UNIVERSITÀ DI PARMA

UNIVERSITA' DEGLI STUDI DI PARMA

DOTTORATO DI RICERCA IN
"*Scienze Chimiche*"

CICLO XXXVIII

Design and biological evaluation of metal complexes with Schiff-base derived ligands: insights into anticancer and antimicrobial activity

Coordinatore:
Chiar.mo Prof. Giovanni Maestri

Tutore:
Chiar.ma Prof.ssa Dominga Rogolino

Dottorando: Alessio Zavaroni

Anni Accademici 2022/2023 – 2024/2025

Abstract

Bioinorganic chemistry gives access to opportunities for the design of therapeutic agents not achievable with organic molecules. The role of complexes of biologically relevant metals such as copper and zinc is becoming more and more important in the development of novel anticancer and antimicrobial compounds. Among the plethora of different classes of ligands used to synthesize bioactive metal complexes, Schiff bases and Schiff-base derived molecules are particularly attractive due to their relatively facile and cheap synthesis and their wide spectrum of biological activities. In this context, Schiff base-derived ligands were designed in order to endow the corresponding metal complexes with specific physical and chemical properties, such as solubility in aqueous medium, and/or specific bioactivity, like selective targeting of cancer cells with respect to normal cells.

The following classes of ligands were investigated for the design of anticancer complexes: bis-(thio)carbohydrazones, (thio)semicarbazones and (thio)acylhydrazones. The introduction of sulfonate groups in the scaffold of the ligands allowed to obtain copper(II) and zinc(II) complexes with excellent solubility in aqueous medium, but unfortunately with lower antiproliferative activity compared to the non-functionalized compounds. On the contrary, conjugation of glucosyl moieties led to obtain copper(II) complexes that were at the same time water soluble and selective against cancer cell lines, such as pancreatic adenocarcinoma, that are known to overexpress glucose transporter proteins.

In the research for novel antimicrobials, a panel of iminophosphine-copper(I) complexes was synthesized by template reactions and the coordination geometry of the compounds was elucidated by means of single crystal X-ray diffraction. The in vitro antimicrobial activity of the complexes was tested against methicillin resistant *Staphylococcus aureus* (MRSA), *Escherichia coli* and *Candida albicans*. All the complexes proved to be active against MRSA in the low micromolar range, while they were not effective against *E. coli* and *C. albicans*.

Abbreviations

δ	Chemical shift
ΔG	Gibbs' free energy
3-AP	Triapine
AMR	Antimicrobial Resistance
ATP	Adenosine 5´-triphosphate
ATR	Attenuated Total Reflection
Bis-CH	Bis-carbohydrazone
Bis-TCH	Bis-thiocarbohydrazone
Boc	*tert*-butoxycarbonyl
CA	Carbonic Anhydrase
CHES	2-(Cyclohexylamino)ethanesulfonic acid
COSY	Correlation Spectroscopy
DCM	Dichloromethane
DFT	Density Functional Theory
DMF	*N,N*-dimethylformamide
DMSO	Dimethyl sulfoxide
DNA	Deoxyribonucleic acid
Eq.	Equivalents
ER	Endoplasmic Reticulum
ESI-MS	Electrospray Ionization Mass Spectrometry
Et_2O	Diethyl ether
EtOAc	Ethyl Acetate
EtOH	Ethanol
FBS	Fetal Bovine Serum
FLC	Friend erythroleukemia cells
FT-IR	Fourier transform infrared spectroscopy
GI_{50}	Concentration for 50% of maximal inhibition of cell proliferation
GLUT	Glucose Transporter
hCTR1	human copper transporter 1
HEPES	4-(2-Hydroxyethyl)piperazine-1-ethanesulfonic acid

HPKTBH	Di-2-pyridylketone thiobenzoylhydrazone
HSQC	Heteronuclear Single Quantum Coherence
IC_{50}	Concentration for 50% of maximal inhibition of a certain activity
LC	Liquid Chromatography
LLC	Lewis Lung Carcinoma
LR	Lawesson's reagent
MD	Molecular Dynamics
MeCN	Acetonitrile
MES	4-Morpholineethanesulfonic acid
MIC	Minimum Inhibitory Concentration
MLCT	Metal to Ligand Charge Transfer
MRSA	Methicillin resistant *Staphylococcus aureus*
MT	Metallothionein
MTS	3-(4,5-dimethylthiazol-2-yl)-5-(3-carboxymethoxyphenyl)-2-(4-sulfophenyl)-2H-tetrazolium
MTT	3-(4,5-dimethylthiazol-2-yl)-2,5-diphenyltetrazolium bromide
MU	Maynooth University
n.a.	Not active
NAD	Nicotinamide adenine dinucleotide
NAH	*N*-acylhydrazone
NHC	N-Heterocyclic carbene
NMR	Nuclear Magnetic Resonance
OBC	Optimal Bactericidal Concentration
OD	Optical density
ORTEP	Oak Ridge Thermal-Ellipsoid Plot
PAC-1	Procaspase activating compound-1
PBS	Phosphate Buffer Saline
PCM	Polarizable Continuum Model
PDI	Protein Disulfide Isomerase
PetEt	Petroleum Ether
PTA	1,3,5-triaza-7-phosphaadamantane
P-XRD	Powder X-ray diffraction

RDF	Radial distribution function
ROS	Reactive Oxygen Species
RR	Ribonucleotide Reductase
SC	Semicarbazone
SC-XRD	Single crystal X-ray diffraction
SD	Standard Deviation
S.I.	Selectivity Index
SOD	SuperOxide Dismutase
TGA	Thermogravimetric Analysis
TFA	Trifluoroacetic acid
THF	Tetrahydrofuran
thp	tris(hydroxymethyl)-phosphine
TLC	Thin Layer Chromatography
Topo	Topoisomerase
TSC	Thiosemicarbazone
UV	Ultraviolet
WHO	World Health Organization
ZIP	Zrt- and Irt-like proteins
ZnT	Zinc Transporters

Index

Chapter 1:

Water soluble bis-(thio)carbohydrazones and their copper(II) and zinc(II) complexes as anticancer agents

Introduction

Copper is the third most abundant essential trace metal in organisms. Its redox chemistry, based on oxidation states Cu^{I} and Cu^{II}, makes it fundamental for many enzyme functions.[1] Copper is involved in several essential processes, such as energy generation in the mitochondrial respiratory chain[2], antioxidant defence[3] and iron acquisition[4].

Copper can be cytotoxic if present in quantities that exceed cellular needs. Similarly to iron, copper can take part in reactions leading to the formation of reactive oxygen species (ROS)[5], like $\cdot O_2^-$, ·OH and ·OOH, that are responsible for oxidative stress and oxidative damage, with the partial or total destruction of the lipid bilayer in cell membranes. Unbound copper ions may in fact give rise to Fenton-type reactions (Scheme 1.1), generating hydroxyl and hydroperoxyl radicals.[6]

$$Cu^{+} + H_2O_2 \rightarrow Cu^{2+} + \cdot OH + OH^{-}$$

$$Cu^{2+} + H_2O_2 \rightarrow Cu^{+} + \cdot OOH + H^{+}$$

Scheme 1.1: Fenton-type reactions catalysed by copper ions.

The redox activity of copper is the reason why the cell and the organism, under normal conditions, have very controlled mechanisms for delivering and loading the metal.[1]

Zinc is the second most abundant essential trace metal in the human body. It is an essential constituent of thousands of enzymes where exerts structural and catalytic roles. In cell biology, zinc is involved in regulation of gene expression, DNA metabolism, chromatin structure, cell proliferation, maturation, death, immune responses, and antioxidant defences.[7]

Given the broad spectrum of functions that require zinc, its levels within the cell are tightly regulated to maintain adequate physiological concentrations. Zinc homeostasis is efficiently controlled by proteins like Zrt- and Irt-like proteins (ZIP), zinc transporters (ZnT), and metallothioneins (MT).[8]

Metals like copper and zinc play important roles in the proliferation of tumour cells[1,9].

Cancer is the second leading cause of death worldwide. It comprises a wide group of diseases that can affect any part of the body.[10] According to the World Health Organization (WHO), one defining feature of cancer is the rapid creation of abnormal cells that grow beyond their usual boundaries and which can then spread to other organs; the latter process is referred to as metastasis.[11]

The connection between cancer and copper can be traced back to the concept of "cuproplasia", defined as copper-dependent cell growth and proliferation.[12] Copper is found in higher levels in cancer cells with respect to normal ones.[13] It is in fact required in angiogenesis[14], i.e. the process of formation of blood vessels. The disposal of blood flow is a requisite for cancer tissue growth and for this reason tumour cells have higher demands for copper.[15] Nevertheless, this metal is not only a need for cancer cells, but it can be also toxic for them. Its redox chemistry makes copper a potential source for ROS, which can damage tumour tissues.[16]

Differently from copper, the role of zinc in cancer varies depending on the type of tumour.[7] In some tumours, high zinc levels have been associated with a reduction in telomere attrition, which is a significant cause of chromosome instability.[17] Therefore, a high level of zinc appears to play a role in maintaining DNA integrity and may help to prevent cancer progression. However, the activity of zinc transporters, which are crucial for cell division, is increased in certain cancers and has been linked to poorer prognosis.[18]

Copper complexes as anticancer agents: the mechanisms of action

Metal complexes are much less employed as drugs compared to organic molecules. Nevertheless, the few examples of metal-based pharmaceuticals play a fundamental role in medicine, especially in cancer treatment. Currently, three platinum(II) complexes, cisplatin, carboplatin and oxaliplatin (Figure 1.1), are approved worldwide as anticancer agents.[19] In spite of their remarkable activity, their efficacy is limited by several drawbacks, such as low selectivity, severe side effects (nephrotoxicity, neurotoxicity and ototoxicity),[20] the development of innate or acquired drug resistance[21] and low solubility in water.[22]

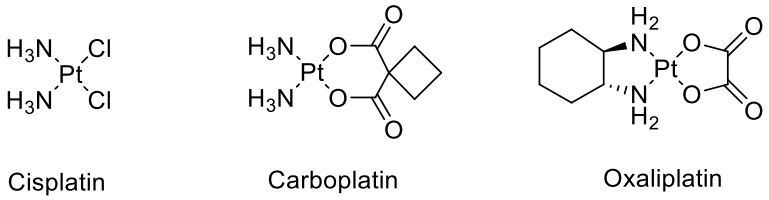

Figure 1.1: Chemical structure of the platinum-based anticancer agents cisplatin, carboplatin and oxaliplatin.

The important drawbacks related to the use of platinum drugs in oncology prompted the scientific community to study the anticancer activity of complexes of endogenous metals, since they could be less toxic to healthy cells and they may circumvent cisplatin resistance.[23] In this context, copper complexes have been attracting attention for a long time.

The dual role of copper, which on one hand is essential for the growth of tumour tissues and on the other hand is toxic at high concentration, can be exploited in the development of anticancer compounds. Two strategies may therefore be pursued: the design of novel organic chelators capable of sequestering copper, thus hindering cancer cell proliferation,[24,25] and the design of anticancer copper complexes that selectively delivery high amounts of metal to cancer cells, thus triggering tumour cell death processes. The latter approach is more strictly related to coordination chemistry and was applied in the projects described in this dissertation.

Based on literature data, copper compounds proved to have a broader activity compared to platinum drugs, whose mechanism of action is mainly based upon covalent binding of DNA of cancer cells.[1] Among the multiple modes of action of copper-based antitumor agents (Figure 1.2), we can find ROS generation, DNA binding and inhibition of proteins such as the Topoisomerases, the Proteasome and the Protein Disulfide Isomerase (PDI). Here follows a brief description of such mechanisms.

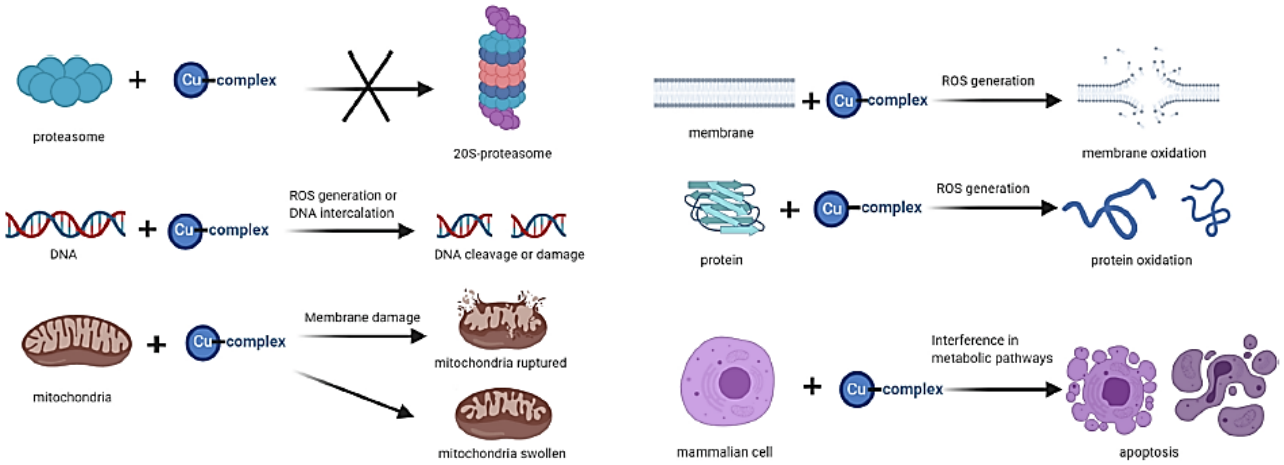

Figure 1.2: Modes of action of copper complexes in a mammalian cell. Adapted from Ref.[1]

Some of the accepted mechanisms of anticancer activity of copper complexes are the production of ROS species[26,27] and/or the ability of acting as CuZnSOD (Copper-Zinc SuperOxide Dismutase, an enzyme implicated in antioxidant defence) mimetics.[28] The effect is a redox imbalance, that combined with the already greater ROS levels of cancer cells leads to excessive oxidative stress that activates programmed cell death. For instance, some bis- and tris-chelate copper complexes bearing 1,10-phen ligands showed a good anticancer activity and act as SOD mimetics in mammalian cells causing cell apoptosis.[29,30]

Several copper complexes showed anticancer activity based on noncovalent interactions with DNA double helix, which is different from the formation of DNA-complex covalent adducts observed for platinum drugs. The noncovalent DNA interactions included intercalative, electrostatic and groove binding of metal complexes.[31] In this context, copper(II) complexes including N-donor ligands (such as diimines) are particularly interesting due to their high DNA interaction ability and *in vitro* antitumor efficiency.[32]

The mechanism of action of some copper complexes is based on inhibition of Topoisomerases (Topos), enzymes that regulate the topological state of DNA, such as the interconversion between knotted and unknotted forms.[33] Since these enzymes are fundamental in DNA replication and transcription, they represent an important target in anticancer research. A copper salicylaldoxime complex, which effectively inhibited the L1210 leukemia cell proliferation, blocked Topo II enzyme, disrupting Topo II dimer formation with consequent induction of single-strand breaks in the DNA.[34]

Proteasome inhibition is another mode of action exerted by copper complexes, especially those that contain ligands of the 8-hydroxy quinoline family.[35] The Proteasome is a large multiprotein complex located in the nucleus and cytoplasm that regulates the degradation of intracellular proteins. Proteasome inhibition affects more cancer cells than normal cells, driving them to apoptosis.[36-38]

Recently, another target of copper-based anticancer agents has been discovered: the Protein Disulfide Isomerase (PDI).[39] PDI is the name for a group of enzymes located in the endoplasmic reticulum, in the cell surface and in the cytosol.[40] It is involved in processes such as protein folding, and disulfide bond isomerization/formation/cleavage[41] (Figure 1.3). It was found that PDI is also a copper binding protein[42] and that, for its role in cell migration and adhesion, it is implicated in many diseases including cancer[43]. In this context, it was identified as a target of some copper(II) complexes with anticancer activity.[44,45]

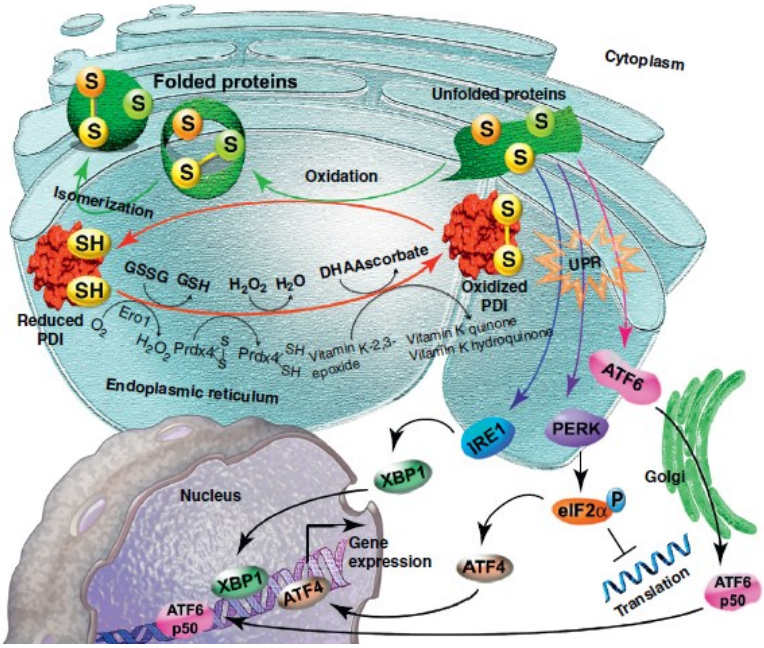

Figure 1.3: In the endoplasmic reticulum (ER), PDI catalyses oxidation and isomerization reactions, mediating disulfide bond formation and rearrangement for oxidative protein folding. Adapted from Ref.[41]

In the last three years, researchers found out that, in human cells, an excess of copper triggers a regulated cell death process distinct from the other known cell death mechanisms (apoptosis, paraptosis, ferroptosis, etc).[46-48] In this process, called "cuproptosis", copper induces cytotoxicity by determining an increased mitochondrial-dependent energy metabolism and accumulation of reactive oxygen species (ROS).[46] This mechanistically distinct pathway gives a promising therapeutic strategy for selectively targeting various forms of tumour.[49]

Copper complexes as anticancer agents: some important examples

The great majority of copper complexes reported in the literature comprises species with the metal in oxidation states Cu^{II} and Cu^{I}, while very few examples of copper(III) compounds are known.[50]

Cu^{II} is a d^9 metal ion and it has a hard-soft intermediate character: it typically forms coordination compounds with ligands bearing N, O and S donor atoms. Copper(II) complexes are characterized by coordination numbers that range from four to six, including four-coordinate square planar, five-coordinate trigonal bipyramidal, five-coordinate square pyramidal and six-coordinate tetragonally distorted geometries.

Cu^{I} is a d^{10} metal ion and it has a soft character: it prefers ligands with soft donor atoms, like phosphorus and sulphur. Copper(I) complexes show low coordination numbers ranging from two to four; the typical geometries are linear, trigonal planar and tetrahedral.

For both Cu^{II} and Cu^{I} compounds, their anticancer activity is strongly determined by the choice of the ligands,[31] that can modulate the hard/soft properties and the redox potential of the metal center. In addition, they can confer hydrophilic or lipophilic characteristics to the complexes, affecting their solubility in extracellular fluids and/or their capacity to cross the lipidic bilayer of the cell membranes. The stability of the complex is also determined by the ligands, which should be designed in order to make the final coordination compound stable enough to reach the desired target, but sufficiently labile to interact with the binding site of a target biomolecule. All these aspects affect not only the anticancer activity of the metal complex, but also its bioavailability and toxicity.

In bioinorganic chemistry, copper(II) compounds are much more investigated with respect to copper(I) species. Although the former are paramagnetic species and their characterization is not always trivial (due to the impossibility of using NMR techniques), their stability makes them much easier to synthesize and facilitates the investigation of their biological properties with respect to copper(I) compounds. Nevertheless, in spite of the plethora of copper(II) complexes that showed promising *in vitro* anticancer activity, few studies were carried out to determine the activity *in vivo*[31] or reached clinical stage.[51] The Casiopeinas® (Figure 1.4), that are patented Cu^{II} mixed-chelate compounds, are the unique class of copper(II) complexes that have reached clinical trials on humans.[52] In the specific, Casiopeina III-ia (Figure 1.4) entered phase I clinical trials in Mexico.[53]

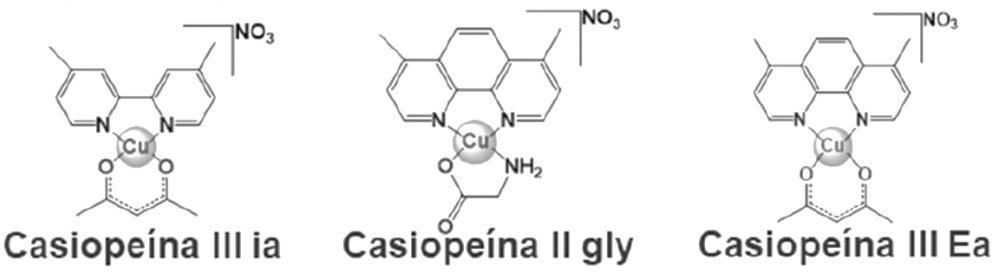

Figure 1.4: Chemical structure of some Casiopeinas. Adapted from Ref.[52]

Although it is known that mammalian cells internalize copper in the oxidation state Cu^{I}, very few studies were carried out to investigate the anticancer activity of copper(I) complexes. This is mainly due to the difficulty to prevent the disproportionation of Cu^{I} to metallic copper and Cu^{II}, a task that is particularly complicated in aqueous media.[31] Only soft ligands like phosphines and N-heterocyclic carbenes (NHCs) are able to stabilize copper(I). To the best of our knowledge, no copper(I) complexes have entered clinical trials. Nevertheless, Cu^{I}-phosphine species represent a class of compounds with promising anticancer activity. A significant

example is the water-soluble tetrakis-(tris(hydroxymethyl)-phosphine-copper(I)) hexafluorophosphate complex (Figure 1.5), which showed a remarkable antitumour activity both *in vitro* and in *in vivo* models.[54]

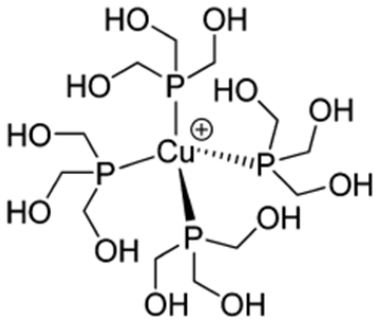

Figure 1.5: Structure of the cationic portion of tetrakis-(tris(hydroxymethyl)-phosphine-copper(I)) hexafluorophosphate. Adapted from Ref.[31]

Zinc complexes as anticancer agents: the mechanisms of action

In the field of anticancer research, also zinc complexes have been studied as potential metallodrugs alternative to platinum compounds. Zinc complexes are interesting mainly because of the very low toxicity of zinc(II) compared with other metals (like iron and copper),[55-57] and also because they undergo fast ligand exchange, can promote Lewis acid activation and can catalyse hydrolytic reactions, such as hydrolysis and cleavage of DNA, thus exerting an antitumour activity.[58,59]

Several zinc complexes showed promising antiproliferative activity, but the reported data are usually limited to *in vitro* studies.[60] In addition, there is still uncertainty on their mechanisms of action: at the moment, the most recognized target of zinc species is DNA and the identified process of cancer cell death is apoptosis.[60]

Zinc complexes as anticancer agents: some important examples

There have been no zinc complexes that have reached clinical trials for anticancer research, and no zinc-based "lead compounds" have been discovered. Despite this, some zinc complexes have shown significant antitumor activity *in vivo*. Some examples are provided below.

A zinc complex of a benzimidazole-derived ligand (Figure 1.6a) showed a significant cytotoxic effect against SK-MEL-1, Hep-G2, HT018, MDA-MB-231 and HeLa cancer cell lines.[61] No anticancer effect was observed with the free ligand. The complex is able to inhibit cancer cell adhesion and migration properties, leading to a decrease in the metastatic potential of cancer cells. In addition, in *in vivo* studies performed in mice, it proved to be highly tolerable and showed low hematologic and liver toxicity.

A zinc complex with an oxoaporphine ligand (Figure 1.6b) was reported to have higher cytotoxic activity against selected cancer cell lines compared to the free ligand.[62] It is able to induce S-phase arrest in Hep-G2 cells at low concentration. In addition, production of ROS, activation of p53 and increase of intracellular Ca^{2+} were detected. The *in vivo* antitumor activity of the compound was tested in a Hep-G2 xenograft model: administration of the zinc complexes led to reduction in tumour weight and volume of Hep-G2 xenograft without any significant loss in mice body weight with respect to the control group, showing better safety profile than cisplatin.

The pyrithione-zinc complex showed in Figure 1.6c induced apoptosis in OSCC cells and reduced migration and metastatic potential in a dose-dependent way.[63] Notably, it induced a decrease in tumour xenograft volume in immunocompromised NOD/SCID/Crl mice without evident toxicity to normal tissues.

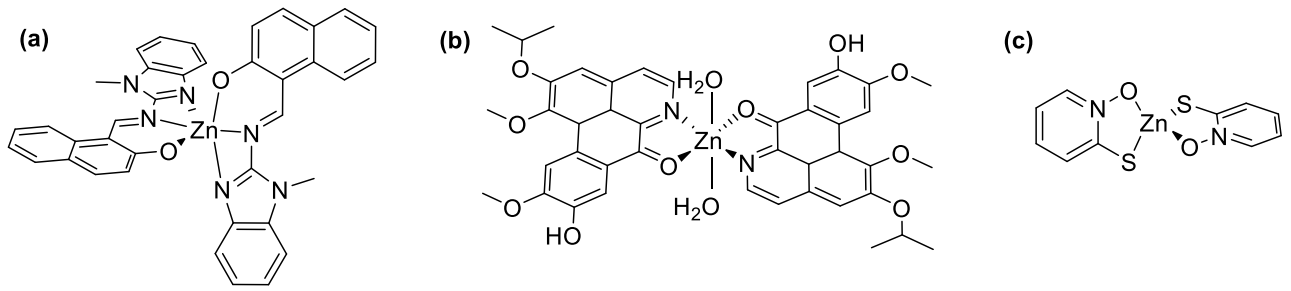

Figure 1.6: Chemical structure of (a) $Zn(bimnap)_2$, (b) oxoaporphine-zinc(II) complex and (c) pyrithione-zinc(II) complex.

Chalcogensemicarbazones and bis-chalcogencarbohydrazones

Among the plethora of different classes of ligands used to synthesize coordination compounds with anticancer activity, chalcogensemicarbazones and bis-chalcogencarbohydrazones are particularly attractive due to their relatively facile and cheap synthesis and their wide spectrum of biological activities (anticancer, antifungal, antibacterial and antiviral).[55]

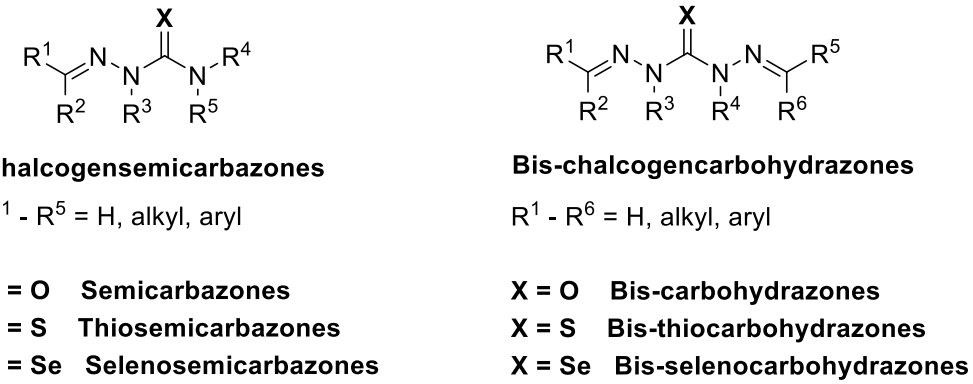

Figure 1.7: General structure of chalcogensemicarbazones and bis-chalcogencarbohydrazones.

The general structure of these two classes of molecules is shown in Figure 1.7. Since these molecules contain the imine functional group, they can be considered as derivatives of Schiff bases. They are obtained by condensation reaction between carbonyl compounds (aldehydes or ketones) and chalcogensemicarbazides or chalcogencarbohydrazides (Scheme 1.2).[64] From a structural point of view, the bis-chalcogencarbohydrazones can be further divided into symmetrical and asymmetrical derivatives, depending on the nature of the two carbonyl precursors (Scheme 1.2b).[65] The synthesis of the asymmetrical ones requires the isolation of an intermediate mono-chalcogencarbohydrazone (Scheme 1.2b).

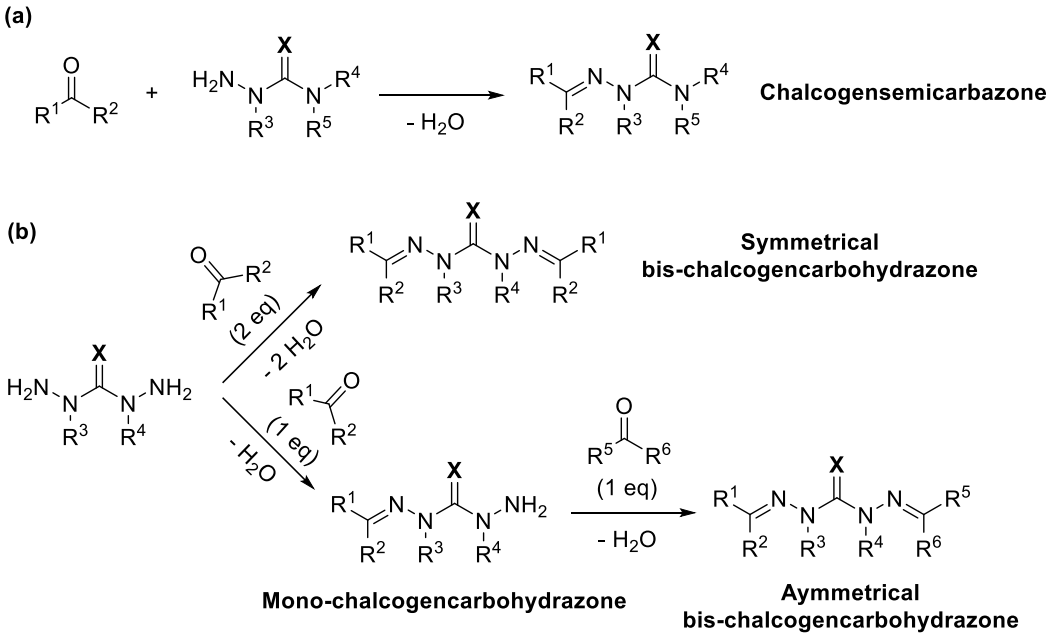

Scheme 1.2: General reaction for the synthesis of (a) chalcogensemicarbazones and (b) bis-chalcogencarbohydrazones.

In this work, we will focus on **semicarbazones (SCs)**, **thiosemicarbazones (TSCs)**, **symmetrical bis-carbohydrazones (bis-CH)** and **bis-thiocarbohydrazones (bis-TCH)**.

SCs and **TSCs** with R^3 = H (Figure 1.7) can exist in solution as two tautomers: keto/thione and enol/thiolene (Scheme 1.3, top).[31] In addition, if the two groups R^1 and R^2 are different, these compounds can also exist as two geometric isomers (*E* and *Z*) with respect to the imine bond (Scheme 1.3, bottom).[66]

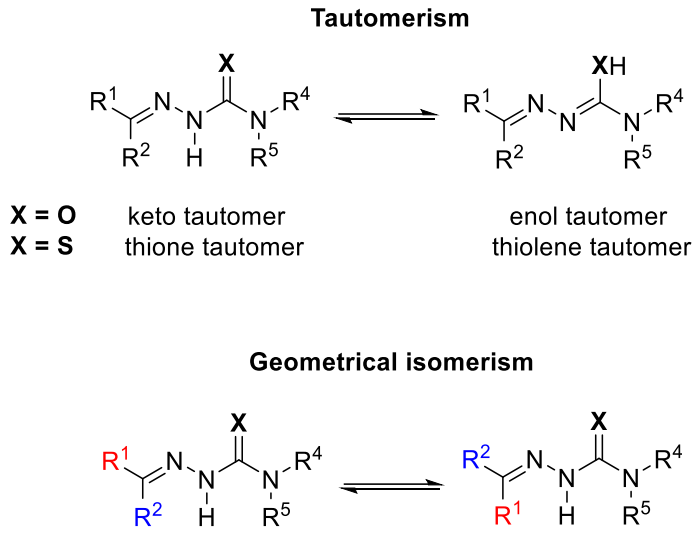

Scheme 1.3: Tautomerism (top) and geometrical isomerism (bottom) of semicarbazones and thiosemicarbazones.

The chalcogensemicarbazones can coordinate transition metals as neutral thiones or, after deprotonation, as thiolene anions. Several different binding modes are possible, depending on the presence of donor atoms in the R^1 and R^2 substituents. They can act as X-monodentate, X,N-bidentate or X,N,D_n (D = donor atom, n = 1,2) tri- or tetra-dentate ligands if additional donor atoms are present on the ligand scaffold.[67,68]

The symmetrical **bis-CHs** and **bis-TCHs** with $R^3 = R^4$ = H display a higher number of possible isomers, compared to **SCs** and **TSCs**. As will be described in detail in Results and Discussion, these compounds can exist as different tautomers, conformational isomers and configurational isomers.[65,69]

The symmetrical bis-chalcogencarbohydrazones possess a further binding site compared to chalcogensemicarbazones and they can give rise both to mono-metallic and bi-metallic complexes. The tautomeric and isomeric versatility of these systems leads to a wide variety of coordination motifs, that also depend on the presence of donor atoms in the R^1 and R^2 substituents. Although being symmetrical molecules, they can arrange in order to bind two metal ions with different donor atoms sets (Figure 1.8a).[70] In addition, they are reported to give rise to quite unusual multinuclear metal complexes, such as the azine-bridged octa-nuclear copper(II) complex depicted in Figure 1.8b.[71]

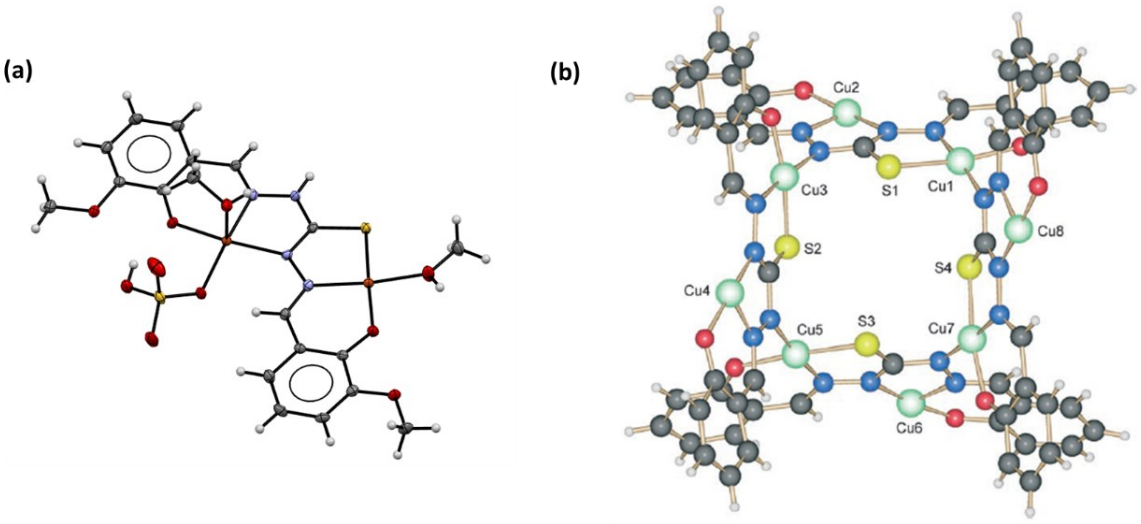

Figure 1.8: (a) Crystal structure of a copper(II) complex with bis-(3-methoxysalicylaldehyde)-thiocarbohydrazone: the ligand binds to the two copper ions with two different donor atom sites (ONN and ONS) (oxygen atoms in red; sulphur in yellow; nitrogen in blue; carbon in grey and hydrogens in white; copper ions in orange). (b) Representation of the copper(II) octa-nuclear species $\{Cu_8L_4\}$ with four bis(salicylaldehyde)thiocarbohydrazone ligands in nonparallel pairs (as before, but copper ions in green). Adapted from Ref.[71]

Anticancer activity of chalcogensemicarbazones and bis-chalcogencarbohydrazones

The thiocarbonyl moiety is a functional group found in a huge number of molecules of pharmaceutical interest and several studies reported the gain in biological activity upon substitution of oxygen with sulphur in compounds that contain carbonyl groups.[72] There is in fact a huge amount of scientific research carried on **thiosemicarbazones** compared to **semicarbazones**.

The antineoplastic activity of **TSCs** is known since the 1950s, when some molecules of this class were reported to have antileukemic activity.[73] The antitumour properties of these ligands have been linked to the inhibition of ribonucleotide reductase (RR), a mammalian enzyme that is involved in the synthesis of deoxyribonucleotides required for DNA replication and repair and that is overexpressed in cancer cells. The catalytic activity of RR is due to its di-iron active site: the **TSCs** exert their anticancer activity by chelating the iron ions in RR.[74]

The most important example of anticancer **TSC** is Triapine (3-AP, Figure 1.9), a compound that was able to enter several phase I and II clinical trials.[75-78] Other significant examples are COTI-2 (synthesized by Critical Outcome Technologies Inc.) and DpC (produced by Oncochel Therapeutics) (Figure 1.9),[73] that are currently in phase I clinical trials.

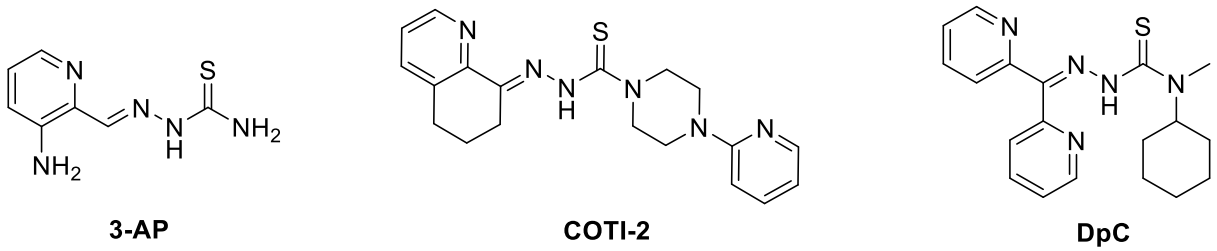

Figure 1.9: Chemical structures of anticancer thiosemicarbazones that entered clinical trials.

Similarly to what is observed for chalcogensemicarbazones, among the bis-chalcogencarbohydrazones the sulphur containing **bis-TCHs** have received more attention compared to **bis-CHs**, both in terms of investigation of coordination properties and of biological activity.[65] The great majority of studies on their biological properties are focused on their use as antimicrobials,[79-81] with only a small number of screenings as antitumour compounds.

Curiously, the **bis-thiocarbohydrazones** have been much less investigated compared to **thiosemicarbazones**. While the biological properties of **TSCs** were under study since the 1950s, the first report on the antifungal activity of **bis-TCHs** appeared only in the 1970s,[82] probably because the thiocarbohydrazide precursor was not commercially available until the late 1970s. Until the first half of the 1990s, however, most studies were limited to the chemistry of these compounds and only recently the biological potential of these systems was recognized.

Examples of anticancer **bis-TCHs** and **bis-CHs** are the bis-(2-acetylpyrazine)thiocarbohydrazone, that is able to inhibit cell proliferation growth *in vitro* with mild selectivity,[83] and the quinoline-based **bis-TCHs** and **bis-CHs** reported by Bozic *et al.*, which displayed strong activity *in vitro* on two diverse cancer cell lines, acute monocytic leukemia (THP-1) and pancreatic adenocarcinoma cancer stem cells (AsPC-1), both in a 2D monolayer model and in spheroidal 3D culture.[84] Some symmetrical **bis-CHs** were also reported to be potent carbonic anhydrase (CA) inhibitors.[85] CA inhibitors (such as acetazolamide, dichlorophenamide and methazolamide) have been employed in the treatment of glaucoma during the past three decades.

Copper(II) and zinc(II) complexes of chalcogensemicarbazones and bis-chalcogencarbohydrazones with anticancer activity

Several examples in the literature[86,87] suggest that the coordination of molecules with known anticancer activity might result in improved antitumour properties of the corresponding metal complexes, which often display multiple mechanisms of action compared to the parent organic ligands. In this context, chalcogensemicarbazones and bis-chalcogencarbohydrazones have been employed to design novel potential chemotherapy drugs.

In spite of the enormous literature on chalcogensemicarbazone-based copper(II) complexes with *in vitro* anticancer activity, only a few were tested *in vivo*. The copper(II) complex with the ligand bis-(4-methyl-4-phenyl-3-thiosemicarbazone)-glyoxal (Figure 1.10a) showed significant cytotoxic activity against a human colorectal tumor (HCT116) xenografts model,[88] while the copper(II) complex with thiophene-2-carboxaldehyde thiosemicarbazone (Figure 1.10b) showed *in vivo* antiproliferative activity against Friend erythroleukemia (FLC) cells even at low doses.[89] Previous studies from our research group showed that the 3-methoxy-2-hydroxy-phenyl thiosemicarbazone copper(II) complex in Figure 1.10c is able to inhibit tumour growth in C57BL mice with implanted Lewis lung carcinoma (LLC) without inducing significant body losses.[44]

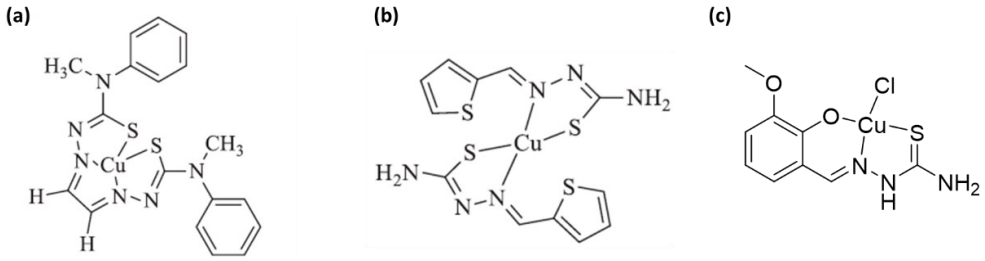

Figure 1.10: Chemical structure of copper(II) complexes with (a) bis-(4-methyl-4-phenyl-3-thiosemicarbazone)-glyoxal, (b) thiophene-2-carboxaldehyde thiosemicarbazone and (c) 3-methoxy-2-hydroxy-phenyl thiosemicarbazone.

Even if to a lesser extent compared to copper(II) species, also some TSC-zinc(II) complexes showed promising antiproliferative activity against cancer cells. For example, the Zn^{II} complexes with cyclohexanone thiosemicarbazone and cyclohexanone N(4)-phenyl thiosemicarbazone ligands (Figure 1.11) are capable of inhibiting human Topoisomerase I even at low concentrations.[90] The results of *in vitro* antiproliferative assays performed on different human cancer cells (MCF-7, Caki-2, CaSki, NCI-H322M and Co-115) indicated GI_{50} values ranging between 0.77 and 4.7 mg/mL (GI_{50} refers to the concentration of a compound that induces 50% growth inhibition in tumour cells in *in vitro* assays).

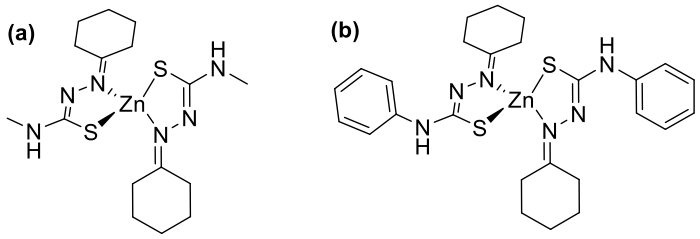

Figure 1.11: Chemical structure of zinc(II) complexes with (a) cyclohexanone thiosemicarbazone and (b) cyclohexanone N(4)-phenyl thiosemicarbazone.

Few studies can be found on the anticancer properties of bis-chalcogencarbohydrazone metal complexes, which in turn received much more attention for their antimicrobial activity. The complexes [CuLCl] · 2 H_2O and [CuL(OAc)] · 2 H_2O with ligand L = bis-(isatin)thiocarbohydrazone (Figure 1.12a) showed antitumor activity against Ehrlich Ascites Carcinoma in *in vivo* tests carried on Swiss Albino mice.[91] Another interesting compound is the bis-CH copper(II) complex shown in Figure 1.12b: in *in vitro* studies, it proved to be a potent anticancer agent able to bind to DNA and induce double strand breaks, to act as a Topoisomerase II inhibitor and to induce, in combination with plumbagin, synergistic cytotoxic activity in breast cancer cells.[92]

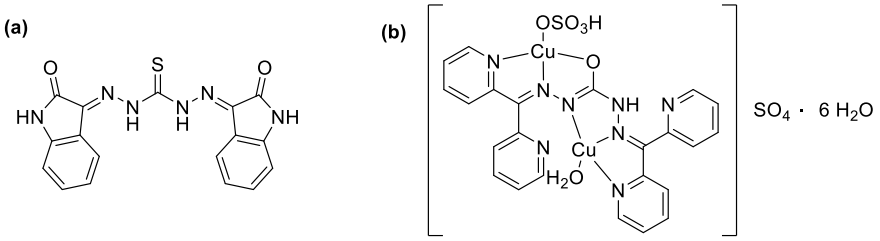

Figure 1.12: Chemical structure of (a) bis-(isatin)thiocarbohydrazone and (b) a copper(II) complex with bis-(dipyridylketone)carbohydrazone.

As the structures of **SCs**, **TSCs**, **bis-TCHs** and **bis-CHs** suggest, their limited water solubility frequently complicates research of these systems and their related complexes. The solubility in aqueous medium is a critical parameter in the development of novel drugs, affecting its bioavailability.[93,94] In addition, low solubility in water can be accompanied to important side effects.[95,96] For example, the copper(II) complexes of substituted salicylaldehyde **thiosemicarbazones** in Figure 1.13 demonstrated a very high cytotoxicity against cancer cells *in vitro*, but they were sparingly soluble in aqueous medium and during *in vivo* experiments performed to determine the activity against Lewis lung carcinoma (LLC), it was observed extensive precipitation of the compounds in the lungs of the tested mice.[44]

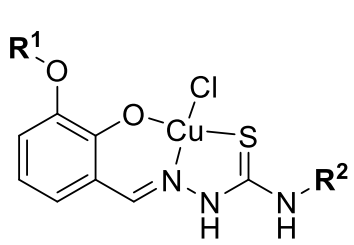

R^1	R^2
Me	H
Me	Ph
Me	Et
H	H
H	Ph
H	Et

Figure 1.13: General structure of the copper(II) complexes of substituted salicylaldehyde thiosemicarbazones previously studied in our research group.[44]

These findings led our group to introduce a sulfonic group in the scaffold of the thiosemicarbazonic ligands, in order to improve water solubility. Five ligands and their corresponding copper(II) complexes (Figure 1.14) were synthesized and tested *in vitro* against a panel of cancer cell lines.[45]

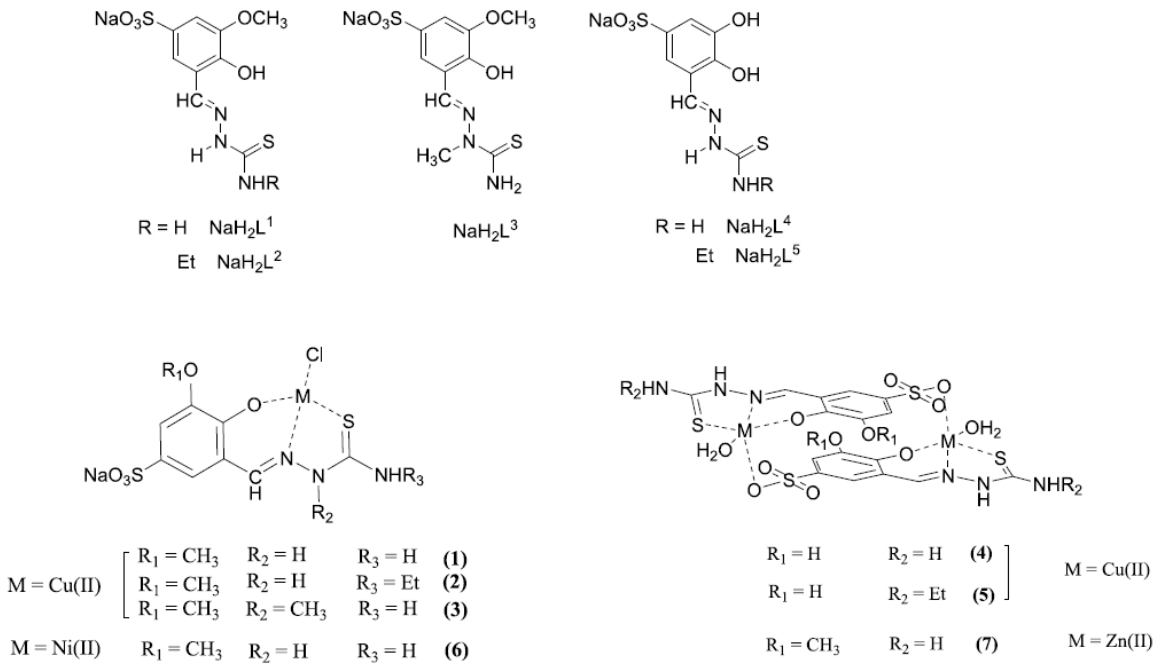

Figure 1.14: General structure of the ligands NaH_2L^1-NaH_2L^5 and of the corresponding copper(II), nickel(II) and zinc(II) complexes. Other possible water molecules in the structures of the complexes are omitted. Adapted from Ref.[45]

While the free ligands did not affect cancer cell viability, copper(II) complexes displayed low to sub-micromolar cytotoxic activity (Table 1.1), which was maintained in 3D spheroidal models. Remarkably, the complexes proved to be selective towards cancer cells, showing high selectivity indexes (Table 1.2). Studies on their mechanism of action indicated that the PDI is a molecular target in cells, which is the same found for the non-sulfonated complexes. Furthermore, preliminary *in vivo* experiments carried out with the most promising complex (complex 5) in the murine Lewis Lung Carcinoma, evidenced its significant anticancer efficacy and better tolerability profile compared to the reference metallodrug (cis-platin) and to the non-sulfonated compounds. The biological assays highlighted also the fundamental role of Cu^{II} in improving the thiosemicarbazone metal complex antiproliferative potential: *in vitro* tests were performed also on the nickel(II) and zinc(II) complexes, but they did not exert any cytotoxic effect.[45]

Table 1.1: 2D cytotoxic activity of the TSC ligands and their metal complexes. Cells (3–5 x 10^3 cell/well) were treated for 72 h with tested compounds. Cell viability was estimated by means of the MTT test. The IC_{50} values were calculated by a four-parameter (4-PL) logistic model ($p < 0.05$). S.D. = standard deviation. Adapted from Ref.[45]

IC_{50} (μM) ± S.D.						
	HCT-15	2008	PSN-1	A431	MCF-7	MDA-MB-231
NaH_2L^1	>100	>100	>100	>100	>100	>100
NaH_2L^2	>100	>100	>100	>100	>100	>100
NaH_2L^3	>100	>100	>100	>100	>100	>100
NaH_2L^4	>100	>100	>100	>100	>100	>100
NaH_2L^5	>100	>100	>100	>100	>100	>100
(1)	5.9 ± 0.8	8.1 ± 2.8	4.7 ± 1.4	8.3 ± 1.1	4.1 ± 1.0	7.2 ± 1.1
(2)	6.4 ± 1.9	9.2 ± 1.1	6.5 ± 2.2	9.8 ± 1.4	8.3 ± 0.2	8.1 ± 1.3
(3)	6.0 ± 1.1	6.9 ± 1.1	5.4 ± 0.4	4.5 ± 0.8	8.9 ± 0.4	6.3 ± 1.7
(4)	0.3 ± 0.1	7.5 ± 0.3	4.1 ± 0.9	2.9 ± 1.2	1.3 ± 0.4	5.4 ± 1.1
(5)	0.9 ± 0.3	6.2 ± 1.5	1.8 ± 0.7	1.8 ± 0.4	1.7 ± 1.0	2.6 ± 0.3
(6)	>100	>100	>100	>100	>100	>100
(7)	>100	>100	>100	>100	>100	>100
Cisplatin	13.9 ± 1.6	2.1 ± 1.3	12.1 ± 2.8	2.0 ± 0.8	8.8 ± 0.2	30.5 ± 2.6

Table 1.2: IC_{50} values for TSC-Cu^{II} complexes towards HEK293 cells (normal cells), with indication of the selectivity index (S.I.). Cells (3–5 x 10^3 cell/well) were treated for 72 h with tested compounds. Cell viability was estimated by means of the MTT test. The IC_{50} values were calculated by a four-parameter (4-PL) logistic model ($p < 0.05$). S.D. = standard deviation. S.I. = IC_{50} toward normal cells/average IC_{50} toward malignant cells. Adapted from Ref.[45]

IC_{50} (μM) ± S.D.		
	HEK 293	S.I.
(1)	51.7 ± 5.0	8.2
(2)	62.8 ± 3.2	7.8
(3)	58.0 ± 6.4	9.2
(4)	111.6 ± 15.6	31
(5)	137.5 ± 10.8	55
Cisplatin	24.7 ± 0.9	2.4

The good results obtained with sulfonated **TSCs** prompted the application of the sulfonation strategy to the two classes of ligands investigated in this project: the **bis-thiocarbohydrazones** and the **bis-carbohydrazones**. As pointed out for the chalcogensemicarbazones, the derivatives reported in literature often display severe solubility issues. To the best of our knowledge, no sulfonated **bis-TCHs/bis-CHs** have ever been reported. This work focuses on symmetrical systems obtained from sodium 3-methoxy-5-sulfonate-salicylaldehyde. Figure 1.15 reports the structures of the ligands **AZ11** and **AZ26** studied in this work.

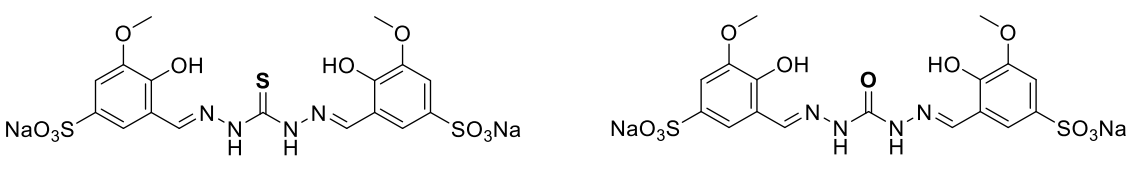

AZ11 **AZ26**

Figure 1.15: Chemical structures of the sulfonated **bis-TCH AZ11** and **bis-CH AZ26**.

A thorough characterization of their isomerization processes in solution was carried out.[97] In addition, thanks to their excellent water solubility, a complete profile of their protonation equilibria and metal binding behaviour was obtained. Mono-nuclear and bi-nuclear copper(II) and zinc(II) complexes were synthesized and characterized. A preliminary study was also performed to determine the *in vitro* anticancer activity of both ligands and complexes.[98]

All the spectral data and other information relevant to the characterization of the synthesized compounds are reported in Appendix. Reference to these data in the text is indicated as Figure/Scheme/Table Axxx, with xxx = number.

Results and discussion

Synthesis and characterization of the ligands

Two novel ligands, the **bis-TCH $Na_2H_4L^1 \cdot 5.5\ H_2O$** (**AZ11**) and the **bis-CH $Na_2H_4L^2 \cdot 5\ H_2O$** (**AZ26**), were synthesized in good yields as sodium salts. The synthetic strategy is shown in Scheme 1.4.

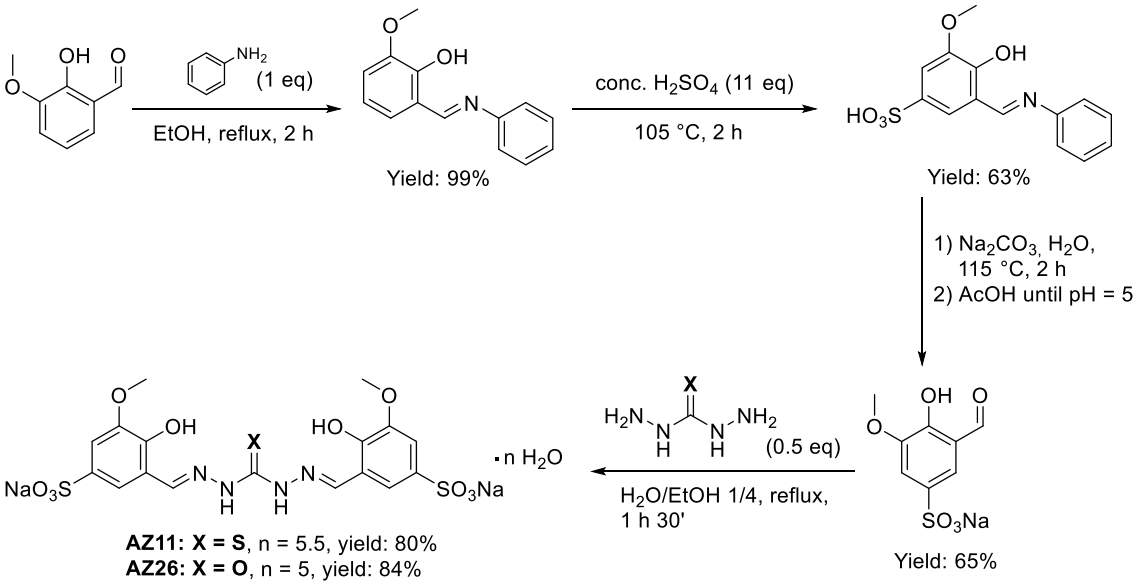

Scheme 1.4: Synthetic pathway to obtain **AZ11** and **AZ26**.

The IR spectrum of **AZ11** (Figure 1.16, left) is characterized by two absorption bands at 1647 and 1612 cm^{-1}, relative to the stretching of the C=N bonds; the absence of the S-H stretching band around 2600 cm^{-1} indicates that in the solid state the ligand is in the thione form. The IR spectrum of **AZ26** (Figure 1.16, right) displays a band at 1663 cm^{-1} (stretching of the C=O group), and two bands at 1614 and 1586 cm^{-1}, attributable to the C=N stretching.

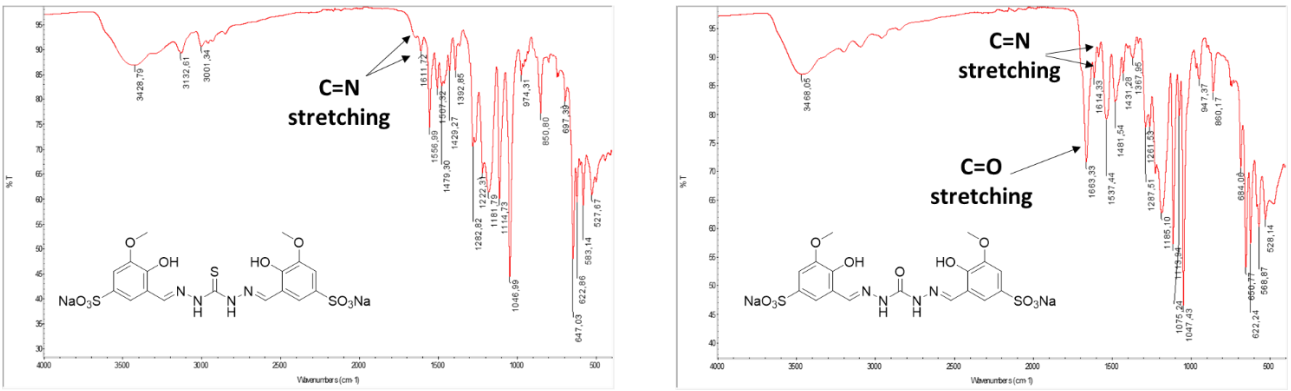

Figure 1.16: FT-IR spectrum of **AZ11** (left) and **AZ26** (right).

Thanks to the presence of the sulfonate groups, the two ligands show good solubility in water at room temperature: their values are approximately 10 g/L and 23 g/L for **AZ11** and **AZ26**, respectively. Elemental analysis (see the experimental section) and TGA (Thermogravimetric analysis, Figures 1.17-18) confirmed the formulas **$Na_2H_4L^1 \cdot 5.5\ H_2O$** (**AZ11**) and **$Na_2H_4L^2 \cdot 5\ H_2O$** (**AZ26**).

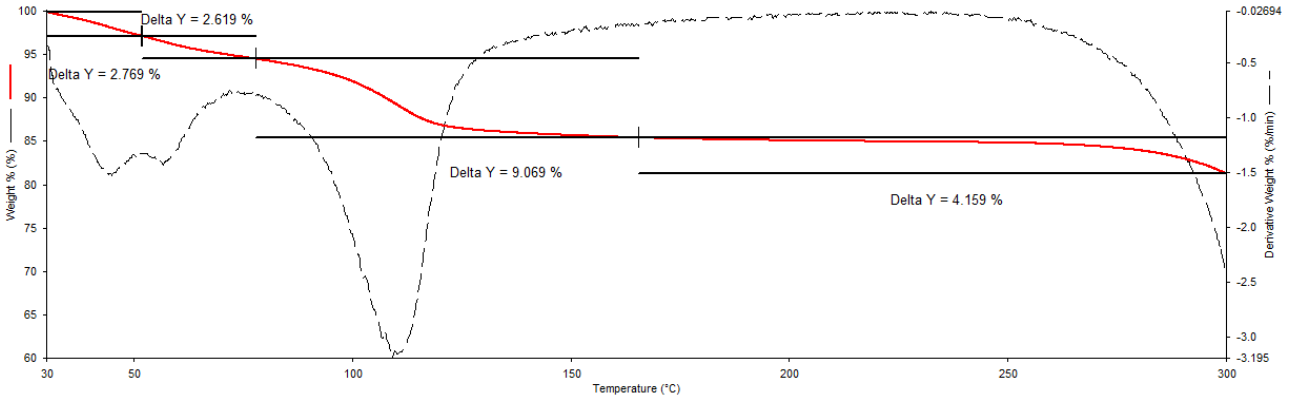

Figure 1.17: TGA plot (temperature range: 30–300 °C, heating rate: 10 °C/min; under atmosphere of air) for **$Na_2H_4L^1 \cdot 5.5\ H_2O$** (**AZ11**). The first event at 30-50 °C (weight loss: 2.769 %) is consistent with the loss of one water molecule; the second event at 50-80 °C (weight loss: 2.619 %) is related to the loss of another water molecule. The third event at 80-170 °C (weight loss: 9.069 %) is consistent with the loss of 3.5 water molecules.

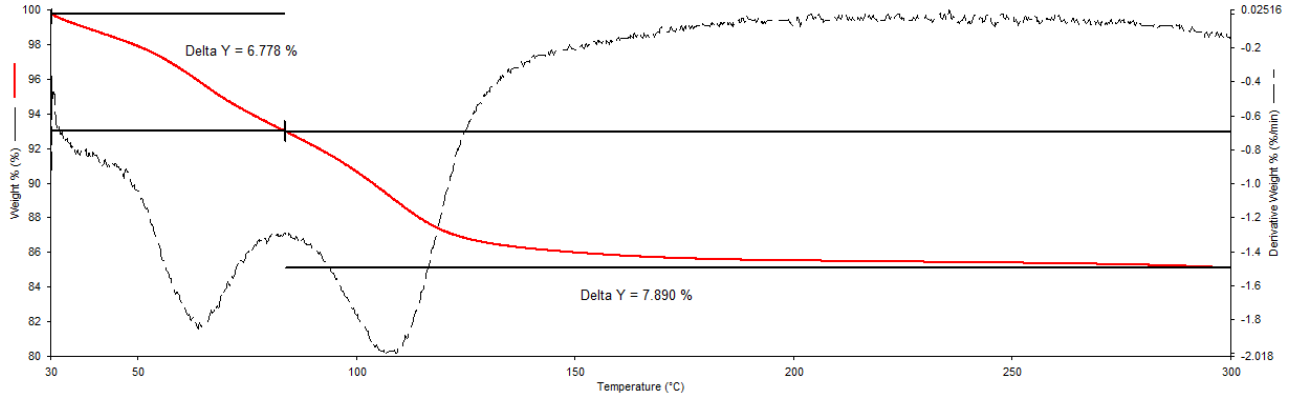

Figure 1.18: TGA plot (temperature range: 30–300 °C, heating rate: 10 °C/min; under atmosphere of air) for **$Na_2H_4L^2 \cdot 5\ H_2O$** (**AZ26**). The first event at 30-80 °C (weight loss %: 6.778 %) is consistent with the loss of 2.5 water molecules; the second event at 80-300 °C (weight loss: 7.890 %) is consistent with the loss of 2.5 water molecules.

Analysis of the isomerization processes in solution

The ^{1}H NMR spectrum of **AZ11** in DMSO-d_6 at 298 K (Figure 1.19) shows a pattern of signals that is not consistent with the symmetrical structure of the **bis-TCH**. Indeed, there are two distinct peaks for the hydroxyl protons (11.84 ppm and 9.52 ppm), the imine protons (8.66 ppm and 8.56 ppm) and for one of the two couples of aromatic protons (7.85 ppm and 7.32 ppm). The spectrum recorded in dry DMSO-d_6 showed a splitting also for the hydrazidic NH protons (Figure 1.21A). The unambiguous assignment of the NH groups was achieved by performing the 2D ^{1}H-^{15}N HSQC experiment (Figure A1.7).

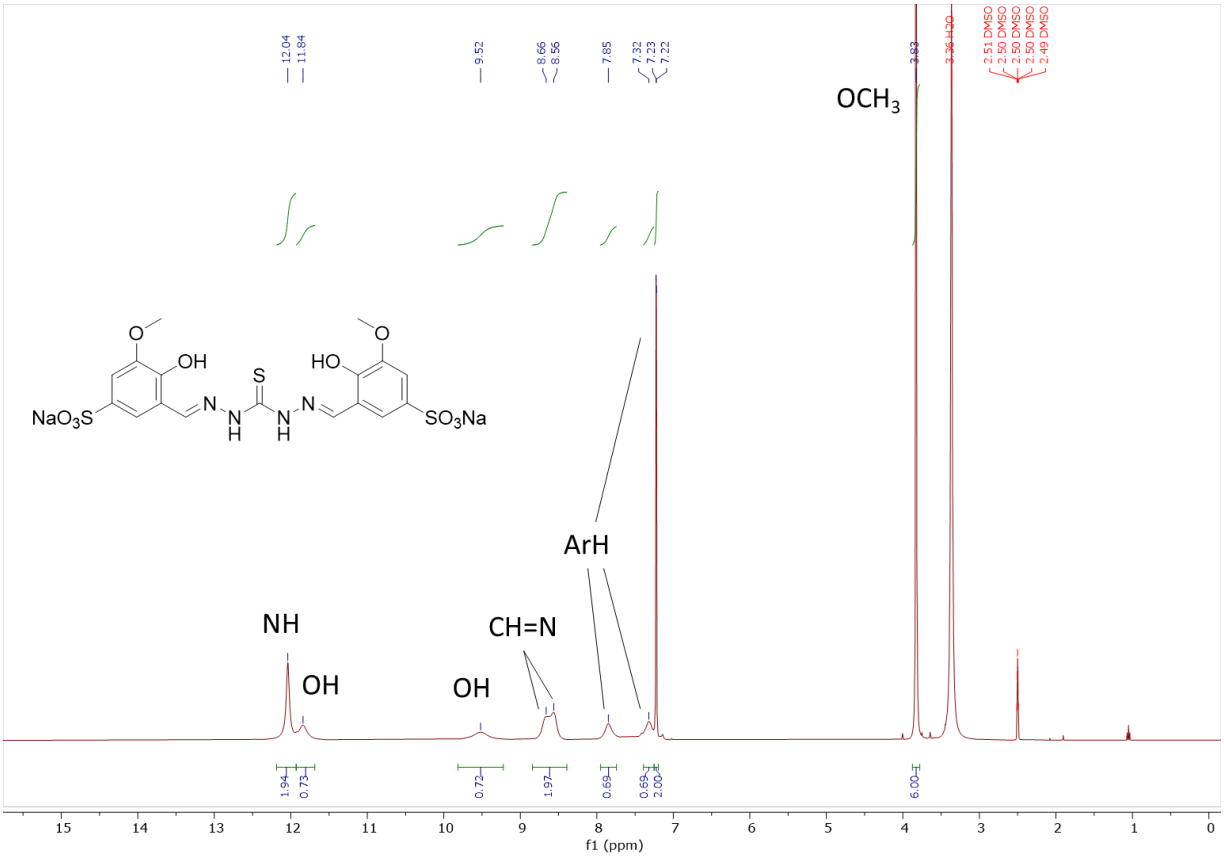

Figure 1.19: ^{1}H NMR (400 MHz) spectrum of **AZ11** in DMSO-d_6 at 298 K.

Although the only difference between **AZ11** and **AZ26** is the nature of the X atom in the central C=X bond, the ^{1}H NMR spectrum of **AZ26** in DMSO-d_6 at 298 K (Figure 1.20) shows a completely different pattern of peaks with respect to **AZ11**. In this case the number of signals is consistent with a symmetrical structure.

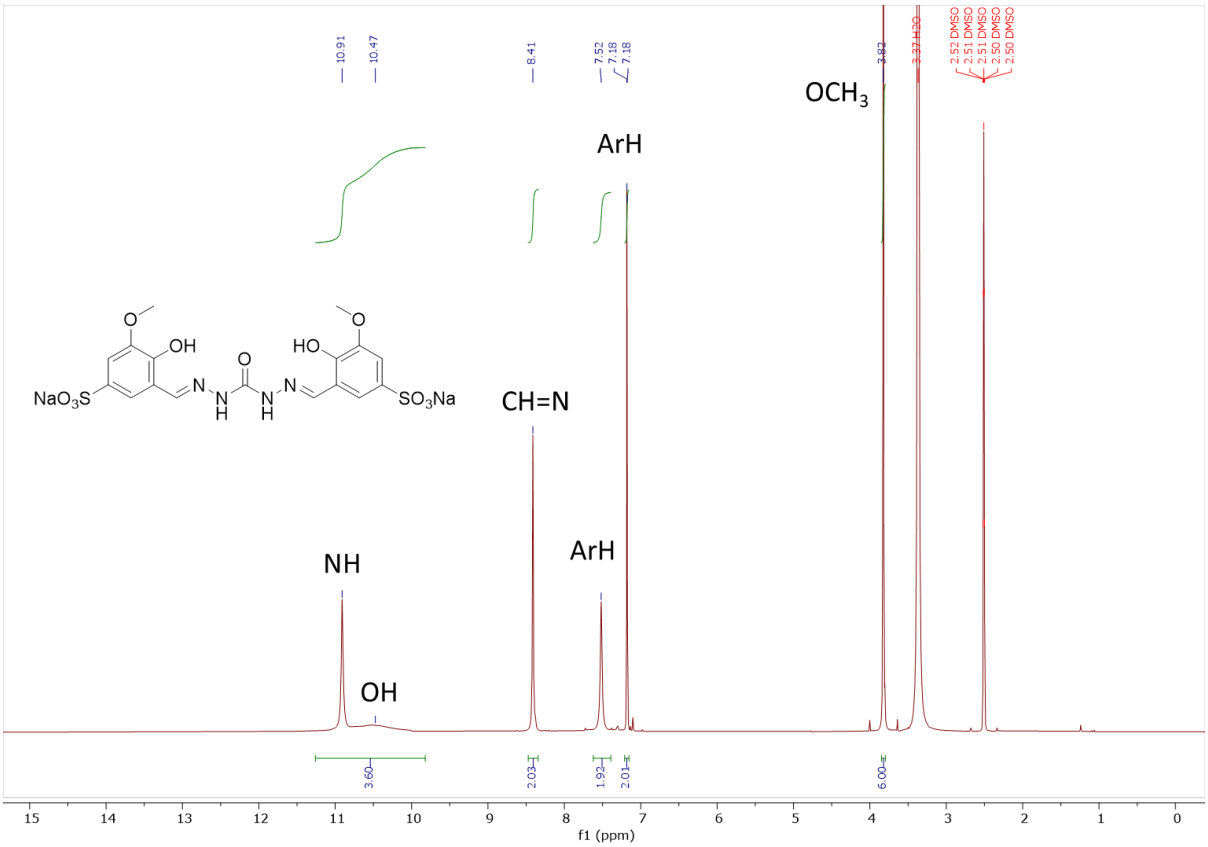

Figure 1.20: ^{1}H NMR (400 MHz) spectrum of **AZ26** in DMSO-d_6 at 298 K.

The different behaviour of the two ligands in solution is confirmed also by their ^{13}C NMR spectra in DMSO-d_6 at 298 K (Figures A1.6 and A1.12). In fact, in the ^{13}C NMR spectrum of **AZ11** (Figure A1.6) there are two signals for the imine carbons (147.50 ppm and 141.97 ppm) and three signals for the aromatic CH groups (119.27 ppm, 116.07 ppm and 111.04 ppm), while for **AZ26** (Figure A1.12) it is possible to observe one peak for the imine carbons (142.98 ppm) and two peaks for the aromatic CH groups (117.19 ppm and 110.37 ppm). Such attributions agree with the ^{1}H-^{13}C HSQC spectra (Figures A1.8 and A1.14).

By inspecting the NMR data related to substituted salicylaldehyde-based **bis-TCHs** and **bis-CHs** reported in the literature,[84,99] it was found, for couples of symmetrical **bis-TCH** and **bis-CH** derived from the same aldehyde, a behaviour in solution identical to that displayed by our systems. To the best of our knowledge, no investigation to explain these observations has been performed, with the exception of a study carried out by Ebrahim Tehrani *et al*.[100] In this work, however, it is discussed the different pattern of signals in ^{1}H and ^{13}C NMR spectra between symmetrical **bis-TCHs** derived from aldehydes and symmetrical **bis-TCHs** derived from ketones, with no comparison with the corresponding **bis-CHs**. As it is observed for **AZ11**, **bis-(aldehyde)thiocarbohydrazones** showed two diastereomeric carbazone moieties, while **bis-(ketone)thiocarbohydrazones** were characterized by a pattern of peaks consistent with symmetrical molecules. The authors explained this behaviour by taking into account the geometrical isomerism around imine bonds (*E/Z*), the formation of intramolecular hydrogen bonds and the bulkiness of the substituents, but they did not consider the conformational dynamics of the C(X)-N groups, and no computational investigation was performed.

The two ligands **AZ11** and **AZ26** can exist as different tautomers (**thione** and **thiolene** for the **bis-TCH AZ11**; **keto** and **enol** for the **bis-CH AZ26**), conformational isomers (***cis-cis***, ***cis-trans*** and ***trans-trans*** with respect to the central C(X)-N bonds) and geometric isomers (***EE***, ***EZ*** and ***ZZ*** with respect to the imine bonds) (Scheme 1.5).[65,69]

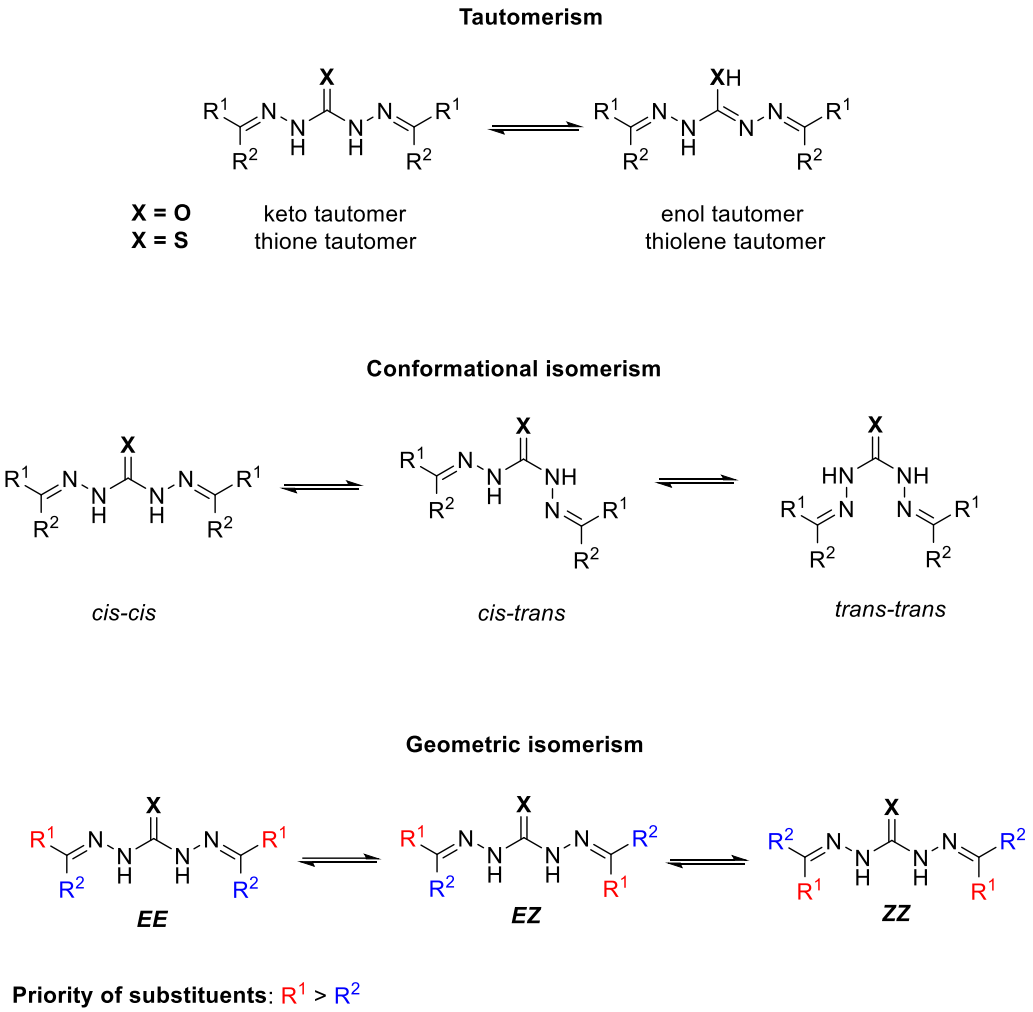

Scheme 1.5: Tautomers, conformational isomers and geometric isomers of bis-carbohydrazones and bis-thiocarbohydrazones.

In the ^{1}H NMR spectrum of **AZ11** in DMSO-d_6 at 298 K (Figure 1.19), there are no signals attributable to the SH group (typically at ca. 15 ppm), suggesting that in solution, like in the solid state, the ligand exists as **thione tautomer**. This is confirmed also by the C=S signal at about 174 ppm in the ^{13}C NMR spectrum (Figure A1.6). Similarly, the chemical shift of the C=O peak in the ^{13}C NMR spectrum of **AZ26** in DMSO-d_6 at 298 K (Figure A1.12), which is around 152 ppm, indicates that the **bis-CH** in solution exists as **keto tautomer**.

The broadening of the signals in the spectra of the ligands in dry DMSO-d_6 (Figure 1.21) indicate that in this solvent chemical exchange processes occur, and that they are different for the two species. Since the only difference between the two ligands is related to the C=X group, it is reasonable to hypothesize that such processes are due to *cis-trans* isomerism around the C(X)-N bonds. Indeed, even though the ligands are in the thione/keto form, the C(X)-N bonds have a partial character of double bonds. This implies that the rotation

around the C(X)-N bonds could be slow on the NMR time scale, explaining why, at least for the **bis-TCH AZ11**, the NMR technique is able to discriminate between the *cis* and *trans* branches of the molecule.

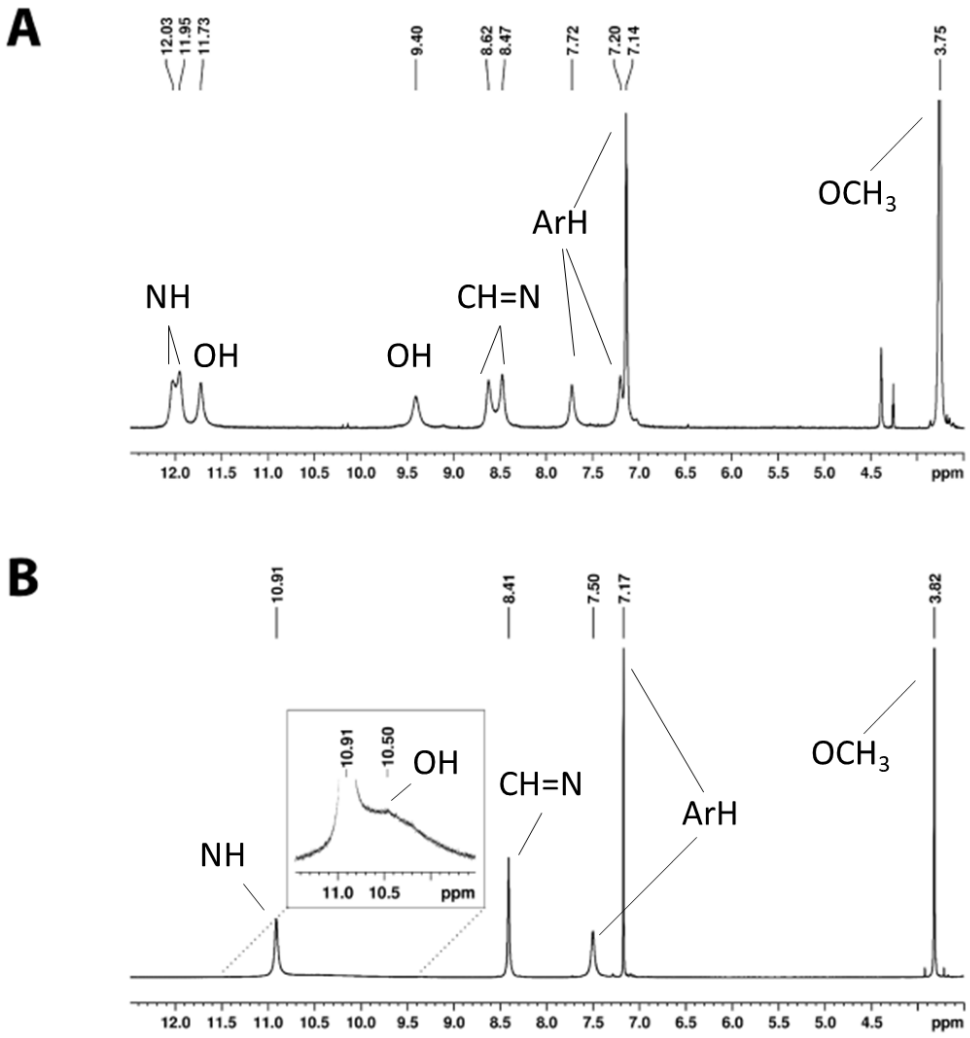

Figure 1.21: ^{1}H NMR (600 MHz) spectra of **AZ11** (A) and **AZ26** (B) in dry DMSO-d_6 at 298 K.

An integrated theoretical–computational and NMR characterization of both ligands was performed in collaboration with the research group of Prof. Greta Donati of University of Napoli Federico II.[97]

In Figure 1.22, the optimized configurational isomers *EE* are shown for both **AZ11** and **AZ26**. For each compound, the rotation along the C(X)–N bond gives rise to either symmetric *cis–cis* or asymmetric *cis–trans* *EE* conformers, and both species were considered and modelled in implicit DMSO solvent (Figure 1.22).

Preliminary DFT calculations allowed to exclude the energetically unfavoured *trans-trans* isomers for both ligands. They also allowed to discard the *EZ* and *ZZ* configurations for both ligands and for both *cis-cis* and *cis-trans* isomers, since they proved to be higher in energy than the *EE* ones. The *EE* configurations are indeed stabilized by the formation of two intramolecular hydrogen bonds between the phenolic groups and the imine nitrogen atoms (Figure 1.22).

The **asymmetric *cis–trans*, *EE* forms** are lower in energy with respect to the corresponding **symmetric *cis–cis*, *EE* ones** of about 2.34 and 2.10 kcal/mol for **AZ11** and **AZ26**, respectively. As it will be discussed in the

next sections, crystallographic data showed that the *cis–trans*, *EE* form of **AZ11** is the one chelating copper(II) ions. Although it is not a direct proof that the *cis–trans EE* form is favoured for the isolated ligand, these data suggested that this species should at least be considered for the modelling at a first stage.

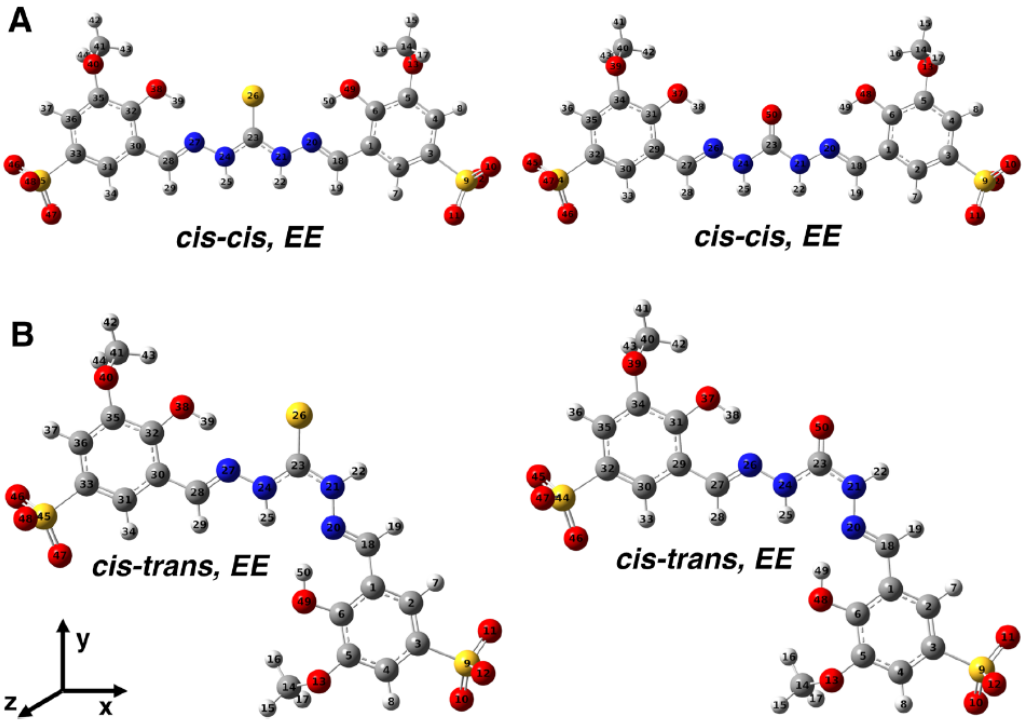

Figure 1.22: Optimized geometries of **bis-TCH AZ11** and **bis-CH AZ26** *cis-cis*, *EE* (A) and *cis-trans*, *EE* (B) isomers in implicit DMSO solvent (oxygen atoms in red; sulphur in yellow; nitrogen in blue; carbon in grey and hydrogens in white). Adapted from Ref.[97]

In Table A1.1, the main structural parameters are reported for the *cis–cis* **bis-TCH** and **bis-CH** species. Both ligands present an almost symmetric structure with respect to a plane passing through the central C–X bond and perpendicular to the molecules (Figure 1.22A). Given such symmetry, both compounds show overall the same bond distance values for the two branches. The comparison between **AZ11** and **AZ26** only reveals, as a main difference, that the C(X)–N bond distances are slightly shorter when sulphur is present instead of oxygen, i.e. 1.368 vs 1.384 Å, respectively. This trend probably suggests a slightly more pronounced double bond character of C(X)–N in **AZ11** with respect to the **AZ26**.

In Table A1.2, the structural parameters of the optimized *cis–trans* **bis-TCH** and **bis-CH** are presented. Again, the C(X)–N bond distances are slightly shorter in **AZ11** with respect to **AZ26**. For C23-N24, the values are 1.357 Å for **AZ11** and 1.376 Å for **AZ26**; for C23-N21, the values are 1.363 Å for **AZ11** and 1.380 Å for **AZ26**. As expected, the lack of the symmetry plane previously mentioned is reflected in structural parameters showing larger discrepancies between the two arms of the ligand, except for the bond distances. For example, the intramolecular hydrogen bonds between the hydroxyl hydrogens and imine nitrogen atoms show a difference of 0.075 (**AZ11**) and 0.074 (**AZ26**) Å between the two sides of the anions. In both cases, the intramolecular hydrogen bond distances are higher on the *trans* side of the molecules.

An analysis of the molecular dipole moments was also carried out (Table 1.3). From the inspection of the *cis–cis* forms, a slightly larger value of the dipole (9.0 D) is detected for the **bis-TCH AZ11** with respect to **bis-CH AZ26** (8.2 D), reflecting a slightly more pronounced asymmetry in the electronic density distribution. This

discrepancy is reduced in the *cis–trans* isomers that also reach larger values (14.2 and 14.5 D for **bis-TCH AZ11** and **bis-CH AZ26**, respectively), meaning that they are more stabilized in DMSO, given the polar character of the solvent.

Table 1.3: Molecular electric dipole moment (D, Debye) of **bis-TCH AZ11** and **bis-CH AZ26** isomers in DMSO implicit solvent.

Dipole moment	**bis-TCH** *cis–cis*	**bis-TCH** *cis–trans*	**bis-CH** *cis–cis*	**bis-CH** *cis–trans*
Total	9.0	14.2	8.2	14.5
x	0.0	−3.8	0.0	4.7
y	9.0	13.6	8.2	13.7
z	−0.1	−0.8	0.0	0.3

The computed ^{1}H NMR chemical shifts for **AZ11** and **AZ26** in DMSO solution in both the *cis–cis* and *cis–trans* forms are presented in Figures 1.23 and 1.24 and compared with those from the experimental NMR spectra.

By inspecting the experimental NMR spectrum of the **AZ11** (Figure 1.21A), the number of peaks suggests that the molecule is characterized by a lack of symmetry with respect to a plane passing through the central C=S bond and perpendicular to the molecule. The contemporary presence of two isomers (both *cis–cis* and *cis–trans*) in solution should be set aside since we should have found a higher number of peaks in the NMR spectrum arising from both isomers. Only one conformational isomer is present and it is the *cis-trans* one. At room temperature, the rotation around the C(S)–N bond is slow on the NMR timescale, which enables the clear observation of the *cis-trans* form. In fact, this slow rotation allows to distinguish the protons on the *cis* and *trans* sides, since their different signals are resolved in the spectrum. Conversely, for fast rotation dynamics on the NMR timescale, averaged signals deriving from the protons of each branch would be observed and the different chemical environments of the two arms could not be appreciated.

The model in the implicit solvent description for the *cis-trans* isomer of **AZ11** successfully reproduces the overall trend of the experimental NMR peaks for **AZ11** (Figure 1.23). This finding validates the hypothesis to consider only the *cis-trans* isomer. The rotation dynamics in which the ligand is involved are depicted in Scheme 1.6.

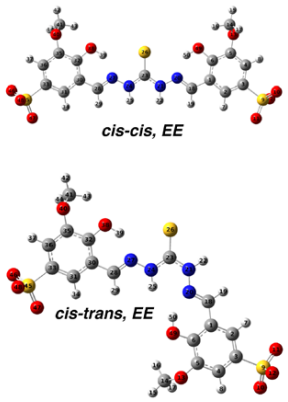

Proton	*cis–cis*	*cis–trans*	Experimental
H(C14)	3.83	3.84	3.75
H(C41)	3.83	3.84	3.75
H(C4)	7.54	7.56	7.14
H(C36)	7.54	7.56	7.14
H(C2)	7.54	7.56	7.20
H(C31)	7.54	7.56	7.72
H(C18)	8.10	7.85	8.47
H(C28)	8.10	8.26	8.62
H(O49)	11.21	9.55	9.40
H(O38)	11.21	11.19	11.73
H(N21)	8.24	8.26	11.95
H(N24)	8.24	9.25	12.03

Figure 1.23: Calculated and experimental 1D ^{1}H NMR chemical shifts δ (ppm) for the **bis-TCH AZ11** in DMSO solvent. The PCM is employed to model the solvent. Adapted from Ref.[97]

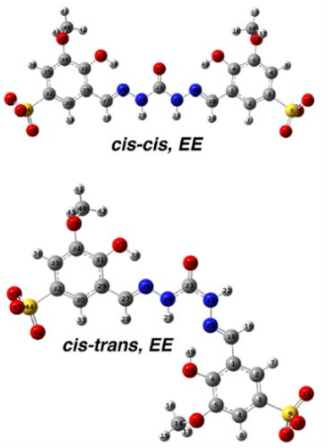

Proton	*cis–cis*	*cis–trans*	Experimental
H(C14)	3.82	3.84	3.82
H(C40)	3.82	3.84	3.82
H(C4)	7.49	7.51	7.17
H(C35)	7.49	7.51	7.17
H(C2)	7.49	7.51	7.50
H(C30)	7.49	7.51	7.50
H(C18)	7.90	7.80	8.41
H(C27)	7.90	8.05	8.41
H(O48)	11.24	9.67	10.50[a]
H(O37)	11.24	11.25	10.50[a]
H(N21)	7.42	7.18	10.91
H(N24)	7.42	8.36	10.91

[a]Very broad signal.

Figure 1.24: Calculated and experimental 1D ^{1}H NMR chemical shifts δ (ppm) for the **bis-CH AZ26** in DMSO solvent. The PCM is employed to model the solvent. Adapted from Ref.[97]

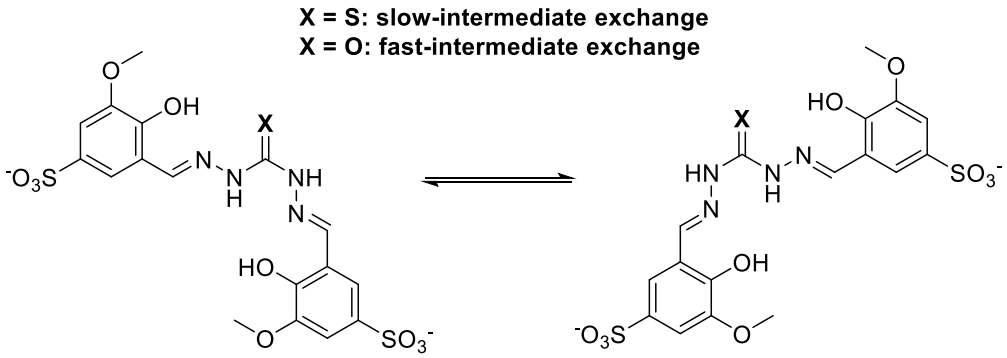

Scheme 1.6: Rotation dynamics around the C(X)-N bonds in the *cis-trans EE* form of **AZ11** (X = S) and **AZ26** (X = O).

NMR spectra for the **bis-TCH AZ11** were performed at different temperatures (Figure 1.25): by increasing the temperature, the peaks start broadening and gradually coalescing, giving rise to an averaged pattern of signals analogous to the one observed in the spectrum of the **bis-CH AZ26** recorded at room temperature. This is in line with a faster rotation around the C(S)–N bond due to temperature increase. This further suggests that in DMSO-d_6 at 298 K **AZ11** and **AZ26** exist in the same form, but in different conformational exchange regimen.

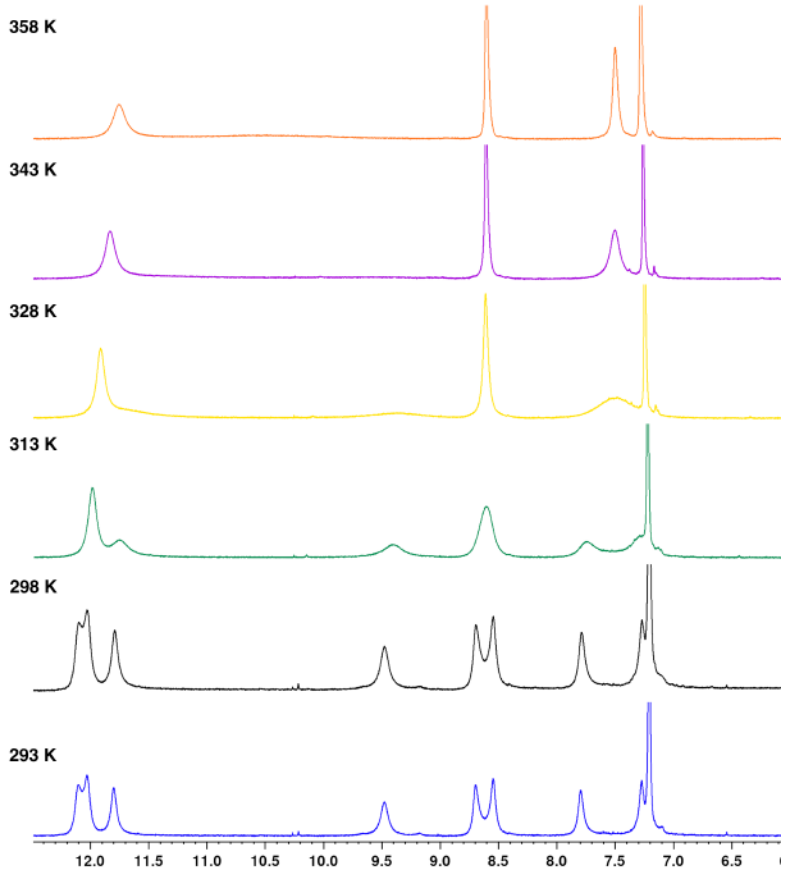

Figure 1.25: ^{1}H NMR (600 MHz) spectra of **AZ11** in dry DMSO-d_6 measured at different temperatures.

The presence of only the *cis–trans* isomer in solution at 298 K is further predicted by the Boltzmann population,

$$\frac{p_i}{p_j} = e^{\frac{(E_j - E_i)}{RT}} \tag{1.1}$$

where p_i and p_j are the populations of the *cis–cis* and *cis–trans* forms, respectively, E_j and E_i are their energies (kcal/mol), R is the gas constant, and T is the reference temperature (298 K). From the DFT model, we obtained a population ratio of $1.9 \cdot 10^{-2}$, suggesting that the *cis–cis* isomer is negligible at room temperature and further supporting the assignment of the NMR spectrum to the *cis–trans* form. Regarding the N–H chemical shifts, the lack of a quantitative reproduction of the experimental values and also a non-correct relative position in the spectrum with respect to the hydroxyl ones (Figures 1.23 and 1.24) suggest that the model should be improved and that the deshielded nature of these hydrogens is underestimated. Furthermore, the model is not able to represent the non-degeneracy of the aromatic protons H(C2) and H(C31) observed in the experimental spectrum of **AZ11**. These results underline that the implicit solvent model is not sufficient to properly describe the solvent effects on this molecule and that a more accurate description should be included.

The experimental spectrum of **AZ26** shows only five peaks (Figure 1.21B), suggesting that at 298 K the conformational dynamics are faster than in **AZ11** and that the distinction between the two sides of the molecule is not possible. Hydroxyl protons show a very broad signal at about 10.5 ppm (inset of Figure 1.21B).

Probably, at 298 K they are in the intermediate exchange regimen close to their coalescence temperature. As a matter of fact, the signal becomes sharper as the temperature increases (Figure 1.26).

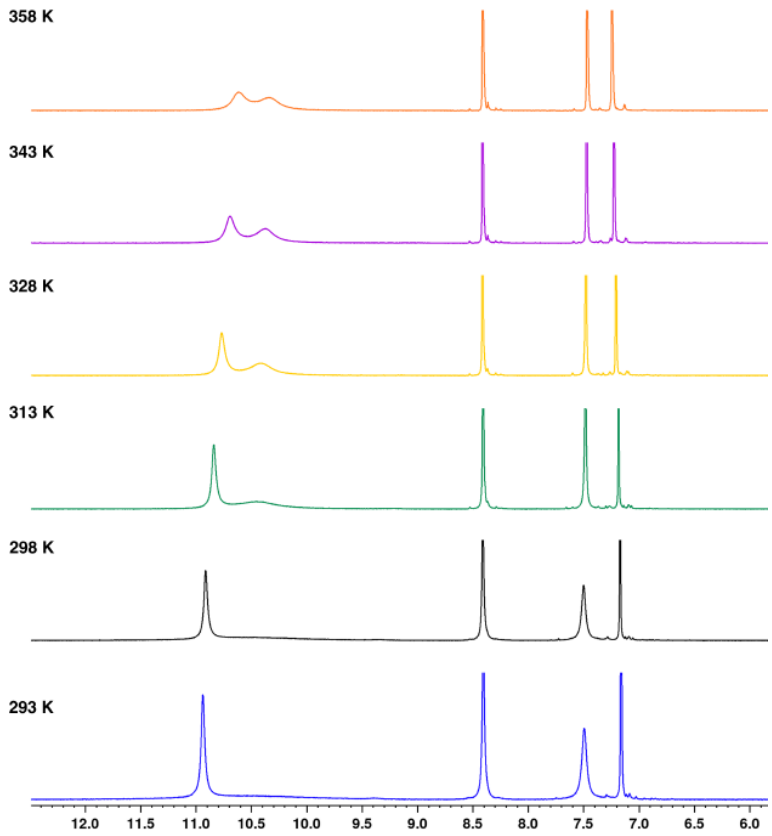

Figure 1.26: ^{1}H NMR (600 MHz) spectra of **AZ26** in dry DMSO-d_6 measured at different temperatures.

For the **bis-CH AZ26** as well, the population ratio of the *cis–cis* and *cis–trans* forms was evaluated, displaying a value similar to the **bis-TCH AZ11** (about 10^{-2}) and thus further confirming the prevalence of the *cis–trans* form in solution. Since **AZ26** exists in the fast-intermediate exchange regimen, the calculated signals for the *cis-trans* isomer (Figure 1.24) have to be elaborated as the average of the two branches of the molecule (Table 1.4).

Table 1.4: Calculated (average of the two branches of the molecule as *cis-trans* isomer) and experimental 1D ^{1}H NMR chemical shifts δ (ppm) for **AZ26** in DMSO-d_6.

Protons	*Cis-trans*	Experimental
H(C14), H(C40)	3.84	3.82
H(C4), H(C35)	7.51	7.17
H(C2), H(C30)	7.51	7.50
H(C18), H(C27)	7.92	8.41
H(O48), H(O37)	10.46	10.50
H(N21), H(N24)	7.77	10.91

As for the **AZ11**, the N–H chemical shifts are quantitatively underestimated, suggesting a limit in the model to describe the NMR features for this functional group.

What emerges from the experimental data is that the two ligands **AZ11** and **AZ26** are characterized by different dynamics rates in solution, as depicted in Scheme 1.6. At room temperature, **AZ11** is in slow-intermediate exchange regimen and by NMR it is possible to distinguish the two branches of the molecule; on the contrary, **AZ26** is in fast-intermediate exchange regimen and the exchange process becomes too rapid to influence directly the experimental NMR spectrum. Consequently, for each branch of the **AZ26** molecule, we observe in the NMR spectrum a situation that is the average between *cis* and *trans*.

The fact that in DMSO-d_6 at 298 K **AZ11** and **AZ26** exist in the same form, the **keto *cis-trans* EE isomer**, but in **different conformational exchange regimen** (slow-intermediate and fast-intermediate at room temperature, respectively) is also confirmed by the study of the kinetics of the conformational dynamics, estimated by using Eyring's equation. The rate constant for the rotation along the C(X)–N bond is

$$\kappa = \frac{\kappa_B T}{h} \cdot e^{-\frac{\Delta G^{\ddagger}}{RT}} \tag{1.2}$$

where κ is the rate constant in s^{-1}, κ_B is the Boltzmann constant, T is the temperature, h is the Planck constant, R is the gas constant, and $\Delta G^{\ddagger}$ is the computed activation energy barrier evaluated as the difference between the Gibbs' free energies of the transition state and the reactant. The calculated half-lifetimes are presented in Table 1.5 by assuming first order kinetics. For **AZ11**, $t_{1/2}$ is 0.23 ms, while for **AZ26**, $t_{1/2}$ is 0.02 ms, almost one order of magnitude smaller than the first one. Therefore, the latter dynamics are reasonably too fast to be detected by NMR and the different chemical environments felt by protons on the *cis* or *trans* side of **AZ26** cannot be disentangled by this technique. Conversely, **AZ11** represents a borderline situation in which the different hydrogen chemical environments are still observed at room temperature. By increasing the temperature, the peaks start broadening and gradually coalescing, resembling **AZ26** (Figure 1.25).

Starting from the Eyring's equation it is possible to derive the following expression,[101,102] that allows to estimate the rate parameters from the experimental ^{1}H NMR spectra:

$$\Delta G^{\ddagger} = RT_c[22.96 + \ln\left(\frac{T_c}{\Delta \nu}\right)] \tag{1.3}$$

where R is the gas constant, T_c is the coalescence temperature (the temperature where the dynamic process transitions change from fast to slow or vice versa) and Δν is the difference in chemical shifts (Hz) at low temperature. In our case, the difference between the hydroxyl hydrogen peaks of **AZ11** at 298 K was employed as Δν value (∼ 1624 Hz) and 343 K was chosen as Tc for these peaks. The rate parameters obtained from the experimental spectrum of **AZ11** are presented in Table 1.5. Despite a difficult accurate estimation of both the coalescence temperature (Tc) and the difference in chemical shift in the low temperature spectrum (Δν), a good qualitative agreement between the experimental and computed rate parameters was achieved.

Table 1.5: Computed rotational barrier energy (kcal/mol), rotational rate constant (s−1), and half-lifetime ($t_{1/2} = \frac{ln2}{\kappa}$, s) for **bis-TCH AZ11** and **bis-CH AZ26** *cis–trans* isomers in implicit solvent. The same quantities evaluated from the experimental 1D ^{1}H NMR spectrum for the **bis-TCH AZ11** are also presented. Adapted from Ref.[97]

	$\Delta G^{\ddagger}$	κ	$t_{1/2}$
bis-TCH	12.71	$2.970 \cdot 10^{3}$	$2.334 \cdot 10^{-4}$
bis-TCH (NMR)	14.59	$1.238 \cdot 10^{2}$	$5.599 \cdot 10^{-3}$
bis-CH	11.23	$3.618 \cdot 10^{4}$	$1.916 \cdot 10^{-5}$

The origin of the difference in conformational dynamics rate between the **bis-TCH AZ11** and the **bis-CH AZ26** can be found in the different extent of partial double bond character of the C(X)-N bonds: the higher partial double bond character of the C(S)-N bonds hinders the rotation around them and therefore slows down the conformational dynamics. This property is also strongly related to the acidity of the C(X)-**NH** groups: as it will be discussed in the next section, the presence of the sulphur atom increases the acidic character of the NH groups. This finding aligns with previous literature.[103] A qualitative analysis[104] of the factors influencing the acidity of N-H bonds in compounds of type RC(=X)NH, (X = O, NH or S) attributes a key role to three aspects: the field-inductive factor, polarizability and resonance. The field-inductive effect decreases in the order of dipole moments, with C=S (2.95 D) having a higher moment than C=O (2.5 D).[104] In addition, both the polarizability and resonance effects are more pronounced in sulfur compounds. This is attributed to the relative weakness of the C=S bond and sulfur superior ability to stabilize a negative charge compared to oxygen. Consequently, these three effects collectively account for the differing conformational dynamics of **AZ11** and **AZ26**.

The discrepancies in terms of quantitative agreement of the calculated chemical shifts with the experimental ones and, in some cases, of relative peak positions, could arise from a poor representation of the micro-solvation environment of the compounds. It is well known that DMSO is able to establish specific interactions with organic molecules and, for this reason, we decided to explicitly model solvent molecules surrounding the ligands. Molecular Dynamics (MD) simulations were performed to investigate the micro-solvation of the ligands. Radial distribution functions (RDFs) were calculated for both the N–H groups and the hydroxyl oxygen atoms with respect to the DMSO oxygens (Figure A1.16). The MD results unveil that **AZ11** and **AZ26** display different microsolvations for the nitrogen belonging to the cis side. While **AZ11** could be stably surrounded by one DMSO molecule on the cis arm, **AZ26** does not trigger a well-defined DMSO structuring. These results suggest that the **AZ11** molecule is more capable of interacting and establishing specific interactions with DMSO across both its branches. In contrast, the **AZ26** molecule is better solvated only on its *trans* side, while the N–H moiety at the *cis* site is less capable of specific interactions with the solvent. These results clearly highlight that there are significant and different solvent dynamics around both N–H sites, and they are reasonably involved in specific interactions with DMSO. **AZ11** engages a total of two DMSO molecules—one at each N–H site—while **AZ26** shows an asymmetry on its two branches, with only the trans side tightly interacting with the solvent.

The MD analysis suggests that, overall, two DMSO molecules should be explicitly included in both cases to build a cluster representation in order to achieve a more realistic description of the systems.

Optimized clusters including two DMSO molecules were prepared (Figure 1.27). The structural parameters are reported in Table A1.3.

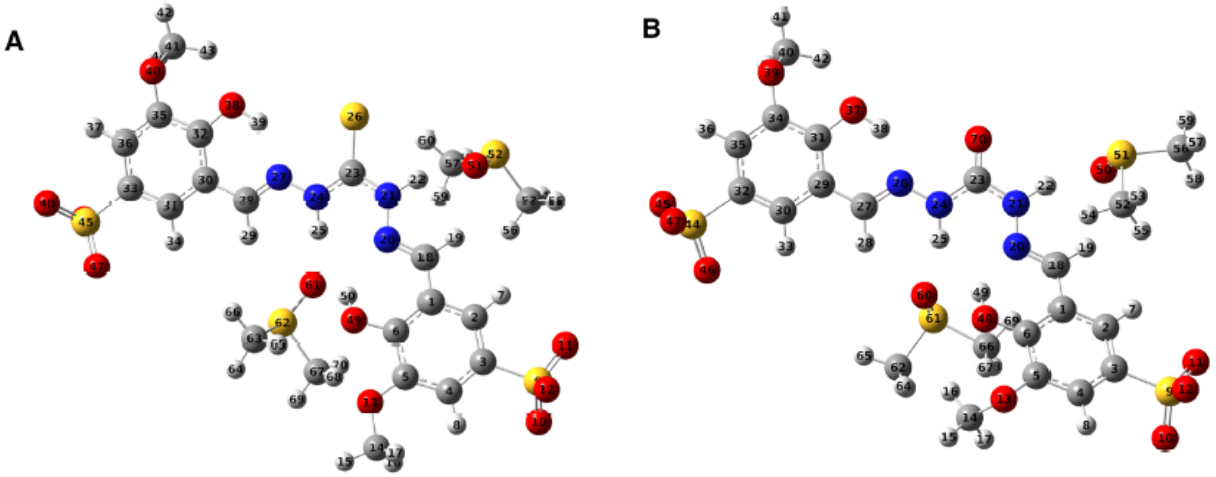

Figure 1.27: Optimized geometries of the **bis-TCH AZ11** (A) and the **bis-CH AZ26** (B) clusters including two DMSO molecules. Adapted from Ref.[97]

The only main difference with respect to the implicit solvent model is shown for the dihedral angles, especially for the N–C–N–N, in which differences of 8.5° and 14.3° are found for **AZ11** and **AZ26**, respectively. This fact suggests that the explicit solvent inclusion enhances the molecular distortion, providing a more realistic picture in which the DMSO interactions perturb the molecular symmetry. By inspecting the dipole moments upon inclusion of explicit solvent molecules, an increase in their values is observed (Table A1.4).

The calculated chemical shifts for the **AZ11** and the **AZ26** clusters are presented in Table 1.6. Again, since **AZ26** exists in the fast-intermediate exchange regimen, the calculated signals (Table 1.6) have to be elaborated as the average of the two branches of the molecule (Table 1.7).

Table 1.6: Calculated and experimental 1D ^{1}H NMR chemical shifts δ (ppm) for the **bis-TCH AZ11** and the **bis-CH AZ26** in cluster representation with two explicit DMSO solvent molecules. The bulk solvent is modelled by PCM.[130-132]

bis-TCH	Calculated	Experimental	**bis-CH**	Calculated	Experimental
H(C14)	3.84	3.75	H(C14)	3.92	3.82
H(C41)	3.84	3.75	H(C40)	3.92	3.82
H(C4)	7.22	7.14	H(C4)	7.42	7.17
H(C36)	7.50	7.14	H(C35)	7.42	7.17
H(C2)	7.50	7.20	H(C30)	7.49	7.50
H(C31)	7.50	7.72	H(C2)	7.56	7.50
H(C28)	8.62	8.47	H(C18)	8.58	8.41
H(C18)	9.02	8.62	H(C27)	8.88	8.41
H(O49)	9.50	9.40	H(O48)	9.76	10.50[a]
H(O38)	11.61	11.73	H(O37)	11.88	10.50[a]
H(N21)	12.19	11.95	H(N21)	11.08	10.91
H(N24)	12.60	12.03	H(N24)	12.69	10.91

[a]Very broad signal.

Table 1.7: Calculated (average of the two branches of the molecule as *cis-trans* isomer) and experimental 1D ^{1}H NMR chemical shifts δ (ppm) for the **bis-CH AZ26** in cluster representation with two explicit DMSO solvent molecules.

Protons	*Cis-trans*	Experimental
H(C14), H(C40)	3.92	3.82
H(C4), H(C35)	7.42	7.17
H(C2), H(C30)	7.52	7.50
H(C18), H(C27)	8.73	8.41
H(O48), H(O37)	10.82	10.50
H(N21), H(N24)	11.88	10.91

For both ligands, the signals showing the largest improvements are undoubtedly the N–H ones; indeed, the shift at larger ppm is nicely and quantitatively reproduced by the cluster model.

The data highlight that the role of hydrogen bond formation between the **bis-TCH AZ11** and DMSO is not negligible to interpret at the molecular level the NMR spectrum of this compound. The importance of these specific interactions is also confirmed by the cluster binding energies, calculated according to the following equation:

$$\Delta G_{binding} = G_{complex} - (G_{solute} + nG_{DMSO}) \quad (1.4)$$

The ΔG values showed that the hydrogen bonds stabilize **AZ11** of 1.63 kcal/mol. This solute–solvent favourable interaction is another cause for the lower conformational freedom of the solute to the point of allowing the NMR technique to clearly detect the molecule *cis* and *trans* sides.

Regarding the **bis-CH AZ26**, probably it makes weaker interactions with DMSO, as testified by the experimental chemical shift values (10.91 vs 11.95 and 12.03 ppm). This evidence is also confirmed by MD simulations and by the cluster binding energy: the solvated **AZ26** does not show a stabilization trend with respect to the isolated molecule; indeed, the complex is a little destabilized at about 1.82 kcal/mol. This result is in line with the faster conformational dynamics of **AZ26**: the solute is less hindered by DMSO and by the less efficient solvation at one of the N–H sites.

The inclusion of explicit solvent molecules in the model allowed to represent more properly the behaviour of the ligands in DMSO. Nevertheless, there are still some features that need a deeper explanation: the pattern of signals for the aromatic protons is not well represented and the reason for the non-degeneracy of only one of the two couples of these protons in the spectrum of **AZ11** is not clear. Trying to investigate this aspect, it has to be underlined that the picture of the DFT model is a static and well-defined hydrogen bonded case representing an ideal situation that is more complex and transient in nature. More importantly, when recording a series of spectra at different temperatures, there may be multiple coalescence temperatures associated with the same single exchange process.[105] If multiple pairs of nuclei experience interconversion during the exchange, it is very likely that the frequency separations between each pair would not be identical. Consequently, the rate constant *k* at which each pair would experience coalescence would differ, determining different coalescence temperatures for each pair of nuclei. In other words, it is possible that exchanging sites with a small frequency difference may be beyond coalescence (fast-intermediate regimen) whereas those with a greater separation may be yet to coalesce (slow-intermediate regimen). This is probably what happens

to the two couples of aromatic protons: the *cis-trans* isomer should give rise to four different signals for the four aromatic protons (because the species is asymmetrical), but the H(C4)-H(C36) couple experiences a different coalescence temperature with respect to the H(C2)-H(C31) couple.

To demonstrate such hypothesis, there was the need to go down in temperature in order to see if there could be the splitting of peaks also for the other couple of aromatic protons of the **bis-TCH AZ11**. Consequently, we studied the behaviour of **AZ11** at low temperatures in D_2O and CD_3OD (Figures 1.28 and 1.29).

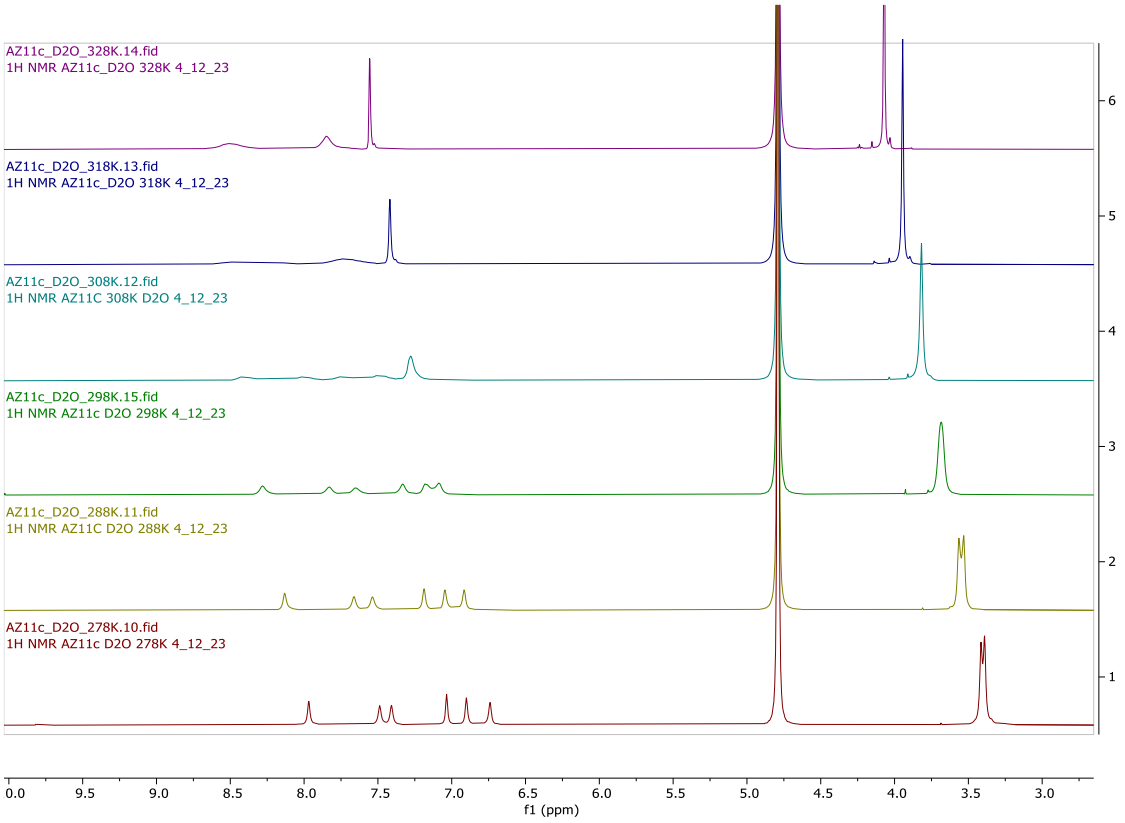

Figure 1.28: ^1H NMR (400 MHz) spectra of **AZ11** in D_2O measured at different temperatures. For each spectrum, the signal of H_2O is maintained fixed at 4.79 ppm.

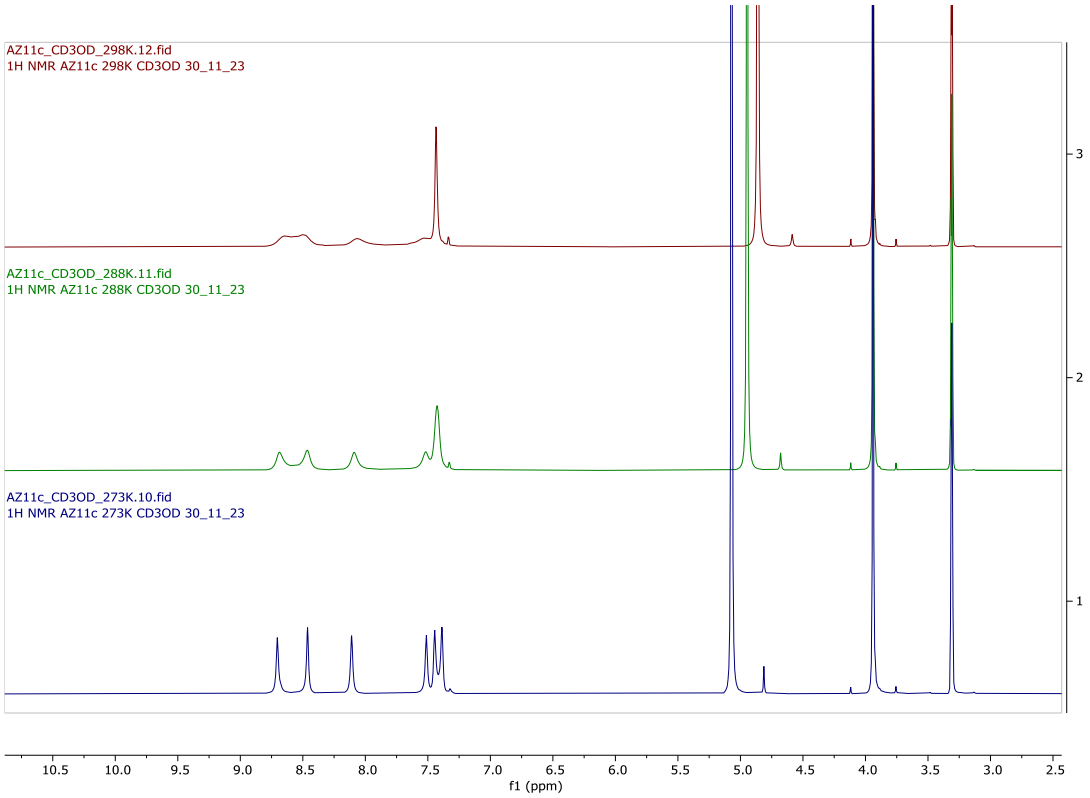

Figure 1.29: ^{1}H NMR (400 MHz) spectra of **AZ11** in CD_3OD measured at different temperatures.

Since water and methanol are polar protic solvents, the NH and OH signals of the ligand disappear and only the imine, aromatic and methoxy protons peaks are visible. As it is evident in both solvents, at low temperatures two signals are visible for the imine protons and four signals for the aromatic hydrogens. The spectra recorded in CD_3OD better show the small frequency difference of the most shielded couple of aromatic protons with respect to the other couple. Although the solvent is different, the patterns of signals at the various temperatures are comparable to the ones observed in DMSO-d_6. The difference in coalescence temperatures may be therefore the reason for the unusual pattern of signals of **AZ11** in DMSO-d_6.

Variable-temperature experiments were performed also for **AZ26**. At low temperatures in D_2O and CD_3OD, the spectrum of **AZ26** (Figures 1.30 and 1.31) resembles the spectrum of **AZ11**, further confirming all the results and conclusions of the study on the isomerization processes.

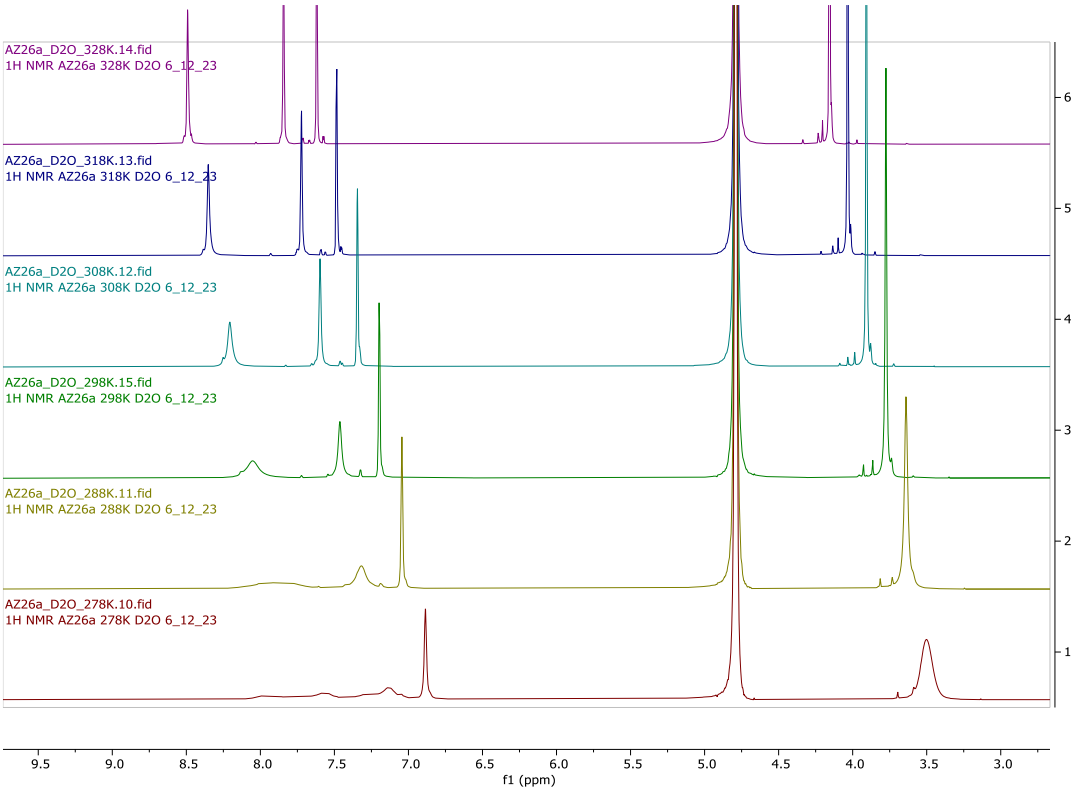

Figure 1.30: ^{1}H NMR (400 MHz) spectra of **AZ26** in D_2O measured at different temperatures. For each spectrum, the signal of H_2O is maintained fixed at 4.79 ppm.

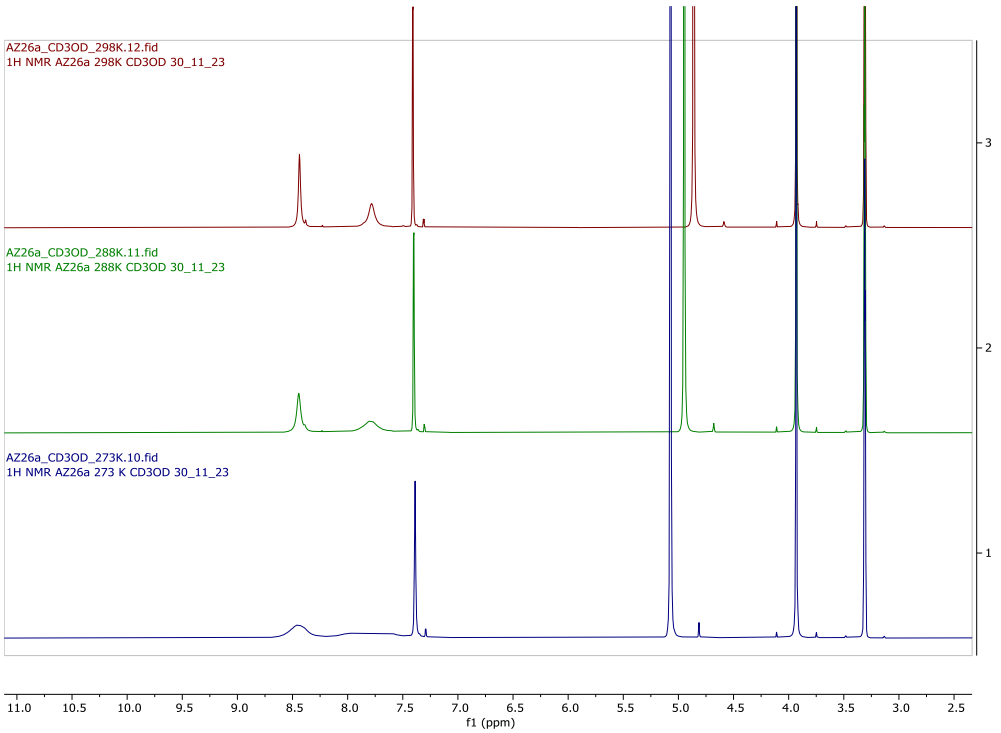

Figure 1.31: ^{1}H NMR (400 MHz) spectra of **AZ26** in CD_3OD measured at different temperatures.

Proton dissociation processes of the ligands

Proton dissociation constants provide information on the capacity of a ligand to form complexes at different pH values and provide an opportunity for deeper comprehension of its biological activity. In fact, the total charge of a molecule (either as a free ligand or in the form of a metal complex) can strongly influence its capacity to interact with biomolecules and cell membranes and affects its pharmacokinetic and pharmacodynamic properties.[106]

In their fully protonated state, the two ligands can be regarded as hexa-protic acids (H_6L, Scheme 1.7); however, in aqueous solution, they behave as triprotic acids in the pH range 2 – 12.

As seen in the previous section, the ligands in solution exist as *cis-trans* isomers, but in Scheme 1.7 they are represented as symmetrical molecules for simplicity. To note that, although it is possible to infer from the NMR data and the DFT model which of the two hydroxyl or NH groups of the *cis-trans* isomer is the most acidic, this is not possible for the sulfonic acid groups.

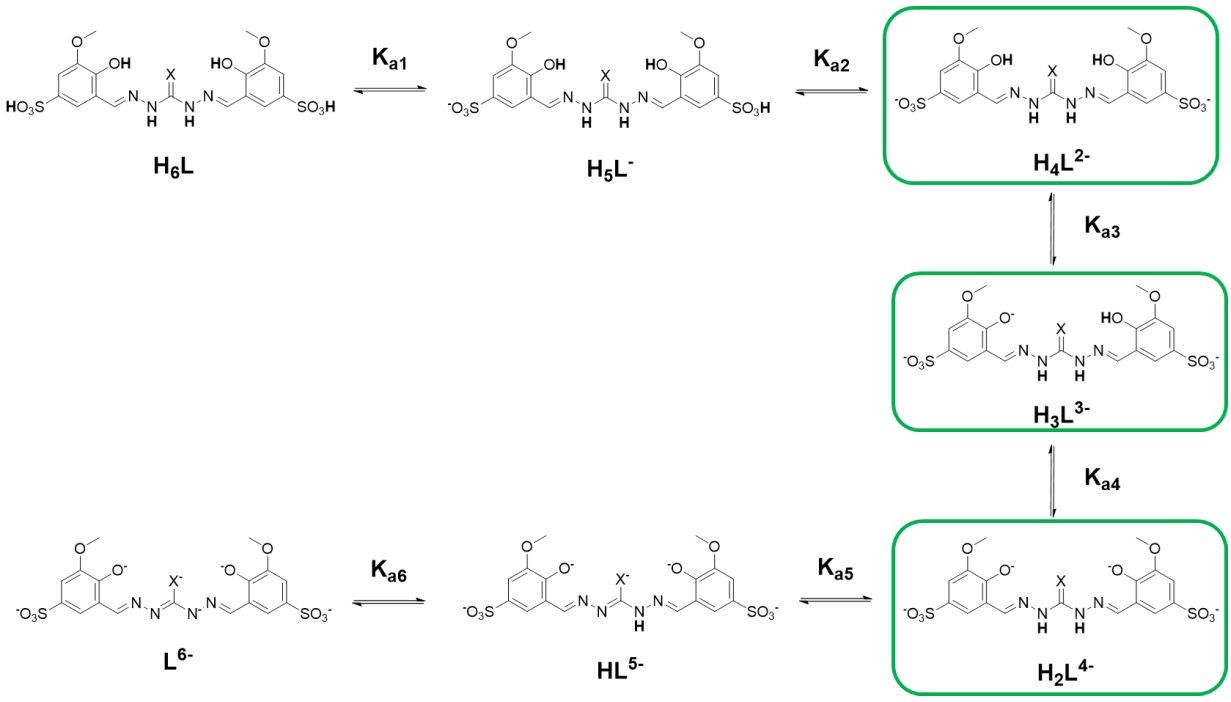

Scheme 1.7: Proton-dissociation equilibria for the two ligands (X = S, O); species present in the pH range 4 - 10 are evidenced in green rectangles.

The proton dissociation constants of **$Na_2H_4L^1 \cdot 5.5\ H_2O$** (**AZ11**) were studied by registering the UV-visible spectra in aqueous solution between pH 3.98 and 10.00 (Figure 1.32A).

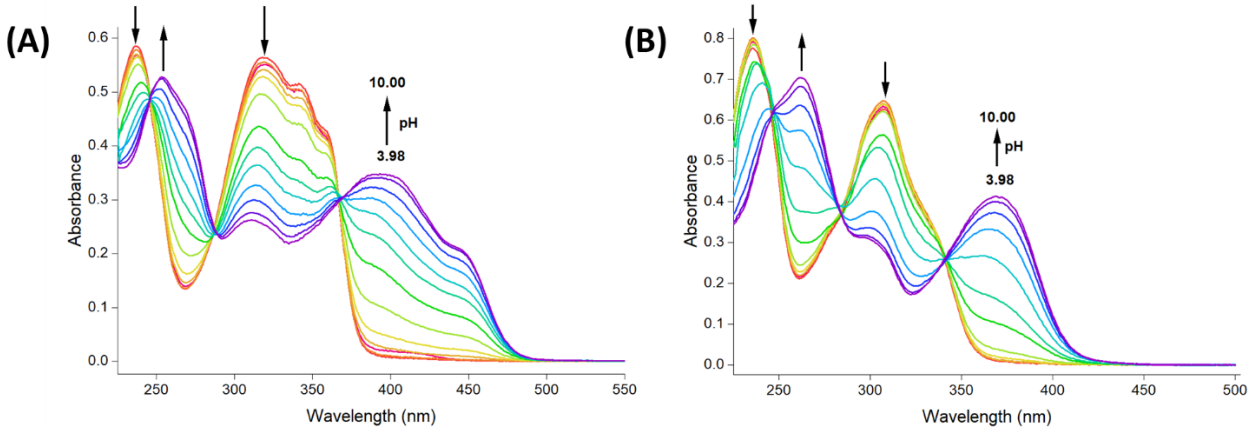

Figure 1.32: UV-visible absorption spectra for (A) **AZ11** and (B) **AZ26** in aqueous solution at different pH values (pH range: 3.98 – 10.00; T = 298.2 K, I = 0.1 M NaCl, C_L = 17 µM).

Between pH = 3.98 and 6.00, the solutions of **AZ11** were colourless with absorption maxima at 237 and 320 nm. From pH = 6.49, the solution was pale green, and the colour became more intense until pH = 10.00: the colour change was accompanied by the appearance of bands at 253 and 393 nm, with a shoulder at 445 nm.

There are three apparent isosbestic points at 246, 288, and 368 nm (Figure 1.32A). The presence of an isosbestic point typically indicates that only two species that vary in concentration contribute to the absorption in that range of wavelengths. If a third one is taking part in the process, the spectra typically intersect at varying wavelengths as concentrations change, creating the impression that the isosbestic point is "out of focus".[107] A careful look at the spectra reveals that this is exactly what happens in our system: in Figure A1.17 is clearly shown this kind of "defocusing" for the isosbestic point at 288 nm, but this phenomenon is common to all three isosbestic points. This finding suggested the presence of three species rather than two, and therefore of two dissociation equilibria contemporary occurring.

Spectroscopic data treatment with the HypSpec2014 software[108] allowed us to determine two pK_a values (Table 1.8), that were referred to the dissociation of the two phenolic groups (pK_{a3} =6.78(1) and pK_{a4} = 8.77(1), Scheme 1.7). Therefore, the single-site pK_a value of the phenolic groups can be estimated as the average pK_a, which is 7.78. This value is similar to that reported for the deprotonation of the phenolic moiety of sodium 5-sulfonate-salicylaldehyde thiosemicarbazones.[109] The values of pK_{a1} and pK_{a2}, associated to the proton dissociation of the sulfonic groups, are expected at much lower values (below 3), and could not be determined from these experiments.

In order to understand if at extreme pH values it was possible to detect some variations to the absorption spectra, also the UV-visible spectra of the ligand at pH 0.99 and 12.67 were collected. In Figure 1.33A representative spectra along the whole pH range studied are depicted. The spectra of **AZ11** at extreme pH values suggest the formation of another species above pH 10 and of another below pH 4. Regarding the species which should be present at extremely basic pH, we expect that it is the HL^{5-} species and therefore it should be possible to determine even the pK_{a5}. In addition, the increase of the band at 320 nm between pH 1 and 4 suggests that in such range a certain amount of the H_5L^- species is present at equilibrium.

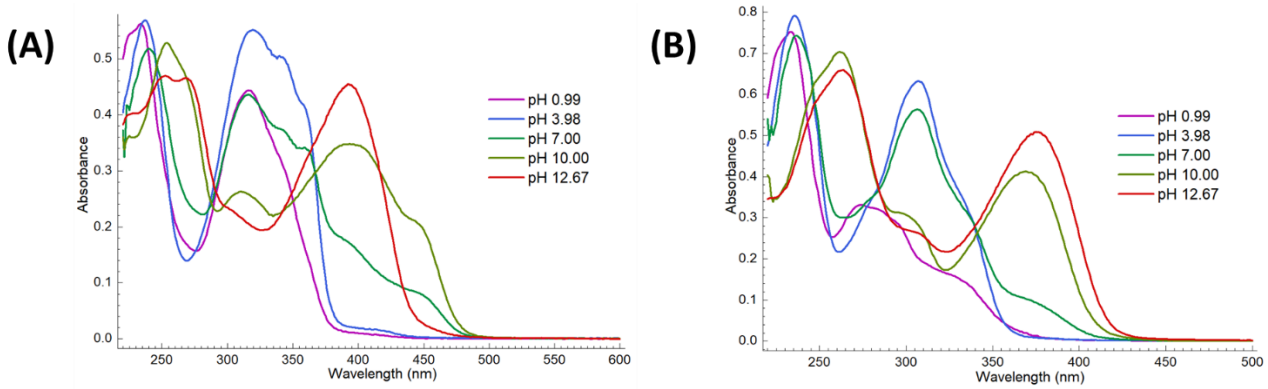

Figure 1.33: (A) Representative UV-visible absorption spectra of **AZ11** (C_{ligand} = 17 µM) at different pH values. It is remarkable the disappearance of the shoulder at 445 nm at pH 12.67, which is consistent with the colour change of the solution (from intense green at pH 10 to nearly colourless at pH 12.67). **(B)** Representative UV-visible absorption spectra of **AZ26** (C_{ligand} = 17 µM) at different pH values.

Potentiometric titrations were performed by the research group of Prof. Matteo Tegoni (Department of Chemistry, Life Sciences and Environmental Sustainability, University of Parma) in the attempt to determine the value of the pK_a of the hydrazidic NH protons (pK_{a5} and pK_{a6}), and, possibly, those of the protonated sulfonate groups. Effectively, potentiometric data allowed us to determine the pK_{a5} value, along with pK_{a3} and pK_{a4} (Table 1.8). The values of pK_{a3} and pK_{a4} obtained by potentiometry measurements are consistent with those obtained by spectrophotometric titrations. A representation of the distribution diagram for the **bis-TCH AZ11** is reported in Figure 1.34A.

Table 1.8: Logarithms of the proton dissociation constants (pK_a) of **bis-TCH AZ11** and **bis-CH AZ26** determined in aqueous solution at T = 298.2 K by UV-visible spectrophotometry and pH potentiometry. Standard deviations are reported in parentheses.

	bis-TCH		bis-CH	
	UV–Visible Spectrophotometry	pH Potentiometry	UV–Visible Spectrophotometry	pH Potentiometry
p*Ka2*	-	-	-	1.70(10)
p*Ka3*	6.78(1)	7.08(4)	7.34(1)	7.77(3)
p*Ka4*	8.77(1)	8.54(4)	8.58(1)	8.45(3)
p*Ka5*	-	11.29(2)	-	-

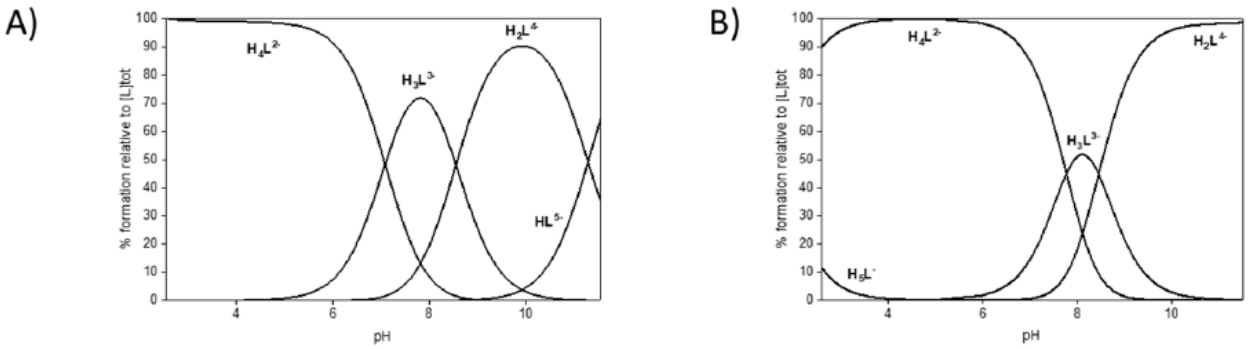

Figure 1.34: Representative distribution diagram of A) **bis-TCH AZ11** and B) **bis-CH AZ26** in aqueous solution (C_L = 3 mM, I = 0.1 M KCl, T = 298.2 K). For each pH value (x axis), the amount of ligand in its different protonation states is reported as a % of the total ligand in solution. At physiological pH, the major species are H_4L^{2-} and H_3L^{3-}. The former corresponds to the ligand deprotonated on the sulfonic groups, while the latter to the ligand deprotonated on the two sulfonic groups and one phenolic group.

Similarly, the proton dissociation constants of **$Na_2H_4L^2 \cdot 5\ H_2O$** (**AZ26**) were studied spectrophotometrically in aqueous solution between pH = 3.98 and 10.00 (Figure 1.32B). At pH values between 3.98 and 6.49, the spectrum of the ligand did not change, and two strong bands at 235 and 308 nm were observed. A significant spectral change was observed in the pH range 7.00–10.00 (Figure 1.32B). As for **AZ11**, the isosbestic points at 247, 284, and 341 nm (Figure A1.18) shift in the course of the titration, suggesting the presence of three species in this pH range and therefore two dissociation equilibria. The spectrophotometric data were processed by means of HypSpec2014 software, leading to pK_{a3} = 7.34(1) and pK_{a4} = 8.58(1), which were assigned to the deprotonation of the two phenolic OH groups (Table 1.8). As for **AZ11**, the single-site pK_a value of the phenolic groups can be estimated as the average pK_a (7.96).

As for **AZ11**, also for **AZ26** were collected the UV-visible spectra at pH 0.99 and 12.67. In Figure 1.33B are depicted representative spectra along the whole pH range studied. The dramatic change of the spectrum between pH 1 and 4 suggested the possibility of determining also the pK_{a2} value.

To complete the analysis, potentiometric titrations were carried out for **AZ26** starting from a very acidic pH. Starting from pH = 2.60, we were able to observe three dissociation equilibria, with pK_a values of 1.70(10), 7.77(3), and 8.45(3), respectively (Table 1.8). The values obtained by potentiometry are consistent with those obtained by spectrophotometric titrations (Table 1.8), and the lowest of the pK_a values was associated with the proton dissociation of H_5L^- on the second sulfonic group (pK_{a2} = 1.70). Importantly, no dissociation of the hydrazidic NH groups was observed, a behaviour consistent with that reported in the literature.[110] A representative distribution diagram of the **bis-CH AZ26** is reported in Figure 1.34B.

The fact that we were able to determine the value of pK_{a5} only for **AZ11** indicates that the C(S)-NH group is more acidic than the C(O)-NH group, as expected.

Synthesis and characterization of the copper(II) and zinc(II) complexes

The ligands were reacted with copper(II) or zinc(II) ions in 1:1 or 2:1 metal:ligand ratio, leading to the formation of the complexes **PP8**, **PP9**, **PP10**, **PP11**, **PP17**, **PP18**, **PP19** and **PP20** (Table 1.9). All the metal complexes were characterized by FT-IR spectroscopy, elemental analysis, ESI mass spectrometry and, in the case of the zinc(II) complexes, also by ^{1}H NMR spectroscopy.

Table 1.9: Overview of the synthesized copper(II) and zinc(II) complexes.

Metal	Ligand	M:L ratio	Complex	M:L ratio	Complex
Cu^{II}	**AZ11**	1:1	**PP8**	2:1	**PP17**
	AZ26	1:1	**PP10**	2:1	**PP19**
Zn^{II}	**AZ11**	1:1	**PP9**	2:1	**PP18**
	AZ26	1:1	**PP11**	2:1	**PP20**

The copper(II) complexes **PP8** and **PP10** were prepared by reacting $CuCl_2$ respectively with **AZ11** and **AZ26** with a 1:1 metal to ligand ratio in H_2O/MeOH at room temperature (Scheme 1.8).

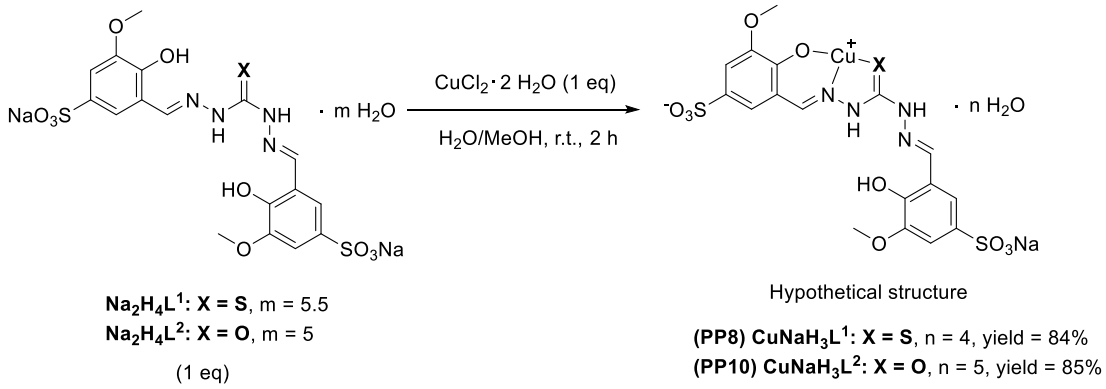

Scheme 1.8: Synthesis of the 1:1 Cu^{II}:ligand complexes. Coordinated water molecules are omitted.

The involvement of the imine nitrogen atoms in copper coordination is confirmed by the IR spectra (Figure 1.35): the bands relative to C=N stretching of the free ligands shift to lower frequencies and gain in intensity in **PP8** (from 1647, 1612 cm^{-1} to 1607, 1586 cm^{-1}) and **PP10** (from 1614, 1586 cm^{-1} to 1604, 1558 cm^{-1}). In the IR spectrum of **PP10** (Figure 1.35B)**,** the C=O stretching band has a moderate shift to lower values (from 1663 in the ligand to 1651 cm^{-1}, $\Delta\nu$ = 12 cm^{-1}), confirming the participation of the keto oxygen in the metal ion coordination. IR data and elemental analysis (see the experimental section) suggested that **PP8** and **PP10** have the common formula **$CuNaH_3L \cdot n\ H_2O$**, with the salicylic oxygen deprotonated and the ligands behaving as ONX tridentate. The coordination sphere of copper is completed by water molecules; however, the lack of single crystal XRD information did not allow to know the number of such molecules, together with the coordination geometry around the metal.

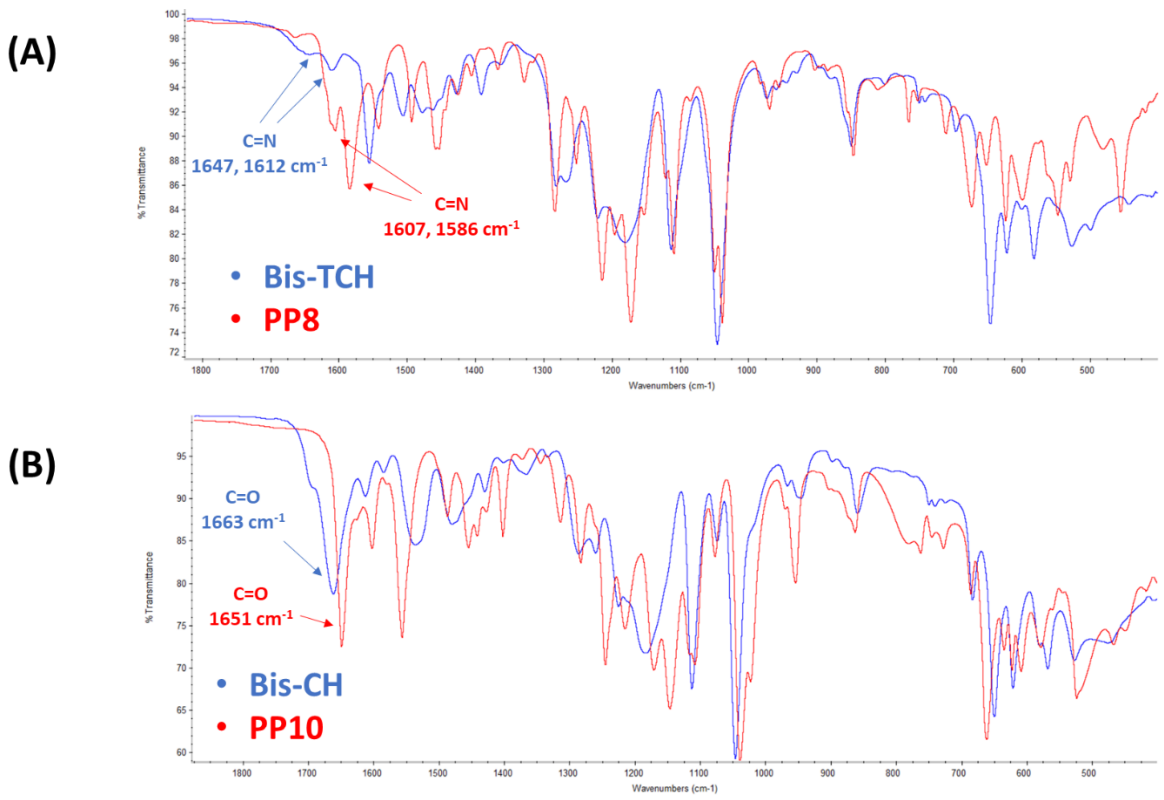

Figure 1.35: FT-IR spectra of **AZ11** (**bis-TCH**) and **PP8** (A), and of **AZ26** (**bis-CH**) and **PP10** (B).

The zinc(II) complexes **PP9** and **PP11** were prepared by reacting $Zn(CH_3COO)_2$ with the two ligands in a 1:1 metal to ligand ratio (Scheme 1.9).

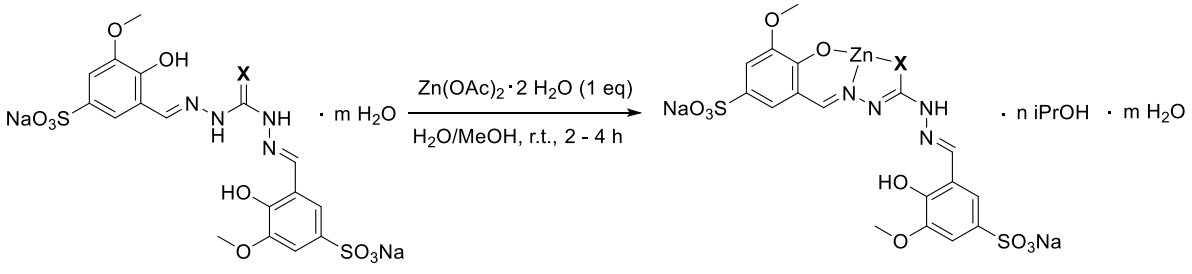

$Na_2H_4L^1$: X = S, m = 5.5
$Na_2H_4L^2$: X = O, m = 5

(1 eq)

Hypothetical structure

(PP9) $ZnNa_2H_2L^1$: X = S, n = 0.33, m = 6, yield = 76%
(PP11) $ZnNa_2H_2L^2$: X = O, n = 0.5, m = 5, yield = 80%

Scheme 1.9: Synthesis of the 1:1 Zn^{II}:ligand complexes. Coordinated water molecules are omitted.

As for the copper complexes, the shift of the C=N stretching vibrations to lower frequencies indicates the involvement of the imine nitrogen atoms in zinc coordination (Figure 1.36). In the IR spectrum of **PP11**, the C=O band is now significantly shifted to lower frequencies with respect to the same band of the **bis-CH AZ26** ($\Delta\nu$ = 63 cm^{-1}, Figure 1.36B). In this case and in **PP9**, the ligand seems bi-deprotonated (salicylic and hydrazidic hydrogens), and coordinates to the metal ion in the **enol** form in a tridentate ONO fashion. Elemental analyses

(see the experimental section) allowed to assign the general formula **$ZnNa_2H_2L \cdot n\ iPrOH \cdot m\ H_2O$** for both **PP9** (n = 0.33; m = 6) and **PP11** (n = 0.5, m= 5). The presence of 2-propanol in the structures of the complexes is confirmed by the ^1H NMR spectra in D_2O (Figure A1.19).

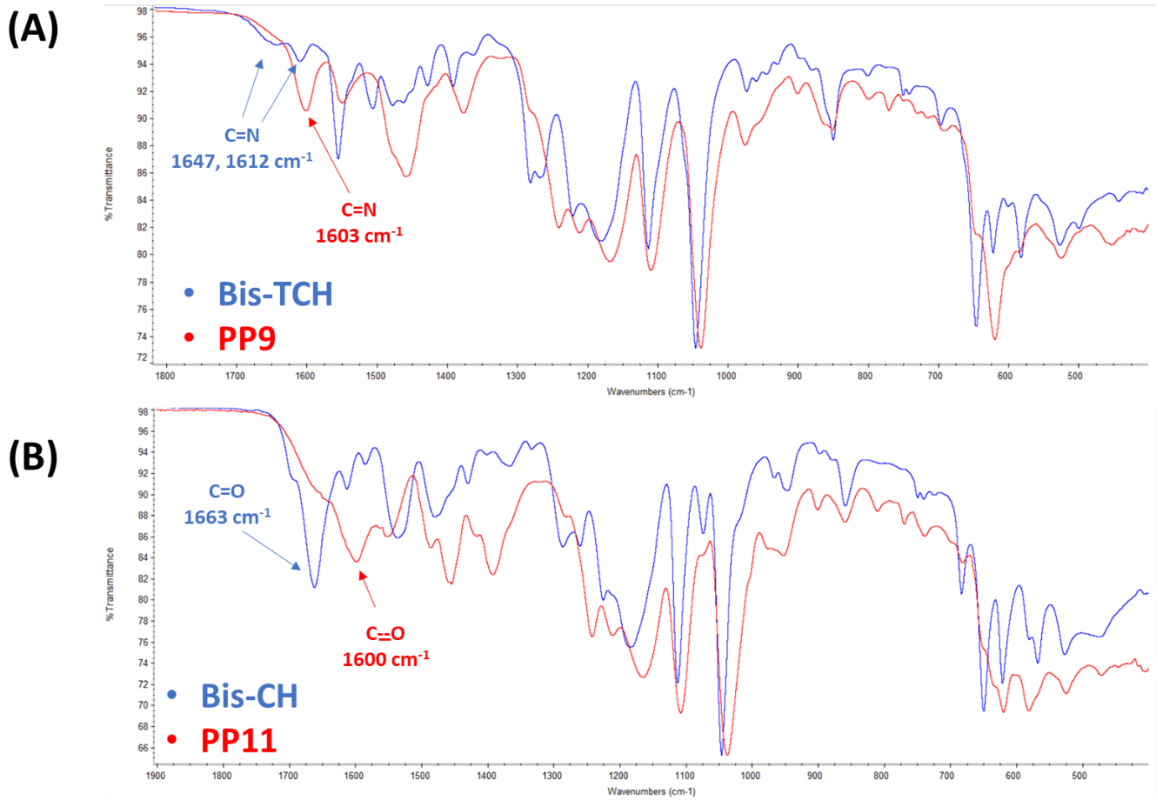

Figure 1.36: FT-IR spectra of **AZ11** (**bis-TCH**) and **PP9** (A), and of **AZ26 (bis-CH**) and **PP11** (B).

The copper(II) complexes **PP17** and **PP19** were prepared by reacting $CuCl_2$ respectively with **AZ11** and **AZ26** in a 2:1 metal to ligand ratio (Scheme 1.10).

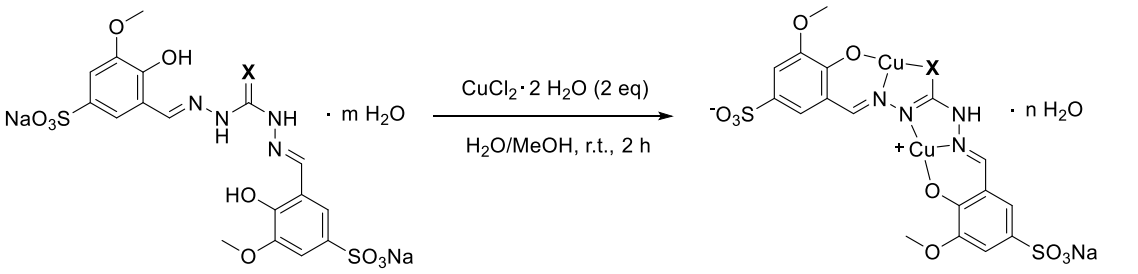

$Na_2H_4L^1$: X = S, m = 5.5
$Na_2H_4L^2$: X = O, m = 5
(1 eq)

Hypothetical structure

(PP17) Cu_2NaHL^1: X = S, n = 7, yield = 33%
(PP19) Cu_2NaHL^2: X = O, n = 7, yield = 87%

Scheme 1.10: Synthesis of the 2:1 Cu^{II}:ligand complexes. Coordinated water molecules are omitted.

In the IR spectrum of **PP19**, the band of C=O stretching falls at 1596 cm^{-1}, indicating that the ligand **AZ26** is coordinated in the **enol** form (Figure 1.37). The elemental analyses suggested that **PP17** and **PP19** have formula **$Cu_2NaHL \cdot n\ H_2O$**, as supported also by ESI mass spectrometry (Figures 1.38 and A1.31) and X-ray diffraction analysis of $[Cu_2(NaHL^1)(H_2O)_7] \cdot 3.5\ H_2O$ (see the crystallography section).

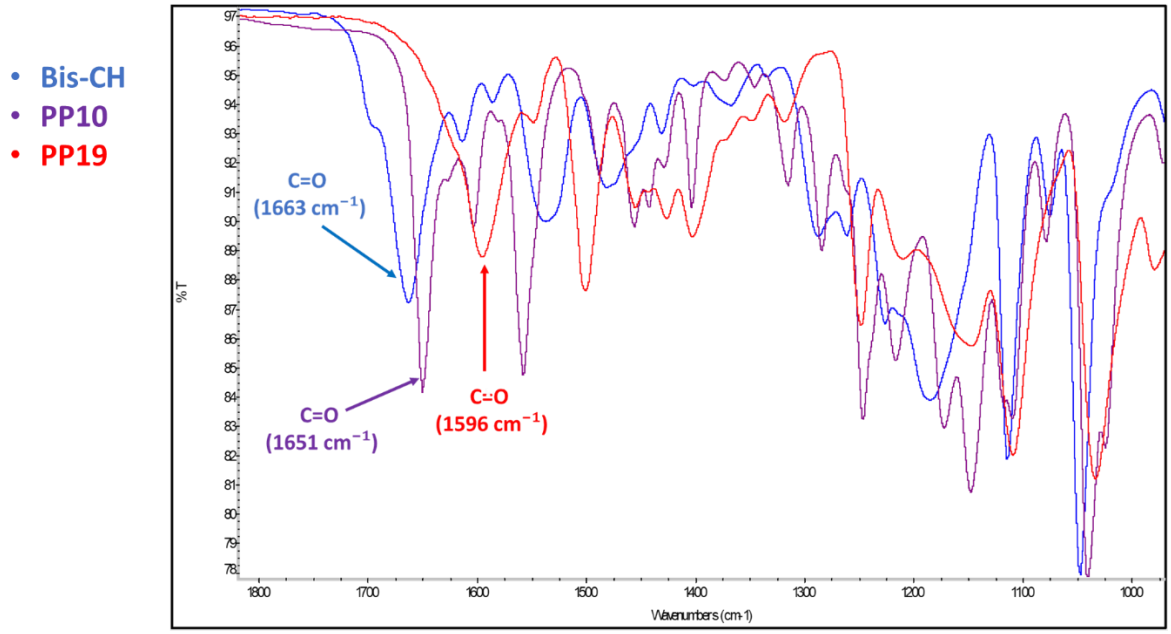

Figure 1.37: Comparison of the FT-IR spectra of **AZ26** (**bis-CH**), **PP10** and **PP19**. It is evident the wavenumber shift of the band associated to the carbonyl group of the ligand upon coordination to one (**PP10**) and two (**PP19**) copper ions.

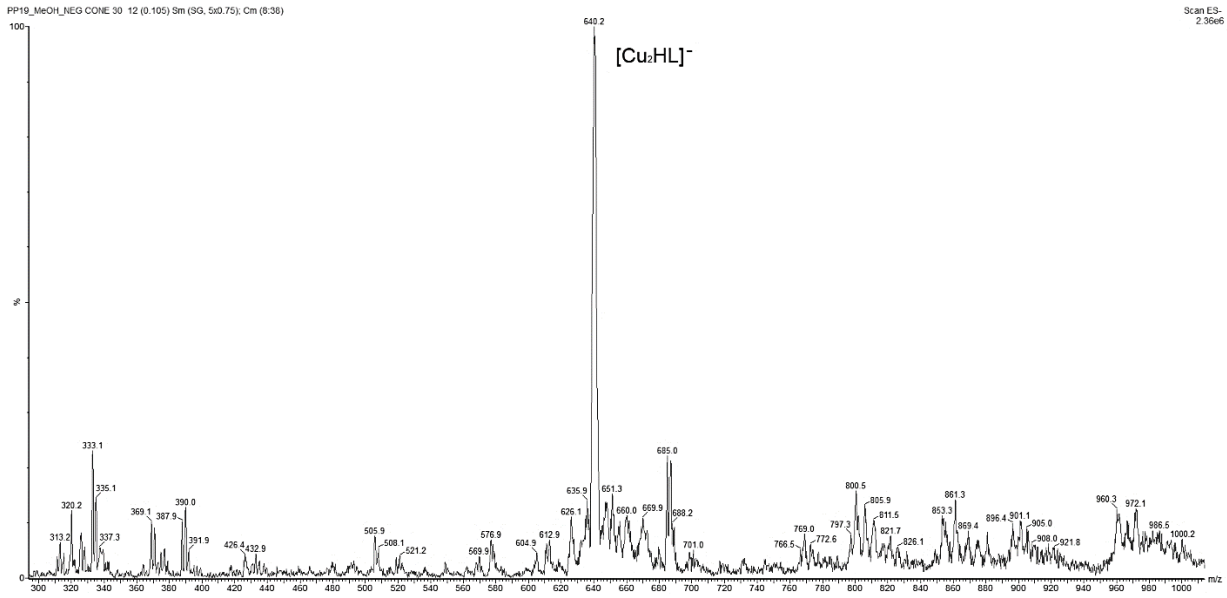

Figure 1.38: ESI-MS spectrum (negative ions) for complex **PP19** in methanol.

The complexes **PP18** and **PP20** were prepared by reacting $Zn(CH_3COO)_2$ respectively with **AZ11** and **AZ26** in a 2:1 metal to ligand ratio (Scheme 1.11).

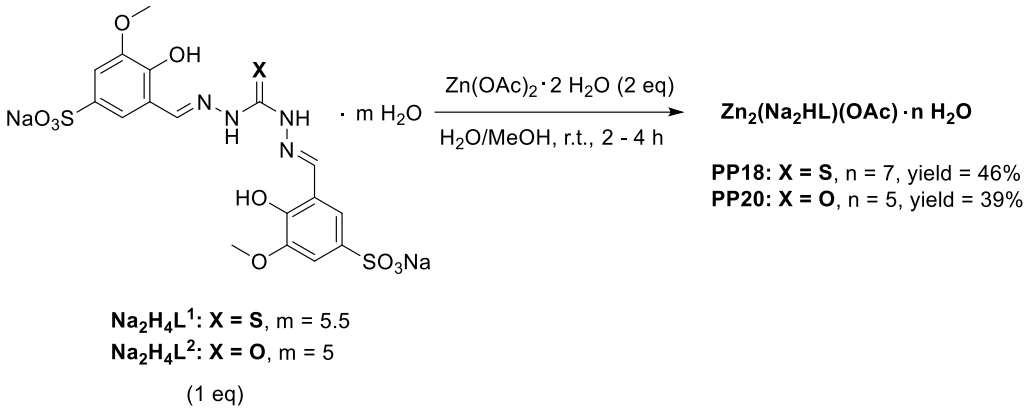

Scheme 1.11: Synthesis of the 2:1 Zn^{II}:ligand complexes.

Like for **PP11** and **PP19**, even for **PP20** the IR spectrum is characterized by a C=O stretching band at lower frequencies with respect to the free ligand (1595 cm^{-1}, Figure 1.39).

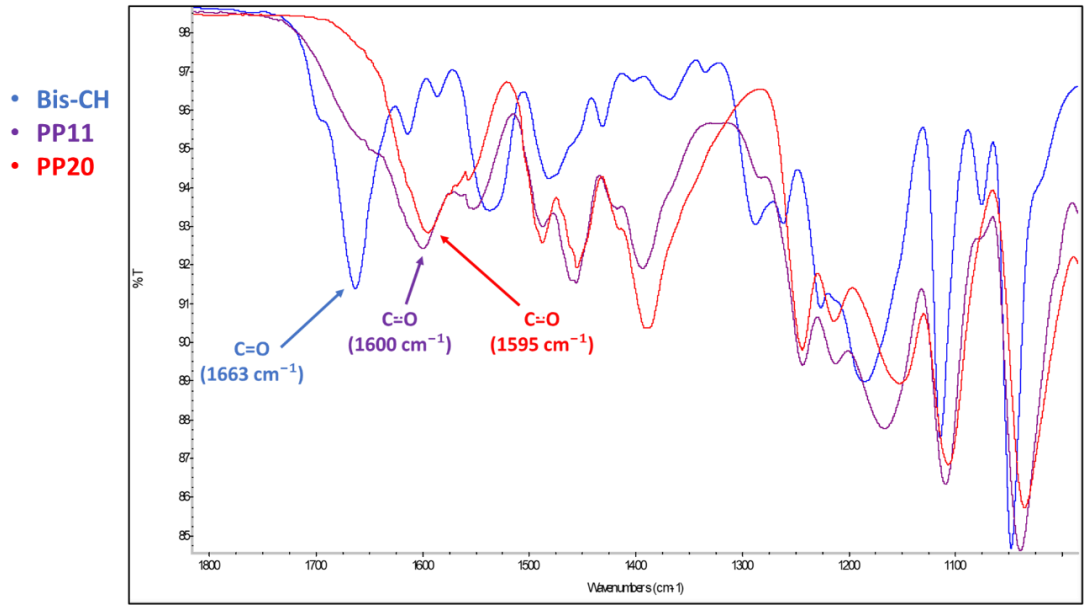

Figure 1.39: Comparison of the FT-IR spectra of **AZ26** (**bis-CH**), **PP11** and **PP20**. It is evident the wavenumber shift of the band associated to the carbonyl group of the ligand upon coordination to one (**PP11**) and two (**PP20**) copper ions.

In the ^1H NMR spectra of both **PP18** and **PP20**, the peak associated to the methyl protons of the acetate group is present (Figures 1.40a and A1.20). As an example, below are reported the ^1H NMR spectrum of complex **PP18** in D_2O (Figure 1.40a) and its comparison with the spectrum of the free ligand **AZ11** in the same solvent

(Figure 1.40b). In D_2O, zinc(II) coordination determines a downfield shift of the imine protons of the ligand, together with the merge of the four aromatic protons peaks into two broad signals (Figure 1.40b).

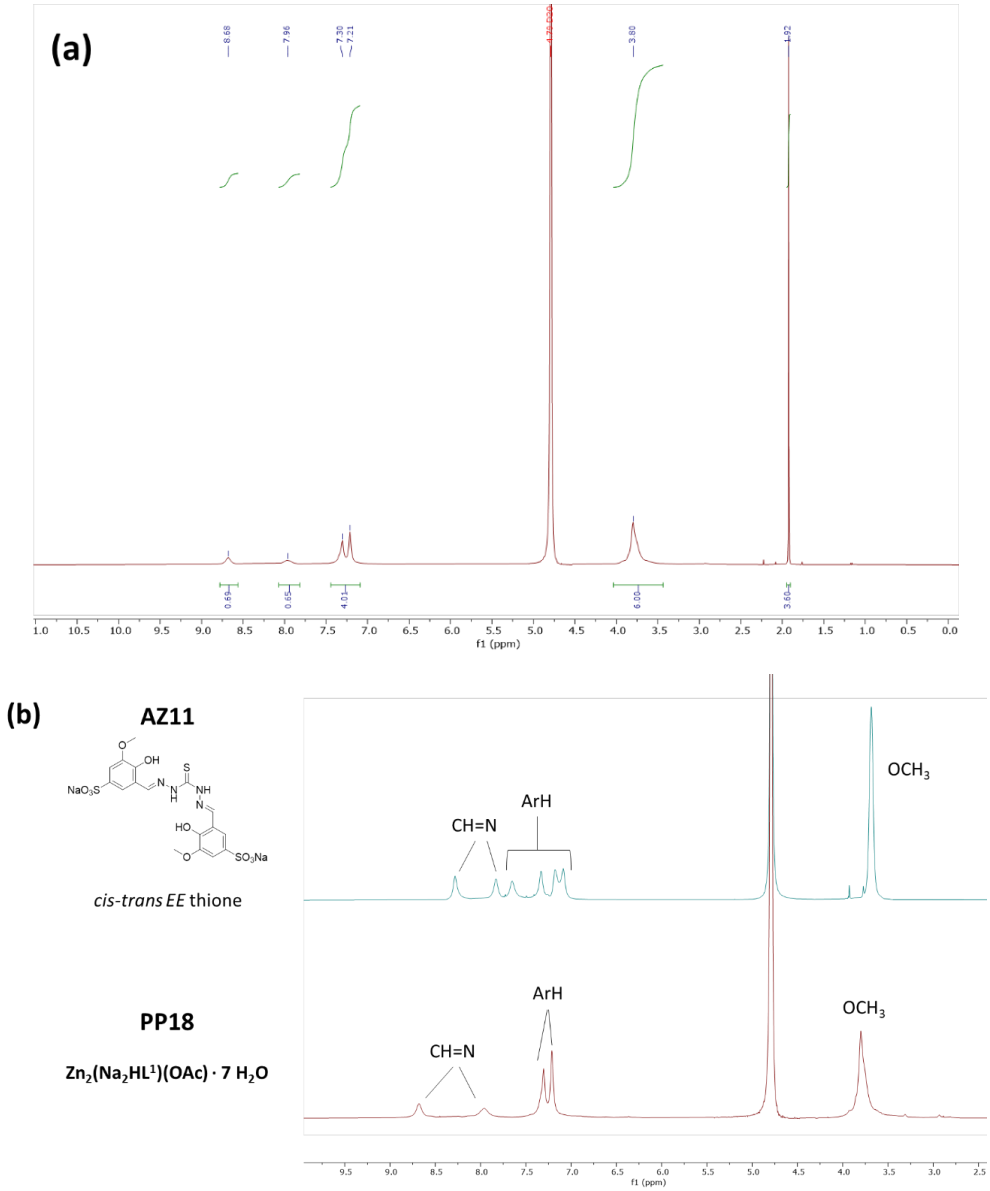

Figure 1.40: (a) ^{1}H NMR (400 MHz) spectrum of **PP18** in D_2O at 298 K. The peak at 1.92 ppm confirms the presence of the acetate ion in the structure of the complex; **(b)** Selected range (2.50 – 10.00 ppm) of the ^{1}H NMR (400 MHz, 298 K) spectra of **AZ11** (top) and **PP18** (bottom) in D_2O.

These results, together with elemental analysis, lead to propose **$Zn_2(Na_2HL)(CH_3COO) \cdot n\ H_2O$** as general formula for **PP18** and **PP20**.

It is relevant to note that the characterization of the complexes **PP17-20** is complicated by their hygroscopic nature.

Crystallography

Slow evaporation of mother liquors of **PP8** led to the formation of dark green crystals of the 2:1 copper(II)/**AZ11** complex $[Cu_2(NaHL^1)(H_2O)_7] \cdot 3.5\ H_2O$. The crystal data (Figure 1.41) reveal a structure in which the **bis-TCH AZ11** coordinates the copper ion in the ***cis–trans*, EE thiolene** form, similarly to what is observed for the complex reported by Dragancea et al.[70] The thiocarbohydrazide fragment shows indeed a thiolic C-S single bond (1.725 Å) and a strongly delocalized π system over the NNCNN system.

The configuration of the ligand allows for a double chelation, one with an ONS and the other with an NNO tridentate system. The ligand is asymmetrically deprotonated and presents a total of five negative charges. In fact, one of the two hydrazidic nitrogen atoms that potentially can undergo deprotonation, even upon chelation remains protonated. These charges agree with the presence of a sodium ion, in addition to the two chelated Cu^{II} ions, for a total of five positive charges.

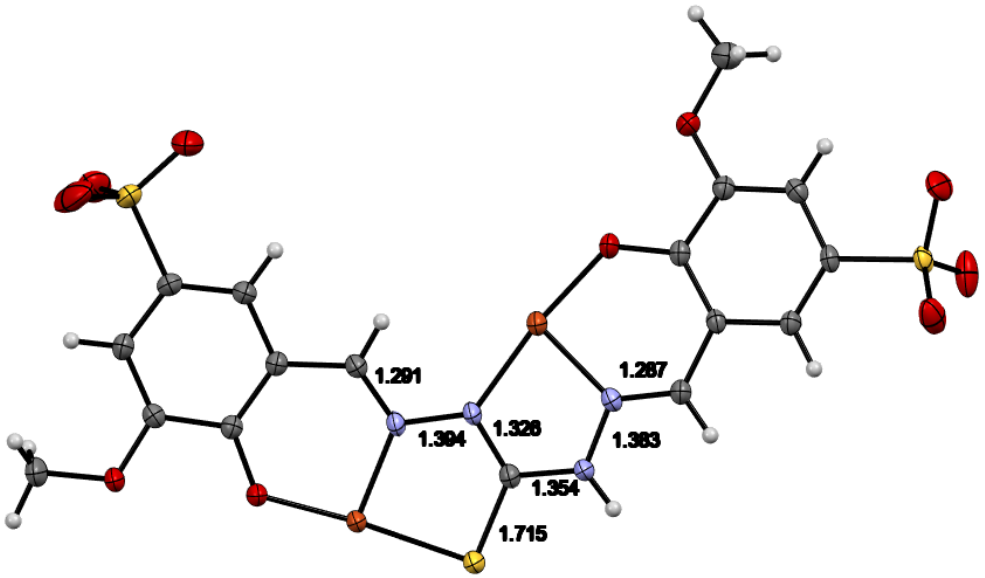

Figure 1.41: Crystal structure of the ligand arranged for chelation of the two copper(II) ions in $[Cu_2(NaHL^1)(H_2O)_7]\cdot 3.5H_2O$ (oxygen atoms in red; sulphur in yellow; nitrogen in blue; carbon in grey and hydrogens in white; copper ions in orange).

The coordination geometries of the two copper atoms are remarkably different (Figure 1.42). The SNO coordinated copper ion presents a more regular square planar coordination with the fourth position of the equatorial plane occupied by a water molecule; a further apical water molecule is found to complete a square pyramidal geometry with a very elongated Cu-O coordination bond (2.458 Å). The other copper atom presents a very distorted geometry that approaches a trigonal bipyramid in which the axial ligands are the three donor atoms from the ligand (NNO), while the two remaining equatorial positions are occupied by two water molecules. The sodium ion coordinates one sulfonate oxygen, two oxygens from the salicylic moiety and three water molecules in a regular octahedral geometry. The bond of sodium with the sulfonate creates in the crystal a head-to-tail system that gives rise to dimers (Figure 1.42).

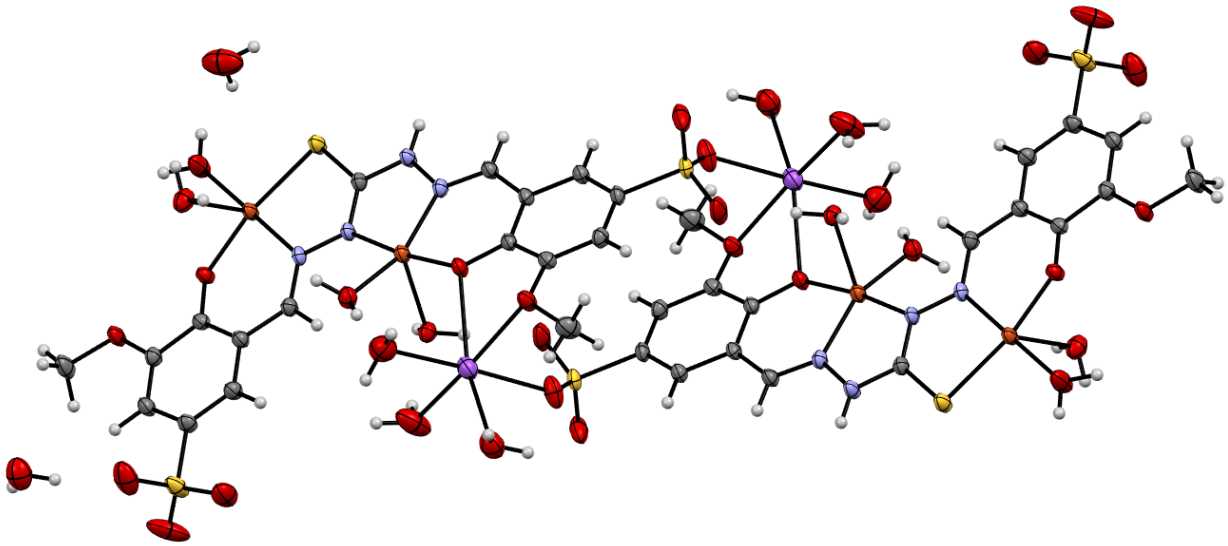

Figure 1.42: The bond of the sodium ion with the sulfonate of one ligand molecule and two oxygens from the salicylic moiety of another ligand molecule gives rise to dimers in the crystal structure of $[Cu_2(NaHL^1)(H_2O)_7] \cdot 3.5\ H_2O$ (oxygen atoms in red; sulphur in yellow; nitrogen in blue; carbon in grey and hydrogens in white; copper ions in orange; sodium ions in purple).

Complexation equilibria in aqueous solution

The complexation equilibria of **bis-TCHs** and **bis-CHs** in solution are poorly investigated in literature. Only Maity and coworkers studied the coordination properties of **bis-TCHs** and **bis-CHs** derived from 8-hydroxyjulolidinal.[99] For such ligands were determined the formation constants of the corresponding 2:1 Cu^{II}:ligand complexes in aqueous medium: logβ values were obtained in the range 13.5 – 14.5, but the authors performed only Job's plots and mass spectrometry experiments to find out the complex stoichiometries and they did not take into account the possibility of forming metal complexes with different stoichiometries.

Below are reported the results obtained from the studies of the complexation equilibria of **AZ11** and **AZ26** with copper(II) and zinc(II) ions in aqueous medium.

Cu^{II}/AZ11 complexation equilibria

The copper(II) complexation equilibria of **AZ11** were studied by means of spectrophotometric titration of the ligand with Cu^{II} in aqueous solution at pH = 2.5 and pH = 7.4. It is worth noting that these titrations, being performed at constant pH, did not allow to establish the protonation state of the ligand but only the possible stoichiometry (Cu/L) of the species. For this reason, in the speciation models L identifies the ligand irrespective of its protonation state, and the charges of the complexes are omitted. Spectral data at pH = 2.5 were collected by titration of **AZ11** (C_L ca. 17 µM) with Cu^{2+} ions, up to a metal:ligand ratio of 5 (Figure 1.43). The two bands at 237 and 318 nm, observed in the spectrum of the free ligand, decrease in absorbance upon addition of Cu^{II}, while the two bands at 259 and 400 nm increase. A thorough examination of the titration data showed that three species are present in solution, the ligand and two complex species.

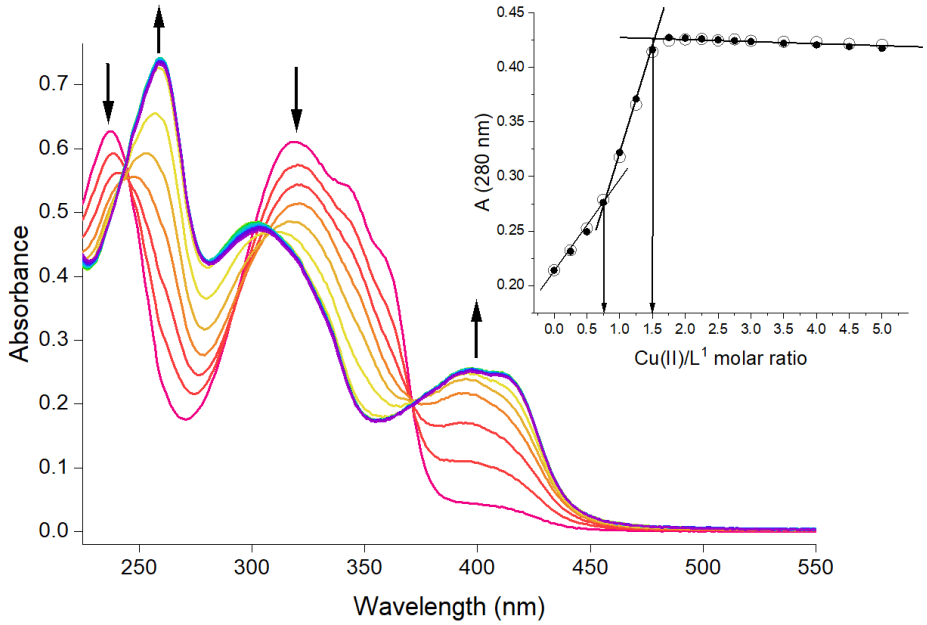

Figure 1.43: UV-visible spectra for the titration of **AZ11** with Cu^{II} in aqueous solution at pH = 2.5 (C_L = 17 µM; Cu^{II}:L = 0-5; I = 3.2 mM HCl). Inset: plot of the observed (circles) and calculated (dots) absorbance values at 280 nm vs Cu^{II}/ligand molar ratio.

Plot of absorbance at 280 nm vs Cu^{II}/ligand molar ratio (Figure 1.43, inset) quite clearly evidenced that two equivalence points are present: one at ca. 0.75 eq. and one at ca. 1.5 eq. of metal added, corresponding to

the formation of $[Cu_3L_4]$ and $[Cu_3L_2]$ species. Data treatment with these two species in the model resulted in the fitting of the curve and the determination of the log β values (Table 1.10): the complex species have a remarkable stability and are already formed at low pH. On the contrary, a model with [CuL] and $[Cu_2L]$ does not allow fitting of the data consistently with the observed Cu/L ratios at the titration end points.

Although in solid state copper(II):**AZ11** complexes with 1:1 and 2:1 stoichiometries were isolated, these species were not observed in solution. This is perhaps not surprising, since the structure of a metal complex in solid state is not necessarily the same observed in solution, where multiple equilibria can be found and where the solvent may be involved in the formation of further species. $[Cu_3L_4]$ species could form in solution taking into account that, in addition to the coordinating possibilities offered by the central skeleton (ONSNO), the ligand has two sulfonic groups that can also behave as binding sites for the metal. Moreover, both the ligands have a great affinity for Cu^{2+} ions, but **AZ11** is more acidic than **AZ26**, and this implies that it coordinates more stably Cu^{II} already at pH 2.5. It will be seen further in the discussion that in the case of **AZ26** at pH = 2.5, the [CuL] species is identified, while, at the same pH, **AZ11** is able to compete more efficiently for the Cu^{2+} ions in solution, and the result is $[Cu_3L_4]$, a species with a higher ligand to metal ratio.

Table 1.10: Logarithms of the conditional formation constants of the Cu^{II} complexes with ligands **AZ11** and **AZ26** in aqueous solution at pH = 2.5 and T = 298.2 K. Standard deviations are reported in parentheses.

	AZ11	**AZ26**
$Log\beta([Cu_3L_4])$	38.6(1)	-
$Log\beta([CuL])$	-	6.26(2)
$Log\beta([Cu_3L_2])$	26.4(1)	-
$Log\beta([Cu_2L])$	-	11.30(2)

Titration spectral data were collected on a solution of **AZ11** (C_L ca. 17 μM) in aqueous 25 mM HEPES buffer at pH 7.4 titrated with Cu^{2+} ions up to a metal:ligand ratio of 3. Figure 1.44 reports the entire spectral set of the titration, together with the plot of the absorbance values at 333 nm with respect to the equivalents of Cu^{II} added to the ligand solution. With the addition of copper(II), the light green colour of the solution turned darker. There are two equivalence points, at ca. 0.75 and 1.5 eq. of Cu^{II} added, which are consistent with the formation of $[Cu_3L_4]$ and $[Cu_3L_2]$ species, as observed at pH 2.5.

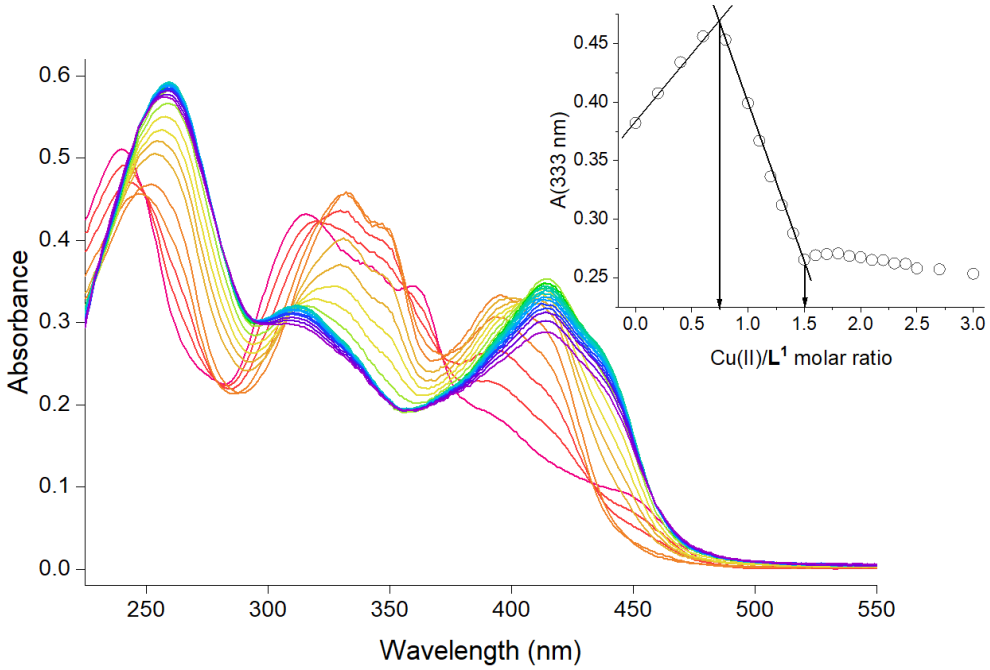

Figure 1.44: UV-visible spectra for the titration of **AZ11** with Cu^{II} in aqueous solution at pH 7.4 (25 mM HEPES buffer, I = 11 mM (Na(HEPES)); C_L = 17 µM; Cu^{II}:L = 0-3). Inset: plot of the observed absorbance values at 333 nm vs Cu^{II}/ligand molar ratio.

The analysis revealed the presence of three families of spectra. The first comprises the spectra collected after addition of copper(II) between 0 and 0.8 equivalents with respect to the ligand (Figure 1.45): we can note the presence of at least six isosbestic points at 250, 280, 321, 357, 371, and 433 nm. We can see the decrease in intensity of the bands at 240, 316, 361 and 448 nm, the formation of bands at 252, 333, 346 nm and the increase in intensity of the band at 396 nm.

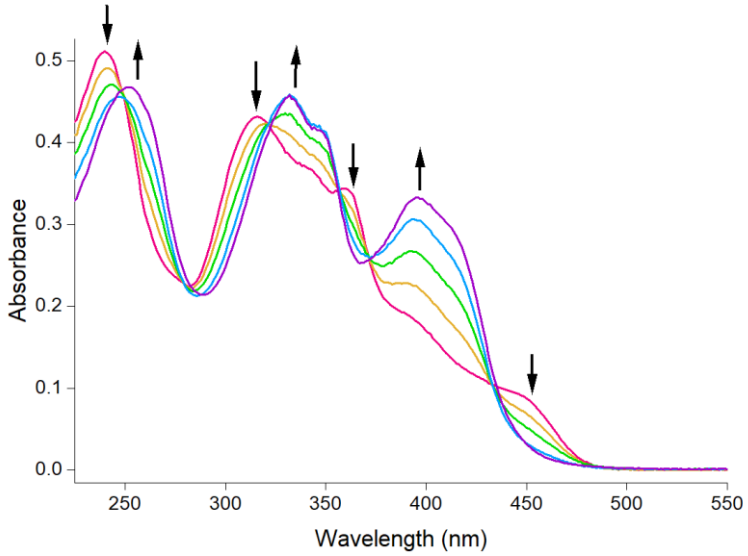

Figure 1.45: UV-visible spectra for the titration of **AZ11** with Cu^{II} in aqueous solution at pH 7.4 (25 mM HEPES buffer, I = 11 mM (Na(HEPES)); C_L = 17 µM; Cu^{II}:L = 0-0.8).

The second group (Figure 1.46) comprises the spectra collected after the addition of copper(II) between 0.8 and 1.5 equivalent. This family is characterized by the presence of three isosbestic points at 232, 310 and 405 nm. The band at 333 nm decreases its intensity while there is an increase of the intensities of the bands at 261 and 415 nm.

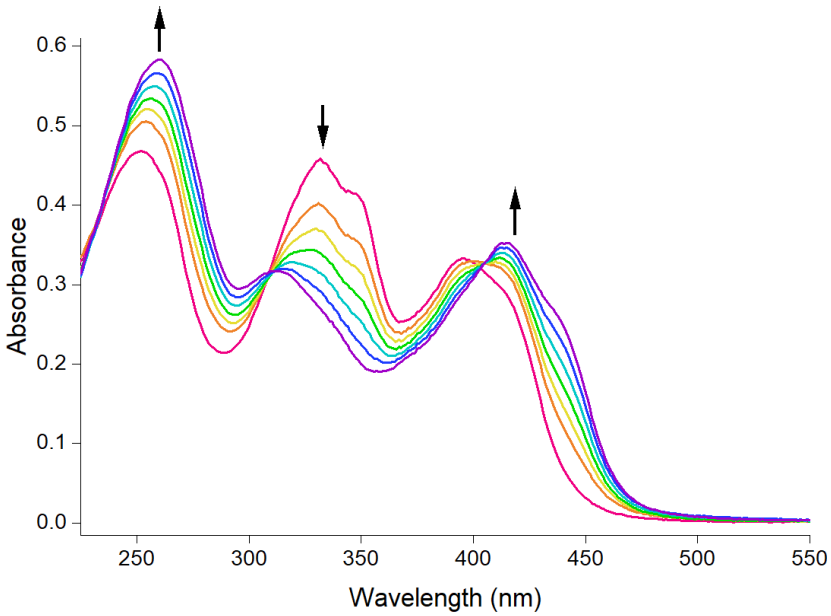

Figure 1.46: UV-visible spectra for the titration of **AZ11** with Cu^{II} in aqueous solution at pH 7.4 (25 mM HEPES buffer, I = 11 mM (Na(HEPES)); C_L = 17 µM; Cu^{II}:L = 0.8-1.5).

The trend in the absorbance after 1.5 eq. of metal cannot be accounted by simple dilution (e.g. the decrease in absorbance at 413 nm after 1.5 eq. of copper(II) added, as shown in Figure 1.47). Therefore, a third family of spectra can be identified (Figure 1.48). These spectra are characterized by the little increase in intensity of the band at 261 nm, the slight decrease of the band at 415 nm, and by the presence of one isosbestic point at 380 nm.

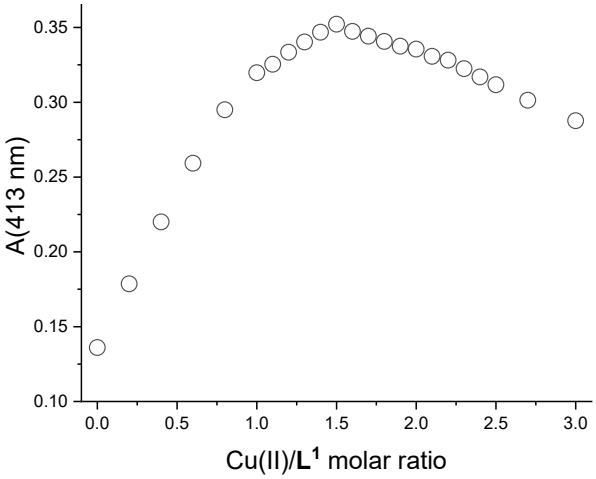

Figure 1.47: Variation of the absorbance at 413 nm and pH 7.4 increasing metal to ligand ratio (ligand = **AZ11**).

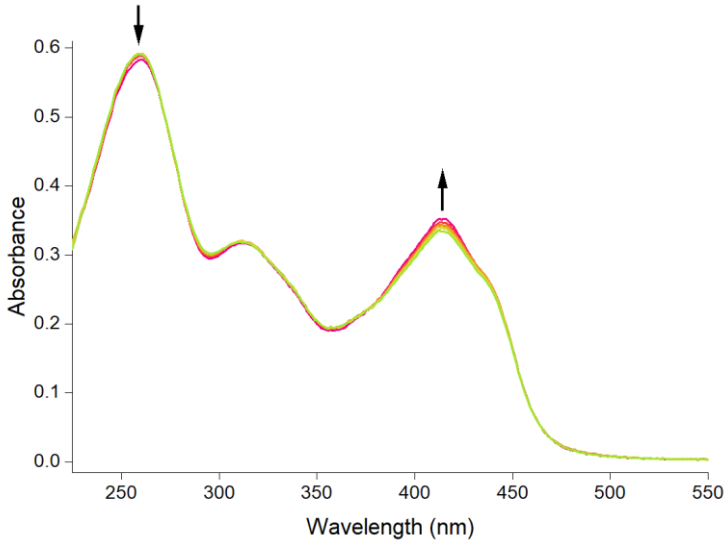

Figure 1.48: UV-visible spectra for the titration of **AZ11** with Cu^{II} in aqueous solution at pH 7.4 (25 mM HEPES buffer, I = 11 mM (Na(HEPES)); C_L = 17 µM; Cu^{II}:L = 1.5-2).

As already stated, the change in absorbance after the addition of 1.5 eq. of Cu^{II} was not accounted by simple dilution effect: we made the hypothesis that in excess of copper(II) a species such as $[Cu_2L]$ can be formed at pH 7.4. Unfortunately, and contrarily to what obtained from data collected at pH 2.5, we could not obtain a reasonable convergence in the log β values. Although a speciation model consisting of the $[Cu_3L_4]$, $[Cu_3L_2]$, and $[Cu_2L]$ species seems reasonable based on the spectral dataset, the steep inflection points in the absorbance values *vs.* metal added (Figure 1.44, inset) suggest that at pH 7.4 the formation constants are too high to be determined.

For an accurate titration, a good general rule is to collect as many data points as possible where the p value is between 0.2 and 0.8. The value of p is defined as the ratio of the complex concentration to the highest possible complex concentration.[111] For a simple system such as M + L = ML, this ensures that the concentrations of all three species involved in the equilibrium are of a similar magnitude.

If this condition is not met, the titration endpoint will be very pronounced, and the experimental data points might fit curves for K values that differ by orders of magnitude. This situation, known as *saturation conditions*, makes it impossible to accurately determine a K value, allowing only a rough estimation of its lower limit. Under *saturation conditions*, the mole ratio method can only be used to determine the stoichiometry of the complex species, not its stability constant.[112]

Cu^{II}/AZ26 complexation equilibria

The copper(II) complexation equilibria of **AZ26** were studied by means of spectrophotometric titrations at pH = 2.5 and 7.4. Again, it is worth noting that titrations conducted at constant pH did not allow to establish the protonation state of the ligand, that is simply reported as L irrespective of its protonation state, but only the possible stoichiometry (Cu/L) of the species. Spectral data at pH = 2.5 were collected by titration of **AZ26** (C_L ca. 17 µM) in acidic solution with Cu^{2+} ions up to a metal:ligand ratio of 7 (Figure 1.49). As observed also with **AZ11**, significant changes in the spectra of the ligand upon addition of copper(II) show that complexes are formed also at this low pH. The best fit of the spectrophotometric data was obtained by considering the formation of [CuL] and [Cu_2L] species, with log β values of 6.26(2) and 11.30(2), respectively (Table 1.10). A representative speciation diagram is reported in Figure A1.21.

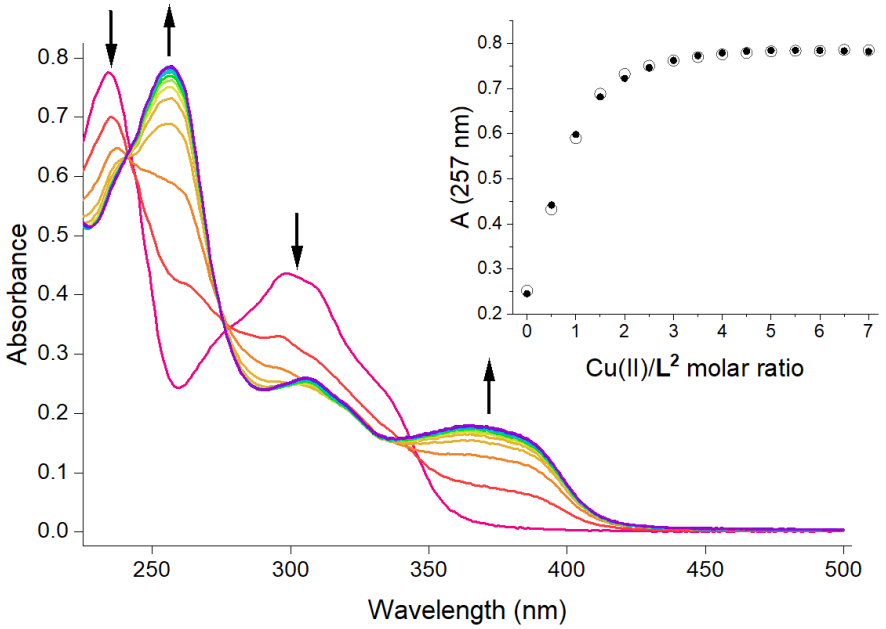

Figure 1.49: UV-visible spectra for the titration of **AZ26** with Cu^{II} in aqueous solution at pH 2.5 (C_L = 17 µM; Cu^{II}:L = 0-7; I = 3.2 mM HCl). Inset: plot of the observed (circles) and calculated (dots) absorbance values at 257 nm vs Cu^{II}/ligand molar ratio.

Spectral data were collected by titration of a solution of **AZ26** (C_L ca. 17 µM) in aqueous 25 mM HEPES buffer at pH 7.4 with Cu^{2+} ions up to a metal:ligand ratio of 3 (Figure 1.50). Differently from data at pH 2.5, these spectral data reveal a steep equivalence point at 1.5 eq. of Cu^{II} *vs.* L (Figure 1.50, inset). This behaviour corresponds to the formation of a predominant complex species of stoichiometry Cu/L 3:2. As for **AZ11**, the presence of this pronounced titration endpoint did not allow to calculate a conditional formation constant for a hypothetical [Cu_3L_2] species.

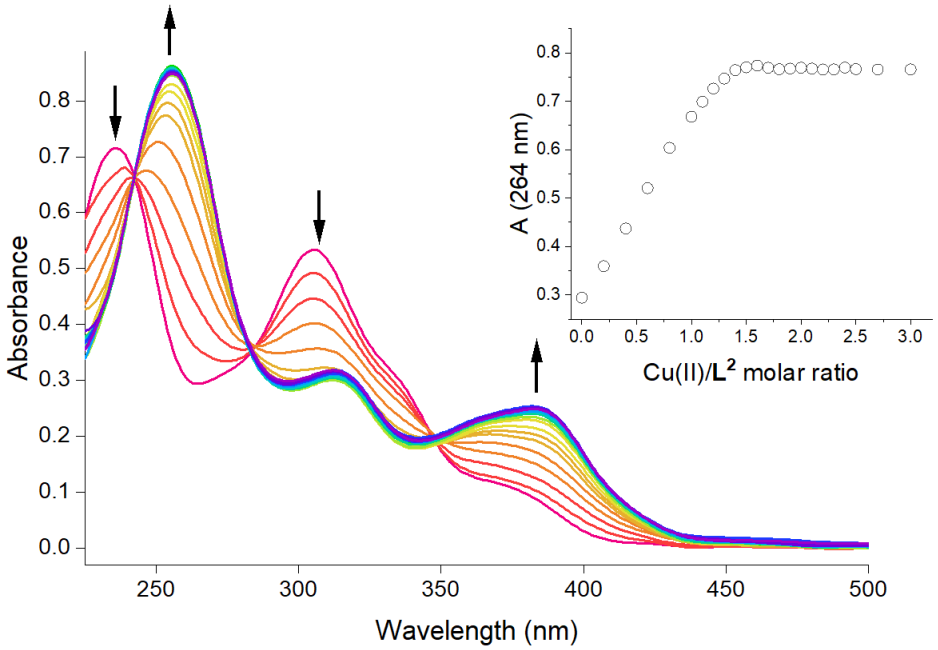

Figure 1.50: UV-visible spectra for the titration of **AZ26** with Cu^{II} in aqueous solution at pH 7.4 (25 mM HEPES buffer, I = 11 mM (Na(HEPES)); C_L = 17 µM; Cu^{II}:L = 0-3). Inset: plot of the observed absorbance values at 264 nm vs Cu^{II}/ligand molar ratio.

Zn^{II}/AZ11 and Zn^{II}/AZ26 complex formation equilibria

A solution of **AZ11** (C_L ca. 17 µM) in aqueous 25 mM HEPES buffer at pH 7.4 was titrated with Zn^{2+} ions up to a metal:ligand ratio of 3 (Figure 1.51).

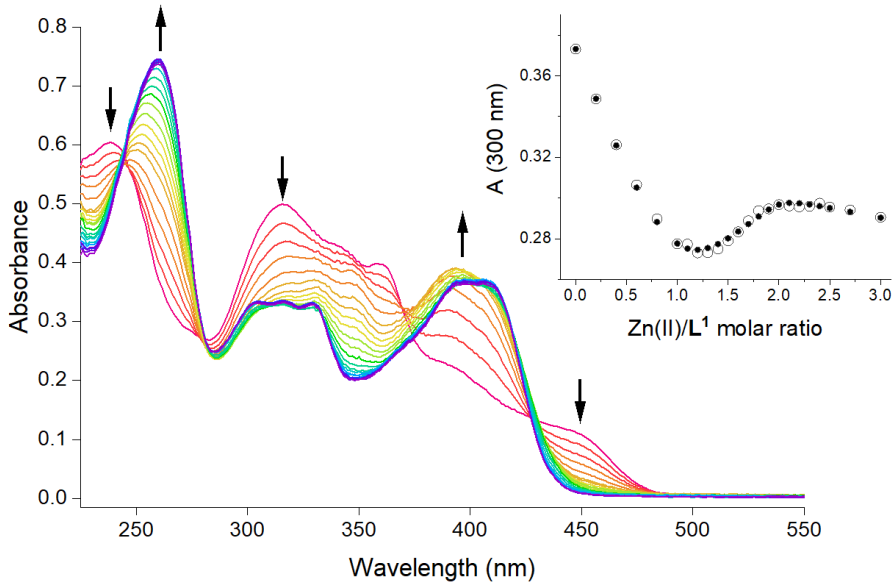

Figure 1.51: UV-visible spectra for the titration of **AZ11** with Zn^{II} in aqueous solution at pH 7.4 (25 mM HEPES buffer, I = 11 mM (Na(HEPES)); C_L = 17 µM; Zn^{II}:L = 0-3). Inset: plot of the observed (circles) and calculated (dots) absorbance values at 300 nm vs Zn^{II}/ligand molar ratio.

The best fit was obtained using a speciation model that consists of the sequential formation of a monometallic [ZnL] and a bimetallic [Zn_2L] species. In fact, two families of spectra were observed, according to the presence in solution of two complex species and the free ligand. A first family of spectra (Zn/L = 0 - 1) (Figure 1.52) is characterized by a decrease in intensity for the bands of the free ligand at 239, 315 and 450 nm, and the appearance of bands at 251 and 394 nm. There are four isosbestic points at 245, 280, 371 and 429 nm.

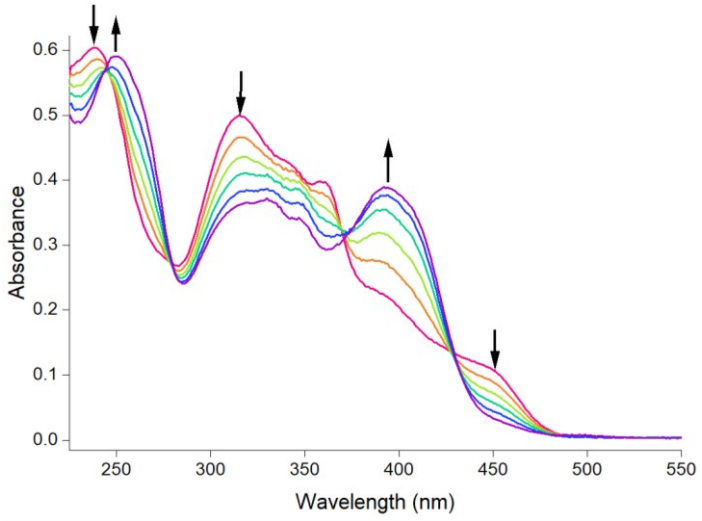

Figure 1.52: UV-visible spectra for the titration of **AZ11** with Zn^{II} in aqueous solution at pH 7.4 (25 mM HEPES buffer, I = 11 mM (Na(HEPES)); C_L = 17 µM; Zn^{II}:L = 0-1).

A second family of spectra (Zn/L = 1 - 2) (Figure 1.53) presents red shift and increase in absorbance of the band at 251 nm, the disappearance of the band at 349 nm, and red shift with decrease of absorbance of the band at 394 nm.

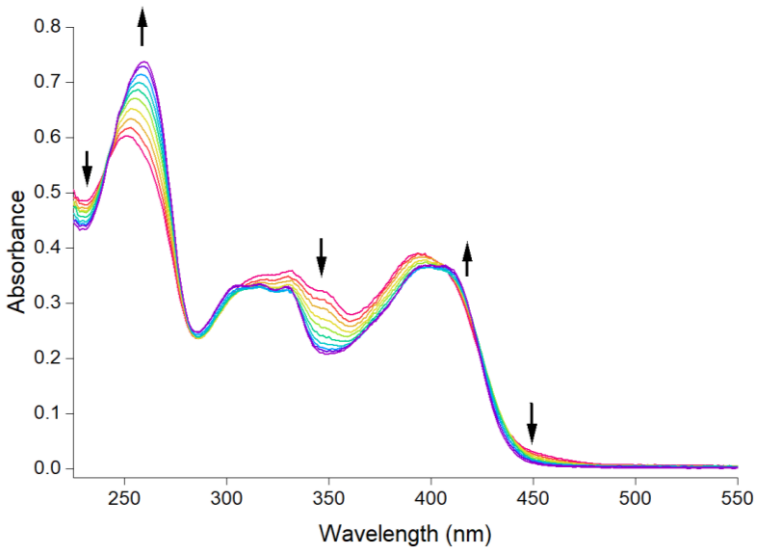

Figure 1.53: UV-visible spectra for the titration of **AZ11** with Zn^{II} in aqueous solution at pH 7.4 (25 mM HEPES buffer, I = 11 mM (Na(HEPES)); C_L = 17 µM; Zn^{II}:L = 1-2).

A plot of the absorbance values at 300 nm clearly shows the two equivalence points at 1 and 2 eq. of metal *vs.* ligand, consistent with the formation of [ZnL] and [Zn_2L] species (Figure 1.51, inset). The elaboration of the spectrophotometric data furnished a value of the Logβ([ZnL]) which is quite high (8.40 ± 0.06), as confirmed by the pronounced endpoint at 1 equivalent of added metal (Figure 1.51, inset). This means that binding occurs under saturation conditions and this does not allow an accurate determination of the formation constant: the obtained value can only be regarded as an estimate. The estimated log β values for the formation of zinc(II) complexes with **AZ11** are shown in Table 1.11, and a representative distribution diagram is reported in Figure A1.22.

Table 1.11: Logarithms of the conditional formation constants of the zinc(II) complexes with the ligands in aqueous 25 mM HEPES buffer at pH 7.4 and at 25°C. Standard deviations are reported in parentheses.

	AZ11	**AZ26**
Logβ([ZnL])	8.40(6)	7.08(3)
Logβ([Zn_2L])	15.29(10)	13.61(4)

The same study was undertaken with **AZ26**: titration of the ligand (C_L ca. 17 µM) was performed in aqueous 25 mM HEPES buffer at pH 7.4 with Zn^{2+} ions up to a metal:ligand ratio of 3 (Figure 1.54).

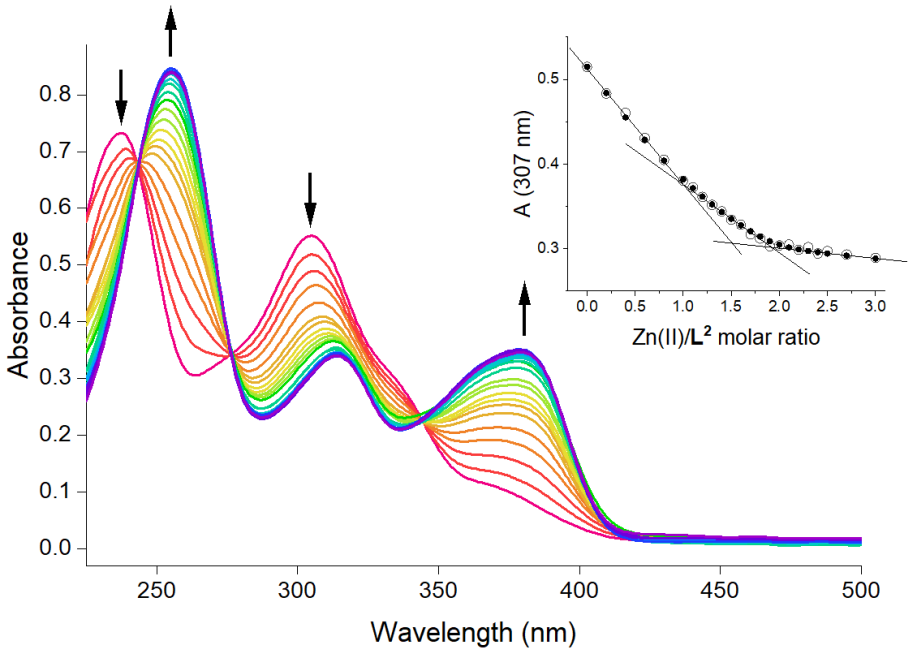

Figure 1.54: UV-visible spectra for the titration of **AZ26** with Zn^{II} in aqueous solution at pH 7.4 (25 mM HEPES buffer, I = 11 mM (Na(HEPES)); C_L = 17 µM; Zn^{II}:L = 0-3). Inset: plot of the observed (circles) and calculated (dots) absorbance values at 307 nm vs Zn^{II}/ligand molar ratio.

The spectra are characterized by four bands at *ca.* 238, 255, 305 and 371 nm, those at 255 and 371 nm increasing in intensity with the addition of metal ions. The presence of these separated absorption bands led to the observation of three apparent isosbestic points at 243, 276 and 345 nm. Analogously to the Zn^{II}/**AZ11** system, the best fit was obtained using a speciation model that consists of the sequential formation of a monometallic [ZnL] and a bimetallic [Zn_2L] species. In the inset of Figure 1.54, the absorbance values at 307 nm are reported as a function of the equivalents of added zinc(II). The absorbance trend presents two almost linear regions between 0 and 1 eq. of zinc(II), and between 1 and 2 eq., respectively. This is in fact consistent with the sequential formation of two species with Zn:L ratio 1:1 and 2:1, respectively. The calculated log β values are reported in Table 1.11 and a representative distribution diagram in Figure A1.23. Overall, the comparison of the log β values for the formation of zinc(II) complexes with **AZ11** and **AZ26** indicate that the former gives rise to more stable complexes (*ca*. 1.5 log units for both species). This behaviour is perhaps expected taking into account the softer nature of the thiocarbohydrazonic group.

Overall, the stability of the copper(II) complexes is higher than those of zinc(II); in fact, the conditional constants of the former ion are too high to be determined at pH 7.4. This is in line with the Irving‑Williams series, which predicts higher stability constants for Cu^{II} compared to Zn^{II}.

Stability of ligands and complexes in simulated physiological conditions

UV-visible absorption measures were performed to investigate the stability of both ligands and complexes at room temperature in DPBS (Dulbecco's Phosphate Buffered Saline) 1x without Ca^{2+} and Mg^{2+}, that is the medium used to solubilize the compounds in the biological assay (see next section). Its composition is: 0.2 g/L KCl, 0.2 g/L KH_2PO_4, 8.0 g/L NaCl and 1.15 g/L Na_2HPO_4 (with the pH adjusted to 7.0 - 7.1 using HCl).[113]

The spectra were measured immediately after the preparation of the working solutions, and then after 1, 24, 48, 72 hours and 1 week (Figures 1.55-57). During the time between two consecutive measures, the samples were stored at room temperature in the dark.

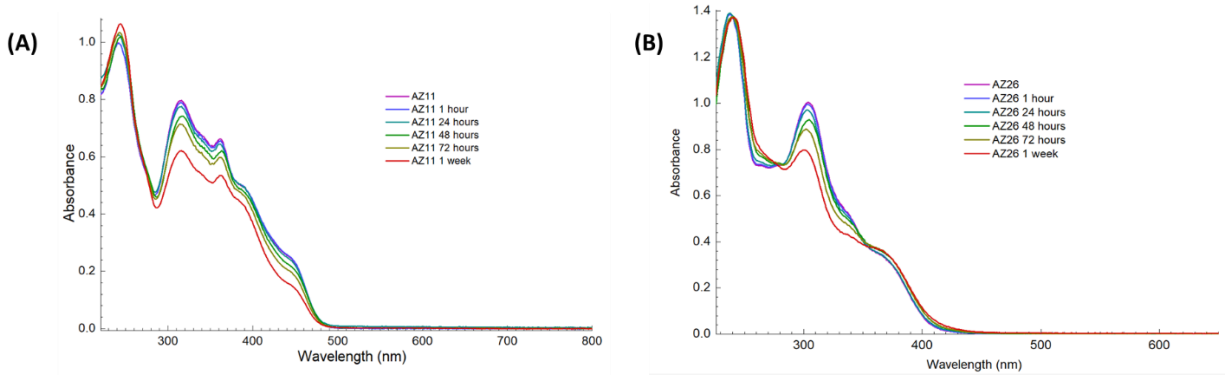

Figure 1.55: UV-visible spectrum of (A) a 17 µM solution of **AZ11** and (B) a 18 µM solution of **AZ26** in DPBS at room temperature over time.

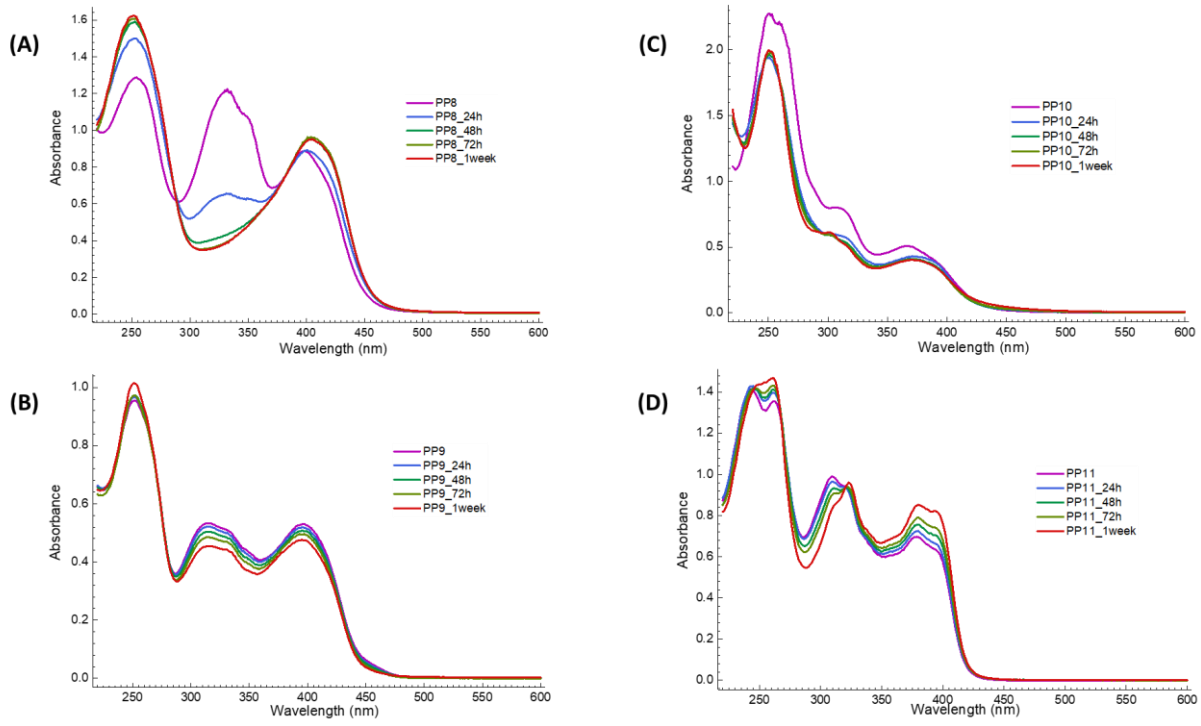

Figure 1.56: UV-visible spectrum of (A) a 35 µM solution of **PP8**, (B) a 42 µM solution of **PP9**, (C) a 33 µM solution of **PP10** and (D) a 40 µM solution of **PP11** in DPBS at room temperature over time.

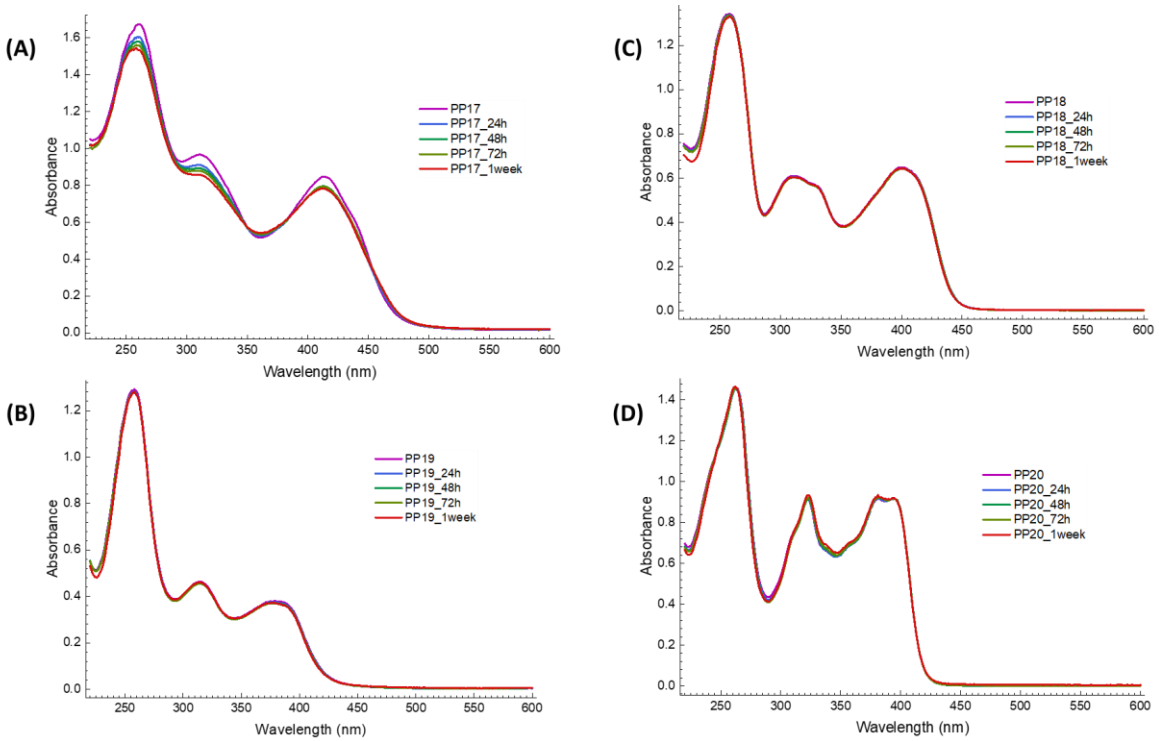

Figure 1.57: UV-visible spectrum of (A) a 45 µM solution of **PP17**, (B) a 32 µM solution of **PP18**, (C) a 25 µM solution of **PP19** and (D) a 28 µM solution of **PP20** in DPBS at room temperature over time.

The absorption spectra of the two ligands remain almost unchanged after 24 hours. After that time, significant variations in their spectra are detected and it is possible to note the presence of isosbestic points (Figure 1.55). This result suggests that in phosphate buffer there is a change in the ligand isomers population over time. Probably, the high ionic strength of the solution strongly affects the conformational dynamics of **AZ11** and **AZ26**. This may be the reason also for the variations observed in the spectra of the 1:1 metal to ligand complexes over time (Figure 1.56).

On the contrary, the 2:1 metal to ligand complexes showed good stability in the medium over time (Figure 1.57). Probably, chelation of two metal centres freezes the conformational dynamics of the ligands and hinders their interaction with buffer ions.

Cytotoxicity against U937 and Hs27 cell lines

The antiproliferative profile of the ligands **AZ11** and **AZ26** and of the complexes **PP8 - 11** was investigated in collaboration with the group of Prof. Annamaria Buschini at the Centre for Molecular and Translational Oncology of the University of Parma, by using a normal fibroblast cell line (Hs27) and leukemia cell line U937, an *in vitro* cell model system systematically used to validate the toxicological profile of new potential anticancer agents.[114,115] For the cytotoxicity assay, Hs27 and U937 cells were treated with five different concentrations of compound, ranging from 12.5 to 100 µg/mL, for 24, 48 and 72 hours.

In a first attempt, the MTS assay was used to evaluate the *in vitro* antiproliferative activity of the compounds. The MTS assay is a colorimetric method for determining the number of viable cells in proliferation or cytotoxicity assays, based on the use of tetrazolium compound 3-(4,5-dimethylthiazol-2-yl)-5-(3-carboxymethoxyphenyl)-2-(4-sulfophenyl)-2H-tetrazolium inner salt or MTS. The yellow MTS tetrazolium compound is bio-reduced by cells into a brown formazan product that is soluble in tissue culture medium (Figure 1.58, top).[116] This conversion is probably accomplished by NADPH or NADH produced by dehydrogenase enzymes in metabolically active cells.[117] The assay is performed by adding a small amount of the reactive directly to culture wells, incubating for 1 – 4 hours and then recording the absorbance at 485 nm with a 96-well plate reader. The quantity of formazan product as measured by absorbance at 485 nm is directly proportional to the number of living cells.

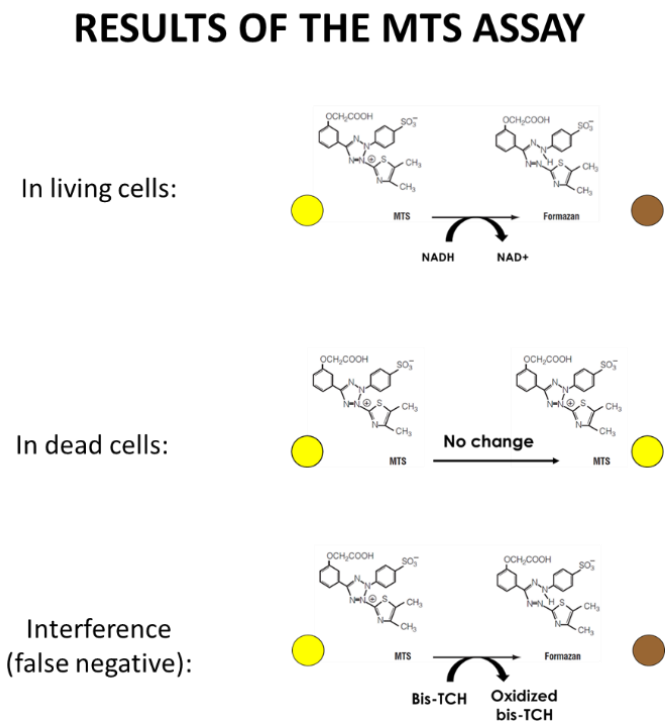

Figure 1.58: Results of the MTS assay in case of living cells (top), dead cells (middle) and interference of the tested compound with the reactant (bottom).

Unfortunately, it was found that all of our tested compounds interfered with the MTS reagent, probably due to their redox activity. Indeed, in the assay, all the wells that contained the cells treated with the ligands and the complexes showed brown coloration (indicative of formazan production). In addition, extensive formation of bubbles was detected in the wells, which prevented a correct reading of the absorbance values. To make sure that the cause for such results was effectively interference of the tested compounds, the MTS assay was

repeated on solutions that contained only the tested compounds and no cells: also in this case, the formation of the formazan was observed (Figure 1.58, bottom).

Consequently, the antiproliferative activity was evaluated by means of the Trypan blue assay, which implies the manual count of cells through Bürker chamber. In this assay, cells are suspended in PBS containing Trypan blue and then examined with a transmission microscope to determine the percentage of cells that have clear cytoplasm (viable cells) *versus* cells that have blue cytoplasm (non-viable cells).[118] It should be stressed that the use of Trypan blue is likely to underestimate the toxicity of the compounds, because it only detects the cells with ruptured membrane, while the cells can be non-functional still retaining the intact membrane.

The dose-response curves (Figure 1.59) showed that the **bis-TCH AZ11** was able to induce a growth inhibition effect between 40% and 45% in both cell lines in a dose- and time-dependent manner, and for U937 cell line it was able to cause a 50% reduction in cell viability only at the highest dose after 72 h of treatment. The **bis-CH AZ26** did not produce a reduction in cell viability in normal Hs27 cells but revealed mild antiproliferative activity after 72 h of application to U937 cancer cells (GI_{50} = 46.5 ± 4.94 µg/mL) (Figure 1.59, right). The coordination of copper(II) ions increased the toxicity of the compounds. The dose-response curves of **PP8** showed an important increase in cytotoxic effect on both cell lines. Particularly, in U937 cancer cells, a growth inhibition of 70% was achieved already at 24 h of treatment (Figure 1.59, right). The dose-response curves of **PP10** showed a high reduction of proliferation, comparable in the two cell lines, that was also dose- and time-dependent. In contrast, zinc(II) coordination was not able to increase the cytotoxic activity of the two ligands (Figure A1.30). The GI_{50} values are reported in µg/mL in Table 1.12 (they are also reported in µM in Table A1.5).

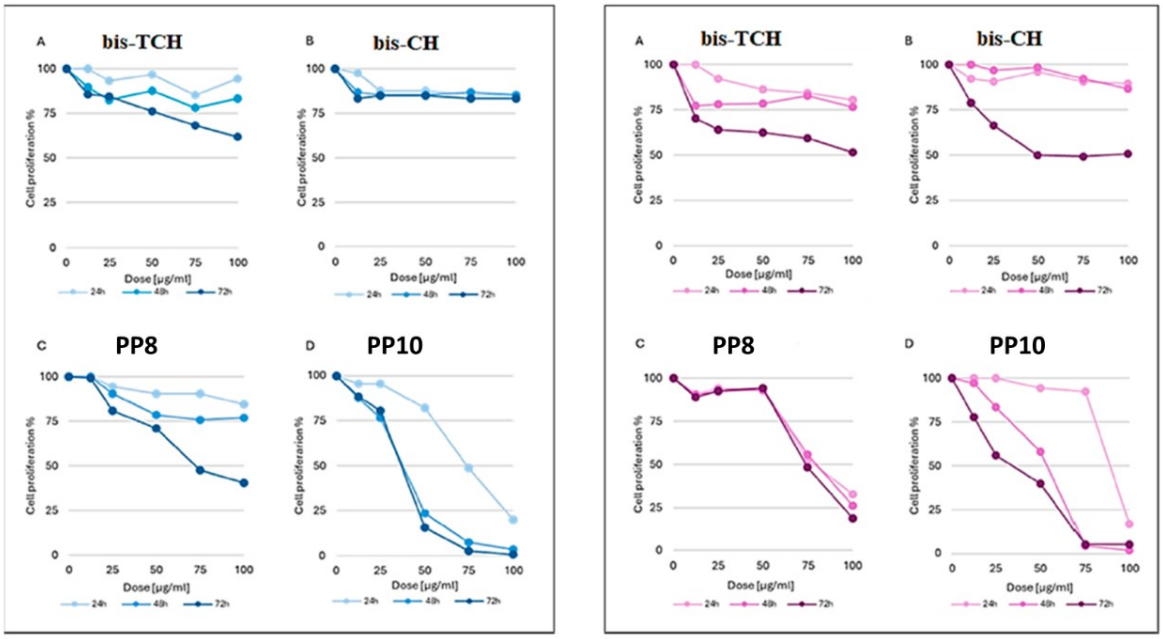

Figure 1.59: Dose-response curves obtained on Hs27 (left) and U937 cells (right) after 24, 48 and 72 h treatment with (A) **bis-TCH (AZ11)**; (B) **bis-CH (AZ26)**; (C) **PP8**; (D) **PP10**. Data are expressed as cell proliferation percentage in comparison with control cells.

Table 1.12: GI_{50} values (µg/mL) obtained in Hs27 and U937 cell lines after 24, 48, and 72 h treatment with the two ligands (**bis-TCH AZ11** and **bis-CH AZ26**) and the complexes **PP8-11**.

Compound	GI_{50} Value (µg/mL)					
	Hs27			U937		
	24 h	48 h	72 h	24 h	48 h	72 h
bis-TCH	-	-	-	-	-	98.00 ± 2.82
bis-CH	-	-	-	-	-	46.50 ± 4.94
PP8	-	-	69.50 ± 3.18	78.50 ± 6.36	82.75 ± 0.35	76.50 ± 2.12
PP10	74.25 ± 11.66	38.00 ± 4.94	36.50 ± 0.71	89.75 ± 0.35	53.50 ± 4.24	34.25 ± 10.25
PP9	-	-	91.00 ± 7.77	-	-	-
PP11	-	-	-	-	-	-

The antiproliferative properties of the 2:1 metal:ligand complexes **PP17-20** on leukemia U937 cells were also studied. In this case, the Luminescent cell viability assay with CellTiter-Glo® 2.0 kit was performed.

The assay determines the number of viable cells in a culture by quantification of ATP. The test is based on the mono-oxygenation of luciferin, a reaction catalysed by the luciferase enzyme in the presence of Mg^{2+}, ATP (produced by metabolically active cells), and molecular oxygen (Figure 1.60). The result is the generation of a stable luminescent signal.[119]

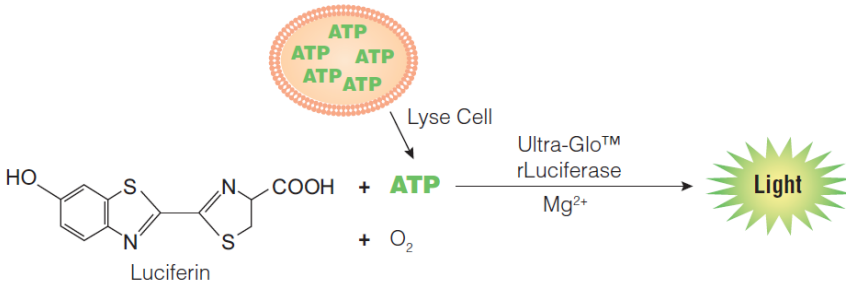

Figure 1.60: Schematic representation of the CellTiter-Glo® 2.0 reaction. Adapted from Ref.[119]

For the cytotoxicity assay, U937 cells were treated with five different concentrations of compounds, ranging from 12.5 to 100 µM, for 24, 48 and 72 hours. Unfortunately, the complexes induced only a negligible growth inhibition on cancer cells: the best result was obtained with the bis-CH copper(II) complex **PP19**, which showed a growth inhibition effect around 40% after 72 h treatment at 75 µM concentration (Figure 1.61). However, for none of the 2:1 metal:ligand complexes was possible to determine a GI_{50} value.

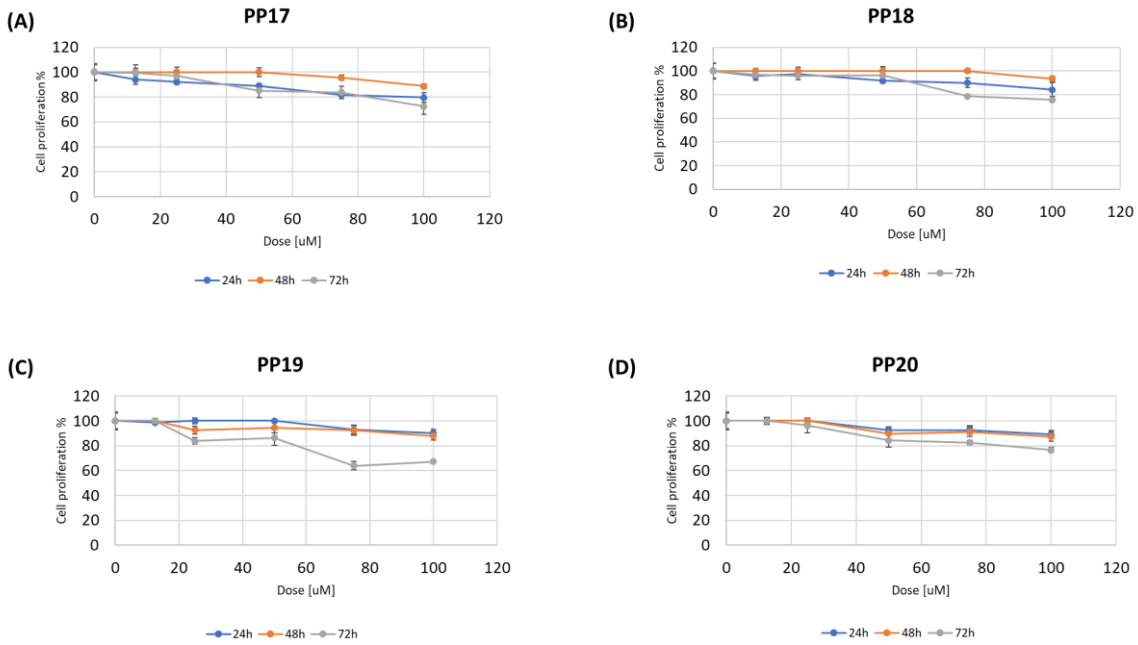

Figure 1.61: Dose–response curves obtained on U937 cells after 24, 48 and 72 h treatment with (A) **PP17**; (B) **PP18**; (C) **PP19**; (D) **PP20**. Data are expressed as cell proliferation percentage compared with control cells.

Overall, the 1:1 metal:ligand complexes proved to be the most cytotoxic, with the copper(II) derivatives showing higher activity compared to the zinc(II) ones. Unfortunately, even for the most active compound **PP10**, the effect on cancer cells can be considered only mildly antiproliferative. In addition, although the study was limited to two cell lines, the compounds were not selective towards U937 cancer cells and induced growth inhibition also in the normal Hs27 cells.

Conclusions

The **bis-TCHs** and the **bis-CHs** are ligands with a broad spectrum of coordination properties and promising biological activities, but they are much less investigated compared to the well-known **TSCs** and **SCs**. Prompted by the potentialities of these classes of ligands, two sulfonated symmetrical **bis-TCH** and **bis-CH** (**AZ11** and **AZ26**, respectively) were synthesized and investigated in this project. They proved to be species highly soluble in aqueous medium, differently to the great majority of ligands of the same class reported in the literature.

This study focused first on the complete characterization of the behaviour of the ligands in solution, both in terms of conformational dynamics and acid-base properties. An integrated theoretical‑computational and NMR investigation on **AZ11** and **AZ26** in a non-protic solvent (DMSO) was performed and unravelled the presence of the two compounds in solution as keto tautomers and *cis‑trans EE* isomers, characterized by a significant conformational freedom at room temperature. The presence of oxygen or sulfur heteroatoms can tune the molecular conformational dynamics driving also a different interaction with the solvent. A study of the protonation processes of the ligands was also carried out in aqueous medium by means of spectrophotometric and potentiometric techniques.

The coordination properties of the ligands towards Cu^{II} and Zn^{II} were studied in aqueous solution by means of UV-visible spectrophotometric titrations: it was found that **AZ11** and **AZ26** are chelators able to complex Cu^{II} ions already at low pH, giving rise to mono- and polymetallic complexes. Both copper(II) and zinc(II) ions showed a thermodynamic preference for **AZ11** with respect to **AZ26**: this finding is consistent with the intermediate to soft nature of the two studied metal ions.

The mono-metallic and bi-metallic complexes of copper(II) and zinc(II) with the two ligands were isolated and all of them showed good solubility in water. The elucidation of the binding mode of the ligands in the 2:1 metal:ligand complexes was possible thanks to the X-ray diffraction analysis of $[Cu_2(NaHL^1)(H_2O)_7]\cdot 3.5H_2O$. The crystal data revealed a structure in which **AZ11** coordinates the copper ions in the *cis–trans*, EE thiolene form and with two different sets of donor atoms, O,N,S and N,N,O.

We were aware that the introduction of the sulfonic groups in the ligand molecular skeleton could limit the cytotoxicity of the new compounds, for example by limiting their ability to cross the cell membrane, but it was reasonable to suppose that the formation of the metal complex, by increasing lipophilicity, could mitigate these possible negative effects. Preliminary cytotoxicity measurements with 1:1 metal:ligand complexes **PP8-11** seem to confirm this hypothesis: the copper(II) complexes showed a cytotoxicity that is decidedly higher than that of the corresponding free ligands. However, these values are modest compared to the nanomolar activity presented by some copper(II) thiosemicarbazone complexes.[44] It is worth noting that, due to interference with MTS, the results of antiproliferative activity were obtained by the Trypan blue assay, which is likely to underestimate the toxicity of the tested compounds.

Another point that deserves consideration is that the most cytotoxic complex **PP10** was obtained from the **bis-CH AZ26** and not from the **bis-TCH AZ11**, a result that is consistent with some literature data on similar systems.[92] It is a widely shared opinion that once Cu^{II} ion is transported inside the cell as a complex, it is reduced to Cu^{I} and then it produces its activity. Thinking about the remarkably high affinity of **AZ11** for copper(II), which we have identified by means of the solution studies, it is possible that in the case of **PP8** the reduction of the metal ions by the endogenous reductants is difficult, leading to a limited activity compared to **PP10**; however, at this point of the research, this remains only an intriguing hypothesis.

Overall, in contrast to the Cu^{II} complexes, the Zn^{II} ones showed only a negligible antiproliferative activity. This finding is in agreement with many studies in literature: in comparison with analogous Cu^{II} or other bivalent metal complexes, the zinc derivatives often resulted much less potent, probably because the very small changes in zinc concentration due to drug uptake are not enough to trigger a strong antitumour effect.

Finally, based on these results, it is possible to conclude that the introduction of two sulfonic groups in the scaffold of bis-(aldehyde)chalcogencarbohydrazones is likely to limit their bioactivity, at least as anticancer compounds. Nevertheless, the insertion of one sulfonic group in the **TSC** scaffold allowed to obtain systems with higher selectivity towards cancer cells. In this context, future work may be focused on the synthesis and biological investigation of asymmetrical bis-chalcogencarbohydrazones bearing only one sulfonic group and their copper(II) complexes.

Experimental section

Chemistry

Materials and methods

Commercial reagents were purchased from Sigma-Aldrich. The purity of the synthesized compounds was determined by elemental analysis and verified to be ≥ 95%. ^{1}H, ^{13}C and 2D NMR spectra were recorded at 25°C on a Bruker Advance 400 MHz FT spectrometer. The ATR-IR spectra were recorded by means of a Perkin Elmer spectrophotometer by using a diamond crystal plate in the range of 4000-400 cm^{-1}. Elemental analyses were performed by using a Thermo Fisher FlashSmart CHNS/O analyser with gas-chromatographic separation. Thermogravimetric analysis (TGA) was performed with a PerkinElmer TGA 8000 instrument (mass sample: 1 – 3 mg), under an atmosphere of air in the temperature range 30–300 °C, at 10 °C/min. Electrospray ionization mass spectral analyses (ESI-MS) were performed with an ESI time-of-flight Micromass 4LCZ spectrometer and the samples were dissolved in methanol. The UV-visible spectra were collected by means of a Thermo Scientific Evolution 260 Bio spectrophotometer equipped with a Peltier temperature controller and quartz cuvettes with 1 cm path length were used.

Synthesis

2-Methoxy-6-((phenylimino)methyl)phenol (AZ1)

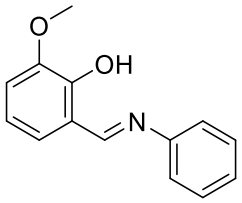

2-Hydroxy-3-methoxybenzaldehyde (3.000 g, 0.02 mol, 1.0 eq) was dissolved in 40 mL of EtOH and a solution of aniline (1.82 mL, 0.02 mol, 1.0 eq) in 4 mL of EtOH was added to the reaction mixture. The resulting brilliant red solution was refluxed for 2 h and 30 min, cooled to room temperature and the solvent was removed under vacuum. 2-Methoxy-6-((phenylimino)methyl)phenol was isolated as an orange crystalline solid (4.341 g, yield = 95%).

IR (cm^{-1}): ν = 3082 (w) (OH), 2957 (w) (CH sp^2), 2838 (w) (CH sp^3), 1655 (m-s) (C=N).

^{1}H NMR (400 MHz, DMSO-d_6, 298 K): δ(ppm) = 3.82 (s, 3H, OCH_3), 6.91 (t, *J* = 7.9 Hz, 1H, ArH), 7.13 (dd, *J* = 8.1, 1.4 Hz, 1H, ArH), 7.25 (dd, *J* = 7.8, 1.5 Hz, 1H, ArH), 7.35 – 7.29 (m, 1H, ArH), 7.50 – 7.39 (m, 4H, ArH), 8.96 (s, 1H, CH=N), 13.24 (s, 1H, OH). (Figure A1.1)

Sodium 3-methoxy-5-sulfonate-salicylaldehyde (AZ3)

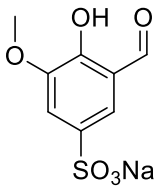

To solid 2-methoxy-6-((phenylimino)methyl)phenol (3.659 g, 0.016 mol, 1.0 eq), concentrated H_2SO_4 (9.50 mL, 0.176 mol, 11.0 eq; d = 1.83 g/mL) was added and the resulting mixture was stirred at 105°C for 2 h. Then,

ice water was added to the mixture and a yellow precipitate formed, which was filtered off, washed with cold water and solubilized in hot water. The resulting solution was left at 4°C for one day and a precipitate formed, which was filtered off, washed with cold water and dried under vacuum. 4-hydroxy-3-methoxy-5-((phenylimino)methyl)benzenesulfonic acid was obtained as a beige solid (3.108 g). To a suspension of 4-hydroxy-3-methoxy-5-((phenylimino)methyl)benzenesulfonic acid (3.108 g, 0.010 mol, 1.0 eq) in 7 mL of H_2O, a solution of Na_2CO_3 (1.503 g, 0.014 mol, 1.4 eq) in 7 mL of H_2O was added dropwise. The resulting solution was stirred and boiled in an open flask for 2 h, then cooled to room temperature and glacial acetic acid was added till pH ca. 5. Subsequently, EtOH (25 mL) was added to the solution, which was left at 4°C overnight. A precipitate was obtained, which was filtered off, washed with EtOH and dried under vacuum. Sodium 3-methoxy-5-sulfonate-salicylaldehyde was isolated as a brown-beige solid (1.674 g, yield = 65%).

IR (cm^{-1}): ν = 1668 (m-s) (C=O).

^{1}H NMR (400 MHz, DMSO-d_6, 298 K): δ(ppm) = 3.85 (s, 3H; OCH_3), 7.37 (d, J = 1.9 Hz, 1H; ArH), 7.52 (d, J = 1.9 Hz, 1H; ArH), 10.26 (s, 1H, CH=O). (Figure A1.2)

^{1}H NMR (400 MHz, D_2O, 298 K): δ(ppm) = 3.94 (s, 3H; OCH_3), 7.51 (d, J = 1.9 Hz, 1H; ArH), 7.72 (d, J = 1.9 Hz, 1H; ArH), 10.01 (s, 1H, CH=O). (Figure A1.3)

Bis-(sodium 3-methoxy-5-sulfonate-salicylaldehyde)-thiocarbohydrazone (AZ11, $Na_2H_4L^1 \cdot 5.5\ H_2O$)

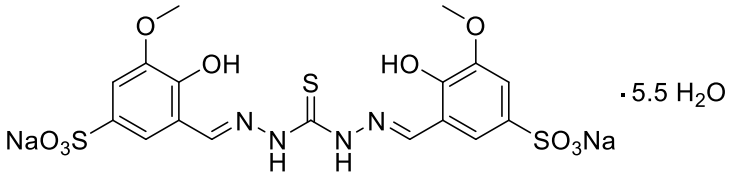

Sodium3-methoxy-5-sulfonate-salicylaldehyde (500 mg, 1.97 mmol, 2.0 eq.) was solubilized in a refluxing H_2O/EtOH mixture (5 mL of H_2O, 20 mL of EtOH). Thiocarbohydrazide (104 mg, 0.98 mmol, 1.0 eq.) was added to the solution, and after a few minutes a greenish precipitate formed. The resulting mixture was refluxed for 1 h and 30 min, then cooled to room temperature; the precipitate was filtered off, washed with EtOH, and dried under vacuum. A pale green solid was obtained (538 mg, yield = 80%).

IR (cm^{-1}): ν = 3429 (m) (OH), 3133 (m) (NH), 1647 and 1612 (m) (C=N).

^{1}H NMR (400 MHz, DMSO-d_6, 298 K): δ(ppm) = 3.83 (s, 6H; OCH_3), 7.22 (d, J = 1.6 Hz, 2H; ArH), 7.32 (s, br, 1H; ArH), 7.85 (s, br, 1H; ArH), 8.56‑8.66 (m, br, ovlp, 2H; CH=N), 9.52 (s, br, 1H; OH), 11.84 (s, br, 1H; OH), 12.04 (s, 2H; NH).

^{1}H NMR (400 MHz, D_2O, 298 K): δ(ppm) = 3.69 (s, br, 6H; OCH_3); 7.09‑7.17 (m, br, ovlp, 2H; ArH); 7.33 (s, br, 1H; ArH); 7.65 (s, br, 1H; ArH); 7.83 (s, br, 1H; CH=N); 8.28 (s, br, 1H; CH=N). (Figure A1.4)

^{1}H NMR (400 MHz, CD_3OD, 298 K): δ(ppm) = 3.94 (s, 6H; OCH_3); 7.43 (s, 2H; ArH); 7.55 (s, br, 1H; ArH); 8.06 (s, br, 1H; ArH); 8.50‑8.64 (m, br, ovlp, 2H; CH=N). (Figure A1.5)

^{13}C NMR (101 MHz, DMSO-d_6, 298 K): δ(ppm) = 55.92, 111.04, 116.07, 117.08, 119.27, 139.31, 141.97, 147.01, 147.50, 149.39, 174.53. (Figure A1.6)

UV/Vis (aqueous 25 mM HEPES buffer at pH 7.4; nm, $mol^{-1}dm^3cm^{-1}$): λ_{max} (ε)= 316 (29000), 241 (35000).

ESI-MS (negative ions): m/z (%): 266 (20) $[H_4L]^{2-}$, 533 (30) $[H_5L]^-$, 555 (100) $[NaH_4L]^-$. (Figure A1.9)

Elem. anal. calcd (%) for $C_{17}H_{16}N_4Na_2O_{10}S_3 \cdot 5.5\ H_2O$: C 30.13, H 4.02, N 8.27, S 14.19; found: C 30.05, H 3.79, N 8.17, S 14.46.

Bis-(sodium 3-methoxy-5-sulfonate-salicylaldehyde)-carbohydrazone (AZ26, $Na_2H_4L^2 \cdot 5\ H_2O$).

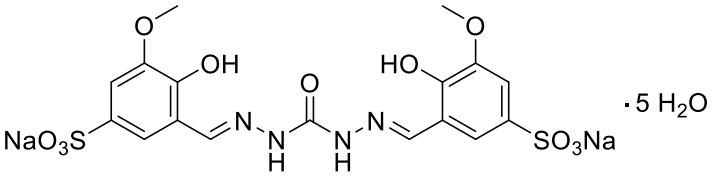

Sodium 3-methoxy-5-sulfonate-salicylaldehyde (500 mg, 1.967 mmol, 2.0 eq) was solubilized in a refluxing H_2O/EtOH mixture (5 mL of H_2O, 20 mL of EtOH). Carbohydrazide (88 mg, 0.977 mmol, 1.0 eq) was added to the solution and the resulting mixture was refluxed for 1 h and 30 min. After few minutes a grey precipitate formed. The mixture was then cooled to room temperature and the resulting precipitate was filtered off, washed with EtOH and dried under vacuum. A pale grey granular solid was obtained (541 mg, yield = 84%).

IR (cm^{-1}): ν = 3468 (m) (OH), 3200 and 3100 (m) (NH), 1663 (s) (C=O), 1614 and 1586 (m) (C=N).

^{1}H NMR (400 MHz, DMSO-d_6, 298 K): δ(ppm) = 3.81 (s, 6H; OCH_3), 7.16 (s, 2H; ArH), 7.50 (s, br, 2H; ArH), 8.40 (s, 2H; CH=N), 10.47 (s, br, 2H, OH), 10.90 (s, br, 2H, NH).

^{1}H NMR (400 MHz, D_2O, 298 K): δ (ppm) = 3.78 (s, 6H; OCH_3), 7.20 (d, J = 1.7 Hz, 2H; ArH), 7.46 (s, br, 2H; ArH), 8.05 (s, br, 2H; CH=N). (Figure A1.10)

^{1}H NMR (400 MHz, CD_3OD, 298 K): δ (ppm) = 3.93 (s, 6H; OCH_3), 7.41 (d, J = 2 Hz, 2H; ArH), 7.78 (s, br, 2H; ArH), 8.44 (s, br, 2H, CH=N). (Figure A1.11)

^{13}C NMR (101 MHz, d_6-DMSO, 298 K): δ (ppm)= 55.88, 110.37, 117.19, 118.62, 139.38, 142.98, 146.50, 146.90, 151.97. (Figure A1.12)

UV/Vis (aqueous 25 mM HEPES buffer at pH 7.4; nm, $mol^{-1}dm^3cm^{-1}$): λ_{max} (ε)= 305 (31400), 236 (42000).

MS-ESI (negative ions): m/z (%): 258 (100) $[H_4L]^{2-}$, 539 (80) $[NaH_4L]^-$. (Figure A1.15)

Elem. anal. calcd (%) for $C_{17}H_{16}N_4Na_2O_{11}S_2 \cdot 5\ H_2O$: C 31.29, H 4.02, N 8.59, S 9.83; found: C 31.44, H 4.05, N 8.68, S 9.93.

$CuNaH_3L^1 \cdot 4\ H_2O$ (PP8)

$Na_2H_4L^1 \cdot 5.5\ H_2O$ (80.0 mg, 0.118 mmol, 1.0 eq) was dissolved in a H_2O/MeOH mixture (2 mL of H_2O, 10 mL of MeOH; pH ca. 8) at 70°C. A solution of $CuCl_2 \cdot 2\ H_2O$ (20.5 mg, 0.120 mmol, 1.0 eq) in 2 mL of MeOH was added and immediately the reaction mixture turned dark green (pH ca. 2). After few minutes a green precipitate formed. The mixture was stirred at room temperature for 2 h. The solvent was partially evaporated, the reaction mixture was cooled at -20°C and the solid separated by centrifugation, washed with absolute EtOH and dried under vacuum. A green powder was obtained (68 mg, yield = 84%).

IR (cm^{-1}): ν = 3534 and 3410 (w) (OH), 3294 (w) (NH), 1607 and 1586 (m) (C=N).

MS-ESI (positive ions): m/z (%): 596 (100) $[CuH_5L]^+$, 618 (60) $[Cu_4H_{13}L_3]^{3+}$, 640 (50) $[Cu_4Na_3H_{10}L_3]^{3+}$. (Figure A1.24)

MS-ESI (negative ions): m/z (%): 594 (100) $[CuH_3L]^-$, 616 (15) $[CuNaH_2L]^-$, 657 (15) $[Cu_2HL]^-$.

Elem. anal. calcd (%) for $C_{17}H_{15}CuN_4NaO_{10}S_3 \cdot 4H_2O$: C 29.59, H 3.36, N 8.12, S 13.94; found: C 29.73, H 3.44, N 8.21, S 13.69.

$ZnNa_2H_2L^1 \cdot 6\ H_2O \cdot 0.33$ iPrOH (PP9)

$Na_2H_4L^1 \cdot 5.5\ H_2O$ (80.3 mg, 0.118 mmol, 1.0 eq) was dissolved in a H_2O/MeOH mixture (2 mL of H_2O, 10 mL of MeOH; pH ca. 8) at 70°C. A solution of $Zn(CH_3COO)_2 \cdot 2\ H_2O$ (26 mg, 0.118 mmol, 1.0 eq) in 3 mL of MeOH was added and the reaction mixture (pH ca. 7) was stirred at room temperature for 2 h. The solvent was partially evaporated, and 2-propanol (15 mL) was added: immediately, a beige precipitate formed. The suspension was cooled to -20 °C and the precipitate was filtered off, washed with 2-propanol and Et_2O and dried under vacuum. A beige powder was obtained (69 mg, yield = 76%).

IR (cm^{-1}): ν = 3420 (m) (OH), 3160 (m) (NH), 1603 (m) (C=N).

MS-ESI (negative ions): m/z (%): 330 (30) $[Zn_2L]^{2-}$, 597 (50) $[ZnH_3L]^-$, 608 (20) $[Zn_2NaH_5L_2]^{2-}$, 619 (20) $[ZnNaH_2L]^-$, 630 (20) $[Zn_2Na_3H_3L_2]^{2-}$, 641 (20) $[ZnNa_2HL]^-$, 660 (15) $[Zn_2HL]^-$. (Figure A1.25)

Elem. anal. calcd (%) for $C_{17}H_{14}N_4Na_2O_{10}S_3Zn \cdot 0.33\ (CH_3)_2CHOH \cdot 6\ H_2O$: C 28.08, H 3.75, N 7.28, S 12.49; found: C 27.87, H 3.21, N 7.03, S 12.48.

$CuNaH_3L^2 \cdot 5\ H_2O$ (PP10)

$Na_2H_4L^2 \cdot 5\ H_2O$ (100.0 mg, 0.153 mmol, 1.0 eq) was dissolved in a H_2O/MeOH mixture (3 mL of H_2O, 7 mL of MeOH; pH ca. 8) at 70°C. A solution of $CuCl_2 \cdot 2\ H_2O$ (26.5 mg, 0.155 mmol, 1.0 eq) in 2 mL of MeOH was added and immediately the reaction mixture turned dark green (pH ca. 2). After few minutes a green fine precipitate formed. The mixture was stirred at room temperature for 4 h. The suspension (pH ca. 2-3) was reduced to a small volume, cooled to -20°C and centrifuged. The resulting solid was washed with absolute EtOH and dried under vacuum. A light green powder was obtained (90 mg, yield = 85%).

IR (cm^{-1}): ν = 3416 (m) (OH), 3315 (m) (NH), 1651 (s) (C=O), 1604 (m) and 1558 (s) (C=N).

MS-ESI (negative ions): m/z (%): 579 (40) $[CuH_3L]^-$, 590 (20) $[Cu_2NaH_5L_2]^{2-}$, 610 (20) $[Cu_2Na_3H_3L_2]^{2-}$, 641 (20) $[Cu_2HL]^-$. (Figure A1.26)

Elem. anal. calcd (%) for $C_{17}H_{15}CuN_4NaO_{11}S_2 \cdot 5\ H_2O$: C 29.50, H 3.64, N 8.10, S 9.27; found: C 29.68, H 3.36, N 8.00, S 9.28.

$ZnNa_2H_2L^2 \cdot 0.5$ iPrOH $\cdot 5\ H_2O$ (PP11)

The ligand $Na_2H_4L^2 \cdot 5\ H_2O$ (99.7 mg, 0.153 mmol, 1.0 eq) was dissolved in a 1/2 H_2O/MeOH mixture (4 mL of H_2O, 7 mL of MeOH; pH ca. 8) at 70°C. A solution of $Zn(CH_3COO)_2 \cdot 2\ H_2O$ (33.3 mg, 0.152 mmol, 1.0 eq) in 3 mL of MeOH was added and the reaction mixture (pH ca. 7) was stirred at room temperature for 4 h. The resulting solution (pH ca. 7) was reduced to a small volume and 2-propanol (15 mL) was added: immediately, a yellow-beige precipitate formed. The suspension was cooled to -20 °C and the precipitate was filtered off, washed with 2-propanol and Et_2O and dried under vacuum. A cream-coloured powder was obtained (91 mg, yield = 80%).

IR (cm^{-1}): ν = 3418 (m) (OH), 3200 (m) (NH), 1600 (m) (C=O), 1555 (m) (C=N).

MS-ESI (negative ions): m/z (%): 289 (50) $[ZnH_2L]^{2-}$, 581 (20) $[ZnH_3L]^-$, 592 (15) $[Zn_2NaH_5L_2]^{2-}$, 603 (15) $[ZnNaH_2L]^-$, 614 (15) $[Zn_2Na_3H_3L_2]^{2-}$, 625 (15) $[ZnNaH_2L]^-$. (Figure A1.27)

Elemental analysis calcd (%) for $C_{17}H_{14}N_4Na_2O_{11}S_2Zn \cdot 0.5\ (CH_3)_2CHOH \cdot 5\ H_2O$: C 29.79, H 3.78, N 7.51, S 8.60; found: C 29.68, H 3.82, N 7.46, S 8.60.

$Cu_2NaHL^1 \cdot 7\ H_2O$ (PP17)

The ligand $Na_2H_4L^1 \cdot 5.5\ H_2O$ (188.0 mg, 0.277 mmol, 1.0 eq) was dissolved in 13 mL of MeOH (pH ca. 8) at 30°C. A solution of $CuCl_2 \cdot 2\ H_2O$ (95 mg, 0.557 mmol, 2.0 eq) in 3 mL of MeOH was added and immediately a dark green suspension (pH ca. 2-3) formed, which was stirred at room temperature for 2 h. The resulting suspension (pH ca. 2-3) was cooled to -20°C, centrifuged and the precipitate was washed with MeOH and dried under vacuum. A dark green hygroscopic powder was obtained (74 mg, yield = 33%).

IR (cm^{-1}): ν̃= 3379 (m) (OH), 3160 (m) (NH), 1598 (s) and 1546 (m) (C=N).

MS-ESI (negative ions): m/z (%): 328 (80) $[Cu_2L]^{2-}$, 656 (80) $[Cu_2HL]^-$. (Figure A1.31)

Elemental analysis calcd (%) for $C_{17}H_{13}Cu_2N_4NaO_{10}S_3 \cdot 7\ H_2O$: C 25.34, H 3.38, N 6.95, S 11.94; found: C 25.33, H 2.98, N 6.94, S 11.62.

$Zn_2(Na_2HL^1)(OAc) \cdot 7\ H_2O$ (PP18)

The ligand $Na_2H_4L^1 \cdot 5.5\ H_2O$ (151.0 mg, 0.223 mmol, 1.0 eq) was dissolved in 11 mL of MeOH (pH ca. 8) at 30°C. A solution of $Zn(CH_3COO)_2 \cdot 2\ H_2O$ (98.0 mg, 0.446 mmol, 2.0 eq) in 3 mL of MeOH was added and the reaction mixture (pH ca. 6) was stirred at room temperature for 2 h. The resulting solution (pH ca. 6) was reduced to a small volume and 2-propanol (15 mL) was added: a fine precipitate formed, which was filtered off, washed with cold 2-propanol and dried under vacuum. A beige hygroscopic powder was obtained (91 mg, yield = 46%).

IR (cm^{-1}): ν = 3390 (m) (OH), 3200 (m) (NH), 1600 and 1549 (m) (C=N).

^1H NMR (400 MHz, D_2O, 298 K): δ(ppm) = 1.92 (s, 3H; CH_3, OAc), 3.70-3.85 (m, br, 6H; OCH_3), 7.15-7.35 (m, br, 4H; ArH), 7.96 (s, br, 1H; CH=N), 8.68 (s, br, 1H; CH=N).

MS-ESI (negative ions): m/z (%): 330 (100) $[Zn_2L]^{2-}$, 440 (20) $[Zn_4HL_2]^{3-}$, 660 (30) $[Zn_2HL]^-$, 682 (30) $[Zn_2NaL]^-$. (Figure A1.28)

Elemental analysis calcd (%) for $C_{19}H_{16}N_4Na_2O_{12}S_3Zn_2 \cdot 7\ H_2O$: C 25.60, H 3.39, N 6.28, S 10.79; found: C 25.57, H 3.07, N 5.84, S 11.37.

$Cu_2NaHL^2 \cdot 7\ H_2O$ (PP19)

The ligand $Na_2H_4L^2 \cdot 5\ H_2O$ (150.0 mg, 0.230 mmol, 1.0 eq) was dissolved in a 2/5 H_2O/MeOH mixture (4 mL of H_2O, 10 mL of MeOH; pH ca. 8) at 70°C. A solution of $CuCl_2 \cdot 2\ H_2O$ (79.0 mg, 0.463 mmol, 2.0 eq) in 3 mL of MeOH was added and immediately a dark green suspension (pH ca. 2) formed, which was stirred at room temperature for 4 h. The resulting suspension (pH ca. 2) was cooled to -20°C, centrifuged and the precipitate was washed with MeOH and dried under vacuum. A green hygroscopic powder was obtained (158 mg, yield = 87%).

IR (cm^{-1}): ν̃= 3400 (m) (OH), 3211 (m) (NH), 1596 (s) (C=O), 1547 (m) (C=N).

MS-ESI (negative ions): m/z (%): 640 (100) $[Cu_2HL]^-$.

Elemental analysis calcd (%) for $C_{17}H_{13}Cu_2N_4NaO_{11}S_2 \cdot 7\ H_2O$: C 25.86, H 3.45, N 7.10, S 8.12; found: C 26.13, H 3.22, N 7.09, S 8.05.

$Zn_2(Na_2HL^2)(OAc) \cdot 5\ H_2O$ (PP20)

The ligand $Na_2H_4L^2 \cdot 5\ H_2O$ (135.0 mg, 0.207 mmol, 1.0 eq) was dissolved in a 2/5 H_2O/MeOH mixture (4 mL of H_2O, 10 mL of MeOH; pH ca. 8) at 70°C. A solution of $Zn(CH_3COO)_2 \cdot 2\ H_2O$ (91.0 mg, 0.414 mmol, 2.0 eq) in 3 mL of MeOH was added and the reaction mixture (pH ca. 7) was stirred at room temperature for 4 h. The resulting solution (pH ca. 7) was reduced to a small volume and 2-propanol (15 mL) was added: a precipitate was obtained, which was filtered off, washed with cold 2-propanol and dried under vacuum. A brown hygroscopic powder was obtained (69 mg, yield = 39%).

IR (cm^{-1}): v = 3408 (m) (OH), 3221 (m) (NH), 1595 (s) (C=O), 1558 (m) (C=N).

MS-ESI (negative ions): m/z (%): 290 (50) $[ZnH_2L]^{2-}$, 322 (100) $[Zn_2L]^{2-}$, 429 (45) $[Zn_4HL_2]^{3-}$, 644 (40) $[Zn_2HL]^-$, 653 (30) $[Zn_4NaHL_2]^{2-}$. (Figure A1.29)

Elemental analysis calcd (%) for $C_{19}H_{16}N_4Na_2O_{13}S_2Zn_2 \cdot 5H_2O$: C 26.68, H 3.06, N 6.55, S 7.50; found: C 27.03, H 3.24, N 6.80, S 7.90.

Crystallography

Crystals of $[Cu_2(NaHL^1)(H_2O)_7]\cdot 3.5H_2O$ were obtained by slow evaporation of the solvent from the mother solution of **PP8** synthesis, after resting several days at room temperature.

Crystallographic data: $C_{17}H_{34}Cu_2N_4NaO_{20.5}S_3$, triclinic, P-1, a= 9.2804(2) Å, b= 14.1111(3) Å, c= 14.2995(3) Å, 63.355(1), 73.025(1), 77.203(1)°; V=1591.82(6) $Å^3$; Z=2; d_{calc}=1.812 mg/cm^3 , F(000)= 890, CuKα radiation (λ = 1.54178), mu=4.456. Tot. refl.= 25831, hkl range= -11<h<11, -17<k<17, -17<l<17; Theta range 3.524-70.219, unique reflections= 6049, number of parameters = 469, GooF= 1.058, R=0.037, wR2=0.114.

Single crystals were mounted on a glass fiber and the intensity data were collected with a SMART APEX2 diffractometer equipped with a Bruker AXS CCD detector. The SAINT1986[120] software was used for the integration of reflection intensities and scaling, and SADABS1996[121] for the absorption correction. The structures were solved by direct methods using SIR97[122] and refined by full-matrix least-squares on all F2 using SHELXL97[123] implemented in the WinGX package.[124] All the non-hydrogen atoms in the molecules were refined anisotropically. The hydrogen atoms were partly found and partly placed in ideal positions using riding models. The structures were solved by direct methods and difference Fourier synthesis using the SHELX suite of programs as implemented within the WINGX software. Thermal ellipsoid plots were generated using the program ORTEP-333 integrated within the WinGX suite of programs.

Spectrophotometric determination of pK_a values

The UV-visible spectra were collected using a Thermo Scientific Evolution 260 Bio spectrophotometer equipped with a Peltier temperature controller. Aqueous buffer stock solutions (50 mM) were prepared as follows: acetate buffer solutions (pH = 3.98, 4.62 and 5.00) were prepared by mixing appropriate volumes of AcOH 50 mM and $AcONa\cdot 3H_2O$ 50 mM solutions. MES (pH = 5.51, 6.00 and 6.49), HEPES (pH = 7.00, 7.48 and 8.01) and CHES (pH = 8.62, 9.01, 9.51 and 10.00) buffer solutions were obtained by suspending appropriate

amounts of solid MES/HEPES/CHES in water, adding aqueous NaOH 100 mM until the desired pH was reached. For 0.99 and 12.67 pH values were used HCl 100 mM and NaOH 100 mM aqueous solutions, respectively. The pH was measured using a Crison Basic 20 pH-meter connected with a Hamilton glass electrode. Calibration of the glass electrode was carried out daily. All solutions were prepared using bi-distilled water. For all the solutions, the ionic strength was 100 mM NaCl.

Working solutions for spectroscopic analysis consisted of 50 mM buffer or 100 mM HCl or 100 mM NaOH, 100 mM NaCl and 17 μM analyte in distilled H_2O at each pH value. Solutions were placed into quartz cuvettes with 1 cm optical length and UV-visible spectral scans were taken from 220 nm to 600 nm for **AZ11** and from 220 nm to 500 nm for **AZ26**. Before the addition of the analyte, the spectrum of each working solution was collected and used as reference. The spectral data collection was carried out at 298.2 K immediately after the addition of the analyte and repeated after 3 and 10 minutes for all the samples at different pH. With the exception of the samples at pH 0.99 and 12.67, for all systems the collected spectra did not change within 10 minutes after ligand addition. All the experiments were performed in duplicate.

The pK_a values were calculated from the spectral dataset using the HypSpec2014 software.[108] In the software, all equilibrium constants are defined as overall association constants: a brief description of the mathematics that allow the determination of pK_a values from proton-base association constants is reported in HypSpec2014 software manual.

UV–visible spectrophotometric titrations

The UV-visible spectra were collected using a Thermo Scientific Evolution 260 Bio spectrophotometer equipped with a Peltier temperature controller. Stock solutions of **AZ11** and **AZ26** were prepared in water at concentration *ca.* 1 mM. Stock solutions of $CuCl_2 \cdot 2\ H_2O$ and $ZnCl_2$ (*ca.* 10 mM) were prepared in water by weight of the salts. HCl and NaOH stock solutions were prepared in water at concentration 100 mM.

The complex formation equilibria at pH 2.5 or 7.4 of the **bis-TCH AZ11** and the **bis-CH AZ26** with Cu^{II} and Zn^{II} ions were studied by direct spectrophotometric titrations of solutions of the ligands with the metal ions, and the samples were prepared as follows. Appropriate aliquots of the stock solutions of the ligands were diluted in a quartz cuvette of 1 cm path length using HEPES buffer (pH 7.4) or by adding HCl aqueous solution (pH 2.5) to obtain *ca.* 17 μM ligand solutions in a total volume of 2.6 mL. The obtained ligand solutions were titrated with copper(II) or zinc(II) titrant solutions (*ca.* 442 μM) up to a metal:ligand ratio of 3 for the studies at pH 7.4, and up to a copper(II):ligand ratio of 5 (for **AZ11**) and 7 (for **AZ26**) for the studies at pH 2.5. For each solution, the absorption spectrum was collected in the 220-600 nm range at 298.2 K. All experiments were performed in triplicate.

The logarithms of the apparent stability constants were calculated from the spectral dataset using the HypSpec2014 software.[108] In all titrations, the molar spectrum of the ligand at the appropriate pH has been used as the fixed parameter. All equilibria were studied at fixed pH, and therefore the determined log β values are logarithms of conditional formation constants. In the speciation models the L component identifies the studied ligand irrespective of its protonation state; for this reason, the charges of the complexes are omitted. Speciation diagrams were calculated using the Hyss2009 software.[125] Where appropriate, the complexation equilibria of copper(II) with HEPES were considered in the calculations, using a conditional log β for the copper(II)/HEPES adduct at pH 7.4 of 2.91 (calculated from literature[126]). No significant competing role of HEPES in zinc complexation is documented in the literature.[127]

Potentiometric titrations

The glass-electrode potentiometric titrations of **AZ11** and **AZ26** were carried out in aqueous solution at T = 298.2 ± 0.1 K and I = 0.1 M (KCl) under a N_2 stream, using 1.5 mL samples. The potentiometric titrations were carried out using an automatic Metrohm OMNIS titrator provided with a Metrohm semi-micro analogic glass electrode. The system was controlled by a PC to monitor the attainment of the equilibrium through pH measurements vs. time, and the addition of titrant aliquots. The Metrohm combined glass electrode was calibrated in terms of $[H^+]$ (hereafter pH=-log$[H^+]$) by titrating HCl solutions with KOH solutions previously standardized against potassium hydrogen phthalate.[128,129] The pK_w value resulted to be in the 13.75-13.77 range. The protonation constants of $Na_2H_4L^1 \cdot 5.5\ H_2O$ and $Na_2H_4L^2 \cdot 5\ H_2O$ were determined by alkalimetric titration of 3 samples (3.0 – 4.5 mM). All samples were prepared by weight of the pure solids, and dissolved in freshly prepared, N_2 fluxed, doubly distilled water. Potentiometric data treatment was carried out using Hyperquad2013 software.[108] Distribution diagrams were obtained using Hyss2009 software.[125]

Stability of ligands and complexes

The UV-visible spectra were collected using a Thermo Scientific Evolution 260 Bio spectrophotometer. Absorption measures were performed at room temperature, using quartz cuvettes with 1 cm optical path length. The tests for stability of ligands and complexes were performed in DPBS (Dulbecco's Phosphate Buffered Saline) 1x without Ca^{2+} and Mg^{2+}. The range of wavelengths which was explored was between 220 nm and 850 nm. A cuvette containing only DPBS buffer was used as blank for the UV-visible measures.

The concentrations of the working solutions were: 17 µM for **AZ11**, 18 µM for **AZ26**, 35 µM for **PP8**, 42 µM for **PP9**, 33 µM for **PP10**, 40 µM for **PP11**, 45 µM for **PP17**, 32 µM for **PP18**, 25 µM for **PP19** and 28 µM for **PP20**. The spectra were measured immediately after the preparation of the working solutions, after 1, 24, 48, 72 hours and after 1 week. During the time between two consecutive measures, the samples were stored at room temperature in the dark.

Computational chemistry

DFT calculations

The **bis-TCH AZ11** and the **bis-CH AZ26** were modelled at the DFT level, while the solvent was initially described by using the implicit picture based on the Polarizable Continuum Model (PCM).[130-132] More in detail, all the geometry optimizations were performed at the B3LYP[133,134]/6-311+G(d) level, including Grimme' s empirical dispersion (GD3),[135] and all the obtained stationary points were confirmed to be minima on the potential energy surface by running frequency calculations and checking the absence of imaginary frequencies. Cluster systems, including explicit DMSO molecules (built based on the MD simulations discussed below), were optimized and modelled at the same theory level. Regarding the optimizations of the transition states for the rotation along the C(X)-N bond, the presence of one imaginary frequency confirmed that they were first order saddle points and their corresponding vibrational mode composition confirmed that they were transition states for that rotation. Then, activation free energies were further calculated for both **AZ11** and **AZ26**. To simulate the 1D ^{1}H-NMR spectra on the previously optimized geometries, the B3LYP/TZVP[136,137] potential was chosen. DFT has already proved to be efficient in calculating NMR chemical shifts,[138-141] and the triple − ζ basis sets have demonstrated the ability to improve the accuracy of the predicted chemical shifts, representing a balance between accuracy and computational cost.[139] The nuclear magnetic shielding tensor is computed according to the expression using the mixed second derivative of the energy with respect to the external magnetic field, $\vec{B}$, and the magnetic moment on nucleus N, m_N,

$$\sigma_{ji}^{N} = \frac{\delta^2 E}{\delta B_i \delta m_{Nj}} \quad (1.5)$$

where i and j are the components of the external magnetic field and induced magnetic moment, respectively. The gauge-including atomic orbital (GIAO)[142,143] method was used for all the NMR calculations to obtain the nuclear magnetic shielding tensors. Since NMR experiments measure chemical shifts, δ_i, which is the difference between the chemical shielding of the target nucleus σ_i and that of a reference nucleus σ_{ref}, to make a direct comparison with experiments, the calculated absolute chemical shieldings σ_i had to be converted to chemical shifts via the appropriate referencing according to the following expression:

$$\delta_i = (\sigma_{ref} - \sigma_i)/(1 - \sigma_{ref}) \quad (1.6)$$

where, for light nuclei such as ^{1}H and ^{13}C, the expression can be approximated to $\delta_i = (\sigma_{ref} - \sigma_i)$. The computational chemical shift referencing scale chosen for the predicted chemical shieldings was tetramethylsilane (TMS), a common choice for ^{1}H and also adopted in the NMR experiments of this work. First, TMS was modelled at the same theory level as the target nuclei in terms of geometry optimization and frequency calculations; then, NMR calculations to achieve its chemical shielding used in Eq. () were made to evaluate all the hydrogens δ_i. Finally, to make a more quantitative comparison with the experimental chemical shifts, all the calculated values were scaled with respect to the experimental ones.

The binding free energies of the complexes with DMSO molecules hydrogen bonded to either **AZ11** or **AZ26** were calculated in the following way:

$$\Delta G_{binding} = G_{complex} - (G_{solute} + nG_{DMSO}) \quad (1.4)$$

where Gc_{omplex} are the cluster energies, Gs_{olute} are the isolated solute energies, G_{DMSO} is the isolated DMSO energy, and n is the number of DMSO molecules present in the complex. The inclusion of the implicit solvent description in the energy terms makes it closer to the real environment of the molecules and allows to mimic more realistic conditions under which the hydrogen bonds are formed. At the same time, it already takes into account the long-range electrostatics, reducing the hydrogen bond interactions to short range contributions, possibly causing an underestimation of $\Delta G_{binding}$. Indeed, the molecules are already polarized in the conductor medium and the energy gain would be the net contribution arising from a reaction in which the pre-polarized educts form a hydrogen bond. Accordingly, two molecules forming a cluster within the conductor embedding will not gain any attractive electrostatic interaction energy because they already were electrostatically perfectly embedded individually. In this picture, the long-range electrostatics does not contribute to the attractive hydrogen bond energy in the calculation that could be substantially ascribed to the covalent contribution to the hydrogen bonds that can be caught only by the explicit solvent molecules picture.[144]

The Gaussian commercial version G16 revision A.03[145] was used for all the *ab initio* calculations, and GaussView (version 6.1.1)[146] was used for outputs visualization, graphical representations of the systems, and visualization of their vibrational normal modes composition.

Atomistic molecular dynamics simulations

As a first step, a box of DMSO molecules was built and equilibrated before exploring the solute dynamics. In detail, a cubic DMSO box was generated using packmol software,[147] with a side of 49.5 Å and consisting of 1024 DMSO molecules (in agreement with a density of about 1.09 g/cm^3). The parameters for the DMSO box were obtained from the optimized AMBER force field parameters for organic solvents,[148] while the Restrained Electrostatic Potential (RESP) atomic partial charges[149] were achieved through the Antechamber[150] accessory module of AmberTools.[151] In detail, a geometry optimization on a DMSO molecule was performed first at the

B3LYP/6-311+G(d) level, and then, the electrostatic potential (ESP)[152] was calculated at the HF/6-31G(d) theory level to obtain the RESP charges subsequently derived from a two-stage fitting procedure implemented in Antechamber, in line with the AMBER force fields parameterization.[153] Finally, the leap program available in AmberTools was used to obtain the solvent box coordinates and topology files. All the MD calculations were performed by using version 2020.6 of GROMACS software.[154] The box was equilibrated by first performing an energy minimization 20 000 steps long and without constraints by using the steepest descent algorithm. For these steps, a gradual decrease in the Coulomb and Lennard-Jones potentials was imposed between 1 and 1.2 nm. Then, the box was heated by increasing the temperature with three subsequent MD runs in the canonical ensemble (NVT) using the weak-coupling Berendsen[155] scheme. In particular, three 500 ps long NVT steps were performed to gradually increase the temperature from 100 K up to 300 K. A further NPT equilibration run of 1 ns was finally performed to adjust the box volume using the Berendsen algorithm for pressure coupling. For all the simulations, the Verlet cutoff scheme was used for non-bonded interactions neighbour search; the Smooth Particle-Mesh Ewald (SPME)[156] method was employed for long-range electrostatic interactions, while the cutoff for long-range van der Waals interactions was set to 1.2 nm. Regarding the modelling of the solute/solvent systems, **AZ11** and **AZ26** were described by the parameters of the latest version of the generalized Amber force field while the RESP atomic partial charges were obtained according to the same procedure described for DMSO. The leap program was used to place each molecule in the center of the previously equilibrated box, including a layer of solvent molecules of about 18 Å, affording a box of ~50 × 50 × 50 $Å^3$. Due to the presence of negatively charged sulfonated groups, neutrality was ensured by adding Na^+ ions, modelled with Joung and Cheatham parameters.[157] Finally, coordinates and topology files were obtained for the solute/solvent systems. To explore the micro-solvation of these molecules, the solute was kept rigid applying harmonic restraints of 1000 kJ mol^{-1} nm^{-2} to the solute heavy atoms. The equilibration consisted of two energy minimization steps (only in one of these steps, the solute was allowed to freely move), each 20 000 steps long. These steps were followed by the same NVT and NPT MD runs described before to allow the solvent to equilibrate around the solute. In this case, a further NPT step of 5 ns was performed. Finally, MD simulations of 220 ns were run and temperature and pressure controls were carried out with the velocity-rescale[158] and Parrinello‐Rahman[159] scheme, respectively. For all the MD simulations (either equilibrations or production), the leap-frog algorithm[160] for integrating Newton's equations of motion was used, a time step of 2 fs was chosen, and the LINCS algorithm[161] was employed to constrain bonds involving hydrogen atoms. Radial distribution functions (RDFs) were calculated from the obtained trajectories using GROMACS software, with a bin resolution of 0.02 Å. The RDFs were evaluated for each of the N‐H nitrogens and the hydroxyl oxygens with respect to the DMSO oxygens. The trajectories were visualized with Visual Molecular Dynamics (VMD) molecular visualization software[162], all the graphics were made with Xmgrace software, and the figures were made using the image manipulator GIMP program (2.10.22 revision 3).

NMR experiments

The samples for NMR spectroscopy were prepared by dissolving 1 mg of **AZ11** and **AZ26** in 0.60 mL of DMSO-d_6. All the spectra were acquired with a Bruker Avance NMR spectrometer operating at 600 MHz ^1H Larmor frequency equipped with a z-gradient 5 mm triple-resonance probe head. 1D and 2D NMR spectra were recorded at 298 K unless otherwise specified. 1D ^1H-NMR spectra were acquired with 32 scans, a spectral width of 20 ppm, a relaxation delay of 1 s, and 64k points. For the 2D ^1H‐^{15}N Heteronuclear Single Quantum Coherence (HSQC) experiments, the acquisition parameters included 32 scans, a spectral width of 13 ppm in t_2 and 400 ppm in t_1, a transmitter frequency offset of 6.5 ppm in t_2 and 200 ppm in t_1, and 20k points in t_2 and 256 points in t_1.

Biology

Cell line and culture conditions

U937 cells (ATCC, CRL-1593.2) were obtained from the American Tissue Culture Collection (Rockville, MD, USA) and were cultured in Roswell Park Memorial Institute Medium (RPMI-1640) (Euroclone, Italy); Hs27 cells (ATCC, CRL1634) were grown in DMEM medium. Both media were supplemented with 10% (v/v) foetal bovine serum (Euroclone, Italy), 1% L-glutamine (2 mM) (Euroclone, Italy), and 1% penicillin (100 U/mL)/streptomycin (100 µg/mL) (Euroclone, Italy), added with 10% (v/v) foetal bovine serum (Euroclone, Italy), 1% L-glutamine (2 mM) (Euroclone, Italy), and 1% penicillin (100 U/mL)/streptomycin (100 µg/mL) (Euroclone, Italy). Flasks were maintained at 37 °C and 5% CO_2 in a humidified atmosphere. Cultures media were refreshed every two or three days during sub-culturing.

MTS assay

The antiproliferative activity of the ligands **AZ11**, **AZ26** and the complexes **PP8-11** was evaluated *in vitro* on U937 cells by CellTiter 96® AQueous One Solution Cell Proliferation Assay (Promega Corporation, Madison WI, USA). In the exponential growth phase, cells were seeded at 5 × 10^4/mL into 96-well flat bottom microplates (FALCON®, Becton Dickinson, Meylan Cedex, France). Cells were cultured in RPMI-1640 supplemented with 5% FBS, 1% L-glutamine and 1% penicillin/streptomycin, at 37 °C, 5% CO2, in the absence of phenol red. After 24 h from seeding, increasing concentrations of compounds, ranging from 12.5 to 100 µg/mL, were added to the medium and cells were incubated for 24 h. An equal volume of DMSO was added to RPMI-1640 medium in the negative control wells. After treatment period, 20 µL MTS reagent was added to each well, incubated for 4 h and the absorbance recorded at 485 nm with a 96-wells plate reader (TECAN SpectraFluor Plus, Mannedorf, Switzerland). Extensive formation of bubbles in the wells prevented a correct reading of the absorbance values. The repetition of the assay on solutions containing the compounds without cells evidenced the interference of all the molecules with the MTS reagent.

Trypan blue assay

The antiproliferative activity of the ligands **AZ11**, **AZ26** and the complexes **PP8-11** was evaluated *in vitro* on U937 and Hs27 cell lines. In the exponential growth phase, cells were seeded at 5 × 10^4/mL into 12-well flat-bottom microplates. Cells were cultured in complete medium supplemented with 10% FBS, 1% L-glutamine, and 1% penicillin/streptomycin at 37 °C, 5% CO_2. After seeding, different concentrations of compounds in the range from 12.5 to 100 µg/mL in a sterile PBS 1X solution were added to the wells and incubated for 24-, 48- and 72- hours. Negative control was obtained treating cells with PBS 1X. To detect if the treatments caused a defect in cell viability, following 24-, 48- and 72- hours treatments with the compounds, cells were stained with Trypan Blue (TB, 0.4 %) (Gibco™, Thermofisher Scientific, Waltham, MA, USA). Cells were then counted using Burker chamber. The GI_{50} value, i.e. the concentration causing 50% reduction in the cell number in comparison with control cells, was calculated taking into account the guidelines of the US National Cancer Institute (NCI).[163] Values are reported as the mean of the GI_{50} calculated on two independent experiments.

Luminescent cell viability assay

The antiproliferative activity of the complexes **PP17-20** was evaluated *in vitro* on U937 cell lines. In the exponential growth phase, cells were seeded at 5 × 10^4/mL into 96-well flat bottom microplates (FALCON®, Becton Dickinson, Meylan Cedex, France). Cells were cultured in RPMI-1640 supplemented with 10% FBS, 1%

L-glutamine and 1% penicillin/streptomycin, at 37 °C, 5% CO_2, in the absence of phenol red. After seeding, different concentrations of compounds in the range from 12.5 to 100 µM in a sterile PBS 1X solution were added to the wells and incubated for 24, 48 and 72 hours. The plates were left to equilibrate in the dark at room temperature for 15 minutes, then the appropriate volume of CellTiter-Glo® 2.0 Reagent was added (100 µL/well). The plates were mixed in the dark for 2 minutes on an orbital shaker to induce cell lysis, then they were incubated in the dark at room temperature for 10 minutes to stabilize the luminescent signal. Luminescence was recorded by means of a 96-wells plate reader (TECAN SpectraFluor Plus, Mannedorf, Switzerland).

Chapter 2:

Glyco-conjugated Schiff bases and their copper(II) complexes as anticancer agents

Introduction

Glucose metabolism in cancer cells

Cancer cells are characterized by a different metabolism compared to normal cells. While in normal cells the generation of the energy needed for cellular processes is based principally on mitochondrial oxidative phosphorylation, in cancer cells it is based on glycolysis, regardless of the presence of oxygen (Figure 2.1).[164] This phenomenon is called aerobic glycolysis or "Warburg effect".[165]

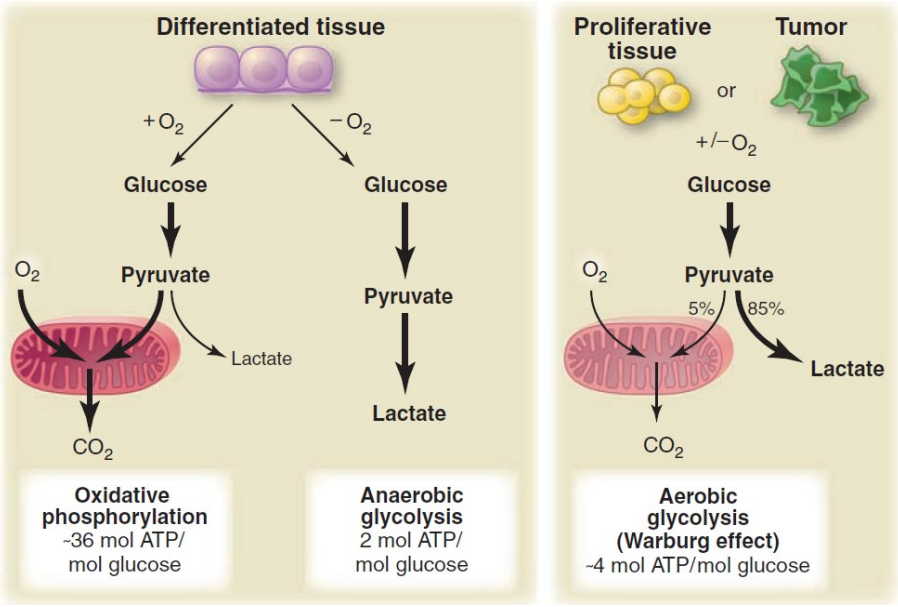

Figure 2.1: Schematic representation of the differences between oxidative phosphorylation, anaerobic glycolysis, and aerobic glycolysis (Warburg effect). Adapted from Ref.[165]

The aerobic glycolysis is an inefficient way to generate adenosine 5´-triphosphate (ATP) (Figure 2.1) and it is still not clear what is the advantage that this process confers to cancer cells. It has been proposed that the metabolism of tumour cells is adapted to favour the uptake and incorporation of nutrients needed to sustain their abnormally high proliferation rate, rather than to generate high amounts of energy.[165] In any case, one of the consequences of the Warburg effect is the enhanced uptake and use of glucose by many types of cancer cells.[166] This implies that malignant cells need a corresponding increase in glucose transport across the membrane[167] and several tumours overexpress glucose transporter proteins, especially the GLUT1 protein.[168]

Glyco-conjugation: a useful tool to increase drug selectivity towards cancer cells

Recognizing that deregulation of cellular energetics is a cancer hallmark and that tumour glycolysis could represent a promising target for clinical intervention, has driven researchers towards the development of new drugs. One strategy involves developing inhibitors that target critical glycolytic enzymes.[169] These inhibitors aim to disrupt the cancer cell primary energy-producing pathway, leading to a decrease in ATP and an inhibition of anabolic processes necessary for cell proliferation. Another strategy is glyco-conjugation, which involves attaching a sugar moiety or a glycomimetic substrate directly to a therapeutic agent.[170-173] The overexpression of GLUTs in cancer cells could in fact be exploited to achieve site-specific delivery of cytotoxic compounds. The chemical scaffold anchored to the glucose should be recognized by GLUTs and internalized as a whole. This could enhance the drug uptake in the tumour cells, improving its activity and selectivity towards cancer cells, avoiding the severe side-effects of a carpet-bombing chemotherapy. Notably, the insertion of a sugar moiety on the molecular backbone of the anticancer agents offers also the possibility to overcome water solubility issues. In addition, the low toxicity and remarkable biocompatibility of carbohydrates further facilitate drug-delivery.[174]

The first compound bearing a glycosidic moiety to be explicitly designed and tested as a cancer-targeting cytotoxic drug is glufosfamide (Figure 2.2a), also known as glucophosphamide or D-glucose isophosphoramide mustard.[175] It is a conjugate of β-D-glucose and the active alkylating moiety of ifosfamide, an anticancer drug. In malignant cells, glufosfamide is metabolized by glucosidases to form ifosforamide. The latter is the active metabolite, which forms DNA crosslinks, therefore inhibiting DNA replication and cancer cell growth.[176] Glufosfamide proved to be less myelotoxic and showed a higher antitumour activity both *in vitro* and *in vivo* than the parent aglycone ifosfamide.[177]

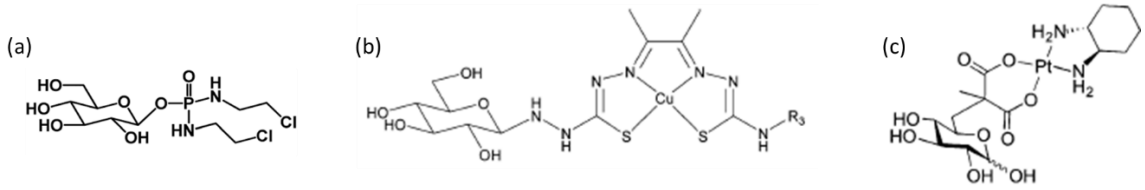

Figure 2.2: Chemical structure of (a) glufosfamide, (b) copper(II)-64-radiolabelled bis-thiosemicarbazonato complexes (R_3 = methyl, ethyl, allyl), (c) a glucose-platinum(II) conjugate with anticancer activity.

Other examples of successful application of the glyco-conjugation strategy in the field of anticancer research are the glycosyl-geldanamycin derivatives reported by Cheng *et al*,[178] the chlorambucil-based neoglycosides synthesized by Goff *et al*[179] and the D-rhamnose-emodin conjugates designed by Xing *et al*.[180]

Glyco-conjugation has not been exploited only with organic molecules, but also on metal complexes, both for radiolabelling methods[181] (Figure 2.2b) and, more recently, for the selective delivery of platinum-based anticancer drugs[182-185] (an example is reported in Figure 2.2c). Even though platinum scaffolds account for the largest class of anticancer glyco-conjugated metal complexes,[186] also other metals such as ruthenium,[187-188] gold[189] and iron[190] are being investigated more and more.

Glyco-conjugated Schiff bases and their copper(II) complexes as anticancer agents

Schiff bases and their copper(II) complexes exhibit a wide spectrum of biological activities, including anticancer activity.[64] The substituted salicylaldehyde-thiosemicarbazone copper(II) complexes previously synthesized by our research group[44] (Figure 2.3) were taken as starting point for the preparation of novel glyco-conjugated derivatives.

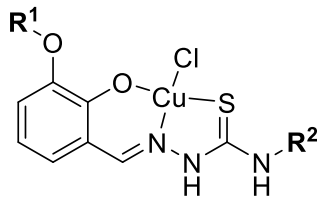

R^1	R^2
Me	H
Me	Ph
Me	Et
H	H
H	Ph
H	Et

Figure 2.3: General structure of the copper(II) complexes of substituted salicylaldehyde thiosemicarbazones previously studied.[44]

The parent complexes shown in Figure 2.3 proved to be highly cytotoxic against different cancer cell lines *in vitro* and studies on their mechanism of action identified the PDI (Protein Disulfide Isomerase) as the molecular target in cells. Unfortunately, they showed low selectivity towards cancer cells, together with poor solubility in aqueous medium.[44] Based on these results, the glyco-conjugation of the thiosemicarbazonic ligands was chosen as suitable approach to design and obtain copper(II) complexes with better selectivity and solubility profiles.

The introduction of the sugar moiety in a Schiff base ligand can involve the carbonyl precursor (in our case, a substituted salicylaldehyde) or the amine/hydrazide precursor. In some examples reported in literature,[191-193] glycosylated thiosemicarbazides were synthesized and used to obtain panels of thiosemicarbazones which were tested for their antimicrobial activity. In another case,[194] glyco-conjugated aldehydes were prepared by O-glycosylation of 4-hydroxyl-aldehydes: the resulting carbonyl precursors were reacted with amines to obtain glycosylated Schiff bases which showed anti-parasitic properties. This last strategy has been previously adopted also by our research group in order to synthesize novel glycosylated **TSCs** bearing per-acetylated glucose or glucose moieties.[195]

The resulting ligands have been employed to prepare copper(II) complexes (**FMM7**, **FMM9**, **FMM11** and **FMM13**, Scheme 2.1). The complexes have been synthesized both with the per-acetylated and the deprotected sugar moiety, in order to evaluate the impact of such fragment on the anticancer activity and cellular uptake of the final compounds.[195] The ligands and the relative complexes have indeed different hydrophilicity. The presence of the lipophilic per-acetylated glucose moiety may hinder the entrance of the complexes in the cells by means of glucose transporters, but it can favour transport by diffusion through the membrane.

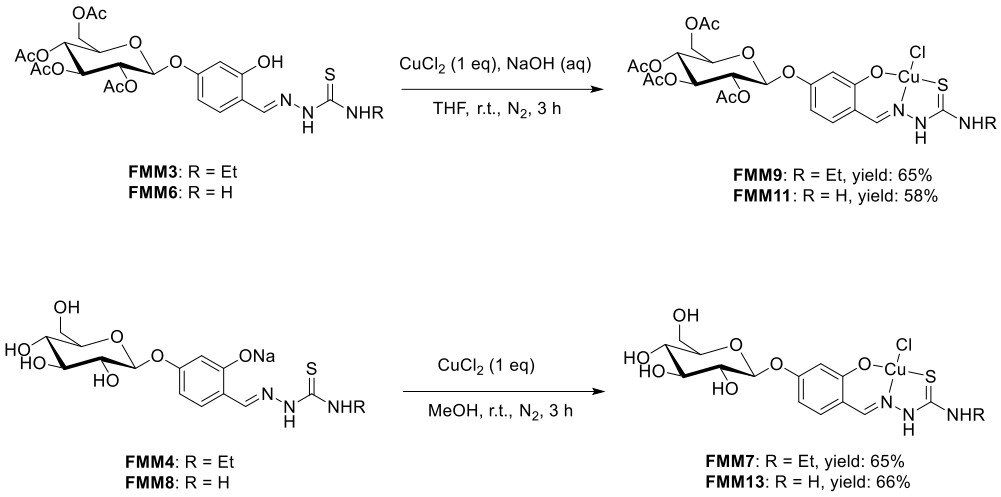

Scheme 2.1: Synthesis of the glucosyl-**TSC** copper(II) complexes.[195]

Both ligands and copper(II) complexes have been tested in preliminary *in vitro* assays for their anticancer activity against a panel of cancer cell lines by the group of prof. Valentina Gandin at the Department of Pharmaceutical and Pharmacological Sciences of the University of Padova. The results are summarized in Table 2.1.

Table 2.1: 2D cytotoxic activity of the **TSC** ligands and their copper(II) complexes. Cells (3–5 x 10^3 cell/well) were treated for 72 h with tested compounds. Cell viability was estimated by means of the MTT test. The IC_{50} values were calculated by a four-parameter (4-PL) logistic model ($p < 0.05$). S.D. = standard deviation.

	IC_{50} (μM) ± S.D.		
Compound	HCT-15	BxPC-3	2008
FMM3	> 50	5.7 ± 0.4	>25
FMM4	> 50	3.1 ± 0.6	>25
FMM6	> 50	5.1 ± 0.1	>25
FMM8	> 50	7.8 ± 1.4	>25
FMM9	23.4 ± 4.4	1.2 ± 0.4	17.3 ± 4.1
FMM7	43.1 ± 5.9	1.8 ± 0.9	> 25
FMM11	28.5 ± 3.2	2.7 ± 0.5	> 25
FMM13	13.4 ± 1.8	0.5 ± 0.2	15.2 ± 3.8
Cisplatin	12.8 ± 2.3	7.0 ± 1.2	2.2 ± 1.7

All the tested compounds have shown moderate or low cytotoxic activity against ovarian carcinoma (2008) and human colorectal adenocarcinoma (HCT-15) cells, while they have proved to be highly effective against pancreatic adenocarcinoma (BxPC-3) cells. Note that the pancreatic cancer cells are known to overexpress the glucose transporters GLUT.[167,168] Further studies are currently ongoing in order to elucidate the mechanism of action of the tested compounds.

These preliminary results have highlighted the effectiveness of the glyco-conjugation strategy and have triggered the interest of our research group towards the development of a wider panel of glucosyl-Schiff bases and related copper(II) complexes.

In this context, it is interesting to evaluate the effect of changing the thiocarbonyl group of **TSCs** with the carbonyl group both on the coordination properties of the ligands and on their anticancer activity (Figure 2.4).

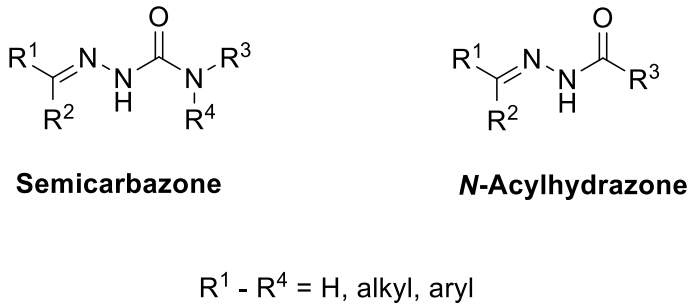

Figure 2.4: General structure of **semicarbazones** (**SCs**) and ***N*-acylhydrazones** (**NAHs**).

Similarly to **TSCs** and **SCs**, ***N*-acylhydrazones NAHs** have a wide spectrum of biological activities,[196] such as antitumour,[197-199] antibacterial,[200] antiviral,[201] antifungal,[202] anti-inflammatory[203] and anticonvulsant.[204] They are obtained by condensation reaction of an aldehyde or ketone with an acylhydrazide.

Remarkable examples of anticancer ***N*-acylhydrazones** are Procaspase activating compound-1 (PAC-1, Figure 2.5, left) and Aldoxorubicin (Figure 2.5, right).

In 2015, PAC-1 entered phase I clinical trials,[197] which allowed to define phase 2 recommended dose of the drug. PAC-1 was found to be safe in heavily pretreated patients with advanced cancers of different types and on-target/off-tumour toxicity did not cause any unexpected or irreversible adverse effects.[205] Regarding its mechanism of action, PAC-1 is able to induce apoptotic death in cancer cells. The ortho-hydroxyl-N-acylhydrazone motif in PAC‑1 is necessary for the anticancer action: it allows the chelation of zinc, which is a strong inhibitor of the enzymatic activity of procaspase 3,[206-207] a protein involved in the promotion of apoptosis.

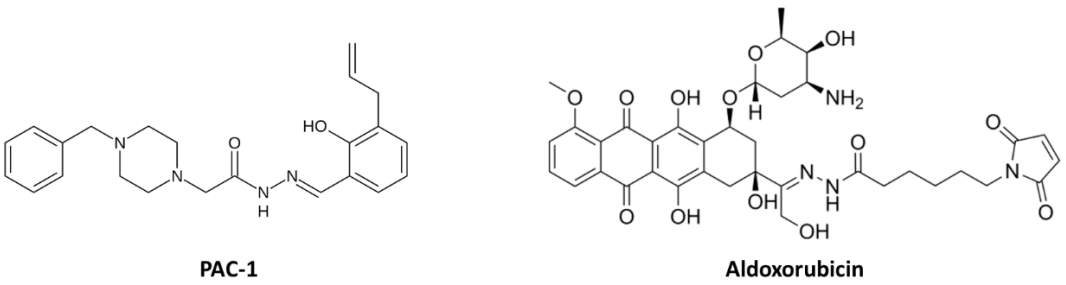

Figure 2.5: Chemical structure of anticancer **NAHs** PAC-1 (left) and Aldoxorubicin (right).

Aldoxorubicin entered phase III clinical trials for the treatment of metastatic, locally progressed, or unresectable soft tissue sarcoma.[208] Through the maleimide moiety, this doxorubicin derivative covalently binds with endogenous serum albumin. Aldoxorubicin is then transported to the target tumour by albumin.

Once there, the acidic environment of the tumour causes the hydrolysis of the hydrazone moiety and the release of doxorubicin at the site of action.[209] Aldoxorubicin can deliver a higher dose of the active species at the cancerous tissue with fewer systemic side effects when compared to doxorubicin. Aldoxorubicin also exhibited no cardiotoxicity, a side effect typically linked to doxorubicin therapy.[208]

Aim of the project

For our study, semicarbazide hydrochloride was selected to synthesize **SC** ligands to be compared with the **TSCs FMM6** and **FMM8**; instead, for the synthesis of novel glucosyl-**acylhydrazones**, octanoic hydrazide was chosen as starting material (Figure 2.6) to confer higher lipophilicity to the final ligands.

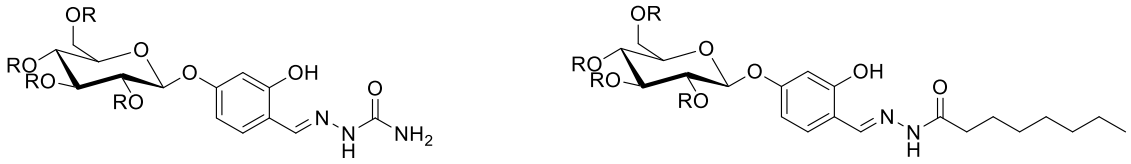

CM2: R = Ac
CM4: R = H

CM7: R = Ac
CM9: R = H

Figure 2.6: Chemical structure of the new glyco-conjugated **SCs** (**CM2** and **CM4**) and **NAHs** (**CM7** and **CM9**).

The ligands were employed to prepare the corresponding copper(II) complexes. Furthermore, the coordination properties of the de-acetylated ligands **FMM8** and **CM4** towards Cu^{II} and Zn^{II} were studied in aqueous solution by means of UV-visible spectrophotometric titrations.

Results and discussion

Synthesis and characterization of the glyco-conjugated ligands

The glyco-conjugation strategy that was previously adopted in our research group implied the deprotection of the per-acetylated Schiff bases, with consequent chromatographic purification for each final compound (Scheme 2.2).[195]

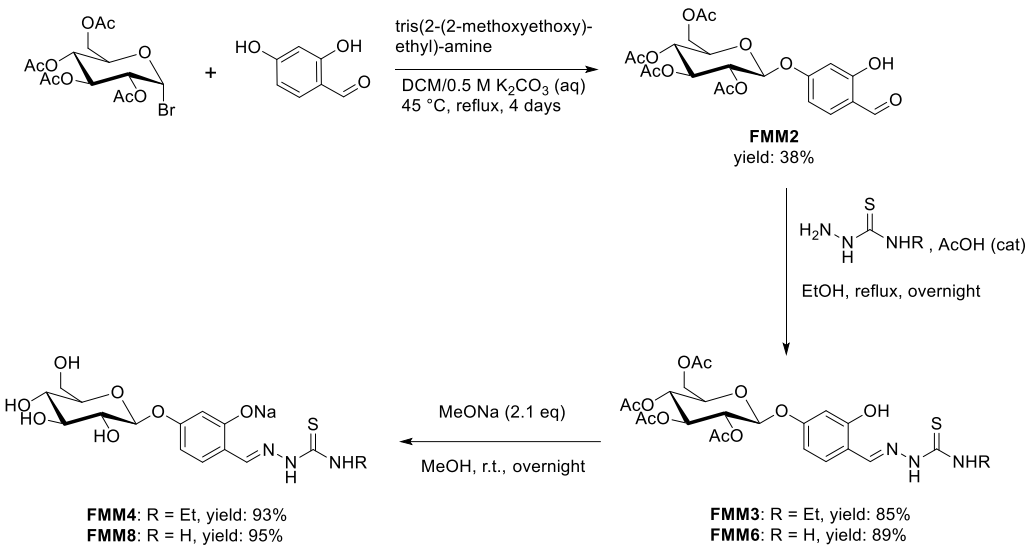

Scheme 2.2: Synthetic pathway to glucosyl-**TSCs**.

The aromatic O-glycosylation reaction between acetobromo-α-D-glucose and 2,4-dihydroxy-benzaldehyde allows to obtain the key precursor **FMM2**. The reaction is performed using a procedure similar to the one reported by Brouillard and coworkers,[210] which is based on the phase-transfer method.[211] The synthesis takes place in an aqueous-organic two-phase-system in the presence of a phase-transfer catalyst, that in this case is tris(2-(2-methoxyethoxy)ethyl)amine.

The per-acetylated glucosyl-**TSCs FMM3** and **FMM6** are obtained by condensation reaction with the desired thiosemicarbazide, while the glucosyl-**TSCs FMM4** and **FMM8** are synthesized by deprotection reaction of the per-acetylated ligands with MeONa, following a procedure reported in literature.[191] Although this last step allows to isolate the glucosyl-**TSCs** in high yields, the purification of the crude by column chromatography is mandatory. This means that, for the preparation of a wide panel of deprotected ligands, a chromatographic separation would be necessary for each of the final products, therefore requiring time and large volumes of solvents. In addition, the products are isolated as sodium salts.

In order to optimize the protocol, the synthetic procedure was varied and the deprotection step was performed directly after the preparation of the per-acetylated glucosyl-aldehyde **FMM2** (Scheme 2.3). The resulting deprotected glucosyl-aldehyde **AZ24** was used to synthesize the deprotected **TSCs** in their neutral form (Scheme 2.3). This procedure modification allows to perform only two chromatographic separations (during the synthesis of **FMM2** and **AZ24**) yielding to an aldehyde precursor that can be used to create a panel of ligands.

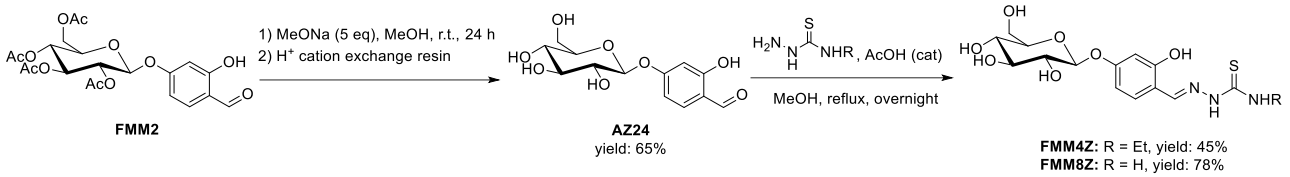

Scheme 2.3: Optimized synthesis of glucosyl-TSCs **FMM4Z** (H_2L^1) and **FMM8Z** (H_2L^2).

The novel glucosyl-aldehyde **AZ24** was obtained in good yields by reaction of the per-acetylated precursor **FMM2** with 5 equivalents of MeONa. The product was characterized by means of FT-IR (Figure A2.6) and NMR spectroscopies, mass spectrometry (Figures A2.8 and A2.9) and elemental analysis (see the experimental section).

The IR spectrum (Figure A2.6) of **AZ24** is characterized by the presence of large OH stretching bands at 3481 cm^{-1} and 3261 cm^{-1} and by the absence of the ester C=O band, which is in turn observed at 1744 cm^{-1} in the spectrum of **FMM2** (Figure A2.1).

The ^1H NMR (400 MHz, 298 K) spectrum of **AZ24** in DMSO-d_6 (Figure 2.8) shows a doublet at 4.96 ppm with a coupling constant value of 7.4 Hz. This peak corresponds to the anomeric proton and its J value gives information on the stereochemistry of the O-glycosidic bond. J values of 7 – 9 Hz are associated to di-axial coupling and therefore to the β-configuration of the glucose moiety (Figure 2.7, right), while J values of 2 – 4 Hz are associated to axial-equatorial coupling and thus to the α-configuration of the glucose moiety[212] (Figure 2.7, left). The J value measured for the anomeric proton of the glucosyl-aldehyde **AZ24** confirms the expected β configuration of the O-glycosidic linkage.

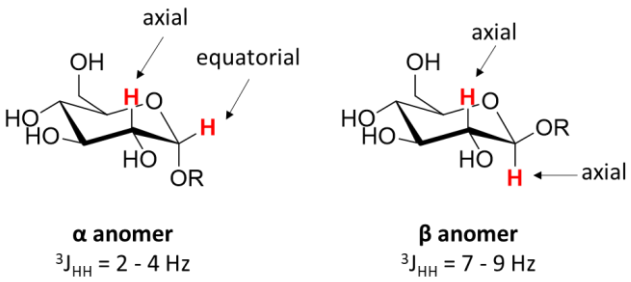

Figure 2.7: Structure of the α and β anomers of a glucose derivative. The value of the coupling constant of the anomeric proton is dependent on the stereochemistry of the glycosidic bond.

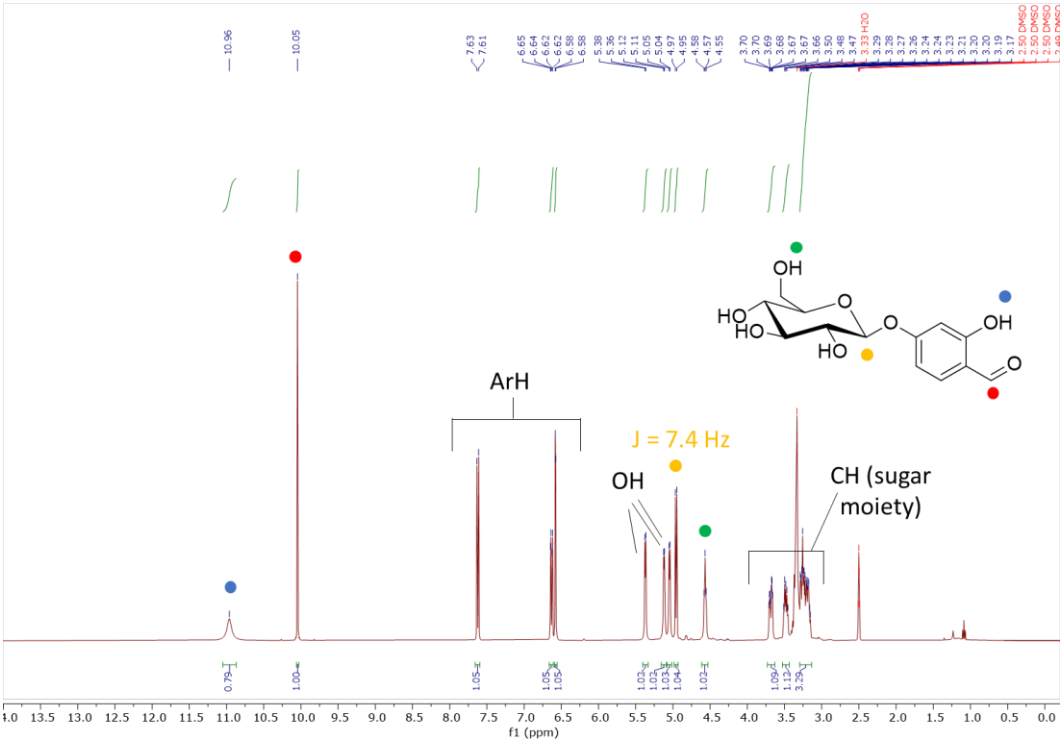

Figure 2.8: ^{1}H NMR (400 MHz, 298 K) spectrum of **AZ24** in DMSO-d_6.

The two aldehydes **FMM2** and **AZ24** were reacted with semicarbazide hydrochloride to synthesize, respectively, ligands **CM2** and **CM4** (Scheme 2.4).

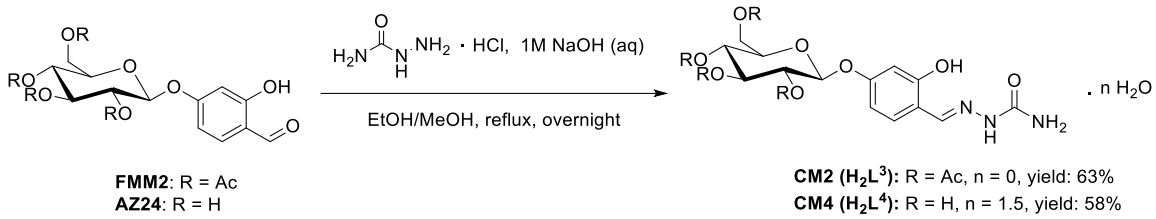

Scheme 2.4: Synthesis of the **SC** ligands **CM2** and **CM4**.

The novel ligands were characterized by means of FT-IR (Figures A2.15 and A2.21) and NMR spectroscopies, mass spectrometry (Figures A2.19, A2.20 and A2.24) and elemental analysis (see the experimental section). In Figure 2.9 are reported the ^{1}H NMR spectra (400 MHz, 298 K) of **CM2** and **CM4** in DMSO-d_6. In both cases, in solution the ligand exists as the keto *E* isomer with respect to the C=N bond.

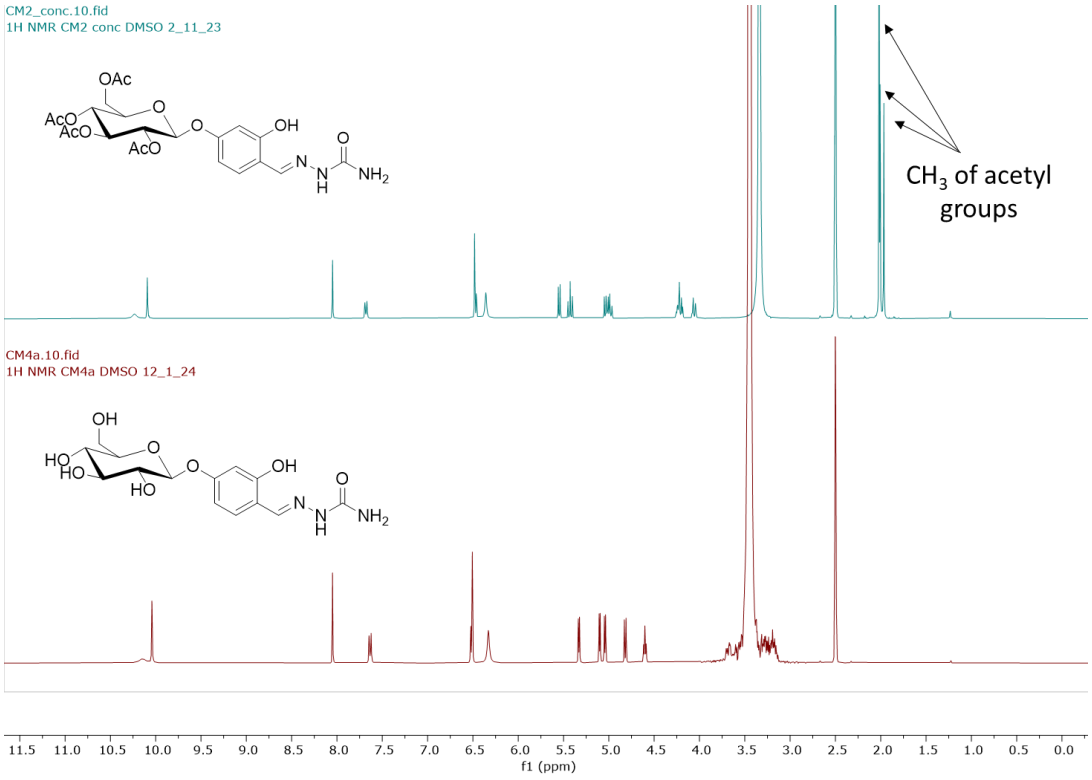

Figure 2.9: ^{1}H NMR spectra (400 MHz, 298 K) of **CM2** (top) and **CM4** (bottom) in DMSO-d_6.

Single crystals of **CM4** were obtained by slow evaporation from an ethanol solution of the ligand. The asymmetric unit of the SC-XRD crystal structure of **CM4** is shown in Figure 2.10. As in solution, in the solid state the semicarbazone is present as keto *E* isomer: the *E* configuration is favoured by the formation of an intramolecular hydrogen bond between the phenolic OH and the iminic N atom. In the crystal packing, all the hydroxyl groups and the N-NH-C=O group are involved in hydrogen bonds with adjacent molecules, while the terminal NH_2 moiety is not involved in hydrogen bonding.

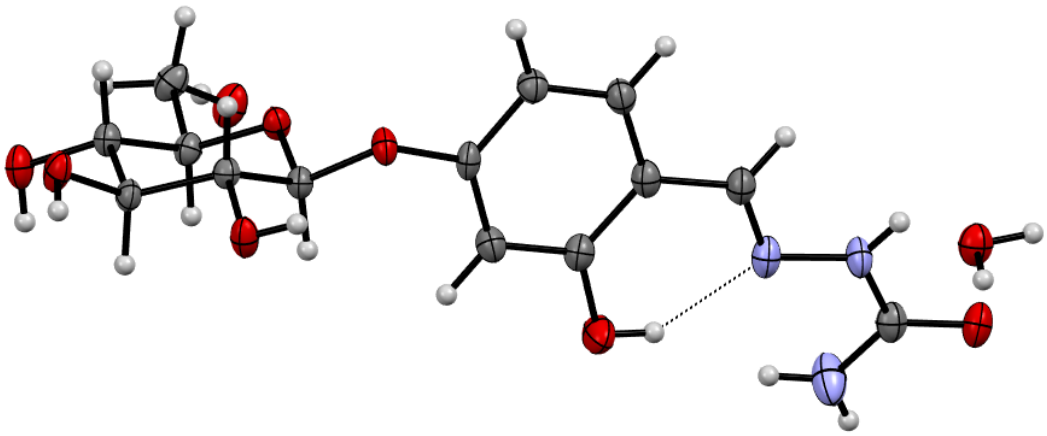

Figure 2.10: Asymmetric unit of the SC-XRD structure of **CM4.** The dashed line evidences the intramolecular hydrogen bond between the phenolic OH and the iminic N atom (oxygen atoms in red; nitrogen in blue; carbon in grey and hydrogens in white).

The packing in the crystal is determined by a high number of hydrogen bonds formed by the hydroxyl groups of the sugar, which is in chair conformation, and by the crystallization water molecule. The latter contributes to the formation of a bridge of hydrogen bonds between adjacent molecules.

The two aldehydes **FMM2** and **AZ24** were reacted with octanoic hydrazide to synthesize, respectively, **CM7** and **CM9** (Scheme 2.5).

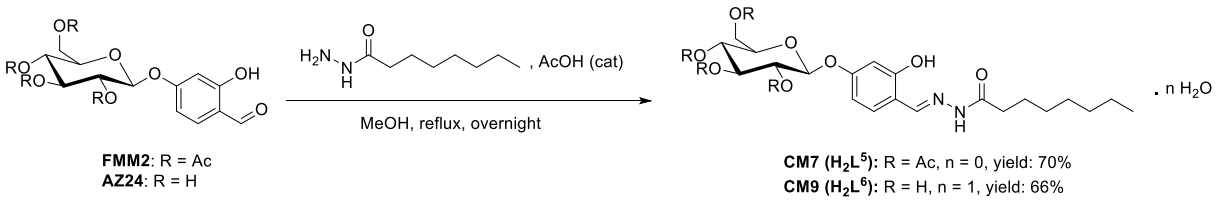

FMM2: R = Ac
AZ24: R = H

CM7 (H_2L^5): R = Ac, n = 0, yield: 70%
CM9 (H_2L^6): R = H, n = 1, yield: 66%

Scheme 2.5: Synthesis of the **N-acylhydrazones CM7** and **CM9**.

The novel ligands were characterized by means of FT-IR (Figures A2.29 and A2.37) and NMR spectroscopies, mass spectrometry (Figures A2.33, A2.34, A2.40 and A2.41) and elemental analysis (see the Experimental section).

Contrarily to what was observed for the **SCs**, NMR experiments indicate that both ligands exist in solution as a mixture of two isomers, **A** (major isomer) and **B** (minor isomer). The ratio between the two isomers is **70:30 A:B**, irrespective of the solvent (DMSO-d_6 and $CDCl_3$) and of the presence of acetyl groups. As an example, in Figure 2.11 the ^{1}H NMR spectrum (400 MHz, 298 K) of **CM7** in DMSO-d_6 is reported.

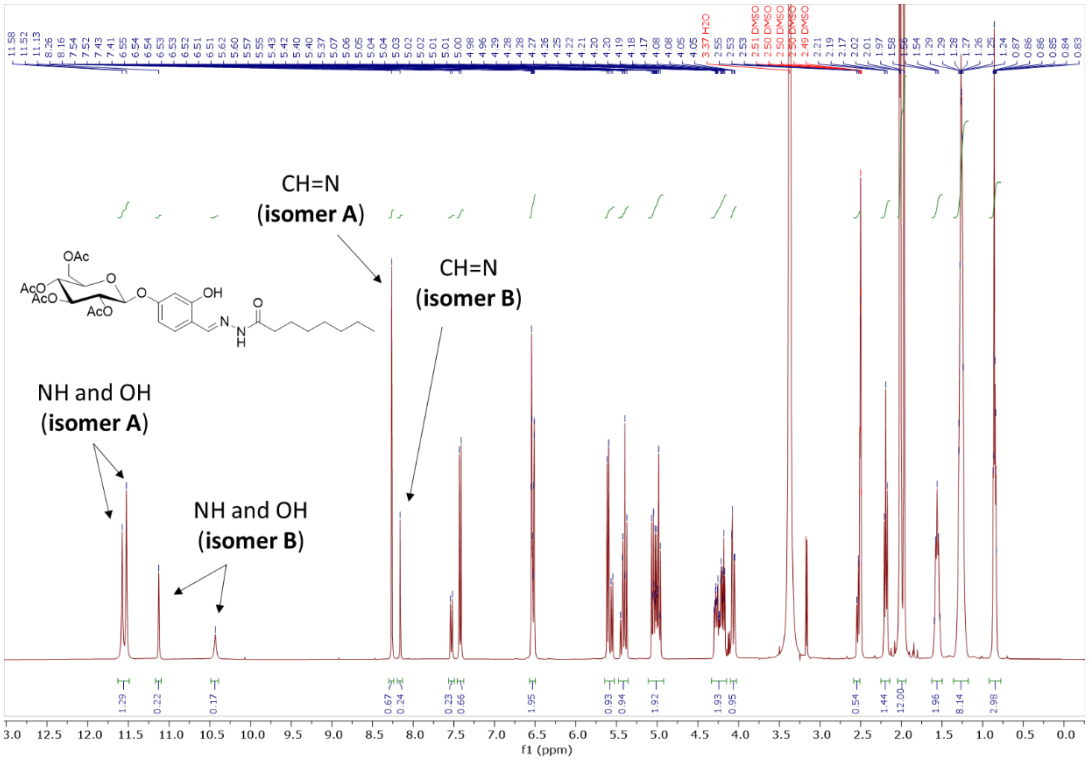

Figure 2.11: ^{1}H NMR spectrum (400 MHz, 298 K) of **CM7** in DMSO-d_6.

The ^{1}H NMR spectrum of **CM7** is characterized by two sets of signals for the following protons: phenolic OH, hydrazidic NH, iminic proton, aromatic protons, anomeric proton (Figure 2.12, in blue) and the methylene groups linked to the hydrazonic carbonyl (Figure 2.12, in red).

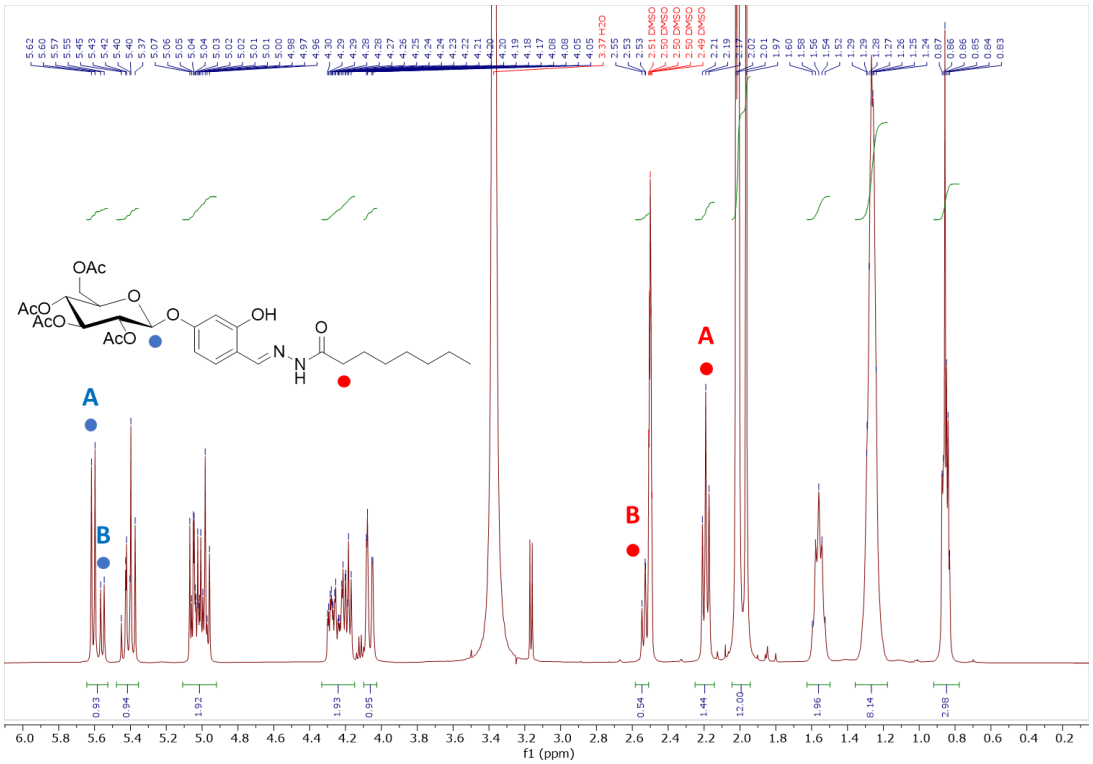

Figure 2.12: Selected range (6.00 – 0.00 ppm) of the ^{1}H NMR spectrum (400 MHz, 298 K) of **CM7** in DMSO-d_6. The peaks of the anomeric protons of the two isomers are indicated in blue, while the signals of the C(=O)-$\underline{CH_2}$-R group of the two isomers are indicated in red.

In solution, the aldehyde-based ***N*-acylhydrazones** can exist as two different geometric isomers (***E*** and ***Z***), but they can also exist as two rotational conformers (***syn*-** and ***anti*-periplanar**, which can be also referred to as ***cis*** and ***trans***) with respect to the C(=O) – N bond[196,213,214] (Figure 2.13). Typically, the **NAHs** derived from aldehydes with an ortho-hydroxy substituent are in ***E*** configuration, since such configuration is stabilized by an intramolecular hydrogen bond between the phenolic OH and the iminic nitrogen atom.[215] This could be true also for **CM7** and **CM9**, in which a ***Z*** configuration may be even less probable due to the steric hindrance of both the glucosyl-aromatic moiety and the alkyl chain. Therefore, we can hypothesize that the ligands in solution exist as ***E*** isomers, but as a mixture of ***cis*** and ***trans*** conformers (Figure 2.14).

Ortho-hydroxyl aldehyde-based **N-acylhydrazones** ligands bind to the copper(II) ion in the ***E trans*** configuration in order to act as O,N,O tridentate chelators, regardless of the favoured isomer in solution.

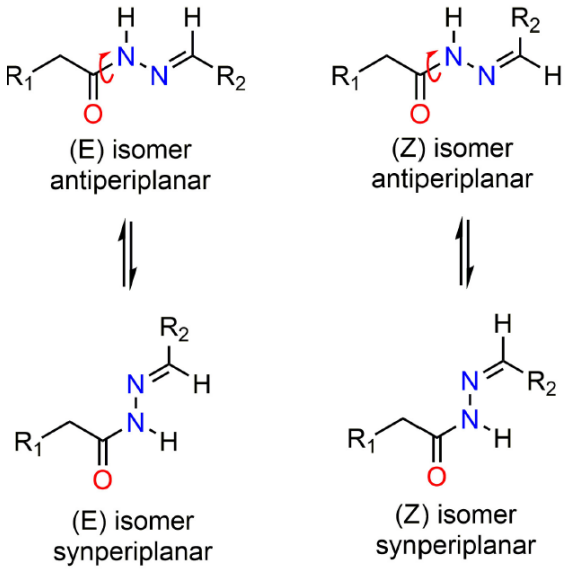

Figure 2.13: Geometric isomers and conformers of **N-acylhydrazones**. Adapted from Ref.[215]

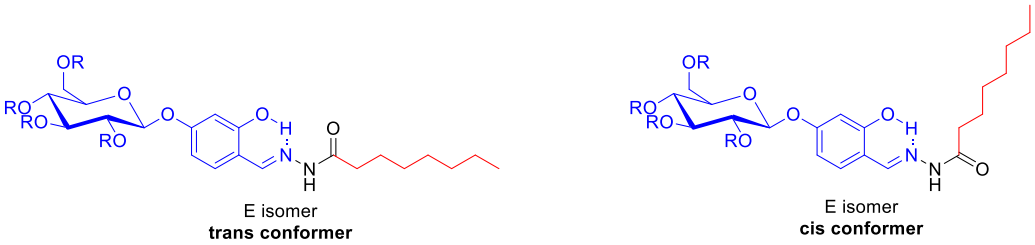

Figure 2.14: Proposed structures for isomers **A** and **B** observed for **CM7** and **CM9** in solution. The coloured parts refer to the moieties involved in the identification of the *cis/trans* species.

Synthesis and characterization of the glyco-conjugated copper(II) complexes

The **SC** ligands **CM2** and **CM4** were reacted with $CuCl_2 \cdot 2\ H_2O$ in 1:1 metal:ligand ratio in MeOH at room temperature to give the complexes **CM5** and **CM6**, respectively (Scheme 2.6).

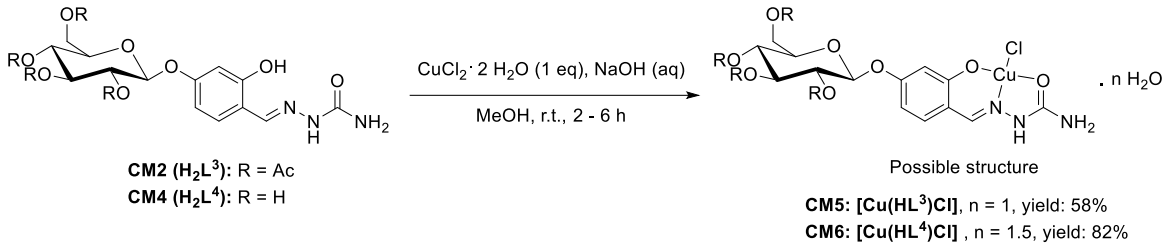

CM2 (H_2L^3): R = Ac
CM4 (H_2L^4): R = H

CM5: [Cu(HL^3)Cl], n = 1, yield: 58%
CM6: [Cu(HL^4)Cl] , n = 1.5, yield: 82%

Scheme 2.6: Synthesis of the copper(II) complexes **CM5** and **CM6**.

The novel complexes were characterized, as usual, by means of FT-IR (Figures A2.25 and A2.27) spectroscopy, mass spectrometry (Figures 2.16, A2.26 and A2.28) and elemental analysis (see the experimental section).

The involvement of the semicarbazonic carbonyl oxygen and of the imine nitrogen atoms in copper coordination is confirmed by the IR spectra (Figures 2.15-16). The band relative to C=O stretching of the free ligand **CM2** shifts to lower frequencies in **CM5** (from 1682 cm^{-1} to 1661 cm^{-1}), while the two bands associated to C=O stretching of ligand **CM4** change into a single band in **CM6** (from 1672 and 1656 cm^{-1} to 1667 cm^{-1}). The two bands of C=N stretching in **CM2** become a single band in the spectrum of **CM5** (from 1628 and 1605 cm^{-1} to 1612 cm^{-1}); the same trend is observed for the **CM4**/**CM6** system (Figure 2.16). For both complexes **CM5** and **CM6**, data suggest that the glucosyl-**SCs** behave as mono-deprotonated O,N,O tridentate ligands.

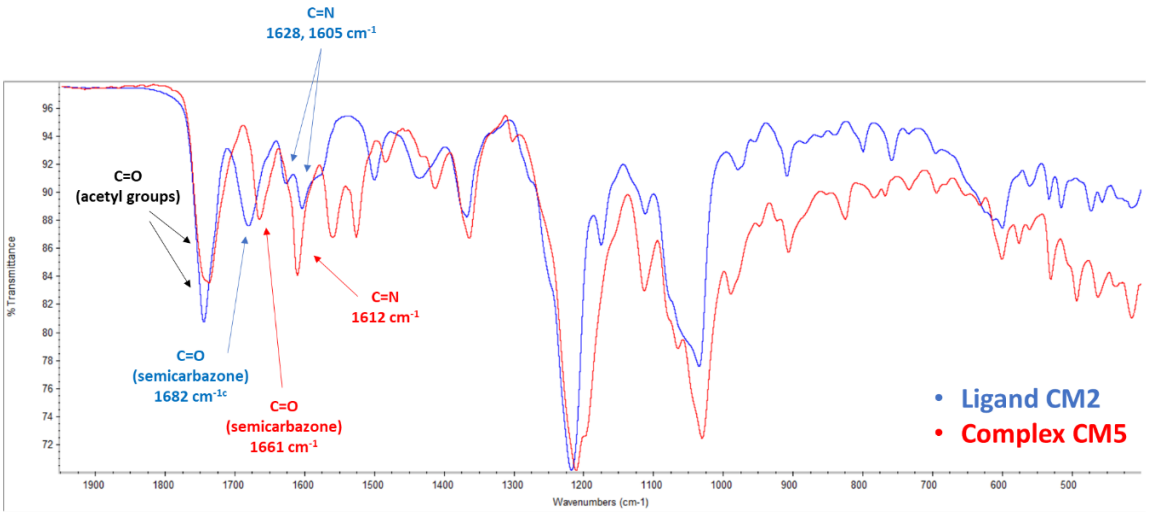

Figure 2.15: FT-IR spectra of ligand **CM2** (in blue) and its copper(II) complex **CM5** (in red).

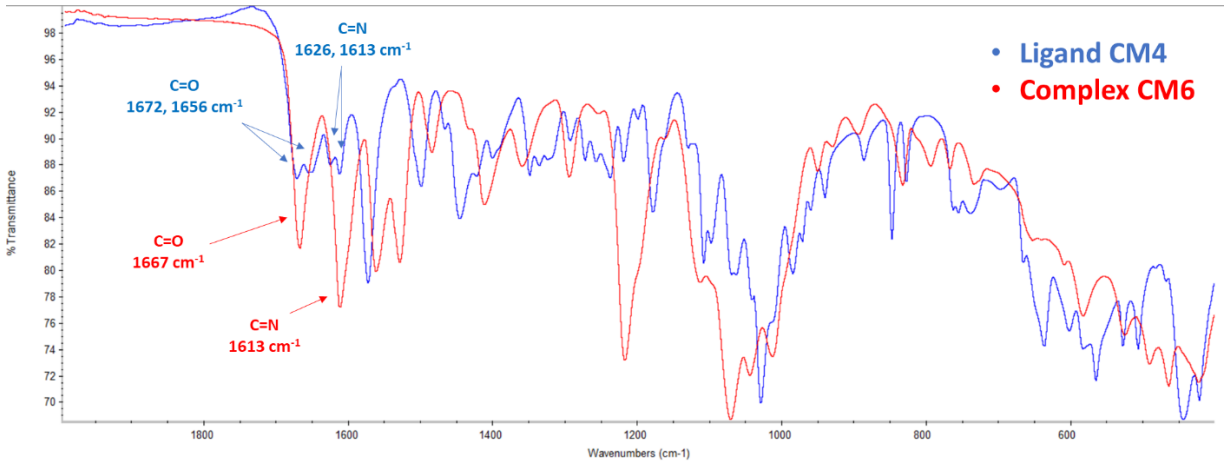

Figure 2.16: FT-IR spectra of ligand **CM4** (in blue) and its copper(II) complex **CM6** (in red).

The complexes have formula **[Cu(HL)Cl] · n H_2O** and the presence of chloride in their structure is confirmed by elemental analysis and ESI-MS (negative ions) data (Figure 2.17). The coordination sphere of copper is completed by water molecules: the lack of single crystal XRD information does not allow to know the number of such molecules, together with the coordination geometry around the metal.

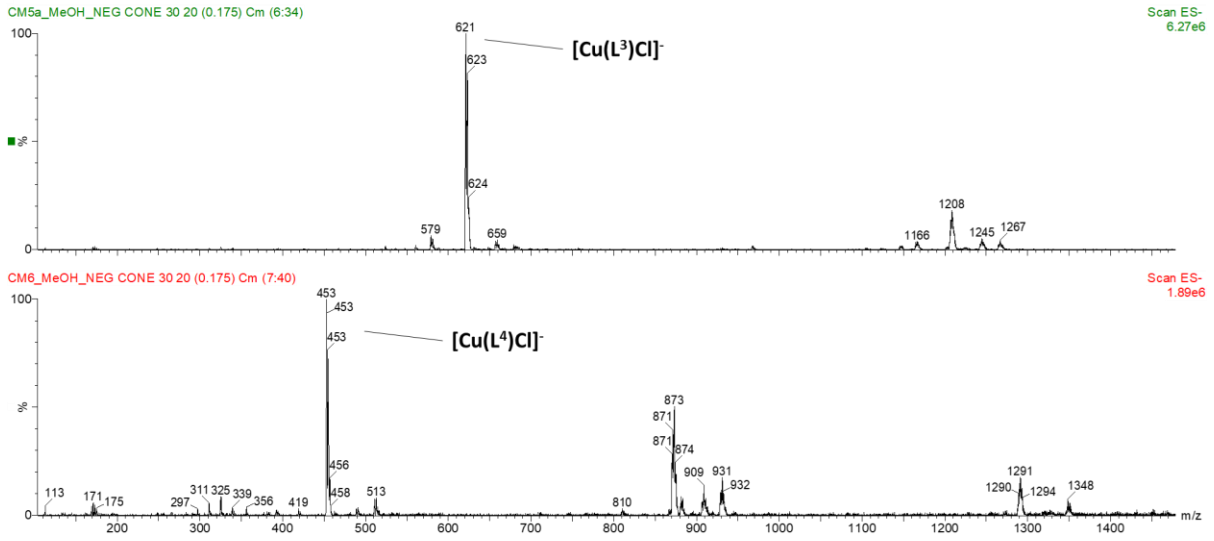

Figure 2.17: ESI-MS (negative ions) spectra of **CM5** (**top**) and **CM6** (**bottom**). The samples were prepared in MeOH.

As expected, the complex **CM6**, which contains the deprotected glucosyl moiety, is soluble in water.

Analogously to the **SCs**, the **NAH** ligands **CM7** and **CM9** were reacted with $CuCl_2 \cdot 2\ H_2O$ in 1:1 metal:ligand ratio in EtOH at room temperature to give the complexes **CM8** and **CM10**, respectively (Scheme 2.7).

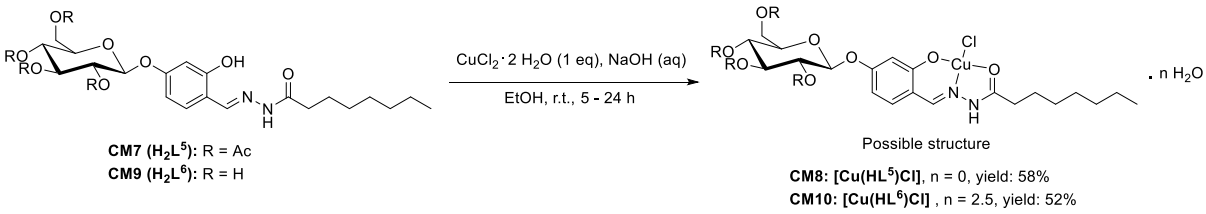

CM7 (H_2L^5): R = Ac
CM9 (H_2L^6): R = H

CM8: [Cu(HL^5)Cl], n = 0, yield: 58%
CM10: [Cu(HL^6)Cl] , n = 2.5, yield: 52%

Scheme 2.7: Synthesis of the copper(II) complexes **CM8** and **CM10**.

The novel complexes were characterized by means of FT-IR (Figures A2.35 and A2.42) spectroscopy, mass spectrometry (Figures 2.20, A2.36 and A2.43) and elemental analysis (see the experimental section).

As for the **SC**-based systems, a) the acylhydrazonic carbonyl oxygen and the imine nitrogen atoms are involved in copper coordination (Figures 2.18-2.19), and b) the glucosyl-**NAHs** behave as mono-deprotonated O,N,O tridentate ligands. The complexes have the common formula **[Cu(HL)Cl] · n H_2O** and the presence of chloride in their structure is confirmed by elemental analysis and ESI-MS (negative ions) data (Figure 2.20). Note that in **CM8** water molecules are not present, as can be expected due to the lipophilic character of the ligand **CM7**.

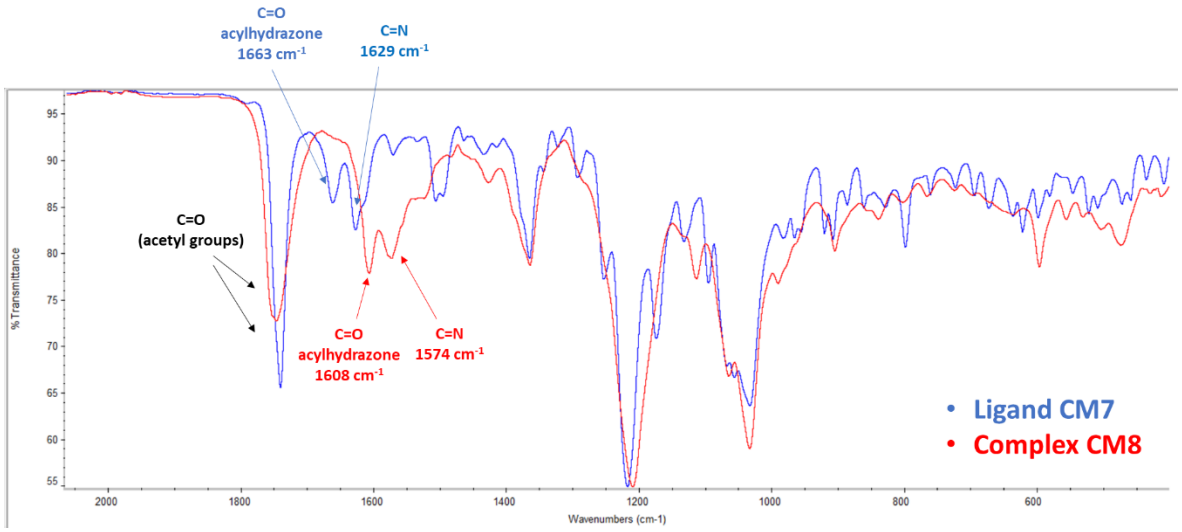

Figure 2.18: FT-IR spectra of ligand **CM7** (in blue) and its copper(II) complex **CM8** (in red).

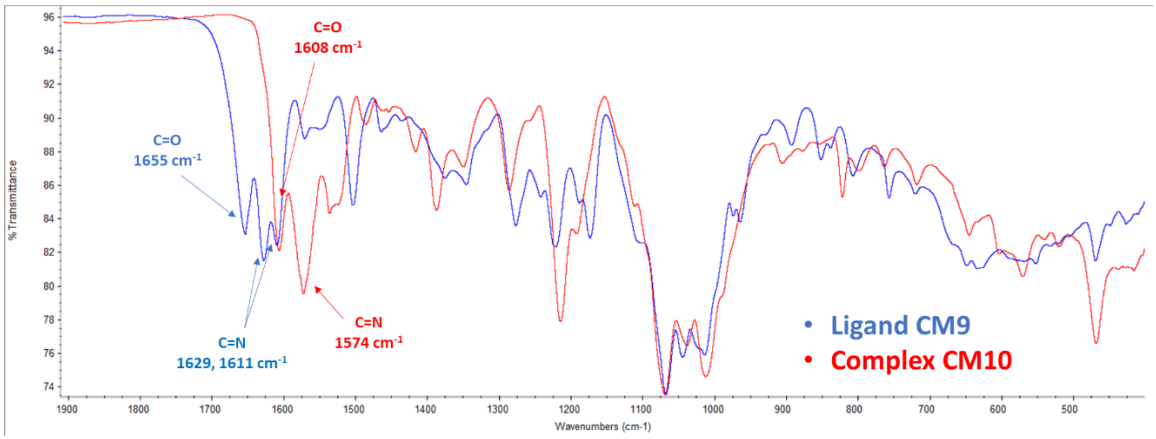

Figure 2.19: FT-IR spectra of ligand **CM9** (in blue) and its copper(II) complex **CM10** (in red).

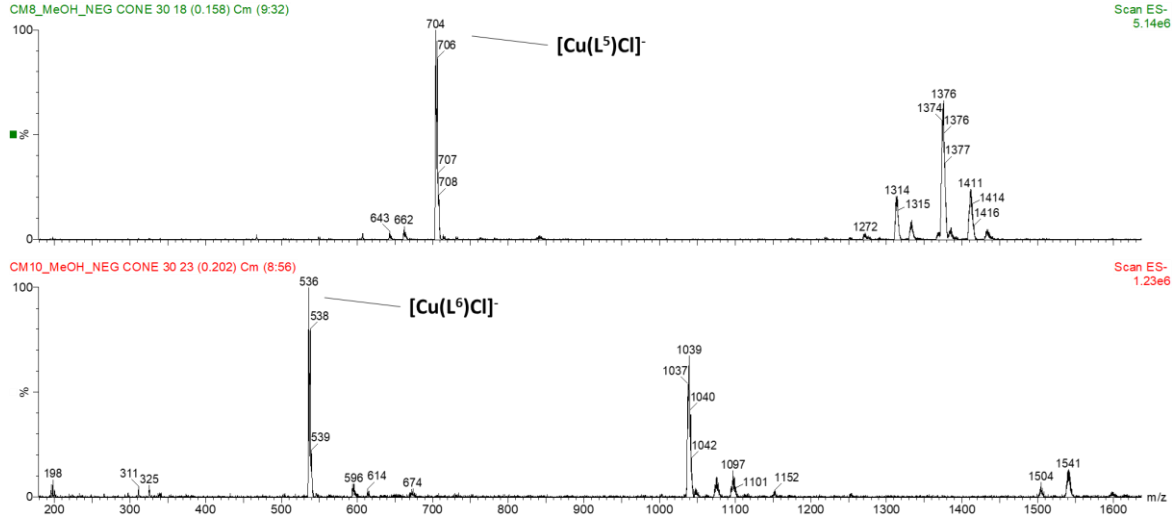

Figure 2.20: ESI-MS (negative ions) spectra of **CM8** (**top**) and **CM10** (**bottom**). The samples were prepared in MeOH.

As expected, the complex **CM10**, which contains the deprotected glucosyl moiety, is soluble in water.

Complexation equilibria in aqueous solution

For a large number of potentially bioactive ligands and metal complexes, solubility issues prevent their characterization in aqueous solution. This is an important limit, since knowledge of the most plausible chemical forms of drugs in aqueous solution and in physiological conditions is a mandatory prerequisite for determining their mechanism of action and might help in the design of more effective and selective medicines. The study of the behaviour of metallodrugs in the solid state and in solution of organic solvents may be not sufficient to understand their bio-transformations in the biological fluids.[216]

The insertion of the glucosyl-moiety in their structure conferred hydro-solubility to the **TSC FMM8Z** (**H_2L^2**) and to the **SC CM4** (**H_2L^4**) (Figure 2.21) and allowed to study their coordination properties in aqueous solution.

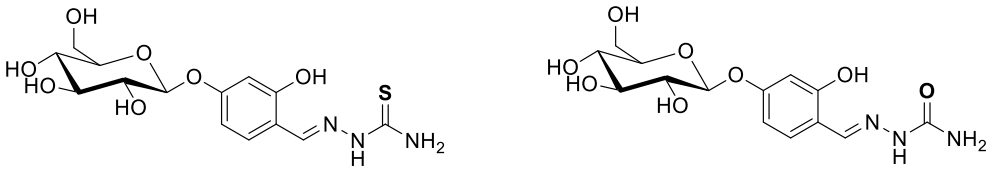

H_2L^2 **H_2L^4**

Figure 2.21: Chemical structure of the **TSC** ligand **H_2L^2** (**FMM8Z**) and of the **SC** ligand **H_2L^4** (**CM4**).

The copper(II) complexation equilibria of **H_2L^2** were studied by means of direct UV-visible spectrophotometric titration of the ligand with Cu^{II} in aqueous solution at pH = 7.4 at 298.2 K. This titration and the titrations that follow, being performed at constant pH, did not allow to establish the protonation state of the ligand but only the possible stoichiometry (M/L) of the species. For this reason, in the speciation models, L identifies the ligand irrespective of its protonation state, and the charges of the complexes are omitted. The HEPES buffer was chosen for the titration, since it has been reported to have a weak competing role in metal ion complexation ($\log K_{Cu(HEPES)}$ = 2.91 at pH = 7.4).[126]

Spectral data were collected by titration of **H_2L^2** (C_L ca. 25 μM) with Cu^{2+} ions up to a metal:ligand ratio of 3 (Figure 2.22). Unexpectedly, the titration data show two families of spectra. The first family of spectra (Cu/L = 0 - 1) (Figure 2.23) is characterized by the appearance of the bands at 257 and 364 nm and by the decrease of the band at 330 nm. There are two isosbestic points at 279 and 350 nm.

The second family of spectra (Cu/L = 1 – 3) (Figure 2.24) is characterized by the increase of the bands at 257 nm and 314 nm, the very slight increase of a shoulder at 414 nm and by the slight decrease of the band at 364 nm. There are two isosbestic points at 333 and 390 nm.

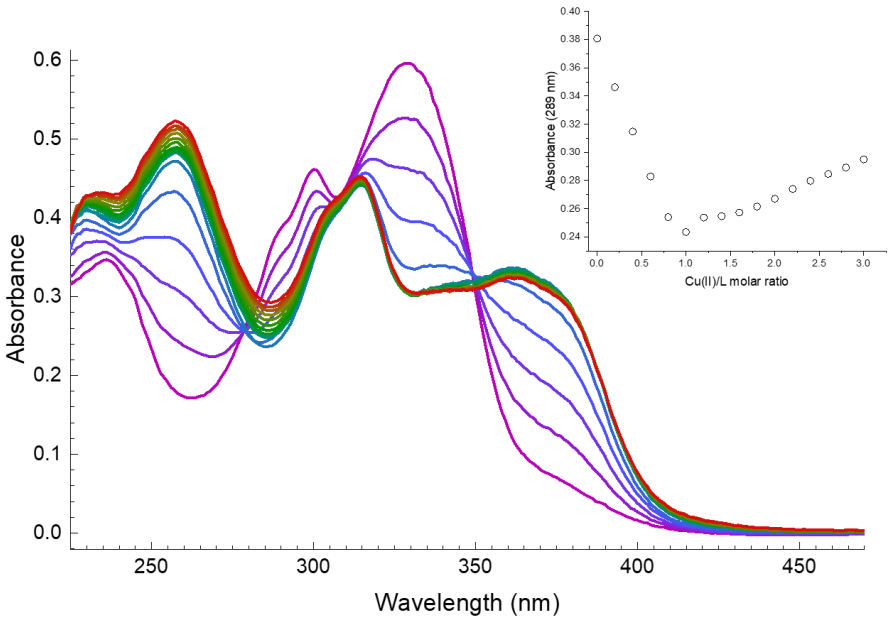

Figure 2.22: UV-visible spectra for the titration of **H_2L^2** with Cu^{II} in aqueous solution at pH 7.4 at 298.2 K (25 mM HEPES buffer, I = 11 mM (Na(HEPES)); C_L = 25 µM; Cu^{II}:L = 0-3). Inset: plot of the experimental absorbance values at 289 nm vs Cu^{II}/ligand molar ratio.

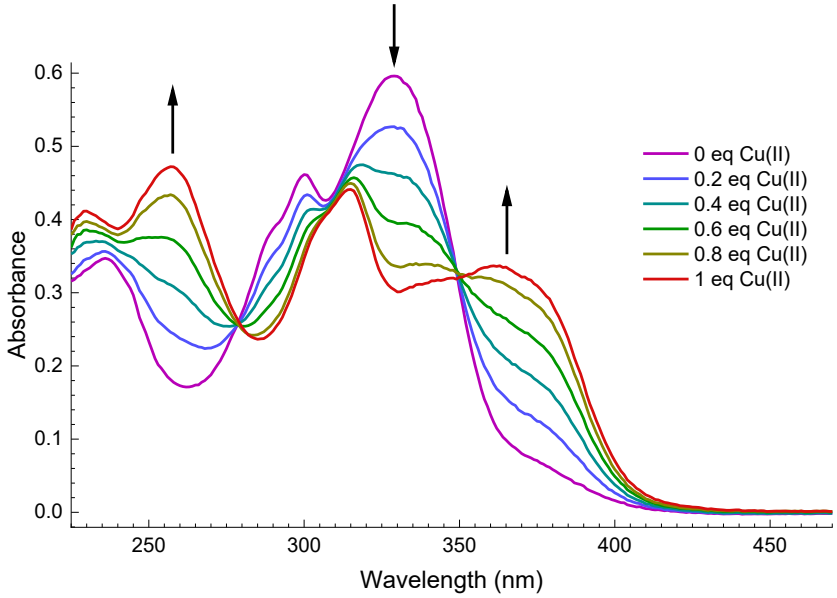

Figure 2.23: UV-visible spectra for the titration of **H_2L^2** with Cu^{II} in aqueous solution at pH 7.4 at 298.2 K (25 mM HEPES buffer, I = 11 mM (Na(HEPES)); C_L = 25 µM; Cu^{II}:L = 0-1).

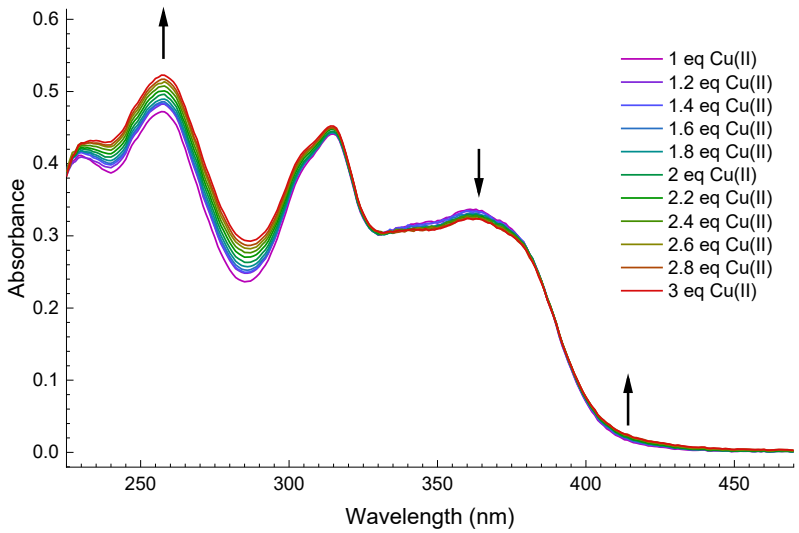

Figure 2.24: UV-visible spectra for the titration of **H_2L^2** with Cu^{II} in aqueous solution at pH 7.4 at 298.2 K (25 mM HEPES buffer, I = 11 mM (Na(HEPES)); C_L = 25 µM; Cu^{II}:L = 1-3).

The observed spectral trend suggests the formation of two complex species in aqueous solution: a 1:1 Cu^{II}:L^2 complex, that forms between 0 and 1 equivalents of copper(II), and another species, probably a 2:1 Cu^{II}:L^2 complex, that forms between 1 and 3 equivalents of added metal. This is further supported by the plot of the absorbance value at 289 nm with respect to the Cu/L ratio: a steep inflection point is observed at 1 eq. of added copper, after which there is an increase in the absorbance value, instead of a plateau (Figure 2.21, inset).

This result is curious, since the ligand was expected to coordinate the metal centre with the O,N,S donor set only, to give a 1:1 metal:ligand complex and/or a 1:2 metal:ligand complex. Indeed, in spectrophotometric studies reported in literature,[44,109,216] the equilibria of similar salicylaldehyde-thiosemicarbazonic ligands with copper(II) and zinc(II) ions in solution are characterized by the formation of ML and ML_2 species, only. The formation of M_2L complexes has been reported only for **TSCs** with two vicinal hydroxyl substituents on the aromatic ring of the aldehydic precursor.[44]

We can therefore hypothesize that the 2:1 Cu^{II}:L^2 complex forms in solution thanks to the interaction of the glucosyl moiety with a second copper(II) ion. It is known that, in solution, saccharides can give rise to transition metals complexes with very low formation constants, through their weakly chelating hydroxyl groups.[217-219] In the case of ligand **H_2L^2**, the equatorial hydroxyl groups of the glucosyl moiety in $^4C_1$ chair conformation are unlikely to chelate the metal ion. A possible explanation of the titration data may involve a change in the chair conformation of the sugar, induced by the metal ion (Scheme A2.1). The involvement of the oxygen atom of the glycosidic bond in copper(II) coordination may also explain the change in the UV-visible spectrum upon coordination, being the oxygen atom attached to the aromatic ring of the ligand. However, at present, this remains hypothetical.

The steep inflection point observed in correspondence of 1 equivalent of copper(II) in the binding isotherm (Figure 2.22, inset) indicates that the experimental conditions are not adequate for an accurate determination of the formation constant of the 1:1 Cu^{II}:ligand complex, because the equilibrium composition is completely shifted towards the formation of the complex species. According to literature,[112] in this case only a rough estimation of the lower limit for the β(CuL) value can be calculated:

$$\beta(CuL) > \frac{100}{[L]_0} \qquad (2.1)$$

where $[L]_0$ is the initial concentration of the ligand solution in the cuvette. Since in the titration the $[L^2]_0$ value was 25 µM, it is only possible to say that, in these experimental conditions, the logβ(CuL^2) value is higher than 6.60. The impossibility of determining an accurate value for the logβ(CuL^2) prevented the determination of the logarithm of the formation constant of the hypothetical Cu_2L^2 species.

Since there is no inflection point at 2 equivalents of metal and the absorbance value at 289 nm keeps on increasing in intensity even after the addition of several equivalents of metal (Figure 2.22, inset), it is only possible to say that the formation constant of the 2:1 metal:ligand species is much lower than the formation constant of the 1:1 metal:ligand species.

We tried to determine the logβ(CuL^2) value by adopting a strategy based on the use of Zn^{II} as competing metal ion for the complexation of **H_2L^2**. If the **TSC** forms a 1:1 Zn^{II}:ligand complex as unique species in solution and if its formation constant is known, it is possible to perform a competitive titration and determine the logβ(CuL^2) value by studying the following equilibrium (the charges of the complexes are omitted):

$$[ZnL^2] + Cu^{2+} = [CuL^2] + Zn^{2+} \qquad (2.2)$$

In order to find the logβ(ZnL^2) value, a solution of **H_2L^2** (C_L ca. 25 µM) in aqueous 25 mM HEPES buffer at pH 7.4 was titrated with Zn^{2+} ions up to a metal:ligand ratio of 4 (Figure 2.25).

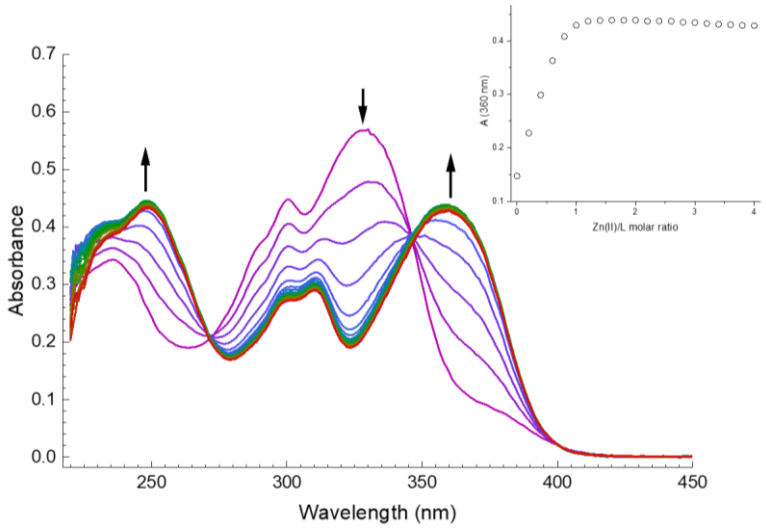

Figure 2.25: UV-visible spectra for the titration of **H_2L^2** with Zn^{II} in aqueous solution at pH 7.4 at 298.2 K (25 mM HEPES buffer, I = 11 mM (Na(HEPES)); C_L = 25 µM; Zn^{II}:L = 0-4). Inset: plot of the experimental absorbance values at 360 nm vs Zn^{II}/ligand molar ratio.

In this case, only one family of spectra was observed. Upon addition of zinc(II) to the ligand solution, a decrease of the band at 328 nm was observed, together with a red shift and an increase of the band at 236 nm and a blue shift and an increase of the band at 380 nm. Two isosbestic points were detected at 271 and 347 nm.

The plot of the absorbance values at 360 nm vs the Zn^{II}/L^2 ratio showed a linear increase in intensity until 1 equivalent of zinc, followed by a plateau (Figure 2.25, inset). This trend suggested that only a 1:1 zinc(II):ligand species formed in aqueous solution and that the binding occurred under saturation conditions, thus preventing an accurate determination of logβ(ZnL^2). However, the spectral data were elaborated by means of

the HypSpec2014 software[108] and the best fitting was obtained by using a speciation model based on a 1:1 metal:ligand complex. The calculated value for logβ(ZnL^2) is 6.84 ± 0.01, a value which is higher than the limit value for accurate determination of formation constants (6.60), and that therefore can be considered only as an estimate.

Lacking the accurate value of logβ(ZnL^2), it was not possible to perform the competitive titration. The **TSC H_2L^2** demonstrated a very high affinity towards both copper(II) and zinc(II) ions.

As for **H_2L^2**, the copper(II) complexation equilibria of the **SC H_2L^4** were studied by means of direct UV-visible spectrophotometric titration of the ligand (C_L ca. 50 µM) with Cu^{II} in aqueous solution at pH = 7.4 and at 298.2 K (Figure 2.26). Metal ions were added up to a copper(II):ligand ratio of 5.

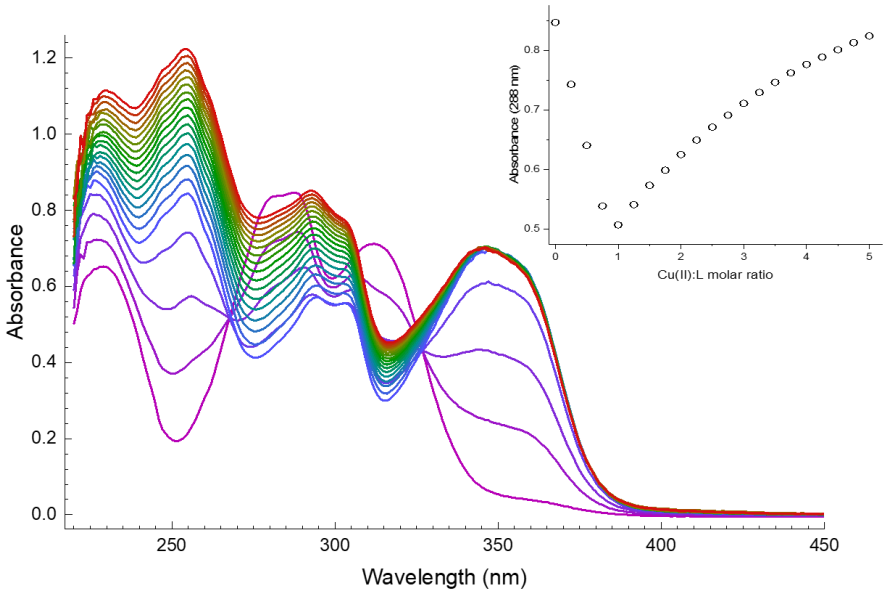

Figure 2.26: UV-visible spectra for the titration of **H_2L^4** with Cu^{II} in aqueous solution at pH 7.4 at 298.2 K (25 mM HEPES buffer, I = 11 mM (Na(HEPES)); C_L = 50 µM; Cu^{II}:L = 0-5). Inset: plot of the experimental absorbance values at 288 nm vs Cu^{II}/ligand molar ratio.

Analogously to the copper(II)-**H_2L^2** system, also in this case two family of spectra were observed. The first family of spectra (Cu/L = 0 - 1) (Figure 2.27) is characterized by the increase of the band at 230 nm, the appearance of the bands at 254 and 348 nm and by the decrease of the band at 288 and 311 nm. There are two isosbestic points at 268 and 327 nm.

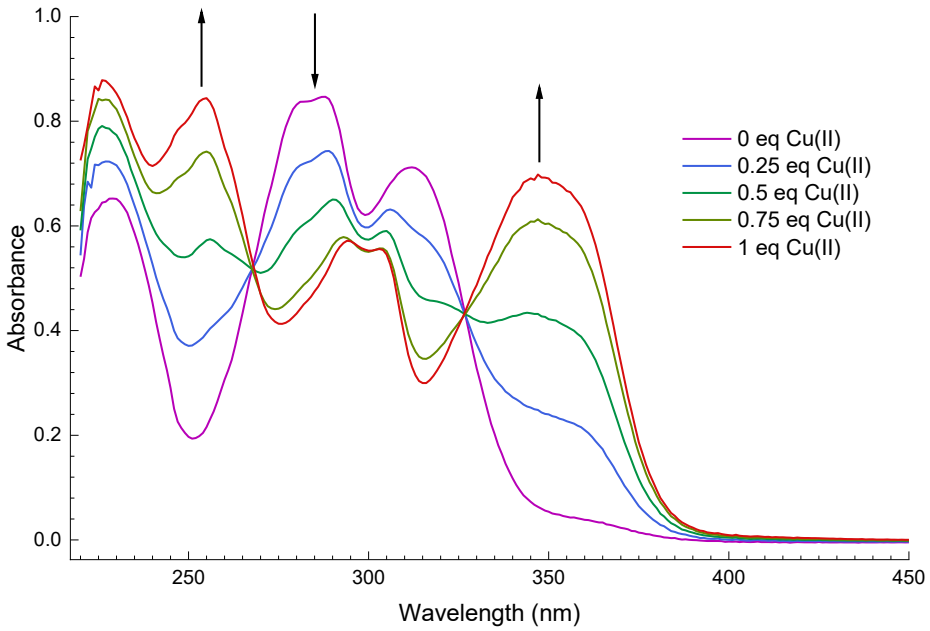

Figure 2.27: UV-visible spectra for the titration of **H_2L^4** with Cu^{II} in aqueous solution at pH 7.4 at 298.2 K (25 mM HEPES buffer, I = 11 mM (Na(HEPES)); C_L = 25 µM; Cu^{II}:L = 0-1).

The second family of spectra (Cu/L = 1 – 5) (Figure 2.28) is characterized by the increase of the bands at 230, 255 and 293 nm and by the very slight decrease of a shoulder around 357 nm. There is an isosbestic point at 348 nm.

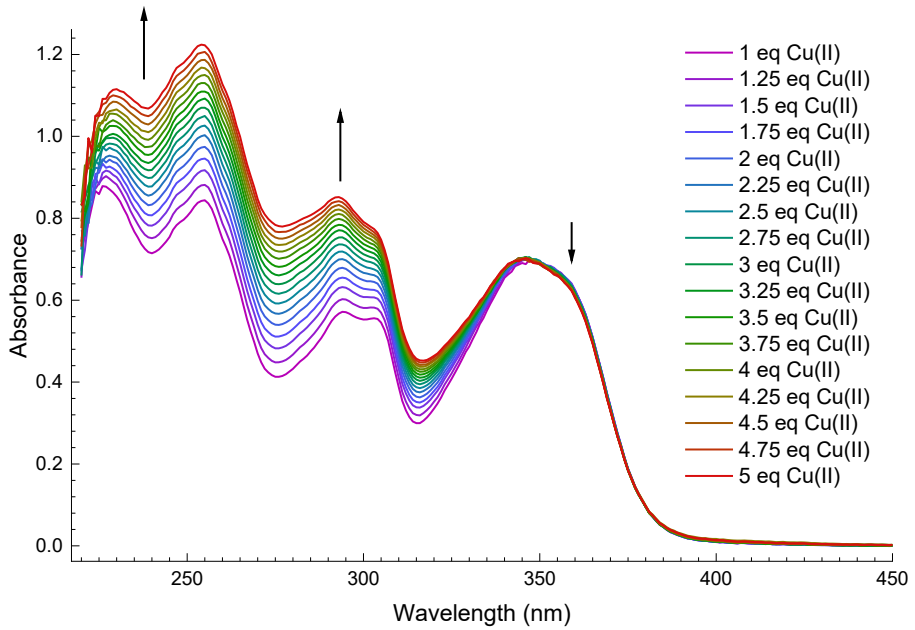

Figure 2.28: UV-visible spectra for the titration of **H_2L^4** with Cu^{II} in aqueous solution at pH 7.4 at 298.2 K (25 mM HEPES buffer, I = 11 mM (Na(HEPES)); C_L = 25 µM; Cu^{II}:L = 1-5).

The observed spectral trend suggests the formation of two complex species in aqueous solution: a 1:1 Cu^{II}:L^4 complex, that forms between 0 and 1 equivalents of copper(II), and another species, probably a 2:1 Cu^{II}:L^4 complex, that forms between 1 and 4 equivalents of added metal.

This finding is further supported by the plot of the absorbance values at 288 nm with respect to the Cu/L ratio: a steep inflection point is observed at 1 eq. of added copper, after which there is an increase in the absorbance value, instead of a plateau (Figure 2.26, inset).

If we look at the plot of the absorbance value at 347 nm with respect to the Cu/L ratio, we can see the formation of a plateau after 1 equivalent (Figure 2.29). Similarly to what was observed for the titration of the **thiosemicarbazone** with copper(II), the second family of spectra is characterized by an unusual evolution of the bands upon addition of metal ions. In fact, the absorption bands that are observed between 220 and 300 nm experiment a significant increase in intensity, while the bands over 300 nm are characterized by slight variations in intensity (Figure 2.28).

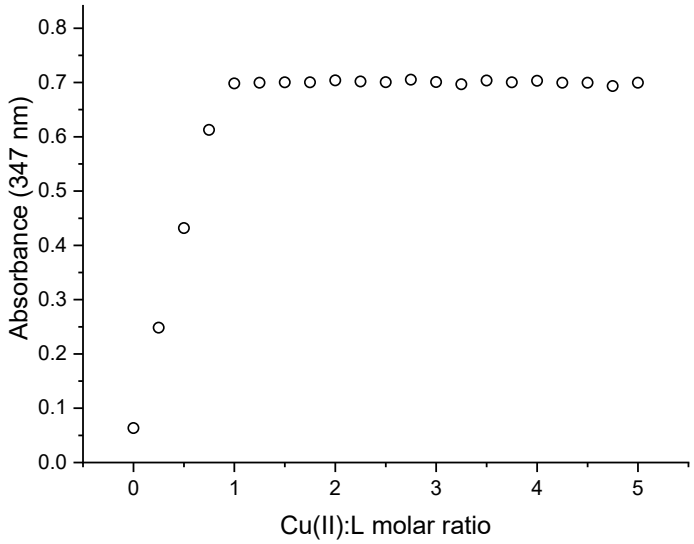

Figure 2.29: Plot of the experimental absorbance values at 347 nm vs Cu^{II}/L^4 molar ratio.

Looking again at the plot of the absorbance values at 288 nm vs Cu^{II}/L^4 molar ratio (Figure 2.26, inset), we can note a linear decrease in absorbance value until 1 equivalent: this suggests that also the formation constant of the CuL^4 species is too high to be determined with accuracy and, according to equation 2.1, we can only estimate that $\log\beta(CuL^4)$ is higher than 6.30.

Regarding the formation of the hypothetical Cu_2L^4 species, as it was observed for the **TSC**, there is only a gradual increase in absorbance value at 288 nm upon addition of copper(II) (Figure 2.26, inset). There is no inflection point at 2 equivalents of metal and the absorbance value keeps on increasing in intensity even after the addition of several equivalents of metal. These results suggest that the formation constant of the 2:1 metal:ligand species is much lower than the formation constant of the 1:1 metal:ligand species.

As we did for $\mathbf{H_2L^2}$, we tried to determine the $\log\beta(CuL^4)$ value by adopting a strategy based on the use of Zn^{II} as competing metal ion for the complexation of $\mathbf{H_2L^4}$. A solution of $\mathbf{H_2L^4}$ (C_L ca. 50 μM) in aqueous 25 mM HEPES buffer at pH 7.4 was titrated with Zn^{2+} ions up to a metal:ligand ratio of 7 (Figure 2.30).

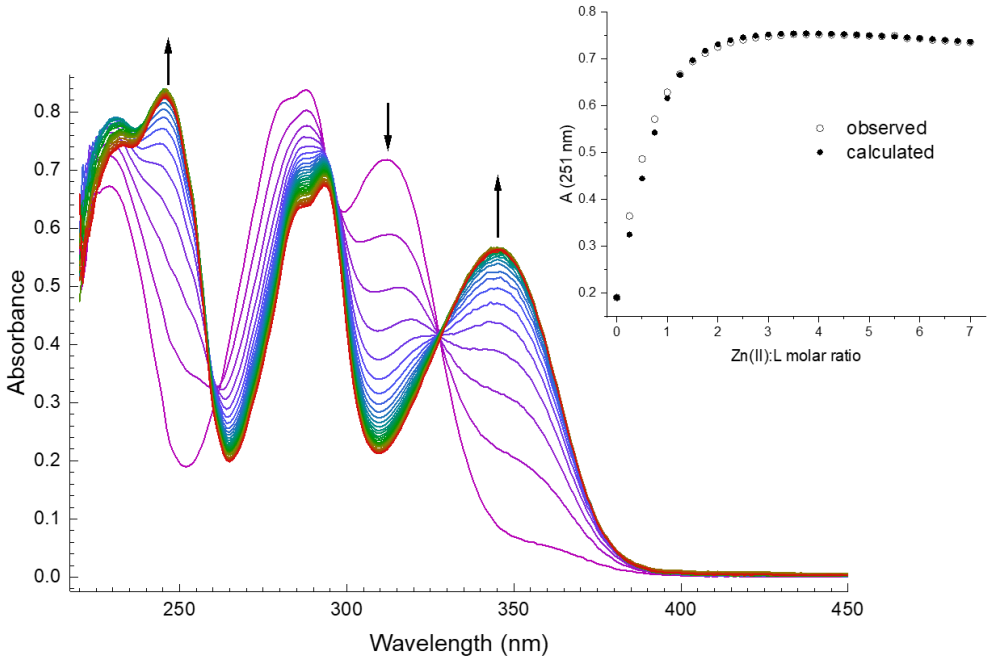

Figure 2.30: UV-visible spectra for the titration of $\mathbf{H_2L^4}$ with Zn^{II} in aqueous solution at pH 7.4 at 298.2 K (25 mM HEPES buffer, I = 11 mM (Na(HEPES)); C_L = 50 µM; Zn^{II}:L = 0-7). Inset: plot of the observed (empty circles) and calculated (black circles) absorbance values at 251 nm vs Zn^{II}/ligand molar ratio.

The titration data are consistent with only one family of spectra, which is characterized by the increase in intensity of the absorption bands at 230, 246 and 345 nm, and by the decrease of the bands at 288 and 312 nm. There are two isosbestic points at 260 and 328 nm.

The spectral data were elaborated by means of the HypSpec2014 software[108] and the best fitting was obtained by using a speciation model based on a 1:1 zinc(II):ligand complex. The calculated value for $\log\beta(ZnL^4)$ is 5.10 ± 0.01. Such value falls below the calculated limit for reliable results ($\log\beta_{limit}$ = 6.30), therefore the obtained formation constant can be considered accurate.

With the knowledge of the formation constant of the 1:1 zinc(II):**semicarbazone** complex, it was possible to run a competitive titration in the attempt of determining the value of $\log\beta(CuL^4)$. A UV-visible spectrophotometric titration was carried out with copper(II) chloride on an aqueous solution (25 mM HEPES buffer; pH 7.4; 298.2 K) containing zinc(II) chloride and $\mathbf{H_2L^4}$ (Figure 2.31). A speciation simulation of the Zn^{II}-$\mathbf{H_2L^4}$ system in the initial conditions of the titration (C_L ca. 50 µM) was run with the Hyss2009 software[125] in order to determine the metal:ligand ratio necessary to assume that all the ligand in the cuvette was involved in zinc coordination, based on the $\log\beta(ZnL^4)$ value. In this way, it was obtained 6:1 as optimal zinc:ligand ratio for the initial conditions of the competitive titration (Figure A2.44). Therefore, a 6:1 zinc(II): $\mathbf{H_2L^4}$ aqueous solution was titrated with copper(II) ions up to a copper(II):ligand ratio of 5 (Figure 2.32).

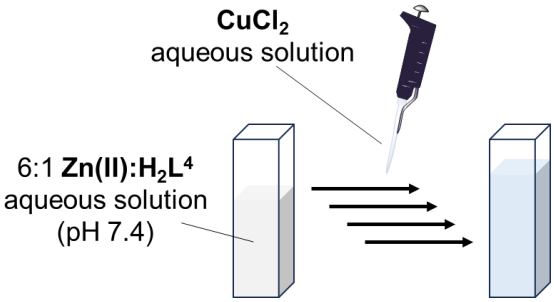

Figure 2.31: Schematic representation of the competitive titration for the system Zn^{II}:**H_2L^4**:Cu^{II}.

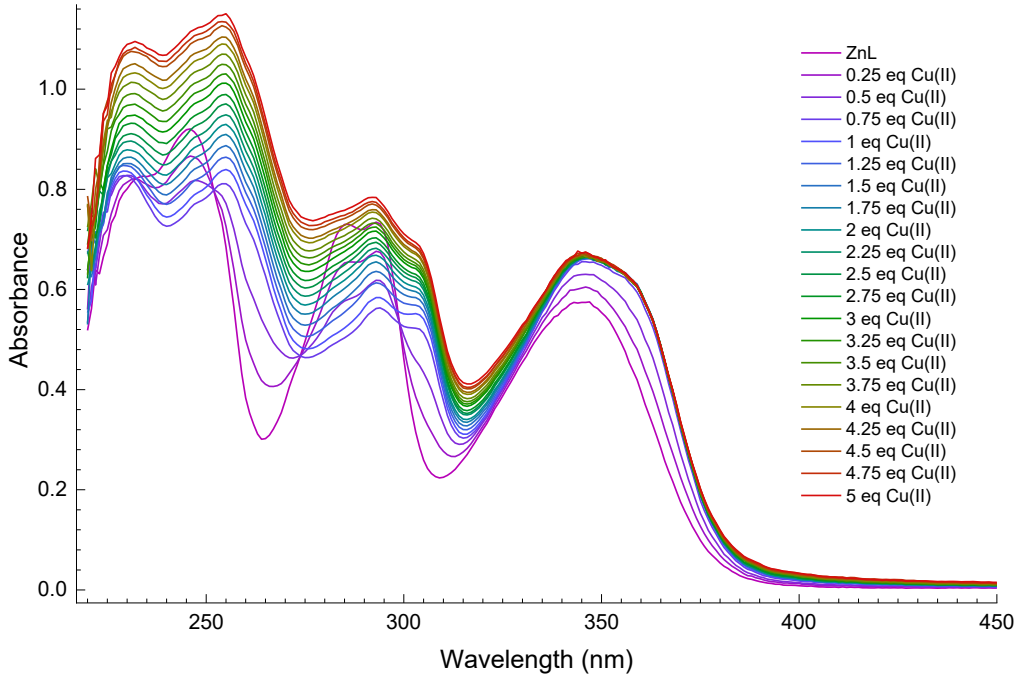

Figure 2.32: UV-visible spectra for the titration of a 6:1 Zn^{II}:**H_2L^4** aqueous solution with Cu^{II} at pH 7.4 and at 298.2 K (25 mM HEPES buffer, I = 11 mM (Na(HEPES)); C_L = 50 µM; Cu:ZnL = 0-5).

Again, the spectral data show the presence of two families of spectra. The first family of spectra (Cu/ZnL = 0 - 1) (Figure 2.33) is characterized by the appearance of a band at 254 nm, by the increase of the band at 348 nm, by the disappearance of the band at 246 nm and by the decrease of the band at 293 nm. There are two isosbestic points at 252 and 298 nm.

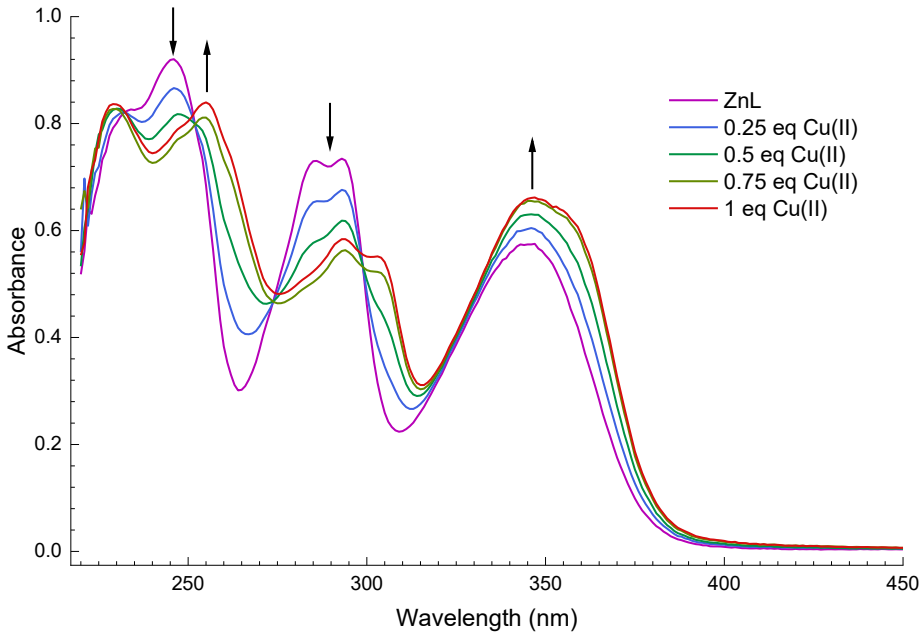

Figure 2.33: UV-visible spectra for the titration of a 6:1 Zn^{II}:$\mathbf{H_2L^4}$ aqueous solution with Cu^{II} at pH 7.4 and at 298.2 K (25 mM HEPES buffer, I = 11 mM (Na(HEPES)); C_L = 50 µM; Cu:ZnL = 0-1).

The second family of spectra (Cu/ZnL = 1 – 5) (Figure 2.34) is characterized by the increase in intensity of the bands at 231, 254 and 292 nm.

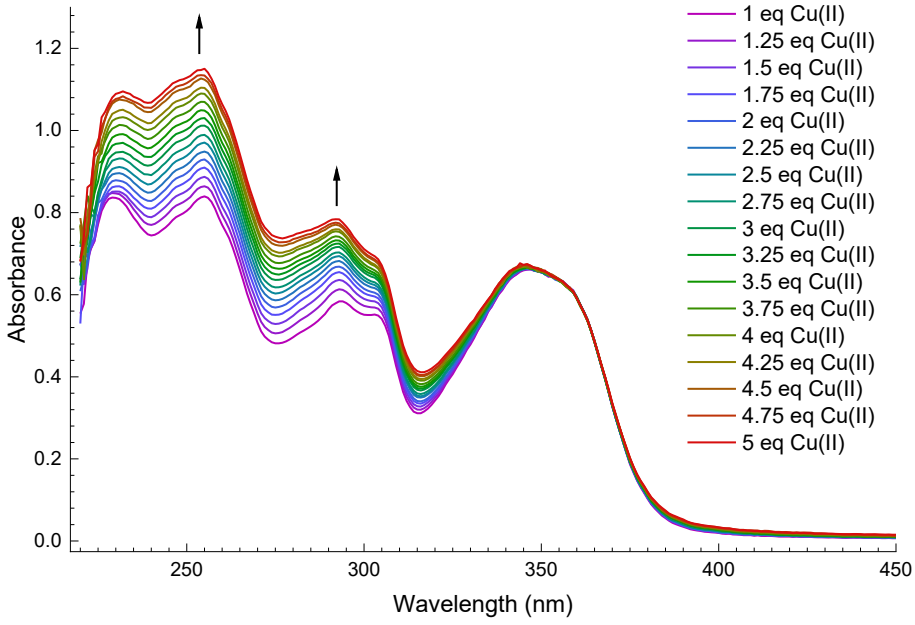

Figure 2.34: UV-visible spectra for the titration of a 6:1 Zn^{II}:$\mathbf{H_2L^4}$ aqueous solution with Cu^{II} at pH 7.4 and at 298.2 K (25 mM HEPES buffer, I = 11 mM (Na(HEPES)); C_L = 50 µM; Cu:ZnL = 1-5).

The first family of spectra is associated to the substitution of zinc(II) with copper(II) in ligand coordination. This statement is supported by the fact that the spectrum of the Zn^{II}:$\mathbf{H_2L^4}$ system after the addition of 1

equivalent of copper(II) is the same as the spectrum of the ligand $\mathbf{H_2L^4}$ after the addition of 1 equivalent of copper(II) in the direct titration (Figure 2.35). This means that the affinity of the glucosyl-**SC** for copper(II) is too high to be determined even by competitive titration, because the equation described below is actually completely shifted towards the formation of the CuL^4 species:

$$[ZnL^4] + Cu^{2+} \rightarrow [CuL^4] + Zn^{2+}$$

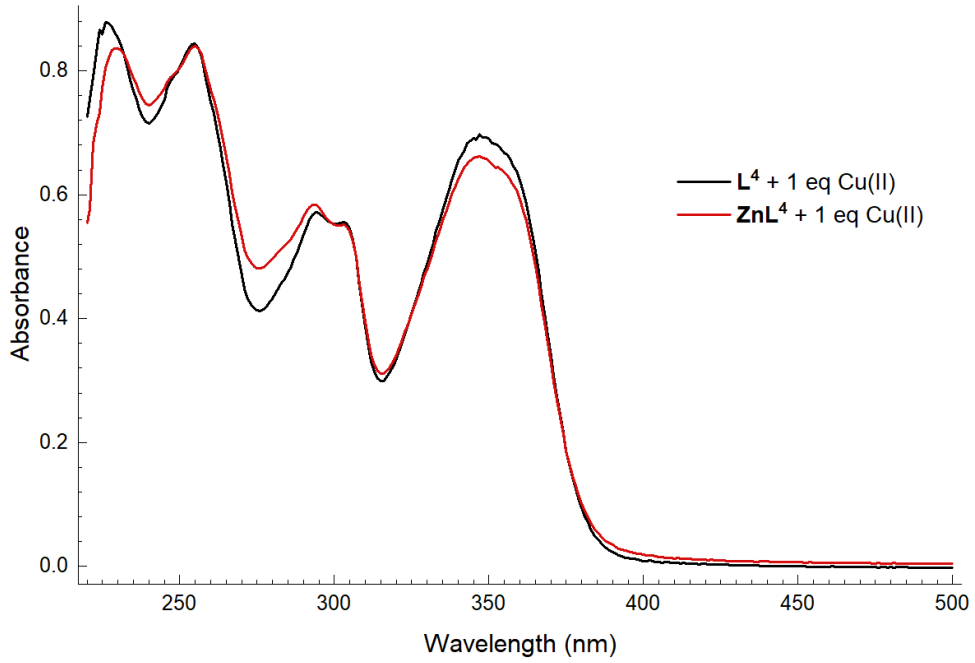

Figure 2.35: UV-visible spectrum of the aqueous solution (25 mM HEPES buffer, pH 7.4, 298.2 K) of the ligand $\mathbf{H_2L^4}$ after the addition of 1 equivalent of copper(II) (in purple) and UV-visible spectrum of the 6:1 Zn^{II}:$\mathbf{H_2L^4}$ aqueous solution (25 mM HEPES buffer, pH 7.4, 298.2 K) after the addition of 1 equivalent of copper(II) (in red).

The second family of spectra shows the same trend as observed for the simple $\mathbf{H_2L^4}$-Cu^{II} system, that is the increase in intensity of the sole absorption bands between 220 and 300 nm. This behaviour is explained by taking into account the formation of another species, such as the hypothetical 2:1 copper(II):ligand complex proposed for the study of **TSC**-copper(II) equilibria (Scheme A2.1).

Conclusions

Four novel glyco-conjugated Schiff bases (**CM2**, **CM4**, **CM7** and **CM9**) and their copper(II) complexes (**CM5**, **CM6**, **CM8** and **CM10**) were successfully synthesized and characterized. The synthesis of the de-acetylated derivatives was performed by means of an optimized protocol based on the isolation of the deprotected glucosyl-aldehyde **AZ24**.

The coordination properties of the de-acetylated ligands **FMM8Z** and **CM4** towards Cu^{II} and Zn^{II} were studied in aqueous solution by means of UV-visible spectrophotometric titrations. Both ligands proved to be excellent chelators of the two metal ions.

Similarly to what was observed for the **bis-TCH AZ11** and the **bis-CH AZ26** in Chapter 1, the stability of the glyco-conjugated **SC**-copper(II) complex is higher with respect to the glyco-conjugated **SC**-zinc(II) complex; in fact, the conditional constant of the former ion is too high to be determined at pH 7.4. A similar behaviour can be hypothesized also for the **TSC**-complexes, although it was not possible to determine the formation constants for both CuL^2 and ZnL^2 species.

The study of the copper(II) complexation equilibria highlighted the possibility for the ligands to form bi-metallic complexes in aqueous solution. The involvement of the glucosyl moiety in metal coordination was hypothesized to explain such unexpected result.

The evaluation of the antiproliferative activity of both ligands and copper(II) complexes is currently ongoing.

Experimental section

Materials and methods

Commercial reagents were purchased from Sigma-Aldrich. Dowex H^+ cation exchange resin was activated by washing with aqueous 2M HCl, followed by washing with water and MeOH. The purity of the synthesized compounds was determined by elemental analysis and verified to be ≥ 95%. ^1H and ^{13}C NMR spectra were recorded at 25°C on a Bruker Advance 400 MHz FT spectrometer. The ATR-IR spectra were recorded by means of a Perkin Elmer spectrophotometer by using a diamond crystal plate in the range of 4000-400 cm^{-1}. Elemental analyses were performed by using a Thermo Fisher FlashSmart CHNS/O analyser with gas-chromatographic separation. Electrospray ionization mass spectral analyses (ESI-MS) were performed with an ESI time-of-flight Micromass 4LCZ spectrometer and the samples were dissolved in methanol. The UV-visible spectra were collected by means of a Thermo Scientific Evolution 260 Bio spectrophotometer equipped with a Peltier temperature controller and quartz cuvettes with 1 cm path length were used.

Synthesis

4-(2',3',4',6'-Tetra-O-acetyl-β-D-glucopyranosyloxy)-2- hydroxybenzaldehyde (FMM2 or AZ22)

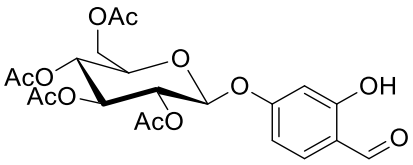

2,4-dihydroxy-benzaldehyde (1.512 g, 10.944 mmol, 1.5 eq) was dissolved in an aqueous K_2CO_3 solution (0.5 M, 15 mL) with tris(2-(2-methoxyethoxy)ethyl)amine (2.3 mL, 7.296 mmol, 1 eq), then a solution of acetobromo-α-D-glucose (3.000 g, 7.296 mmol, 1 eq) in DCM (15 mL) was added. The resulting red-orange emulsion was left stirring vigorously at 45°C for 4 days. After that time the reaction was cooled to r.t. and 40 mL of water are added. The organic phase was separated and the aqueous phase was extracted 3 times with DCM. The combined organic phases were washed one time with 1M HCl and twice with water, then dried over Na_2SO_4, filtered and concentrated. The resulting oily residue was purified by column chromatography (PetEther/EtOAc 65/35) and triturated with n-hexane to obtain the product as a white solid (1.291 g, yield = 38%).

IR (cm^{-1}): ν = 2951 (w) (CH), 1744 (s) (C=O, acetyl groups), 1660 (m-s) (C=O, aldehyde). (Figure A2.1)

^1H NMR (400 MHz, Chloroform-*d,* 298 K): δ(ppm) = 11.37 (s, 1H, OH), 9.77 (s, 1H, CH=O), 7.47 (d, *J* = 8.6 Hz, 1H, ArH), 6.60 (dd, *J* = 8.6, 2.3 Hz, 1H, ArH), 6.54 (d, *J* = 2.3 Hz, 1H, ArH), 5.35 – 5.25 (m, 2H, CH), 5.20 – 5.11 (m, 2H, CH), 4.27 (dd, *J* = 12.3, 6.0 Hz, 1H, CH), 4.18 (dd, *J* = 12.2, 2.4 Hz, 1H, CH), 3.92 (ddd, *J* = 10.1, 6.0, 2.4 Hz, 1H, CH), 2.10 (s, 3H, CH_3), 2.06 (m, ovlp, 6H, CH_3), 2.04 (s, 3H, CH_3). (Figure A2.2)

^{13}C NMR (126 MHz, Chloroform-*d*, 298 K): δ(ppm) = 194.97 (CH=O), 170.74, 170.31, 169.54, 169.36, 164.17, 163.31, 135.52, 116.79, 109.81, 103.73, 97.86, 72.68, 72.56, 71.02, 68.27, 61.99, 20.78 (CH_3), 20.74 (CH_3), 20.73 (CH_3), 20.73 (CH_3). (Figure A2.3)

ESI-MS (positive ions): m/z (%): 491 (100) $[M + Na]^+$. (Figure A2.4)

ESI-MS (negative ions): m/z (%): 467 (100) $[M – H]^-$. (Figure A2.5)

Elem. anal. calcd (%) for $C_{21}H_{24}O_{12}$: C 53.85, H 5.16; found: C 54.47, H 5.23.

4-(β-D-glucopyranosyloxy)-2- hydroxybenzaldehyde (AZ24)

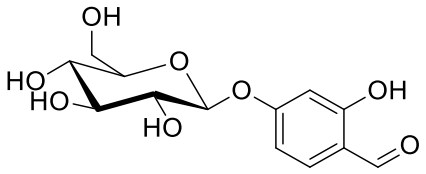

The aldehyde **FMM2** (500 mg, 1.067 mmol, 1 eq) was suspended in MeOH and solid MeONa (288 mg, 5.331 mmol, 5 eq) was added: the resulting suspension was left stirring at room temperature overnight (after 2 hours stirring, a red solution was obtained). The complete consumption of the reagent was confirmed by TLC (DCM/MeOH 4/1). The mixture was neutralized by addition of Dowex H^+ cation exchange resin, then it was filtered and the filtrate was concentrated under vacuum. An orange oil was obtained, which was purified by column chromatography (DCM/MeOH 4/1) and triturated with Et_2O to obtain the product as a pink solid (208 mg, yield = 65%).

IR (cm^{-1}): ν = 3481 (m), 3284 (m) (OH), 2924 (w) (CH), 1631 (m-s) and 1610 (s) (C=O). (Figure A2.6)

^{1}H NMR (400 MHz, DMSO-d_6, 298 K): δ(ppm) = 10.96 (s, br, 1H, OH), 10.05 (s, 1H, CH=O), 7.62 (d, *J* = 8.7 Hz, 1H, ArH), 6.63 (dd, *J* = 8.7, 2.3 Hz, 1H, ArH), 6.58 (d, *J* = 2.2 Hz, 1H, ArH), 5.37 (d, *J* = 4.9 Hz, 1H, OH), 5.12 (d, *J* = 4.6 Hz, 1H, OH), 5.04 (d, *J* = 5.3 Hz, 1H, OH), 4.96 (d, *J* = 7.3 Hz, 1H, anomeric CH), 4.57 (t, *J* = 5.7 Hz, 1H, CH_2OH), 3.68 (dq, *J* = 11.8, 2.1 Hz, 1H, CH), 3.48 (dt, *J* = 11.5, 5.4 Hz, 1H, CH), 3.29 – 3.14 (m, 3H, CH).

^{13}C NMR (101 MHz, DMSO-d_6, 298 K): δ(ppm) = 191.04 (CH=O), 163.79, 162.68, 131.93, 117.11, 108.51, 103.36, 99.71, 77.17, 76.46, 73.09, 69.46, 60.51. (Figure A2.7)

ESI-MS (positive ions): m/z (%): 323 (100) $[M + Na]^+$, 623 (70) $[2M + Na]^+$. (Figure A2.8)

ESI-MS (negative ions): m/z (%): 299 (100) $[M – H]^-$. (Figure A2.9)

Elem. anal. calcd (%) for $C_{13}H_{16}O_8$: C 52.00, H 5.37; found: C 51.74, H 5.48.

4-(β-D-glucopyranosyloxy)-2-hydroxybenzaldehyde-4-ethyl-3- thiosemicarbazone (FMM4Z, $H_2L^1 \cdot H_2O$)

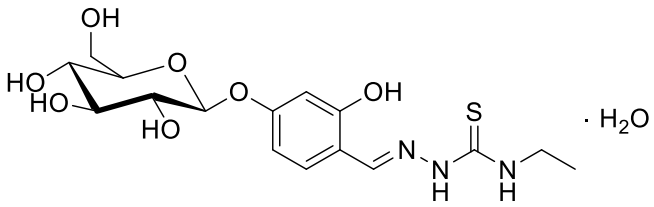

The aldehyde **AZ24** (200 mg, 0.666 mmol, 1 eq) was solubilized in hot MeOH (8 mL) and solid 4-ethyl-3-thiosemicarbazide (79 mg, 0.666 mmol, 1 eq) was added, followed by three drops of glacial acetic acid. The resulting pale pink-yellow solution was refluxed for 4 hours. The mixture was dried and the crude was recrystallized from absolute EtOH/Et_2O. A white solid was obtained (121 mg, yield = 43%).

IR (cm^{-1}): ν = 3600 – 3020 (m) (OH, NH), 2980 (w), 2878 (w) (CH), 1629 (C=N), 1545 (C=C). (Figure A2.10)

^{1}H NMR (400 MHz, DMSO-d_6, 298 K): δ(ppm) = 11.24 (s, 1H, NH), 9.99 (s, br, 1H, OH), 8.39 (t, *J* = 5.9 Hz, 1H, NH), 8.27 (s, 1H, CH=N), 7.85 (d, *J* = 8.4 Hz, 1H, ArH), 6.53 (m, 2H, ArH), 5.31 (d, *J* = 5.0 Hz, 1H, OH), 5.09 (d, *J* = 5.0 Hz, 1H, OH), 5.02(d, *J* = 5.0 Hz, 1H, OH), 4.83 (d, *J* = 7.5 Hz, 1H, anomeric CH), 4.56 (t, *J* = 5.7 Hz, 1H, CH_2OH), 3.72 – 3.64 (m, 1H, CH), 3.61 – 3.52 (m, 2H, CH_2), 3.49 (dt, *J* = 11.6, 5.7 Hz, 1H, CH), 3.30 – 3.14 (m, 4H, CH), 1.13 (t, *J* = 7.1 Hz, 3H, CH_3). (Figure A2.11)

^{13}C NMR (101 MHz, DMSO-d_6, 298 K): δ(ppm) = 176.25 (C=S), 159.77, 157.50, 139.10, 127.79, 114.58, 107.79, 103.39, 100.10, 77.13, 76.59, 73.16, 69.56, 60.56, 38.22 (CH_2), 14.71 (CH_3). (Figure A2.12)

Elem. anal. calcd (%) for $C_{16}H_{23}N_3O_7S \cdot H_2O$: C 45.82, H 6.01, N 10.02, S 7.64; found: C 45.60, H 5.88, N 10.06, S 7.65.

4-(β-D-glucopyranosyloxy)-2- hydroxybenzaldehyde-3-thiosemicarbazone (FMM8Z, H_2L^2)

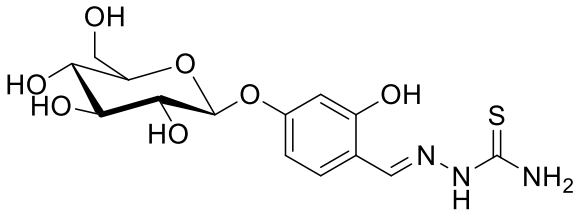

The aldehyde **AZ24** (119 mg, 0.396 mmol, 1 eq) was solubilized in hot MeOH (8 mL) and solid thiosemicarbazide (36 mg, 0.396 mmol, 1 eq) was added, followed by one drop of glacial acetic acid. The resulting solution was refluxed overnight, then it was cooled to r.t., reduced to half volume and Et_2O (20 mL) was added. A white precipitate formed, which was filtered, washed with Et_2O and dried *in vacuo*. A white solid was obtained (116 mg, yield = 78%).

^{1}H NMR (400 MHz, DMSO-d_6, 298 K): δ(ppm) = 11.26 (s, 1H, NH), 9.96 (s, br, 1H, OH), 8.27 (s, 1H, CH=N), 8.01 (s, br, 1H, NH), 7.84 – 7.81 (m, 2H, NH, ArH), 6.52 (m, 2H, ArH), 5.31 (d, *J* = 5.1 Hz, 1H, OH), 5.09 (d, *J* = 4.7 Hz, 1H, OH), 5.02 (d, *J* = 5.2 Hz, 1H, OH), 4.83 (d, *J* = 7.5 Hz, 1H, anomeric CH), 4.56 (t, *J* = 5.8 Hz, 1H, CH_2OH), 3.68 (ddd, *J* = 11.7, 5.4, 2.0 Hz, 1H, CH), 3.48 (dt, *J* = 11.7, 5.8 Hz, 1H, CH), 3.20 (dtd, *J* = 22.9, 8.8, 5.0 Hz, 3H, CH). (Figure A2.13)

^{13}C NMR (101 MHz, DMSO-d_6, 298 K): δ(ppm) = 175.57 (C=S), 160.30, 156.56, 139.92, 127.18, 116.03, 108.30, 103.87, 100.55, 77.56, 77.02, 73.63, 70.00, 61.01. (Figure A2.14)

4-(2',3',4',6'-Tetra-O-acetyl-β-D-glucopyranosyloxy)-2- hydroxybenzaldehyde-3-semicarbazone (CM2, H_2L^3)

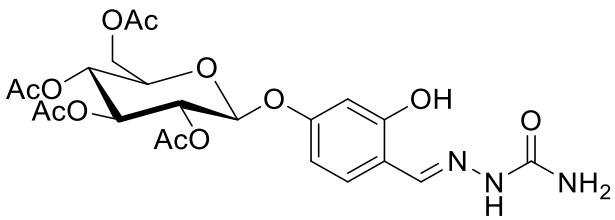

The per-acetylated aldehyde **FMM2** (400 mg, 0.854 mmol, 1 eq) was dissolved in EtOH (5 mL) at 60 °C. In another flask, semicarbazide hydrochloride (96 mg, 0.861 mmol, 1 eq) was solubilized in EtOH (5 mL) and the solution was neutralized with aqueous 1 M NaOH (830 µL, 0.830 mmol, 0.96 eq). The semicarbazide solution was added to the aldehyde solution and a light orange mixture was obtained, which was stirred under reflux overnight. The mixture was left to cool to r.t., concentrated and left at -21 °C overnight. A precipitate formed, which was filtered, washed with cold EtOH and dried *in vacuo*. A light pink solid was obtained (280 mg, yield = 63%).

IR (cm^{-1}): ν = 1746 (s) (C=O, acetyl groups), 1682 (m-s) (C=O, semicarbazone), 1628 (m) and 1605 (m-s) (C=N). (Figure A2.15)

^{1}H NMR (400 MHz, DMSO-d_6, 298 K): δ(ppm) = 10.23 (s, br, 1H, OH), 10.09 (s, 1H, NH), 8.05 (s, 1H, CH=N), 7.68 (d, *J* = 9.0 Hz, 1H, ArH), 6.50 – 6.45 (m, 2H, ArH), 6.36 (s, br, 2H, NH_2), 5.55 (d, *J* = 8.0 Hz, 1H, CH), 5.43 (t, *J* = 9.6 Hz, 1H, CH), 5.08 – 4.93 (m, 2H, CH), 4.28 – 4.16 (m, 2H, CH), 4.06 (d, *J* = 9.9 Hz, 1H, CH), 2.01 (m, 9H, CH_3), 1.97 (s, 3H, CH_3). (Figure A2.16)

^{1}H NMR (400 MHz, Chloroform-*d*, 298 K): δ(ppm) = 10.04 (s, br, 1H, OH), 9.99 (s, 1H, NH), 7.89 (s, 1H, CH=N), 7.11 (d, *J* = 8.5 Hz, 1H, ArH), 6.58 (d, *J* = 2.4 Hz, 1H, ArH), 6.53 (dd, *J* = 8.5, 2.4 Hz, 1H, ArH), 5.42 (s, br, 2H, NH_2), 5.34 – 5.21 (m, 2H, CH), 5.19 – 5.07 (m, 2H, CH), 4.27 (dd, *J* = 12.3, 5.7 Hz, 1H, CH), 4.19 (dd, *J* = 12.3, 2.5 Hz, 1H, CH), 3.90 (ddd, *J* = 10.0, 5.7, 2.5 Hz, 1H, CH), 2.10 (s, 3H, CH_3), 2.05 – 2.02 (m, 9H, CH_3). (Figure A2.17)

^{13}C NMR (101 MHz, Chloroform-*d*, 298 K): δ(ppm) = 170.83, 170.37, 169.60, 169.44, 159.32, 158.92, 157.14, 146.17, 132.19, 113.23, 109.17, 104.39, 98.41, 72.75, 72.32, 71.15, 68.39, 62.09, 20.84 (CH_3), 20.76 (CH_3), 20.72 (CH_3). (Figure A2.18)

ESI-MS (positive ions): m/z (%): 548 (100) $[M + Na]^+$, 1073 (30) $[2M + Na]^+$. (Figure A2.19)

ESI-MS (negative ions): m/z (%): 524 (100) $[M – H]^-$, 1049 (60) $[2M – H]^-$. (Figure A2.20)

Elem. anal. calcd (%) for $C_{22}H_{27}N_3O_{12}$: C 50.28, H 5.18, N 8.00; found: C 50.08, H 5.17, 7.48.

4-(β-D-glucopyranosyloxy)-2- hydroxybenzaldehyde-3-semicarbazone (CM4, $H_2L^4 \cdot 1.5\ H_2O$)

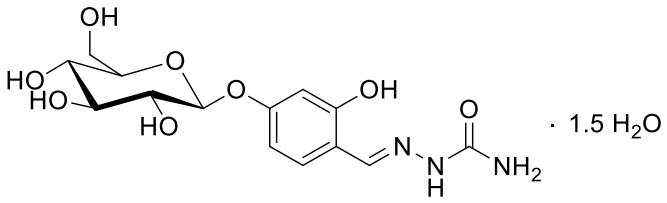

The aldehyde **AZ24** (152 mg, 0.506 mmol, 1 eq) was dissolved in MeOH (5 mL) at 70 °C. In another flask, semicarbazide hydrochloride (56 mg, 0.506 mmol, 1 eq) was solubilized in MeOH (5 mL) and the pH of the resulting solution was brought to ca. 7 – 8 by addition of aqueous 1M NaOH (380 µL). The semicarbazide solution was added to the aldehyde solution and the resulting mixture was stirred under reflux overnight. The mixture was left to cool to r.t., concentrated to few mL and then 2-propanol was added. The resulting suspension was left at -21 °C overnight and the precipitate was filtered, washed with cold 2-propanol and Et_2O and dried *in vacuo*. A white solid was obtained (113 mg, yield = 58%).

IR (cm^{-1}): ν = 3500 – 3350 (m) (OH), 3249 (m) (NH), 1672 (m) and 1656 (m) (C=O), 1626 (m) and 1613 (m) (C=N), 1574 (s) (C=C). (Figure A2.21)

^{1}H NMR (400 MHz, DMSO-d_6, 298 K): δ(ppm) = 10.14 (s, br, 1H, OH), 10.04 (s, 1H, NH), 8.05 (s, 1H, CH=N), 7.63 (d, *J* = 9.2 Hz, 1H, ArH), 6.56 – 6.48 (m, 2H, ArH), 6.33 (s, br, 2H, NH_2), 5.33 (d, *J* = 5.1 Hz, 1H, OH), 5.10 (d, *J* = 4.8 Hz, 1H, OH), 5.04 (d, *J* = 5.3 Hz, 1H, OH), 4.82 (d, *J* = 7.5 Hz, 1H, anomeric CH), 4.60 (t, *J* = 5.7 Hz, 1H, OH), 3.72 – 3.60 (m, 2H, CH), 3.32 – 3.13 (m, 4H, CH). (Figure A2.22)

^{13}C NMR (101 MHz, DMSO-d_6, 298 K): δ(ppm) = 159.14, 157.08, 156.62, 137.74, 127.79, 114.77, 107.66, 103.53, 100.17, 77.08, 76.59, 73.20, 69.58, 60.58. (Figure A2.23)

ESI-MS (positive ions): m/z (%): 380 (100) $[M + Na]^+$, 737 (60) $[2M + Na]^+$. (Figure A2.24)

Elem. anal. calcd (%) for $C_{14}H_{19}N_3O_8 \cdot 1.5\ H_2O$: C 43.75, H 5.77, N 10.93; found: C 43.33, H 5.40, N 10.82.

[Cu(HL^3)Cl] · H_2O (CM5)

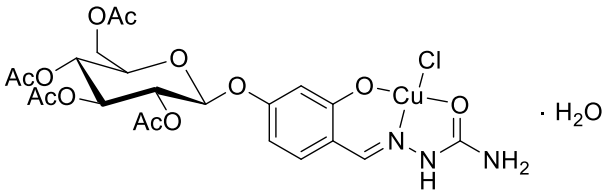

The ligand **CM2** (201 mg, 0.382 mmol, 1 eq) was solubilized in MeOH (10 mL) and two drops of aqueous 1 M NaOH were added: the pink solution turned yellow and the measured pH was 9. A solution of $CuCl_2 \cdot 2\ H_2O$ (64 mg, 0.375 mmol, ca. 1 eq) in MeOH (4 mL) was added and a dark green suspension was obtained (pH = 2 – 3). The mixture was stirred at r.t. for 2 hours, then it was centrifuged and the precipitate was washed three times with MeOH and dried *in vacuo*. A dark green solid was obtained (142 mg, yield = 58%).

IR (cm^{-1}): ν = 3380 (m-w) (OH, water), 3214 (m-w) (NH), 1739 (s) (C=O, acetyl groups), 1661 (m-s) (C=O, semicarbazone), 1612 (s) (C=N), 1561 (m) (C=C). (Figure A2.25)

ESI-MS (positive ions): m/z (%): 587 (100) $[CuHL^3]^+$, 1175 (15) $[Cu_2HL^3{}_2]^+$, 1211 (15) $[Cu_2H_2L^3{}_2Cl]^+$. (Figure A2.26)

ESI-MS (negative ions): m/z (%): 621 $[CuL^3Cl]^-$, 1208 $[Cu_2L^3{}_2Cl]^-$, 1245 $[Cu_2HL^3{}_2Cl_2]^-$, 1267 $[Cu_2NaL^3{}_2Cl_2]$-.

Elem. anal. calcd (%) for $C_{22}H_{26}ClCuN_3O_{12} \cdot 1\ H_2O$: C 41.19, H 4.40, N 6.55; found: C 41.55, H 4.24, N 6.21.

[Cu(HL^4)Cl] · 1.5 H_2O (CM6)

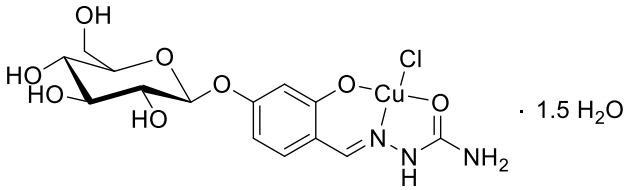

The ligand **CM4** (130 mg, 0.364 mmol, 1 eq) was solubilized in a 1/1 H_2O/MeOH mixture (10 mL) and two drops of aqueous 1 M NaOH were added: a pale-yellow solution with pH = 9 was obtained. A solution of $CuCl_2 \cdot 2\ H_2O$ (61 mg, 0.358 mmol, ca. 1 eq) in MeOH (2 mL) was added and a dark green solution was obtained (pH = 2 – 3), which was stirred at r.t. for 6 hours. The mixture turned into a suspension with a fine precipitate. The suspension was left at -21 °C, then it was centrifuged and the precipitate was washed with 2-propanol and dried *in vacuo*. A light green solid was isolated (142 mg, yield = 82%).

IR (cm^{-1}): ν = 3370 (s) (OH), 3216 (s) (NH), 1667 (s) (C=O, semicarbazone), 1613 (s) (C=N), 1563 (s) (C=C). (Figure A2.27)

ESI-MS (positive ions): m/z (%): 419 (100) $[CuHL^4]^+$, 837 (25) $[Cu_2HL^4{}_2]^+$. (Figure A2.28)

ESI-MS (negative ions): m/z (%): 453 (100) $[CuL^4Cl]^-$, 873 (50) $[Cu_2L^4{}_2Cl]^-$, 909 (10) $[Cu_2HL^4{}_2Cl_2]^-$, 931 (20) $[Cu_2NaL^4{}_2Cl_2]^-$.

Elem. anal. calcd (%) for $C_{14}H_{18}ClCuN_3O_8 \cdot 1.5\ H_2O$: C 34.86, H 4.39, N 8.71; found: C 34.87, H 4.45, N 8.22.

(2R,3R,4S,5R,6S)-2-(acetoxymethyl)-6-(3-hydroxy-4-((2-octanoylhydrazono)methyl)phenoxy)tetrahydro-2H-pyran-3,4,5-triyl triacetate (CM7, H_2L^5)

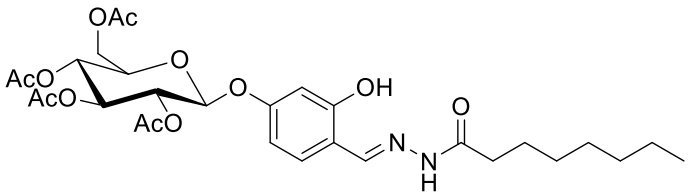

The per-acetylated aldehyde **FMM2** (300 mg, 0.640 mmol, 1 eq) was dissolved in MeOH (5 mL) at 50 °C. A solution of octanoic hydrazide (101 mg, 0.638 mmol, 1 eq) in MeOH (5 mL) was added to the reaction mixture, followed by two drops of glacial acetic acid. The resulting solution was stirred under reflux overnight. The mixture was left to cool to r.t., then it was left at -21 °C for few hours. A precipitate formed, which was filtered, washed with cold MeOH and dried *in vacuo*. A white solid was obtained (272 mg, yield = 70%).

IR (cm^{-1}): ν = 3472 (w) (OH), 3258 (w) (NH), 2927 (m-w) (CH), 1742 (s) (C=O, acetyl groups), 1663 (m) (C=O, acylhydrazone), 1629 (m) (C=N). (Figure A2.29)

^{1}H NMR (400 MHz, DMSO-d_6, 298 K, *isomer ratio A:B 70:30*): δ(ppm) = 11.58 – 11.52 (m, 2H, NH and OH, *isomer A*), 11.13 (s, 1H, NH, *isomer B*), 10.43 (s, 1H, OH, *isomer B*), 8.26 (s, 1H, CH=N, *isomer A*), 8.16 (s, 1H, CH=N, *isomer B*), 7.53 (d, J = 8.4 Hz, 1H, ArH, *isomer B*), 7.42 (d, J = 8.4 Hz, 1H, ArH, *isomer A*), 6.55 – 6.51 (m, 4H, ArH, *ovlp isomers A and B*), 5.61 (d, J = 8.0 Hz, 1H, CH, *isomer A*), 5.56 (d, J = 8.0 Hz, 1H, CH, *isomer B*), 5.45 – 5.37 (m, 2H, CH, *ovlp isomers A and B*), 5.10 – 4.96 (m, 4H, CH, *ovlp isomers A and B*), 4.30 – 4.16 (m, 4H, CH, *ovlp isomers A and B*), 4.08 – 4.05 (m, 2H, CH, *ovlp isomers A and B*), 2.53 (t, J = 7.4 Hz, 2H, CH_2-C=O, *isomer B*), 2.19 (t, J = 7.4 Hz, 2H, CH_2-C=O, *isomer A*), 2.02 – 1.97 (m, 24 H, O-C(=O)CH_3, *ovlp isomers A and B*), 1.60 – 1.52 (m, 4H, CH_2, *ovlp isomers A and B*), 1.29 – 1.24 (m, 16H, CH_2, *ovlp isomers A and B*), 0.87 – 0.83 (m, 6H, CH_3, *ovlp isomers A and B*).

^{1}H NMR (400 MHz, Chloroform-*d*, 298 K, *isomer ratio A:B 70:30*): δ(ppm) = 11.16 (s, 1H, NH, *isomer B*), 10.51 (s, 1H, NH, *isomer A*), 9.45 (s, br, 1H, OH, *isomer A*), 8.39 (s, br, 1H, OH, *isomer B*), 8.31 (s, 1H, CH=N, *isomer B*), 7.86 (s, 1H, CH=N, *isomer A*), 7.14 (d, J = 8.5 Hz, 1H, ArH, *isomer A*), 7.09 (d, J = 8.5 Hz, 1H, ArH, *isomer B*), 6.61 (d, J = 2.4 Hz, 2H, ArH, *ovlp isomers A and B*), 6.56 (dd, J = 8.5, 2.4 Hz, ArH, *isomer A*), 6.51 (dd, J = 8.5, 2.4 Hz, ArH, *isomer B*), 5.33 – 5.24 (m, 4H, CH, *ovlp isomers A and B*), 5.18 – 5.10 (m, 4H, CH, *ovlp isomers A and B*), 4.31 – 4.25 (m, 2H, CH, *ovlp isomers A and B*), 4.20 – 4.16 (m, 2H, CH, *ovlp isomers A and B*), 3.92 – 3.88 (m, 2H, CH, *ovlp isomers A and B*), 2.61 (t, J = 7.6 Hz, 2H, CH_2-C=O, *isomer A*), 2.28 (t, J = 7.6 Hz, 2H, CH_2-C=O, *isomer B*), 2.12 – 2.03 (m, 24 H, O-C(=O)CH_3, *ovlp isomers A and B*), 1.76 – 1.68 (m, 4H, CH_2, *ovlp isomers A and B*), 1.44 – 1.25 (m, 16H, CH_2, *ovlp isomers A and B*), 0.91 – 0.85 (m, 6H, CH_3, *ovlp isomers A and B*). (Figure A2.30)

^{13}C NMR (101 MHz, DMSO-d_6, 298 K, *isomer ratio A:B 70:30*): δ(ppm) = 173.80 (HN-C=O, *isomer A*), 170.05 (O-C(=O)CH_3, *ovlp isomers A and B*), 169.66(O-C(=O)CH_3, *ovlp isomers A and B*), 169.42 (O-C(=O)CH_3, *ovlp isomers A and B*), 169.18 (O-C(=O)CH_3, *ovlp isomers A and B*), 168.42, 158.96, 158.54, 157.69, 146.51, 140.86, 131.07, 128.35, 115.23, 113.73, 108.00, 103.91, 103.64, 96.91, 96.60, 71.93, 70.93, 70.68, 68.09, 68.02, 61.70, 61.59, 33.93, 32.02, 31.19, 28.77, 28.64, 28.47, 24.96, 24.22, 22.10, 20.50 (O-C(=O)CH_3, *ovlp isomers A and B*), 20.44 (O-C(=O)CH_3, *ovlp isomers A and B*), 20.38 (O-C(=O)CH_3, *ovlp isomers A and B*), 20.33 (O-C(=O)CH_3, *ovlp isomers A and B*), 13.99 (CH_2CH_3, *ovlp isomers A and B*). (Figure A2.31)

^{13}C NMR (101 MHz, Chloroform-*d*, 298 K, *isomer ratio A:B 70:30*): δ(ppm) = 174.73, 170.75, 170.66, 170.24, 169.44, 169.30, 168.90, 159.36, 149.67, 145.98, 132.08, 131.85, 112.92, 108.99, 108.86, 104.38, 104.25, 98.33, 98.22, 72.70, 72.65, 72.25, 71.02, 68.33, 68.22, 61.92, 35.32, 32.93, 31.67, 29.35, 29.24, 29.01, 25.36, 24.38, 22.61, 20.62, 14.08. (Figure A2.32)

ESI-MS (positive ions): m/z (%): 609 (65) $[M + H]^+$, 632 (100) $[M + Na]^+$, 1240 (70) $[2M + Na]^+$. (Figure A2.33)

ESI-MS (negative ions): m/z (%): 607 (70) $[M - H]^-$, 1215 (100) $[2M - H]^-$. (Figure A2.34)

Elem. anal. calcd (%) for $C_{29}H_{40}N_2O_{12}$: C 57.23, H 6.62, N 4.60; found: C 56.89, H 6.62, N 4.47.

[Cu(HL^5)Cl] (CM8)

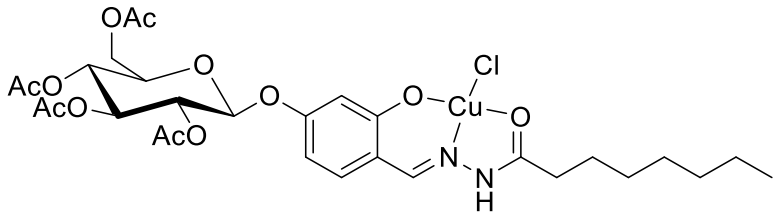

The ligand **CM7** (100 mg, 0.164 mmol, 1 eq) was dissolved in EtOH (10 mL) and two drops of aqueous 1 M NaOH were added: the pH of the resulting yellow solution was 8. A solution of $CuCl_2 \cdot 2\ H_2O$ (29 mg, 0.170 mmol, ca. 1 eq) in EtOH (5 mL) was added and a dark green solution (pH = 4) was obtained. The mixture was stirred at r.t. overnight, then it was concentrated at rotavapor and water (15 mL) was added: a suspension was obtained, which was left at 4 °C for 2 days. The suspension was centrifuged and the obtained precipitate was washed with water and dried *in vacuo*. A light green solid was obtained (67 mg, yield = 58%).

IR (cm^{-1}): ν = 3155 (w) (NH), 2929 (m-w) and 2857 (m-w) (CH), 1748 (s) (C=O, acetyl groups), 1608 (m-s) (C=O, acylhydrazone), 1574 (m-s) (C=N). (Figure A2.35)

ESI-MS (positive ions): m/z (%): 670 (100) $[CuHL^5]^+$, 1279 (20) $[CuH_3L^5{}_2]^+$, 1341 (30) $[Cu_2HL^5{}_2]^+$, 1377 (40) $[CuH_2L^5{}_2Cl]^+$. (Figure A2.36)

ESI-MS (negative ions): m/z (%): 704 (100) $[CuL^5Cl]^-$, 1376 (70) $[Cu_2L^5{}_2Cl]^-$.

Elem. anal. calcd (%) for $C_{29}H_{39}ClCuN_2O_{12}$: C 49.29, H 5.56, N 3.96; found: C 48.95, H 5.63, N 3.83.

N'-(2-hydroxy-4-(((2S,3R,4S,5S,6R)-3,4,5-trihydroxy-6-(hydroxymethyl)tetrahydro-2H-pyran-2-yl)oxy)benzylidene)octanehydrazide (CM9, $H_2L^6 \cdot H_2O$)

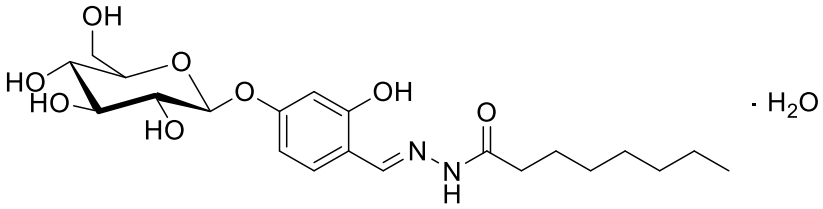

The aldehyde **AZ24** (178 mg, 0.593 mmol, 1 eq) was dissolved in MeOH (10 mL) at 45 °C. A solution of octanoic hydrazide (93 mg, 0.587 mmol, 1 eq) in MeOH (5 mL) was added to the reaction mixture, followed by two drops of glacial acetic acid. The resulting solution was stirred under reflux overnight. The mixture was left to cool to r.t., then it was concentrated at rotavapor and Et_2O (35 mL) was added. A precipitate formed, which was filtered, washed with Et_2O and dried *in vacuo*. A white solid was obtained (179 mg, yield = 66%).

IR (cm^{-1}): ν = 3500 – 3100 (m-s) (OH and NH), 2923 (m-s) and 2854 (m-s) (CH), 1655 (s) (C=O), 1629 (s) and 1611 (s) (C=N). (Figure A2.37)

^{1}H NMR (400 MHz, DMSO-d_6, 298 K, *isomer ratio A:B 70:30*): δ(ppm) = 11.47 (s, br, 2H, NH and OH, *isomer A*), 11.09 (s, 1H, NH, *isomer B*), 10.32 (s, br, 1H, OH, *isomer B*), 8.26 (s, 1H, CH=N, *isomer A*), 8.16 (s, 1H, CH=N, *isomer B*), 7.49 (d, J = 8.6 Hz, 1H, ArH, *isomer B*), 7.38 (d, *J* = 8.6 Hz, 1H, ArH, *isomer A*), 6.61 – 6.50 (m, 4H, ArH, *ovlp isomers A and B*), 5.31 (d, *J* = 4.8 Hz, 2H, OH, *ovlp isomers A and B*), 5.05 (m, 4H, OH, *ovlp isomers A and B*), 4.90 (d, *J* = 7.6 Hz, 1H, anomeric CH, *isomer A*), 4.84 (d, *J* = 7.6 Hz, 1H, anomeric CH, *isomer B*), 4.57 (t, *J* = 4.8 Hz, 2H, OH, *ovlp isomers A and B*), 3.68 (ddd, *J* = 11.8, 5.2, 2.0 Hz, 2H, CH, *ovlp isomers A and B*), 3.47 (dt, *J* = 11.7, 6.3 Hz, 2H, CH, *ovlp isomers A and B*), 3.30 – 3.11 (m, 8H, CH, *ovlp isomers A and B*), 2.53 (t, J = 7.4 Hz, 2H, CH_2-C=O, *isomer B*), 2.19 (t, *J* = 7.4 Hz, 2H, CH_2-C=O, *isomer A*), 1.56 (p, *J* = 7.0 Hz, 4H, CH_2, *ovlp isomers A and B*), 1.35 – 1.18 (m, 16H, CH_2, *ovlp isomers A and B*), 0.86 (m, 6H, CH_3, *ovlp isomers A and B*). (Figure A2.38)

^{13}C NMR (101 MHz, DMSO-d_6, 298 K, *isomer ratio A:B 70:30*): δ(ppm) = 173.66 (HN-C=O, *isomer A*), 172.13 (HN-C=O, *isomer B*), 168.27, 159.84, 159.63, 158.92, 157.67, 146.78, 141.21, 130.85, 128.15, 114.09, 112.80, 107.99, 107.89, 103.58, 100.13, 99.98, 77.08, 76.57, 76.51, 73.19, 69.61, 69.54, 64.95, 60.63, 60.56, 33.93, 31.98, 31.17, 28.76, 28.63, 28.49, 28.45, 24.97, 24.18, 22.09, 13.97 (CH_3, *ovlp isomers A and B*). (Figure A2.39)

ESI-MS (positive ions): m/z (%): 441 (40) $[M + H]^+$, 463 (100) $[M + Na]^+$, 904 (40) $[2M + Na]^+$. (Figure A2.40)

ESI-MS (negative ions): m/z (%): 439 (100) $[M - H]^-$, 880 (60) $[2M - H]^-$. (Figure A2.41)

Elem. anal. calcd (%) for $C_{21}H_{32}N_2O_8 \cdot 1\ H_2O$: C 55.01, H 7.47, N 6.11; found: C 55.59, H 7.31, N 6.14.

[Cu(HL^6)Cl] · 2.5 H_2O (CM10)

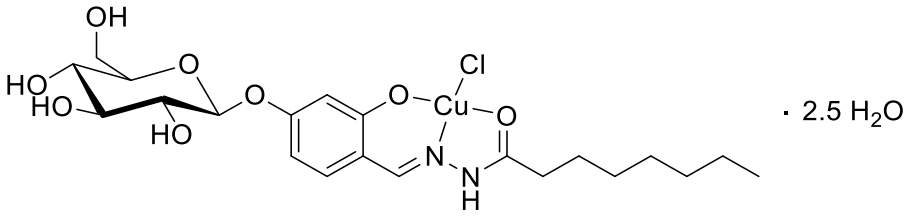

The ligand **CM9** (150 mg, 0.340 mmol, 1 eq) was dissolved in EtOH (10 mL) at 50 °C and three drops of aqueous 1 M NaOH were added: the pH of the resulting yellow solution was 9. A solution of $CuCl_2 \cdot 2\ H_2O$ (58 mg, 0.340 mmol, 1 eq) in EtOH (3 mL) was added and a dark green suspension (pH = 4) was obtained. The mixture was stirred at r.t. for 5 hours, then it was concentrated at rotavapor and left at -21 °C overnight. The suspension was centrifuged and the obtained precipitate was washed with cold EtOH and dried *in vacuo*. A dark green solid was obtained (103 mg, yield = 52%).

IR (cm^{-1}): ν = 3600 – 3100 (m) (OH and NH), 2925 (m-s) and 2855 (m-s) (CH), 1608 (s) (C=O), 1574 (s) (C=N). (Figure A2.42)

ESI-MS (positive ions): m/z (%): 502 (90) $[CuHL^6]^+$, 1006 (20) $[Cu_2HL^6{}_2]^+$, 1041 (25) $[Cu_2ClH_2L^6{}_2]^+$. (Figure A2.43)

ESI-MS (negative ions): m/z (%): 536 (100) $[CuL^6Cl]^-$, 1039 (70) $[Cu_2ClL^6{}_2]^-$.

Elem. anal. calcd (%) for $C_{21}H_{31}ClCuN_2O_8 \cdot 2.5\ H_2O$: C 43.22, H 6.22, N 4.80; found: C 42.69, H 5.78, N 4.68.

Crystallography

Single crystals of **CM4** suitable for X-ray diffraction analysis were obtained by slow evaporation of a solution of the ligand in EtOH.

Crystallographic data: $C_{14}H_{19}N_3O_8 \cdot H_2O$, monoclinic, C2, a= 13.2111(10) Å, b= 7.2718(6) Å, c= 18.2221(17) Å, 90, 111.181(4), 90°; V=1632.3(2) $Å^3$; Z=4; d_{calc}=1.527 mg/cm^3, F(000)= 792, CuKα radiation (λ = 1.54178), mu=1.109. Tot. refl.= 14192, hkl range= -15<h<16, -8<k<9, -22<l<22; Theta range 2.60 - 74.54, unique reflections= 3294, number of parameters = 247.

A suitable crystal was selected and mounted on a diffractometer Bruker D8 Venture. The crystal was kept at 200.00 K during data collection. Using Olex2,[220] the structure was solved with the olex2.solve[221] structure solution program using Charge Flipping and refined with the XL refinement package[123] using Least Squares minimisation.

UV–visible spectrophotometric titrations

The UV-visible spectra were collected using a Thermo Scientific Evolution 260 Bio spectrophotometer equipped with a Peltier temperature controller. Stock solutions of $\mathbf{H_2L^2}$ (**FMM8Z**) and $\mathbf{H_2L^4}$ (**CM4**) were prepared in aqueous 25 mM HEPES buffer at concentrations ca. 0.33 and 0.35 mM, respectively. Stock solutions of $CuCl_2 \cdot 2\ H_2O$ and $ZnCl_2$ were prepared in water at concentrations ca. 32.5 mM and 3.3 mM.

The complex formation equilibria at pH 7.4 of $\mathbf{H_2L^2}$ and $\mathbf{H_2L^4}$ with Cu^{2+} and Zn^{2+} ions were initially studied by direct spectrophotometric titrations of solutions of the ligands with the metal ions, and the samples were prepared as follows. Appropriate aliquots of the stock solutions of $\mathbf{H_2L^2}$ and $\mathbf{H_2L^4}$ were diluted in a quartz cuvette of 1 cm path length using aqueous 25 mM HEPES buffer (pH = 7.4) to obtain, respectively, *ca.* 25 µM and 50 µM ligand solutions in a total volume of 2.6 mL. The obtained ligand solutions were titrated with copper(II) or zinc(II) titrant solutions: for the system $\mathbf{H_2L^2}$ – Cu^{II} was used a 1.3 mM copper(II) working solution and the titration was performed up to a 3:1 metal:ligand ratio; for the system $\mathbf{H_2L^2}$ – Zn^{II} was used a 1.3 mM zinc(II) working solution and the titration was performed up to a 4:1 metal:ligand ratio; for the system $\mathbf{H_2L^4}$ – Cu^{II} was used a 3.3 mM copper(II) working solution and the titration was performed up to a 5:1 metal:ligand ratio; for the system $\mathbf{H_2L^4}$ – Zn^{II} was used a 3.3 mM zinc(II) working solution and the titration was performed up to a 7:1 metal:ligand ratio. For each solution, the absorption spectrum was collected in the 220-500 nm range at 298.2 K. All the experiments were performed in triplicate.

The equilibria at pH 7.4 of the system $\mathbf{H_2L^4}$ – Cu^{II} – Zn^{II} were also studied by competitive titration, as follows. A solution of the ligand $\mathbf{H_2L^4}$ (conc. 50 µM) was prepared in the cuvette by diluting the ligand stock solution in aqueous 25 mM HEPES buffer (pH = 7.4). A proper amount of the 3.3 mM Zn^{II} working solution was added to the ligand solution to obtain a Zn^{II}: $\mathbf{H_2L^4}$ ratio equal to 6:1. The obtained solution (total volume = 2.6 mL) was titrated with 3.3 mM Cu^{II} working solution up to a Cu^{II}: $\mathbf{H_2L^4}$ ratio of 5. For each solution, the absorption spectrum was collected in the 220-500 nm range at 298.2 K. The titration was performed in triplicate.

The logarithms of the apparent stability constants were calculated from the spectral dataset using the HypSpec2014 software.[108] In all titrations, the molar spectrum of the ligand at the appropriate pH was used as the fixed parameter. All equilibria were studied at fixed pH, and therefore the determined log β values are logarithms of conditional formation constants. In the speciation models the L component identifies the studied ligand irrespective of its protonation state; for this reason, the charges of the complexes are omitted. Speciation diagrams were calculated using the Hyss2009 software.[125]

Chapter 3:

Thiohydrazones and their copper(II) complexes as versatile chemical scaffolds in bioinorganic chemistry

Introduction

Thiohydrazones

Thiohydrazones (or **thioacylhydrazones**) are obtained by reaction of an aldehyde or ketone with a **thiohydrazide** (Scheme 3.1) and can be considered as the sulphur analogues of the **acylhydrazones**.[222-224]

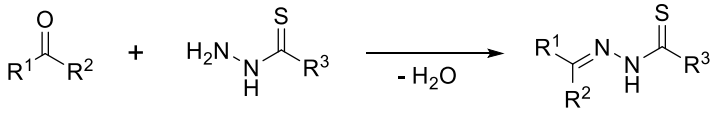

R^1 - R^2 = H, alkyl, aryl
R^3 = alkyl, aryl

Scheme 3.1: Synthesis of **thiohydrazones**.

While many acylhydrazides are commercially available or easily accessible by synthesis,[225-226] the isolation of **thiohydrazides** is not straightforward. Aromatic thiohydrazides are traditionally prepared from aryl halides through a protocol that implies three steps[222,227] (Scheme 3.2): (1) reaction of a Grignard compound with carbon disulphide to obtain the magnesium halide salt of an aryl-dithioacid; (2) reaction of the dithioate salt with sodium chloroacetate to give the key intermediate carboxymethyl dithioate; (3) reaction of the carboxymethyl dithioate with hydrazine.

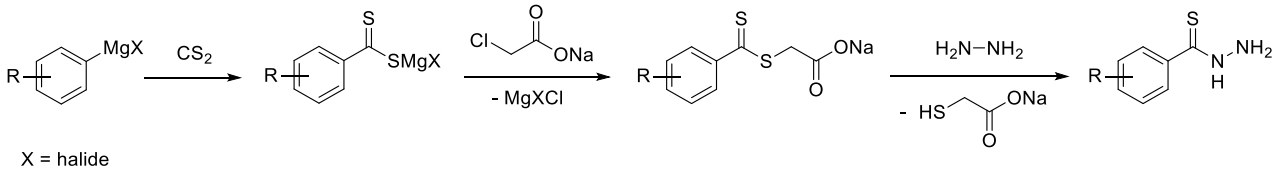

X = halide

Scheme 3.2: Synthetic route to aromatic thiohydrazides (X = halide, R = any group without labile protons).

The synthetic protocol is characterized by the use of toxic, flammable and environmentally hazardous substances (CS_2 and hydrazine) and by the need for strictly anhydrous conditions in the first step. These drawbacks make the synthetic route not attractive and may be in part responsible for the scarce use of **thiohydrazides** as precursors for ligands in coordination chemistry. The only exception is represented by thiobenzohydrazide,[228-230] probably because its precursor *S*-(thiobenzoyl)thioglycolic acid is commercially available (Figure 3.1).

thiobenzohydrazide S-(thiobenzoyl)thioglycolic acid

Figure 3.1: Chemical structure of thiobenzohydrazide (left) and its commercial precursor, *S*-(thiobenzoyl)thioglycolic acid (right).

Among the Schiff bases, the **thiohydrazones** are the unique class of molecules to display a **thione** – **thiolene** – **thiadiazoline** tautomerism (Scheme 3.3). The formation of the cyclic structure of the **thiadiazoline** (also known as 2,3-dihydro-1,3,4-thiadiazole) is due to the intramolecular ring closure of the thiolene tautomer.[231-233]

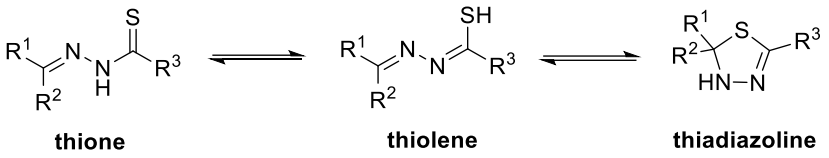

R^1 - R^2 = H, alkyl, aryl
R^3 = alkyl, aryl

Scheme 3.3: Tautomers of thiohydrazones.

Similarly to ***N*-acylhydrazones**, the **thiohydrazones** with different R^1 and R^2 substituents can exist as two different geometric isomers (***E*** and ***Z***) with respect to the C=N bond,[233] but they can also exist as two different rotational conformers (***syn*-** and ***anti*-periplanar**, which can be also referred to as ***cis*** and ***trans***) with respect to the C(=S) – N bond (Figure 3.2).

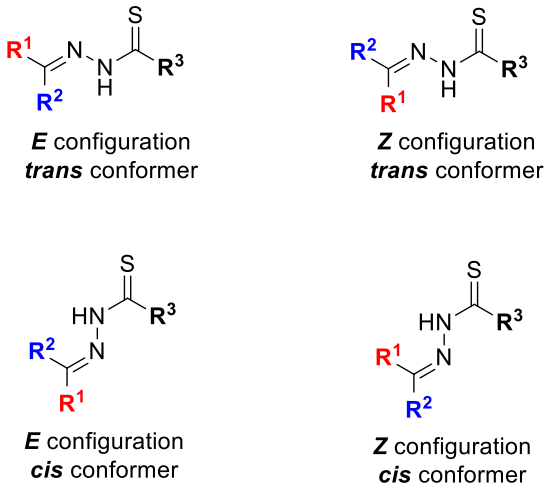

Figure 3.2: Geometric isomers and conformers of thiohydrazones.

The existence of such a high number of possible structures makes the characterization of these compounds quite difficult, especially in solution. In addition, the literature on these systems is scarce. The first reported syntheses of **thiohydrazones** date back to the works carried out by Holmberg in the 1940s,[227] but it was only in the 1980s that it was discovered the possibility for these molecules to give rise to cyclic tautomers, thanks to the works of Zelenin,[231] Evans and Taylor.[232,234] It is reported that several factors can affect the tautomeric and configurational equilibria in solution, such as the nature of the aldehyde/ketone precursor, the polarity of the solvent and the temperature.[224,231,233]

Regarding the aldehyde-based **thiohydrazones**, ^{1}H and ^{13}C NMR spectroscopies allow to discriminate among **thione** and **thiadiazoline** tautomers in solution. Indeed, if the molecule is in the **thione** form, the chemical shift of the signal of the methine proton at C2 falls in the range 8 – 9 ppm; on the contrary, if the molecule is in the **thiadiazoline** form, the peak of the same proton falls between 6 and 7 ppm[232] (Figure 3.3). For what concerns ^{13}C NMR, the C2 signal of the **thione** appears around 140 – 150 ppm, compatibly with the sp^2 hybridization of the carbon atom; in contrast, the C2 signal of the **thiadiazoline** is typically observed in the range 70 – 100 ppm, coherently with its sp^3 hybridization[231,232] (Figure 3.3).

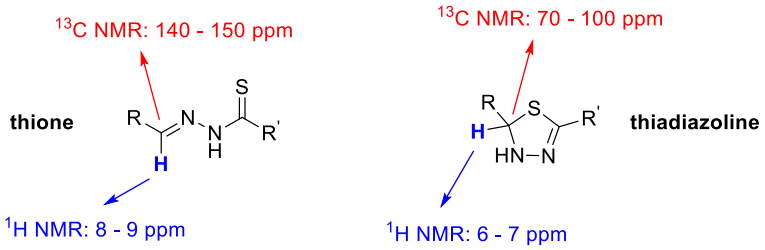

Figure 3.3: Relevant NMR signals of thione and thiadiazoline tautomers of thiohydrazones.

To the best of our knowledge, in literature examples of detection of the **thiolene** tautomer in solution are not reported.

In solution, the cyclic **thiadiazoline** is in equilibrium with the acyclic **thione**, which allows **thiohydrazones** to act as metal chelators.[224] Indeed, metal coordination shifts the equilibrium towards the acyclic form of the ligands.

Many of the thiohydrazone-metal complexes reported in literature are based on tridentate ligands. Among the most important examples there are the chloro(phenyl 2-pyridyl ketone thiobenzoylhydrazonato)palladium(II) complex (Figure 3.4a) reported by Pelagatti et al., which displays catalytic activity in the homogeneous hydrogenation of phenylacetylene;[230] the copper(II) (Figure 3.4b), cobalt(II) and nickel(II) complexes of 5-(4-oxo-4H-chromen-3-yl)-4,5-dihydro-1,3,4-thiadiazole-2-carboxamide reported by Myannik et al., that are characterized by a dimeric structure with bridging halides,[235] and the iron complexes synthesized by Kalinowski et al., that display interesting biological activity and that will be described in the next section. The most representative compound of the latter class is the $Fe^{II}(PKTBH)_2$ complex (Figure 3.4c). [224]

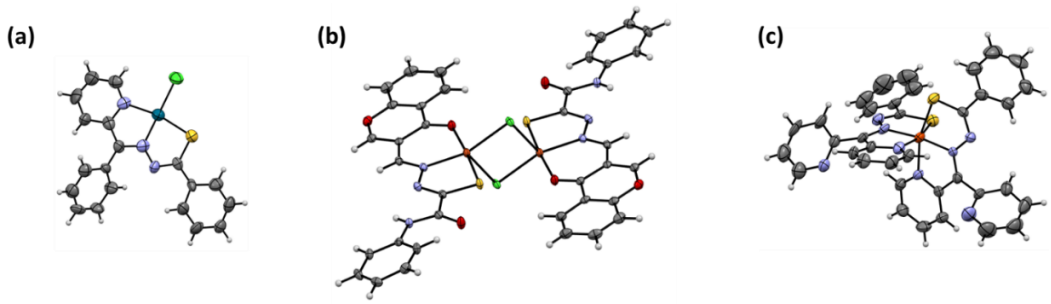

Figure 3.4: ORTEP diagrams of (a) chloro(phenyl 2-pyridyl ketone thiobenzoylhydrazonato)palladium(II), (b) the copper(II) complex of 5-(4-oxo-4H-chromen-3-yl)-4,5-dihydro-1,3,4-thiadiazole-2-carboxamide and c) the iron(II) complex $Fe^{II}(PKTBH)_2$ (HPKTBH = di-2-pyridylketone benzoyl thiohydrazone) Oxygen atoms in red, sulphur in yellow, nitrogen in blue, chlorine in green, carbon in grey, hydrogens in white, copper in orange, palladium in dark green.

Biological activity of thiohydrazones and their metal complexes

A careful survey of the literature highlighted the scarcity of data about the biological properties of **thiohydrazones**. Naik and coworkers reported the synthesis of two **bis-thiohydrazones** which showed some antibacterial and antifungal activity,[236,237] but the screening of their activity was limited to a small number of pathogens and no investigation on their mechanism of action was performed.

To the best of our knowledge, only Kalinowski and coworkers performed a thorough investigation of the biological properties of some **thiohydrazones** (Figure 3.5).[224] They studied the structure-activity relationships of a panel of anticancer ligands and related iron(II) and iron(III) complexes.

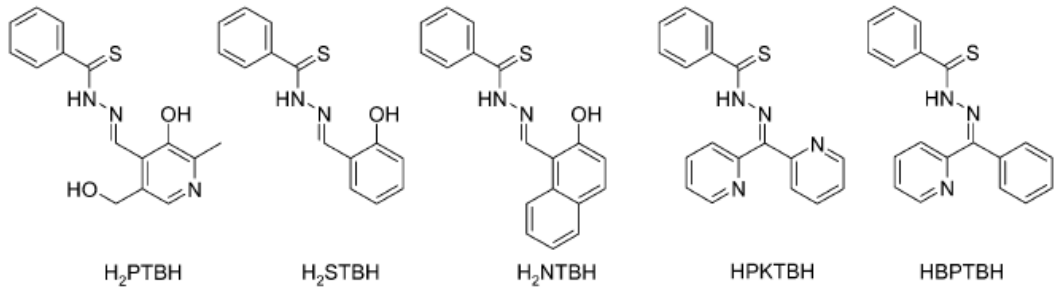

Figure 3.5: Chemical structures of the thiohydrazones H_2PTBH, H_2STBH, H_2NTBH, HPKTBH and HBPTBH. Adapted from Ref.[224]

Interestingly, while some of the ligands synthesized by Kalinowski et al. crystallized in the **thione** form (Figure 3.6a-b), the thiohydrazone HPKTBH crystallized as **thiadiazoline** tautomer (Figure 3.6c).

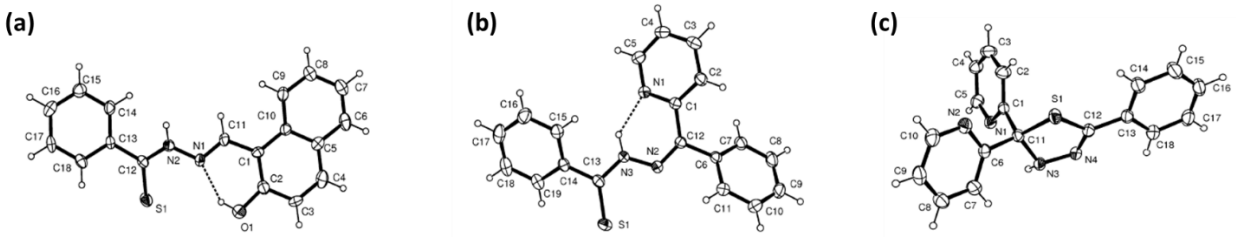

Figure 3.6: ORTEP diagrams of (a) H_2NTBH, (b) HBPTBH and (c) HPKTBH. Adapted from Ref.[224]

Since metal coordination shifts the equilibrium towards the acyclic form of **thiohydrazones**, all the ligands reported in Figure 3.5 acted as tridentate chelators towards iron.[224]

The **O,N,S-thiohydrazones** (H_2PTBH, H_2STBH and H_2NTBH) displayed reduced antiproliferative activity against SK-N-MC neuroepithelioma cells compared to that of their O,N,O-hydrazone analogues. In contrast, the **N,N,S-thiohydrazones** (HPKTBH and HBPTBH) proved to have largely increased anticancer activity with respect to their oxygen analogues, with IC_{50} values similar to the ones showed by highly effective thiosemicarbazones like HDp44mT.[74] In addition, all the tested **thiohydrazones** showed a significant decrease in anti-proliferative activity in normal cells in comparison with tumour cells, thus being characterized by an appreciable therapeutic index. Regarding the mechanism of action, the authors correlated the

antiproliferative activity of the **thiohydrazones** to their capability of chelating iron, a metal required by cancer cells to sustain their rapid replication.[224]

The authors synthesized also iron(II) and iron(III) complexes of the five thiohydrazones; $Fe^{II}(PKTBH)_2$ (Figure 3.4c), with an IC_{50} of 0.14 ± 0.01 μM against neuroepithelioma cells, was the most active one.

Design of novel thiohydrazones

Thiohydrazones and their metal complexes constitute an underrated class of bioactive compounds. Although their key precursors, the **thiohydrazides**, are known since the 1940s, they have been mainly employed for the synthesis of 1,3,4-thiadiazoles[238-240] or *N*-acylthiadiazolines[241-243] rather than **thiohydrazones**. Attracted by the unexplored potential of these systems, we decided to investigate the thiohydrazonic scaffold with the aim of preparing novel anticancer compounds. We started our investigations from the design and synthesis of precursors different from the widely used thiobenzohydrazide. In collaboration with the group of Prof. Alex Manicardi of the University of Parma, a different protocol for the preparation of **thiohydrazides** was applied. The obtained 4-(dimethylamino)benzothiohydrazide and 2-propylpentanethiohydrazide were used to synthesize four novel **thiohydrazones** (Figure 3.7).

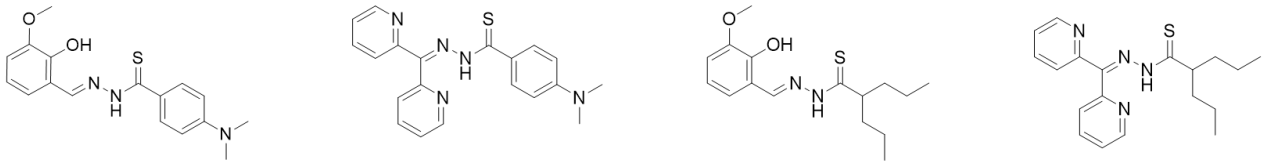

AZM8a H_2L^1 | **AZM14b** HL^2 | **AZM12** H_2L^3 | **AZM16** HL^4

Figure 3.7: Chemical structures of the four novel **thiohydrazones** synthesized in this project.

Two of the ligands were then employed to prepare the corresponding copper(II) complexes, in order to evaluate their cytotoxic profile.

This project was carried out during a period of research under the supervision of Prof. Diego Montagner in the Department of Chemistry of Maynooth University, Ireland.

Results and discussion

Synthesis and characterization of thiohydrazides

As stated in the introduction, the traditional procedure for the synthesis of aromatic **thiohydrazides** involves the use of highly toxic and hazardous reagents, such as carbon disulfide and hydrazine.[222,227] Instead we used a modified version of protocols reported in the literature,[238,241-243] starting from a carboxylic acid: (1) synthesis of Boc-hydrazide, (2) thionation with Lawesson's reagent, (3) Boc deprotection (Scheme 3.4).

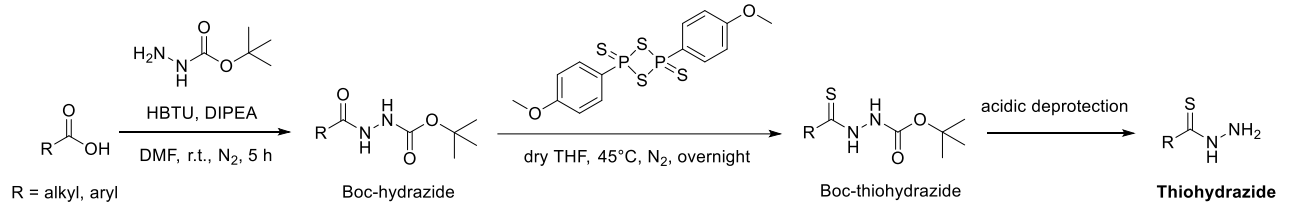

Scheme 3.4: Synthetic route to thiohydrazides.

The conversion of the carbonyl group of the Boc-protected hydrazide into thiocarbonyl implies the use of the Lawesson's reagent (LR, Scheme 3.5). LR is an arylthionophosphine sulfide which is commonly used as an alternative to hazardous phosphorus pentasulfide for the conversion of a wide variety of carbonyl compounds to thiocarbonyl compounds.[244] The accepted mechanism of thionation of carbonyl groups proceeds via 1,3,2-oxathiaphosphetane derivatives as Wittig-type intermediates (Scheme 3.5).[245-247]

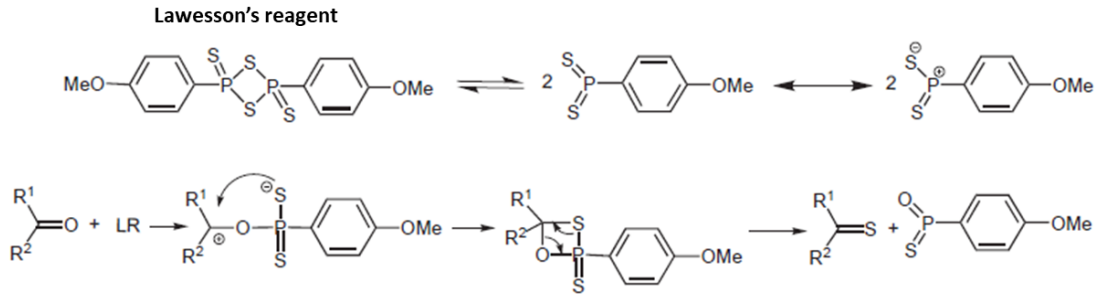

Scheme 3.5: Mechanism of the thionation reaction using Lawesson's reagent. Adapted from Ref.[247]

Within this project, three carboxylic acids were selected as starting materials for the synthesis of thiohydrazides: two aromatic carboxylic acids, namely 4-(dimethylamino)benzoic acid and 4-(nitro)benzoic acid, and an alkyl carboxylic acid, namely 2-propylpentanoic acid or valproic acid (Figure 3.8).

The two aromatic precursors were chosen with the aim of studying the effect that the presence of an electron-donating and an electron-withdrawing group in position 4 can have on both the reactivity and the anticancer activity of the related **thiohydrazones**, making a direct comparison with the properties of **thiohydrazones** derived from unsubstituted thiobenzohydrazide. The choice of these two carboxylic acids was also motivated by the fact that the 4-(dimethylamino)phenyl and 4-(nitro)phenyl fragments are present in a large number of drugs and bioactive compounds.[248-250]

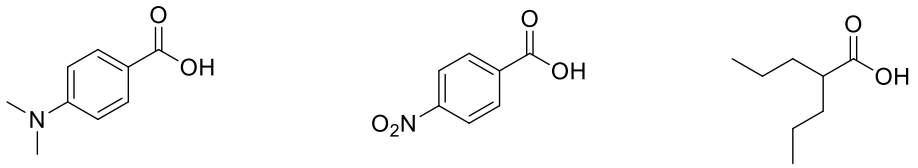

4-(dimethylamino)benzoic acid 4-(nitro)benzoic acid valproic acid

Figure 3.8: Chemical structure of the three carboxylic acids used in this project as precursors for thiohydrazides.

The synthetic protocol described in Scheme 3.5 was initially applied for the preparation of 4-(dimethylamino)benzothiohydrazide[243] and 4-(nitro)benzothiohydrazide.[251]

The syntheses of 4-(dimethylamino)benzothiohydrazide (**AZM4c**) and its hydrochloride salt (**AZM4-hydrochloride**) are shown in Scheme 3.6.

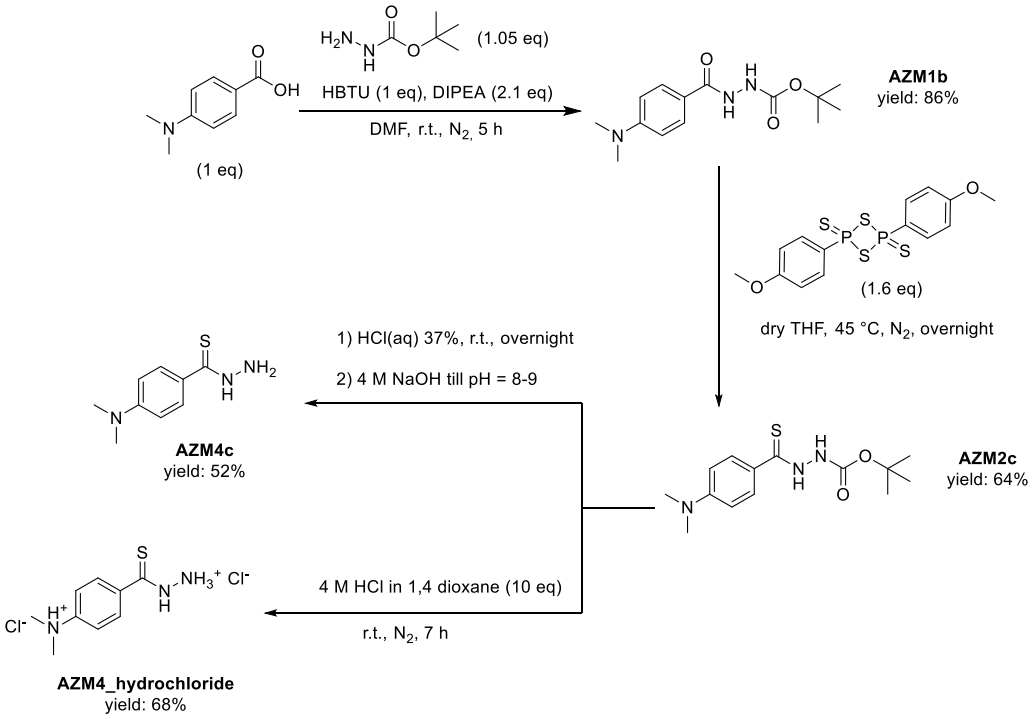

Scheme 3.6: Synthetic routes to 4-(dimethylamino)benzothiohydrazide (**AZM4c**) and its double hydrochloride salt (**AZM4-hydrochloride**).

The product of the coupling reaction between 4-(dimethylamino)benzoic acid and *tert*-butyl carbazate, the Boc-hydrazide **AZM1b**, was obtained in good yields by performing the reaction in DMF at room temperature. No chromatographic separation was necessary to purify the product, but several extractions of the organic phase were needed to completely remove the tetramethylurea by-product. The same protocol was applied with similar results for the other two synthesized Boc-hydrazides (**AZM3** and **AZM6**).

Attempts were made in order to use solvents safer than DMF, but solubility issues did not allow to completely get rid of it. A 5:1 MeCN:DMF mixture was found suitable to carry out the coupling instead of pure DMF.

In the subsequent step, the Boc-hydrazide **AZM1b** was converted into the Boc-thiohydrazide **AZM2c** by reaction with LR in THF (Scheme 3.6). The desired pure Boc-thiohydrazide was isolated in moderate yields, but the reaction showed several drawbacks related to the need for strict anhydrous conditions and to the formation of a side-product. The purification of the product from the side-product proved to be challenging even by column chromatography and partial coelution of the two species did not allow to collect the Boc-thiohydrazide in high yields. However, the compound **AZM2c** was obtained in pure form, and it was characterized by FT-IR (Figure A3.6) and NMR spectroscopies (Figures 3.9 and A3.7) and mass spectrometry (Figure A3.8). In Figure 3.9 it is reported the ^{1}H NMR (500 MHz) spectrum of **AZM2c** in DMSO-d_6.

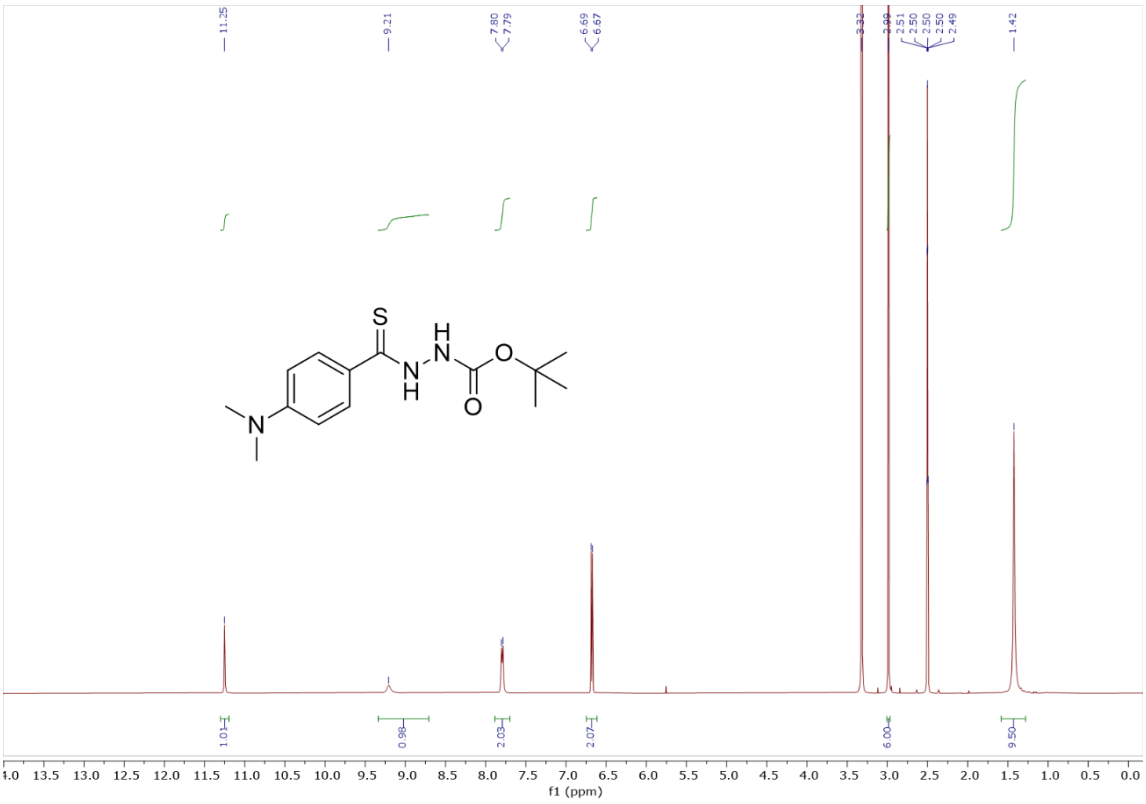

Figure 3.9: ^{1}H NMR (500 MHz, 298 K) spectrum of **AZM2c** in DMSO-d_6.

The side-product of the reaction was also fully characterized. ^{1}H NMR (figure A3.10), elemental analysis (see the experimental section), mass spectrometry (Figure A3.11) and literature data[246] suggested that it was the 2,3-dihydro-1,3,4,2-thiadiazaphosphole reported in Figure 3.10.

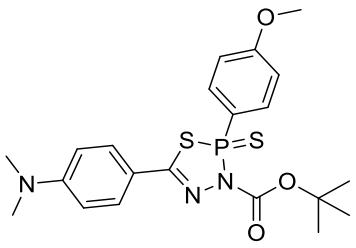

Figure 3.10: Chemical structure of the 2,3-dihydro-1,3,4,2-thiadiazaphosphole side-product.

Attempts were made in order to prevent the formation of this heterocyclic compound. Hypothesizing that the side-product was a reaction intermediate, we tried to apply longer reaction times (2-3 days) and higher temperatures (55 °C) to force the conversion into the desired product. Unfortunately, the heterocycle still formed. A patent[252] reported that such compound may be hydrolysed in basic conditions and with heating to give the corresponding thiohydrazide. Treatment of the crude of **AZM2c** with sat. $NaHCO_3$ aqueous solution at room temperature was not sufficient to hydrolyse the side-product. No attempts with harsher conditions were performed, in order to avoid undesired cyclization reactions.

With the Boc-thiohydrazide in our hands, a series of different procedures were tested to determine the optimal conditions for the acidic deprotection of Boc. Quite unexpectedly, all the attempts to achieve complete deprotection with trifluoroacetic acid (TFA) in DCM failed, even using TFA concentrations higher than 60%. Consequently, since **AZM2c** proved to be soluble in aqueous 37% HCl, the deprotection was performed directly in acid without further dilution. The desired 4-(dimethylamino)benzothiohydrazide (**AZM4c**) was obtained in moderate yields in the form of free base after the addition of aqueous NaOH until pH 8-9. Unfortunately, the sample proved to be contaminated by traces (2% in mass, NMR based) of a 1,3,4-thiadiazolic side-product (Figure 3.11, left), as indicated by the ^{1}H NMR spectrum (Figure 3.11) and LC-MS spectra (Figure A3.18) of **AZM4c**. All the attempts made to purify the product by column chromatography were unsuccessful.

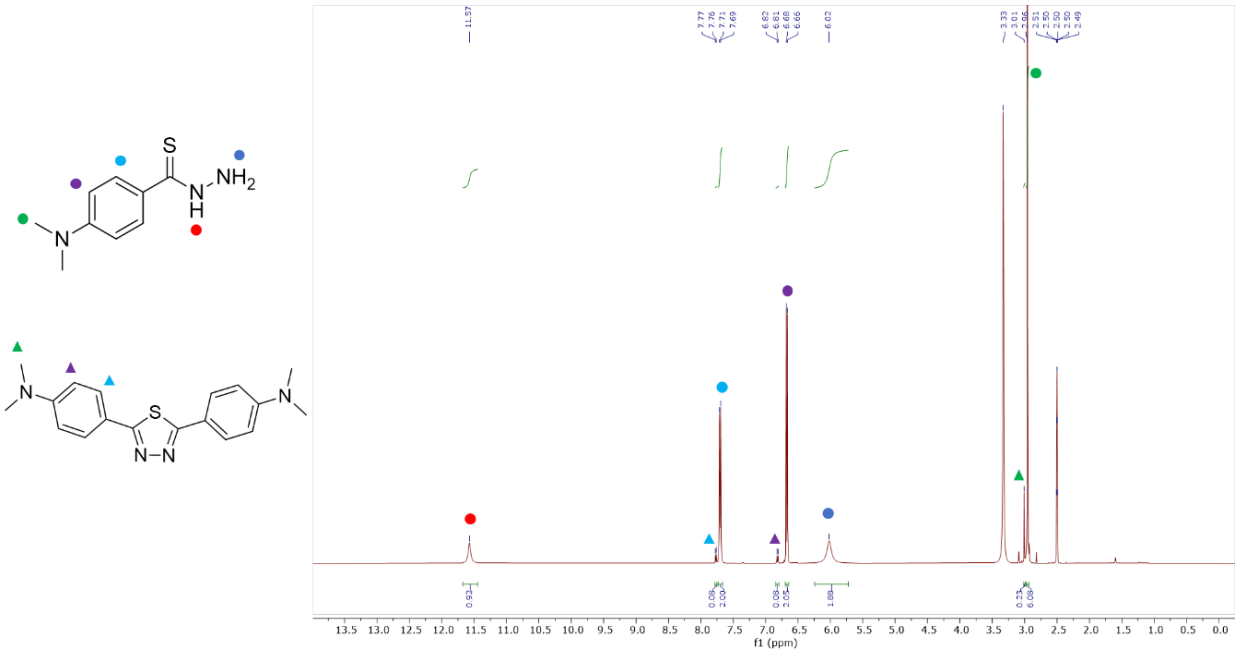

Figure 3.11: ^{1}H NMR (500 MHz, 298 K) spectrum of **AZM4c** in DMSO-d_6. The chemical structures of 4-(dimethylamino)benzothiohydrazide (top) and the 1,3,4-thiadiazolic side-product (bottom) are shown on the left.

In order to avoid the formation of the 1,3,4-thiadiazolic impurity, which was supposed to be triggered by atmospheric oxygen or by the addition of the base, we tried also another protocol for deprotection, based on the use of HCl in 1,4-dioxane under anhydrous conditions and inert atmosphere (Scheme 3.6). Such procedure was already reported to be effective for the synthesis of various thiohydrazide hydrochloride salts.[238,241,242] The deprotection reaction was therefore run by using 10 equivalents of HCl in 1,4-dioxane under anhydrous conditions and inert atmosphere. The product (**AZM4_hydrochloride**) was obtained as double hydrochloride salt by precipitation after the addition of Et_2O. Although the yield of the reaction was raised, also in this case the product was contaminated by traces of the impurity (2% in mass), as indicated by its ^{1}H NMR spectra in DMSO-d_6 (Figure A3.19) and D_2O (Figure A3.20).

The formation of the 1,3,4-thiadiazole seemed therefore to be triggered by the acidic conditions employed for the deprotection. The obtainment of 1,3,4-thiadiazoles during the synthesis of thiohydrazides was observed also by Jensen and Pedersen in the 1960s.[253] More recently, Angeles and coworkers reported the

formation of an analogue impurity during the preparation of 2,4-(difluoro)benzothiohydrazide hydrochloride salt.[242]

Both **AZM4c** and **AZM4_hydrochloride** were however used for the synthesis of **thiohydrazones**. As it will be described, this side-product did not contaminate the final ligands.

The synthesis of 4-(nitro)benzothiohydrazide proved to be even more problematic compared to 4-(dimethylamino)benzothiohydrazide. The Boc-hydrazide **AZM3** was easily isolated in high yields, while very low yields (15%) and difficult purification affected the preparation of Boc-thiohydrazide **AZM5a** (Scheme 3.7). Even the use of a large excess of LR and longer reaction times did not allow to improve the yield. In addition, the obtained Boc-thiohydrazide contained traces of impurities (Figure A3.21).

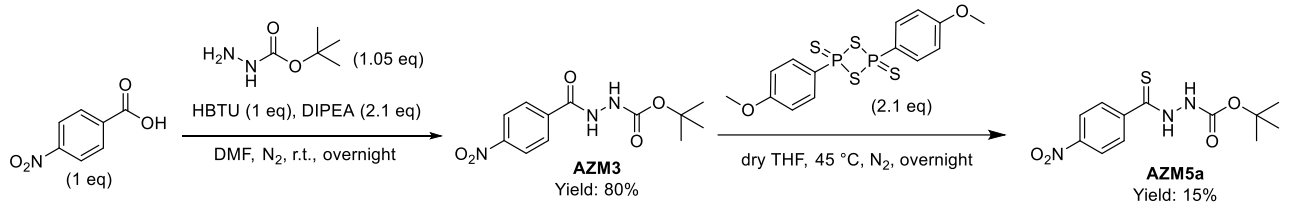

Scheme 3.7: Synthesis of Boc-thiohydrazide **AZM5a**.

Further problems encountered in the deprotection step prevented the isolation of the desired thiohydrazide: treatment with TFA in DCM was unsuccessful and attempts of deprotection with aqueous 37% HCl failed due to insolubility of **AZM5a** in the acidic mixture. Time constraints and the limited amount of available Boc-thiohydrazide prevented the application of the deprotection protocol based on HCl in 1,4 dioxane.

Overall, the thionation reaction appeared to be the critical step in the synthesis of 4-(nitro)benzothiohydrazide. In light of these results, we decided to temporarily abandon the synthesis 4-(nitro)benzothiohydrazide to focus our efforts towards the preparation of 2-propylpentanethiohydrazide.

Contrarily to what was observed for aromatic **thiohydrazides**, the application of the synthetic protocol allowed to isolate 2-propylpentanethiohydrazide hydrochloride (or valproic thiohydrazide hydrochloride) **AZM11** in good yields and in pure form (Scheme 3.8).

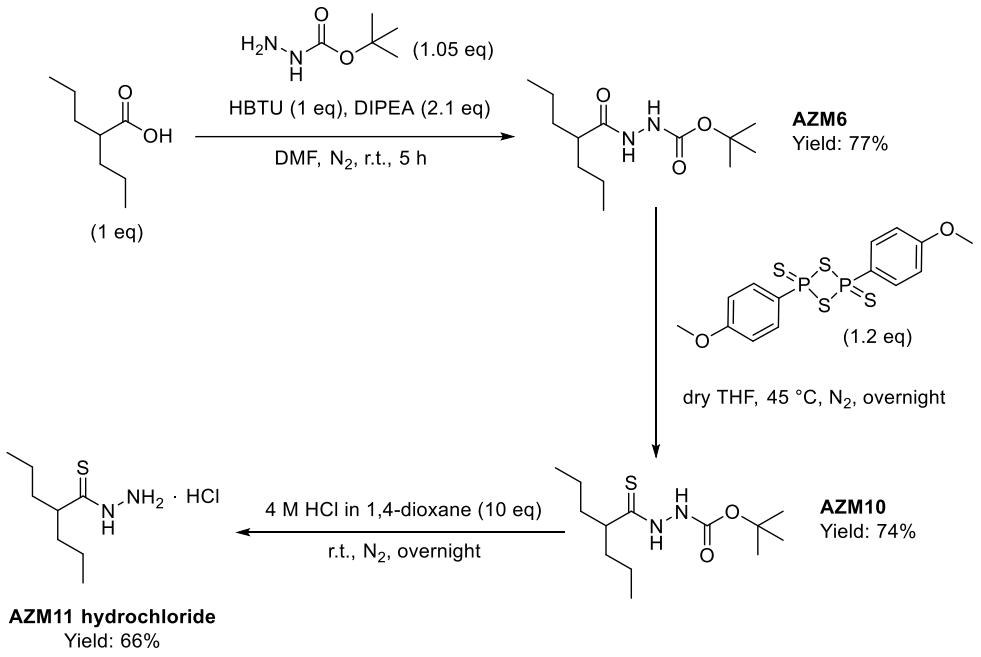

Scheme 3.8: Synthetic route to 2-propylpentanethiohydrazide hydrochloride (**AZM11**).

The ^{1}H NMR (500 MHz) spectrum of the Boc-hydrazide **AZM6** in DMSO-d_6 showed the presence of two isomers in solution, as suggested by the splitting of the signals of the two NH groups (Figure A3.23).

The thionation reaction allowed to obtain the desired Boc-thiohydrazide **AZM10**. ^{1}H NMR spectrum in $CDCl_3$ (Figure A3.38) indicated the presence of traces of a thiadiazaphosphole side-product similar to the one obtained during the synthesis of **AZM2c**, but the intermediate was used in the next step without further purification.

Boc-removal was achieved by using HCl in 1,4-dioxane and the target thiohydrazide (**AZM11**) was precipitated and isolated as hydrochloride salt after addition of Et_2O. No contamination of the product by thiadiazaphosphole or 1,3,4-thiadiazole was observed. The purity of **AZM11** was confirmed by NMR spectroscopy (Figures 3.11 and A3.40-41), mass spectrometry (Figure A3.42) and elemental analysis (see the experimental section). **AZM11** was isolated as hydrochloride and in its ^{1}H NMR (500 MHz, 298 K) spectrum in DMSO-d_6 (Figure 3.12) it is possible to observe two very broad signals attributable to the NH protons. The peak at 12.19 ppm can be assigned to the NH group, while the broad signal between 7.00 and 4.00 ppm can be attributed to the protonated terminal NH_3^+ group. Such peak is probably overlapped to the signal of H_2O.

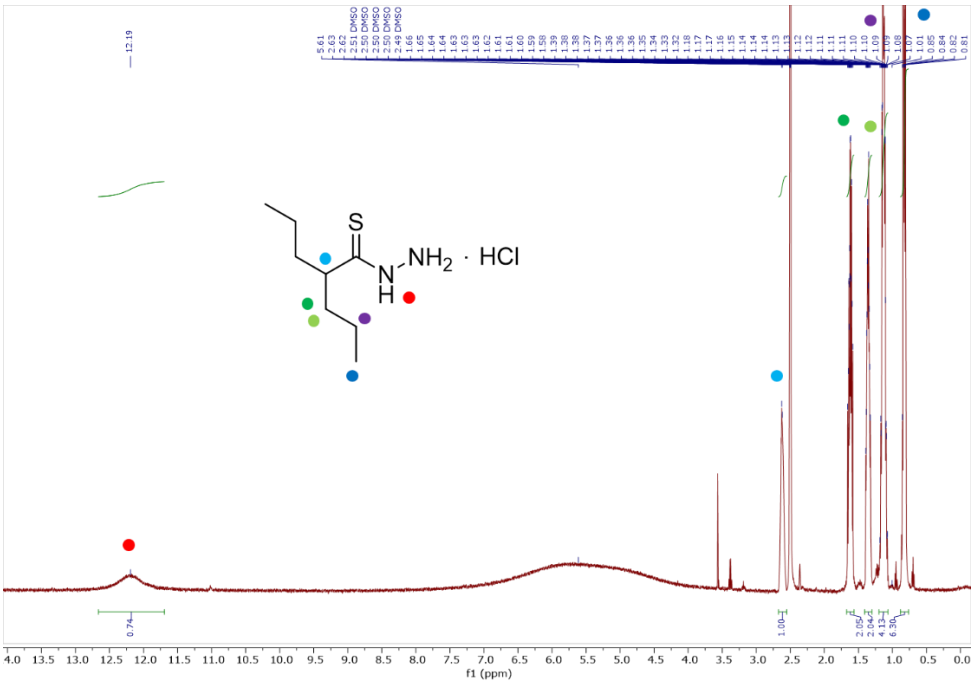

Figure 3.12: ^{1}H NMR (500 MHz, 298 K) spectrum of **AZM11** in DMSO-d_6.

A careful inspection of the spectrum made us notice the splitting of the signals of the β-CH_2 groups of the thiohydrazide (Figure 3.13). Although being achiral, the molecule possesses diastereotopic β-CH_2 groups. This is because substitution of any one of the four β-CH_2 hydrogens generates two chiral centres at once, and the two possible hydrogen substitution products at any one β-CH_2 carbon will be diastereomers (Figure 3.14). Obviously, the same considerations are valid also for the precursors of **AZM11**.

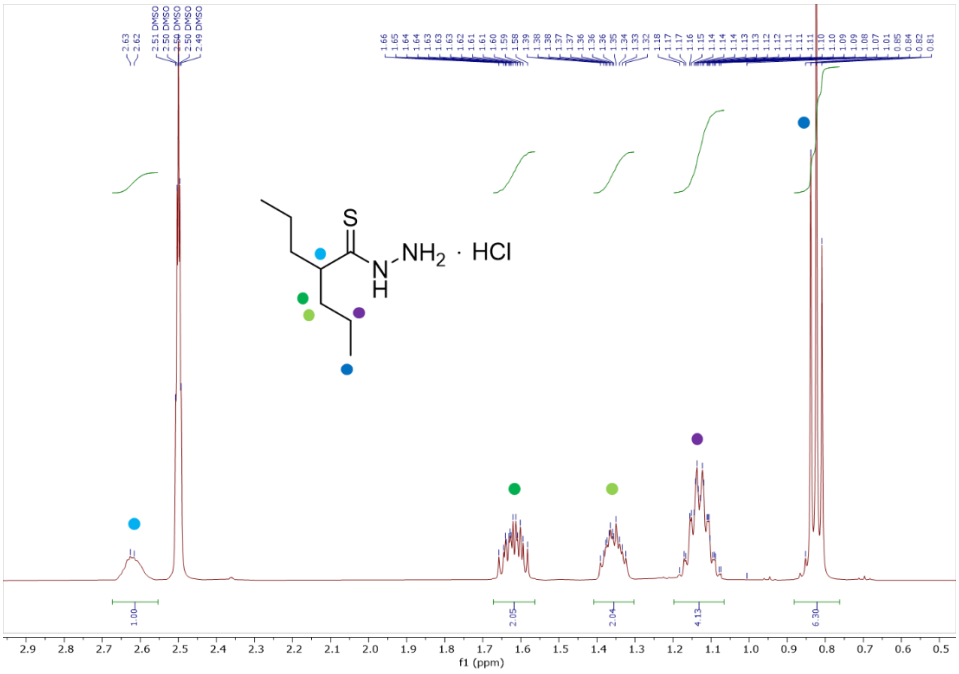

Figure 3.13: Selected range (0.50 – 3.00 ppm) of the ^{1}H NMR (500 MHz, 298 K) spectrum of **AZM11** in DMSO-d_6.

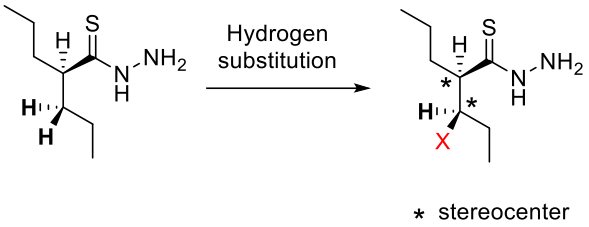

Figure 3.14: Diastereotopic hydrogens in compound **AZM11**. Hydrogen substitution at any one β-CH_2 carbon generates two stereocentres.

Overall, the applied synthetic protocol proved particularly efficient for the preparation of the alkyl **thiohydrazide AZM11**, while various problems were encountered during the synthesis of aromatic **thiohydrazides**, particularly in the case of 4-(nitro)benzothiohydrazide. The need for strictly anhydrous conditions in the step involving LR and the possibility of formation of different heterocyclic side-products in the steps (2) and (3) were identified as the main drawbacks of the method. Time constraints did not allow to systematically explore different conditions to optimize the syntheses: this aspect will be the focus of future work.

Synthesis and characterization of thiohydrazones

The 4-(dimethylamino)benzothiohydrazide, both as free base (**AZM4c**) and as hydrochloride salt (**AZM4_hydrochloride**), and the valproic thiohydrazide hydrochloride (**AZM11**) were used to synthesize four novel **thiohydrazones** (Figure 3.15).

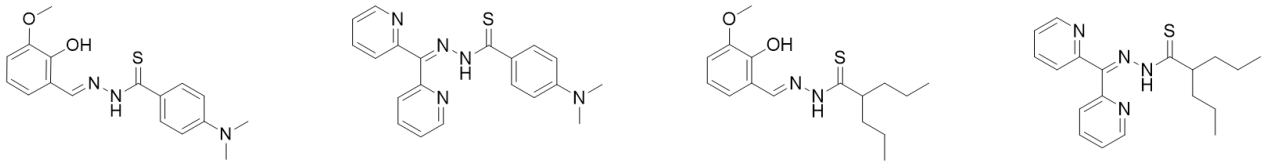

AZM8a H_2L^1 | **AZM14b** HL^2 | **AZM12** H_2L^3 | **AZM16** HL^4

Figure 3.15: Chemical structures of the four novel **thiohydrazones** synthesized in this project.

Two different carbonyl precursors were employed: ortho-vanillin and di(2-pyridyl)ketone (Figure 3.16).

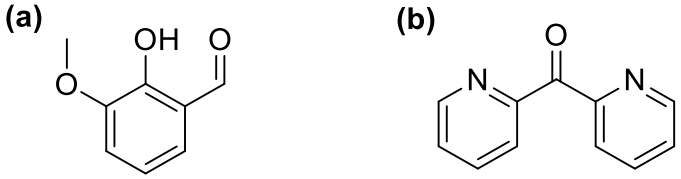

Figure 3.16: Chemical structures of (a) ortho-vanillin and (b) di(2-pyridyl)ketone.

Ortho-vanillin was selected also because of the promising results in terms of anticancer activity that our research group obtained with thiosemicarbazones derived from this aldehyde,[44,45] while di(2-pyridyl)ketone was chosen because of the excellent anti-proliferative activity and selectivity towards cancer cells displayed by known **thiosemicarbazones** derived from this ketone, like Dpc and HDp44mT.[74] In addition, we wanted to make a direct comparison with the ligand HPKTBH (Figure 3.5) reported by Kalinowski and coworkers.[224]

As already mentioned, aldehyde-based **thiohydrazones** can display not only **thione-thiolene-thiadiazoline** tautomerism and conformational isomerism, but also geometric isomerism with respect to the imine bond. Differently, **thiohydrazones** derived from symmetrical ketones such as di(2-pyridyl)ketone are characterized by tautomerism and conformational isomerism only. In agreement with this, the behaviour in solution of the di(2-pyridyl)ketone derivatives **AZM14b** and **AZM16** proved to be less complicated compared to the one showed by the ortho-vanillin based **thiohydrazones**. For this reason, the synthesis and the characterization of the ketone-based ligands will be described first.

The ligand **AZM14b** was obtained by condensation reaction of **AZM4_hydrochloride** with di(2-pyridyl)ketone (Scheme 3.9). Two equivalents of base (NaOH) were added to neutralize the hydrochloric acid of the thiohydrazide salt.

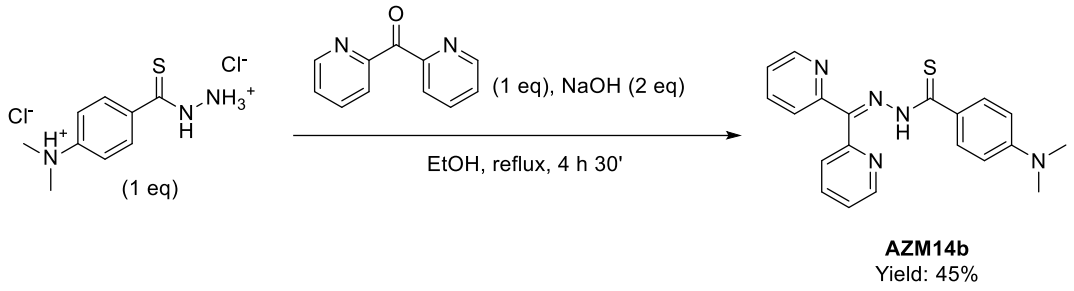

Scheme 3.9: Synthesis of the **thiohydrazone AZM14b**.

The novel ligand was characterized by means of FT-IR (Figure A3.53), 1D and 2D NMR spectroscopies (Figures 3.17-18, A3.54-60), mass spectrometry (Figures A3.61-62) and elemental analysis (see the experimental section).

^{1}H NMR (500 MHz, 298 K) experiments showed that, in both $CDCl_3$ and DMSO-d_6, the **thiohydrazone** exists as a mixture of **thiadiazoline** and **thione** in equilibrium (Scheme 3.10), in accord with what observed by Kalinowski et al. with ligand HPKTBH.[224] Even though the ratio between the two tautomers changes depending on the solvent, the **thiadiazoline** is the major species in both $CDCl_3$ and DMSO-d_6 (Scheme 3.10). As an example, in Figures 3.17-18 the ^{1}H NMR (500 MHz, 298 K) spectrum of **AZM14b** in $CDCl_3$ is reported.

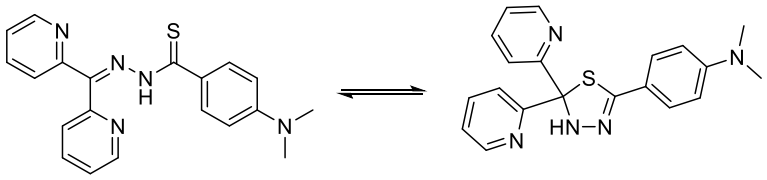

	Thione	Thiadiazoline
DMSO-d_6	9%	91%
$CDCl_3$	17%	83%

Scheme 3.10: Tautomerism of **AZM14b** in DMSO-d_6 and $CDCl_3$.

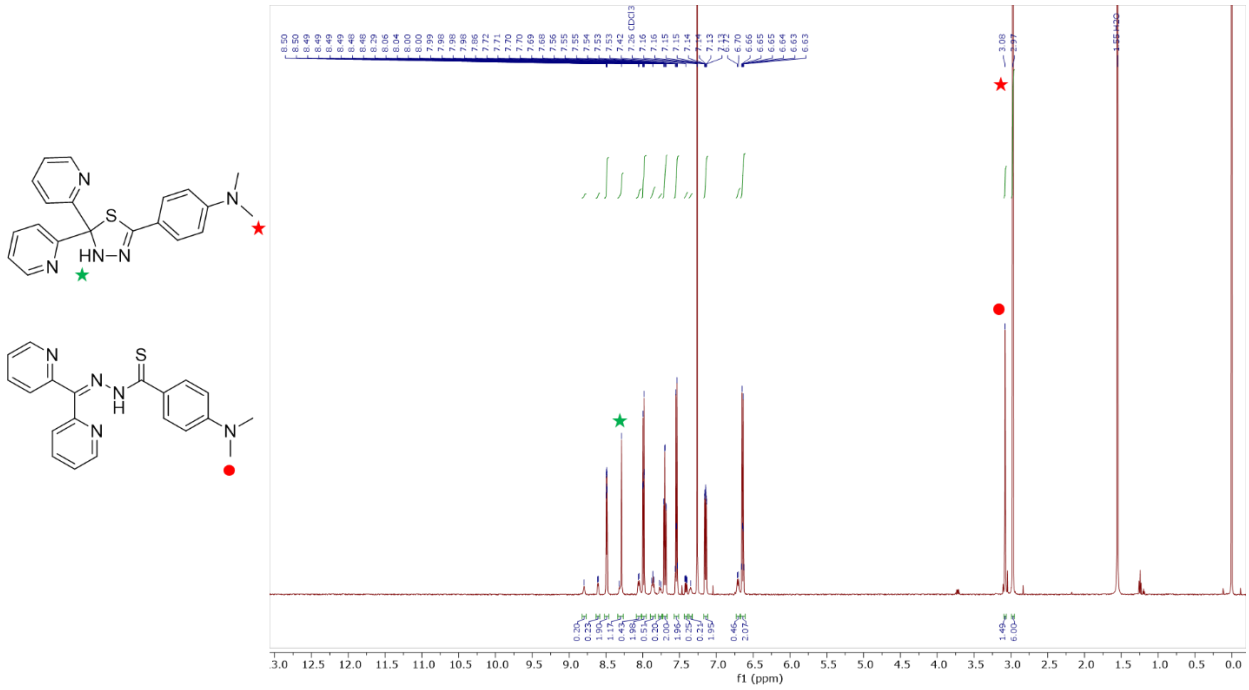

Figure 3.17: ^{1}H NMR (500 MHz, 298 K) spectrum of **AZM14b** in $CDCl_3$. The chemical structures of the **thiadiazoline** and **thione tautomers** are shown on the left.

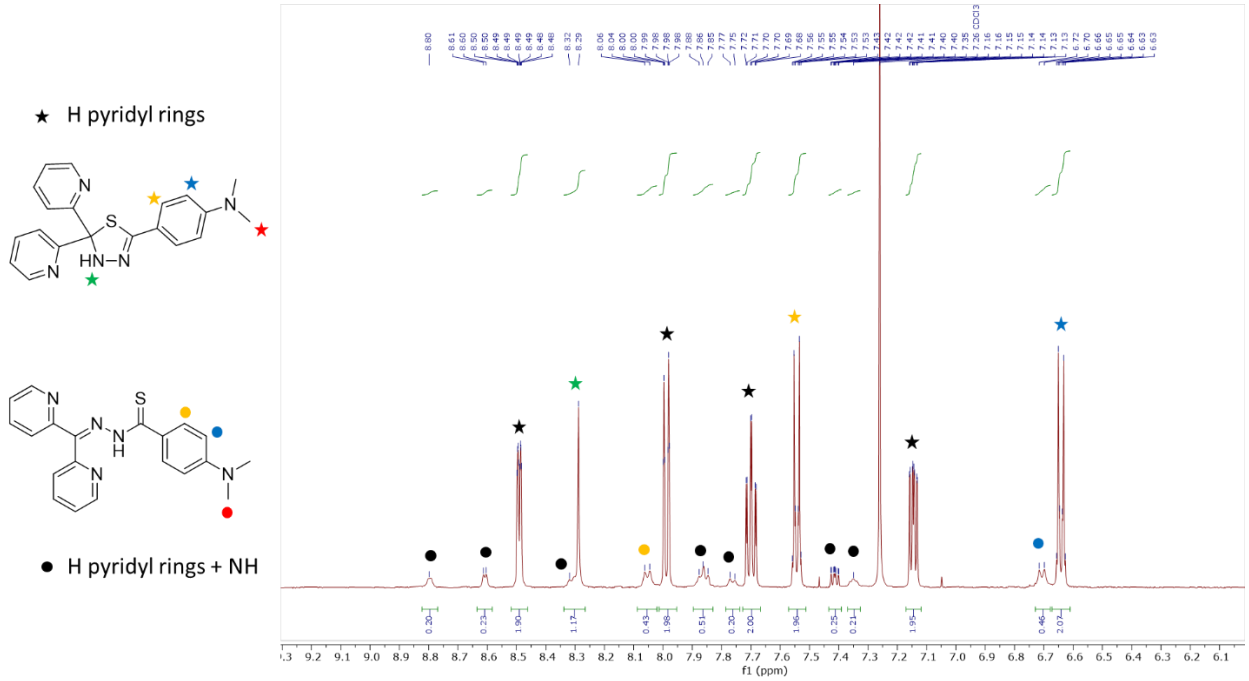

Figure 3.18: Selected range (6.00 – 9.30 ppm) of the ^{1}H NMR (500 MHz, 298 K) spectrum of **AZM14b** in $CDCl_3$ with the chemical structures of the **thiadiazoline** and **thione tautomers** on the left.

The distinction between the cyclic and the acyclic structures of the ligand in solution is possible by inspecting the NMR peaks of the protons of the pyridyl rings (Figure 3.18). In the structure of the **thiadiazoline**, both pyridyl rings experiment the same chemical environment and therefore give rise to four signals only: this is exactly what it is observed for the prevalent species in the ^{1}H NMR spectra of **AZM14b**. Contrarily, in the

structure of the **thione**, the nitrogen atom of one of the pyridyl rings is involved in an intramolecular H bond (Figure 3.19): consequently, the protons of the two rings are not chemically equivalent and eight signals are observed. The pattern of signals observed for the minor species is consistent with the **thione** structure and it is also comparable with the ^{1}H NMR spectra of di(2-pyridyl)ketone **thiosemicarbazones**.[254]

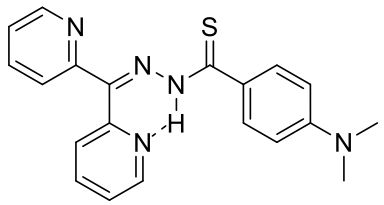

Figure 3.19: Intramolecular hydrogen bond in **AZM14b**.

In the ^{13}C NMR (126 MHz, 298 K) spectrum of **AZM14b** in $CDCl_3$ (Figure A3.58) it is present a signal at 89.32 ppm, attributable to the *sp*^{3} hybridized quaternary carbon (C2) of the **thiadiazolinic** ring (Figure 3.3): this finding further confirms the identity of the major isomer in solution. The signals of the major species (the **thiadiazoline**) and a peak at 40.30 ppm associated to the methyl carbon atoms of the minor tautomer (the **thione**) are also observed.

In the ESI-MS spectrum (positive ions) of **AZM14b** it is possible to observe the signals of the $[M + H]^+$ molecular ion and of the $[M + Na]^+$ adduct, together with peaks generated by fragmentation processes (Figure A3.61). A tentative assignment is reported in Figure A3.61.

The N,N,S tridentate ligand **AZM16** was obtained by condensation of **AZM11_hydrochloride** with di(2-pyridyl)ketone (Scheme 3.11).

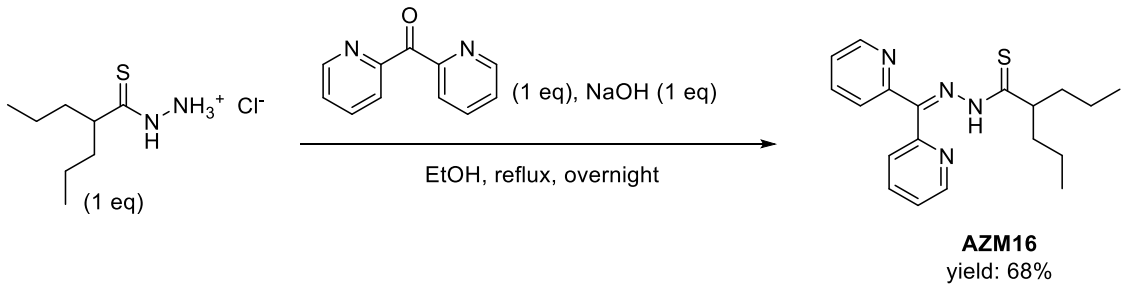

Scheme 3.11: Synthesis of the thiohydrazone **AZM16**.

The novel ligand was characterized by means of FT-IR (Figure A3.63), 1D and 2D NMR spectroscopies (Figures 3.20-22, A3.64-72), and mass spectrometry (Figures A3.73-74).

The solution behaviour of **AZM16** proved to be more complex than the one displayed by **AZM14b**. Indeed, the ^{1}H NMR (500 MHz, 298 K) experiments showed that, in both $CDCl_3$ and DMSO-d_6, the **thiohydrazone** exists as a mixture of three isomers in equilibrium. As an example, in Figures 3.20-22 selected ranges of the ^{1}H NMR (500 MHz, 298 K) spectrum of **AZM16** in DMSO-d_6 are reported.

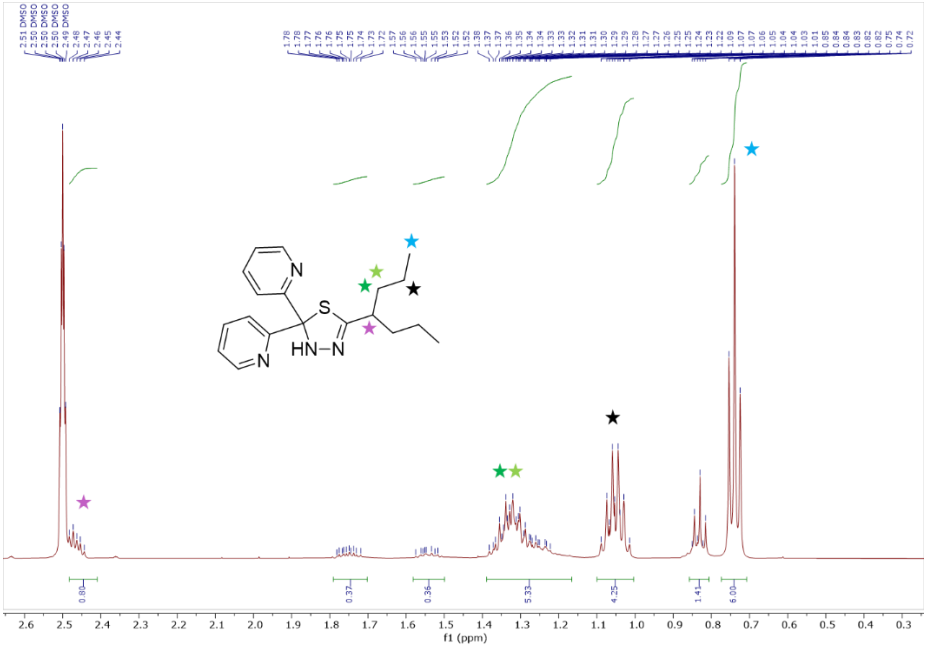

Figure 3.20: Selected range (0.20 – 2.70 ppm) of the ^{1}H NMR (500 MHz, 298 K) spectrum of **AZM16** in DMSO-d_6. The peak attributions are reported for the major isomer only (the **thiadiazoline**).

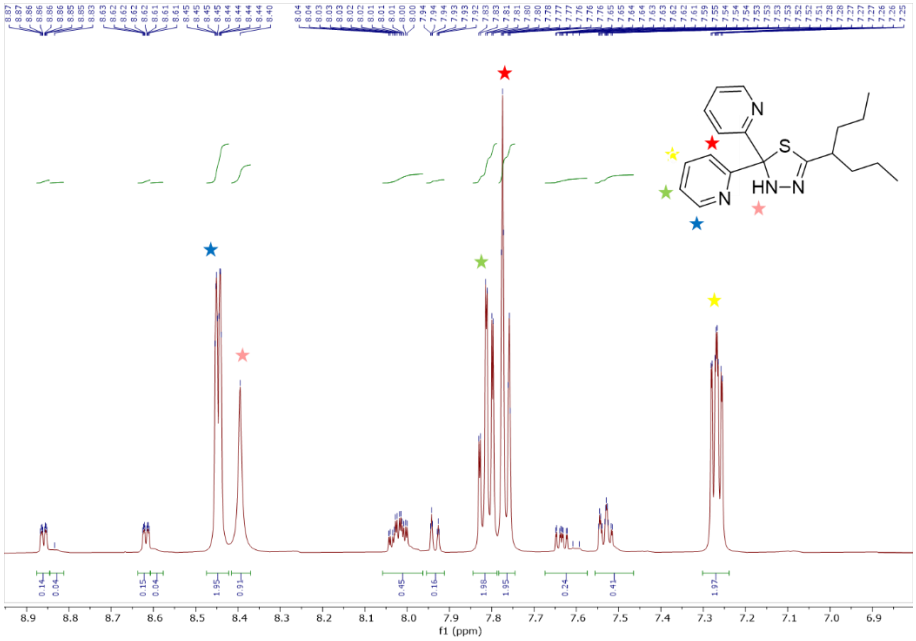

Figure 3.21: Selected range (6.80 – 8.95 ppm) of the ^{1}H NMR (500 MHz, 298 K) spectrum of **AZM16** in DMSO-d_6. The peak attributions are reported for the major isomer only (the **thiadiazoline**).

Similarly to **AZM14b**, the major isomer in both solvents is the **thiadiazoline** (81 – 85 %), as indicated by the pattern of signals in the ^{1}H NMR spectra (Figures 3.20-22 and A3.64-67) and by the presence of the diagnostic peak at ca. 90 ppm in the ^{13}C NMR spectrum in DMSO-d_6 (Figure A3.70). Instead, the identity of the other two minor species (that we will refer to as **isomer 2** and **isomer 3**) in equilibrium with the thiadiazolinic form of

AZM16 is uncertain. The identification is hindered by their low concentration in solution and by the high number of peaks they give rise. Nevertheless, it is possible to observe in Figure 3.22 that they show a higher number of aromatic protons peaks with respect to the **thiadiazoline**, therefore suggesting that they are acyclic species. The possible acyclic species for the **thiohydrazone** are: **thione** (Figure 3.23a), **thiolene** (Figure 3.23b) and **zwitterionic thiolene** (Figure 3.23c).

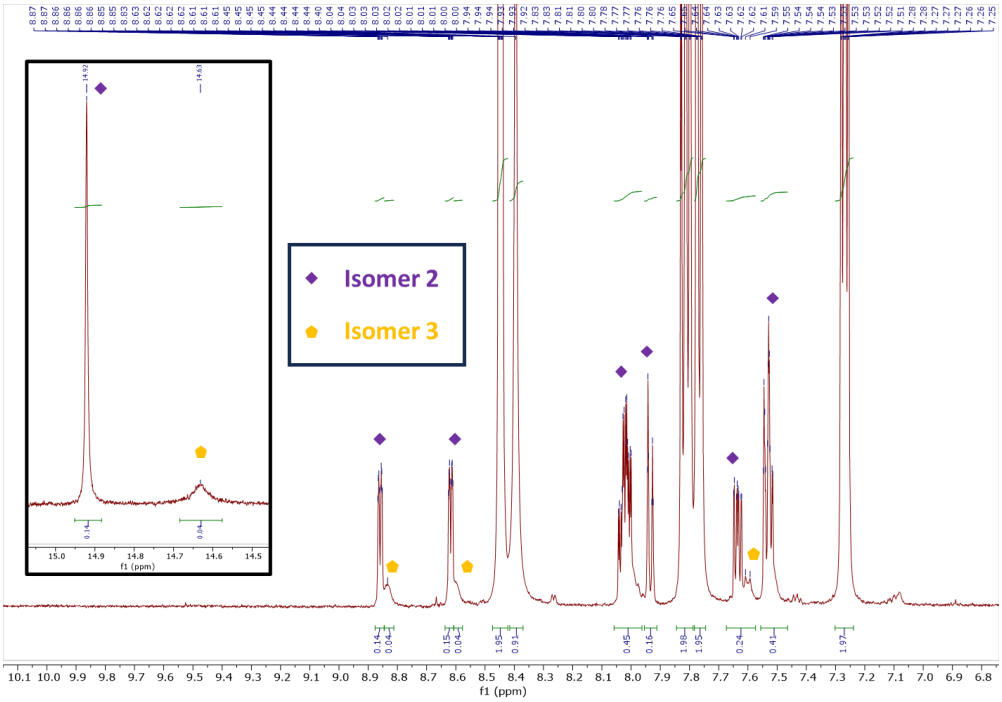

Figure 3.22: Selected range (6.85 – 10.15 ppm) of the ^{1}H NMR (500 MHz, 298 K) spectrum of **AZM16** in DMSO-d_6. The inset shows the signals observed at 14.50 – 15.10 ppm. The peak attributions are reported for the minor isomers (**isomer 2** and **isomer 3**).

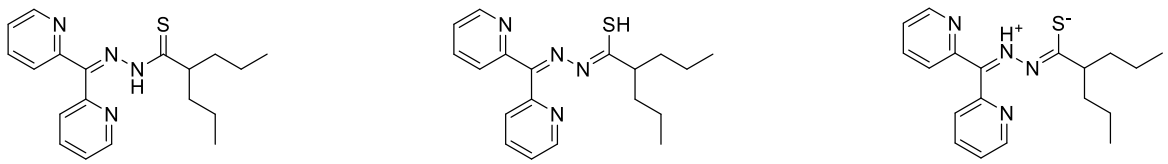

Figure 3.23: Chemical structures of the possible acyclic tautomers of **AZM16**: (a) **thione**, (b) **thiolene** and (c) **zwitterionic thiolene**.

The NH signal for the two unknown species is shifted to very low fields in both $CDCl_3$ and DMSO-d_6 (in the range 14.60 – 16.00 ppm, Figures 3.22 and A3.67). Hypothesizing that these signals were due to the SH groups of two configurations of the **thiolene** tautomer (Figure 3.23b), the FT-IR spectrum of a solution of **AZM16** in $CDCl_3$ was measured (Figure A.3.76). No bands in the range 2500 – 2600 cm^{-1} were detected, thus excluding the presence of SH groups, as well as the existence of the **thiolene** tautomer for the ligand in solution.

If we take into account the **thione** tautomer (Figure 3.23a), a plausible way that it has to give rise to two species in solution consists of rotation around the thioamidic C-N bond. The resulting isomers would be the

cis (or synperiplanar) and ***trans*** (or antiperiplanar) conformers (Figure 3.24), the same hypothesized for the ***N*-acylhydrazones** described in Chapter 2. The intramolecular hydrogen bond of the thione species would explain the quite high chemical shift observed for the NH groups of both isomers **2** and **3**.

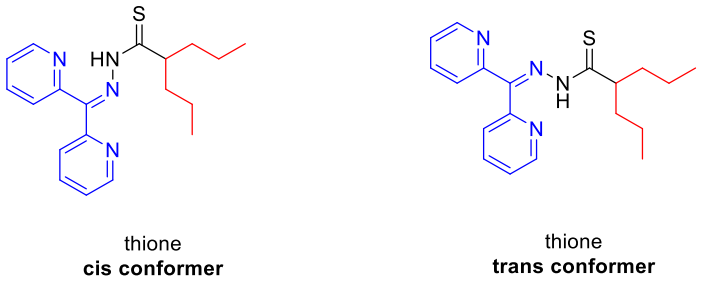

Figure 3.24: ***Cis*** and ***trans*** rotational conformers of the **thione** tautomer of **AZM16**.

The other possibility is the **zwitterionic thiolene**: also this form could explain the very high chemical shift of the NH signals, the absence of the SH band in the IR spectrum of the chloroform solution of **AZM16** and the presence of two isomers in solution (***E*** and ***Z*** with respect to the S-**C=N**-N bond, Figure 3.25). Furthermore, on the basis of the high nucleophilic character of the RS^- group and the high electrophilicity of the iminium carbon, the zwitterionic **thiolene** could be seen also as a precursor form for the generation of the **thiadiazoline** cycle.

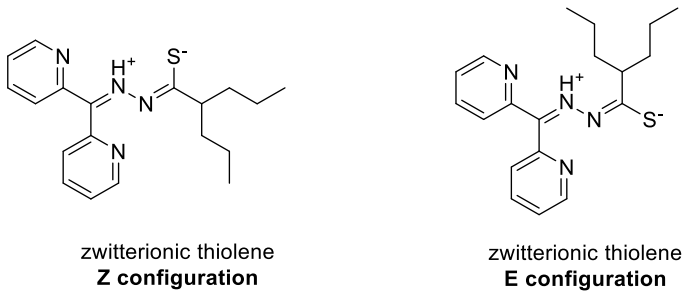

Figure 3.25: ***Z*** and ***E*** configurations of the **zwitterionic thiolene** tautomer of **AZM16**.

Both **thione** and **zwitterionic thiolene** tautomers are therefore plausible forms to explain the detection of the isomers **2** and **3** by NMR.

In the ESI-MS spectrum (positive ions) of **AZM16** it is possible to observe the signals of the $[M + H]^+$ molecular ion and of the $[M + Na]^+$ adduct, together with the peak at m/z = 262 of a cationic fragment formed upon ring closure and loss of a pyridyl ring (Figure 3.26). The latter is analogous to the fragment observed in the ESI-MS spectrum of the other di(2-pyridyl)ketone-thiohydrazone **AZM14b** (Figure A3.61).

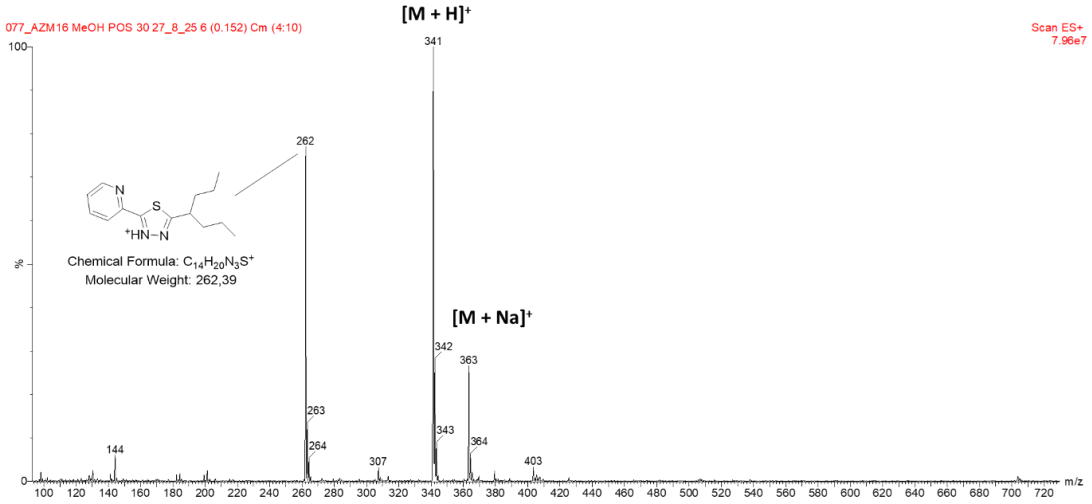

Figure 3.26: ESI-MS spectrum (positive ions) of a solution of **AZM16** in MeOH.

The two novel di(2-pyridyl)ketone-thiohydrazones **AZM14b** and **AZM16** were found to exist in solution as mixtures of multiple isomers in equilibrium, but always with the **thiadiazoline** tautomer as the major species. This result is in accord with the data reported for the **thiohydrazone HPKTBH** synthesized by Kalinowski and coworkers.[224]

As previously mentioned, the characterization of the ortho-vanillin based **thiohydrazones AZM8a** and **AZM12** proved to be even more challenging compared to the ketone-based ligands.

In the case of ligand **AZM8a**, the characterization was further complicated by the fact that it was not possible to isolate the product in the pure form. In fact, the condensation reaction between the **thiohydrazide AZM4c** and ortho-vanillin always led to obtain the ligand **AZM8a** (Scheme 3.12) with traces of an oxidation side-product (3-4%, NMR based), identified as the 1,3,4-thiadiazole reported in Figure 3.27, as suggested also by LC-MS data (Figure A3.37).

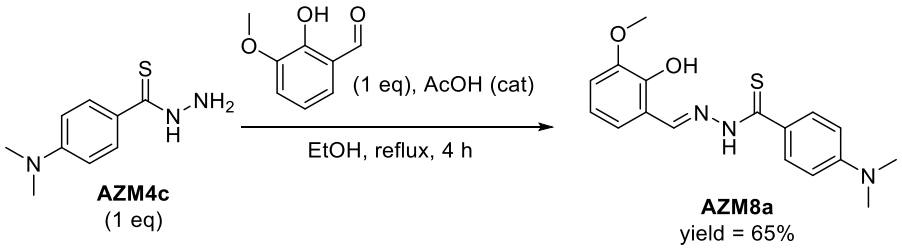

Scheme 3.12: Synthesis of the **thiohydrazone AZM8a**.

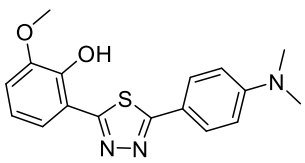

Figure 3.27: Chemical structure of the 1,3,4-thiadiazolic side-product obtained in the synthesis of **AZM8a**.

The synthesis of the ligand was performed in air and at high temperatures, therefore atmospheric dioxygen may be responsible for the oxidation side-reaction.[233] Time constraints did not allow to perform the reaction in inert atmosphere.

Although the product was not pure, some considerations can however be drawn from its ^{1}H NMR spectra (Figures A3.28-35). Excluding the side-product, at least three isomers (Scheme 3.13) were detected in both $CDCl_3$ and DMSO-d_6. Interestingly, the isomeric composition proved to be strongly dependent on the solvent, as summarized in Scheme 3.13.

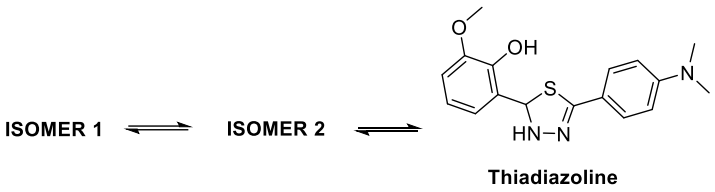

DMSO-d_6	87%	traces	13%
$CDCl_3$	25%	10%	65%

Scheme 3.13: Isomerism of **AZM8a** in DMSO-d_6 and $CDCl_3$.

The identification of the **thiadiazoline** tautomer was possible thanks to the presence of a singlet at 6.49 ppm in the ^{1}H NMR spectrum in DMSO-d_6 (Figure A3.30) and at 6.31 ppm in the ^{1}H NMR spectrum in $CDCl_3$ (Figure A3.34). As already discussed, such peak in the range of 6 – 7 ppm is associated to the methine proton at C2 and it is diagnostic for the aldehyde-based thiadiazolines.

Regarding the other two species, isomers **1** and **2**, several structures are possible. The signals of their NH protons fall between 12.80 and 13.20 ppm in DMSO-d_6 (Figure A3.31) and between 10.00 and 12.00 ppm in $CDCl_3$ (Figure A3.35), thus being more shielded than the NH protons of the minor isomers of compound **AZM16**. This suggests that the isomers **1** and **2** can be both **thione** tautomers. However, the ligand can give rise not only to ***cis*** and ***trans*** conformers, but also to ***E*** and ***Z*** isomers with respect to the imine bond. The species **1** and **2** can therefore be two of the following isomers: ***E cis***, ***E trans***, ***Z cis***, ***Z trans***. Since the intramolecular hydrogen bond involving the phenolic OH and the imine nitrogen favours the ***E*** configuration, we can hypothesize that **1** and **2** are the ***E trans*** and ***E cis*** **thione** isomers (Figure 3.28).

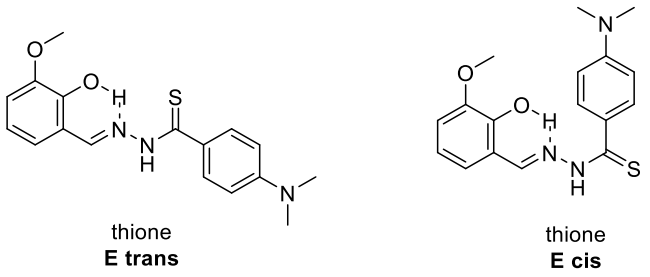

Figure 3.28: Proposed structures for isomers **1** and **2** of **AZM8a**.

Remarkably, while in the polar DMSO-d_6 the hypothesized ***E trans* thione** is the major isomer, in the less polar $CDCl_3$ the **thiadiazoline** is the prevalent species.

The second O,N,S tridentate ligand **AZM12** was obtained by condensation reaction of **AZM11_hydrochloride** with ortho-vanillin, as reported in Scheme 3.14.

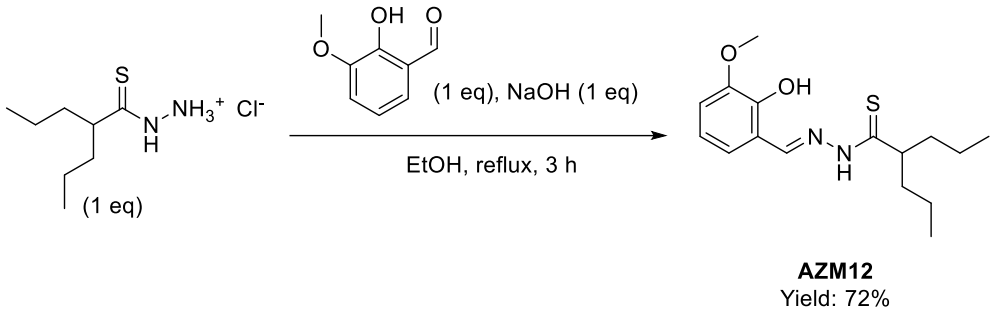

AZM12
Yield: 72%

Scheme 3.14: Synthesis of the **thiohydrazone AZM12**.

Although also in this case the synthesis was performed by refluxing the reaction mixture in air, no oxidation side-products were obtained. Probably the formation of the 1,3,4-thiadiazole is favoured with aromatic **thiohydrazides**, since in that case the oxidation product would be a highly conjugated system.

The novel ligand was characterized by means of FT-IR (Figure A3.43), 1D and 2D NMR spectroscopies (Figures A3.44-51), mass spectrometry (Figure A3.52) and elemental analysis (see the Experimental section).

As it was observed for **AZM8a**, ^{1}H NMR (500 MHz, 298 K) experiments showed that, in both $CDCl_3$ and DMSO-d_6, **AZM12** exists as a mixture of at least three isomers (**1**, **2** and **thiadiazoline**) and the isomers relative concentrations are strongly affected by the solvent (Scheme 3.15). In fact, while the **isomer 1** is prevalent in DMSO-d_6, the **thiadiazoline** is the major species in $CDCl_3$. In Figures 3.29-30 selected ranges of the ^{1}H NMR spectra of **AZM12** in $CDCl_3$ and DMSO-d_6 are reported.

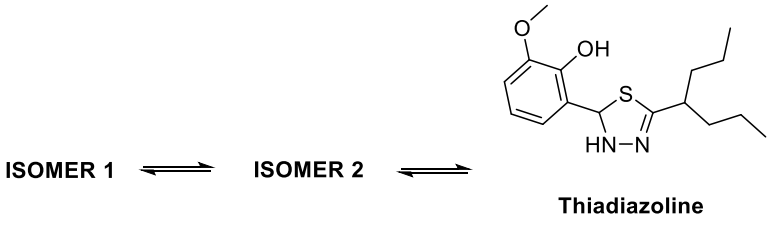

DMSO-d_6	80%	15%	5%
$CDCl_3$	30%	10%	60%

Scheme 3.15: Isomerism of **AZM12** in DMSO-d_6 and $CDCl_3$.

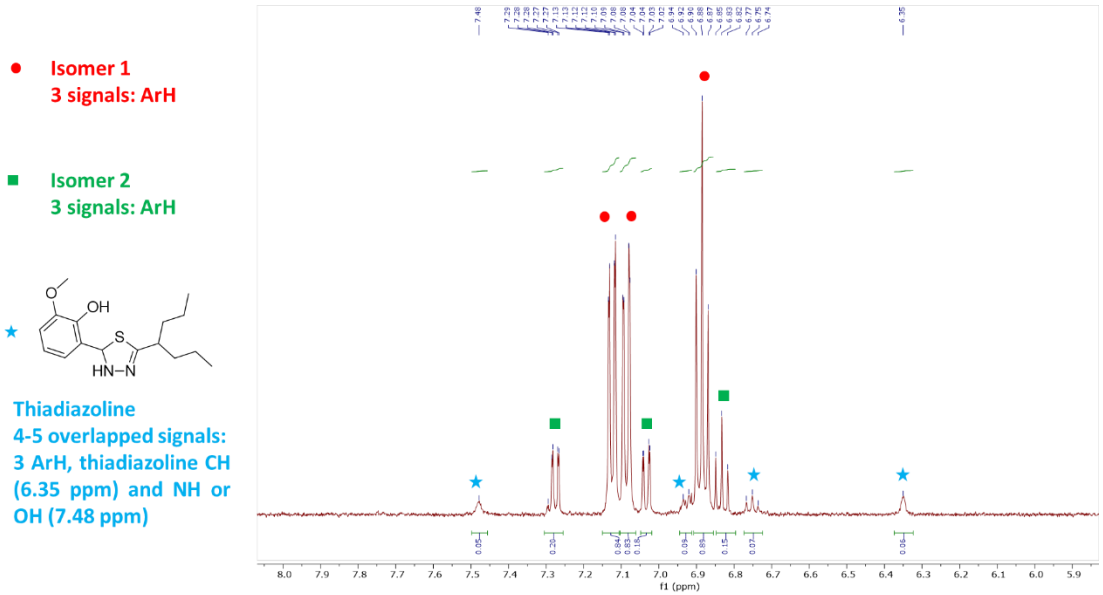

Figure 3.29: Selected range (5.80 – 8.10 ppm) of the ^{1}H NMR (500 MHz, 298 K) spectrum of **AZM12** in DMSO-d_6. The proposed peak attributions are reported for all the isomers.

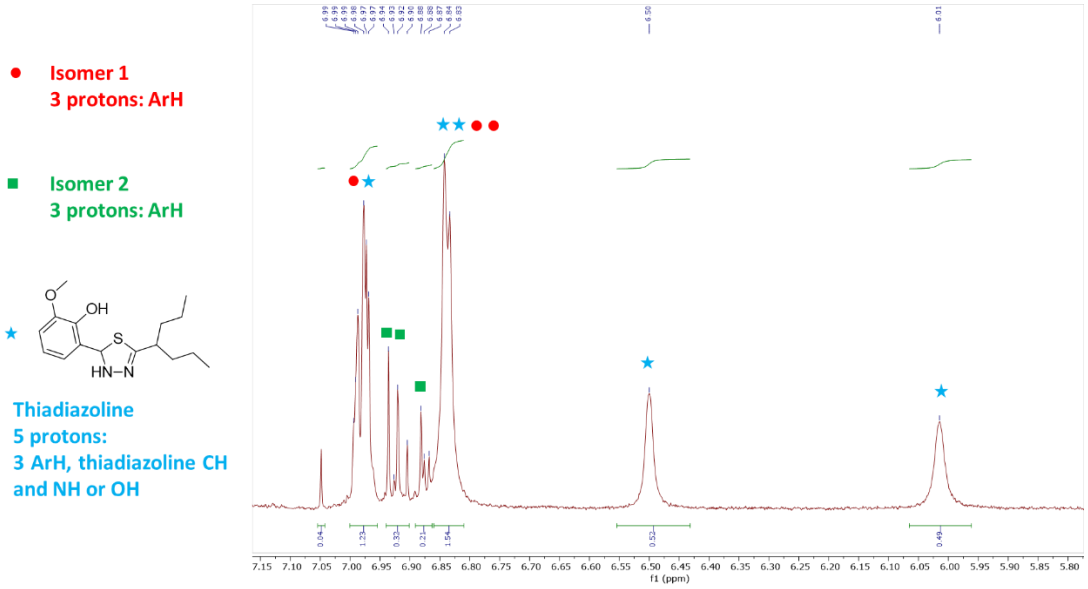

Figure 3.30: Selected range (5.80 – 8.10 ppm) of the ^{1}H NMR (500 MHz, 298 K) spectrum of **AZM12** in $CDCl_3$. The proposed peak attributions are reported for all the isomers.

Regarding the identity of the isomers **1** and **2**, the same considerations drawn for **AZM8a** can be applied also to **AZM12**: we hypothesize that these two species are the ***E trans*** and ***E cis*** **thione** isomers.

To sum up, the four synthesized **thiohydrazones** display a complicated behaviour in solution, due to the formation, among others, of the **thiadiazoline** tautomer. The latter proved to be the prevalent species for the 2-(dipyridyl)ketone-based ligands irrespective of the solvent used to measure their NMR spectra, while for

the ortho-vanillin-based ligands the isomeric composition proved to be strongly affected by the solvent, with the **thiadiazoline** being the major species in the less polar $CDCl_3$. It is interesting to note that, for aldehyde and asymmetrical ketone **thiohydrazones**, ring closure leads to the formation of a stereocenter in C2. The resulting **thiadiazolines** are therefore chiral compounds and they are present in solution as racemic mixtures.

Copper(II) complexes of thiohydrazones

The ligands **AZM12** and **AZM16** were used to synthesize novel copper(II) complexes by reaction with $CuCl_2 \cdot 2\ H_2O$ in ethanol at room temperature. The resulting complexes **AZM15** and **AZM18** were characterized by means of FT-IR spectroscopy, mass spectrometry and elemental analysis.

The complex **AZM15** was obtained in high yields as described in Scheme 3.16.

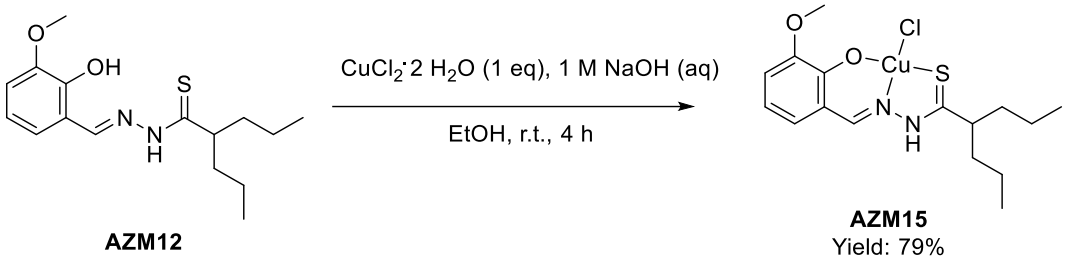

Scheme 3.16: Synthesis of the copper(II) complex **AZM15**.

In Figure 3.31, the comparison of the FT-IR spectra of the ligand **AZM12** and the complex **AZM15** highlights the disappearance of the OH stretching band at 3224 cm^{-1} upon copper(II) coordination. For what concerns the C=N band, a significant increase in intensity is observed by passing from the free ligand to the coordinated one. These findings support the hypothesis of the **thiohydrazone** binding the metal ion as a mono-deprotonated O,N,S tridentate ligand. The formula **[Cu(HL^3)Cl]** is therefore proposed for complex **AZM15**, based also on mass spectrometry (Figure 3.32) and elemental analysis data (see the experimental section).

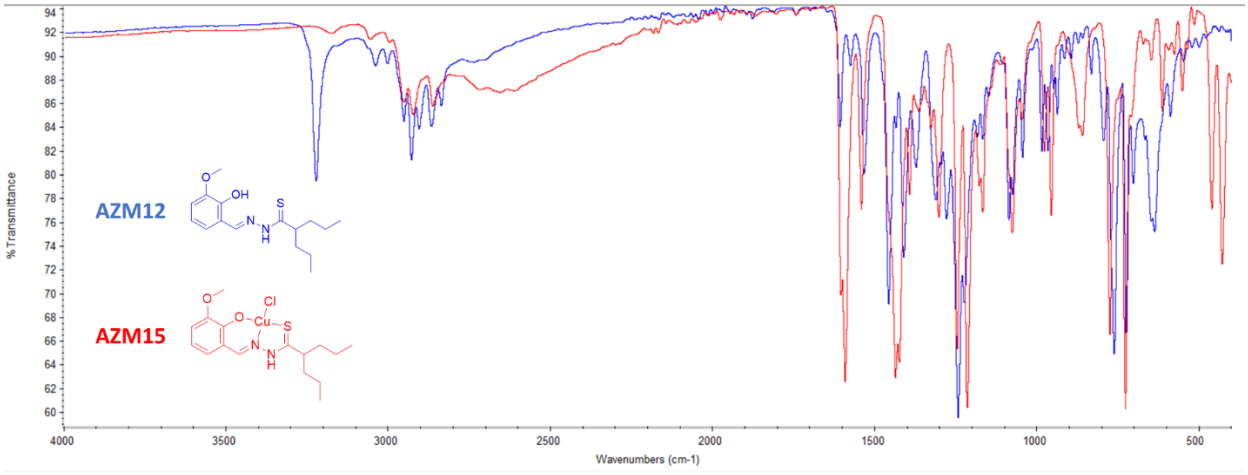

Figure 3.31: FT-IR spectrum of **AZM12** (in blue) and **AZM15** (in red).

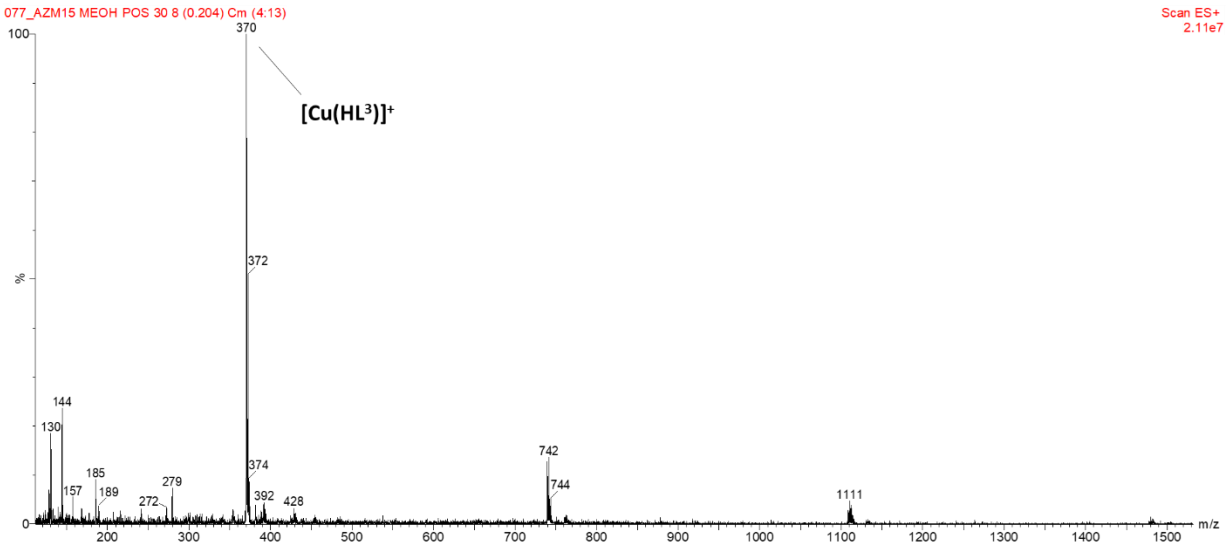

Figure 3.32: ESI-MS spectrum (positive ions) for **AZM15** in methanol.

The complex **AZM18** was synthesized as described in Scheme 3.17.

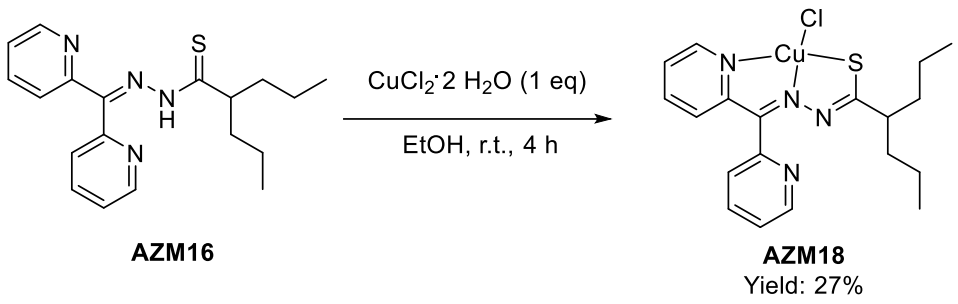

AZM16

AZM18
Yield: 27%

Scheme 3.17: Synthesis of the copper(II) complex **AZM18**.

In the structure of complex **AZM18**, the deprotonated ligand **AZM12** coordinates the copper(II) ion in a N,N,S tridentate fashion. The loss of the NH proton upon coordination is indicated by the disappearance of the band at 3258 cm^{-1} in the spectrum of the complex (Figure 3.33). The proposed formula **[Cu(L^4)Cl]** is supported also by mass spectrometry (Figure A3.75) and elemental analysis data (see the experimental section).

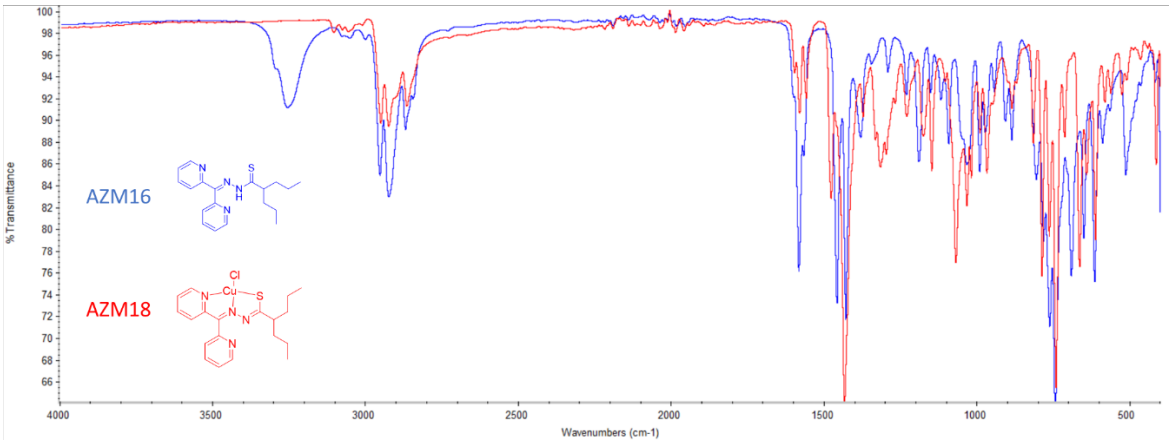

Figure 3.33: FT-IR spectrum of **AZM16** (in blue) and **AZM18** (in red).

The hypothesized structure for both complexes **AZM15** and **AZM18** is square-planar, but such coordination geometry is not the only one possible. Although less common, the alternative structure consists of a binuclear system $Cu_2L_2Cl_2$ with bridging chlorides between the two copper centres, analogous to the system reported by Myannik and coworkers (Figure 3.4b).[235] In this case, the coordination geometry of the metal ions would be trigonal bipyramidal, which is not possible to exclude in absence of single crystal X-ray diffraction analysis.

Conclusions

In spite of the huge literature about the chemical and biological properties of **TSCs** and **NAHs**, the **thiohydrazones** and their metal complexes are much less investigated. Continuing our work on Schiff base-derived ligands and copper(II) complexes with anticancer activity, four novel **thiohydrazones** were synthesized starting from 4-(dimethylamino)benzothiohydrazide (**AZM4c**) and valproic thiohydrazide hydrochloride (**AZM11**) precursors. Being these two precursors not commercially available, they were prepared by means of a three steps protocol. The protocol proved to be highly effective for the synthesis of the alkyl **thiohydrazide AZM11**, while several drawbacks related to formation of oxidation side-products and difficult purification affected the synthesis of the aromatic **thiohydrazide AZM4c**. Furthermore, the attempts performed to prepare another aromatic thiohydrazide, 4-(nitro)benzothiohydrazide, were unsuccessful.

The four synthesized **thiohydrazones** were the ortho-vanillin-derived **AZM8a** and **AZM12** and the 2-(dipyridyl)ketone-based **AZM14b** and **AZM16**. All of them displayed a complicated behaviour in solution, due to **thione-thiadiazoline** tautomerism, ***cis-trans*** conformational isomerism and, in the case of the aldehyde derivatives, also ***E/Z*** configurational isomerism. Interestingly, the **thiadiazoline** tautomer proved to be the prevalent species in solution for the 2-(dipyridyl)ketone-based ligands irrespective of the solvent used to measure their NMR spectra, while for the ortho-vanillin-based ligands the isomeric composition proved to be strongly affected by the solvent, with the **thiadiazoline** being the major species in the less polar $CDCl_3$.

The valproic thiohydrazide-based ligands **AZM12** and **AZM16** were used to prepare two novel copper(II) complexes, **AZM15** and **AZM18** respectively, which were characterized by means of IR spectroscopy, mass spectrometry and elemental analysis. Data suggested that both ligands behave as mono-deprotonated tridentate chelators towards copper(II). Time constraints, the insufficient amount of ligand **AZM14b** and the failure in isolating pure ligand **AZM8a** did not allow to prepare the copper(II) complexes of these two chelators.

Future investigation shall focus on further optimization of the synthesis of aromatic **thiohydrazides** and on the preparation of a large panel of these precursors, as well as on the assessment of their anticancer properties. Also, a thorough study of the conditions affecting the isomeric composition of the resulting **thiodrazone** ligands in different solvents would be helpful to deepen the chemistry of these fascinating systems. Indeed, although they are quite small molecules, they display an unexpectedly complicated behaviour in solution.

Experimental section

Materials and methods

Commercial reagents were purchased from Sigma-Aldrich. ^{1}H, ^{13}C and 2D NMR spectra were recorded at 25°C on a Bruker Advance 400 MHz FT spectrometer or on a Bruker Advance 500 MHz FT spectrometer. The ATR-IR spectra were recorded by means of a Perkin Elmer spectrophotometer by using a diamond crystal plate in the range of 4000-400 cm^{-1}. Elemental analyses were performed by using a Thermo Fisher FlashSmart CHNS/O analyser with gas-chromatographic separation. Electrospray ionization mass spectral analyses (ESI-MS) were performed with an ESI time-of-flight Micromass 4LCZ spectrometer and the samples were dissolved in methanol. Mass spectral characterization of crude compounds was performed with a Waters LCT Premier XE Spectrometer and the samples were dissolved in DCM or acetonitrile/DMSO mixtures.

Synthesis

Tert-butyl 2-(4-(dimethylamino)benzoyl)hydrazine-1-carboxylate (AZM1b)

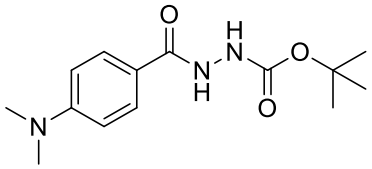

DMF was purged with N_2 prior to use in order to remove dimethylamine. The reaction was carried out under N_2. HBTU (3.595 g, 9.480 mmol, 1.0 eq) and 4-(dimethylamino)benzoic acid (1.566 g, 9.480 mmol, 1.0 eq) were added to DMF (36 mL) and the mixture was left stirring for 2 minutes at 0 °C. DIPEA (3.5 mL, 19.908 mmol, 2.1 eq) was added and the pale-yellow mixture was stirred for 15 minutes at 0 °C, then for 15 minutes at r.t.. Tert-butylcarbazate (1.315 g, 9.954 mmol, 1.05 eq) was added and the mixture was left stirring at 0 °C for 15 minutes, then for 5 hours at r.t.. The mixture was concentrated and the resulting beige oil was diluted with DCM, washed two times with sat. aq. $NaHCO_3$, two times with brine and six times with water, dried over Na_2SO_4 and concentrated *in vacuo*. The desired Boc-hydrazide was obtained as an off-white solid (2.276 g, yield = 86%).

IR (cm^{-1}): ν = 3301 (m) (NH), 2987 (w) (CH sp^2), 2904 (w) (CH sp^3), 1696 (m-s) (tBuO-C=O), 1632 (s) (Ar-C=O), 1610 (s) (C=C). (Figure A3.1)

^{1}H NMR (400 MHz, Chloroform-*d*, 298 K): δ(ppm) = 7.74 (s, br, 1H, NH), 7.71 (d, *J* = 9.0 Hz, 2H, ArH), 6.74 - 6.60 (m, 3H, NH and ArH), 3.02 (s, 6H, N-$(CH_3)_2$), 1.49 (s, 9H, C-$(CH_3)_3$). (Figure A3.2)

^{13}C NMR (126 MHz, Chloroform-*d*, 298 K): δ(ppm) = 167.07, 156.15, 153.02, 129.01 (CH), 118.48, 111.14 (CH), 81.74(CMe_3), 40.18(NMe_2), 28.32 (CMe_3). (Figure A3.3)

ESI-MS (positive ions): m/z (%): 148 (80) $[M - C_5H_{11}N_2O_2]^+$, 224 (35) $[M - C_4H_7]^+$, 280 (90) $[M + H]^+$, 302 (90) $[M + Na]^+$, 560 (25) $[2M + H]^+$, 582 (100) $[2M + Na]^+$. (Figure A3.5)

Tert-butyl 2-(4-(dimethylamino)phenylcarbonothioyl)hydrazine-1-carboxylate (AZM2c)

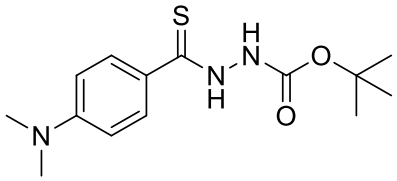

In an oven dried flask were introduced 3 Å molecular sieves, the Boc-hydrazide (513 mg, 1.836 mmol, 1.0 eq) and the Lawesson's reagent (1166 mg, 2.883 mmol, 1.6 eq). Anhydrous THF (22 mL) was added under N_2 and the mixture was stirred at r.t. for 20 minutes. The resulting yellow mixture was left stirring at 45 °C under N_2 overnight. After removal of molecular sieves, the mixture was concentrated and sat. $NaHCO_3$ aqueous solution (ca. 150 mL) was added to the resulting yellow slurry. The suspension was extracted twice with EtOAc and the combined organic phases were washed twice with sat. $NaHCO_3$ aqueous solution and twice with brine, then dried over Na_2SO_4, filtered and concentrated. The crude was dissolved in the minimum volume of DCM, silica was added and then all was dried. Column chromatography (EtPet/DCM 1/4, then DCM, then DCM/EtOAc 1/1) with dry load of the crude allowed to obtain the desired Boc-thiohydrazide as a yellow solid (348 mg; yield = 64%).

IR (cm^{-1}): ν = 3303 (m) and 3236 (m) (NH), 2984 (w) (CH sp^2), 2904 (w) (CH sp^3), 1699 (s) (tBuO-C=O), 1610 (s) (C=C). (Figure A3.6)

^{1}H NMR (500 MHz, DMSO-d_6, 298 K): δ(ppm) = 11.25 (s, 1H, NH), 9.21 (s, br, 1H, NH), 7.79 (d, *J* = 8.3 Hz, 2H, ArH), 6.68 (d, *J* = 9.1 Hz, 2H, ArH), 2.99 (s, 6H, N-$(CH_3)_2$), 1.42 (s, 9H, C-$(CH_3)_3$).

^{13}C NMR (126 MHz, DMSO-d_6, 298 K): δ(ppm) = 154.54, 152.42, 129.33 (CH), 110.41 (CH), 79.47(CMe_3), 28.07(CMe_3). (Figure A3.7)

ESI-MS (positive ions): m/z (%): 240 (100) $[M - C_4H_7]^+$, 296 (65) $[M + H]^+$, 318 (60) $[M + Na]^+$. (Figure A3.8)

Tert-butyl-5-(4-(dimethylamino)phenyl)-2-(4-methoxyphenyl)-3H-1,3,4,2-thiadiazaphosphole-3-carboxylate 2-sulfide (side-product of the synthesis of AZM2c)

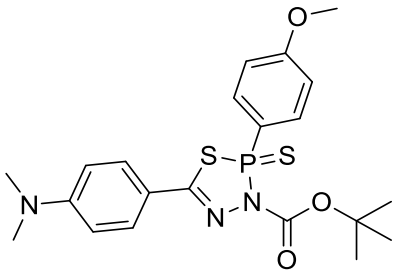

IR (cm^{-1}): ν = 3090 - 2987 (w) (CH sp^2), 2911 (w) (CH sp^3), 1735 (m-s) (tBuO-C=O), 1604 (m-s) and 1590 (m-s) (C=N). (Figure A3.9)

^{1}H NMR (400 MHz, Chloroform-*d*, 298 K): δ(ppm) = 8.06 – 7.95 (m, 2H, ArH), 7.66 (d, *J* = 8.8 Hz, 2H, ArH), 7.00 (dd, *J* = 8.8, 3.5 Hz, 2H, ArH), 6.67 (d, *J* = 9.0 Hz, 2H, ArH), 3.89 (s, 3H, O-CH_3), 3.03 (s, 6H, N-$(CH_3)_2$), 1.30 (s, 9H, C-$(CH_3)_3$). (Figure A3.10)

ESI-MS (positive ions): m/z (%): 496 (100) $[M + MeOH + H]^+$. (Figure A3.11)

Elem. anal. calcd (%) for $C_{21}H_{26}N_3O_3PS_2 \cdot 0.5\ H_2O$: C 53.37, H 5.76, N 8.89, S 13.57; found: C 53.62, H 5.75, N 8.41, S 13.55.

Tert-butyl 2-(4-nitrobenzoyl)hydrazine-1-carboxylate (AZM3)

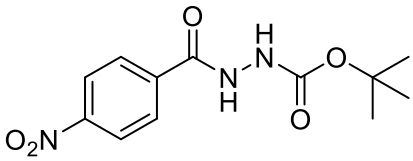

DMF was purged with N_2 prior to use in order to remove dimethylamine. The reaction was carried under N_2. HBTU (3.826 g, 10.088 mmol, 1.0 eq) and 4-(nitro)benzoic acid (1.686 g, 10.088 mmol, 1.0 eq) were added to DMF (35 mL) and the mixture was left stirring for 2 minutes at 0 °C. DIPEA (3.69 mL, 21.185 mmol, 2.1 eq) was added and the mixture was stirred for 15 minutes at 0 °C, then for 15 minutes at r.t.. t-butylcarbazate (1.400 g, 10.593 mmol, 1.05 eq) was added and the resulting dark red solution was left stirring at 0 °C for 15 minutes, then at r.t. overnight. The mixture was concentrated and the crude was diluted with EtOAc (ca. 100 mL), washed two times with sat. aq. $NaHCO_3$, two times with brine and eight times with water, dried over Na_2SO_4 and concentrated *in vacuo*. The desired Boc-hydrazide was obtained as a yellow-beige solid (2.276 g, yield = 80%).

IR (cm^{-1}): ν = 3396 (m) and 3318 (m) and 3230 (m) (NH), 2983 (w-m) (CH sp^2), 1716 (m) (tBuO-C=O), 1672 (s) (Ar-C=O), 1599, 1521 (s) (C=C). (Figure A3.12)

^{1}H NMR (500 MHz, Chloroform-*d*, 298 K): δ(ppm) = 8.45 (s, br, 1H, NH), 8.27 (d, *J* = 8.6 Hz, 2H, ArH), 7.97 (d, *J* = 8.6 Hz, 2H, ArH), 6.80 (s, br, 1H, NH), 1.51 (s, 9H, C-$(CH_3)_3$). (Figure A3.13)

^{13}C NMR (126 MHz, Chloroform-*d*, 298 K): δ(ppm) = 164.91, 155.76, 150.18, 137.37, 128.69 (CH), 124.01 (CH), 82.84 (CMe_3), 28.27 (CMe_3). (Figure A3.14)

4-(Dimethylamino)benzothiohydrazide (AZM4c)

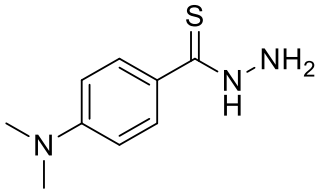

The Boc-thiohydrazide **AZM2c** (341 mg, 1.154 mmol) was dissolved in 20 mL of 37% HCl (aq) at 0 °C and the resulting yellow-green solution was left stirring at 0 °C for ten minutes, then at r.t. overnight with open flask. 4 M NaOH (aq) was added dropwise to the mixture at 0 °C till pH ca. 8 – 9 (1M NaOH was used when pH was near to the desired value). The resulting green suspension was left at 4 °C for three hours, then it was filtered, washed with water and dried *in vacuo*. A greenish granular solid was obtained (115 mg, yield = 52%).

IR (cm^{-1}): ν = 3280 – 3100 (m) (NH), 2902 (w-m) (CH), 1597 (s) (C=C). (Figure A3.15)

^{1}H NMR (500 MHz, DMSO-d_6, 298 K): δ(ppm) = 11.57 (s, br, 1H, NH), 7.70 (d, *J* = 8.9 Hz, 2H, ArH), 6.67 (d, *J* = 9.0 Hz, 2H, ArH), 6.02 (s, br, 2H, NH_2), 2.96 (s, 6H, $N(CH_3)_2$).

^{13}C NMR (126 MHz, DMSO-d_6): δ(ppm) = 183.43 (C=S), 151.72(C-C=S), 128.53(CH), 125.22 (C-NMe_2), 110.65(CH), 39.75 ($N(CH_3)_2$). (Figure A3.16)

LC-MS (positive ions): m/z (%): 164 (100) $[M - N_2H_3]^+$. (Figure A3.17)

The product was contaminated by traces (2% in mass, NMR based) of 4,4'-(1,3,4-thiadiazole-2,5-diyl)bis(N,N-dimethylaniline):

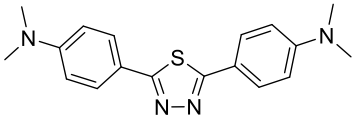

^{1}H NMR (500 MHz, DMSO-d_6, 298 K): δ(ppm) = 7.76 (d, *J* = 8.9 Hz, 4H, ArH), 6.81 (d, *J* = 8.9 Hz, 4H, ArH), 3.01 (s, 12H, $N(CH_3)_2$).

LC-MS (positive ions): m/z (%): 325 (100) $[M + H]^+$. (Figure A3.18)

4-(Dimethylamino)benzothiohydrazide bis-hydrochloride (AZM4_hydrochloride)

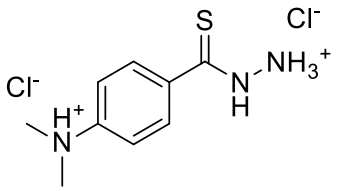

HCl in 1,4-dioxane (4 M, 10 eq) was added at 0 °C under N_2 to solid Boc-thiohydrazide **AZM2c** (199 mg, 0.674 mmol, 1 eq). The resulting orange suspension was left stirring under N_2 at r.t. for 7 hours. Et_2O (12 mL) was added and the resulting yellow suspension was left at 4 °C overnight. The precipitate was filtrated, washed with Et_2O and dried *in vacuo*. A green granular solid was obtained (123 mg, yield = 68%).

^{1}H NMR (500 MHz, DMSO-d_6, 298 K): δ(ppm) = 7.84 (d, *J* = 9.1 Hz, 2H, ArH), 6.76 (d, *J* = 9.0 Hz, 2H, ArH), 3.01 (s, 6H, $N(CH_3)_2$). (Figure A3.19)

^{1}H NMR (500 MHz, Deuterium Oxide, 298 K) δ 7.90 (d, *J* = 8.8 Hz, 2H, ArH), 7.68 (d, *J* = 8.8 Hz, 2H, ArH), 3.32 (s, 6H, $N(CH_3)_2$). (Figure A3.20)

The product was contaminated by traces (2% in mass, NMR based) of 4,4'-(1,3,4-thiadiazole-2,5-diyl)bis(N,N-dimethylaniline), probably in its bis-hydrochloride form.

Tert-butyl 2-(4-(nitro)phenylcarbonothioyl)hydrazine-1-carboxylate (AZM5a)

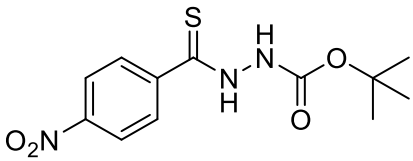

In an oven dried flask were introduced 3 Å molecular sieves, the Boc-hydrazide **AZM3** (505 mg, 1.795 mmol, 1.0 eq) and the Lawesson's reagent (1552 mg, 3.837 mmol, 2.1 eq). Anhydrous THF (22 mL) was added under N_2 and the orange mixture was stirred at r.t. for 20 minutes. The resulting red suspension was left stirring at 45°C under N_2 overnight (after few minutes it turned into a red solution). After removal of molecular sieves, the mixture was concentrated and sat. $NaHCO_3$ aqueous solution (ca. 150 mL) was added to the crude. The

suspension was extracted twice with EtOAc and the combined organic phases were washed twice with 1M HCl (aq) and twice with brine, then dried over Na_2SO_4, filtered and concentrated. The crude was dissolved in the minimum volume of EtOAc, silica was added and then all was dried. Column chromatography (EtOAc/EtPet 4/6) with dry load of the crude allowed to obtain the Boc-thiohydrazide as a beige-orange solid (81 mg, yield = 15%).

^{1}H NMR (500 MHz, DMSO-d_6, 298 K): δ(ppm) = 10.01 (s, 1H, NH), 8.26 (d, *J* = 8.9 Hz, 2H, ArH), 7.78 (d, *J* = 8.8 Hz, 2H, ArH), 1.43 (s, 9H, 3 CH_3). (Figure A3.21)

Tert-butyl 2-(2-propylpentanoyl)hydrazine-1-carboxylate (AZM6)

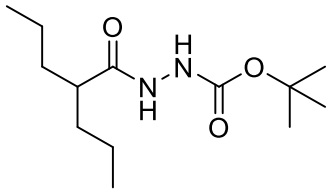

DMF was purged with N_2 prior to use in order to remove dimethylamine. The reaction was carried under N_2. HBTU (1197 mg, 3.155 mmol, 1.0 eq) and valproic acid (0.5 mL, 3.155 mmol, 1.0 eq) were added to DMF (10 mL) and the mixture was left stirring for 2 minutes at 0 °C. DIPEA (2.1 eq) was added and the mixture was stirred for 15 minutes at 0 °C, then for 15 minutes at r.t.. Then, t-butylcarbazate (1.05 eq) was added and the resulting colourless solution was left stirring at 0 °C for 15 minutes, then for 5 hours at r.t.. The mixture was concentrated and the resulting oil was diluted with DCM, washed two times with sat. aq. $NaHCO_3$, two times with brine and eight times with water, dried over Na_2SO_4, filtered and concentrated *in vacuo*. The resulting pale-yellow oil was triturated with EtPet until a white solid was obtained. The solid was dried *in vacuo* (628 mg, yield = 77%).

IR (cm^{-1}): ν = 3246 (m-s) (NH), 3000 – 2800 (m-s) (CH), 1714 (s) (tBuO-C=O), 1673 (m-s) and 1640 (s) (C-C=O). (Figure A3.22)

^{1}H NMR (500 MHz, DMSO-d_6, 298 K): δ (ppm) = 9.52 (s, br, 1H, NH*, minor isomer*), 9.45 (s, 1H, NH, *major isomer*) 8.65 (s, 1H, NH, *major isomer*), 8.20 (s, br, 1H, NH*, minor isomer*), 2.17 – 2.08 (m, 1H, CH), 1.49 – 1.32 (m, 11H, tBu + CH_2), 1.24 (m, 6H, 3 CH_2), 0.84 (t, *J* = 7.0 Hz, 6H, 2 CH_3). (Figure A3.23)

^{13}C NMR (126 MHz, DMSO-d_6): δ (ppm) = 174.52, 155.26, 78.77 (CMe_3), 43.01(CH), 34.70, 28.09, 19.98, 13.99. (Figure A3.24)

ESI-MS (positive ions): m/z (%): 127 (95) $[M - C_5H_{11}N_2O_2]^+$, 181 (100) $[M – C_5H_8O_2 + Na]^+$, 203 (95) $[M – C_4H_7]^+$, 281 (95) $[M + Na]^+$. (Figure A3.26)

4-(Dimethylamino)-N'-(2-hydroxy-3-methoxybenzylidene)benzothiohydrazide (AZM8, H_2L^1)

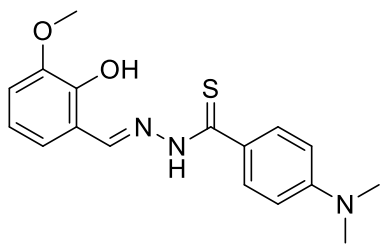

Solid thiohydrazide **AZM4c** (68 mg, 0.348 mmol, 1.0 eq) was added to a solution of ortho-vanillin (53 mg, 0.348 mmol, 1.0 eq) in EtOH (13 mL), followed by one drop of AcOH. The resulting orange-green suspension was left stirring under reflux for 4 hours. An orange-green solution with a crystalline precipitate was obtained. The mixture was concentrated to half volume and then left at 4 °C overnight. The crystalline product was filtered, washed with cold EtOH and dried *in vacuo*. A beige crystalline solid was obtained (75 mg, yield = 65%).

IR (cm^{-1}): ν = 3317 (w) (OH, NH), 3000 - 2780 (CH), 1600 (C=N), 1516 (C=C). (Figure A3.27)

^{1}H NMR (500 MHz, DMSO-d_6, 298 K): complex pattern of signals (Figures A3.28-31).

^{1}H NMR (500 MHz, Chloroform-*d*, 298 K): complex pattern of signals (Figures A3.32-35).

^{13}C NMR (126 MHz, DMSO-d_6, 298 K): δ(ppm) = 191.25 (C=S), 152.70, 152.05, 148.12, 147.61, 129.75, 128.56, 127.49, 125.32, 122.35, 118.95, 118.01, 114.59, 111.68, 110.53, 55.87 (OCH_3). (Figure A3.36)

The product was contaminated by 2-(5-(4-(dimethylamino)phenyl)-1,3,4-thiadiazol-2-yl)-6-methoxyphenol (3-4% in mass, NMR based):

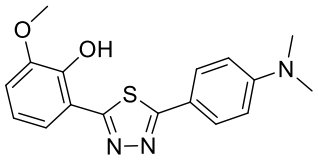

LC-MS (positive ions): m/z (%): 328 (100) $[M + H]^+$. (Figure A3.37)

Tert-butyl 2-(2-propylpentanethioyl)hydrazine-1-carboxylate (AZM10)

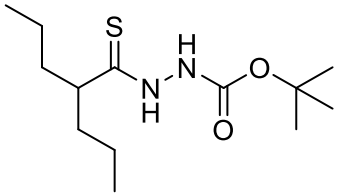

In an oven dried flask were introduced 3 Å molecular sieves, the Boc-hydrazide **AZM6** (460 mg, 1.780 mmol, 1.0 eq) and the Lawesson's reagent (853 mg, 2.109 mmol, 1.2 eq). Anhydrous THF (20 mL) was added under N_2 and the mixture was stirred at r.t. for 20 minutes. The resulting pale-yellow suspension was left stirring at 45°C under N_2 overnight (after two hours it turned into a colourless solution). After removal of molecular sieves, the mixture was concentrated and sat. $NaHCO_3$ aqueous solution (ca. 125 mL) was added to the resulting oil. The suspension was extracted twice with EtOAc and the combined organic phases were washed twice with sat. $NaHCO_3$ aqueous solution and twice with brine, then dried over Na_2SO_4, filtered and concentrated. The crude oil was dissolved in the minimum volume of EtOAc, silica was added and then all was dried. Column chromatography (EtPet/EtOAc 4/1) with dry load of the crude allowed to obtain the Boc-thiohydrazide as a pale greenish oil (363 mg, yield = 74%).

^{1}H NMR (500 MHz, Chloroform-*d*, 298 K): δ(ppm) = 9.25 (s, br, 1H, NH), 8.88 (s, br, 1H), 2.37 (tt, *J* = 9.4, 4.9 Hz, 1H, CH), 1.76 (dddd, *J* = 13.4, 10.3, 9.2, 5.2 Hz, 2H, CH_2), 1.56 – 1.50 (m, 11H, CH_2, $C(CH_3)_3$), 1.32 – 1.18 (m, 4H, CH_2), 0.89 (t, *J* = 7.3 Hz, 6H, CH_3). (Figure A3.38)

2-Propylpentanethiohydrazide hydrochloride (AZM11)

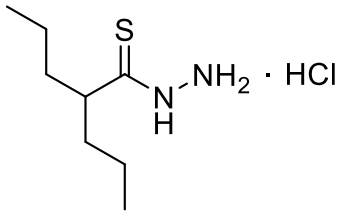

4 M HCl in 1,4-dioxane (3.1 mL, 12.353 mmol, 10 eq) was added at 0 °C under N_2 to the oily Boc-thiohydrazide **AZM10** (339 mg, 1.235 mmol, 1 eq) and the resulting solution was left stirring at r.t. under N_2. After few minutes, it turned into a milky suspension, which was left stirring overnight. Et_2O (12 mL) was added and the mixture was left at 4 °C for two hours. The resulting white precipitate was filtered, washed with Et_2O and dried *in vacuo*. A white crystalline solid was obtained (171 mg, yield = 66%).

IR (cm^{-1}): ν = 3129 (m) and 3067 (m) (NH), 2960 - 2600 (s) (CH). (Figure A3.39)

^{1}H NMR (500 MHz, DMSO-d_6, 298 K): δ (ppm) = 12.19 (s, br, 1H, NH), 7.00 – 4.00 (s, br, ovlp, 3H, NH_3^+), 2.62 (m, 1H, CH), 1.67 – 1.56 (m, 2H, CH_2), 1.41 – 1.30 (m, 2H, CH_2), 1.20 – 1.07 (m, 4H, CH_2), 0.82 (t, *J* = 7.3 Hz, 6H, CH_3).

^{13}C NMR (126 MHz, DMSO-d_6, 298 K): δ(ppm) = 49.28 (CH), 37.29 (CH_2), 19.81 (CH_2), 13.86 (CH_3). (Figure A3.40)

ESI-MS (positive ions): m/z (%): 215 (100) $[M + H_2O + Na]^+$. (Figure A3.42)

Elem. anal. calcd (%) for $C_8H_{19}ClN_2S$: C 45.59, H 9.09, N 13.29, S 15.21; found: C 45.14, H 9.02, N 13.05, S 15.37.

N'-(2-hydroxy-3-methoxybenzylidene)-2-propylpentanethiohydrazide (AZM12, H_2L^3)

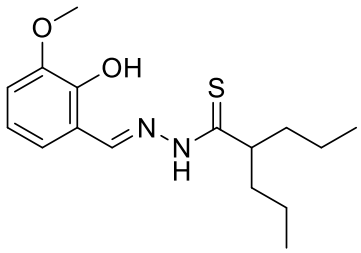

The thiohydrazide salt **AZM11** (63.6 mg, 0.302 mmol, 1 eq) was solubilized in absolute EtOH (7 mL) at r.t.. 1M NaOH (aq) (302 µL, 0.302 mmol, 1 eq) was added and a white precipitate started to form. Temperature was raised to 40 °C and a solution of orthovanillin (45.6 mg, 0.302 mmol, 1 eq) in EtOH (3 mL) was added to the suspension. The resulting yellow-green mixture was left stirring under reflux for 3 hours (TLC in EtOAc/EtPet 1/1 indicated total consumption of the aldehyde). A yellow-green solution was obtained, which was reduced to half volume and then left at 4 °C overnight. A small amount (2 mg) of white precipitate was obtained: it was probably unreacted thiohydrazide. It was removed by filtration and the mother liquors were

concentrated to a small volume, then water was added: immediately, a yellow-green precipitate formed. The solid was filtrated, washed with water and dried *in vacuo*. A yellow solid was isolated (67 mg, yield = 72%).

IR (cm^{-1}): ν = 3224 (s) (OH, NH), 3040 - 2838 (m) (CH), 1608 (m-s) (C=N), 1577 (w) and 1535 (s) (C=C). (Figure A3.43)

^{1}H NMR (500 MHz, DMSO-d_6, 298 K): complex pattern of signals (Figures A3.44-46).

^{1}H NMR (500 MHz, Chloroform-*d*, 298 K): complex pattern of signals (Figures A3.47-49).

^{13}C NMR (126 MHz, DMSO-d_6, 298 K): δ(ppm) = 204.31 (C=S), 152.79, 148.09, 147.69, 144.54, 122.20, 120.05, 119.41, 119.04, 117.81, 117.55, 114.88, 113.68, 55.90, 50.73, 37.90, 37.62, 19.97, 19.88, 13.94. (Figure A3.50)

ESI-MS (positive ions): m/z (%): 150 (50) $[M - C_8H_{16}NS]^+$, 309 (100) $[M + H]^+$, 331 (70) $[M + Na]^+$. (Figure A3.52)

Elem. anal. calcd (%) for $C_{16}H_{24}N_2O_2S$: C 62.31, H 7.84, N 9.08, S 10.39; found: C 62.52, H 7.90, N 8.94, S 10.39.

(Di(pyridin-2-yl)methylene)-4-(dimethylamino)benzothiohydrazide (AZM14b, HL^2)

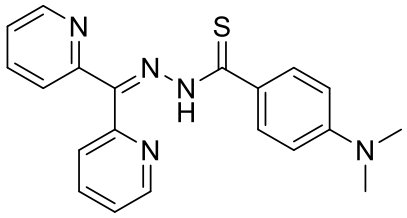

The thiohydrazide salt **AZM4_hydrochloride** (60 mg, 0.224 mmol, 1 eq) was solubilized in absolute EtOH (6 mL) and 4 M NaOH (aq) (112.2 µL, 0.448 mmol, 2 eq) was added: a suspension formed, which was stirred at 50 °C for 20 minutes. Then, a solution of di-2-pyridylketone (41.5 mg, 0.224 mmol, 1 eq) was added and the resulting mixture was stirred under reflux. After 10 minutes, an orange solution was obtained. The mixture was refluxed for 4 hours and 30 minutes, then it was left to cool at r.t., concentrated to dryness and recrystallized from EtOH. The mixture was left at – 20 °C overnight, then it was filtered, washed with cold EtOH and dried *in vacuo*. A grey-brown solid was obtained (36 mg, yield = 45%).

IR (cm^{-1}): ν = 3286 (m-w) (NH), 3090 - 2770 (CH), 1612 (C=N), 1582, 1524 (C=C). (Figure A3.53)

^{1}H NMR (500 MHz, DMSO-d_6, 298 K): (Figure A3.54)

Thiadiazoline: 91 % Thione: 9 %

Thiadiazoline: δ(ppm) = 8.80 (s, 1H, NH), 8.47 (dt, J = 4.7, 1.4 Hz, 2H, ArH), 7.86 – 7.79 (m, 4H, ArH), 7.42 – 7.35 (m, 2H, ArH), 7.28 (td, J = 4.8, 3.8 Hz, 2H, ArH), 6.74 – 6.67 (m, 2H, ArH), 2.93 (s, 6H, NMe_2).

Thione: δ(ppm) = 8.94 (s, br, 1H, NH), 8.64 (s, br, 1H, ArH), 8.08 – 7.87 (m, br, 6H, ArH), 7.67 – 7.61 (m, br, 2H, ArH), 7.53 (s, br, 1H, ArH), 6.83 – 6.80 (m, br, 1H, ArH), 3.04 (s, br, 6H, NMe_2).

^{1}H NMR (500 MHz, Chloroform-*d*, 298 K):

Thiadiazoline: 83 % Thione: 17 %

Thiadiazoline: δ(ppm) = 8.49 (ddd, J = 4.8, 1.8, 0.9 Hz, 2H, ArH), 8.29 (s, 1H, NH), 7.99 (dt, J = 8.0, 1.1 Hz, 2H, ArH), 7.70 (td, J = 7.8, 1.8 Hz, 2H, ArH), 7.57 – 7.51 (m, 2H, ArH), 7.15 (ddd, J = 7.5, 4.8, 1.1 Hz, 2H, ArH), 6.67 – 6.61 (m, 2H, ArH), 2.97 (s, 6H, NMe_2).

Thione: δ(ppm) = 8.80 (d, J = 4.8 Hz, 1H, ArH), 8.61 (d, J = 4.8 Hz, 1H, ArH), 8.32 (m, 1H, NH), 8.05 (d, J = 8.6 Hz, 2H, ArH), 7.90 – 7.84 (m, 3H, ArH), 7.76 (d, J = 8.3 Hz, 1H, ArH), 7.41 (ddd, J = 7.6, 4.9, 1.2 Hz, 1H, ArH), 7.37 – 7.33 (m, 1H, ArH), 6.71 (d, J = 8.7 Hz, 2H, ArH), 3.08 (s, 6H, NMe_2).

^{13}C NMR (126 MHz, DMSO-d_6, 298 K): δ(ppm) = 161.60, 148.47, 137.04, 127.37, 122.75, 120.98, 111.70. (Figure A3.57)

^{13}C NMR (126 MHz, Chloroform-*d*, 298 K): δ(ppm) = 162.06, 159.99, 148.74, 137.00, 128.43, 122.67, 121.73, 111.73, 89.32 (S-C-NH of thiadiazoline), 40.36 (NMe_2 of thiadiazoline), 40.30 (NMe_2 of thione). (Figure A3.58)

ESI-MS (positive ions): m/z (%): 164 (60) $[M - C_{11}H_9N_4]^+$, 283 (25) $[M - C_5H_4N]^+$, 332 (50) $[M - HN_2]^+$, 362 (100) $[M + H]^+$, 384 (40) $[M + Na]^+$. (Figures A3.61-62)

Elem. anal. calcd (%) for $C_{20}H_{19}N_5S \cdot 1.5\ H_2O$: C 61.83, H 5.71, N 18.03, S 8.25; found: C 61.39, H 4.94, N 17.35, S 8.46.

[Cu(HL^3)Cl] (AZM15)

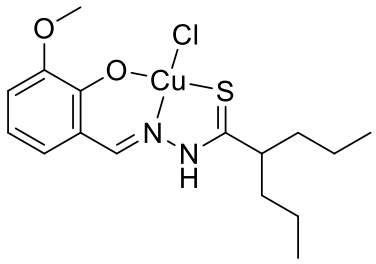

The ligand **AZM12** (41 mg, 0.133 mmol, 1 eq) was solubilized in EtOH (6 mL) and 1 M NaOH (aq) was added to the yellow solution till pH ca. 7 – 8. The solution turned orange and $CuCl_2 \cdot 2\ H_2O$ (22.4 mg, 0.133 mmol, 1 eq) in EtOH (5 mL) was added dropwise. Immediately, a dark green suspension formed (pH ca. 3), which was left stirring at r.t. for 4 hours, then concentrated to half volume and left at -20 °C overnight. The resulting dark green precipitate was filtered, washed with cold EtOH and cold Et_2O and dried *in vacuo*. A dark green solid was obtained (43 mg, yield = 79%).

IR (cm^{-1}): ν = 3173 (w) and 3061 (w) (NH), 3000 - 2400 (m) (CH), 1606 (s) (C=N), 1593 (s), 1543 (m-s) (C=C).

ESI-MS (positive ions): m/z (%): 370 (100) $[Cu(HL^3)]^+$.

Elem. anal. calcd (%) for $C_{16}H_{23}ClCuN_2O_2S$: C 47.28, H 5.70, N 6.89, S 7.89; found: C 46.86, H 5.70, N 6.67, S 7.75.

N'-(di(pyridin-2-yl)methylene)-2-propylpentanethiohydrazide (AZM16, HL^4)

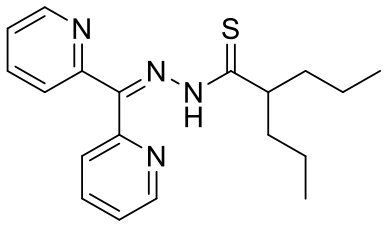

The thiohydrazide salt **AZM11** (54 mg, 0.256 mmol, 1 eq) was dissolved in EtOH (6 mL) and 1M NaOH (aq) (256 µL, 0.256 mmol, 1 eq) was added. Di-2-pyridylketone (47 mg, 0.256 mmol, 1 eq) in EtOH (5 mL) was added and the resulting colourless mixture was left stirring under reflux overnight (TLC in EtOAc indicated total consumption of the ketone). A yellow solution was obtained, which was reduced to half volume and then left at 4 °C overnight. A small amount of white precipitate (unreacted thiohydrazide) formed, which was removed by filtration. Attempts were done to precipitate the ligand, but all of them were unsuccessful. The mixture was therefore dried and the crude was purified by column chromatography in EtOAc. A brown-orange oil was isolated, which was left at 4 °C overnight. A brown solid was isolated (59 mg, yield = 68%).

IR (cm^{-1}): ν = 3258 (m-s) (NH), 2955 - 2820 (m-s) (CH), 1585 (s) (C=N, C=C). (Figure A3.63)

^{1}H NMR (500 MHz, DMSO-d_6, 298 K): complex pattern of signals (Figure A3.64).

^{1}H NMR (500 MHz, Chloroform-*d*, 298 K): complex pattern of signals (Figures A3.65-67).

^{13}C NMR (126 MHz, DMSO-d_6, 298 K): δ(ppm) = 161.54, 150.95, 148.84, 148.36, 137.91, 136.88, 122.69, 121.01, 90.18 (NH-C-S of thiadiazoline), 40.41 (S-C-CH of thiadiazoline), 37.91, 35.79, 19.94, 19.63, 13.98, 13.70. (Figure A3.70).

ESI-MS (positive ions): m/z (%): 262 (80) $[M - C_5H_4N]^+$, 341 (100) $[M + H]^+$, 363 (30) $[M + Na]^+$. (Figures A3.73-74).

[Cu(L^4)Cl] (AZM18)

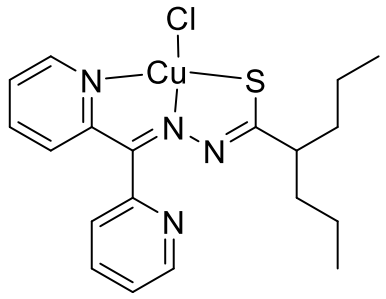

The ligand **AZM16** (51 mg, 0.151 mmol, 1 eq) was solubilized in EtOH (5 mL) and to the resulting orange-green solution was added dropwise a solution of $CuCl_2 \cdot 2\ H_2O$ (25.7 mg, 0.151 mmol, 1 eq) in EtOH (4 mL). A dark green solution formed immediately (pH ca. 3 – 4). The mixture was stirred at r.t. for four hours, then the resulting suspension was concentrated to half volume and left at 4 °C overnight. A dark green precipitate was obtained, which was filtrated, washed with cold EtOH and dried *in vacuo*. A dark green solid was obtained (18 mg, yield = 27%).

IR (cm^{-1}): ν = 2952 - 2867 (m-s) (CH), 1601 - 1561 (m) (C=N, C=C).

ESI-MS (positive ions): m/z (%): 402 (50) $[Cu(L^4)]^+$, 852 (100) $[Cu_4L^4{}_4Cl_2 + H_2O]^{2+}$. (Figure A3.75)

Elem. anal. calcd (%) for $C_{19}H_{23}ClCuN_4S$: C 52.05, H 5.29, N 12.78, S 7.31; found: C 51.90, H 5.30, N 12.64, S 7.06.

Chapter 4:

2-Amino-1,3,4-thiadiazoles:

unexpected synthesis and copper(I) coordination

Introduction

The **1,3,4-thiadiazole** ring (Figure 4.1a) is a five-membered heterocycle with a great potential in pharmaceutical and material chemistry.[240,255,256] Acetazolamide (Figure 4.1b), a carbonic anhydrase inhibitor used in the treatment of glaucoma and other diseases,[257-259] is probably the most famous compound with biological activity based on a **1,3,4-thiadiazole** scaffold. In material chemistry, the electron-deficient nature of the 1,3,4-thiadiazoles, together with their thermal and chemical stability, allow to predict their applications, for example, as luminophores,[260,261] corrosion inhibitors[262] or additives in lubricants.[263]

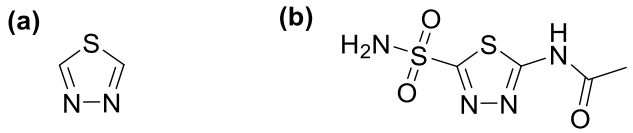

Figure 4.1: (a) General structure of the 1,3,4-thiadiazole ring; (b) chemical structure of the carbonic anhydrase inhibitor acetazolamide.

The coordination behaviour of **1,3,4-thiadiazoles** is less extensively studied compared to their pharmacological or optical properties and is primarily dictated by the nitrogen atoms in the ring,[264] while the sulphur atom is rarely involved in the metal ion complexation; obviously, coordination modes are strongly influenced by the presence of substituents in the ring.[265-268]

Various strategies for the synthesis of **1,3,4-thiadiazoles** exist,[240] mainly based on the cyclization of thiosemicarbazide or substituted thiosemicarbazides, leading to **2-amino-1,3,4-thiadiazoles**. The reaction implies (a) the use of an acylating agent, such as an acid halide[269] or an acid anhydride[270] or (b) the formation of a Schiff base intermediate, through the condensation of the thiosemicarbazide with an aldehyde, followed by oxidative cyclization with a metal oxidant.[271] Nevertheless, due to the instability and reactivity of the precursor formyl chloride, few synthetic methods are reported for obtaining **5-unsubstituted 2-amino 1,3,4-thiadiazoles**, which can be obtained by reaction of 4-substituted thiosemicarbazides with triethyl-orthoformate,[272,273] diethyl chlorophosphite,[274] $TiCl_4$[275] in DMF, or by heterocyclization of thiocarbonohydrazides.[276]

This chapter reports some results obtained in the attempt to extend to thiosemicarbazides the protocol described by S.H. Kwak and Y. Gong for the synthesis of *N,N*-dialkyl formamidines,[277] based on the reaction of amines, hydrazines or acyl hydrazides with *N,N*-dialkyl formamides and phenyl chloroformate (Scheme 4.1a-c). Quite unexpectedly, what we obtained by reacting 4-phenylthiosemicarbazide with DMF and phenyl chloroformate was not a formamidine, but the 2-phenylamino 1,3,4-thiadiazole **AZ42** (**L**, Scheme 4.1d).

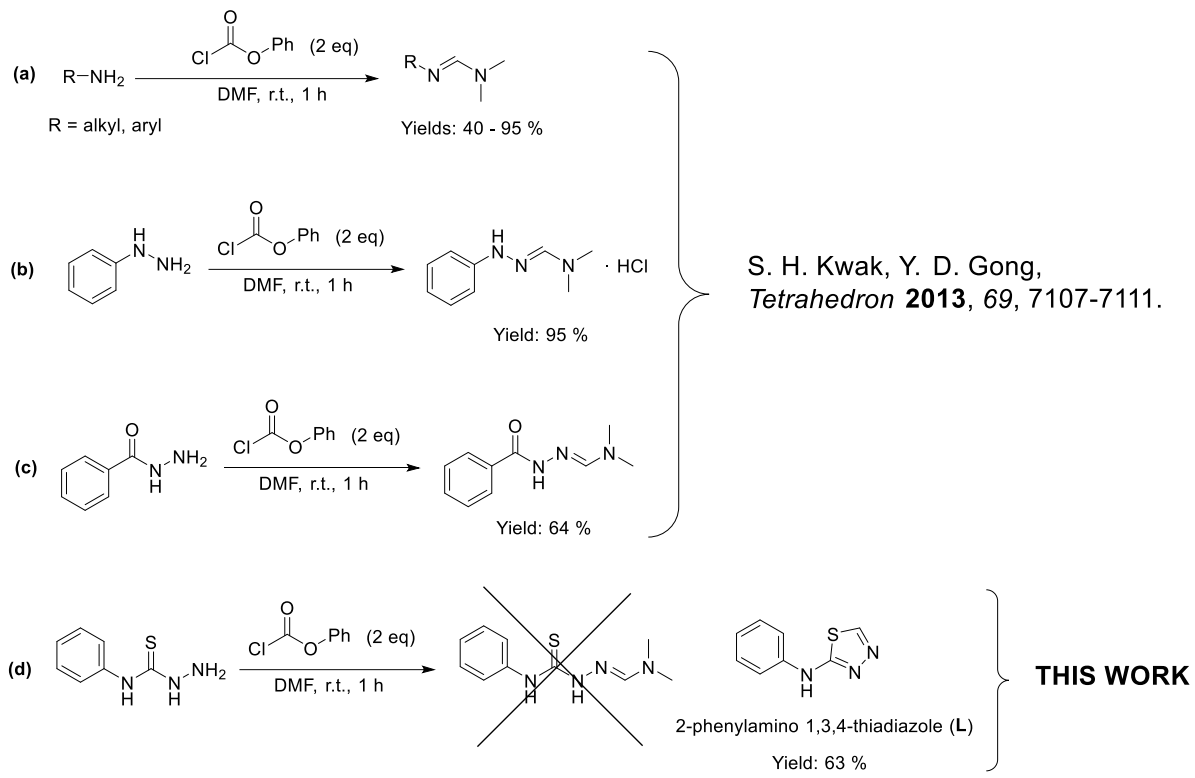

Scheme 4.1: Reaction of (a) amines, (b) hydrazines, (c) acyl hydrazides and (d) 4-phenylthiosemicarbazide with DMF and phenyl chloroformate.

Here we report on the characterization of the obtained 2-amino 1,3,4-thiadiazole and on the complexing behaviour of this scaffold towards CuI: a novel 1D copper(I) coordination polymer **[CuIL]n** (**AZ45**, Figure 4.2) was synthesized and characterized.[278] The X-ray diffraction analysis of its structure and its emission spectrum will be discussed.

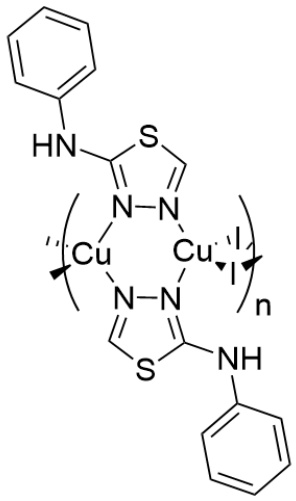

Figure 4.2: Chemical structure of the copper(I) coordination polymer **AZ45**.

Results and discussion

Cyclization of thiosemicarbazides

2-Phenylamino 1,3,4-thiadiazole (**AZ42** or **L**) was obtained in good yield by reacting 4-phenylthiosemicarbazide with DMF and 2 equivalents of phenyl chloroformate (Scheme 4.2), regardless of the addition of the base. Indeed, even without the addition of K_2CO_3, we did not isolate the HCl salt of the **1,3,4-thiadiazole**, but the compound in its neutral form, as confirmed by elemental analysis (see the experimental section).

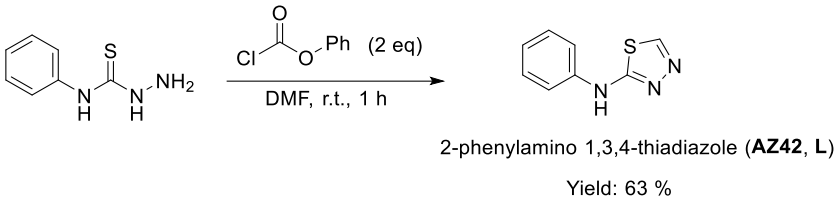

2-phenylamino 1,3,4-thiadiazole (**AZ42**, **L**)

Yield: 63 %

Scheme 4.2: Synthesis of 2-phenylamino 1,3,4-thiadiazole (**AZ42**, **L**).

The synthesis of this compound was already reported in literature,[272,279] although based on different procedures. The **1,3,4-thiadiazole L** was characterized by means of IR (Figure A4.1), ^{1}H, ^{13}C and 2D NMR spectroscopies (Figures 4.3 and A4.2-3), mass spectrometry (Figures A4.5-6) and elemental analysis. In Figure 4.3 is reported the ^{1}H NMR spectrum of **L** in DMSO-d_6.

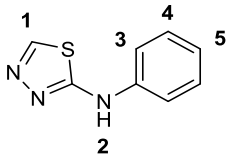

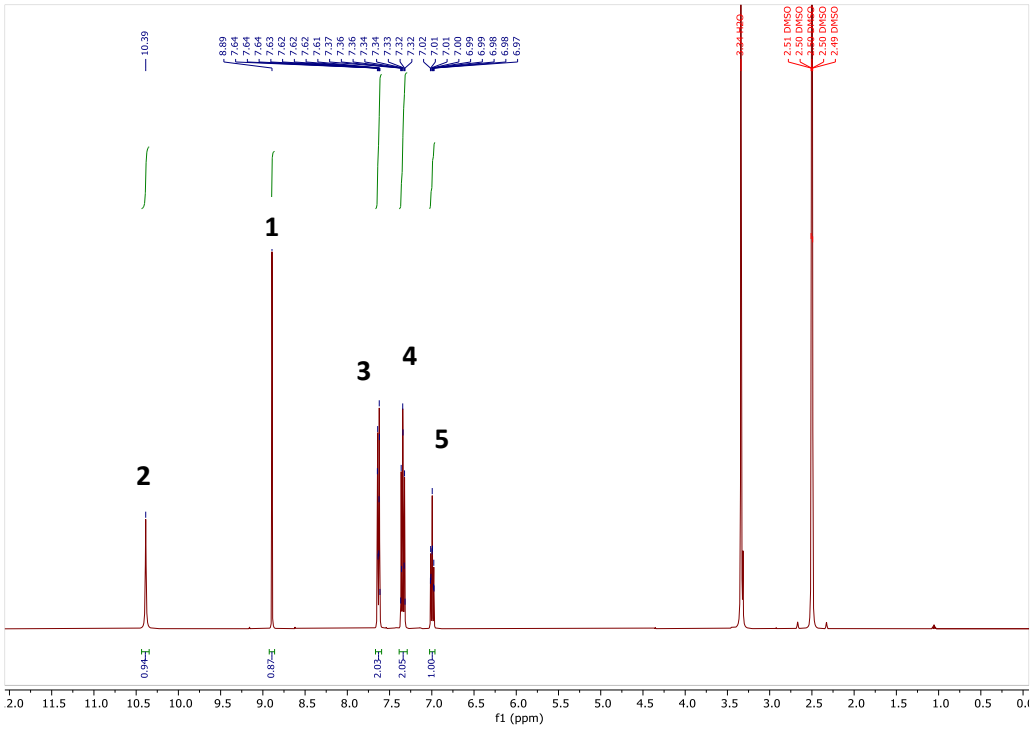

Figure 4.3: ^{1}H NMR (400 MHz, 298 K) spectrum of **L** in DMSO-d_6.

A mechanism for the cyclization that led to the formation of **L** can be proposed, starting from the formation of the iminium salt **1** (Scheme 4.3),[277] or from the salt formed by the phenolate anion and the $[(CH_3)_2N{=}CHCl]^+$ cation (which is the same of the Vilsmeier reagent) (**2** in Scheme 4.3).[280] The evolution of CO_2 bubbles from the reaction mixture is coherent with both the proposed intermediates. Then, the intermediate reacts with the NH_2 group of the thiosemicarbazide, leading to the formation of **3** and phenol as a by-product. Finally, **3** cyclizes with elimination of dimethylammonium chloride. The formation of the latter is probably the reason why it is not necessary to add a base to eliminate HCl.

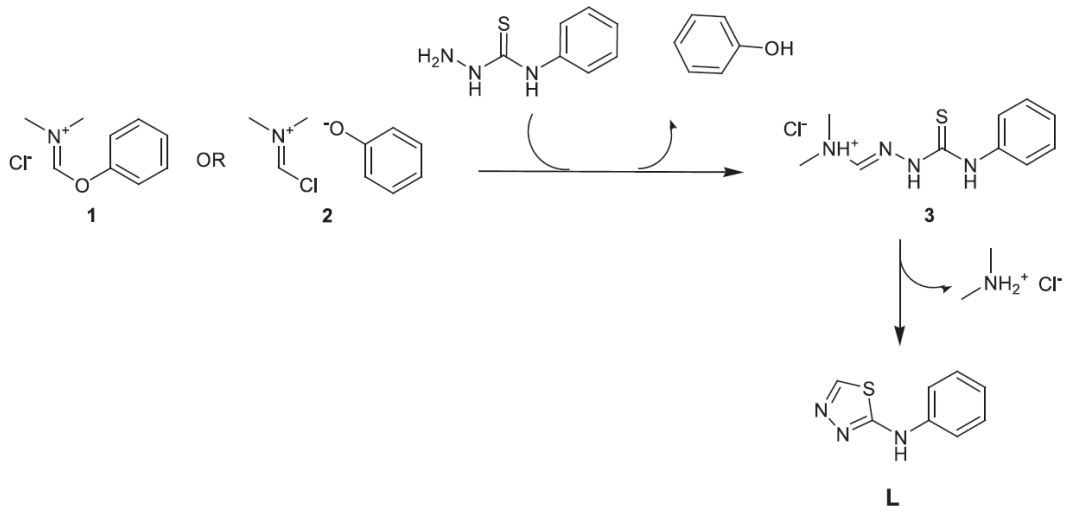

Scheme 4.3: Proposed mechanism of cyclization.

Since the presence of substituents in the **1,3,4-thiadiazole** ring can significantly influence its coordination modes, by altering its electronic and steric properties, we also investigated the use of other thiosemicarbazides as starting reagents. It was found that the yield of the cyclization reaction drops significantly by using thiosemicarbazide or 4-ethylthiosemicarbazide as starting reagents (Scheme 4.4a), suggesting that phenyl chloroformate may be successfully applied as cyclizing reagent in DMF for the synthesis of **2-arylamino-1,3,4-thiadiazoles**, but not for the synthesis of **2-alkylamino-1,3,4-thiadiazoles**. In fact, the application of the previously illustrated protocol to the reaction with 4-ethylthiosemicarbazide or thiosemicarbazide as substrates gave 2-ethylamino 1,3,4-thiadiazole (**AZ50**) and *N,N*-dimethyl-N'-(2-thiadiazolyl)formamidine (**AZ47**) in negligible yield (5% and 6%, respectively; Scheme 4.4a). The spectral characterization of **AZ50** (^{1}H and ^{13}C NMR spectra in Figures A4.7-8) and **AZ47** (IR spectrum in Figure A4.9; ^{1}H and ^{13}C NMR in Figures A4.10-12; ESI-MS in Figures A4.13-14), which are both known compounds,[273,281,282] are reported in the Appendix.

Interestingly, **AZ47** is the result of the reaction of **2-amino-1,3,4-thiadiazole** with a second molecule of DMF. The yield of this reaction increased to 26% by using 3 equivalents of phenyl chloroformate (Scheme 4.4a). Attempts to crystallize this compound as salt from an aqueous solution of hydrogen chloride led to isolate some crystals of the hydrolysis product *N*-(1,3,4-thiadiazol-2-yl)formamide suitable for single crystal X-ray diffraction analysis (Scheme 4.4b).

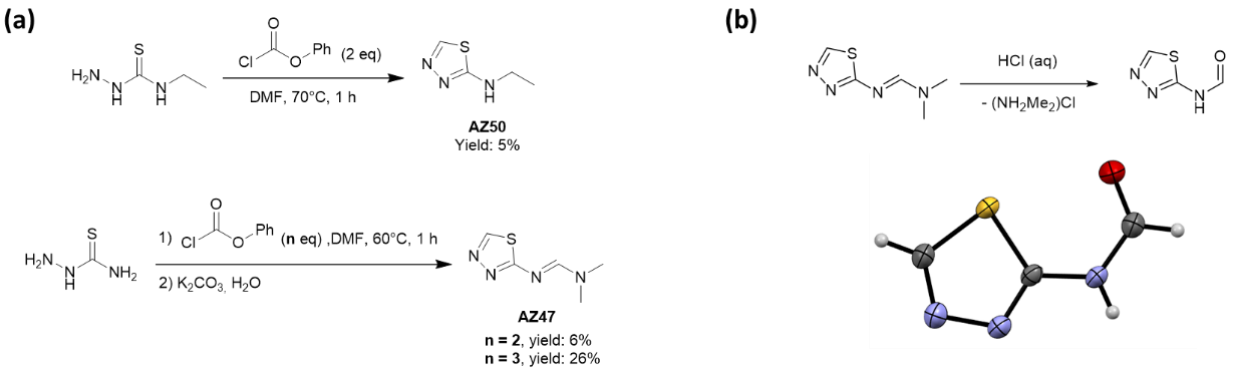

Scheme 4.4: (a) Reaction of 4-ethylthiosemicarbazide (top) and thiosemicarbazide (bottom) with phenyl chloroformate in DMF; (b) Hydrolysis reaction of **AZ47** (top) and ORTEP representation of the hydrolysis product *N*-(1,3,4-thiadiazol-2-yl)formamide (bottom). Carbon atoms in grey, hydrogens in white, oxygen in red, nitrogen in blue and sulphur in yellow.

Synthesis and characterization of [CuIL]n

The reaction of 2-phenylamino 1,3,4-thiadiazole **L** with CuI in 1:1 ratio in acetonitrile led to the isolation of an off-white solid that was characterised as the **[CuIL]n** complex (**AZ45**, Scheme 4.5). Even by changing the ligand:metal ratio to 1:2 or 2:1, the same compound formed.

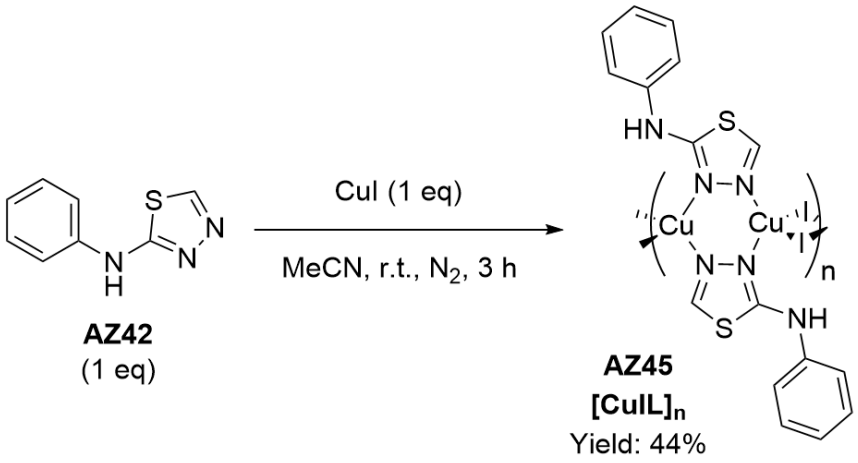

Scheme 4.5: Synthesis of the copper(I) coordination polymer **AZ45.**

The novel complex was characterized by means of FT-IR (Figures 4.4 and A4.15) and ^{1}H NMR spectroscopies (Figures A4.16-17), mass spectrometry (Figure A4.18), elemental analysis (see the experimental section), powder-XRD and single crystal-XRD.

The IR spectra of **L** and of **[CuIL]n** are significantly different. In the IR spectrum of **[CuIL]n** there is one band at 1596 cm^{-1} attributable to C=N stretching, while the IR spectrum of the ligand shows two bands at 1614 and 1598 cm^{-1} (Figure 4.4), indicating the involvement of nitrogen atoms in coordination.

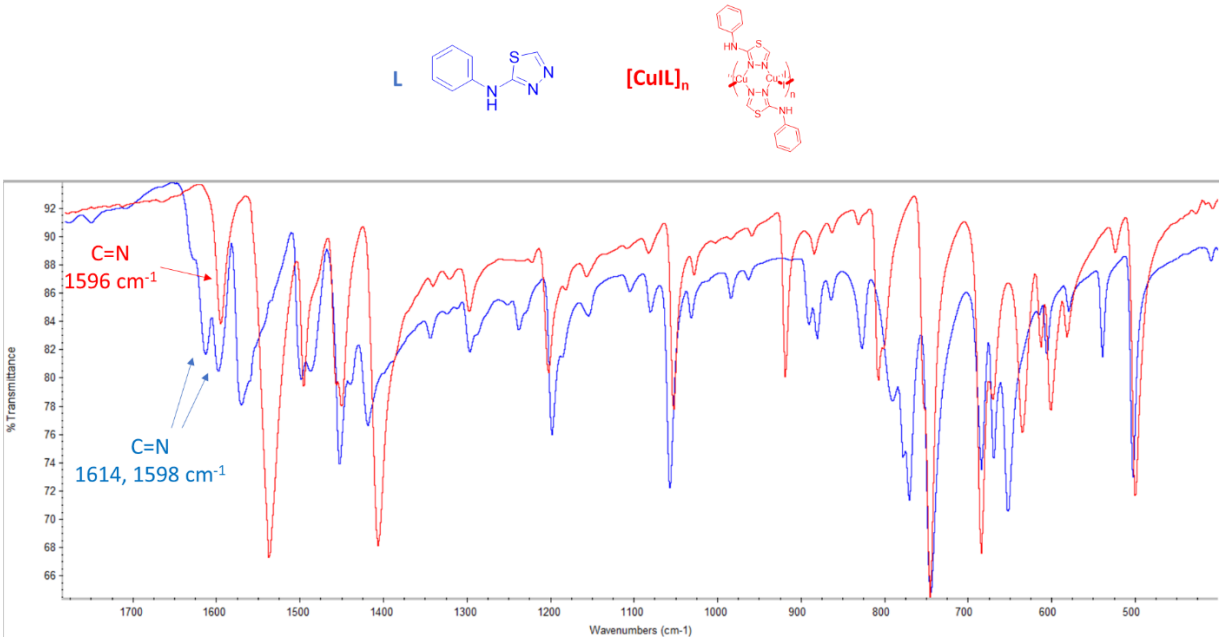

Figure 4.4: IR spectrum of **L** (in blue) and **[CuIL]n** (in red).

Rod-shaped crystals of **[CuIL]n** suitable for X-ray diffraction analysis were isolated by slow evaporation of a MeCN solution of the complex. **[CuIL]n** forms crystals belonging to the monoclinic system, space group *P*21/n. The asymmetric unit consists of one Cu(I) ion, one **L** molecule and one iodide ion (Figure A4.19). Each copper(I) ion is surrounded by two nitrogen atoms of two distinct molecules of **L** and by two iodide ions in a distorted tetrahedral geometry (Figure 4.5a). The 1D chain is characterized by $N_2Cu_2N_2$ units in a chair conformation, which are bridged by μ_2-iodide ligands (Figure 4.5b). The distance between the two copper centres in $N_2Cu_2N_2$ is 3.445 Å, while the Cu···Cu distance in the CuI_2Cu units is 2.868 Å: both are slightly longer than the sum of van der Waals radii of two Cu atoms (2.8 Å), and therefore there is no significant metallophilic interaction. The **1,3,4-thiadiazole** acts as a bridging N,N' ligand and this behaviour is consistent with other Cu(I) and Ag(I) complexes of **2-amino-1,3,4-thiadiazoles** reported in the literature.[283-286] The packing of adjacent 1D chains is characterized by π···π interactions between the edges of the aromatic rings of the 2-phenylamino moieties of a chain and the faces of the aromatic rings of the 2-phenylamino moieties of another chain (Figure 4.5c).

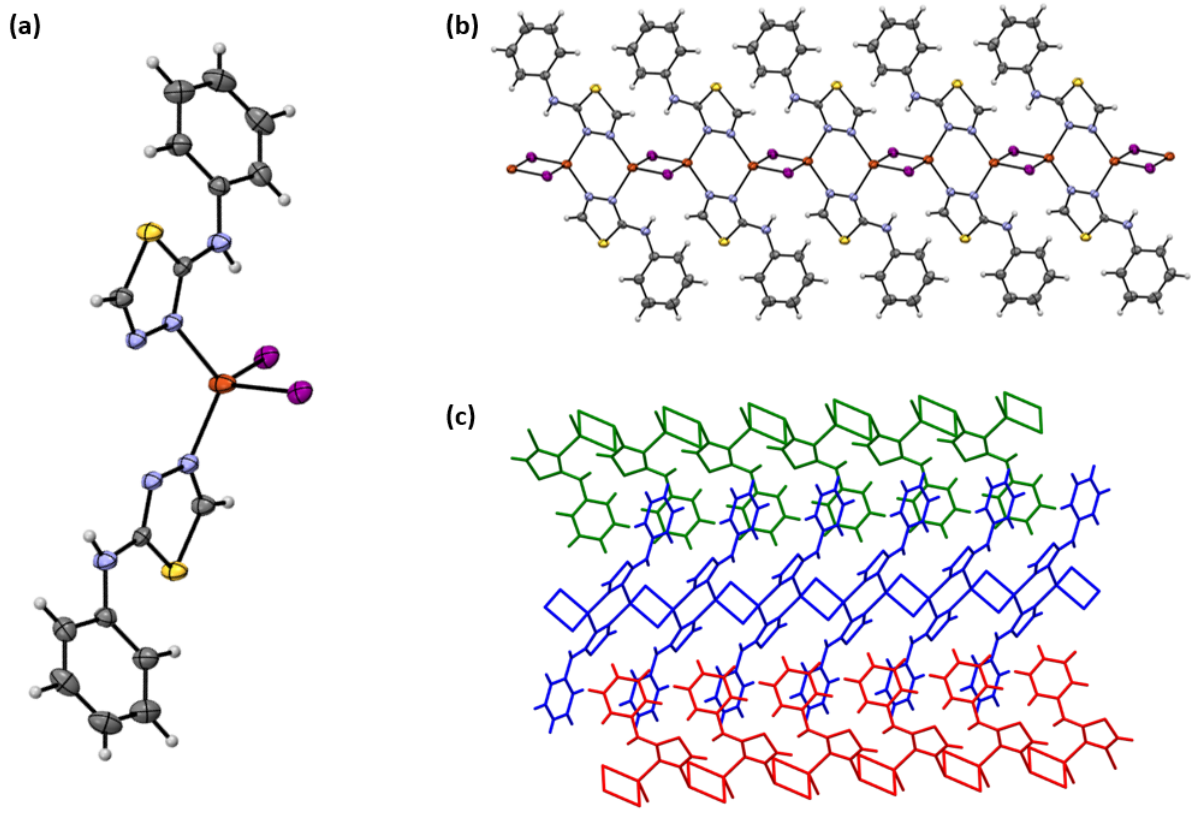

Figure 4.5: (a) Coordination geometry of Cu(I) centre in **[CuIL]n**. The ellipsoids are displayed at a 50% probability level (sulphur atoms in yellow, nitrogen in blue, carbon in grey, hydrogens in white, iodine in purple, copper ion in red). (b) View of 1D chain characterized by the alternation of perpendicular $N_2Cu_2N_2$ and CuI_2Cu units. (c) Packing of 1D chains is characterized by π···π interactions between phenyl moieties (different chains are in different colours).

The diffraction pattern obtained by powder X-ray diffraction (P-XRD) analysis of a sample of **[CuIL]n** matched with the pattern calculated from single crystal X-ray diffraction data (Figure 4.6), confirming the homogeneity of the sample.

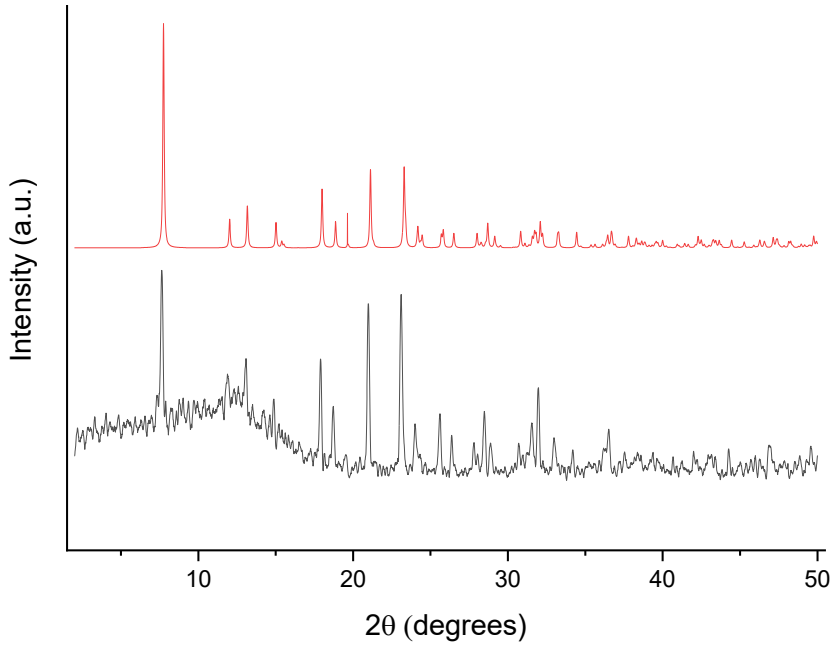

Figure 4.6. Calculated (top) and experimental (bottom) P-XRD pattern for **[CuIL]$_n$**.

[CuIL]n is slightly soluble in acetonitrile and insoluble in chloroform. The ^{1}H NMR spectra of the solution of **[CuIL]n** and of the ligand **L** in CD_3CN show little differences. In the spectrum of **[CuIL]n** the NH peak of the coordinated ligand is broadened and slightly shifted to high field with respect to the spectrum of the free ligand, while the signal of the imine proton is shifted to down field (Figure A4.20). Small variations in chemical shifts are found also for the signals of the aromatic protons. The complex is stable in CD_3CN in the air over time: no significant variations were observed in its ^{1}H NMR spectrum after one week (Figure A4.21). In the ESI-MS spectrum of **[CuIL]n** in MeCN there are two peaks attributable to $[CuL]^+$ and $[CuL_2]^+$ species (Figure A4.18).

The UV–visible spectrum of **L** in MeCN (Figure A4.22) shows two absorption bands with λ_{max} = 282 (ε = 12000 $mol^{-1}dm^3cm^{-1}$) and 245 nm (ε = 4600 $mol^{-1}dm^3cm^{-1}$). In the UV–visible spectrum of **[CuIL]n** in the same solvent, the two bands do not change their maxima, but considerably gain in intensity (λ_{max} = 282 nm, ε = 13600 $mol^{-1}dm^3cm^{-1}$; λmax = 245 nm, ε = 18800 $mol^{-1}dm^3cm^{-1}$; Figure A4.22).

[CuIL]n is soluble also in DMSO, but in this solvent the behaviour of the complex proved to be different, depending on concentration. At room temperature and in the air, the UV–visible spectrum of a micromolar solution of the complex showed an increase in intensity of the band at 285 nm along 48 hours (Figure A4.23). Under the same experimental conditions, a millimolar DMSO solution of the complex was initially colourless, but it turned dark green after few minutes, and a grey precipitate formed. The change in colour could be attributable to MLCT absorption bands observable after coordination of the solvent and/or aggregation phenomena,[287] as suggested by the dependence of the colour change on concentration. To exclude the formation of Cu^{II} species in solution, **[CuIL]n** was dissolved in DMSO-d_6 (concentration was in the millimolar range). In the ^{1}H NMR spectrum of the resulting dark green solution there are all the signals attributable to the coordinated ligand **L**. The main difference with the spectrum of the uncomplexed **L** is the signal at 9.19 ppm (8.89 ppm in **L**), that is broad in the spectrum of the complex (Figure A4.17). No effect of paramagnetism was detected: therefore, regardless of the identity of the complex species in solution, no oxidation of Cu(I) to Cu^{II} seems to take place.

Since many copper(I) complexes display luminescent properties,[240] the emission spectrum of **[CuIL]n** was measured. While in acetonitrile solution at room temperature **[CuIL]n** is non-emissive, it is weakly emissive in the solid state at room temperature (excitation wavelength: 350 nm, Figure 4.7). interestingly, it is characterized by a quite rare white emission[288] with λ_{max} =613 nm.

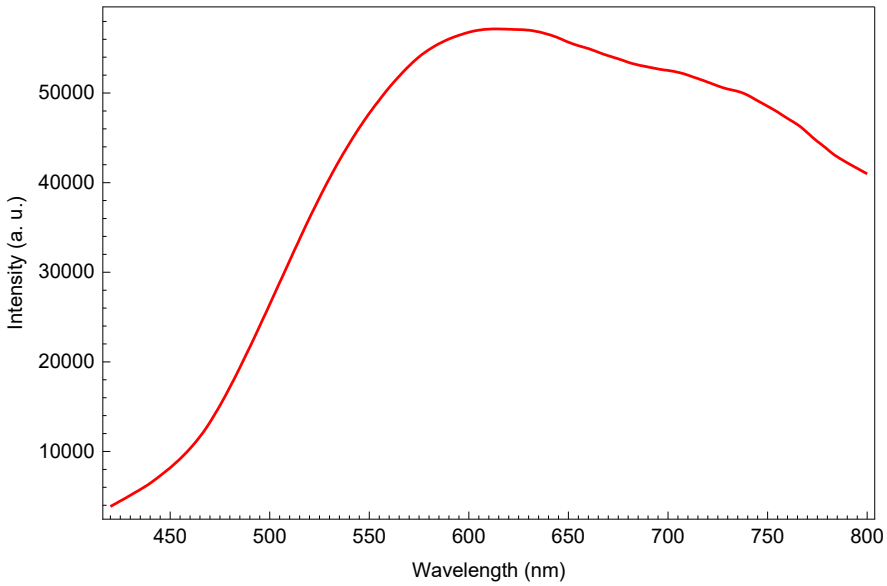

Figure 4.7. Emission spectrum of **[CuIL]$_n$** as powder at room temperature (excitation wavelength: 350 nm).

Conclusions

In this work, it was demonstrated the synthesis of 2-phenylamino-1,3,4-thiadiazole via an unexpected cyclization of 4-phenylthiosemicarbazide, and explored its coordination behaviour towards Cu(I) ions. The synthesized **1,3,4-thiadiazole** scaffold formed a novel 1D coordination polymer with Cu(I), where the metal center is coordinated by nitrogen atoms from two distinct **1,3,4-thiadiazole** ligands and iodide ions, with a distorted tetrahedral geometry. This study highlights the versatility of the **1,3,4-thiadiazole** ring, whose coordination chemistry has been poorly explored. These findings open new possibilities for the design of novel metal-thiadiazole complexes with potential uses in various fields, including luminescent materials and catalysis.

Experimental section

Materials and methods

Commercial reagents were purchased from Sigma-Aldrich. The purity of the synthesized compounds was determined by elemental analysis and verified to be ≥95%. ^{1}H, ^{13}C and 2D NMR spectra were recorded at 25 ◦C on a Bruker Advance 400 MHz FT spectrometer. The ATR-IR spectra were recorded by means of a Perkin Elmer spectrophotometer by using a diamond crystal plate in the range of 4000–400 cm^{-1}. Elemental analyses were performed by using a Thermo Fisher FlashSmart CHNS/O analyzer with gas-chromatographic separation. Electrospray ionization mass spectral analyses (ESI-MS) were performed with an ESI time-of-flight Micromass 4LCZ spectrometer. Samples were dissolved in methanol or acetonitrile. The UV–visible spectra were collected by means of a Thermo Scientific Evolution 260 Bio spectrophotometer and quartz cuvettes with 1 cm path length were used. Emission spectra were collected with a FLS1000 Edinburgh Fluorimeter equipped with a PMT-900 Detector (200–870 nm). Powder X-ray diffraction (P-XRD) data were collected with a Rigaku Smartlab XE diffractometer equipped with a 2D HyPix3000 detector operating in 1D mode. Data were collected under ambient conditions in Bragg–Brentano geometry (Cu Kα =1.5046 Å) in continuous mode, in the 2°–50° 2θ angular range, with a step size of 0.01◦ at a scan speed of 8° min^{-1}.

Synthesis

2-Phenylamino 1,3,4-thiadiazole (L, AZ42)

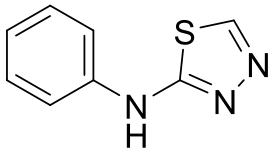

Phenyl chloroformate (1.5 mL, 12 mmol, 2 eq) was added dropwise to DMF (6 mL), then the dark red mixture was stirred for 10 min at r.t.. 4-Phenylthiosemicarbazide (1 g, 6 mmol, 1 eq) was added and the resulting solution was stirred for 1 h at r.t.. Water (ca. 40 mL) was added and a precipitate formed, which was filtered, washed with water and recrystallized in 1/3 EtOH/water. The off-white solid was filtered, washed with water and dried *in vacuo* (665 mg, yield = 63%).

M.p.: 169-171 °C (lit.[266] 168-170 °C).

IR (cm^{-1}): ν = 1614 and 1598 (s) (C=N). (Figure A4.1)

^{1}H NMR (400 MHz, DMSO-d_6, 298 K): δ(ppm) = 10.39 (s, 1H, NH), 8.89 (s, 1H, CH=N), 7.67 – 7.59 (m, 2H, ArH), 7.39 – 7.29 (m, 2H, ArH), 6.99 (tt, *J* = 7.4, 1.1 Hz, 1H, ArH).

^{1}H NMR (400 MHz, acetonitrile-d_3, 298 K): δ(ppm) = 8.61 (s, 1H, NH), 8.47 (s, 1H, CH=N), 7.63 – 7.57 (m, 2H, ArH), 7.41 – 7.33 (m, 2H, ArH), 7.06 (tt, *J* = 7.4, 1.1 Hz, 1H, ArH). (Figure A4.2)

^{13}C NMR (101 MHz, DMSO-d_6, 298 K): δ(ppm) = 164.71, 144.55, 141.22, 129.55, 122.28, 117.75. (Figure A4.3)

MS-ESI (positive ions): m/z (%): 178 (100) $[L + H]^+$. (Figure A4.5)

MS-ESI (negative ions): m/z (%): 176 (100) $[L – H]^-$. (Figure A4.6)

Elem. anal. calcd (%) for $C_8H_7N_3S$: C 54.22, H 3.98, N 23.71, S 18.09; found: C 54.37, H 4.00, N 23.84, S 18.09.

2-Ethylamino 1,3,4-thiadiazole (AZ50)

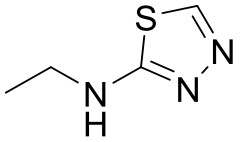

To DMF (3 mL) was added dropwise phenyl chloroformate (0.75 mL, 6 mmol, 2 eq) and the obtained dark red mixture was stirred for 10 min at r.t.. Then, solid 4-ethylthiosemicarbazide (358 mg, 3 mmol, 1 eq) was added and the temperature was raised to 70°C in order to solubilize the substrate. The mixture was left stirring at 70°C for 1 h, then it was left cooling at r.t.. Water (20 mL) was added to the mixture, which was extracted with $CHCl_3$ and washed with water. The organic phase was dried over Na_2SO_4, filtered and concentrated. The crude oil was purified by column chromatography (EtOAc) and the resulting solid was dried *in vacuo*. An off-white powder was obtained (21 mg, yield = 5%).

^{1}H NMR (400 MHz, chloroform-*d*, 298 K): δ(ppm) = 8.39 (s, 1H, CH=N), 5.64 (s, 1H, NH), 3.40 (q, *J* = 7.2 Hz, 2H, CH_2), 1.33 (t, *J* = 7.2 Hz, 3H, CH_3). (Figure A4.7)

^{13}C NMR (101 MHz, chloroform-*d*, 298 K): δ(ppm) = 170.21, 141.41, 42.32, 14.78. (Figure A4.8)

***N,N*-Dimethyl-N'-(2-thiadiazolyl)formamidine (AZ47)**

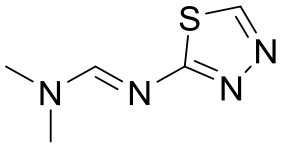

Phenyl chloroformate (1.13 mL, 9 mmol, 3 eq) was added dropwise to DMF (3 mL) and the resulting dark red mixture was stirred for 10 min at r.t.. Thiosemicarbazide (273 mg, 3 mmol, 1 eq) was added and the temperature was raised to 60°C to facilitate the solubilization. The mixture was stirred at 60°C for 1 h, then it was left cooling down at r.t.. Water (20 mL) and solid K_2CO_3 (1.245 g, 9 mmol) were added to the mixture, which was treated with $CHCl_3$ and washed with water. The organic phase was dried over Na_2SO_4, filtered and concentrated. The crude was purified by column chromatography ($CHCl_3$/MeOH 95/5) and the resulting orange oil was triturated with Et_2O and dried *in vacuo*. A brown-orange solid was obtained (124 mg, yield = 26%).

M.p.: 65-70 °C.

IR (cm^{-1}): ν = 1622 (s) (C=N). (Figure A4.9)

^{1}H NMR (400 MHz, DMSO-d_6, 298 K): δ(ppm) = 8.95 (s, 1H, S-CH=N), 8.25 (s, 1H, N-CH=N), 3.12 (s, 3H, CH_3), 2.99 (s, 3H, CH_3). (Figure A4.10)

^{1}H NMR (400 MHz, chloroform-*d*, 298 K): δ(ppm) = 8.65 (s, 1H, S-CH=N), 8.30 (s, 1H, N-CH=N), 3.13 (s, 3H, CH_3), 3.10 (m, 3H, CH_3). (Figure A4.11)

^{13}C NMR (101 MHz, chloroform-*d*, 298 K): δ(ppm) = 175.68, 156.70, 147.33, 41.05, 35.03. (Figure A4.12)

MS-ESI (positive ions): m/z (%): 157 (100) $[M + H]^+$. (Figure A4.13)

MS-ESI (negative ions): m/z (%): 155 (100) $[M – H]^-$. (Figure A4.14)

Elem. anal. calcd (%) for $C_5H_8N_4S$: C 38.45, H 5.16, N 35.87, S 20.52; found: C 38.77, H 5.23, N 35.33, S 19.87.

$[CuIL]_n$ (AZ45)

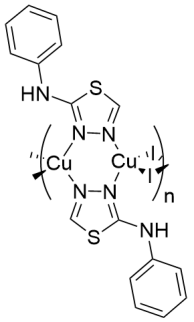

A solution of CuI (128 mg, 0.672 mmol, 1 eq) in 15 mL of MeCN was added under nitrogen to a pale-yellow solution of **L** (120 mg, 0.677 mmol, 1 eq) in 20 mL of MeCN. The resulting yellow solution was stirred at r.t. for 3 h. The obtained suspension was reduced to half volume and then left at 4°C under nitrogen overnight. The precipitate was filtered, washed with cold MeCN, Et_2O and dried *in vacuo*. A sand-coloured powder was obtained (110 mg, yield = 44%).

M.p.: 210-212 °C.

IR (cm^{-1}): ν = 1596 (s) (C=N). (Figure A4.15)

^{1}H NMR (400 MHz, acetonitrile-d_3, 298 K): δ(ppm) = 8.61 (s, 1H), 8.47 (s, br, 1H), 7.63 – 7.56 (m, 2H), 7.41 – 7.34 (m, 2H), 7.10 – 7.03 (m, 1H). (Figure A4.16)

^{1}H NMR (400 MHz, DMSO-d_6, 298 K): δ(ppm) = 10.41 (s, 1H), 9.19 (s, 1H), 7.62 (d, *J* = 7.8 Hz, 2H), 7.33 (t, *J* = 7.5 Hz, 2H), 6.98 (t, *J* = 7.2 Hz, 1H). (Figure A4.17)

MS-ESI (positive ions): m/z (%): 178 (100) $[L + H]^+$, 240 (40) $[CuL]^+$, 417 (20) $[CuL_2]^+$. (Figure A4.18)

Elem. anal. calcd (%) for $C_8H_7CuIN_3S$: C 26.13, H 1.92, N 11.43, S 8.72; found: C 26.39, H 1.93, N 11.41, S 8.52.

Crystallography

Single crystal X-ray diffraction analyses were carried out with a Bruker D8Venture diffractometer equipped with a kappa goniometer and an Oxford cryosystem. Microfocused MoKα radiation (λ =0.71073Å) was used as the X-ray source and Lorentz polarization and absorption correction were applied through the SADABS procedure.[289] The phase problem was solved by direct methods and the structures were refined by full-matrix least-squares on all F2 using SHELXL,[123,290] as implemented in the OLEX2[220] suite of programs. The structure drawings were obtained using ORTEPIII[291] and Mercury.[292]

Single crystals of complex **AZ45** and *N*-(1,3,4-thiadiazol-2-yl)formamide suitable for X-ray diffraction study were obtained by slow evaporation of mother liquors and an aqueous solution, respectively. Crystallographic data for both compounds are reported in Tables A1-2. CCDC 2390360 and 2408774 contain supplementary crystallographic data.

Chapter 5:

Synthesis and biological activity of iminophosphine copper(I) complexes

Introduction

Chemistry of copper(I) complexes

Cu^{I} is a d^{10} metal ion with a soft character: it typically forms coordination compounds with ligands bearing soft donor atoms, like phosphorus, sulphur and nitrogen of aromatic amines. With rare exceptions, copper(I) complexes show low coordination numbers ranging from two to four; the typical geometries are linear for two-coordinated species, trigonal planar for three-coordinated complexes and tetrahedral for four-coordinated compounds. The great majority of copper(I) coordination compounds reported in literature exhibits tetrahedral geometry.[31,293,294]

Depending on the stoichiometry and the nature of the ligands, copper(I) complexes can display either monomeric, dimeric, trimeric, tetrameric or even more complicated structures. An example of this versatility is shown in Figure 5.1, where $(CuI)_x$ motifs found in copper-iodine based clusters[295] are reported.

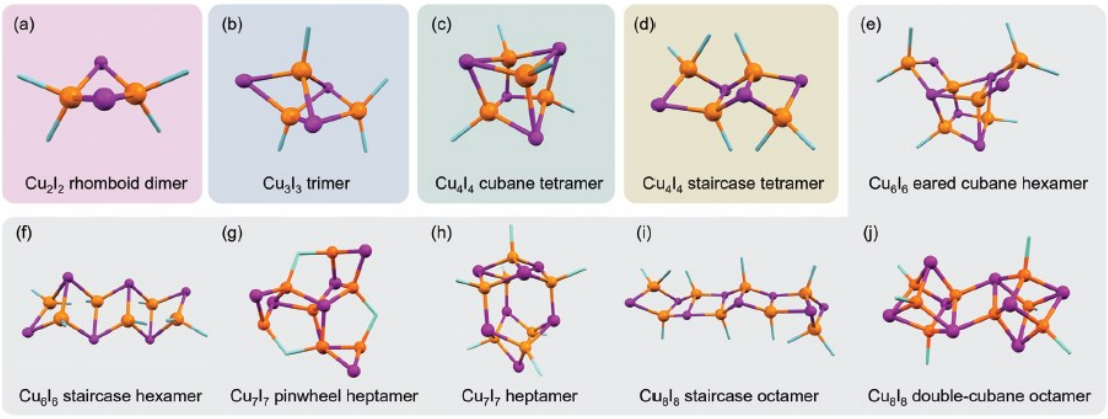

Figure 5.1: $(CuI)_x$ motifs found in copper-iodine based clusters (copper atoms in orange, iodine in purple, organic ligands donor atoms in blue). Adapted from Ref.[295]

The stabilization of copper(I) species can be challenging both in solid state and in solution. Cu^{I} can be oxidized to Cu^{II} by atmospheric oxygen, while in aqueous solution it easily undergoes disproportionation to Cu^{II} and metallic copper:

$$2\ Cu^{+}(aq) \rightarrow Cu^{2+}(aq) + Cu(s)$$

The disproportionation reaction is the difference of the two following half-reactions:

$Cu^{+}(aq) + e^{-} \rightarrow Cu(s)$ $\quad E^{0} = +0.52$ V

$Cu^{2+}(aq) + e^{-} \rightarrow Cu^{+}(aq)$ $\quad E^{0} = +0.16$ V

Consequently, the cell standard potential $E^{0}_{cell} = 0.52\ V - 0.16\ V = +0.36\ V$ and the equilibrium constant for the reaction at 298 K is $K = 1.3 \cdot 10^{6}$. The disproportionation is therefore highly favourable.[296] Only formation of strong Cu(I)-ligand interactions, such as those displayed in the case of copper-tertiary phosphine and copper-NHC (NHC = N-heterocyclic carbene) species (Figure 5.2), can prevent undesired oxidation or disproportionation processes.[31]

Tertiary phosphines

N-heterocyclic carbenes (NHCs)

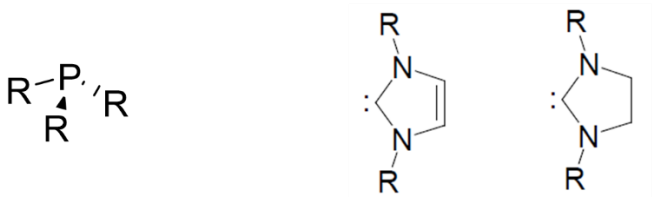

Figure 5.2: General structure of tertiary phosphines (left) and N-heterocyclic carbenes (NHCs).

Biological properties of copper(I) complexes

Copper(I) complexes are principally investigated for their application in catalysis,[293,297,298] photochemistry[299] and structural chemistry,[300] while their biological properties are much less studied. Nevertheless, the few examples of bioactive copper(I) complexes reported in literature display a broad spectrum of activity, ranging from anticancer to antimicrobial. In the following section, the most important literature examples will be briefly described.

Anticancer activity of copper(I) complexes

Both tertiary phosphine-copper(I) and NHC-copper(I) complexes have been studied as potential anticancer agents.

The chemotherapeutic activity of phosphine copper(I) complexes is known since the 1980s, when Berners-Price and Sadler investigated the *in vitro* cytotoxic properties of a panel of cationic copper(I) complexes with bidentate diphosphines (P-P ligands).[95,301] The presence of several phenyl groups appended to the phosphine ligands conferred a strong lipophilic character to the Cu^{I} complexes, which in turn showed potent cytotoxic activity. Unfortunately, this positive combination of lipophilicity and cytotoxicity determined undesired nephrotoxicity in animal models, thus precluding clinical trials in humans.[96]

After these pioneering works, mainly three different groups of phosphine-based copper(I) complexes were studied for their antitumour activity: the homoleptic, cationic $[Cu(P)_4]^+$ species, the mixed-ligand, neutral [Cu(N-N)(P)(X)] complexes and the mixed-ligand [Cu(TRID)(P)] species, where P represents a monodentate phosphine, N-N an aromatic diimine, X a halide or pseudo-halide and TRID an anionic scorpionate ligand (Figure 5.3).

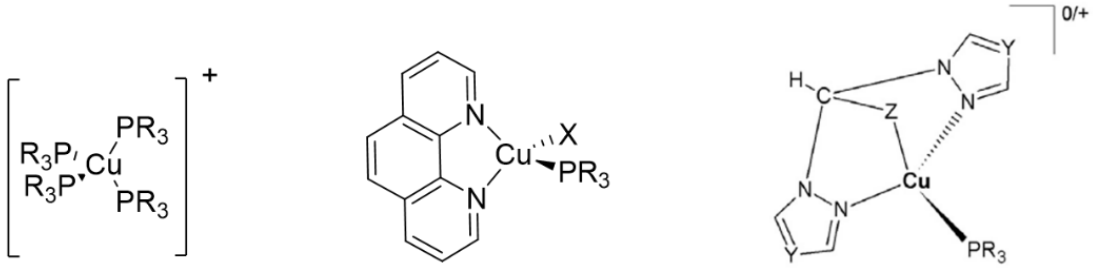

$[Cu(P)_4]^+$ **[Cu(N-N)(P)(X)]** **[Cu(TRID)(P)]**

Figure 5.3: General structures of $[Cu(P)_4]^+$, [Cu(N-N)(P)(X)] and [Cu(TRID)(P)] complexes. R = alkyl or aryl; X = halide or pseudo-halide; Z = COO^- or pyrazole; Y = CH or N.

For all these three classes of compounds, hydrophilic phosphines or aminomethylphosphines were employed to endow the final complexes with solubility in aqueous medium. It is important to note that these hydrophilic ligands alone are not cytotoxic against cancer and normal cells (Figure 5.4).[302]

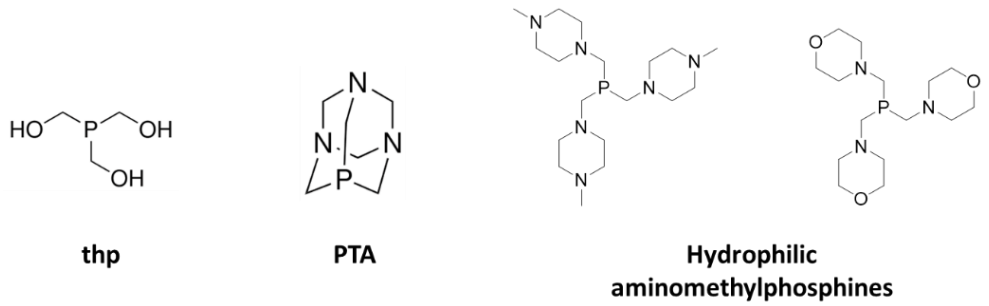

Figure 5.4: Structures of tris(hydroxymethyl)phosphine (thp), 1,3,5-triaza-7-phosphaadamantane (PTA) and aminomethylphosphines derived from 1-methylpiperazine and morpholine.[303]

Among the homoleptic, cationic $[Cu(P)_4]^+$ complexes, the most representative example is $[Cu(thp)_4]^+$ (Figure 5.5). Its hexafluorophosphate salt is characterized by exceptional solubility and stability in aqueous medium and proved to be a highly effective and selective anticancer agent both *in vitro* and *in vivo*.[54,304] The *in vivo* antitumour activity was tested against the aggressive Lewis lung carcinoma and human colorectal cancer implanted in mice. The selectivity of $[Cu(thp)_4]PF_6$ against cancer cells has been linked to a specific mechanism of cellular internalization involving hCTR1 (human copper transporter 1), a transmembrane protein that has been found to be highly overexpressed in several tumour cells.[305] Chemosensitivity tests conducted on various cell lines chosen for their resistance to cisplatin or oxaliplatin showed that $[Cu(thp)_4]PF_6$ was able to overcome platinum drug resistance, thus suggesting that the mechanism of action of this complex was different from the one displayed by platinum(II)-based anticancer drugs. In fact, molecular and cellular studies demonstrated that the cytotoxicity of $[Cu(thp)_4]PF_6$ (but also of other copper(I) compounds) was mainly related to inhibition of Proteasome, a large multiprotein complex located in the nucleus and in the cytoplasm that regulates the degradation of intracellular proteins.[306]

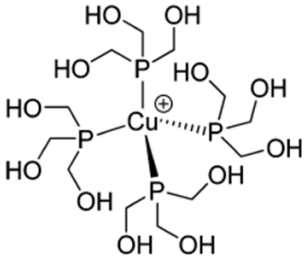

Figure 5.5: Structure of $[Cu(thp)_4]^+$ ion. Adapted from Ref.[31]

Several mixed-ligand, neutral [Cu(N-N)(P)(X)] complexes showed promising anticancer activity against different tumour cell lines.[302] For example, the four complexes reported in Figure 5.6, all derived from 2,9-dimethyl-1,10-phenanthroline (dmp), proved to be highly cytotoxic against CT26 (mouse colon carcinoma) and A546 (human lung adenocarcinoma) cell lines, with IC_{50} values below 10 μM.[307] Gel electrophoresis experiments indicated that all these complexes were comparably efficient in DNA degradation processes and suggested that DNA interaction was the principal mechanism of action. In spite of the presence of hydrophilic aminomethylphosphines in their structure, these compounds have low solubility in water.

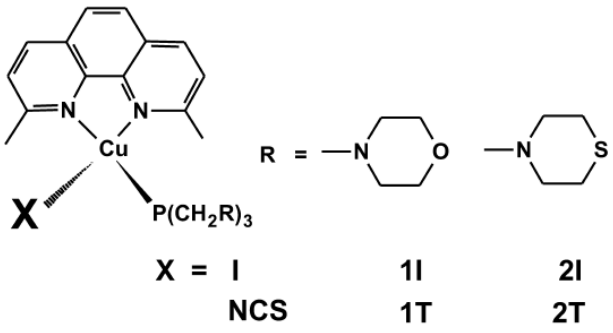

Figure 5.6: General structure of the copper(I) complexes investigated by Starosta and coworkers. Adapted from Ref.[307]

Porchia and coworkers synthesized a panel of neutral and charged phosphine/scorpionate copper(I) complexes which showed remarkable antiproliferative activity towards several cancer cell lines.[308,309] Complexes **9**-**12**, (Figure 5.7) showed *in vitro* antitumour activity comparable or superior to that of cisplatin. The neutral complexes **9** and **10**, with IC_{50} values appreciably lower than those exhibited by cisplatin, proved to be the most promising agents in terms of cytotoxic efficacy.[308]

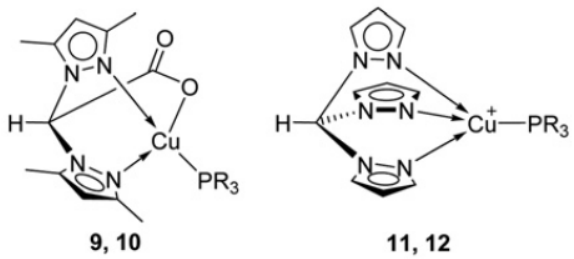

Figure 5.7: Structure of mixed-ligand copper(I) complexes **9-12** synthesized by Porchia and coworkers. PR_3 = PTA or PCN (PCN = tris(2-cyanoethyl)phosphine). Adapted from Ref.[308]

In the last twenty years, copper(I)-NHC complexes have been attracting interest for their application in several research fields, including the design of novel chemotherapeutics.[310] The exact mechanism of action of anticancer NHC-copper(I) complexes is still unknown, but some properties of these compounds affect their biological activity:[311-313]

- Ability to generate reactive oxygen species (ROS). Copper(I)-NHC complexes produce reactive oxygen species upon reaction with intracellular oxygen, thus causing DNA disruption.
- Lipophilicity: high lipophilicity allows easy penetration through the cell membrane. This property can be tuned by varying the N-substituents of the NHC ligands.
- Stability of the Cu-C bond: this allows slow release of the metal ion to the target site, avoiding undesired disproportionation of copper(I).

In Figure 5.8 are shown the structures of some copper(I)-NHC complexes endowed with anticancer activity.

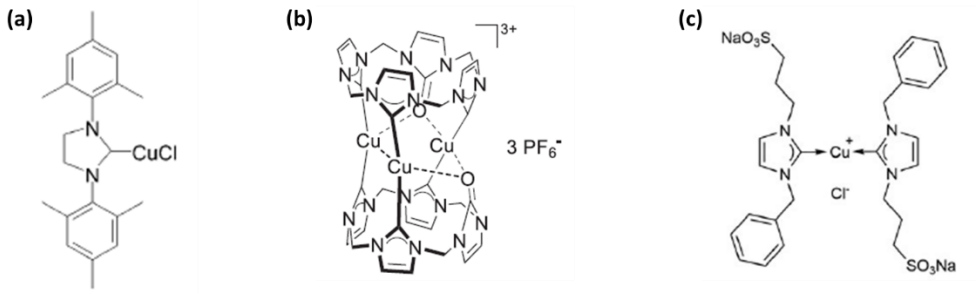

Figure 5.8: Chemical structure of some copper(I)-NHC complexes with anticancer activity. Adapted from Ref.[312,314,315]

Antimicrobial activity of copper(I) complexes

Antimicrobial-resistant (AMR) bacteria are rapidly emerging and spreading. At the same time, the lack of new antibiotics in clinical development determines serious threats to the world healthcare system. Consequently, there is an urgent need for more effective therapies to overcome AMR.[316]

Metal ions have a long history of serving as antimicrobial agents and metal complexes are now attracting more interest from scientific communities in the fight against AMR. The advantages of metallo-antimicrobials over traditional antibiotics lie in their multitargeted mechanisms, which render less likelihood to generate resistance. Moreover, metal complexes may also serve as antibiotic adjuvants to enhance the efficacy of clinically used antibiotics.[317]

In this context, copper compounds represent a great opportunity. Nevertheless, similarly to what is observed in anticancer research, copper(I) complexes have received much less attention than copper(II) species.

A careful inspection of literature highlighted the scarcity of data about the antimicrobial activity of phosphine-based copper(I) complexes. The class of compounds that has received more attention in this context is the class of mixed-ligand, neutral [Cu(N-N)(P)(X)] complexes.[302] These species displayed, together with anticancer properties, a very high *in vitro* antimicrobial activity against the Gram-positive bacterium *Staphylococcus aureus* and the yeast *Candida albicans*. In fact, the complexes with N-N = 2,9-dimethyl-1,10-phenanthroline (Figure 5.6) proved to be effective towards both strands with minimum inhibitory concentration (MIC) values in the range of 1-2 µg/mL.[307]

In a recent work, Pellei et al. reported the antibacterial activity of a novel class of cationic mixed-ligand copper(I) complexes against *Staphylococcus aureus* and the Gram-negative *Escherichia coli*.[318] The synthesized compounds are $[Cu(N)(P)_2]^+$ species, where N is a phenoxy-ketimine and P is a monodentate tertiary phosphine (Figure 5.9). The phosphine ligands PPh_3 (triphenylphosphine) and PTA were chosen in order to tune the lipophilicity of the final complexes. The copper(I) complexes derived from PTA, although being less effective compared to their silver(I) analogues, proved to be moderately active against both *S. aureus* and *E. coli* with MIC_{50} values around 50 – 100 µg/mL. Contrarily, the copper(I) complex with PPh_3 did not exhibit any antibacterial activity.

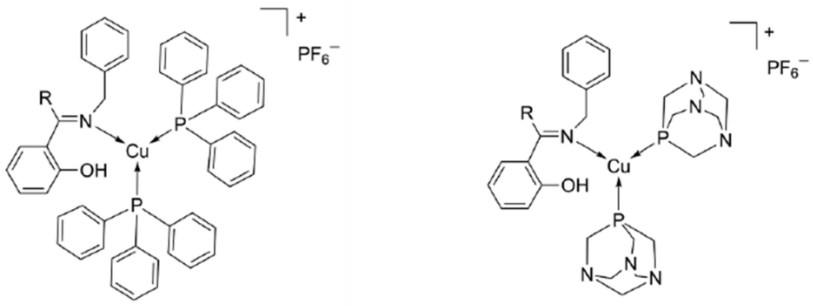

R = Ph R = Ph, Me

Figure 5.9: Chemical structure of the antimicrobial copper(I) complexes reported by Pellei and coworkers. Adapted from Ref.[318]

Similarly to what was observed for phosphine copper(I) complexes, until now most efforts on the development of metal-NHCs have been focused on their antitumour activities.[310] In contrast, the antimicrobial properties of metal-NHCs are less explored and are mainly limited to the silver(I) derivatives,

whose inhibition capacity comes from the release of silver ions. However, silver-NHCs often suffer deactivation by light due to the relatively unstable Ag-C bonds.[319] On the other hand, copper(I)-NHCs have been less studied although they are characterized by excellent stability towards air, moisture and light.[31,320]

Recently, Bernardi and coworkers performed a high-throughput screening of metal-NHC complexes against biofilm formation by several pathogenic bacteria.[321] In this study, copper(I)-NHCs displayed a remarkable inhibitory activity against *Listeria monocytogenes*, *Pseudomonas aeruginosa*, *Staphylococcus aureus*, and *Escherichia coli*. It was also found that copper(I)-NHCs exhibited comparable activity to silver(I)-NHCs, suggesting that copper-NHCs could serve as potential antibacterial agents.

Touj and coworkers found that the benzimidazole-based copper-NHCs presented significant inhibitory activity against food-borne pathogens and clinical microorganisms,[322] while Pan demonstrated the potential of copper(I)-NHC **Cu1** (Figure 5.10) as broad-spectrum inhibitor to treat oral bacteria, in particular for diminishing biofilm formation of *Streptococcus mutans*, one of the major agents responsible of dental caries.[323]

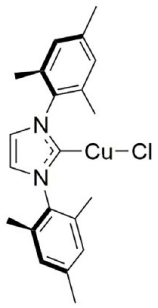

Cu1

Figure 5.10: Chemical structure of copper(I)-NHC **Cu1**, an antibacterial complex with a reported MIC value < 2 µg/mL against *Streptococcus mutans*. Adapted from Ref.[323]

Design of novel copper(I) complexes

To the best of our knowledge, no biological data are available for copper(I) complexes with P,N ligands. An interesting class of P,N ligands is the one of **iminophosphines**. They have been used extensively for the synthesis of complexes with gold[324] and palladium,[325-329] while few iminophosphine Cu(I) complexes are reported in literature.[330,331] Iminophosphines can act as **P-monodentate** or **P,N-bidentate ligands** towards Cu(I), as shown in Figure 5.11.

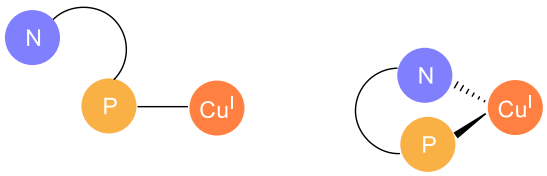

Figure 5.11: Coordination modes of iminophosphine ligands.

In this project, the iminophosphine **L^{1}** (Figure 5.12) was chosen as prototype ligand for a series of copper(I) complexes.

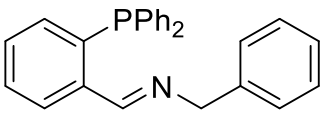

Figure 5.12: Chemical structure of iminophosphine **L^{1}**.

A synthetic strategy based on template reactions allowed to prepare a panel of iminophosphine copper(I) complexes by varying the stoichiometric ratio of the reagents and the nature of the anion of the copper(I) precursor (Scheme 5.1).

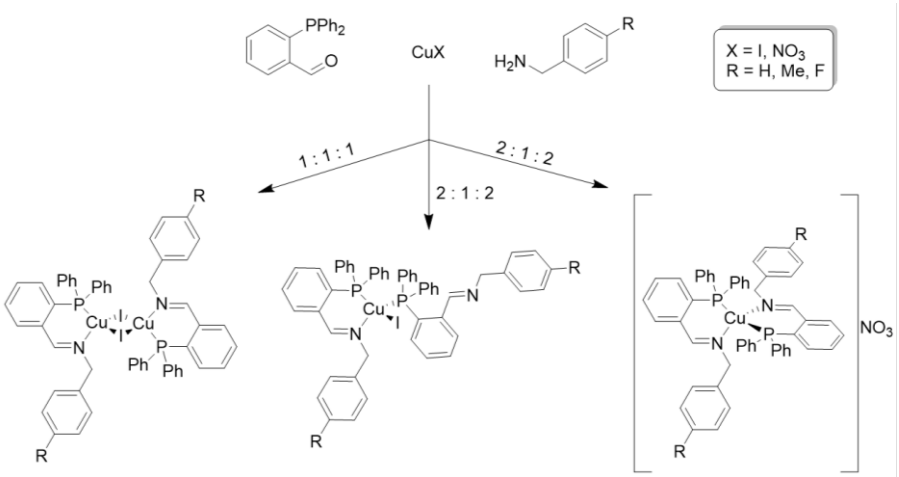

Scheme 5.1: Schematic representation of the synthetic routes to the iminophosphine copper(I) complexes studied in this project.

Some of the synthesized copper(I) complexes were investigated for their biological activity, showing promising antibacterial properties.

Results and discussion

Synthesis and characterization of iminophosphine copper(I) complexes

The iminophosphine **L[1]** was obtained by condensation reaction between 2-(diphenylphosphino)benzaldehyde and benzylamine (Scheme 5.2).

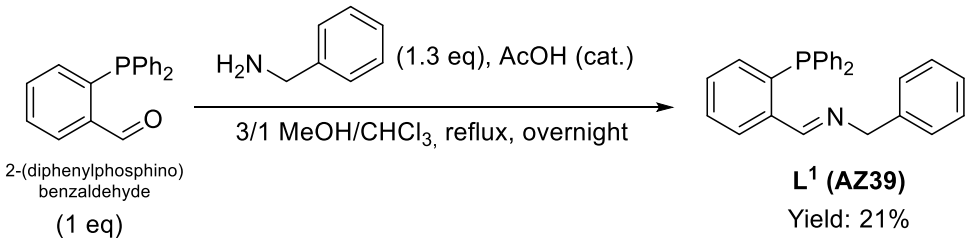

Scheme 5.2: Direct synthesis of iminophosphine **L[1]** (**AZ39**).

The direct synthesis of the iminophosphine proved to be affected by some drawbacks. The product was isolated only in poor yield (21%). In addition, **L[1]** was unstable on silica and therefore no column chromatography could be performed to purify the crude of the reaction. Consequentially, we carried out a template reaction between 2-(diphenylphosphino)benzaldehyde, benzylamine and a copper(I) precursor.

Copper(I) iodide was reacted with the aldehyde and benzylamine in 1:1:1 stoichiometric ratio in acetonitrile/chloroform mixture under inert atmosphere and the **1:1 iminophosphine:copper(I)** dimeric complex **[Cu(μ-I)L[1]]$_2$** (**AZ46**) was obtained as a red-orange powder (Scheme 5.3).

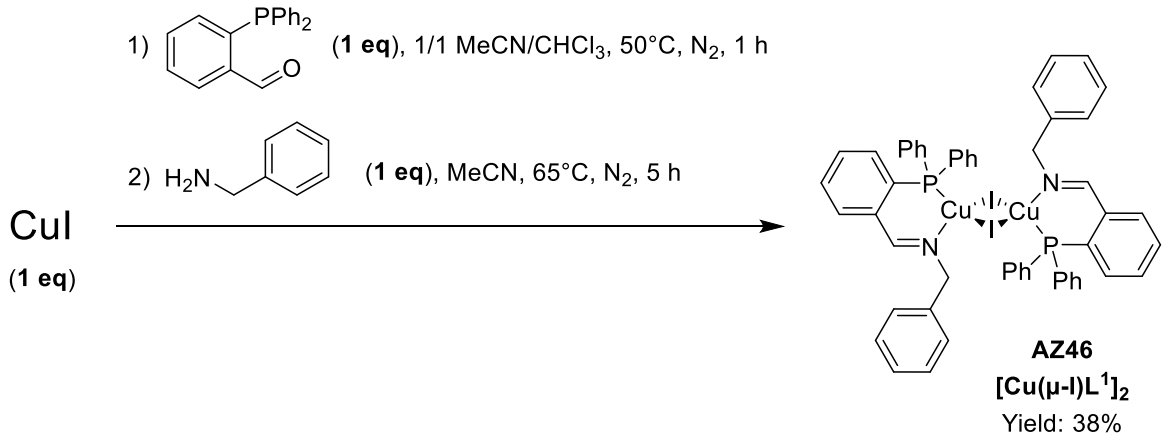

Scheme 5.3: Template synthesis of the dinuclear complex **[Cu(μ-I)L[1]]$_2$** (**AZ46**).

[Cu(μ-I)L[1]]$_2$ was characterized by means of FT-IR, ^{1}H and ^{31}P NMR spectroscopies, mass spectrometry, elemental analysis (see the experimental section) and single crystal XRD. The formation of the imine bond, and therefore the success of the template synthesis, was confirmed by the presence of a band at 1628 cm^{-1} in the IR spectrum of the complex. A comparison between the IR spectra of **[Cu(μ-I)L[1]]$_2$** and 2-(diphenylphosphino)benzaldehyde is shown in Figure 5.13.

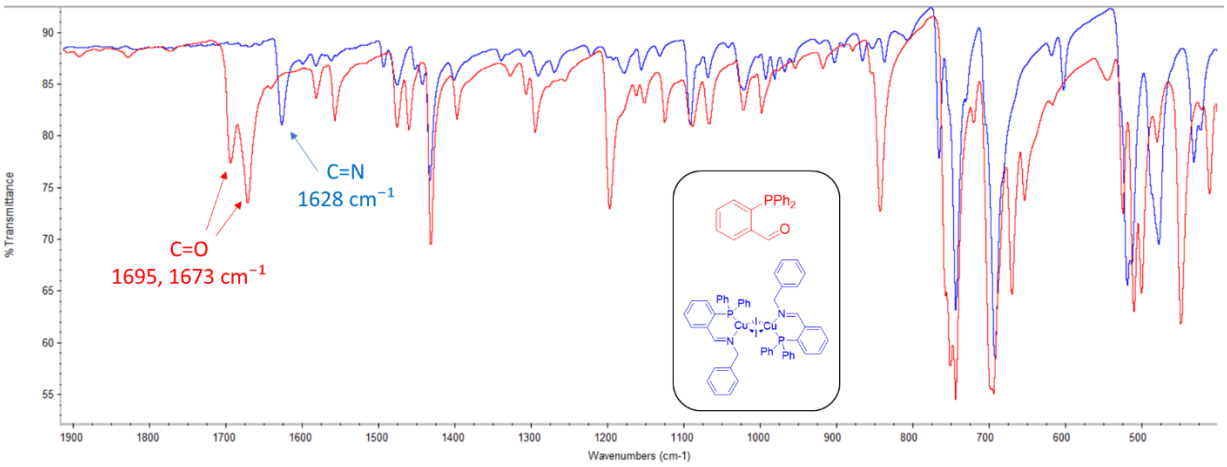

Figure 5.13: FT-IR spectra of **[Cu(μ-I)L^1]$_2$** (in blue) and 2-(diphenylphosphino)benzaldehyde (in red).

A comparison of the FT-IR spectrum of complex **[Cu(μ-I)L^1]$_2$** with ligand **L^1** shows the slight shift of the C=N stretching band towards lower wavenumbers upon coordination (Figure 5.14).

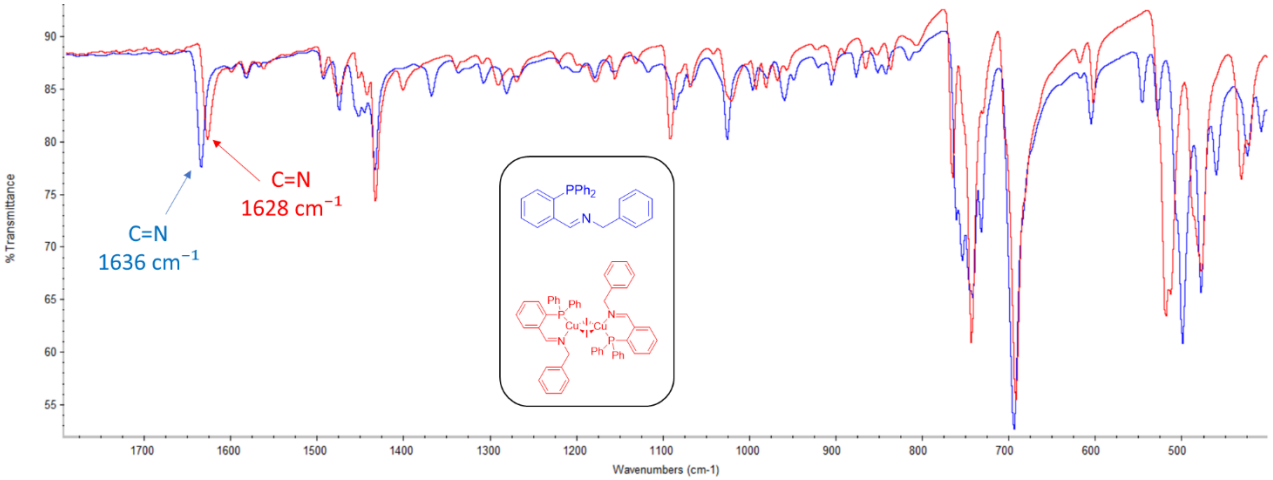

Figure 5.14: FT-IR spectra of **[Cu(μ-I)L^1]$_2$** (in red) and **L^1** (in blue).

Red-orange single crystals suitable for XRD analysis were obtained by slow evaporation of a solution of the complex in $CHCl_3$. The crystal data revealed a dinuclear structure with each copper atom coordinated to the P,N-bidentate iminophosphine and two iodine atoms (Figure 5.15a). The iodine atoms bind to the metal centres in a bridging mode. The phosphorus and nitrogen atoms of the two coordinated ligands adopt a *trans* configuration. The bite angle of the ligands is 90.6° and the coordination geometry of copper(I) is distorted tetrahedral (Figure 5.15b). The Cu-Cu distance is 3.049 Å, thus higher than the sum of the Van der Waals radii of two copper atoms (2.80 Å): this excludes the formation of any significant metallophilic interaction.

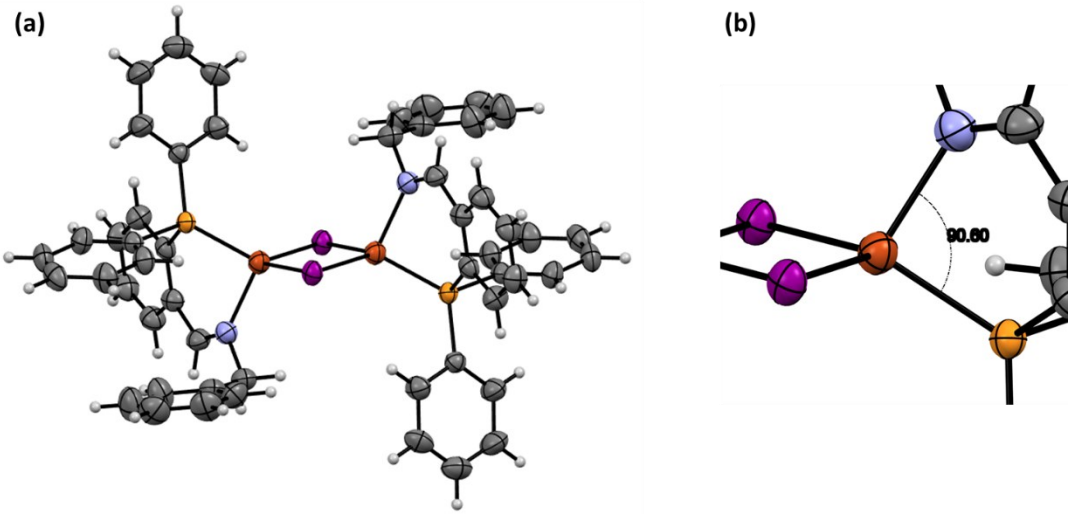

Figure 5.15: (a) ORTEP diagram of the crystal structure of complex **AZ46**, drawn with 50% probability ellipsoids; (b) coordination geometry of copper(I) centre with indication of the ligand bite angle (phosphorus atoms in light orange, nitrogen in blue, carbon in grey, hydrogens in white, iodine in purple, copper in dark orange).

The obtained complex proved to be the same as the compound reported by Süß and coworkers,[332] by using a different procedure. To the best of our knowledge, this is the unique copper(I) complex of iminophosphines derived from benzylamines to be already present in literature.

The complex is moderately soluble in DMSO, poorly soluble in chloroform, acetonitrile, acetone and insoluble in water, ethanol and *n*-hexane. In spite of its low solubility in chloroform, it was possible to measure the ^{1}H and ^{31}P NMR spectra of the complex in $CDCl_3$ (Figure 5.16).

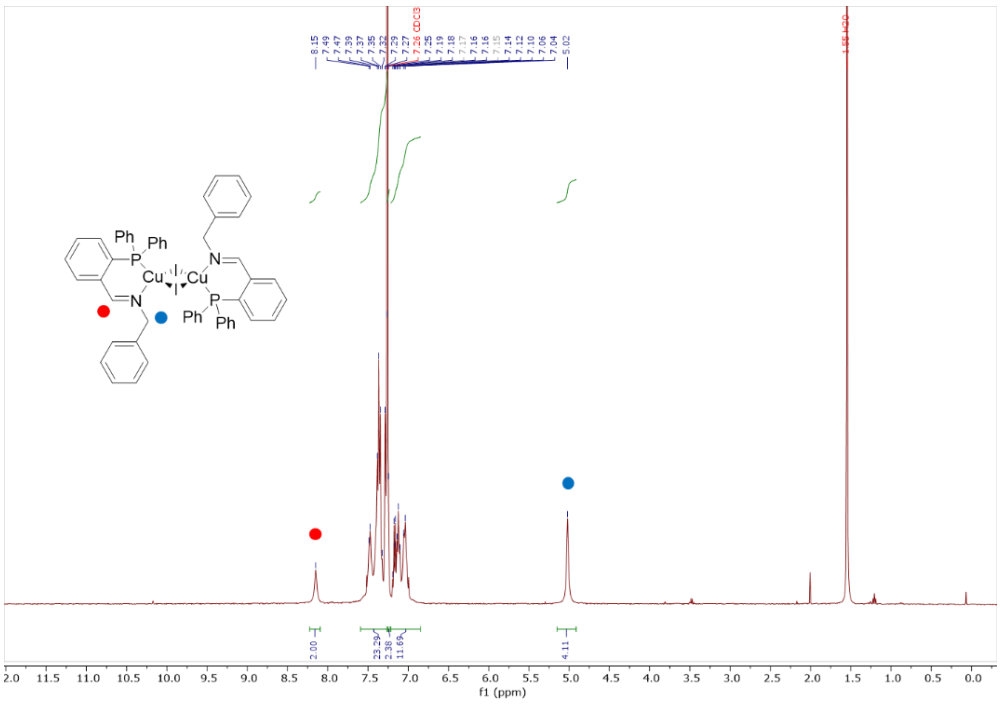

Figure 5.16: ^{1}H NMR (400 MHz, 298 K) spectrum of **$[Cu(\mu\text{-}I)L^{1}]_2$** in $CDCl_3$.

The comparison between the ^{1}H NMR (400 MHz, 298 K) spectra of complex **[Cu(μ-I)L^{1}]$_2$** and ligand **L^{1}** in $CDCl_3$ (Figure 5.17) evidences the broadening of the signals related to the complex. In fact, while in the spectrum of **L^{1}** the peak of the imine proton is a well resolved doublet (because of the coupling with the phosphorus nucleus[324], $J_{H,P}$ = 5.1 Hz), in the spectrum of **[Cu(μ-I)L^{1}]$_2$** the same signal is a broad singlet (Figure 5.17). The broadening is observed also in the ^{31}P NMR (162 MHz, 298 K) spectrum of the complex in $CDCl_3$ (Figure 5.18).

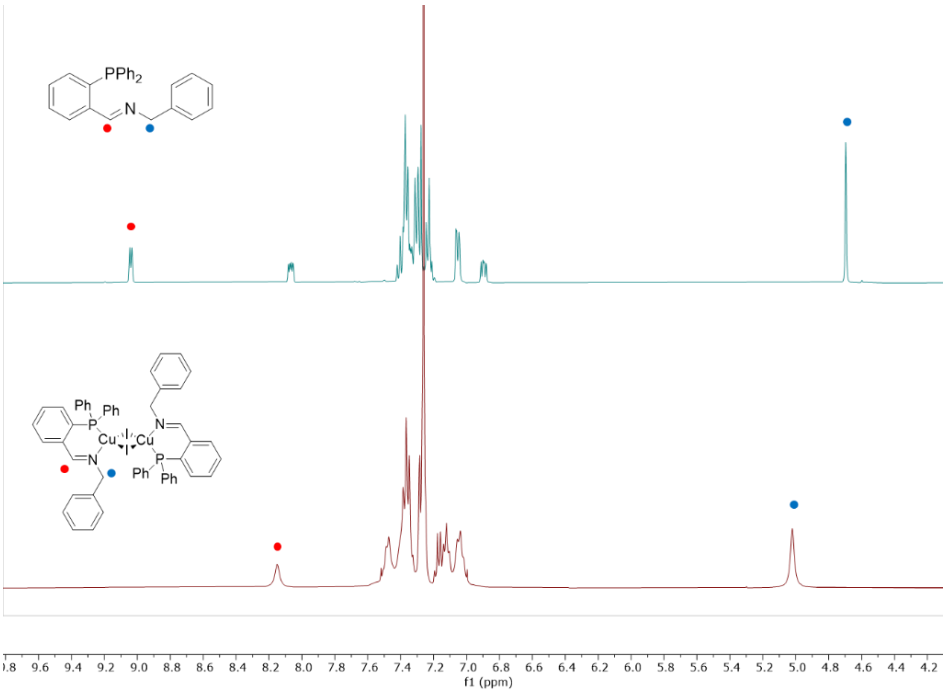

Figure 5.17: Selected range (4.20 – 9.80 ppm) of the ^{1}H NMR (400 MHz, 298 K) spectra of **L^{1}** (top) and **[Cu(μ-I)L^{1}]$_2$** (bottom) in $CDCl_3$.

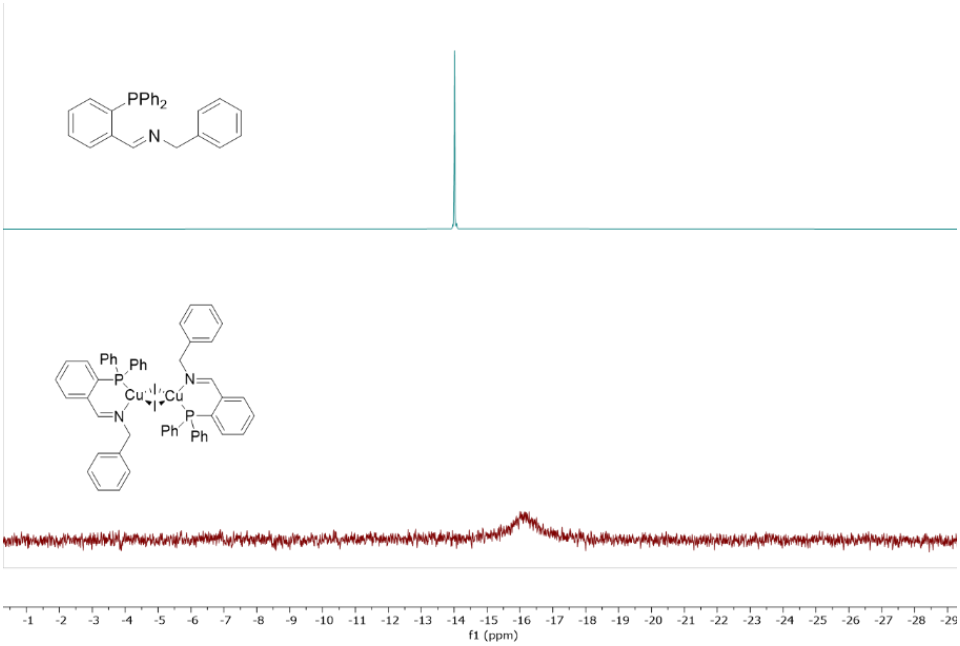

Figure 5.18: ^{31}P NMR (162 MHz, 298 K) spectra of **L^{1}** (top) and **[Cu(μ-I)L^{1}]$_2$** (bottom) in $CDCl_3$.

The NMR spectra measured in $CDCl_3$ show that, for the complex, both the phosphorus nucleus and the imine proton undergo a significant shielding with respect to the free ligand. More precisely, the imine proton signal of the free ligand can be found at 9.04 ppm, while the same peak for the coordinated ligand falls at 8.15 ppm. Similarly, the chemical shift of the phosphorus atom of $\mathbf{L^1}$ is -14.01 ppm, while for $\mathbf{[Cu(\mu\text{-}I)L^1]_2}$ is -16.13 ppm. This can be explained by the presence of coordinated iodide anion: the π-backbonding from the metal centre to the phosphorus atom and the imine moiety may be favoured by the iodide anions, which are σ and π donor ligands and therefore give electron density to the copper centre. Consequently, the electron rich metal centre backdonates to the π acceptor phosphorus and imine nitrogen atoms and their NMR signals result shielded.

The ^1H and ^{31}P NMR spectra of **AZ46** were measured also in DMSO-d_6: two broad signals were detected for the imine proton at 8.74 and 8.64 ppm (Figure A5.9) as well as for the phosphorus nucleus at -9.03 and -17.66 ppm (Figure A5.12). Being DMSO a coordinating solvent, probably it can take part in copper(I) coordination, giving rise to multiple complex species. In addition, it was found that $\mathbf{[Cu(\mu\text{-}I)L^1]_2}$ is not stable in DMSO-d_6 over time, since after one day another set of signals appeared in the ^1H NMR spectrum (Figure A5.10) and a peak at 28.77 ppm, attributable to a phosphine oxide, was detected in ^{31}P NMR spectrum (Figure A5.13).

In the ESI-MS spectrum (positive ions) of **AZ46** in MeCN it is present one signal at m/z = 442, associated to the $[CuL^1]^+$ species (Figure 5.19).

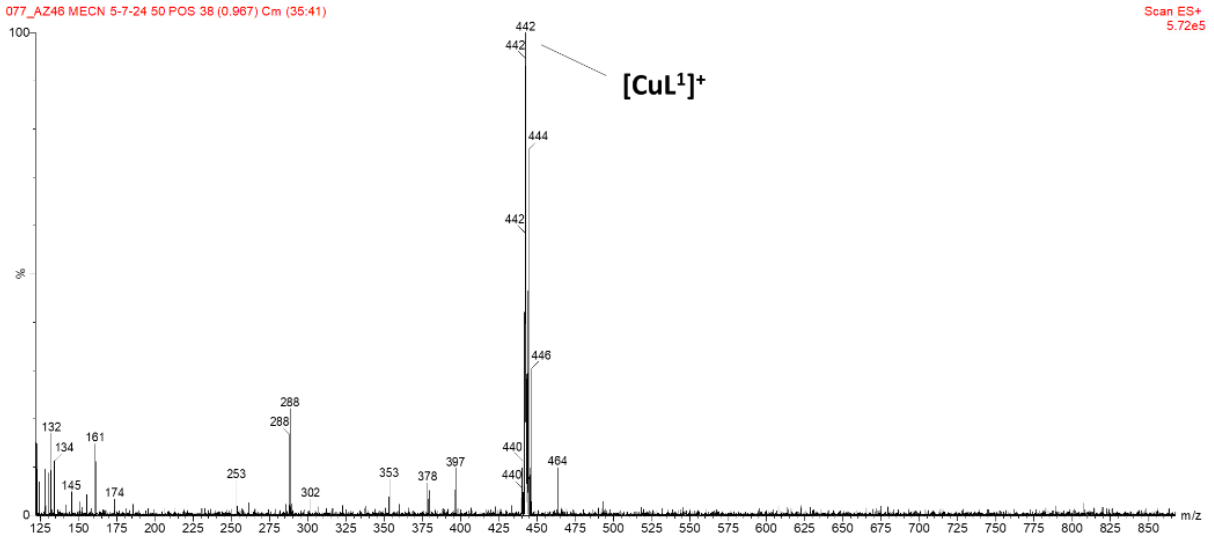

Figure 5.19: ESI-MS spectrum (positive ions) for complex **AZ46** in acetonitrile.

Applying the procedure used for **AZ46**, other two **1:1 iminophosphine:copper(I)** complexes, **AZ52** and **AZ54**, were synthesized and characterized (Scheme 5.4); ligands N-(2-(diphenylphosphino)phenyl)-methylene 4-methylbenzylamine and N-(2-(diphenylphosphino)phenyl)-methylene 4-fluorobenzylamine are indicated as $\mathbf{L^2}$ and $\mathbf{L^3}$, respectively. Single crystal XRD analysis allowed to identify the two complexes as structural analogues of **AZ46**, with general formula $\mathbf{[Cu(\mu\text{-}I)L^n]_2}$ (Figure 5.20).

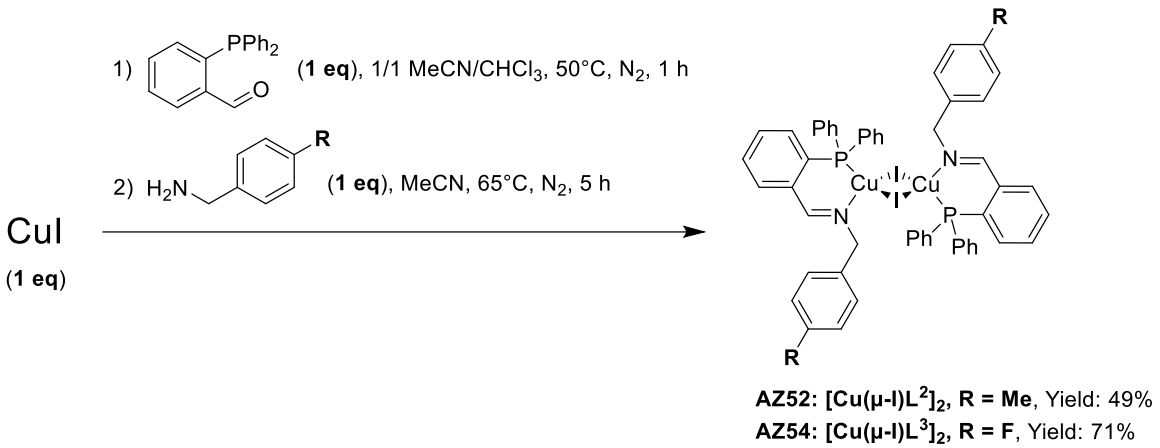

Scheme 5.4: Template synthesis of the dinuclear complexes **[Cu(μ-I)L^2]$_2$** (**AZ52**) and **[Cu(μ-I)L^3]$_2$** (**AZ54**).

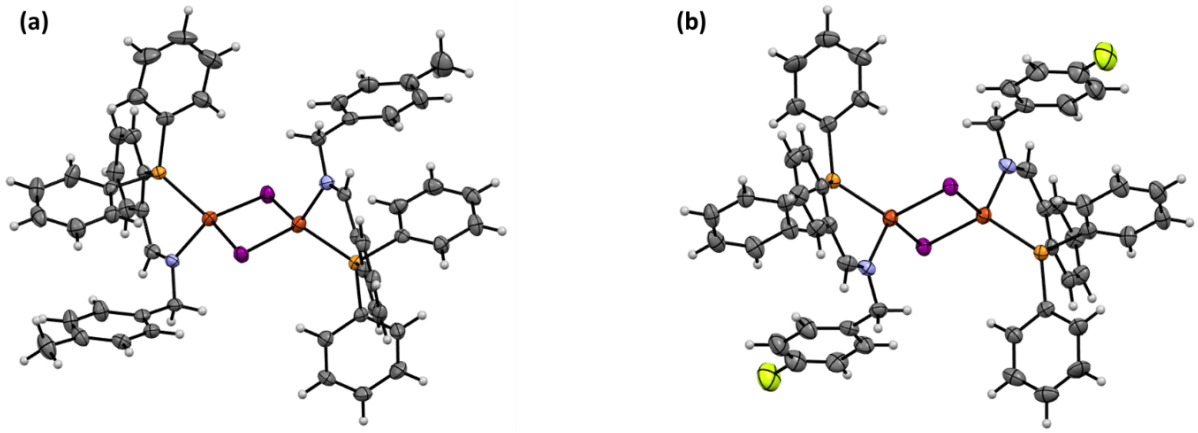

Figure 5.20: ORTEP diagrams of the crystal structures of complexes (a) **AZ52** and (b) **AZ54**, drawn with 50% probability ellipsoids (phosphorus atoms in light orange, nitrogen in blue, carbon in grey, hydrogens in white, iodine in purple, fluorine in yellow, copper in dark orange).

The two novel complexes were characterized by means of FT-IR (Figures A5.14 and A5.18), ^{1}H and ^{31}P NMR spectroscopies (Figures A5.15-16, A5.19 and A5.21), mass spectrometry (Figures A5.17 and A5.23) and elemental analysis (see the experimental section). Similarly to **AZ46**, **AZ54** is poorly soluble in chloroform, while **AZ52** is soluble. The complexes are stable in $CDCl_3$ over three days (Figures A5.20 and A5.22).

To gain some information about the mechanism of the template synthesis of **1:1 iminophosphine:copper(I)** complexes, also the 1:1 2-(diphenylphosphino)benzaldehyde:copper(I) complex, that forms in the initial step, was isolated (Scheme 5.5). The resulting compound (**AZ57, [Cu(μ-I)(MeCN)L^a]$_2$**) was characterized by means of FT-IR (Figure A5.69), ^{1}H and ^{31}P NMR spectroscopies (Figures A5.70-71), mass spectrometry (Figure A5.72), elemental analysis (see the experimental section) and powder XRD (P-XRD, Figure 5.21a).

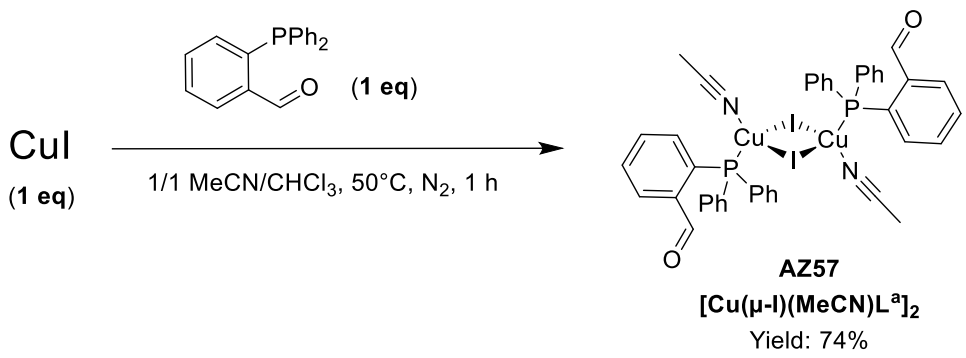

Scheme 5.5: Synthesis of the dimeric complex **[Cu(μ-I)(MeCN)L^a]$_2$** (**AZ57**). **L^a** indicates 2-(diphenylphosphino)benzaldehyde.

No single crystals suitable for XRD characterization were obtained, but the powder isolated from the synthesis was analysed by means of P-XRD. The experimental powder diffractogram of **AZ57** perfectly matched with the P-XRD pattern calculated from the crystallographic data of the complex, already reported in literature[333] (Figure 5.21).

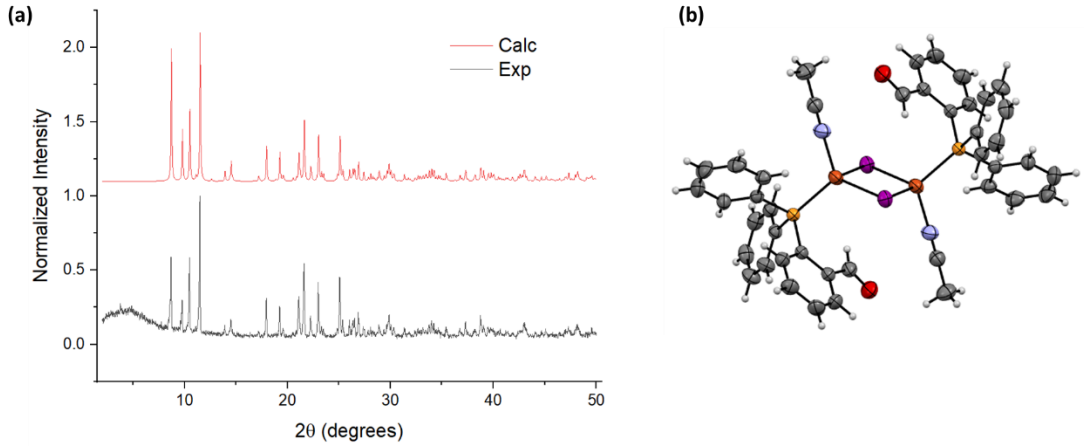

Figure 5.21: (a) Calculated (in red) and experimental (in black) powder diffractogram of complex **[Cu(μ-I)(MeCN)L^a]$_2$**; (b) ORTEP diagram of the crystal structure of **[Cu(μ-I)(MeCN)L^a]$_2$**, drawn with 50% probability ellipsoids[333] (phosphorus atoms in light orange, nitrogen in blue, carbon in grey, hydrogens in white, iodine in purple, oxygen in red, copper in dark orange).

AZ57 is a dinuclear species with the copper(I) centres coordinated to two bridging iodine atoms. The tetrahedral environment that surrounds each metal ion is completed by the nitrogen atom of acetonitrile molecules. It is interesting to note that the "hard" oxygen atoms of 2-(diphenylphosphino)benzaldehyde ligands are not involved in coordination of the "soft" copper(I) ion.

Since in the literature NMR and mass spectrometry data for **AZ57** are not reported, its full characterization is added in Appendix.

The template approach was explored also for the synthesis of **2:1 iminophosphine:copper(I)** complexes. Copper(I) iodide was reacted with 2-(diphenylphosphino)benzaldehyde and the desired benzylamine derivative in 1:2:2 stoichiometric ratio in acetonitrile/chloroform mixture under inert atmosphere (Scheme 5.6).

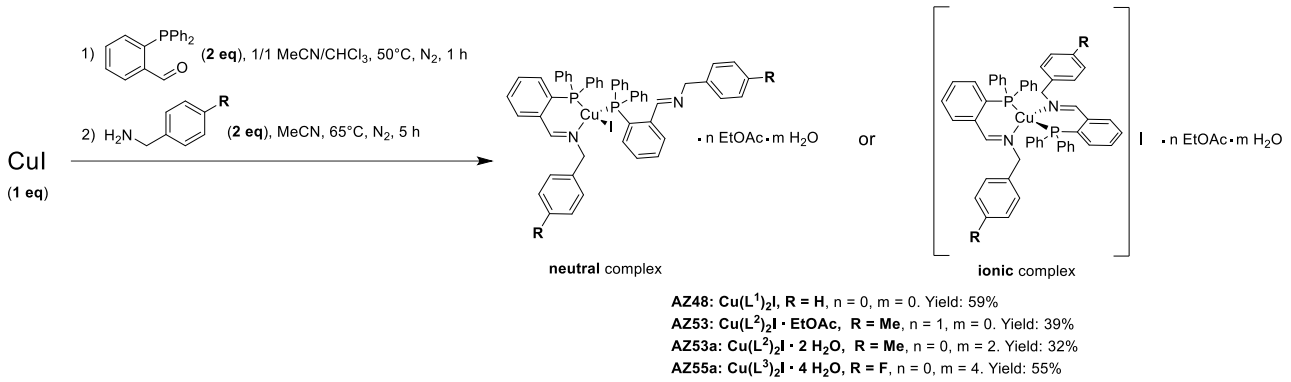

Scheme 5.6: Template synthesis of the **2:1 iminophosphine:copper(I)** complexes **AZ48**, **AZ53**, **AZ53a** and **AZ55a**.

Hypothesizing the formation of tetracoordinated species, the resulting complexes may exist in two possible forms: neutral or ionic (Scheme 5.6). In the structure of the neutral complex, one iminophosphine acts as P,N-bidentate ligand towards copper(I), while the other is P-monodentate and iodide completes the coordination sphere. On the contrary, in the ionic structure, both iminophosphines act as P,N-bidentate ligands and the iodide anion is out of the coordination sphere.

Here we discuss the characterization of the **Cu(L^1)$_2$I** (**AZ48**), that was obtained from benzylamine. The FT-IR spectrum of this 2:1 **L^1**:Cu complex shows little differences compared to the spectrum of the corresponding 1:1 **L^1**:Cu compound **AZ46** (Figure 5.22). Indeed, the Δν between the C=N stretching bands of the two complexes is only 3 cm^{-1}.

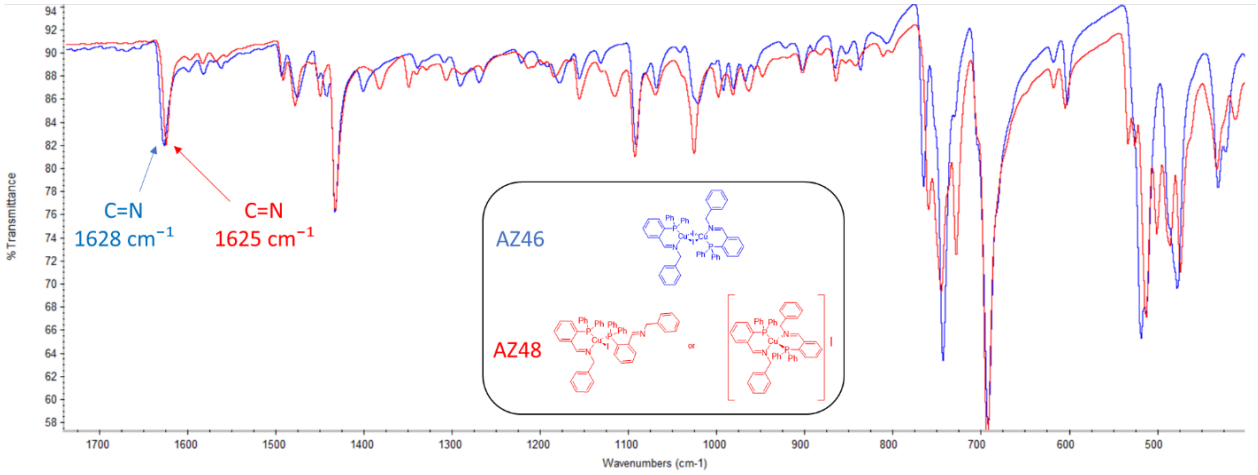

Figure 5.22: FT-IR spectra of **AZ46** (in blue) and **AZ48** (in red).

Contrarily to the dimeric complex, **Cu(L^1)$_2$I** is soluble in acetonitrile, chloroform and DMSO. The ^{1}H and ^{31}P NMR spectra of **AZ48** in $CDCl_3$ were measured and compared with the spectra of **AZ46** and **AZ39** (Figure 5.23).

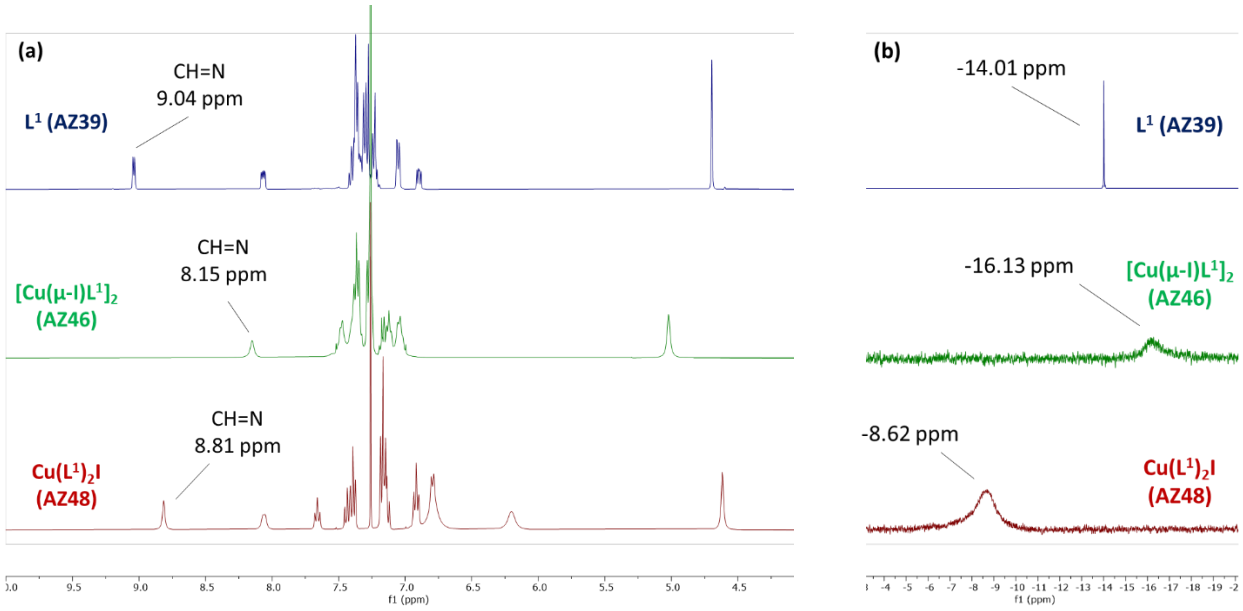

Figure 5.23: (a) **^{1}H NMR (400 MHz, 298 K)** spectra of **L^1** (top), **$[Cu(\mu\text{-}I)L^1]_2$** (middle) and **$Cu(L^1)_2I$** (bottom) in $CDCl_3$; (b) **^{31}P NMR (162 MHz, 298 K)** spectra of **L^1** (top), **$[Cu(\mu\text{-}I)L^1]_2$** (middle) and **$Cu(L^1)_2I$** (bottom) in $CDCl_3$.

The same broadening of signals observed for **AZ46** was found also in the NMR spectra of **AZ48** (Figure 5.23).

It is interesting to note that, in $CDCl_3$, while the signal of the imine proton of the coordinated ligand in complex **AZ48** is slightly shielded with respect to the peak of the imine proton of the free ligand, the phosphorus nucleus of **AZ48** experiments a significant deshielding compared to the phosphorus of **AZ39** (Figure 5.23). This could be consistent with **AZ48** existing in solution in the ionic form: in such form, the two coordinated ligands are both P,N-bidentate and the iodide ligand, being out of the coordination sphere, cannot donate electron density on the copper(I) centre. Consequently, the π-backbonding from the metal centre to the phosphorus atom is unfavoured and the phosphine ligand may act principally as σ donor, leading to a downfield shifted signal in the ^{31}P NMR spectrum.

The ^{1}H and ^{31}P NMR data obtained in $CDCl_3$ showed that the trend of CH=N and P signals observed for the complexes of **L^1** (R = H) is the same also for the complexes of **L^2** (R = F) and **L^3** (R = F) (Tables 5.1 and 5.2).

Table 5.1: Chemical shift values for the CH=N signal in the ^{1}H NMR (400 MHz, chloroform-*d*, 298 K) spectra of the 1:1 and 2:1 iminophosphine:copper(I) complexes derived from CuI.

^{1}H NMR ($CDCl_3$), δ(CH=N) (ppm)	$[Cu(\mu\text{-}I)L]_2$	CuL_2I
R = H	8.15 (**AZ46**)	8.81 (**AZ48**)
R = Me	8.13 (**AZ52**)	8.79 (**AZ53**)
R = F	8.16 (**AZ54**)	8.82 (**AZ55a**)

Table 5.2: Chemical shift values for the phosphorus signal in the ^{31}P NMR (162 MHz, chloroform-*d*, 298 K) spectra of the 1:1 and 2:1 iminophosphine:copper(I) complexes derived from CuI.

$^{31}P\{H\}$ NMR ($CDCl_3$), δ (ppm)	$[Cu(\mu\text{-}I)L]_2$	CuL_2I
R = H	-16.13 (**AZ46**)	-8.62 (**AZ48**)
R = Me	-15.72 (**AZ52**)	-8.74 (**AZ53**)
R = F	-15.77 (**AZ54**)	- 8.90 (**AZ55a**)

The trend of the phosphorus signal in ^{31}P NMR spectra is coherent with what was reported for the copper(I) complexes of another P,N chelate ligand (Figure 5.24).

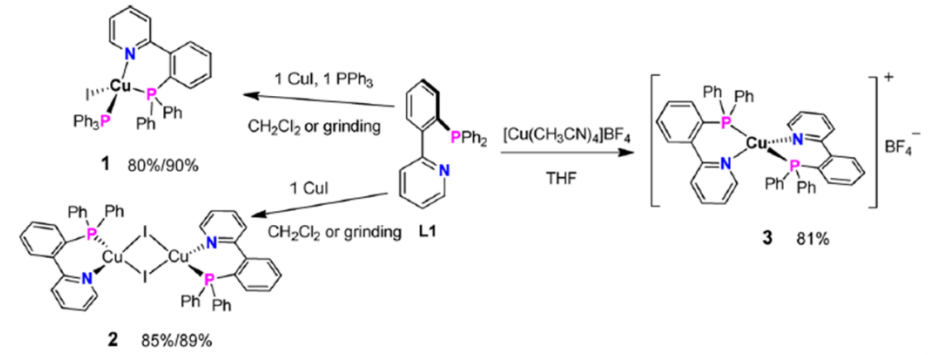

$^{31}P\{H\}$ NMR ($CDCl_3$), δ (ppm)	Free ligand	Complex 1	Complex 2	Complex 3
L1	- 10.1	-13.85	-13.94	-4.68
PPh_3	- 4.93	-1.39	-	-

Figure 5.24: (Top) Synthesis and structure of the copper(I) complexes reported by Zeng and coworkers, adapted from Ref.[334]; (bottom) table with the ^{31}P chemical shift values of the free and coordinated ligands measured in $CDCl_3$.[334,335]

The phosphorus signal of ligand **L1** in the ionic complex **3** was found to be significantly deshielded compared to the same signal in the spectra of the free ligand, the dimeric complex **2** and the neutral complex **1** (Figure 5.24). This finding further supports the hypothesis of complex **AZ48** existing in ionic form in $CDCl_3$.

All the **2:1 iminophosphine:copper(I)** complexes proved to be stable in $CDCl_3$ over one week (only traces of phosphine oxide were detected, as shown in Figure A5.30).

^{1}H and ^{31}P NMR measurements were carried out also in DMSO-d_6 (see Appendix). Here we discuss the data collected for **AZ48**. In DMSO-d_6, **AZ48** was much more stable than **AZ46**, since only traces of phosphine oxide were observed after leaving the sample in air for two days (Figure A5.32). In addition, only one signal was

observed for both the imine proton and the phosphorus nucleus of the coordinated ligand (Figures 5.25 and A5.31), suggesting that the structure of the complex in DMSO-d_6 is the same as the one displayed in $CDCl_3$.

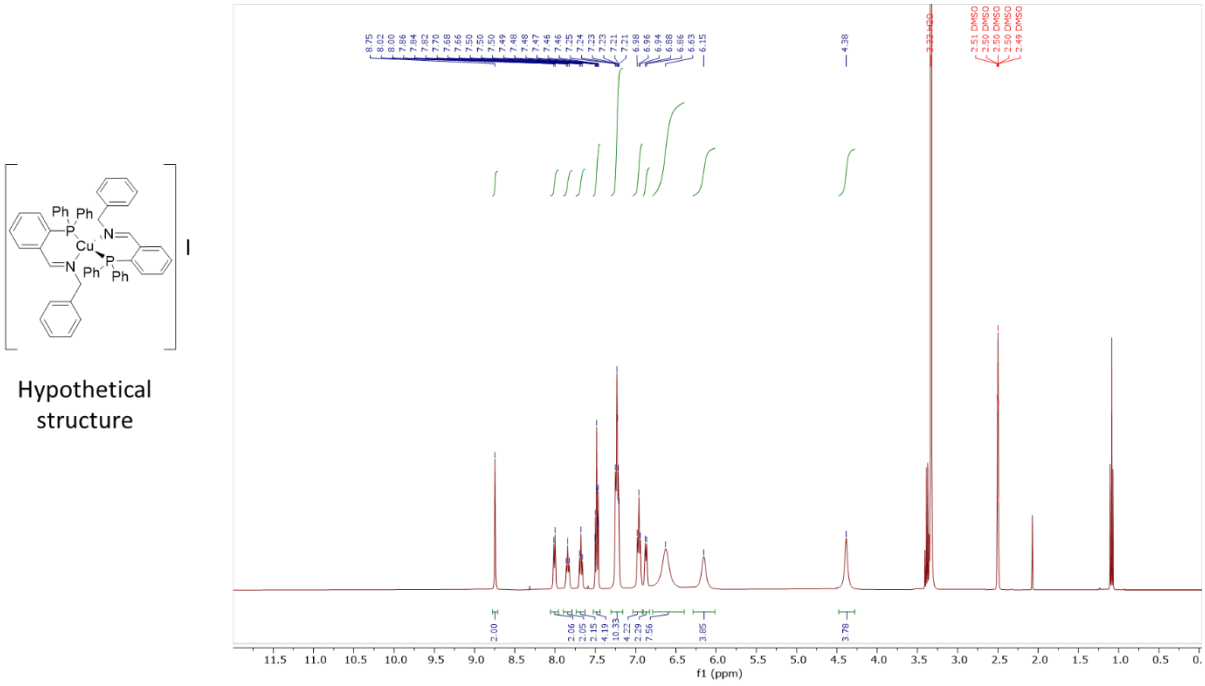

Figure 5.25: ^{1}H NMR (400 MHz, 298 K) spectrum of **AZ48** in DMSO-d_6.

The solubility of the **2:1 iminophosphine:copper(I)** complexes proved to be strongly affected by the para-substituent of the benzylamine precursors. This led to the employment of different work-up conditions for the various products. In fact, while **AZ48** precipitated from the reaction mixture after addition of diethyl ether, this procedure failed for **AZ53** (R = Me), which in turn was isolated by concentration of the reaction mixture and addition of ethyl acetate. The product co-crystallized with the solvent to give complex **Cu(L^2)$_2$I · EtOAc**, as indicated by IR (Figure A5.36), ^{1}H NMR (Figure A5.37) and elemental analysis data (see the experimental section). Remarkably, slow evaporation of mother liquors from the synthesis of **AZ53** afforded single crystals of the complex **Cu(L^2)$_2$I** (Figure 5.26).

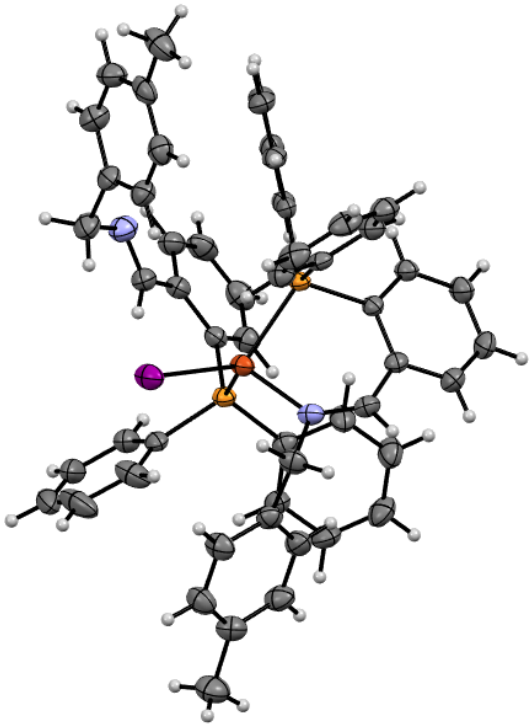

Figure 5.26: ORTEP diagram of the crystal structure of **Cu(L^2)$_2$I**, drawn with 50% probability ellipsoids (phosphorus atoms in light orange, nitrogen in blue, carbon in grey, hydrogens in white, iodine in purple, copper in dark orange).

The complex is in the neutral form, with one ligand acting as P,N-bidentate towards copper(I), and the other in P-monodentate fashion; iodide completes the distorted tetrahedral coordination sphere. Unfortunately, it was not possible to determine by P-XRD analysis if such structure was the same also for the powder isolated from the synthesis. All the attempts made to obtain single crystals from the sample of **AZ53** failed.

In order to isolate the 2:1 **L^2**:Cu^I complex without co-crystallized solvents, the synthesis of the complex was repeated, but the work-up conditions were changed. The reaction mixture was concentrated to dryness and the product was recrystallized from $CHCl_3$/n-hexane mixture. The resulting complex **AZ53a** proved to have formula **Cu(L^2)$_2$I · 2 H_2O**, as confirmed by elemental analysis (see the experimental section).

Both complexes **AZ53** and **AZ53a** were characterized by means of FT-IR (Figures A5.36 and A5.40), ^1H and ^{31}P NMR spectroscopies (Figures A5.37-38 and A5.41-43), mass spectrometry (Figures A5.39 and A5.44) and elemental analysis (see the experimental section).

The isolation of complex **AZ55a** proved to be the most challenging. Indeed, the application of the synthetic protocol used for **AZ48** did not allow to recover the desired 2:1 ligand:metal species, but the dimeric 1:1 **L^3**:Cu^I complex **AZ54**. Only by employing a 1:3:3 copper(I):aldehyde:amine stoichiometric ratio was possible to obtain the 2:1 **L^3**:Cu^I compound in moderate yields. The isolated complex **AZ55a** was hygroscopic and elemental analysis allowed to assign the formula **Cu(L^3)$_2$I · 4 H_2O** (see the experimental section).

Similarly to the template synthesis of 1:1 iminophosphine:copper(I) complexes, also in the preparation of the **2:1 ligand:metal** derivatives it was observed the formation of a precipitate after the addition of CuI to the solution of 2-(diphenylphosphino)benzaldehyde. This compound (**AZ58**) was isolated (Scheme 5.7) and characterized by means of FT-IR (Figure A5.73), ^{1}H and ^{31}P NMR spectroscopies (Figures A5.74-75), mass spectrometry (Figure A5.76), elemental analysis (see the experimental section) and powder XRD (P-XRD, Figure A5.77).

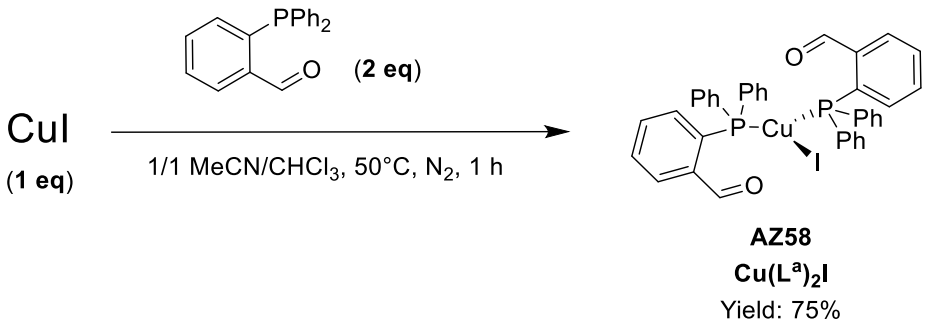

AZ58
Cu(L^{a})$_2$I
Yield: 75%

Scheme 5.7: Synthesis of the complex **Cu(L^{a})$_2$I** (**AZ58**). **L^{a}** indicates 2-(diphenylphosphino)benzaldehyde.

Single crystals suitable for XRD analysis were obtained by slow evaporation of a solution of the complex in $CHCl_3$. The crystal data revealed a slightly distorted trigonal planar complex with both aldehydic ligands binding copper(I) in P-monodentate fashion and the iodine atom completing the coordination sphere (Figure 5.27). This structure was already reported in literature.[333]

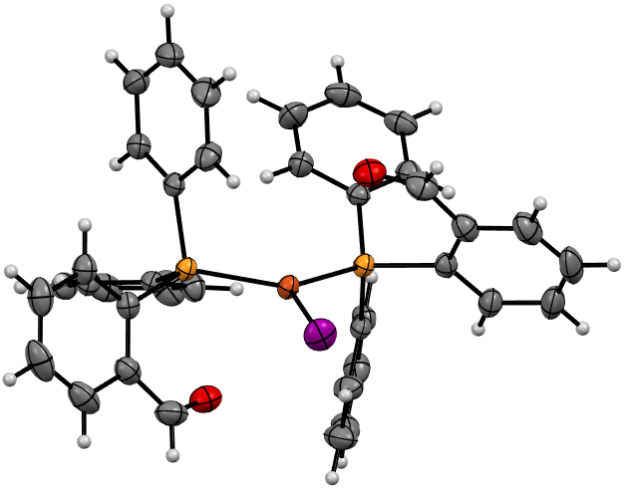

Figure 5.27: ORTEP diagram of the crystal structure of **Cu(L^{a})$_2$I** (**AZ58**), drawn with 50% probability ellipsoids (phosphorus atoms in light orange, carbon in grey, hydrogens in white, iodine in purple, oxygen in red, copper in dark orange).

Powder XRD analysis allowed to confirm that the structure of the complex isolated from the synthesis was the same as the one of the crystallized species (Figure A5.77). As observed for **AZ57**, the "hard" oxygen atoms of 2-(diphenylphosphino)benzaldehyde ligands are not involved in coordination of the "soft" copper(I) ion.

After the detailed characterization of template synthesis with CuI as copper(I) precursor, we wanted to explore the template approach with a counterion different from iodide. The nitrate ion was selected both to study the effect of this less coordinating anion on the structure of the products and to endow the final complexes with solubility in aqueous medium.

Copper(I) nitrate is an unstable inorganic compound that has never been isolated. Nevertheless, it is possible to synthesize the complex $[Cu(MeCN)_4]NO_3$ and use it as copper(I) precursor. As for several other $[Cu(MeCN)_4]X$ complexes, where X = halide, PF_6^-, BF_4^- or ClO_4^-, it can be prepared in two main different ways[336-339] (Scheme 5.8): (**1**) reaction of copper(I) oxide with HX in acetonitrile or (**2**) comproportionation reaction of a copper(II) salt CuX_2 with metallic copper in acetonitrile.

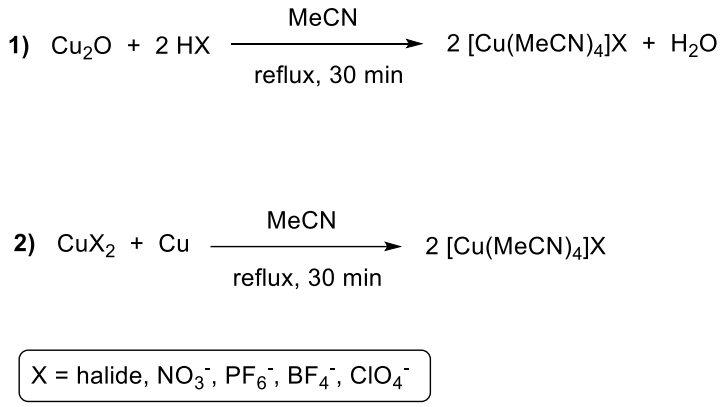

Scheme 5.8: Synthetic routes to $[Cu(MeCN)_4]X$ complexes.

Here, route (**2**) was chosen and a panel of three **2:1 iminophosphine:copper(I)** complexes was prepared (Scheme 5.9). Since $[Cu(MeCN)_4]NO_3$ is reported to be much more stable in solution than in solid state,[336] the applied protocol was based on the direct addition of 2-(diphenylphosphino)benzaldehyde and the desired amine to the solution of $[Cu(MeCN)_4]NO_3$ in acetonitrile obtained *in situ*.

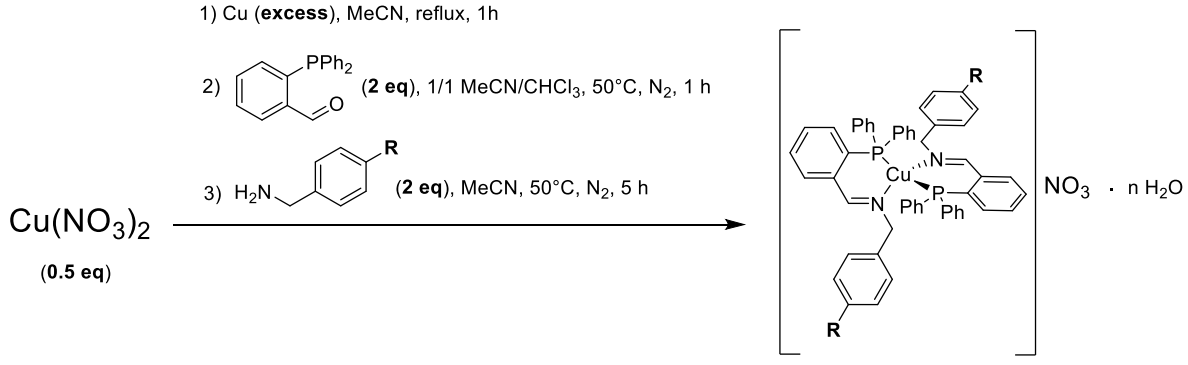

AZ61: $[Cu(L^1)_2]NO_3$, R = H, n = 0. Yield: 64%
AZ65: $[Cu(L^2)_2]NO_3 \cdot H_2O$, R = Me, n = 1. Yield: 69%
AZ66: $[Cu(L^3)_2]NO_3 \cdot 2\ H_2O$, R = F, n =2. Yield: 69%

Scheme 5.9: Template synthesis of the **2:1 iminophosphine:copper(I)** complexes **AZ61**, **AZ65** and **AZ66**.

The complexes were characterized by means of FT-IR, ^{1}H and ^{31}P NMR spectroscopies, mass spectrometry and elemental analysis (see the experimental section). Here we discuss the characterization of complex **[Cu(L^{1})$_2$]NO$_3$** (**AZ61**).

A comparison of the FT-IR spectrum of complex **[Cu(L^{1})$_2$]NO$_3$** with ligand **L^{1}** shows the shift of the C=N stretching band towards lower wavenumbers and the appearance of a strong band at 1344 cm^{-1}, attributable to the nitrate anion, upon coordination (Figure 5.28). The presence of only one strong band in the range 1400 – 1300 cm^{-1} suggests that the complex is ionic in the solid state.[340]

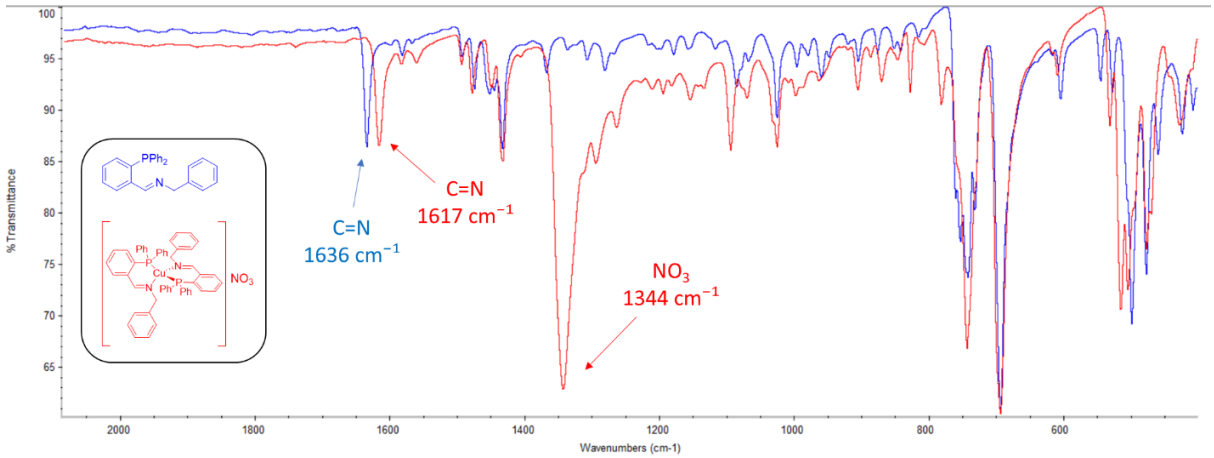

Figure 5.28: FT-IR spectra of **[Cu(L^{1})$_2$]NO$_3$** (in red) and **L^{1}** (in blue).

Single crystals of **[Cu(L^{1})$_2$]NO$_3$** suitable for XRD analysis were obtained by slow evaporation of mother liquors from the synthesis. In agreement with the IR spectrum, the crystal data revealed an ionic structure and a distorted tetrahedral geometry around the copper(I) centre (Figure 5.29). Unfortunately, in the crystal structure, the imine group of one of the two P,N-bidentate ligands is characterized by disorder.

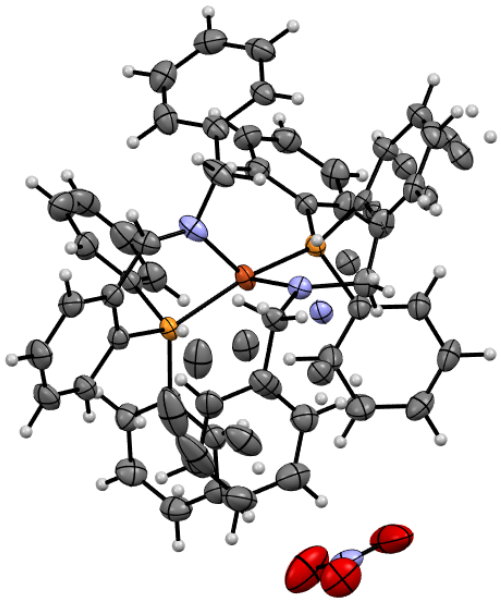

Figure 5.29: ORTEP diagram of the crystal structure of **[Cu(L^{1})$_2$]NO$_3$** (**AZ61**), drawn with 50% probability ellipsoids (phosphorus atoms in light orange, carbon in grey, hydrogens in white, nitrogen in blue, oxygen in red, copper in dark orange).

AZ61 proved to be soluble in acetonitrile, chloroform, DMSO and methanol. Similarly to what was observed for the 2:1 ligand:metal complexes derived from CuI, also in the ^{1}H and ^{31}P NMR spectra of **AZ61** in $CDCl_3$ and DMSO-d_6 are present one signal for the imine proton and one signal for the phosphorus atom, supporting the idea that the complex exhibits an ionic structure also in solution. In Figures 5.30-31 the ^{1}H and ^{31}P NMR spectra of **AZ61** recorded in DMSO-d_6 are reported. In this solvent, the complex showed stability over one week: no formation of phosphine oxide species was detected (Figure 5.31).

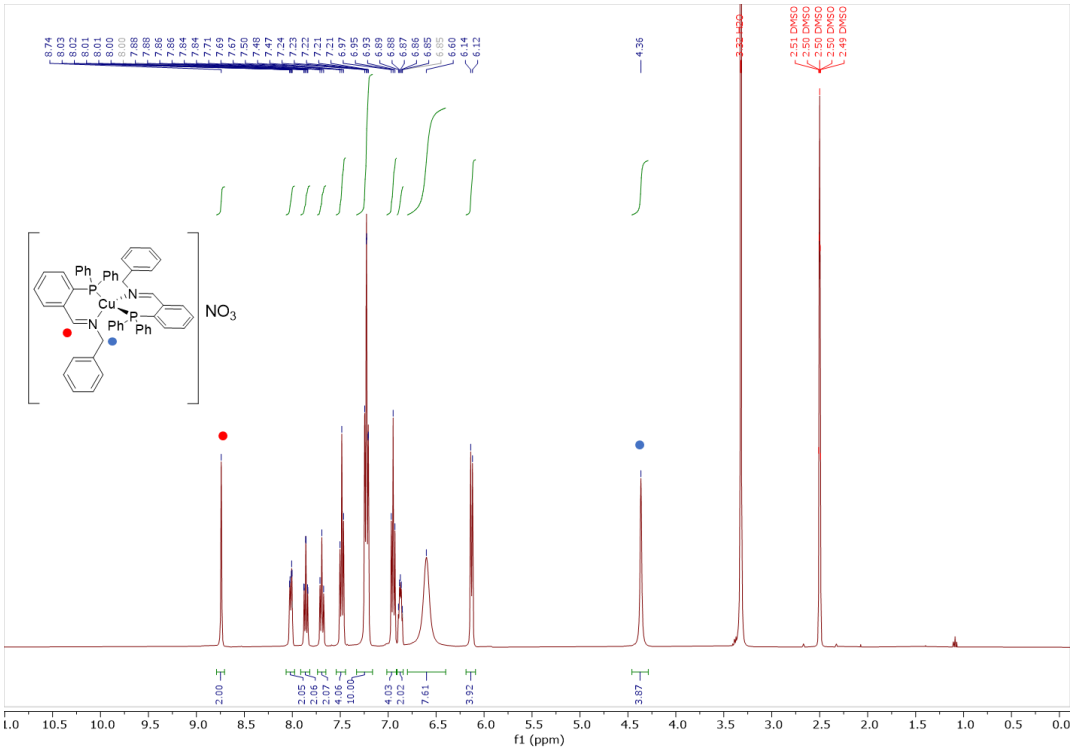

Figure 5.30: ^{1}H NMR (400 MHz, 298 K) spectrum of **AZ61** in DMSO-d_6.

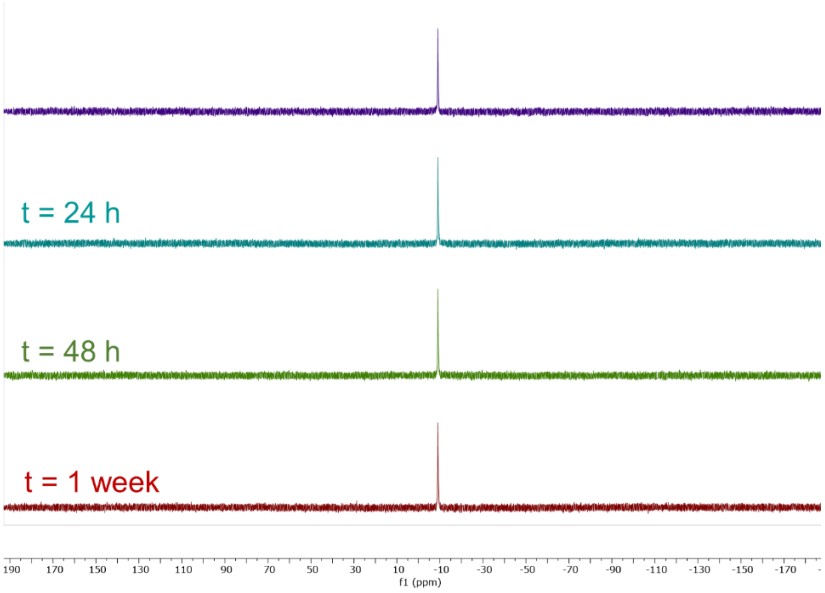

Figure 5.31: ^{31}P NMR (162 MHz, 298 K) spectrum of **AZ61** in DMSO-d_6 measured immediately after preparation of the sample (purple), after 24 hours (blue-green), 48 hours (green) and one week (red).

The behaviour of **AZ65** and **AZ66** was analogous to **AZ61**. In Tables 5.3 and 5.4 the chemical shift values for the CH=N and phosphorus signals of the three complexes in $CDCl_3$ and DMSO-d_6 are reported.

Table 5.3: Chemical shift values for the CH=N signal in the ^1H NMR spectra of the 2:1 iminophosphine:copper(I) complexes with nitrate counteranion in $CDCl_3$ and DMSO-d_6.

^1H NMR, δ(CH=N) (ppm)	$CDCl_3$	DMSO-d_6
AZ61 (R = H)	8.73	8.74
AZ65 (R = Me)	8.69	8.71
AZ66 (R = F)	8.79	8.76

Table 5.4: Chemical shift values for the phosphorus signal in the ^{31}P NMR spectra of the 2:1 iminophosphine:copper(I) complexes with nitrate counteranion in $CDCl_3$ and DMSO-d_6.

$^{31}P\{H\}$ NMR, δ (ppm)	$CDCl_3$	DMSO-d_6
AZ61 (R = H)	-7.68	-9.07
AZ65 (R = Me)	-7.85	-9.13
AZ66 (R = F)	-7.54	-8.96

Contrarily to what was observed in the template synthesis with CuI, no precipitation occurred after addition of 2-(diphenylphosphino)benzaldehyde to the solution of $[Cu(MeCN)_4]NO_3$. In order to elucidate the structure of the "intermediate" 2:1 aldehyde:copper(I) species, such complex was isolated by concentration of the aldehyde-$[Cu(MeCN)_4]NO_3$ mixture and subsequent addition of diethyl ether: yellow crystals of novel complex **AZ67** were obtained. The synthesis is reported in Scheme 5.10.

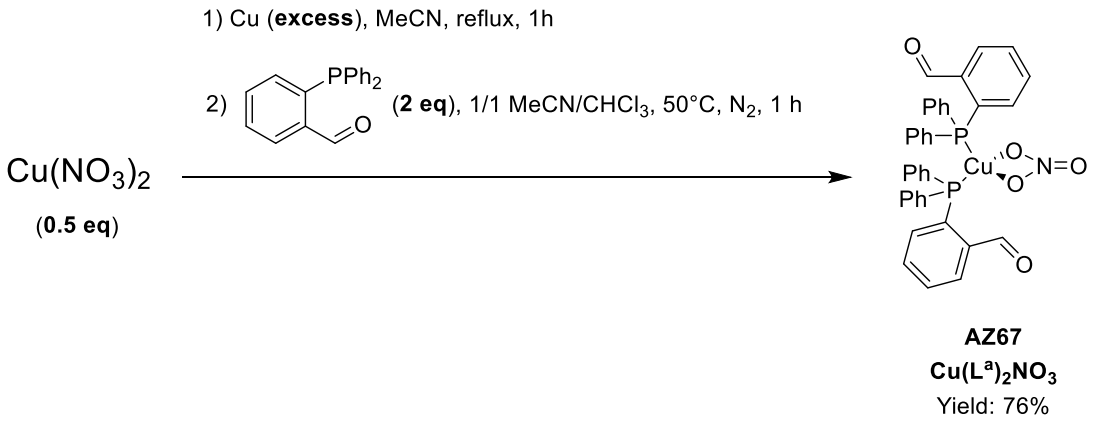

AZ67
$Cu(L^a)_2NO_3$
Yield: 76%

Scheme 5.10: Synthesis of the complex **$Cu(L^a)_2NO_3$** (**AZ67**). **L^a** indicates 2-(diphenylphosphino)benzaldehyde.

A comparison of the FT-IR data of complex **Cu(L^a)$_2$NO$_3$** with ligand **L^a** shows the appearance of two strong bands at 1434 and 1286 cm^{-1} in the spectrum of the former (Figure 5.32). Such bands are ascribable to N-O stretching. According to literature,[340,341] the presence of these two bands indicates that the nitrate group is coordinated to the metal, although it is not possible to determine from IR data if it acts as mono- or bidentate ligand.

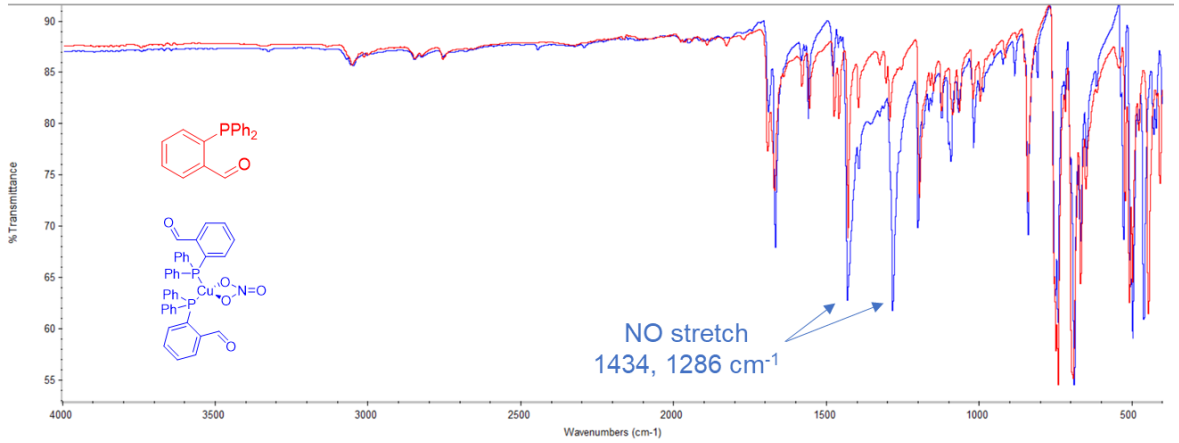

Figure 5.32: FT-IR spectra of **Cu(L^a)$_2$NO$_3$** (in blue) and **L^a** (in red). **L^a** indicates 2-(diphenylphosphino)benzaldehyde.

Single crystals of Cu(L^a)$_2$NO$_3$ useful for X-ray diffraction analysis were selected from the sample. In the crystal structure, the nitrate ligand is bidentate with a bite angle of 56.4° (Figure 5.33b), while the two molecules of 2-(diphenylphosphino)benzaldehyde act as P-monodentate ligands (Figure 5.33a). The P-Cu-P angle is 128.9° (Figure 5.33b) and the coordination geometry around the copper(I) centre is therefore a distorted tetrahedron.

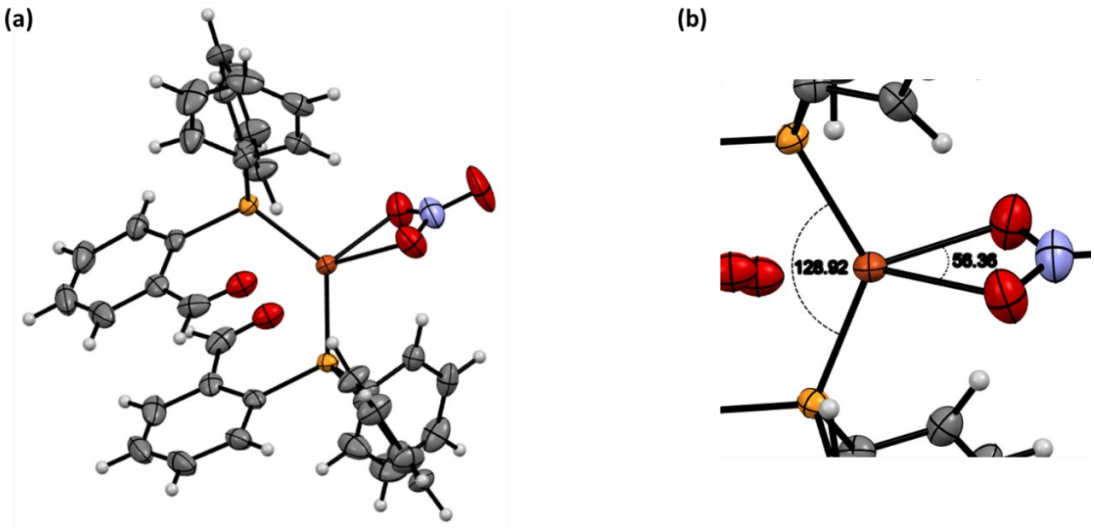

Figure 5.33: (a) ORTEP diagram of the crystal structure of complex **AZ67**, drawn with 50% probability ellipsoids; (b) coordination geometry of copper(I) centre with indication of P-Cu-P and O-Cu-O angles (phosphorus atoms in light orange, nitrogen in blue, carbon in grey, hydrogens in white, oxygen in red, copper in dark orange).

The complex is soluble in acetonitrile, chloroform and DMSO, but in the latter two solvents is not stable. In $CDCl_3$, significant formation of phosphine oxide was detected few hours after preparation of the solution and after two days the precipitation of a green solid indicated oxidation of copper(I) to copper(II). **AZ67** proved to be more stable in DMSO-d_6 than in $CDCl_3$, but also in this solvent was observed a relatively fast formation of phosphine oxide.

Antimicrobial activity of 2.1 iminophosphine:copper(I) complexes

This part of the project was carried out during my period of secondment in Maynooth University (MU), Republic of Ireland. The biological assays were conducted under the supervision of Prof. Kevin Kavanagh of the Department of Biology (MU).

Preliminary assays were performed in order to determine if the **2:1 iminophosphine:copper(I)** complexes **AZ48**, **AZ53a**, **AZ55a**, **AZ61**, **AZ65** and **AZ66** (Figure 5.34) show some activity against methicillin resistant *Staphylococcus aureus* (MRSA), *Escherichia coli* and *Candida albicans*. MRSA is a strain of Gram-positive bacteria, *E. coli* is a Gram-negative bacterium, while *C. albicans* is a yeast.

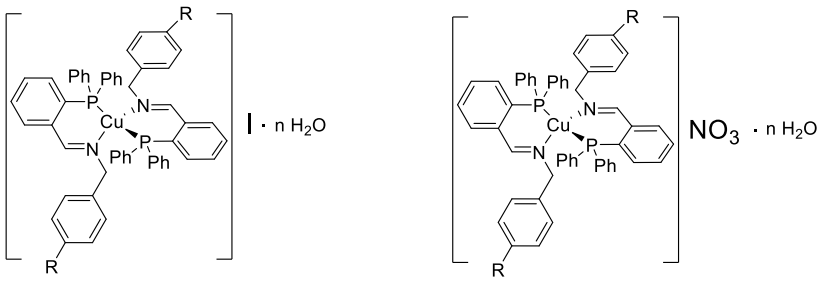

AZ48 R = H, n = 0
AZ53a R = Me, n = 2
AZ55a R = F, n = 4

AZ61 R = H, n = 0
AZ65 R = Me, n = 1
AZ66 R = F, n = 2

Figure 5.34: (Left) General structure for the complexes **AZ48**, **AZ53a** and **AZ55a** (it is reported the ionic structure, which is probably the one found in solution); (right) general structure for the complexes **AZ61**, **AZ65** and **AZ66**.

The set-up for the preliminary biological assays is described in the experimental section. All the complexes were not active against *E. coli* and *C. Albicans*, while they proved to be effective against MRSA.

The **bacteriostatic activity** of the metal complexes against MRSA was therefore evaluated by means of the broth microdilution method. As an example, in Figure 5.35 the results obtained for complex **AZ48** are reported.

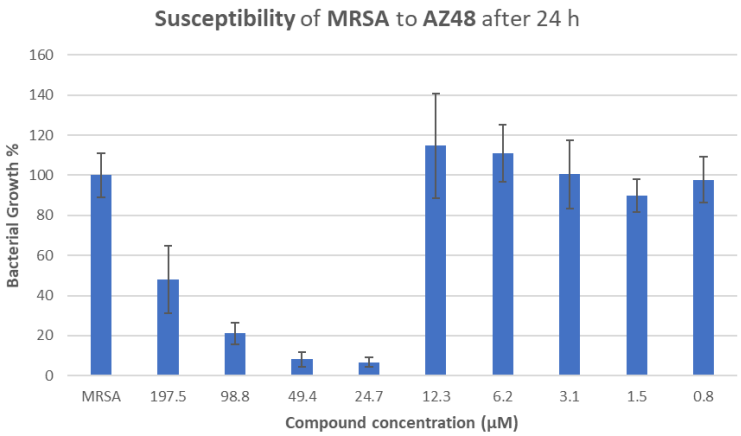

Figure 5.35: Susceptibility of MRSA to complex **AZ48** determined by broth microdilution method. Standard deviation is represented by bars.

As observed for **AZ48** in Figure 5.35, all the complexes showed an anomalous trend in detected bacterial growth % with respect to compound concentration: at high concentrations (190 – 120 µM), a paradoxical high growth % was revealed, which significantly lowers until concentration values around 30 – 8 µM (depending on the compound) and then increases at very low concentrations. Such behaviour can be explained by considering two possible causes: (1) precipitation or formation of aggregates at high compound concentrations, (2) Eagle's effect.

(1) Precipitation or formation of aggregates: the determination of bacterial growth % is an indirect measure, that is, it is a measure of turbidity of samples due to the presence of bacterial cells suspended in solution (see the experimental section). At high concentration of tested compounds, precipitation or formation of aggregates can occur, therefore enhancing the turbidity of the system even without the presence of bacterial cells. Although the copper(I) complexes are soluble in DMSO, working solutions were prepared by dilution with PBS, an aqueous medium. The presence of several phenyl rings in the structures of the complexes confers them high lipophilicity and low solubility in water, although the nitrate containing complexes proved to be soluble in water/acetone mixtures. The phosphate buffer can also affect the solubility of the compounds.

(2) Eagle's effect: phenomenon in which bacteria or fungi exposed to concentrations of antibiotic higher than an optimal bactericidal concentration (OBC) have paradoxically improved levels of survival than at the OBC due to a decreased net rate of cell death.[342] This effect was first described by scientist Harry Eagle in 1948 with regard to penicillin. Currently, Eagle effect is found for a number of antibiotics like beta-lactams, glycopeptides, fluoroquinolones, aminoglycosides and polymyxins. It is also observed in case of various micro-organisms, including *Staphylococcus spp.*, *Streptococcus spp.*, *Enterococcus spp.* and Gram-negative bacteria. In clinical settings, Eagle effect leads to treatment failure due to application of excessive dose of antibiotic.[343]

To unravel the real origin of the anomalous trend of data, a control experiment was designed and performed. **AZ48** and **AZ61**, which were the most promising compounds based on the results of the broth microdilution method, were selected to repeat the assay, but with a different set-up to consider the possibility of precipitation (see the experimental section). The results for **AZ48** are summarized in Figure 5.36.

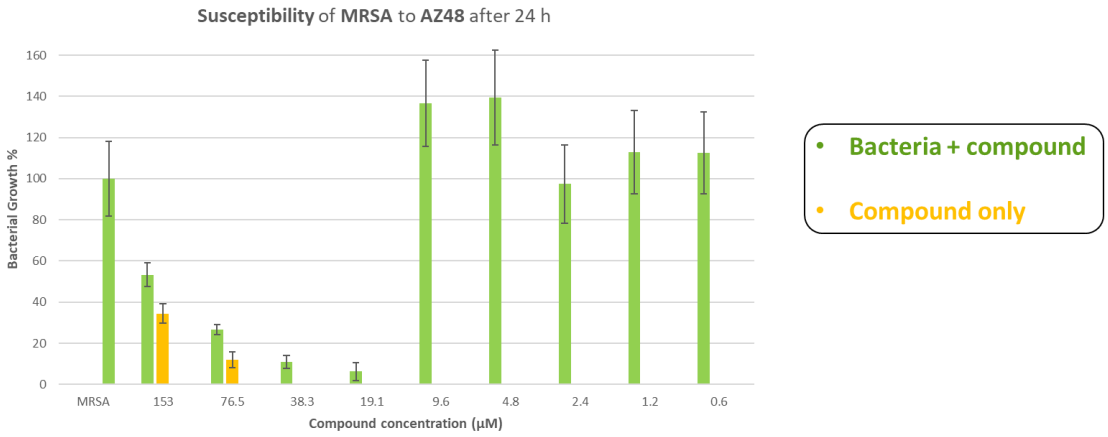

Figure 5.36: Susceptibility of MRSA to **AZ48** determined by broth microdilution method with control for precipitation after 24 hours incubation.

Data suggest that the precipitation of the tested compounds is the reason for the paradoxical results obtained in the assay, thus excluding the occurrence of Eagle's effect. Nevertheless, the optical density values measured for the wells that contained both bacteria and compounds at high concentration were always higher than the ones measured for the wells that contained only the compounds at the same high concentration. Such result can be due to several reasons, including technical errors.

The determination of the **minimum inhibitory concentration** (**MIC**), defined as the lowest concentration of an antibacterial agent which prevents visible growth of the strain of a micro-organism (in this case, MRSA), was performed taking into account the false positive results obtained at high concentrations of the tested compounds. For the complexes **AZ48** and **AZ61**, the MIC was determined based on the assay performed with the control for precipitation. The results are summarized in Table 5.5.

Table 5.5: MIC (expressed in µM) and percentage values of microbial growth with respect to positive control at concentration = MIC for the tested copper(I) complexes.

Compound	MIC (µM)	Percentage value of microbial growth at concentration = MIC (mean ± standard deviation).
AZ48	19.1	6.2 ± 4.4
AZ53a	31.5	12.8 ± 2.3
AZ55a	30.7	23.0 ± 16.8
AZ61	11.1	5.6 ± 4.7
AZ65	-	> 50
AZ66	-	> 50

Despite the limited number of tested compounds, some general considerations can be drawn from the data reported in Table 5.5:

- for all the iodine containing complexes was possible to determine a MIC, while among the nitrate containing complexes this was possible only for **AZ61**.
- Among the complexes synthesized from the same copper(I) precursor, the ones that contain the ligand $\mathbf{L^1}$, namely **AZ48** and **AZ61**, are the best bacteriostatic agents against MRSA.
- Para-substitution of the phenyl ring in the benzylamine precursor decreases the activity of the final complex irrespective of the electronic nature of the substituent.

Conclusions

The template synthesis proved to be an efficient strategy for the preparation of iminophosphine copper(I) complexes with various stoichiometries and counterions. Although the syntheses had to be performed under inert atmosphere, there was no need for dry solvents, thus highlighting the robustness of these systems with respect to disproportionation. All the isolated complexes proved to be stable in the solid state even after one year.

Crystallographic data evidenced also for these complexes the strong preference of copper(I) for a tetrahedral coordination geometry. The only exception is represented by the trigonal planar **Cu(L^a)$_2$I** complex. Interestingly, in the solid state, while all the 2:1 ligand:metal complexes were isolated as monomeric species, all the 1:1 ligand:metal complexes proved to have dimeric structure.

Remarkably, for none of the iminophosphine copper(I) complexes was observed copper(I) oxidation in solution. Instead, probably because of fluxionality, partial oxidation of phosphine to phosphine-oxide was observed mainly for the 1:1 ligand:metal complexes derived from CuI. The 2:1 iminophosphine copper(I) complexes synthesized from CuI showed good stability in $CDCl_3$, while in DMSO-d_6 traces of phosphine-oxide species were detected after few days. A complementary behaviour was displayed by the nitrate containing copper(I) complexes: they showed exceptional stability in DMSO-d_6, while in $CDCl_3$ phosphine-oxide species formed along two days.

The *in vitro* antimicrobial activity of the 2:1 iminophosphine copper(I) complexes was evaluated against the Gram-positive bacterium methicillin resistant *Staphylococcus aureus* (MRSA), the Gram-negative bacterium *Escherichia coli* and the yeast *Candida albicans*. All the complexes were not active against *E. coli* and *C. Albicans*, while they proved to be effective against MRSA, with MIC values in the range 10 – 30 μM.

In order to explore the whole biological potential of this class of copper(I) complexes, *in vitro* studies of their anticancer activity are currently ongoing.

The approach described herein for the synthesis of Cu(I) complexes, together with the promising results obtained in terms of bacteriostatic activity, may pose the basis for the design of novel therapeutic agents.

Experimental section

Chemistry

Materials and methods

Commercial reagents were purchased from Sigma-Aldrich. The purity of the synthesized compounds was determined by elemental analysis and verified to be ≥95%. ^{1}H, ^{13}C, ^{31}P and 2D NMR spectra were recorded at 25 °C on a Bruker Advance 400 MHz FT spectrometer. No special precautions were taken while performing NMR measurements (i.e. no experiments were carried out under nitrogen atmosphere). The ATR-IR spectra were recorded by means of a Perkin Elmer spectrophotometer by using a diamond crystal plate in the range of 4000–400 cm^{-1}. Elemental analyses were performed by using a Thermo Fisher FlashSmart CHNS/O analyzer with gas-chromatographic separation. Electrospray ionization mass spectral analyses (ESI-MS) were performed with an ESI time-of-flight Micromass 4LCZ spectrometer. Samples were dissolved in methanol or acetonitrile. Powder X-ray diffraction (P-XRD) data were collected with a Rigaku Smartlab XE diffractometer equipped with a 2D HyPix3000 detector operating in 1D mode. Data were collected under ambient conditions in Bragg–Brentano geometry (Cu Kα =1.5046 Å) in continuous mode, in the 2°–50° 2θ angular range, with a step size of 0.01◦ at a scan speed of 8° min^{-1}.

Synthesis

N-(2-(Diphenylphosphino)phenyl)-methylene benzylamine (L^1, AZ39)

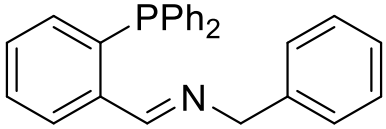

Benzylamine (49 µL, 0.447 mmol, 1.3 eq) was added to a yellow solution of 2-(diphenylphosphino)benzaldehyde (100 mg, 0.344 mmol, 1.0 eq) in 3/1 MeOH/DCM (9 mL/3 mL) mixture and the resulting mixture was stirred under reflux overnight. The obtained colourless solution was allowed to cool to r.t., then it was reduced to a small volume (ca. 1-2 mL) and left at -20 °C overnight. A white precipitate formed, which was filtered, washed with a small volume of cold MeOH and dried *in vacuo*. The desired iminophosphine was isolated as a white solid (28 mg, yield = 21%).

IR (cm^{-1}): ν = 3052 (w) (CH sp^2), 2829 (w) (CH sp^3), 1636 (m) (C=N). (Figure A5.1)

^{1}H NMR (400 MHz, Chloroform-*d*, 298 K): δ(ppm) = 9.04 (d, *J* = 5.1 Hz, 1H, CH=N), 8.07 (ddd, *J* = 7.8, 4.0, 1.4 Hz, 1H, ArH), 7.44 – 7.27 (m, 13H, ArH), 7.25 – 7.21 (m, 2H, ArH), 7.08 – 7.02 (m, 2H, ArH), 6.93 – 6.86 (m, 1H, ArH), 4.70 (s, 2H, CH_2). (Figure A5.2)

^{1}H NMR (400 MHz, DMSO-d_6, 298 K): δ(ppm) = 8.93 (d, *J* = 4.8 Hz, 1H, CH=N), 7.95 (ddd, *J* = 7.6, 4.0, 1.5 Hz, 1H, ArH), 7.50 – 7.36 (m, 8H, ArH), 7.26 – 7.17 (m, 7H, ArH), 7.02 – 6.94 (m, 2H, ArH), 6.82 (ddd, *J* = 7.7, 4.5, 1.4 Hz, 1H, ArH), 4.62 (s, 2H, CH_2). (Figure A5.3)

^{13}C NMR (101 MHz, Chloroform-*d*, 298 K): δ(ppm) = 160.71 ((d, *J* = 22.5 Hz), 139.50 (d, J = 17.3 Hz), 139.08, 137.77, 137.58, 136.45 (d, J = 9.5 Hz), 134.23 (d, J = 20.0 Hz), 133.35, 132.12, 130.53, 129.07, 129.04, 128.84, 128.77, 128.50, 128.15, 127.81 (d, J = 4.4 Hz), 126.93, 65.23. (Figure A5.4)

^{31}P NMR (162 MHz, Chloroform-*d*, 298 K): δ(ppm) = -14.01 (s). (Figure A5.5)

^{31}P NMR (162 MHz, DMSO-d_6, 298 K): δ(ppm) = -14.49 (s). (Figure A5.6)

MS-ESI (positive ions; MeOH): m/z (%): 275 (100) $[M - C_7H_6N]^+$, 380 (98) $[M + H]^+$. (Figure A5.7)

Elem. anal. calcd (%) for $C_{26}H_{22}NP$: C 82.30%, H 5.84%, N 3.69%; found: C 82.06%, H 5.79%, N 3.41%.

General procedure for the synthesis of 1:1 iminophosphine:Cu(I) complexes

The reaction was performed under N_2 atmosphere and the solvents were degassed prior to use. To a solution of 2-(diphenylphosphino)benzaldehyde (100 mg, 0.344 mmol, 1.0 eq) in $CHCl_3$ (10 mL) was added a solution of CuI (65.9 mg, 0.346 mmol, 1.0 eq) in MeCN (10 mL) and the resulting mixture was stirred at 50 °C for 1 h (after 15 minutes a yellow precipitate formed). The desired amine (0.344 mmol, 1.0 eq) in MeCN (10 mL) was added and the resulting suspension was stirred at 60 - 65 °C for 5 h: the initial yellow suspension became an orange-red solution and then an orange precipitate formed. The mixture was allowed to cool to r.t., then it was left at 4 °C under nitrogen overnight. The precipitate was filtrated, washed with cold MeCN and dried *in vacuo*.

$[Cu(\mu\text{-}I)L^1]_2$ (AZ46)

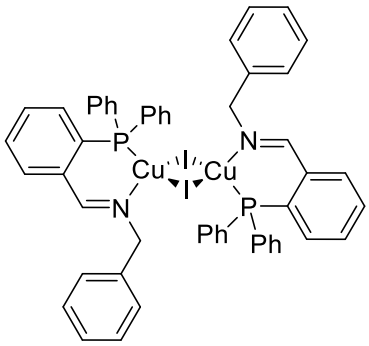

Benzylamine (37.6 µL, 0.344 mmol) was used for the synthesis. The product was isolated as an orange-red powder (75 mg, yield = 38%).

IR (cm^{-1}): ν = 3033 (w) (CH sp^2), 2842 (w) (CH sp^3), 1628 (m) (C=N). (Figure A5.8)

^{1}H NMR (400 MHz, Chloroform-*d,* 298 K): δ(ppm) = 8.15 (s, br, 2H, CH=N), 7.59 – 7.26 (m, 24H, ArH), 7.25 (s, 2H, ArH), 7.22 – 6.85 (m, 12H, ArH), 5.02 (s, br, 4H, CH_2).

^{31}P NMR (162 MHz, Chloroform-*d,* 298 K): δ(ppm) = -16.13 (s, br). (Figure A5.11)

MS-ESI (positive ions; MeCN): m/z (%): 442 $[CuL^1]^+$.

Elem. anal. calcd (%) for $C_{52}H_{44}Cu_2I_2N_2P_2$: C 54.80%, H 3.89%, N 2.46%; found: C 54.76%, H 3.84%, N 2.42%.

Single crystals suitable for XRD analysis were obtained by slow evaporation of a solution of the complex in $CHCl_3$.

$[Cu(\mu\text{-}I)L^2]_2$ (AZ52)

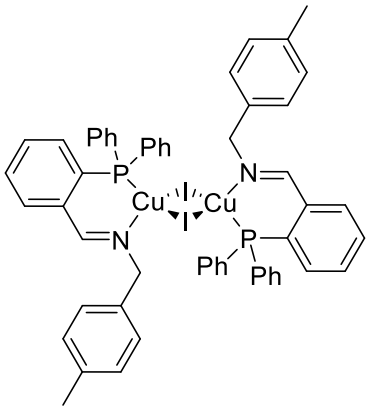

4-Methylbenzylamine (43.8 µL, 0.344 mmol) was used for the synthesis. After the addition of the amine, temperature was raised to 60 °C. The product was isolated as an orange-red powder (99 mg, yield = 49%).

IR (cm^{-1}): ν = 3046 (w) (CH sp^2), 2845 (w) (CH sp^3), 1627 (m) (C=N). (Figure A5.14)

^{1}H NMR (400 MHz, Chloroform-*d*, 298 K): δ(ppm) = 8.13 (s, br, 2H, CH=N), 7.60 – 7.27 (m, 24H, ArH), 7.25 (s, 2H, ArH), 6.99 (m, 10H, ArH), 4.98 (s, br, 4H, CH_2), 2.28 (s, 6H, CH_3). (Figure A5.15)

^{31}P NMR (162 MHz, Chloroform-*d*, 298 K): δ(ppm) = -15.72 (s, br). (Figure A5.16)

MS-ESI (positive ions; MeCN): m/z (%): 456 (100) $[CuL^2]^+$, 850 (25) $[CuL^2{}_2]^+$. (Figure A5.17)

Elem. anal. calcd (%) for $C_{54}H_{48}Cu_2I_2N_2P_2$: C 55.54%, H 4.14%, N 2.40%; found: C 55.65%, H 4.07%, N 2.34%.

Single crystals suitable for XRD analysis were obtained by slow evaporation of mother liquors.

$[Cu(\mu\text{-}I)L^3]_2$ (AZ54)

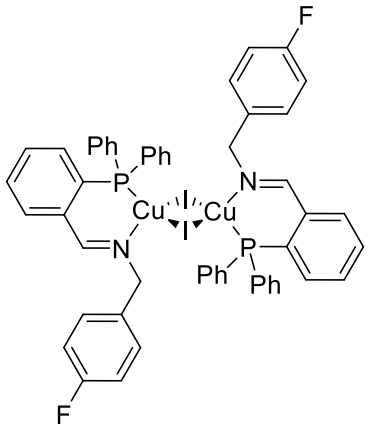

4-Fluorobenzylamine (39.3 µL, 0.344 mmol) was used for the synthesis. After the addition of the amine, temperature was raised to 65 °C. The product was isolated as an orange-red powder (151 mg, yield = 71%).

IR (cm^{-1}): ν = 3046 (w) (CH sp^2), 2841 (w) (CH sp^3), 1628 (m) (C=N). (Figure A5.18)

^{1}H NMR (400 MHz, Chloroform-*d*, 298 K): δ(ppm) = 8.16 (s, br, 2H, CH=N), 7.59 – 7.26 (m, 26H, ArH), 7.06 – 6.98 (m, 6H, ArH), 6.78 (t, *J* = 8.5 Hz, 4H, ArH), 4.96 (s, br, 4H, CH_2). (Figure A5.19)

^{31}P NMR (162 MHz, Chloroform-*d*, 298 K): δ(ppm) = -15.77 (s, br). (Figure A5.21)

MS-ESI (positive ions; MeCN): m/z (%): 460 (100) $[CuL^3]^+$, 857 (40) $[CuL^3{}_2]^+$. (Figure A5.23)

Elem. anal. calcd (%) for $C_{52}H_{42}Cu_2F_2I_2N_2P_2$: C 53.12%, H 3.60%, N 2.38%; found: C 53.25%, H 3.62%, N 2.34%.

Single crystals suitable for XRD analysis were obtained by slow evaporation of mother liquors.

General procedure for the synthesis of 2:1 iminophosphine:Cu(I) complexes derived from CuI

The reaction was performed under N_2 atmosphere and the solvents were degassed prior to use. To a solution of 2-(diphenylphosphino)benzaldehyde (100 mg, 0.344 mmol, 2.0 eq) in $CHCl_3$ (10 mL) was added a solution of CuI (32.8 mg, 0.172 mmol, 1.0 eq) in MeCN (10 mL) and the resulting mixture was stirred at 50 °C for 1 h (after 15-20 minutes a yellow precipitate formed). The desired amine (0.344 mmol, 2.0 eq) in MeCN (10 mL) was added and the resulting suspension was stirred at 50 °C for 5 h: the initial yellow suspension became a bright orange-red solution. The solution was allowed to cool to r.t., then, depending on the amine, it was reduced to a small volume (3 - 4 mL) and an appropriate antisolvent was added, otherwise it was dried and recrystallized with the proper solvent mixture. The resulting precipitate was filtrated, washed with the appropriate solvent and dried *in vacuo*.

$Cu(L^1)_2I$ (AZ48)

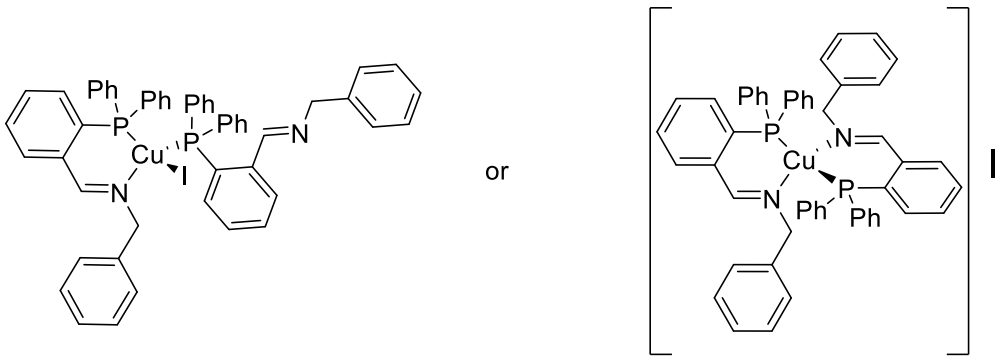

neutral ionic

Benzylamine (37.6 µL, 0.344 mmol) was used for the synthesis. Et_2O was used as antisolvent. The product was isolated as a light orange solid (98 mg, yield = 59%).

IR (cm^{-1}): ν = 3044 (w) (CH sp^2), 2875 (w) (CH sp^3), 1626 (m) (C=N). (Figure A5.24)

^{1}H NMR (400 MHz, Chloroform-*d*, 298 K): δ(ppm) = 8.81 (s, br, 2H, CH=N), 8.05 (s, br, 2H, ArH), 7.66 (t, *J* = 7.6 Hz, 2H, ArH), 7.49 – 7.35 (m, 6H, ArH), 7.20 – 7.10 (m, 10H, ArH), 7.03 – 6.63 (m, 14H, ArH), 6.20 (s, br, 4H, ArH), 4.62 (s, br, 4H, CH_2). (Figure A5.25)

^{1}H NMR (400 MHz, DMSO-d_6, 298 K): δ(ppm) = 8.75 (s, br, 2H, CH=N), 8.01 (d, *J* = 7.6 Hz, 2H, ArH), 7.84 (t, *J* = 7.6 Hz, 2H, ArH), 7.68 (t, *J* = 7.5 Hz, 2H, ArH), 7.48 (tt, *J* = 7.4, 1.2 Hz, 4H, ArH), 7.23 (m, 10H, ArH), 6.96 (t, *J* = 7.6 Hz, 4H, ArH), 6.87 (d, *J* = 7.6 Hz, 2H, ArH), 6.63 (s, br, 8H, ArH), 6.15 (s, br, 4H, ArH), 4.38 (s, br, 4H, CH_2).

^{13}C NMR (126 MHz, DMSO-d_6, 298 K): δ(ppm) = 170.77, 137.48, 136.39, 133.64, 133.15, 132.58, 131.21, 130.47, 129.04, 129.01, 128.97, 128.44, 127.60, 126.95, 67.69. (Figure A5.28)

^{31}P NMR (162 MHz, Chloroform-*d*, 298 K): δ(ppm) = -8.62 (s, br). (Figure A5.29)

^{31}P NMR (162 MHz, DMSO-d_6, 298 K): δ(ppm) = -9.14 (s, br). (Figure A5.31)

MS-ESI (positive ions; MeCN): m/z (%): 442 (100) $[CuL^1]^+$, 822 (60) $[CuL^1{}_2]^+$. (Figure A5.35)

Elem. anal. calcd (%) for $C_{52}H_{44}CuIN_2P_2$: C 65.79%, H 4.67%, N 2.95%; found: C 65.28%, H 4.93%, N 2.92%.

$Cu(L^2)_2I \cdot EtOAc$ (AZ53)

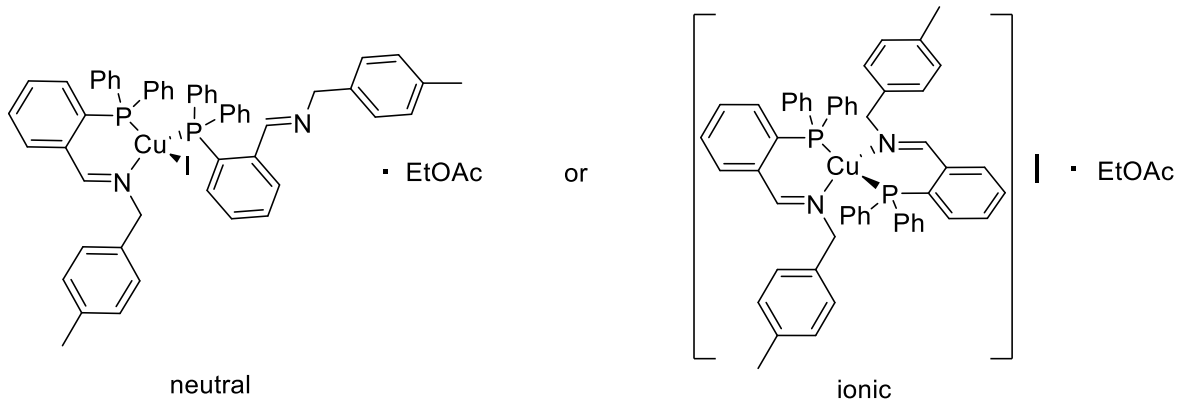

4-Methylbenzylamine (43.8 µL, 0.344 mmol) was used for the synthesis. After the addition of the amine, temperature was raised to 60 °C. EtOAc was used as antisolvent. The product was isolated as a yellow-orange solid (72 mg, yield = 39%).

IR (cm^{-1}): ν = 3054 (w) (CH sp^2), 2884 (w) (CH sp^3), 1736 (m) (C=O, EtOAc), 1626 (m) (C=N). (Figure A5.36)

^{1}H NMR (400 MHz, Chloroform-*d*, 298 K): δ(ppm) = 8.79 (s, br, 2H, CH=N), 8.06 (d, br, *J* = 7.2 Hz, 2H, ArH), 7.66 (t, *J* = 7.5 Hz, 2H, ArH), 7.48 – 7.36 (m, 6H, ArH), 7.17 (t, *J* = 7.6 Hz, 8H, ArH), 6.76 (m, 14H, ArH), 6.07 (s, br, 4H, ArH), 4.56 (s, br, 4H, N$\underline{CH_2}$Ph), 4.12 (q, *J* = 7.1 Hz, 2H, $CH_3C(=O)O\underline{CH_2}CH_3$), 2.28 (s, 6H, Ph$\underline{CH_3}$), 2.04 (s, 3H, $\underline{CH_3}C(=O)OCH_2CH_3$), 1.26 (t, *J* = 7.1 Hz, 3H, $CH_3C(=O)OCH_2\underline{CH_3}$). (Figure A5.37)

^{31}P NMR (162 MHz, Chloroform-*d*, 298 K), δ(ppm): -8.78 (s, br). (Figure A5.38)

MS-ESI (positive ions; MeCN): m/z (%): 456 (100) $[CuL^2]^+$, 850 (65) $[CuL^2{}_2]^+$. (Figure A5.39)

Elem. anal. calcd (%) for $C_{58}H_{56}CuIN_2O_2P_2$: C 65.38%, H 5.30%, N 2.63%; found: C 65.36%, H 4.90%, N 2.67%.

Yellow single crystals suitable for XRD analysis were obtained by slow evaporation of mother liquors.

$Cu(L^2)_2I \cdot 2H_2O$ (AZ53a)

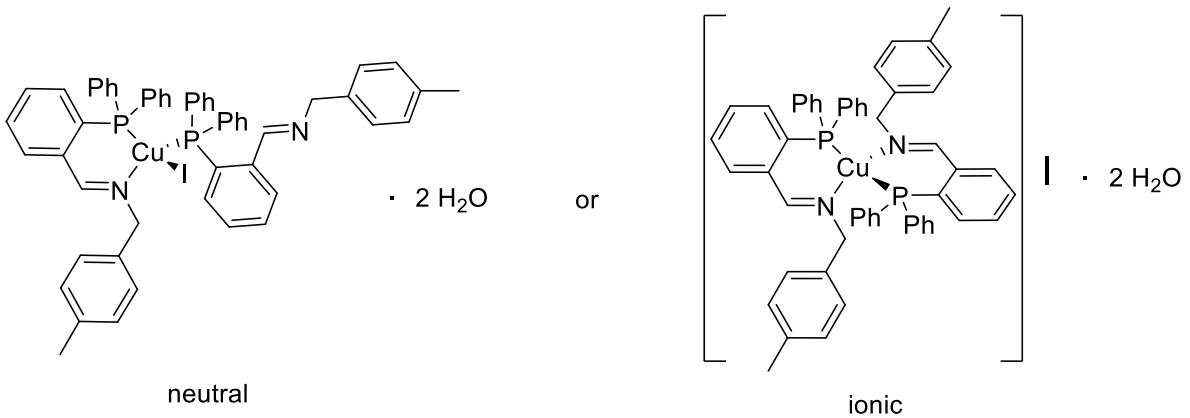

4-Methylbenzylamine (43.8 µL, 0.344 mmol) was used for the synthesis. After the addition of the amine, temperature was raised to 60 °C. After stirring at 60 °C, the reaction mixture was dried and recrystallized in $CHCl_3$/n-hexane. The resulting suspension was left at r.t. overnight, then it was filtrated, washed with n-hexane. The obtained orange solid was triturated with Et_2O and dried *in vacuo*. The product was isolated as a light orange solid (56 mg, yield = 32%).

IR (cm^{-1}): ν = 3049 (w) (CH sp^2), 2834 (w) (CH sp^3), 1626 (m) (C=N). (Figure A5.40)

^{1}H NMR (400 MHz, Chloroform-*d*, 298 K): δ(ppm) = 8.69 (s, br, 2H, CH=N), 7.98 (s, br, 2H, ArH), 7.70 – 7.60 (m, 2H, ArH), 7.46 – 7.36 (m, 6H, ArH), 7.18 (t, *J* = 7.6 Hz, 8H, ArH), 7.01 – 6.59 (m, 14H, ArH), 6.14 (s, br, 4H, ArH), 4.63 (s, br, 4H, CH_2), 2.28 (s, 6H, CH_3). (Figure A5.41)

^{1}H NMR (400 MHz, DMSO-d_6, 298 K): δ(ppm) = 8.70 (s, 2H, CH=N), 7.99 (m, 2H, ArH), 7.85 (m, 2H, ArH), 7.70 (m, 2H, ArH), 7.53 – 7.45 (m, 4H, ArH), 7.23 (s, br, 8H, ArH), 6.98 – 6.44 (m, br, 14H, ArH), 5.98 (d, *J* = 7.7 Hz, 4H, ArH), 4.32 (s, br, 4H, CH_2), 2.26 (s, 6H, CH_3). (Figure A5.42)

^{31}P NMR (202 MHz, DMSO-d_6, 298 K): δ(ppm) = -9.16. (Figure A5.43)

MS-ESI (positive ions; MeCN): m/z (%): 456 (100) $[CuL^2]^+$, 850 (70) $[CuL^2{}_2]^+$. (Figure A5.44)

Elem. anal. calcd (%) for $C_{54}H_{52}CuIN_2O_2P_2$: C 64.00%, H 5.17%, N 2.76%; found: C 64.01%, H 4.97%, N 2.69%.

$Cu(L^3)_2I \cdot 4H_2O$ (AZ55a)

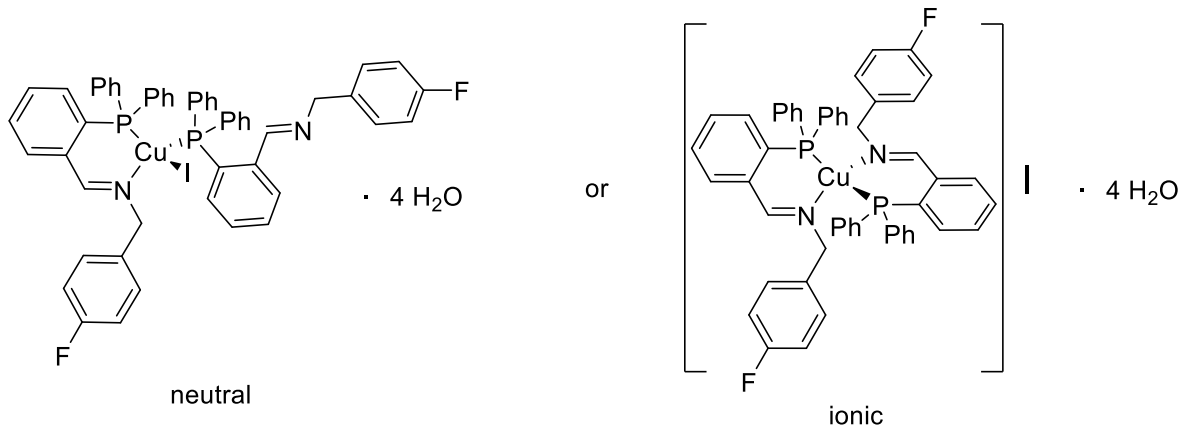

For the synthesis, the following molar ratios were used: 3:1:3 aldehyde:CuI:amine. To a solution of 2-(diphenylphosphino)benzaldehyde (150 mg, 0.516 mmol, 3.0 eq) in $CHCl_3$ (10 mL) was added a solution of CuI (32.8 mg, 0.172 mmol, 1.0 eq) in MeCN (10 mL) and the resulting mixture was stirred at 50 °C for 1 h (after few minutes a yellow precipitate formed). 4-Fluorobenzylamine (59 µL, 0.516 mmol, 3.0 eq) in MeCN (10 mL) was added and the resulting suspension was stirred at 65 °C for 5 h: the initial yellow suspension became a bright orange-red solution. The solution was allowed to cool to r.t., then it was dried and recrystallized in $CHCl_3$/n-hexane. A yellow precipitate formed and the suspension was left at r.t. for 2 h, then it was filtrated, washed with n-hexane and dried *in vacuo*. The product was isolated as a yellow solid (101 mg, yield = 55%).

IR (cm^{-1}): ν = 3049 (w) (CH sp^2), 2922 (w) (CH sp^3), 1627, 1602 (m) (C=N). (Figure A5.45)

^{1}H NMR (500 MHz, Chloroform-*d*): δ(ppm) = 8.85 (s, br, 2H, CH=N), 8.03 (s, br, 2H, ArH), 7.63 (t, *J* = 7.2 Hz, 2H, ArH), 7.41 (t, *J* = 7.4 Hz, 6H, ArH), 7.21 (t, *J* = 7.7 Hz, 8H, ArH), 7.02 – 6.54 (m, 14H, ArH), 6.24 (s, br, 4H, ArH), 4.63 (s, br, 4H, CH_2). (Figure A5.46)

^{31}P NMR (202 MHz, Chloroform-*d*, 298 K), δ(ppm): -9.03 (s, br). (Figure A5.47)

MS-ESI (positive ions; MeCN): m/z (%): 460 (100) $[CuL^3]^+$, 858 (50) $[CuL^3{}_2]^+$. (Figure A5.48)

Elem. anal. calcd (%) for $C_{52}H_{50}CuF_2IN_2O_4P_2$: C 59.07%, H 4.77%, N 2.65%; Trovato: C 59.07%, H 4.23%, N 2.53%.

General procedure for the synthesis of 2:1 iminophosphine:Cu(I) complexes derived from $Cu(NO_3)_2 \cdot 3H_2O$

To a light blue solution of $Cu(NO_3)_2 \cdot 3H_2O$ (20.8 mg, 0.086 mmol, 0.5 eq) in MeCN (15 mL) was added an excess of copper powder (ca. 0.2 mmol) and the mixture was stirred under reflux till complete decolorization of the solution (ca. 30 min). The colourless solution was quickly hot filtered in order to remove unreacted copper powder, then it was degassed, put under N_2 and added to a solution of 2-(diphenylphosphino)benzaldehyde (100 mg, 0.344 mmol, 2.0 eq) in $CHCl_3$ (10 mL). The resulting yellow solution was stirred at 50 °C under N_2 for 1 h. The desired amine (0.344 mmol, 2.0 eq) in MeCN (10 mL) was added and the mixture was stirred at 50 °C under N_2 for 5 h: the initial yellow solution turned red-orange. The solution was allowed to cool to r.t., then it was reduced to a small volume (3 – 4 mL) and Et_2O (ca. 50 mL) was added. The resulting suspension was left at 4 °C under N_2 overnight. The precipitate was filtrated, washed with Et_2O and dried *in vacuo*.

$[Cu(L^1)_2]NO_3$ (AZ61)

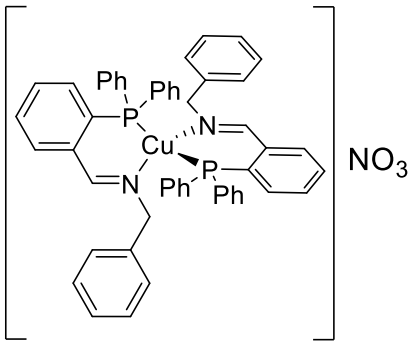

Benzylamine (37.6 µL, 0.344 mmol) was used for the synthesis. The product was isolated as a red powder (98 mg, yield = 64%).

IR (cm^{-1}): ν = 3049 (w) (CH sp^2), 2892 (w) (CH sp^3), 1617 (m) (C=N), 1344 (s) (NO_2 asym. str.). (Figure A5.49)

^{1}H NMR (400 MHz, Chloroform-*d*, 298 K): δ(ppm) = 8.73 (s, 2H, CH=N), 8.12 (d, *J* = 7.5 Hz, 2H, ArH), 7.77 (t, *J* = 7.3 Hz, 2H, ArH), 7.45 (dt, *J* = 34.7, 7.5 Hz, 8H, ArH), 7.21 – 7.09 (m, 10H, ArH), 6.89 – 6.70 (m, 8H, ArH), 6.59 (s, br, 4H, ArH), 5.92 (d, *J* = 7.5 Hz, 4H, ArH), 4.52 (s, br, 4H, CH_2). (Figure A5.50)

^{1}H NMR (400 MHz, DMSO-d_6, 298 K): δ(ppm) = 8.74 (s, 2H, CH=N), 8.06 – 7.98 (m, 2H, ArH), 7.86 (td, *J* = 7.5, 1.3 Hz, 2H, ArH), 7.69 (t, *J* = 7.6 Hz, 2H, ArH), 7.48 (t, *J* = 7.4 Hz, 4H, ArH), 7.33 – 7.16 (m, 10H, ArH), 6.95 (t, *J* = 7.6 Hz, 4H, ArH), 6.87 (dt, *J* = 7.8, 4.0 Hz, 2H, ArH), 6.60 (s, br, 8H, ArH), 6.13 (d, *J* = 7.5 Hz, 4H, ArH), 4.36 (s, 4H, CH_2).

^{1}H NMR (400 MHz, Methanol-d_4, 298 K): δ(ppm) = 8.63 (s, 2H, CH=N), 7.98 (dq, *J* = 7.8, 1.8 Hz, 2H, ArH), 7.83 (td, *J* = 7.6, 1.3 Hz, 2H, ArH), 7.69 – 7.59 (m, 2H, ArH), 7.47 (t, *J* = 7.5 Hz, 4H, ArH), 7.28 – 7.15 (m, 10H, ArH), 7.01 – 6.25 (m, br, 14H, ArH), 6.14 (dd, *J* = 8.2, 1.3 Hz, 4H, ArH), 4.45 (s, 4H, CH_2). (Figure A5.51)

^{31}P NMR (162 MHz, Chloroform-*d*, 298 K): δ(ppm) = -7.68 (s, br). (Figure A5.52)

^{31}P NMR (162 MHz, DMSO-d_6, 298 K): δ(ppm) = -9.07 (s).

MS-ESI (positive ions; MeCN): m/z (%): 442 (100) $[CuL^1]^+$, 822 (10) $[CuL^1{}_2]^+$. (Figure A5.54)

Elem. anal. calcd (%) for $C_{52}H_{44}CuN_3O_3P_2$: C 70.62%, H 5.01%, N 4.75%; found: C 70.85%, H 4.97%, N 4.63%.

Single crystals suitable for XRD analysis were obtained by slow evaporation of mother liquors.

$[Cu(L^2)_2]NO_3 \cdot H_2O$ (AZ65)

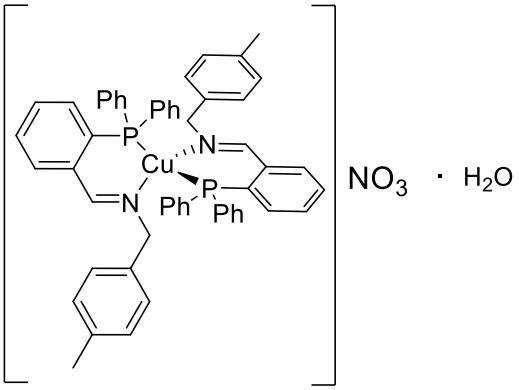

4-Methylbenzylamine (43.8 µL, 0.344 mmol) was used for the synthesis. The product was isolated as an orange sticky solid (110 mg, yield = 69%).

IR (cm^{-1}): ν = 3500-3300 (w) (OH), 3051 (w) (CH sp^2), 2917 (w) (CH sp^3), 1621 (m) (C=N), 1335 (s) (NO_2 asym. str.). (Figure A5.55)

^{1}H NMR (500 MHz, Chloroform-*d*, 298 K): δ(ppm) = 8.69 (s, 2H, CH=N), 8.09 (d, *J* = 6.6 Hz, 2H, ArH), 7.76 (td, *J* = 7.6, 1.0 Hz, 2H, ArH), 7.50 (t, *J* = 7.6 Hz, 2H, ArH), 7.42 (s, 4H, ArH), 7.15 (d, *J* = 6.4 Hz, 8H, ArH), 7.02 – 5.92 (m, 14H, ArH), 5.79 (d, *J* = 7.9 Hz, 4H, ArH), 4.46 (s, 4H, CH_2), 2.28 (s, 6H, CH_3). (Figure A5.56)

^{1}H NMR (400 MHz, DMSO-d_6, 298 K): δ(ppm) = 8.71 (s, 2H, CH=N), 8.04 – 7.97 (m, 2H, ArH), 7.85 (td, *J* = 7.6, 1.3 Hz, 2H, ArH), 7.70 (t, *J* = 7.6 Hz, 2H, ArH), 7.49 (t, *J* = 7.4 Hz, 4H, ArH), 7.22 (t, *J* = 7.6 Hz, 8H, ArH), 6.87 (dt, *J* = 8.0, 4.3 Hz, 2H, ArH), 6.81 – 6.29 (m, br, 12H, ArH), 5.98 (d, *J* = 7.8 Hz, 4H, ArH), 4.32 (s, 4H, CH_2), 2.26 (s, 6H, CH_3). (Figure A5.57)

^{13}C NMR (126 MHz, Chloroform-*d*, 298 K): δ(ppm) = 170.30, 138.01, 137.98, 137.95, 136.90, 135.80, 135.75, 135.70, 134.14, 134.03, 132.06, 132.04, 131.35, 130.66, 130.56, 130.39, 129.29, 128.88, 127.34, 68.94, 21.36. (Figure A5.58)

^{13}C NMR (126 MHz, DMSO-d_6, 298 K): δ(ppm) = 170.30, 137.38, 136.86, 135.40, 133.68, 133.32, 133.12, 132.48, 131.11, 130.45, 128.96, 128.91, 128.87, 128.84, 127.01, 67.59, 20.75. (Figure A5.59)

^{31}P NMR (202 MHz, Chloroform-*d*, 298 K): δ(ppm) = -7.85 (s, br). (Figure A5.60)

^{31}P NMR (162 MHz, DMSO-d_6, 298 K): δ(ppm) = -9.13 (s). (Figure A5.61)

MS-ESI (positive ions; MeCN): m/z (%): 456 (100) $[CuL^2]^+$, 850 (30) $[CuL^2{}_2]^+$. (Figure A5.62)

Elem. anal. calcd (%) for $C_{54}H_{50}CuN_3O_4P_2$: C 69.70%, H 5.42%, N 4.52%; found: C 70.24%, H 5.31%, N 4.63%.

$[Cu(L^3)_2]NO_3 \cdot 2H_2O$ (AZ66)

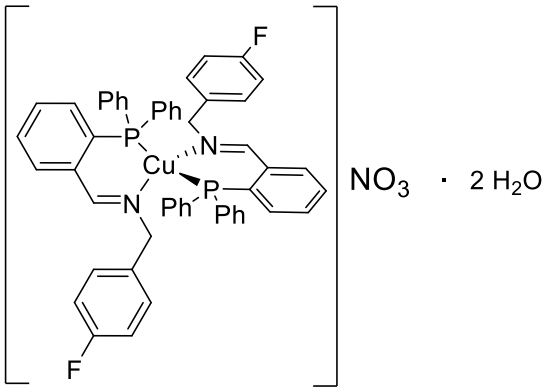

4-Fluorobenzylamine (39.3 µL, 0.344 mmol) was used for the synthesis. The product was isolated as an orange solid (113 mg, 69%).

IR (cm^{-1}): ν = 3057 (w) (CH sp^2), 2979 (w) and 2853 (w) (CH sp^3), 1621 (m) and 1604 (m) (C=N), 1364, 1323 (s) (NO_2 asym. str.). (Figure A5.63)

^{1}H NMR (500 MHz, Chloroform-*d*, 298 K): δ(ppm) = 8.79 (s, 2H, CH=N), 8.15 (d, *J* = 6.6 Hz, 2H, ArH), 7.76 (td, *J* = 7.6, 1.1 Hz, 2H, ArH), 7.47 (dt, *J* = 21.2, 7.2 Hz, 6H, ArH), 7.20 (t, *J* = 7.4 Hz, 8H, ArH), 7.08 – 5.98 (m, 14H, ArH), 5.83 (dd, *J* = 8.5, 5.4 Hz, 4H, ArH), 4.52 (s, 4H, CH_2). (Figure A5.64)

^{1}H NMR (400 MHz, DMSO-d_6, 298 K): δ(ppm) = 8.76 (s, 2H, CH=N), 8.05 – 7.98 (m, 2H, ArH), 7.85 (td, *J* = 7.5, 1.2 Hz, 2H, ArH), 7.74 – 7.66 (m, 2H, ArH), 7.51 (t, *J* = 7.5 Hz, 4H, ArH), 7.26 (t, *J* = 7.6 Hz, 8H, ArH), 6.88 (dt, *J* = 7.9, 4.1 Hz, 2H, ArH), 6.79 – 6.55 (m, br, 12H, ArH), 6.17 (dd, *J* = 8.4, 5.4 Hz, 4H, ArH), 4.36 (s, 4H, CH_2). (Figure A5.65)

^{31}P NMR (162 MHz, Chloroform-*d*, 298 K): δ(ppm) = -7.54 (s, br). (Figure A5.66)

^{31}P NMR (162 MHz, DMSO-d_6, 298 K): δ(ppm) = -8.96 (s). (Figure A5.67)

MS-ESI (positive ions; MeCN): m/z (%): 460 (100) $[CuL^3]^+$, 858 (60) $[CuL^3{}_2]^+$. (Figure A5.68)

Elem. anal. calcd (%) for $C_{52}H_{46}CuF_2N_3O_5P_2$: C 65.30%, H 4.85%, N 4.39%; found: C 65.54%, H 4.86%, N 4.20%.

Synthesis of 2-(diphenylphosphino)benzaldehyde:Cu(I) complexes

$[Cu(\mu\text{-}I)(MeCN)L^a]_2$ (AZ57)

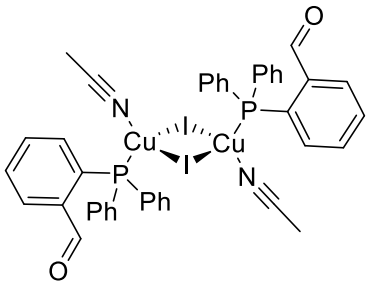

The reaction was performed under N_2 atmosphere and the solvents were degassed prior to use. To a solution of 2-(diphenylphosphino)benzaldehyde (100 mg, 0.344 mmol, 1.0 eq) in $CHCl_3$ (10 mL) was added a solution

of CuI (65.9 mg, 0.346 mmol, 1.0 eq) in MeCN (10 mL) and the resulting mixture was stirred at 50 °C for 1 h. The obtained yellow suspension was allowed to cool to r.t., then it was reduced to half volume. The suspension was left at 4 °C under N_2 for 1 h, then it was filtrated, washed with cold MeCN and dried *in vacuo*. The product was isolated as a yellow powder (132 mg, yield = 74%).

IR (cm^{-1}): ν = 2921 (w), 2829(w) and 2747 (w) (CH), 2295 (w) and 2270 (w) (C≡N), 1688 (s) (C=O). (Figure A5.69)

^{1}H NMR (400 MHz, Chloroform-*d*, 298 K): δ(ppm) = 10.09 (s, br, 2H, CH=O), 7.94 (d, *J* = 7.4 Hz, 2H, ArH), 7.62 – 7.27 (m, 24H, ArH), 7.00 (d, *J* = 7.6 Hz, 2H, ArH), 2.01 (s, 6H, CH_3-CN). (Figure A5.70)

^{31}P NMR (162 MHz, Chloroform-*d*, 298 K): δ(ppm) = -0.13 (s, br). (Figure A5.71)

MS-ESI (positive ions; MeCN): m/z (%): 353 (100) $[Cu(L^a)]^+$, 643 (40) $[Cu(L^a)_2]^+$. (Figure A5.72)

Elem. anal. calcd (%) for $C_{42}H_{36}Cu_2I_2N_2O_2P_2$: C 48.34%, H 3.48%, N 2.68%; found: C 47.88%, H 3.38%, N 2.16%.

$Cu(L^a)_2I$ (AZ58)

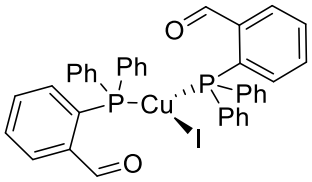

The reaction was performed under N_2 atmosphere and the solvents were degassed prior to use. To a solution of 2-(diphenylphosphino)benzaldehyde (100 mg, 0.344 mmol, 2.0 eq) in $CHCl_3$ (10 mL) was added a solution of CuI (32.8 mg, 0.172 mmol, 1.0 eq) in MeCN (10 mL) and the resulting mixture was stirred at 50 °C for 1 h. The obtained yellow suspension was allowed to cool to r.t., then it was reduced to half volume. The suspension was left at 4 °C under N_2 for 2 h, then it was filtrated, washed with cold MeCN and dried *in vacuo*. The product was isolated as a yellow powder (100 mg, yield = 75%).

IR (cm^{-1}): ν = 3061 (w) and 2921 (w) (CH sp^2), 2838 (w) and 2744 (w) (aldehyde CH), 1696 (m) and 1674 (s) (C=O). (Figure A5.73)

^{1}H NMR (400 MHz, Chloroform-*d*, 298 K): δ(ppm) = 9.98 (s, br, 2H, CH=O), 7.89 (d, *J* = 7.7 Hz, 2H, ArH), 7.60 (td, *J* = 7.5, 1.2 Hz, 2H, ArH), 7.55 – 7.33 (m, 16H, ArH), 7.28 (s, 4H, ArH), 7.24 (s, 2H, ArH), 7.01 (d, *J* = 7.6 Hz, 2H, ArH). (Figure A5.74)

^{31}P NMR (162 MHz, Chloroform-*d*, 298 K): δ(ppm) = -1.53 (s, br). (Figure A5.75)

MS-ESI (positive ions; MeCN): m/z (%): 290 (70) $[L^a]^+$, 353 (85) $[Cu(L^a)]^+$, 643 (100) $[Cu(L^a)_2]^+$. (Figure A5.76)

Elem. anal. calcd (%) for $C_{38}H_{30}CuIO_2P_2$: C 59.19%, H 3.92%; found: C 59.62%, H 3.98%.

Single crystals suitable for XRD analysis were obtained by slow evaporation of a solution of the complex in $CHCl_3$.

$Cu(L^a)_2NO_3$ (AZ67)

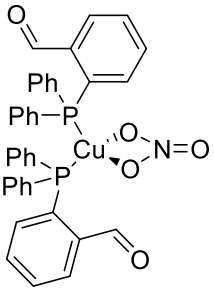

To a light blue solution of $Cu(NO_3)_2 \cdot 3H_2O$ (20.8 mg, 0.086 mmol, 0.5 eq) in MeCN (15 mL) was added an excess of copper powder (ca. 0.2 mmol) and the mixture was stirred under reflux till complete decolorization of the solution (ca. 30 min). The colourless solution was quick hot filtered in order to remove unreacted copper powder, then it was degassed, put under N_2 and added to a solution of 2-(diphenylphosphino)benzaldehyde (100 mg, 0.344 mmol, 2.0 eq) in $CHCl_3$ (10 mL). The resulting yellow solution was stirred at 50 °C under N_2 for 1 h. The solution was allowed to cool to r.t., then it was reduced to a small volume (3 – 4 mL) and Et_2O (ca. 50 mL) was added. The mixture was left at -20 °C under N_2 overnight. The precipitate was filtrated, washed with Et_2O and dried *in vacuo*. The product was isolated as a yellow crystalline solid (92 mg, yield = 76%).

IR (cm^{-1}): ν = 3061 (w) (CH sp^2), 2852 (w) and 2757 (w) (CH aldehyde), 1692 (m) and 1670 (s) (C=O), 1434 (s) (NO stretch), 1286 (s) (NO_2 asym. stretch).

^{1}H NMR (400 MHz, DMSO-d_6, 298 K): δ(ppm) = 9.97 (s, br, 2H, CH=O), 8.00 (s, br, 2H, ArH), 7.73 (dtd, *J* = 18.2, 7.4, 1.5 Hz, 4H, ArH), 7.56 – 6.96 (m, 20H, ArH), 6.85 (d, *J* = 7.5 Hz, 2H, ArH). (Figure A5.78)

MS-ESI (positive ions; MeCN): m/z (%): 353 (100) $[Cu(L^a)]^+$, 643 (65) $[Cu(L^a)_2]^+$. (Figure A5.79)

Elem. anal. calcd (%) for $C_{38}H_{30}CuNO_5P_2$: C 64.63%, H 4.28%, N 1.98%; found: C 65.00%, H 4.35%, N 2.07%.

Single crystals for X-ray diffraction analysis were selected from the prepared sample.

Crystallography

Single crystal X-ray diffraction analyses were carried out with a Bruker D8Venture diffractometer equipped with a kappa goniometer and an Oxford cryosystem. Microfocused MoKα radiation (λ =0.71073Å) was used as the X-ray source and Lorentz polarization and absorption correction were applied through the SADABS procedure.[289] The phase problem was solved by direct methods and the structures were refined by full-matrix least-squares on all F2 using SHELXL,[123,290] as implemented in the OLEX2[220] suite of programs. The structure drawings were obtained using ORTEPIII[291] and Mercury.[292]

Biology

Preliminary assay

Two different media for cell culture were used: nutrient broth (Oxoid) for bacteria and Minimal Medium (2% glucose, 0.5% ammonium sulphate and 0.17% yeast Nitrogen base) for the yeast. Bacteria were sub-cultured from nutrient agar plates and grown in nutrient broth overnight in an orbital shaker at 37 °C and 200 rpm. The yeast *Candida albicans* was sub-cultured from a Minimal Medium plate and grown overnight at 37 °C and 200 rpm in Minimal Medium. Stock solutions of the metal complexes were prepared by dissolving the six compounds in 1 mL of DMSO to give the following stock concentrations: **AZ48** 7.90 mM, **AZ53a** 5.03 mM, **AZ55a** 4.92 mM, **AZ61** 5.43 mM, **AZ65** 7.74 mM, **AZ66** 5.96 mM. Two sets of working solutions, A_1 and A_2, were prepared respectively by 1/10 and 1/100 dilution of compounds stock solutions with PBS. To Petri dishes that contained the proper medium, 100 µL of pathogen inoculum (obtained by dilution of the micro-organism cultures with PBS) were added and spread on the plates (1×10^5 CFU per plate). 10 µL of A_1 and A_2 compounds solutions were added in specific areas on the Petri dishes and the plates were incubated at 37°C for 24 hours under static conditions. The presence or not of inhibition zones on the dishes was evaluated simply by naked eye. A schematic representation of the set-up and the outcomes of the preliminary assay are depicted in Figure 5.37.

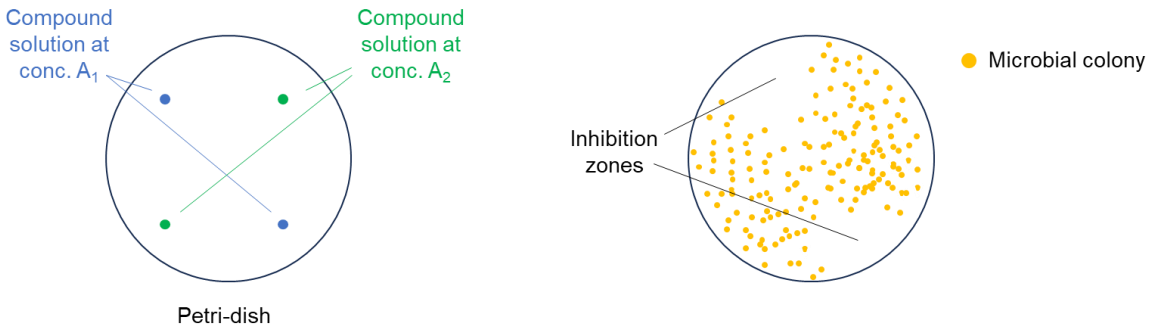

Figure 5.37: Set-up of the preliminary assay: on a Petri-dish containing microbial inoculum, compound solutions are deposited at two different concentrations (duplicates of A_1 and A_2 samples of the same compound are performed on the same plate) (left); outcome of the preliminary assay: the areas on the plate where there are not visible microbial colonies are “inhibition zones” and indicate that the tested compound has antimicrobial activity at the concentration used (right).

Broth microdilution method

One 96-well microtitration plate (Figure 5.38) was used for each compound, with a total of 6 different plates. A multichannel pipette was employed. The following procedure was used for each plate:

- 100 µL of nutrient broth were added to all the wells;
- 100 µL of compound working solution at A_1 concentration were added to all the wells of row 3;
- diluted samples were prepared in the other rows (4 – 11) by progressive two-fold dilutions (100 µL from each well of row 3 were added to each well of row 4 and mixed, then 100 µL were taken from

each well of row 4 and added to each well of row 5 and so on). At the end, each well of the rows from 3 to 11 contained 100 µL of solution (at row 11, the 100 µL of excess solution were thrown to waste);

- each well of rows 2 – 11 was inoculated with a microbial inoculum (100 µL) prepared in the same medium. The total volume in each well of rows 2 – 11 was 200 µL, while the concentration of the compound in each well of row 3 was ¼ of A_1 (the final concentration of DMSO in each well of row 3 is 2.5%);
- after well-mixing, the inoculated 96-well plate was incubated at 37°C for 24 hours under static conditions;
- bacterial cells growth % was determined by spectrophotometric analysis, that is, optical density (OD) measurement for each well. The OD value was recorded at 600 nm. Measurements were performed with a Bio-Tek Synergy HT spectrophotometer.

Rows 1 and 12, containing the medium only, were used as negative controls (no proliferation of bacteria), while row 2, containing the inoculum without tested compound, was used as positive control (proliferation of bacteria).

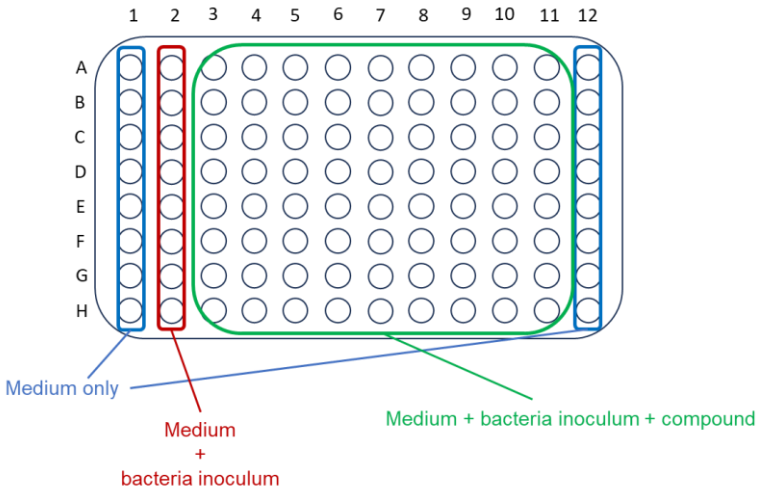

Figure 5.38: Schematic representation of the set-up for broth microdilution method on 96-well plate.

High OD_{600} values are due to high concentrations of bacterial cells in the wells: more bacteria are present, more turbid will be the sample.

High OD values are related to high growth % of bacterial cells and therefore to low or no antibiotic activity of tested compounds. Low OD values are related to low growth % and high antibiotic activity.

Broth microdilution method with control for compound precipitation

One 96-well microtitration plate was used for one compound, with a total of 2 different plates. A multichannel pipette was employed. The following procedure was used for each plate:

- 100 µL of nutrient broth were added to all the wells;
- 100 µL of compound working solution (**AZ48** conc. = 611 µM; **AZ61** conc. = 712 µM) were added to all the wells of row 3;
- diluted samples were prepared in the other rows (4 – 11) by progressive two-fold dilutions;

- the wells of rows 2 – 11 belonging to rows E,F,G and H only were inoculated with a microbial inoculum (100 µL);
- to the wells of rows 2 – 11 belonging to rows A,B,C and D only were added 100 µL of nutrient broth without bacterial cells. Rows A,B,C and D contained the compound only and were used as control for precipitation;
- the total volume in each well of rows 2 – 11 was 200 µL, while the concentration of the compound in each well of row 3 was ¼ of the concentration of the working solution (the final concentration of DMSO in each well of row 3 is 2.5%);
- after well-mixing, the 96-well plate was incubated at 37°C for 24 hours under static conditions;
- bacterial cells growth % was determined by spectrophotometric analysis, that is, optical density (OD) measurement for each well. The measurement was performed with a Bio-Tek Synergy HT spectrophotometer.

In Figure 5.39 it is depicted the set-up for the experiment.

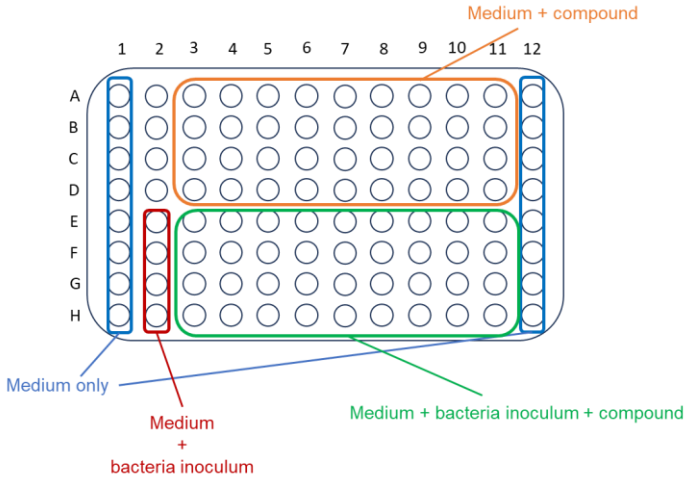

Figure 5.39: Schematic representation of the set-up for broth microdilution method on 96-well plate with control for precipitation.

References

1) D. A. da Silva, A. De Luca, R. Squitti, M. Rongioletti, L. Rossi, C. M. L. Machado, G. Cerchiaro, *J. Inorg. Biochem.* **2022**, *226*, 111634.

2) Y. C. Horng, P. A. Cobine, A. B. Maxfield, H. S. Carr, D. R. Winge, *J. Biol. Chem.* **2004**, *279*, 35334–35340.

3) C. K. Tsang, Y. Liu, J. Thomas, Y. Zhang, X. F. S. Zheng, *Nat. Commun.* **2014**, *5*, 3446.

4) N. E. Hellman, S. Kono, G. M. Mancini, A. J. Hoogeboom, G. J. De Jong, J. D. Gitlin, *J. Biol. Chem.* **2002**, *277*, 46632–46638.

5) I. Bremner, *Am. J. Clin. Nutr.* **1998**, *67*.

6) W. H. Koppenol, *Redox Rep.* **2001**, *6*, 229–234.

7) M. Bendellaa, P. Lelièvre, J-L. Coll, L. Sancey, A. Deniaud, B. Busser, *Int. J. Cancer.* **2024**, *154*, 7‑20.

8) M. I. Costa, A. B. Sarmento-Ribeiro, A. C. Gonçalves, *Int. J. Mol. Sci.* **2023**, *24*, 4822.

9) B. Chen, P. Yu, W. N. Chan, F. Xie, Y. Zhang, L. Liang, K. T. Leung, K. W. Lo, J. Yu, G. M. K. Tse, W. Kang, K. F. To, *Signal Transduct. Target. Ther.* **2024**, 9:6.

10) L. A. Torre, R. L. Siegel, E. M. Ward, A. Jemal, *Cancer Epidemiol. Biomark. Prev. 25.* **2016**, *1*, 16–27.

11) WHO fact sheets, https://www.who.int/news-room/fact-sheets/detail/cancer

12) E. J. Ge, A. I. Bush, A. Casini, *et al*., *Nat Rev Cancer* **2022**, *22*, 102–113.

13) V.C. Shanbhag, N. Gudekar, K. Jasmer, C. Papageorgiou, K. Singh, M.J. Petris, *Biochim. Biophys. Acta, Mol. Cell Res.* **2021**, *1868 (2),* 118893.

14) E.D. Harris, *Nutr. Rev.* **2004**, *62 (2)*, 60–64.

15) F. Soncin, J. D. Guitton, T. Cartwright, J. Badet, *Biochem. Biophys. Res. Commun.* **1997**, *236 (3),* 604–610.

16) B. Halliwell, J. M. C. Gutteridget, *Biochem. J.* **1984**, *219 (1)*, 1–14.

17) E. H. Blackburn, E. S. Epel, J. Lin, *Science* **2015**, *350(6265),* 1193-1198.

18) T. Nimmanon, S. Ziliotto, O. Ogle, A. Burt, J. M. W. Gee, G. K. Andrews, P. Kille, C. Hogstrand, W. Maret, K. M. Taylor, *Cell Mol Life Sci.* **2021**, *78(4),* 1781-1798.

19) E. Armstrong-Gordon, D. Gnjidic, A. J. McLachlan, B. Hosseini, A. Grant, P. J. Beale, N. J. Wheate, *J. Cancer Res. Clin. Oncol.* **2018**, *144*, 1561–1568.

20) P. D. O'Dowd, D. F. Sutcliffe, D. M. Griffith, *Coord. Chem. Rev.* **2023**, *497*, 215439.

21) Z. H. Siddik, *Oncogene* **2003**, *22 (47),* 7265–7279.

22) S. Alassadi, M. J. Pisani, N. J. Wheate, *Dalton Trans.* **2022**, *51*, 10835–10846.

23) M. Frezza, S. Hindo, D. Chen, A. Davenport, S. Schmitt, D. Tomco, Q. P. Dou, *Curr. Pharmaceut. Des.* **2010**, *16*, 1813-1825.

24) X. Ding, H. Xie, Y. Kang, *J. Nutr. Biochem.* **2011**, *22 (4),* 301–310.

25) S. Baldari, G. Di Rocco, G. Toietta*, Int. J. Mol. Sci.* **2020**, *21*, 1069.

26) C. R. Kowol, B. K. Keppler, C. G. Hartinger, U. Jungwirth, *Antioxid. Redox Signal.* **2011**, *15*.

27) J. M. Matés, *Toxicology* **2000**, *153*, 83–104.

28) M. Devereux, D. O'Shea, M. O'Connor, H. Grehan, G. Connor, M. McCann, G. Rosair, F. Lyng, A. Kellett, M. Walsh, et al., *Polyhedron* **2007**, *26*, 4073–4084.

29) M. Devereux, M. Mccann, D. O. Shea, M. O. Connor, E. Kiely, V. Mckee, D. Naughton, A. Fisher, A. Kellett, M. Walsh, et al., *Bioinorg. Chem. Appl.* **2006**, 1–11.

30) B. Coyle, P. Kinsella, M. Mccann, M. Devereux, R. O. Connor, M. Clynes, K. Kavanagh, *Toxicol. Vitr.* **2004**, *18*, 63–70.

31) C. Santini, M. Pellei, V. Gandin, M. Porchia, F. Tisato, C. Marzano, *Chem. Rev.* **2014**, *114*, 815–862.

32) R. Buchtík, Z. Trávníček, J. Vančo, *J. Inorg. Biochem.* **2012**, *116*, 163–171.

33) S. J. McKie, K. C. Neuman, A. Maxwell, *BioEssays* **2021**, *43 (4),* e2000286.

34) D. Jayaraju, A. K. Kondapi, *Curr. Sci.* **2001**, *81*, 787–792.

35) K. G. Daniel, P. Gupta, R. H. Harbach, W. C. Guida, Q. P. Dou, *Biochem. Pharmacol.* **2004**, *67*, 1139–1151.

36) L. D. Fricker, *Annu. Rev. Pharmacol. Toxicol.* **2020**, *60*, 457–476.

37) J. S. Gelman, J. Sironi, I. Berezniuk, S. Dasgupta, L. M. Castro, F. C. Gozzo, E. S. Ferro, L. D. Fricker, *Plos one* **2013**, *8 (1)*, e53263.

38) H. C. Drexler, *Proc. Natl. Acad. Sci.* **1997***, 94*, 855.

39) E. Lee, D.H. Lee, *BMB* **2017**, *Rep 50*, 401-410.

40) C. Grek, D. M. Townsend, *Endoplasmic Reticulum Stress Dis* **2014**, *1 (1),* 4-17.

41) S. Xu, S. Sankar, N. Neamati, *Drug Discovery Today* **2014**, *19 (3),* 222-240.

42) S. Narindrasorasak, P. Yao, B. Sarkar, *Biochem. Biophys. Res. Commun.* **2003**, *311*, 405–414.

43) A. M. Benham, *Antioxidants Redox Signal.* **2012**, *16*, 781–789.

44) M. Carcelli, M. Tegoni, J. Bartoli, C. Marzano, G. Pelosi, M. Salvalaio, D. Rogolino, V. Gandin, *Eur. J. Med. Chem.* **2020**, *194*, 112266.

45) F. Miglioli, M. De Franco, J. Bartoli, M. Scaccaglia, G. Pelosi, C. Marzano, D. Rogolino, V. Gandin, M. Carcelli, *Eur. J. Med. Chem.* **2024***, 276,* 116697.

46) P. Tsvetkov, S. Coy, B. Petrova, M. Dreishpoon, A. Verma, M. Abdusamad, J. Rossen *et al., Science* **2022**, *375*, 1254–1261.

47) D. Tang, X. Chen, G. C. Kroemer, *Cell Res* **2022**, *32*, 417–418.

48) J. Xie, Y. Yang, Y. Gao, Y., J. He, *Mol Cancer* **2023**, *22*, 46.

49) Y. Han, G. Zhu, Y. Jin, C. Li, *ACS Materials Lett.* **2025**, *7*, 3301−3319.

50) M. Melník, M. Kabešová, *J. Coord. Chem.* **2000**, *50*, 323.

51) Y. Wang, T. Tang, Y. Yuan, N. Li, X. Wang, J. Guan, *ChemMedChem* **2024**, *19*, e202400060.

52) Z. Aguilar-Jiménez, A. Espinoza-Guillén, K. Resendiz-Acevedo, I. Fuentes-Noriega, C. Mejía, L. Ruiz-Azuara, *Inorganics* **2023**, *11*, 394.

53) Z. Aguilar-Jiménez, M. González-Ballesteros, S. G. Dávila-Manzanilla, A. Espinoza-Guillén, L. Ruiz-Azuara, *Int. J. Mol. Sci.* **2022**, *23*, 12756.

54) F. Tisato, M. Porchia, C. Santini, V. Gandin, C. Marzano, *Copper(I) Chemistry of Phosphines, Functionalized Phosphines and Phosphorus Heterocycles,* Elsevier Inc, **2019**.

55) H. Beraldo, D. Gambino, *Mini-Rev. Med. Chem.* **2004**, *4*, 31–39.

56) S. Q. Zhang, X. F. Yu, H. B. Zhang, N. Peng, Z. X. Chen, Q. Cheng, X. L. Zhang, S. H. Cheng, Y. Zhang, *Mol. Nutr. Food Res.* **2018**, *62*, e170098.

57) S. A. Rider, S. J. Davies, A. N. Jha, R. Clough, J. W. Sweetman, *J. Anim. Physiol. Anim. Nutr.* **2010**, *94*, 99–110.

58) J. Qian, L. Wang, W. Gu, X. Liu, J. Tian, S. Yan, *Dalton Trans.* **2011**, *40*, 5617–5624.

59) E. Boseggia, M. Gatos, L. Lucatello, F. Mancin, S. Moro, M. Palumbo, C. Sissi, P. Tecilla, U. Tonellato, G. Zagotto*, J. Am. Chem. Soc.* **2004**, *126*, 4543–4549.

60) M Pellei, F. Del Bello, M. Porchia, C. Santini, *Coord. Chem. Rev*. **2021**, *445*, 214088.

61) A. Hussain, M. F. AlAjmi, Md. T. Rehman, A. A. Khan, P. A. Shaikh, R. A. Khan, *Molecules* **2018**, *23*, 1232.

62) J. L. Qin, W. Y. Shen, Z. F. Chen, L. F. Zhao, Q. P. Qin, Y. C. Yu, H. Liang, *Sci. Rep.* **2017***, 7,* 46056.

63) G. Srivastavaa, A. Mattaa, G. Fua, R. T. Somasundarama, A. Dattib, P. G. Walfisha, R. Ralhan, *Molecular Oncology*, **2015**, *9*, 1720-1735.

64) A. Podolski-Renić, A. Čipak Gašparović, A. Valente, O. Lopez, J. H. Bormio Nunes, C. R. Kowol, P. Heffeter, N. R. Filipović, *Eur. J. Med. Chem.* **2024**.

65) C. Bonaccorso, T. Marzo, D. La Mendola, *Pharmaceuticals* **2020**, *13*, 4.

66) B. Sentürk, B. Butschke, F. Eisenreich, *Chem. Sci.* **2025**.

67) I. A. Mir, Q. U. Ain, T. Qadir, A. Q. Malik, Saima Jan, S. Shahverdi, S. A. Nabi, *J. Mol Struct.* **2014**, *1295*, 136216.

68) T. S. Lobana, R. Sharma, G. Bawa, S. Khanna, *Coord. Chem. Rev.* **2009**, *253*, 977‑1055.

69) M. H. Assaleh, A. R. Božić, S. Bjelogrlić, M. Milošević, M. Simić, A. D. Marinković, I. N. Cvijetić, *Struct. Chem.* **2019**, *30*, 2447–2457.

70) D. Dragancea, A. W. Addison, M. Zeller, L. K. Thompson, D. Hoole, M. D. Revenco, A. D. Hunter, *Eur. J. Inorg. Chem.* **2008**, 2530–2536.

71) D. Dragancea, V. B. Arion, S. Shova, E. Rentschler, N. V. Gerbeleu, *Angew. Chem. Int. Ed.* **2005**, *44*, 7938–7942.

72) T. N. Hansen, C. A. Olsen, *Chem. Eur. J.* **2023**, *2023*, e202303770.

73) P. Heffeter, V. F. S. Pape, É. A. Enyedy, B. K. Keppler, G. Szakacs, C. R. Kowol, *Antioxidants Redox Signal.* **2019**, *30*, 1062–1082.

74) Y. Yu, D. S. Kalinowski, Z. Kovacevic, A. R. Siafakas, P. J. Jansson, C. Stefani, D. B. Lovejoy, P. C. Sharpe, P. V. Bernhardt, D. R. Richardson, *J. Med. Chem.* **2009**, *52*, 5271–5294.

75) L. Feun, M. Modiano, K. Lee, J. Mao, A. Marini, N. Savaraj, P. Plezia, B. Almassian, E. Colacino, J. Fischer, et al., *Cancer Chemother. Pharmacol.* **2002**, *50*, 223–229.

76) J. Chao, T. W. Synold, R. J. Morgan, C. Kunos, J. Longmate, H. J. Lenz, D. Lim, S. Shibata, V. Chung, R. G. Stoller, et al., *Cancer Chemother. Pharmacol.* **2012**, *69*, 835–843.

77) M. J. Mackenzie, D. Saltman, H. Hirte, J. Low, C. Johnson, G. Pond, M. J. Moore, *Invest. New Drugs* **2007**, *25*, 553–558.

78) S. Attia, J. Kolesar, M. R. Mahoney, H. C. Pitot, D. Laheru, J. Heun, W. Huang, J. Eickhoff, C. Erlichman, K. D. Holen, *Invest. New Drugs* **2008**, *26*, 369–379.

79) A. Bacchi, M. Carcelli, P. Pelagatti, G. Pelizzi, M. C. Rodriguez-Arguelles, D. Rogolino, C. Solinas, F. Zani, *J. Inorg. Biochem.* **2005**, *99*, 397–408.

80) A. R. Bozic, S. K. Bjelogrlic, I. T. Novakovic, N. R. Filipovic, P. M. Petrovic, A. D. Marinkovic, T. R. Todorovic, I. N. Cvijetic, *ChemistrySelect* **2018**, *3*, 2215 – 2221.

81) A. Bacchi, M. Carcelli, P. Pelagatti, C. Pelizzi, G. Pelizzi, F. Zani, *J. Inorg. Biochem.* **1999***, 75,* 123–133.

82) D. M. Wiles, T. Suprunchuk, *J. Med. Chem.* **1970**, *13*, 323–324.

83) N. Zhang, Y. Tai, M. Li, P. Ma, J. Zhao, J. Niu, *Dalton Trans.* **2014**, *43*, 5182–5189.

84) A. Bozic, A. Marinkovic, S. Bjelogrlic, T. R. Todorovic, I. N. Cvijetic, I. Novakovic, C. D. Muller, N. R. Filipovic, *RSC Adv.* **2016**, *6*, 104763.

85) S. Iqbal, M. Saleem, M. K. Azim, M. Taha, U. Salar, K. M. Khan, S. Perveen, M. I. Choudhary, *Bioorg. Chem.* **2017**, *72*, 89–101.

86) C. R. Kowol, R. Trondl, P. Heffeter, V. B. Arion, M. A. Jakupec, A. Roller, M. Galanski, W. Berger, B. K. Keppler, *J. Med. Chem*. **2009**, *52*, 5032–5043.

87) C. M. Manzano, D. H. Nakahata, R. E. F. de Paiva, *Coord. Chem. Rev*. **2022**, *462*, 214506.

88) D. Palanimuthu, S. V. Shinde, K. Somasundaram, A. G. Samuelson*, J. Med. Chem.* **2013**, *56*, 722–734.

89) J. Garcia-Tojal, A. Garcia-Orad, J. L. Serra, J. L. Pizarro, L. Lezama, M. I. Arriortua, T. Rojo, *J. Inorg. Biochem.* **1999**, *75*, 45‑54.

90) R. Vikneswaran, N. E. Eltayeb, S. Ramesh, R. Yahya, *Polyhedron* **2016**, *105*, 89–95.

91) M. P. Sathisha, V. K. Revankar, K. S. R. Pai, *Metal-Based Drugs* **2008**, *Article ID 362105*, 11 pages.

92) R. S. Nair, M. E. Potti, R. Thankappan, S. K. Chandrika, M. R. P. Kurup, P. Srinivas, *Mol. Carcinog.* **2017**, *56*, 1501‑1514.

93) V. R. Vemula, V. Lagishetty, S. Lingala, *Int. J. Pharm. Sci. Rev. Res.* **2010**, *5 (1),* 41–51.

94) K. T. Savjani, A. K. Gajjar, J. K. Savjani, *ISRN Pharmaceutics* **2012**, *Article ID 195727*, 10 pages.

95) S. J. Berners-Price, P. J. Sadler, *Phosphines and Metal Phosphine Complexes: Relationship of Chemistry to Anticancer and Other Biological Activity*. In *Bioinorganic Chemistry*; Springer: Berlin/Heidelberg, Germany, **1988**, *70*, pp 27–102.

96) G. D. Hoke, R. A. Macia, P. C. Meunier, P. J. Bugelski, C. K. Mirabelli, G. F. Rush, W. D. Matthews, *Toxicol. Appl. Pharmacol.* **1989**, *100*, 293–306.

97) F. Santoro, V. M. D'Amore, A. Zavaroni, I. Diakogiannaki, D. Rogolino, M. Carcelli, A. Carotenuto, L. Marinelli, F. S. Di Leva, D. Brancaccio, G. Donati, *J. Chem. Phys.* **2025***, 162*, 094306.

98) A. Zavaroni, E. Riva, V. Borghesani, G. Donati, F. Santoro, V. M. D'Amore, M. Tegoni, G. Pelosi, A. Buschini, D. Rogolino, M. Carcelli, *Int. J. Mol. Sci.* **2024**, *25*, 10831.

99) D. Maity, A. K. Manna, D. Karthigeyan, T. K. Kundu, S. K. Pati, T. Govindaraju, *Chem. Eur. J.* **2011**, *17*, 11152 – 11161.

100) K. H. M. Ebrahim Tehrani, F. Kobarfard, P. Azerang, M. Mehravar, Z. Soleimani, G. Ghavami, S. Sardari, *Iran. J. Pharm. Res.* **2013**, *12*, 331–346.

101) H. Gunther, *NMR Spectroscopy* (Wiley, New York, NY, **1994**).

102) M. T. Huggins, T. Kesharwani, J. Buttrick, C. Nicholson, *J. Chem. Educ*. **2020**, *97*, 1425.

103) A. Bacchi, A. Bonini, M. Carcelli, F. Ferraro, E. Leporati, C. Pelizzi, G. Pelizzi, *J. Chem. Soc., Dalton Trans.* **1996**, 2699-2704.

104) F. G. Bordwell, G. Z. Ji, *J. Am. Chem. Soc.* **1991**, *113*, 8398.

105) T. D. W. Claridge, *High Resolution NMR Techniques in Organic Chemistry*, 3rd Ed., Elsevier **2016**.

106) C. Hansch, G. Sammer, J. B. Taylor, *Comprehensive Medicinal Chemistry* **1990**, *Vol. IV,* p. 241.

107) J. W. Moore, R. G. Pearson, A. A. Frost, *Kinetics and Mechanism*, 3rd Edition, John Wiley and Sons, **1981**.

108) A. Gans, A. Sabatini, A. Vacca, *Talanta* **1996**, *43,* 1739‑1753.

109) A. Sîrbu, O. Palamarciuc, M. V. Babak, J. M. Lim, K. Ohui, E. A. Enyedy, S. Shova, D. Darvasiová, P. Rapta, W. H. Ang, et al., *Dalt. Trans.* **2017**, *46*, 3833–3847.

110) A. R. Božić, N. R. Filipović, T. Z. Verbić, M. K. Milčić, T. R. Todorović, I. N. Cvijetić, O. R. Klisurić, M. M. Radišić, A. D. Marinković, *Arab. J. Chem.* **2020**, *13*, 932-953.

111) C. S. Wilcox, *Frontiers in Supramolecular Organic Chemistry and Photochemistry*, ed. H.-J. Schneider and H. Durr, VCH, Weinheim, **1991**, pp. 123–144.

112) P. Thordarson, *Chem. Soc. Rev.* **2011**, *40*, 1305.

113) https://www.sigmaaldrich.com/IT/it/product/mm/tms012

114) S. Montalbano, F. Bisceglie, G. Pelosi, M. Lazzaretti, A. Buschini, *Pharmaceutics* **2023**, *15*, 1325.

115) A. I. Vogel, *Quantitative Inorganic Analysis Including Elementary Instrumental Analysis* 3rd ed.; Longmans: London, UK, **1962**.

116) Technical bulletin of *CellTiter 96® Aqueous One Solution Cell Proliferation Assay*, Promega Corporation.

117) M. V. Berridge, A. S. Tan, *Arch. Biochem. Biophys.* **1993**, *303*, 474–482.

118) W. Strober, *Curr. Protoc. Immunol.* **2015**.

119) Technical manual of *CellTiter-Glo® 2.0 assay*, Promega Corporation.

120) *SAINT: SAX, Area Detector Integration*; Siemens Analytical Instruments Inc., Madison, WI, USA, **1986**.

121) G. Sheldrick, *SADABS: Siemens Area Detector Absorption Correction Software*; University of Goettingen: Gottingen, Germany, **1996**.

122) A. Altomare, C. Burla, M. Camalli, G. L. Cascarano, C. Giacovazzo, A. Guagliardi, A. G. G. Moliterni, G. Polidori, R. Spagna, *J. Appl. Crystallogr.* **1999**, *32*, 115-119.

123) G. M. Sheldrick, *Acta Crystallogr. A* **2008**, *64*, 112-122.

124) L. J. Farrugia, *J. Appl. Crystallogr.* **1999**, *32*, 837‑838.

125) L. Alderighi, P. Gans, A. Ienco, D. Peters, A. Sabatini, A. Vacca, *Coord. Chem. Rev.* **1999**, *184*, 311-318.

126) M. Sokołowska, W. Bal, *J. Inorg. Biochem.* **2005**, *99*, 1653‑1660.

127) C. M. H. Ferreira, I. S. S. Pinto, E. V. Soares, H. M. V. M. Soares, *RSC Adv.* **2015**, *5*, 30989‑31003.

128) H.M.V.M. Soares, P.C.F.L. Conde, *Anal. Chim. Acta* **2000**, *421*, 103‑111.

129) G. Gran, *Analyst* **1952**, *77*, 661‑671.

130) S. Miertus, E. Scrocco, J. Tomasi, *Chem. Phys.* **1981**, *55*, 117.

131) B. Mennucci, J. Tomasi, J. *Chem. Phys.* **1997**, *106*, 5151.

132) N. Rega, M. Cossi, V. Barone, *Chem. Phys. Lett.* **1998**, *293*, 221.

133) A. D. Becke, *J. Chem. Phys.* **1993,** *98,* 5648.

134) C. Lee, W. Yang, R. G. Parr, *Phys. Rev. B* **1988**, *37*, 785.

135) S. Grimme, J. Antony, S. Ehrlich, H. Krieg, *J. Chem. Phys.* **2010**, *132*, 154104.

136) A. Schaefer, C. Huber, R. Ahlrichs, *J. Chem. Phys.* **1994**, *100*, 5829.

137) A. Schaefer, C. Huber, R. Ahlrichs, *J. Chem. Phys.* **1992**, *97*, 2571.

138) J. R. Cheeseman, G. W. Trucks, T. A. Keith, M. J. Frisch, J. *Chem. Phys.* **1996**, *104*, 5497.

139) Z. S. Safi, N. Wazzan, *Sci. Rep.* **2022**, *12,* 17798.

140) P. R. Rablen, S. A. Pearlman, J. Finkbiner, *J. Phys. Chem. A* **1999**, *103*, 7357.

141) R. Jain, T. Bally, P. R. Rablen, *J. Org. Chem.* **2009**, *74*, 4017.

142) R. McWeeny, *Phys. Rev.* **1962**, *126*, 1028.

143) R. Ditchfield, *Mol. Phys.* **1974**, *27*, 789.

144) A. Klamt, J. Reinisch, F. Eckert, A. Hellweg, M. Diedenhofen, *Phys. Chem. Chem. Phys.* **2012**, *14*, 955.

145) M. J. Frisch, G. W. Trucks, H. B. Schlegel, G. E. Scuseria, M. A. Robb, J. R. Cheeseman, G. Scalmani, V. Barone, G. A. Petersson, H. Nakatsuji, X. Li, M. Caricato, A. V. Marenich, J. Bloino, B. G. Janesko, R. Gomperts, B. Mennucci, H. P. Hratchian, J. V. Ortiz, A. F. Izmaylov, J. L. Sonnenberg, D. Williams-Young, F. Ding, F. Lipparini, F. Egidi, J. Goings, B. Peng, A. Petrone, T. Henderson, D. Ranasinghe, V. G. Zakrzewski, J. Gao, N. Rega, G. Zheng, W. Liang, M. Hada, M. Ehara, K. Toyota, R. Fukuda, J. Hasegawa, M. Ishida, T. Nakajima, Y. Honda, O. Kitao, H. Nakai, T. Vreven, K. Throssell, J. A. Montgomery, Jr., J. E. Peralta, F. Ogliaro, M. J. Bearpark, J. J. Heyd, E. N. Brothers, K. N. Kudin, V. N. Staroverov, T. A. Keith, R. Kobayashi, J. Normand, K. Raghavachari, A. P. Rendell, J. C. Burant, S. S. Iyengar, J. Tomasi, M. Cossi, J. M. Millam, M. Klene, C. Adamo, R. Cammi, J. W. Ochterski, R. L. Martin, K. Morokuma, O. Farkas, J. B. Foresman, D. J. Fox, *Gaussian 16, Revision A.02*, Gaussian, Inc., Wallingford, CT, **2016**.

146) R. Dennington, T. A. Keith, J. M. Millam, *Gaussview Version 6*, Semichem, Inc., Shawnee Mission, KS, **2019**.

147) L. Martinez, R. Andrade, E. G. Birgin, J. M. Martinez, *J. Comput. Chem.* **2009**, *30*, 2157‑2164.

148) T. Fox, P. A. Kollman, *J. Phys. Chem. B* **1998***, 102*, 8070.

149) C. I. Bayly, P. Cieplak, W. Cornell, P. A. Kollman, *J. Phys. Chem.* **1993**, *97*, 10269.

150) J. Wang, W. Wang, P. A. Kollman, D. A. Case, *J. Mol. Graphics Modell.* **2006**, *25,* 247‑260.

151) D. A. Case, H. M. Aktulga, K. Belfon, D. S. Cerutti, G. A. Cisneros, V. W. D. Cruzeiro et al., *J. Chem. Inf. Model.* **2023***, 64,* 6183‑6191.

152) U. C. Singh, P. A. Kollman, *J. Comput. Chem.* **1984**, *5*, 129.

153) T. Fox, P. A. Kollman, *J. Phys. Chem. B* **1998**, *102*, 8070.

154) M. J. Abraham, T. Murtola, R. Schulz, S. Pall, J. C. Smith, B. Hess, E. Lindahl*, SoftwareX* **2015**, *1–2,* 19.

155) H. J. C. Berendsen, W. F. van Gusteren, A. DiNola, J. R. Haak, *J. Chem. Phys.* **1984***, 81*, 3684.

156) U. Essmann, L. Perera, M. L. Berkowitz, T. Darden, H. Lee, and L. G. Pedersen, *J. Chem. Phys.* **1995**, *103*, 8577.

157) I. S. Joung, T. E. Cheatham III, *J. Phys. Chem. B* **2008**, *112*, 9020.

158) G. Bussi, D. Donadio, M. Parrinello, *J. Chem. Phys.* **2007**, *126*, 014101.

159) M. Parrinello, A. Rahman, *J. Appl. Phys.* **1981***, 52,* 7182.

160) W. F. Van Gunsteren, H. J. C. Berendsen, *Mol. Simul.* **1988**, *1*, 173.

161) B. Hess, H. Bekker, H. J. C. Berendsen, J. G. E. M. Fraaije, *J. Comput. Chem.* **1997**, *18*, 1463.

162) W. Humphrey, A. Dalke, and K. Schulten, *J. Mol. Graphics* **1996**, *14,* 33.

163) R. H. Shoemaker, *Nat. Rev. Cancer* **2006**, *6*, 813–823.

164) O. Warburg, *Science* **1956**, *123*, 309.

165) M. G. Vander Heiden, L. C. Cantley, C. B. Thompson, *Science* **2009**, *324,* 5930.

166) M. Jang, S. S. Kim, J. Lee, *Exp Mol Med* **2013**, *45*, e45.

167) L. Szablewski, *Biochim. Biophys. Acta* **2013**, *1835*, 164–169.

168) M. E. Cameron, A. Yakovenko, J. G. Trevino, *J. Oncol.* **2018**, *Article ID 6214838*, 6 pages.

169) Y. Zhou, Y. Guo, K. Y. Tam, *Expert Opin. Ther. Pat.* **2022**, *32 (4)*, 441-453.

170) A. M. Srour, M. N. El-Bayaa, M. M. Omran, M. M. Sharaky, W. A. El-Sayed, *Anticancer Agents Med Chem*, **2021**, *21 (10)*, 1323 – 1333.

171) E. C. Calvaresi, P. J. Hergenrother, *Chem. Sci.* **2013**, *4*, 2319–2333.

172) F. Hossain, P. R. Andreana, *Pharmaceuticals* **2019**, *12*, 84.

173) A. L. Iorio, E. Lenci, C. Marzano, E. Bucaletti, B. Tirinnanzi, G. Casati, *et al., ACS Med. Chem. Lett.* **2024**, *15 (11),* 1953–1960.

174) M. I. Molejon, G. Weiz, J. D Breccia, M. I. Vaccaro, *World J. Clin. Oncol.* **2020**, *11(3)*, 110–120.

175) J. Stüben, R. Port, B. Bertram, U. Bollow, W. E. Hull, M. Schaper, J. Pohl, M. Wiessler, *Cancer Chemother. Pharmacol.* **1996**, *38*, 355–365.

176) K. S. Stenn, *Am. J. Dermatopathol.* **1979**, *1*, 375–376.

177) J. Pohl, B. Bertram, P. Hilgard, M. R. Nowrousian, J. Stüben, M. D. Wiessler, *Cancer Chemother Pharmacol.* **1995**, *35*, 364–370.

178) H. Cheng, X. Cao, M. Xian, L. Fang, T. B. Cai, J. J. Ji, J. B. Tunac, D. Sun, P. G. Wang, *J Med Chem.* **2005***, 48,* 645–652.

179) R. D. Goff, J. S. Thorson, *J Med Chem.* **2010**, *53*, 8129–8139.

180) J. Y. Xing, G. P. Song, J. P. Deng, L. Z. Jiang, P. Xiong, B. J. Yang, S. S. Liu, *PloS One* **2015**, *10*, e0144781.

181) J. P. Holland, F. I. Aigbirhio, H. M. Betts, P. D. Bonnitcha, P. Burke, M. Christlieb, G. C. Churchill, A. R. Cowley, J. R. Dilworth, P. S. Donnelly, J. C. Green, J. M. Peach, S. R. Vasudevan, J. E. Warren, *Inorg. Chem.* **2007**, *46*, 465-485.

182) M. Patra, T. C. Johnstone, K. Suntharalingam, S. J. Lippard, *Angew. Chem. Int. Ed.* **2016**, *55*, 2550 –2554.

183) P. Liu, Y. Lu, X. Gao, R. Liu, D. Zhang-Negrerie, Y. Shi, Y. Wang, S. Wanga, Q. Gao, *Chem. Commun.* **2013**, *49*, 2421 - 2423.

184) M. E. Cucciolito, F. D. L. Bossa, R. Esposito, G. Ferraro, A. Iadonisi, G. Petruk, L. D'Elia, C. Romanetti, S. Traboni, A. Tuzi, et al*., Inorg. Chem. Front.* **2018**, *5*, 2921‑2933.

185) E. Moynihan, S. Panseri, G. Bassi, A. Rossi, E. Campodoni, E. Dempsey, M. Montesi, T. Velasco-Torrijos, D. Montagner, *Int. J. Mol. Sci.* **2023**, *24*, 6028.

186) F. Brescia, I. Titilas, S. Cacciapuoti, L. Ronconi, *Molecules* **2025**, *30*, 3537.

187) P. R. Florindo, D. M. Pereira, P. M. Borralho, P. J. Costa, M. F. M. Piedade, C. M. P. Rodrigues, A. C. Fernandes, *Dalton Trans.* **2016**, *45,* 11926‑11930.

188) V. Hamala, A. Martišova, L. Cervenkova Štastna, J. Karban, A. Danco, A. Šimarek, M. Lamac, M. Horacek, T. Kolarova, R. Hrstka, et al., *Appl. Organomet. Chem.* **2020**, *34*, e5896.

189) O. Dada, G. Sanchez-Sanz, M. Tacke, X. Zhu, *Tetr. Lett.* **2018**, *59*, 2904‑2908.

190) S. Schoch, D. Iacopini, M. Dalla Pozza, S. Di Pietro, I. Degano, G. Gasser, V. Di Bussolo, F. Marchetti, *Organometallics* **2022**, *41*, 514‑526.

191) K. M. Alexacou, A. C. Tenchiu (Deleanu), E. D. Chrysina, M. D. Charavgi, I. D. Kostas, S. E. Zographos, N. G. Oikonomakos, D. D. Leonidas, *Bioorg. Med. Chem.* **2010**, *18*, 7911–7922.

192) S. Ghosh, A. K. Misra, G. Bhatia, M. M. Khan, A. K. Khanna, *Bioorg. Med. Chem. Lett.* **2009**, *19*, 386–389.

193) N. D. Thanh, N. T. K. Giang, T. H. Quyen, D. T. Huong, V. N. Toan, *Eur. J. Med. Chem.* **2016**, *123*, 532 - 543.

194) A. Reddy, L. S. Sangenito, A. de Azevedo Guedes, M. H. Branquinha, K. Kavanagh, J. McGinley, A. L. S. dos Santos, T. Velasco-Torrijos, *Dalton Trans.* **2017**, *46*, 5297–5307.

195) F. Miglioli, *Ph. D. dissertation*, University of Parma, Italy, **2022**.

196) L. I. Socea, S. F. Barbuceanu, E. M. Pahontu, A. C. Dumitru, G. M. Nitulescu, R. C. Sfetea, T. V. Apostol, *Molecules* **2022**, *27*, 8719.

197) A. E. Kassab, *Arch. Pharm.* **2023**, *356*, e2200548.

198) B. Aneja, N. S. Khan, P. Khan, A. Queen, A. Hussain, M. T. Rehman, M. F. Alajmi, H. R. El-Seedi, S. Ali, M. I. Hassan, et al., *Eur. J. Med. Chem.* **2019**, *163*, 840–852.

199) C. Congiu, V. Onnis, *Bioorg. Med. Chem*. **2013**, *21*, 6592–6599.

200) Y. Zhou, S. Zhang, H. He, W. Jiang, L. Hou, D. Xie, M. Cai, H. Peng, L. Feng, *Bioorg. Med. Chem.* **2018**, *26*, 84–95.

201) Z. X. Zhao, L. P. Cheng, M. Li, W. Pang, F. H. Wu, *Eur. J. Med. Chem.* **2019**, *173*, 305–313.

202) D. Reis, A. Despaigne, J. Silva, N. Silva, C. Vilela, I. Mendes, J. Takahashi, H. Beraldo, *Molecules* **2013**, *18*, 12645–12662.

203) R. C. Maia, L. L. Silva, E. F. Mazzeu, M. M. Fumian, C. M. de Rezende, A. C. Doriguetto, R. S. Correa, A. L. Miranda, E. J. Barreiro, C. A. Fraga, *Bioorg Med Chem* **2009**, *17*, 6517‑6525.

204) S. Ulloora, R. Shabaraya, R. Ranganathan, A. V. Adhikari, *Eur. J. Med. Chem.* **2013**, *70*, 341‑349.

205) O. C. Danciu, M. Holdhoff, R. A. Peterson, J. H. Fischer, L. C. Liu, H. Wang, N. K. Venepalli, R. Chowdhery, M. K. Nicholas, M. J. Russell, T. M. Fan, P. J. Hergenrother, T. M. Tarasow, A. Z. Dudek, *BJC* **2023**, *128*, 783–792.

206) L. K. Charkoudian, D. M. Pham, K. J. Franz, *J. Am. Chem. Soc.* **2006**, *128*, 12424.

207) Q. P. Peterson, D. C. Hsu, D. R. Goode, C. J. Novotny, R. K. Totten, P. J. Hergenrother, *J. Med. Chem.* **2009**, *52*, 5721.

208) E. Sachdev, D. Sachdev, M. Mita, *Expert Opin. Invest. Drugs* **2017**, *26*, 1175.

209) F. Kratz, A. Warnecke, K. Scheuermann, C. Stockmar, J. Schwab, P. Lazar, P. Drückes, N. Esser, J. Drevs, D. Rognan, C. Bissantz, C. Hinderling, G. Folkers, I. Fichtner, C. Unger*, J. Med. Chem.* **2002**, *45*, 5523.

210) H. El Hajji, O. Dangles, P. Figueiredo, R. Brouillard, *Helv. Chim. Acta* **1997**, *80*, 398–413.

211) E. V. Dehmlow, S. S. Dehmlow, *Phase Transfer Catalysis*, 3rd Ed., VCH Verlagsgesellschaft: Weinheim, Germany, **1993**, 39–49.

212) W. A. Bubb, *Concepts in Magnetic Resonance Part A*, **2003**, *Vol. 19A (1)*, 1–19.

213) S. Fernández-Palacios, E. Matamoros, I. Morato Rojas, J. T. López Navarrete, M. C. Ruiz Delgado, Y. Vida, E. Perez-Inestrosa, *Int. J. Mol. Sci.* **2023**, *24*, 14739.

214) K. Kadyan, R. Singh, J. Sindhu, P. Kumar, M. Devi, S. Lal, A. Kumar, D. Singh, H. Kumar, *Top. Curr. Chem.* **2025**, *18*, 383.

215) M. M. Hincapié-Otero, A. Joaqui-Joaqui, D. Polo-Cerón, *Univ.Sci.* **2021**, *26(2)*, 193–215.

216) É. A. Enyedy, É. Zsigó, N. V. Nagy, C. R. Kowol, A. Roller, B. K. Keppler, T. Kiss, *Eur. J. Inorg. Chem.* **2012**, 4036–4047.

217) J. F. Verchere, S. Chapelle, F. Xin, D. C. Crans, *Progress in Inorganic Chemistry,* **1998**, *Vol. 47,* John Wiley & Sons, Inc.

218) S. J. Angyal, *Carbohydr. Res.* **1990***, 200,* 181-188.

219) B. Gyurcsik, L. Nagy, *Coord. Chem. Rev.* **2000**, *203*, 81–149.

220) O. V. Dolomanov, L. J. Bourhis, R. J. Gildea, J. A. K. Howard, H. Puschmann, *J. Appl. Cryst.* **2009**, *42*, 339-341.

221) L. J. Bourhis, O. V. Dolomanov, R. J. Gildea, J. A. K. Howard, H. Puschmann, *Acta Cryst.* **2015**, *A71*, 59-75.

222) K. A. Jensen, C. Pedersen, *Acta Chem. Scand.* **1961**, *15*, 1087-1103.

223) K. A. Jensen, C. Pedersen, *Acta Chem. Scand.* **1961**, *15*, 1109-1123.

224) D. S. Kalinowski, P. C. Sharpe, P. V. Bernhardt, D. R. Richardson, *J. Med. Chem.* **2007,** *50,* 6212-6225.

225) S. Fernández-Palacios, E. Matamoros, I. Morato Rojas, J. T. López Navarrete, M. C. Ruiz Delgado, Y. Vida, E. Perez-Inestrosa, *Int. J. Mol. Sci.* **2023**, *24*, 14739.

226) A. A. Burke, E. S. Severson, S. Mool, M. J. Solares Bucaro, F. T. Greenaway, C. E. Jakobsche, *J. Enzym. Inhib. Med. Chem* **2017**, *32(1),* 496-503.

227) B. Holmberg, *Arkiv Kemi, Mineral. Geol.* **1943**, *17(A)*, 23.

228) S. Sawusch, U. Schilde, A. Lehmann, E. Uhlemann, *Inorg. Chim. Acta* **1998**, *277*, 219-224.

229) L. D. Popov, S. I. Levchenkov*,* I. N. Shcherbakov*,* A. A. Tsaturyan, Yu. P. Tupolova, Z. A. Starikova, A. S. Burlov, V. V. Lukov, V. A. Kogan*, Rus. J. Coord. Chem.* **2013***, 39(5),* 367–372.

230) P. Pelagatti, A. Venturini, A. Leporati, M. Carcelli, M. Costa, A. Bacchi, G. Pelizzi, C. Pelizzi, *J. Chem. Soc*., *Dalton Trans*. **1998**, 2715–2721.

231) K. N. Zelenin, V. A. Khrustalev, V. V. Alekseev, P. A. Sharbatyan, A. T. Lebedev, *Khim. Gererotsikl. Soedin,* **1982**, *7*, 904-910.

232) D. M. Evans, L. Hill, D. R. Taylor, *J. Chem. Soc., Perkin Trans. 1*, **1986**, 1499 – 1505.

233) A. S. Komendantova, A. N. Fakhrutdinov, L. G. Menchikov, A. Y. Sukhorukov, I. V. Zavarzin, Y. A. Volkova, *Eur. J. Org. Chem.* **2019**, 527–536.

234) D. M. Evans, D. R. Taylor, *J. Chem. Soc., Chem. Commun.*, **1982**, *188*.

235) K. A. Myannik, V. N. Yarovenko, E. K. Beloglazkina, A. A. Moiseeva, M. M. Krayushkin, *Polyhedron* **2018**, *139*, 208–214.

236) A. D. Naik, S. M. Annigeri, U. B. Gangadharmath, V. K. Revankar, V. B. Mahale, *Transit. Met. Chem.* **2002**, *27*, 333–336.

237) A. D. Naik, S. M. Annigeri, U. B. Gangadharmath, V. K. Revankar, V. B. Mahale, V. Reddy, *Bull. Chem. Soc. Jpn.* **2002**, *75*, 2161–2167.

238) J. G. Hubert, I. A. Stepek, H. Noda, J. W. Bode, *Chem. Sci.*, **2018**, *9*, 2159.

239) Z. Gan, B. Tian, J. Yuan, D. Ran, L. Zhang, G. Dong, T. Pan, Y. Zeng, Y. Yu, *Tetr. Lett* **2020**, *61*, 152195.

240) Y. Hu, C. Y. Li, X. M. Wang, Y. H. Yang, H. L. Zhu, *Chem. Rev.* **2014**, *114*, 5572–5610.

241) V. Molteni, X. Li, J. Nabakka, F. Liang, J. Wityak, A. Koder, L. Vargas, R. Romeo, N. Mitro, P. A. Mak, H. M. Seidel, J. A. Haslam, D. Chow, T. Tuntland, T. A. Spalding, A. Brock, M. Bradley, A. Castrillo, P. Tontonoz, E. Saez, *J. Med. Chem.* **2007,** *50,* 4255-4259.

242) A. R. Angeles, L. Yang, C. Dai, A. Brunskill, A. D. Basso, M. A. Siddiqui, *Tetr. Lett.* **2010**, *51*, 6236–6239.

243) B. G. Szczepankiewicz, G. Liu, H. S. Jae, A. S. Tasker, I. W. Gunawardana, T. W. von Geldern, S. L. Gwaltney, J. R. Wu-Wong, L. Gehrke, W. J. Chiou, R. B. Credo, J. D. Alder, M. A. Nukkala, N. A. Zielinski, K. Jarvis, K. W. Mollison, D. J. Frost, J. L. Bauch, Y. H. Hui, A. K. Claiborne, Q. Li, S. H. Rosenberg, *J. Med. Chem.* **2001,** *44,* 4416-4430.

244) H. Oshida, A. Ishii, J. Nakayama, *Tetr. Lett.* **2004**, *45*, 1331–1334.

245) T. Ozturk, E. Ertas, O. Mert, *Chem. Rev.,* **2007,** *107*, 5210-5278.

246) M. P. Cava, M. I. Levinson, *Tetrahedron* **1985**, *41*, 5061.

247) M. Jesberger, T. P. Davis, L. Barner, *Synthesis* **2003**, *13,* 1929-1958.

248) S. H. Hausner, D. Alagille, A. O. Koren, L. Amici, J. K. Staley, K. P. Cosgrove, R. M. Baldwin, G. D. Tamagnan, *Bioorg. Med. Chem. Lett.* **2009**, *19*, 543–545.

249) T. Čimbora-Zovko, A. Brozovic, I. Piantanida, G. Fritz, A. Virag, B. Alič, V. Majce, M. Kočevar, S. Polanc, M. Osmak, *Eur. J. Med. Chem* **2011**, *46 (7)*, 2971-2983.

250) Z. Song, Y. Liu, Z. Dai, W. Liu, K. Zhao, T. Zhang, Y. Hu, X. Zhang, Y. Dai, *Bioorg. Med. Chem.* **2016**, *24 (19),* 4723-4730.

251) W. Thiel, R. Mayer, *Journal fur praktische Chemie* **1989**, *331 (4),* 649 – 658.

252) PCT/US2005/036761: N. Almstead, G. M Karp, R. Wilde, E. Welch, J. A Campbell, H. Ren, G. Chen, "Pyrazole or triazole compounds and their use for the manufacture of a medicament for treating somatic mutation-related diseases".

253) K. A. Jensen, C. Pedersen, *Acta Chem. Scand.* **1961**, *15*, 1124-1129.

254) N. Sheernaly, I. Shajan, A. Steinbrueck, B. Albada, N. Metzler-Nolte, *RSC Med. Chem.,* **2025**, *16*, 3512 – 3521.

255) D. M. Kaminski, A. A. Hoser, M. Gagos, A. Matwijczuk, M. Arczewska, A. Niewiadomy, K. Wozniak, *Cryst. Growth Des.* **2010**, *10*, 3480–3488.

256) D. M. Kaminski, A. Matwijczuk, D. Pociecha, E. Gorecka, A. Niewiadomy, M. Dmowska, M. Gagos, *BBA* **2012**, *1818*, 2850–2859.

257) I. P. Kaur, R. Smitha, D. Aggarwal, M. Kapil, *Int. J. Pharm.* **2002**, *248*, 1–14.

258) M. B. Russell, A. Ducros, *Lancet Neurol.* **2011**, *10*, 457–470.

259) H. G. Tiselius, *Curr. Opin. Urol.* **2010**, *20*, 169–173.

260) M. L. Keshtov, I. O. Konstantinov, A. R. Khokhlov, I. E. Ostapov, V. G. Alekseev, Z. Xie, H. Dahiya, G. D. Sharma, *J. Polym. Sci.* **2022**, *60*, 2086–2099.

261) G. Czernel, A. Matwijczuk, D. Karcz, A. Gorecki, A. Niemczynowicz, A. Szczes, G. Gładyszewski, A. Matwijczuk, B. Gładyszewska, A. Niewiadomy, *Molecules* **2018**, *23*, 2861.

262) M. Lebrini, F. Bentiss, H. Vezin, M. Lagrenee, *Corros. Sci.* **2006**, *48*, 1279–1291.

263) J. Dong, Q. Sun, S. Zhang, E. Zhang, W. Ma, Y. Wang, W. Li, X. Wang, *Colloids Surf. A: Physicochem. Eng. Aspects* **2025**, *707*, 135825.

264) M. T. Luís Frija, A. J. L. Pombeiro, M. N. Kopylovich, *Coord. Chem. Rev.* **2016**, *308*, 32–55.

265) M. Cingi, M. Lanfranchi, M. Pellinghelli, M. Tegoni, *Eur. J. Inorg. Chem.* **2000**, *2000*, 703–711.

266) D. P. Singh, S. Pratap, S. K. Pandey, R. J. Butcher, G. Marverti, *J. Coord. Chem.* **2014**, *68*, 261–276.

267) Q. Wang, C. Ma, G. He, Y. Li, *Heteroat. Chem.* **2012**, *23*, 531–538.

268) S. Tunsrichon, K. Chainok, V. Promarak, P. Nalaoh, S. Youngme, J. Boonmak, *Inorg. Chem.* **2022**, *61*, 11734–11745.

269) A. W. Schuettelkopf, L. Gros, D. E. Blair, J. A. Frearson, D. M. F. van Aalten, I. H. Gilbert, *Bioorg. Med. Chem.* **2010**, *18 (23)*, 8334–8340.

270) G. S. Alegaon, K. R. Alagawadi, P. V. Sonkusare, S. M. Chaudhary, D. H. Dadwe, A. S. Shah, *Bioorg. Med. Chem. Lett.* **2012**, *22*, 1917–1921.

271) V. Jatav, P. Mishra, S. Kashaw, J.P. Stables, *Eur. J. Med. Chem.* **2008**, *43*, 1945–1954.

272) B. Stanovnik, M. Tisler, *J. Org. Chem.* **1960**, *25*, 2234–2236.

273) R. A. Coburn, B. Bhooshan, R. A. Glennon, *J. Org. Chem.* **1973**, *38*, 3947–3949.

274) V. N. Yarovenko, A. V. Shirokov, I. V. Zavarzin, O. N. Krupinova, A. V. Ignatenko, M. M. Krayushkin, *Synthesis* **2004**, 17–19.

275) B. Han, Z. Zheng, D. Zheng, L. Zhang, P. Cui, J. Shi, C. Li, *Synth. Commun.* **2019**, *49*, 2512–2520.

276) A. A. Hassan, F. F. Abdel-Latif, M. A. Aziz, S. M. Mostafa, S. Brase, M. Nieger, *Chin. Chem. Lett.* **2015**, *26*, 1183–1186.

277) S. H. Kwak, Y. D. Gong, *Tetrahedron* **2013**, *69*, 7107–7111.

278) A. Zavaroni, G. Pelosi, M. Incerti, M. Carcelli, D. Rogolino, *Inorg. Chem. Comm.* **2025**, *177*, 114432.

279) G. Pulvermacher, *Ber.* **1894**, *27*, 613.

280) O. Meth-Cohn, S. P. Stanforth, In: *Comprehensive Organic Synthesis,* B.M. Trost, I. Fleming (Eds.), C.H. Heathcock (Vol. Ed.), Vol. 2, Pergamon, Oxford, **1991**, pp. 777–794.

281) G. V. Oshovskii, F. F. Tolmachev, A. S. Merkulov, A. M. Pinchuk, *Chem. Heterocycl. Compd.*, **1997**, *33 (10),* 1242-1243.

282) M. Zablocka, G. Oshovsky, C. Duhayon, S. Ladeira, A. M. Caminade, S. Mignani, J. P. Majoral, *Dalton Trans.* **2016**, *45*, 9695.

283) M. Maekawa, M. Munakata, T. Kuroda-Sowa, Y. Suenaga, K. Sugimoto, *Inorg. Chim. Acta* **1999**, *290*, 153–158.

284) K. Xue, W. X. Chai, Y. W. Wu, C. Ling, L. Song, *J. Clust. Sci.* **2014**, *25*, 1005–1017.

285) Y. Geng, W. Zhang, J. F. Song, R.-S. Zhou, W.-Z. Jiao, *Inorg. Chim. Acta* **2021**, *528*, 120596.

286) Y. I. Slyvka, B. R. Ardan, M. G. Myskiv, *J. Struct. Chem.* **2018**, *59 (2)*, 388–394.

287) A. Matwijczuk, D. Kluczyk, A. Gorecki, A. Niewiadomy, M. Gagos, *J. Phys. Chem. B* **2016**, *120*, 7958–7969.

288) A. Mensah, J. J. Shao, J. L. Ni, G. J. Li, F. M. Wang, L. Z. Chen, *Front. Chem.* **2022**, *9*, 816363.

289) Bruker. SAINT and SADABS. Bruker AXS. APEX3, SAINT SADABS. Bruker AXS Inc., Madison, Wisconsin, USA. **2016**.

290) G. M. Sheldrick, *Acta Crystallogr. Sect. C Struct. Chem.* **2015**, *71*, 3–8.

291) M. N. Burnett, C. K. Johnson, *ORTEP-III: Oak Ridge Thermal Ellipsoid Plot Program for Crystal Structure Illustrations*; Citeseer, **1996**.

292) C. F. Macrae, I. Sovago, S. J. Cottrell, P. T. A. Galek, P. McCabe, E. Pidcock, M. Platings, G. P. Shields, J. S. Stevens, M. Towler, *J. Appl. Cryst.* **2020**, *53*, 226–235.

293) J. Beaudelot, S. Oger, S. Perusko, T. A. Phan, T. Teunens, C. Moucheron, G. Evano, *Chem. Rev.* **2022**, *122*, 16365−16609.

294) F. H. Jardine, *Adv. Inorg. Chem. Radiochem.* **1975**, *17*, 115-163.

295) J. Troyano, F. Zamora, S. Delgado, *Chem. Soc. Rev.*, **2021**, *50*, 4606.

296) M. Weller, T. Overton, J. Rourke, F. Armstrong, *Inorganic Chemistry, Sixth Edition*, Oxford University Press, **2014**.

297) F. Himo, T. Lovell, R. Hilgraf, V. V. Rostovtsev, L. Noodleman, K. B. Sharpless, V. V. Fokin, *J. Am. Chem. Soc.*, **2005**, *127*, 210-216.

298) K. Sonogashira, *J. Organomet. Chem.* **2002**, *653 (1–2)*, 46-49.

299) T. H. Kim, Y. W. Shin, J. H. Jung, J. S. Kim, J. Kim, *Angew. Chem. Int. Ed.* **2008**, *47*, 685 –688.

300) B. F. Hoskins, R. Robson, *J. Am. Chem. Soc.* **1989**, *111*, 5962-5964.

301) S. J. Berners-Price, M. E. Sant, R. I. Christopherson, P. W. Kuchel, *Magn. Reson. Med.* **1991**, *18,* 142-158.

302) R. Starosta, *Pharmaceuticals* **2023**, *16*, 766.

303) R. Starosta, M. Florek, J. Król, M. Puchalska, A. Kochel, *New J. Chem.* **2010**, *34*, 1441‑1449.

304) C. Marzano, V. Gandin, M. Pellei, D. Colavito, G. Papini, G. Gioia Lobbia, E. Del Giudice, M. Porchia, F. Tisato, C. Santini, *J. Med. Chem.* **2008,** *51,* 798–808.

305) F. Tisato, C. Marzano, V. Peruzzo, M. Tegoni, M. Giorgetti, M. Damjanovic, et al., *J. Inorg. Biochem.* **2016**, *165*, 80-91.

306) V. Gandin, M. Pellei, F. Tisato, M. Porchia, C. Santini, C. Marzano, *J. Cell Mol. Med.* **2012**, *16*, 142-151.

307) R. Starosta, A. Bykowska, A. Kyzioł, M. Płotek, M. Florek, J. Krol, M. Jezowska-Bojczuk, *Chem Biol Drug Des* **2013**, *82*, 579–586.

308) M. Porchia, A. Dolmella, V. Gandin, C. Marzano, M. Pellei, V. Peruzzo, et al., *Eur. J. Med. Chem.* **2013**, *59*, 218226.

309) V. Gandin, F. Tisato, A. Dolmella, M. Pellei, C. Santini, M. Giorgetti, et al., *J. Med. Chem.* **2014**, *57*, 47454760.

310) S. Nayak, S. L. Gaonkar, *ChemMedChem* **2021**, *16*, 1360–1390.

311) W. Streciwilk, F. Hackenberg, H. Muller-Bunz, M. Tacke, *Polyhedron* **2014**, *80*, 3–9.

312) L. Morel, A. S. Jarrousse, A. Gautier, S. P. Nolan, A. Chevry, M.-L. Teyssot, S. Diez-Gonzalez, C. Beaudoin, A. De Haze, M. Manin, *Chem. Eur. J.* **2008**, *15*, 314–318.

313) M. Elie, G. U. Mahoro, E. Duverger, J. L. Renaud, R. Daniellou, S. Gaillard, *J. Organomet. Chem.* **2019**, *893*, 21–31.

314) C. H. G. Jakob, A. Weigert Muñoz, J. F. Schlagintweit, V. Weißa, R. M. Reich et al., *J. Organomet. Chem.* **2021**, *932*, 121643.

315) M. Pellei, V. Gandin, C. Marzano, M. Marinelli, F. Del Bello, C. Santini, *Appl Organometal Chem.* **2018**, *32*, e4185.

316) Antimicrobial Resistance Collaborators, *Lancet* **2022**, *399*, 629–655.

317) C. Wang, X. Wei, L. Zhong, C. L. Chan, H. Li, H. Sun, *J. Am. Chem. Soc.* **2025**, *147*, 12361−12380.

318) M. Caviglia, Z. Li, C. Santini, J. Del Gobbo, C. Cimarelli, M. Du, A. Dolmella, M. Pellei, *Molecules* **2025**, *30*, 1893.

319) M. E. Garner, W. J. Niu, X. G. Chen, I. Ghiviriga, K. A. Abboud, W. H. Tan, A. S. Veige, *Dalton Trans.* **2015**, *44*, 1914–1923.

320) M. L. Teyssot, A. S. Jarrousse, A. Chevry, A. De Haze, C. Beaudoin, M. Manin, S. P. Nolan, S. Diez-Gonzalez, L. Morel, A. Gautier, *Chem. Eur. J.* **2009**, *15*, 314–318.

321) T. Bernardi, S. Badel, P. Mayer, J. Groelly, P. de Fremont, B. Jacques, P. Braunstein, M. L. Teyssot, C. Gaulier, F. Cisnetti, A. Gautier, S. Roland, *ChemMedChem* **2014**, *9*, 1140–1144.

322) N. Touj, A. Chakchouk-Mtibaa, L. Mansour, A. H. Harrath, J. Al-Tamimi, L. Mellouli, I. Ozdemir, S. Yasar, N. Hamdi, *J. Mol. Struct.* **2019**, *1181*, 209–219.

323) T. Pan, Y. Wanga, F. S. Liu, H. Lin, Y. Zhou, *Polyhedron* **2021***, 197*, 115033.

324) T. Traut-Johnstone, S. Kanyanda, F. H. Kriel, T. Viljoena, P. D. R. Kotze, W. E. van Zyl, J. Coates, D. J. G. Rees, M. Meyer, R. Hewer, D. B. G. Williams, *J. Inorg. Biochem.* **2015**, *145*, 108–120.

325) E. Shirakawa, H. Yoshida, H. Takaya, *Tetr. Lett.,* **1997***, 38 (21),* 3759-3762.

326) J. I. Ortega-Gaxiola, H. Valdés, E. Rufino-Felipe, R. A. Toscano, D. Morales-Morales, *Inorg. Chim. Acta* **2020**, *504*, 119460.

327) D. Bradley, G. Williams, M. Pretorius, *J. Mol. Catal. A Chem.* **2008**, *284*, 77–84.

328) S. Antonaroli, B. Crociani, *J. Organomet. Chem.* **1998**, *560*, 137–146.

329) M. M. Mogorosi, T. Mahamo, J. R. Moss, S. F. Mapolie, J. C. Slootweg, K. Lammertsma, G. S. Smith, *J. Organomet. Chem.* **2011**, *696*, 3585-3592.

330) L. Chen, S. Huo, P. Wang, X. Bai, Y. Gao, Y. Yang, *Polyhedron* **2025**, *265*, 117278.

331) S. Huo, X. Bai, P. Wang, Y. Gao, Y. Yang, *Inorg. Chim. Acta* **2025**, *589*, 122884.

332) J. Süß, U. Monkowius, M. Zabel, *Molbank* **2024**, *2024*, M1808.

333) A. Aguirrechu-Comerón, R. Hernández-Molina, J. González-Platas, *J. Struct. Chem.* **2018,** *59 (4),* 943-948.

334) C. Zeng, N. Wang, T. Peng, S. Wang, *Inorg. Chem.* **2017**, *56*, 1616−1625.

335) J. Flapper, H. Kooijman, M. Lutz, A. L. Spek, P. W. N. M. van Leeuwen, C. J. Elsevier, P. C. J. Kamer, *Organometallics* **2009**, *28*, 1180–1192.

336) B. J. Hathaway, D. G. Holah, J. D. Postlethwaite, *J. Chem. Soc.* **1961**, 3215-3218.

337) G. J. Kubas, *Inorganic Syntheses* **1979**, *19*, 90-92.

338) H. J. Gysling, *Inorganic Syntheses* **1979**, *19*, 92-97.

339) I. S. Kritchenkov, J. R. Shakirova, S. P. Tunik, *RSC Adv.* **2019**, *9*, 15531.

340) N. F. Curtis, Y. M. Curtis, *Inorg. Chem.* **1965**, *4*, 804.

341) J. I. Bullock, *J. Inorg. Nucl. Chem.* **1967**, *29*, 2257-2264.

342) A. Prasetyoputri, A. M. Jarrad, M. A. Cooper, M. A. T. Blaskovich, *Trends in Microbiology* **2019**, *27 (4)*.

343) B. Kowalska-Krochmal, R. Dudek-Wicher, *Pathogens*, **2021**, *10*, 165.

APPENDIX

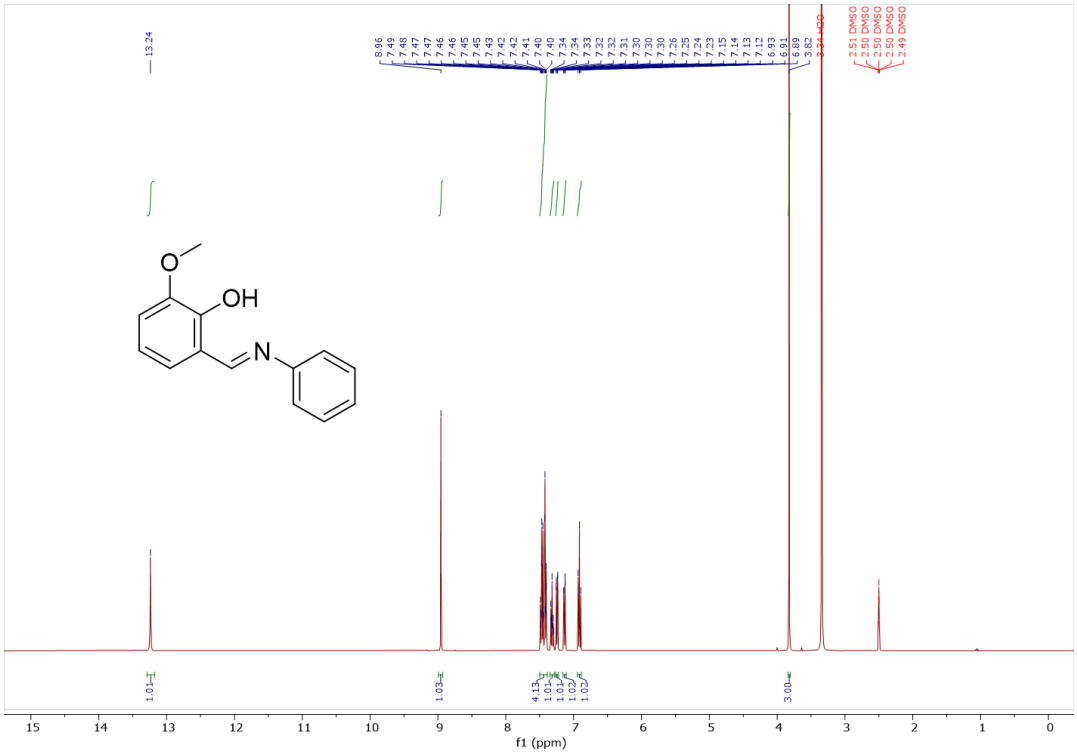

Figure A1.1: ^{1}H NMR (400 MHz, DMSO-d_6, 298 K) spectrum of **AZ1**.

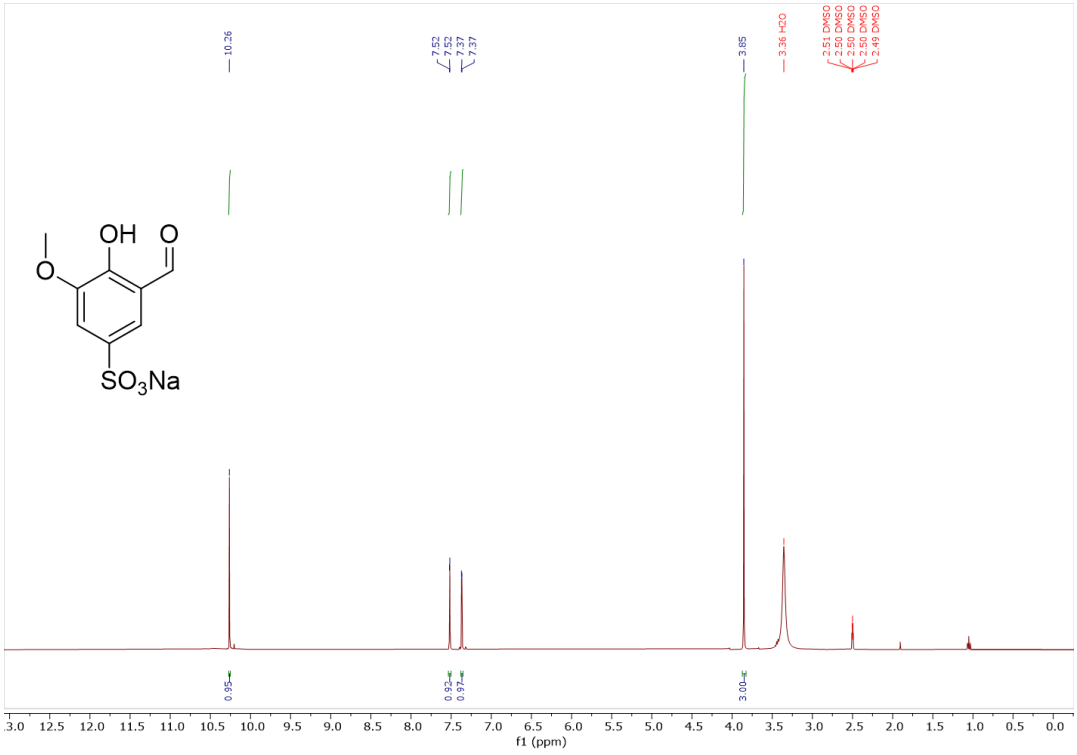

Figure A1.2: ^{1}H NMR (400 MHz, DMSO-d_6, 298 K) spectrum of **AZ3**.

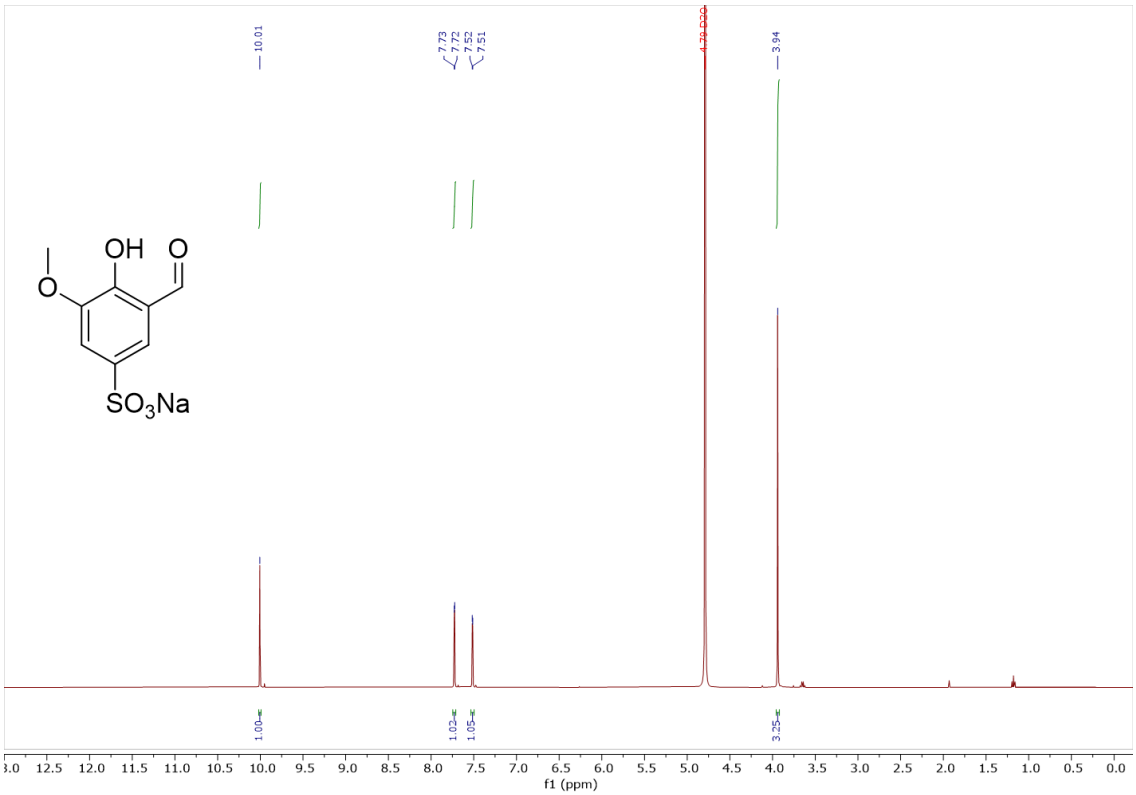

Figure A1.3: ^{1}H NMR (400 MHz, D_2O, 298 K) spectrum of **AZ3**.

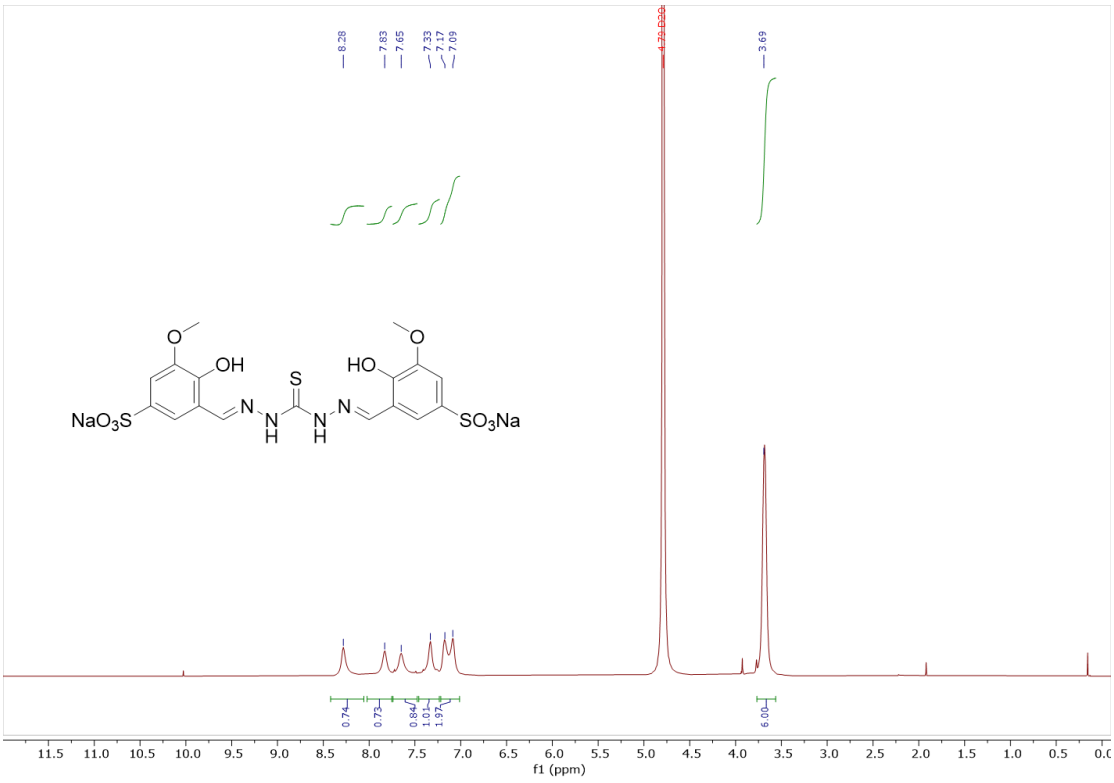

Figure A1.4: ^{1}H NMR (400 MHz, D_2O, 298 K) spectrum of **AZ11**.

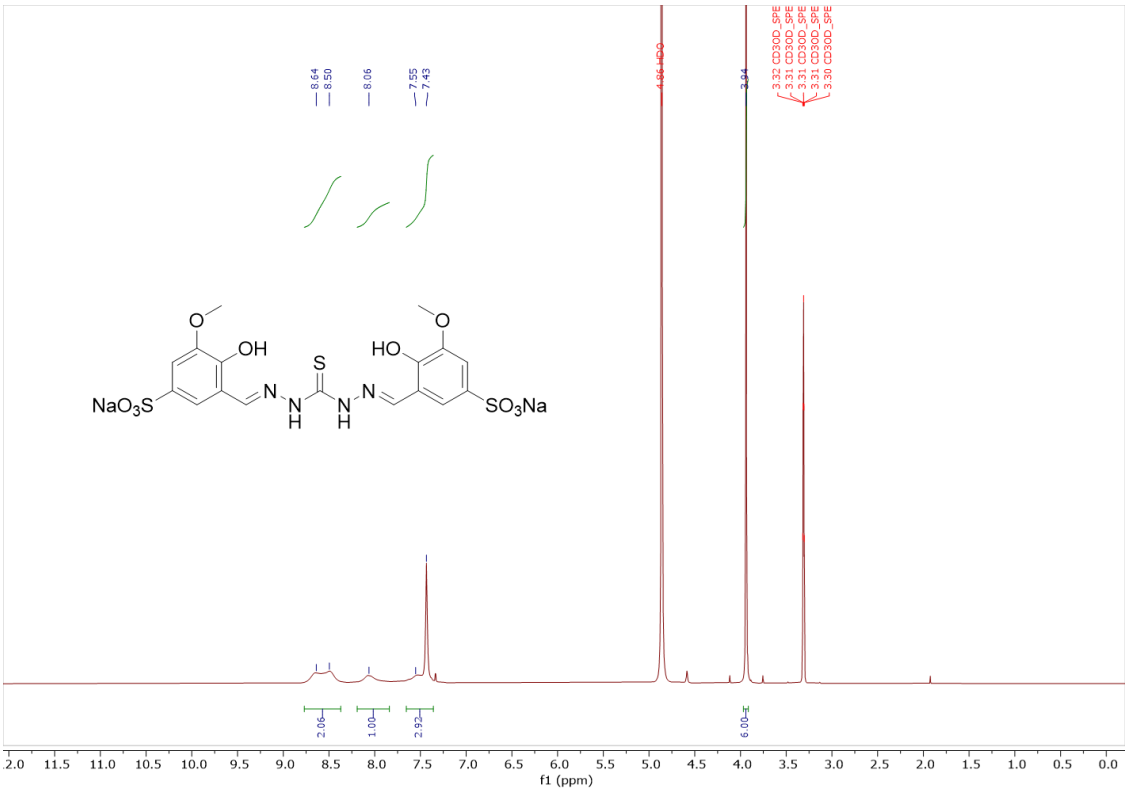

Figure A1.5: ^{1}H NMR (400 MHz, CD_3OD, 298 K) spectrum of **AZ11**.

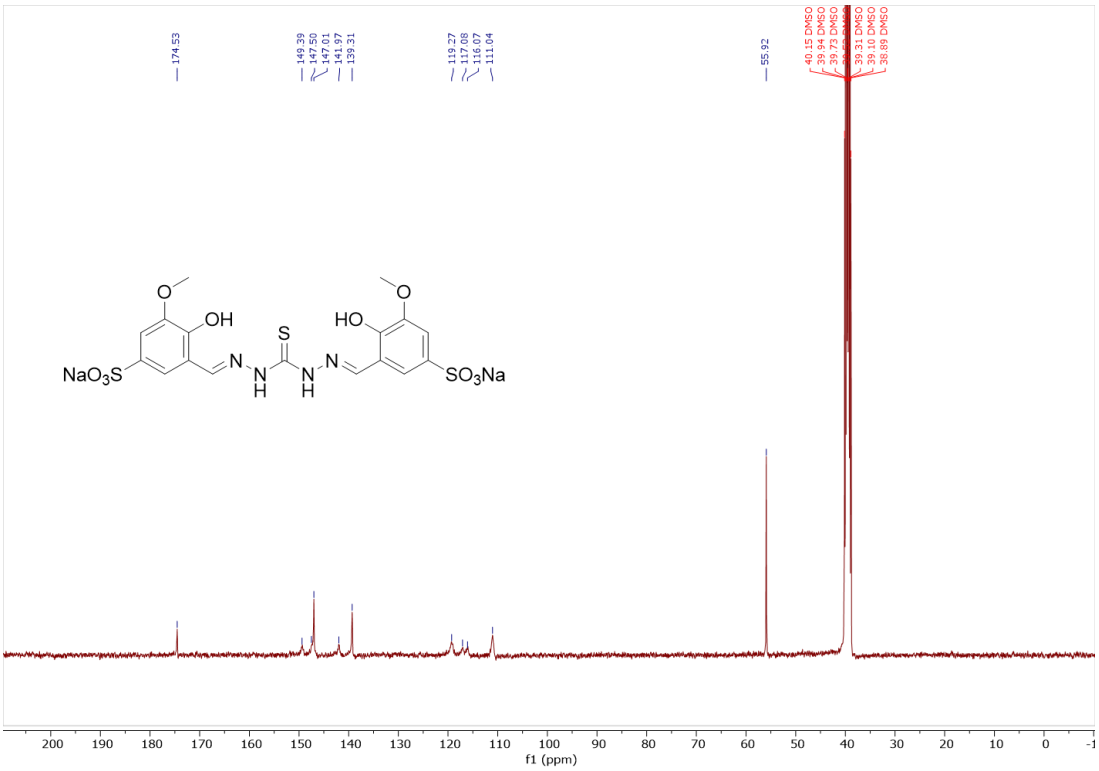

Figure A1.6: ^{13}C NMR (101 MHz, DMSO-d_6, 298 K) spectrum of **AZ11**.

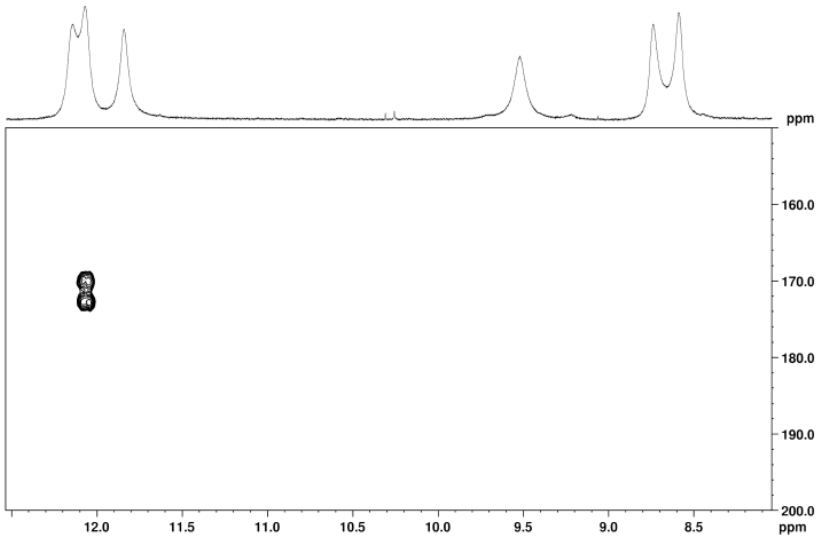

Figure A1.7: 2D ^{1}H-^{15}N HSQC spectrum of **AZ11** at 298 K in DMSO-d_6.

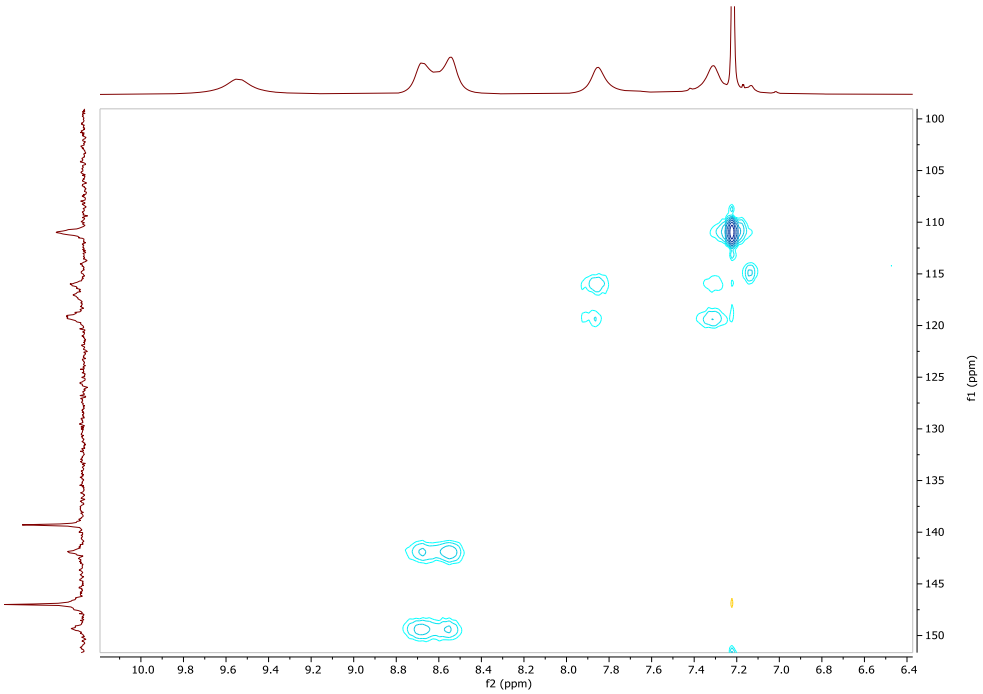

Figure A1.8: 2D ^{1}H-^{13}C HSQC spectrum of **AZ11** at 298 K in DMSO-d_6.

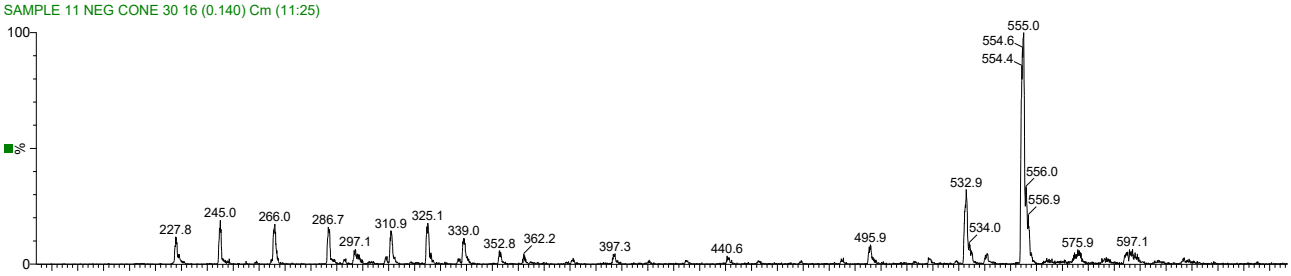

Figure A1.9: ESI-MS spectrum (negative ions) for **AZ11** in methanol.

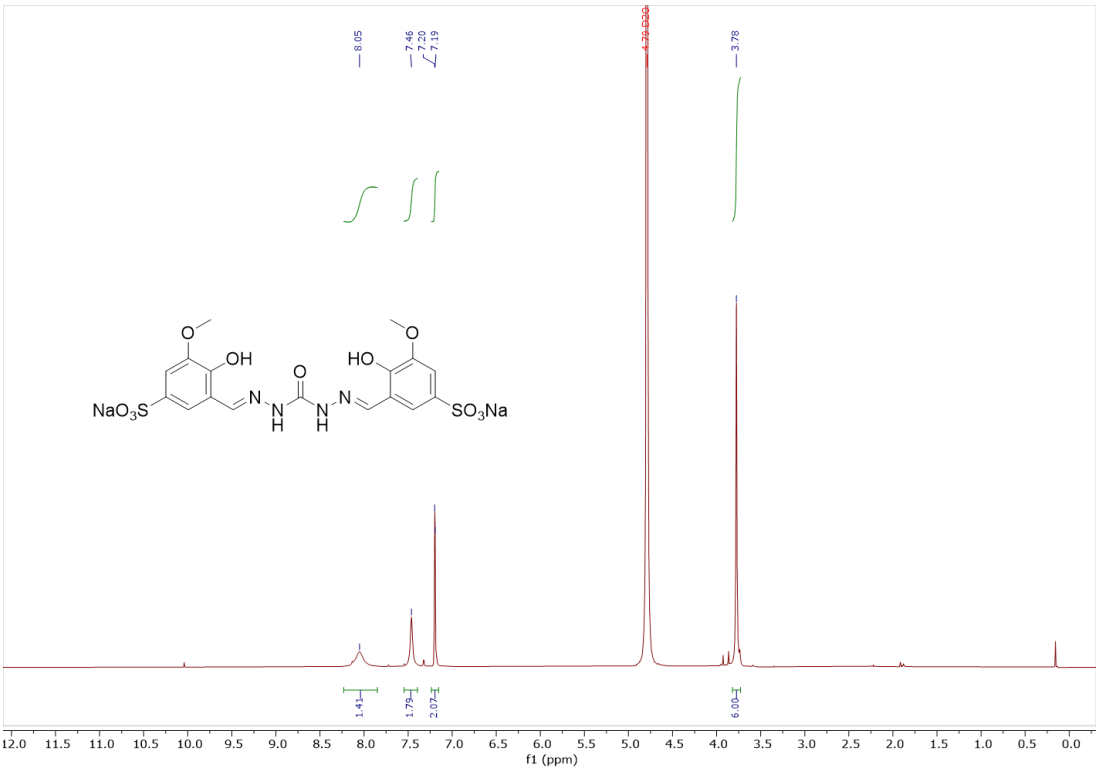

Figure A1.10: ^{1}H NMR (400 MHz, D_2O, 298 K) spectrum of **AZ26**.

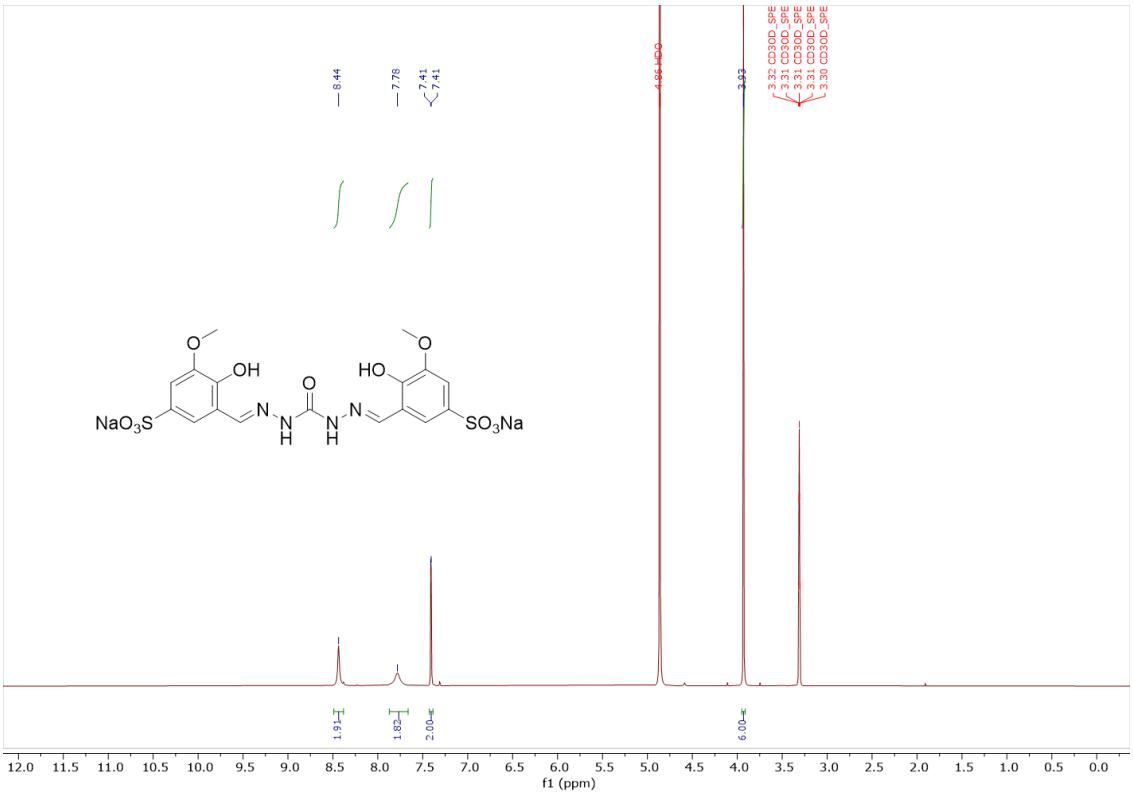

Figure A1.11: ^{1}H NMR (400 MHz, CD_3OD, 298 K) spectrum of **AZ26**.

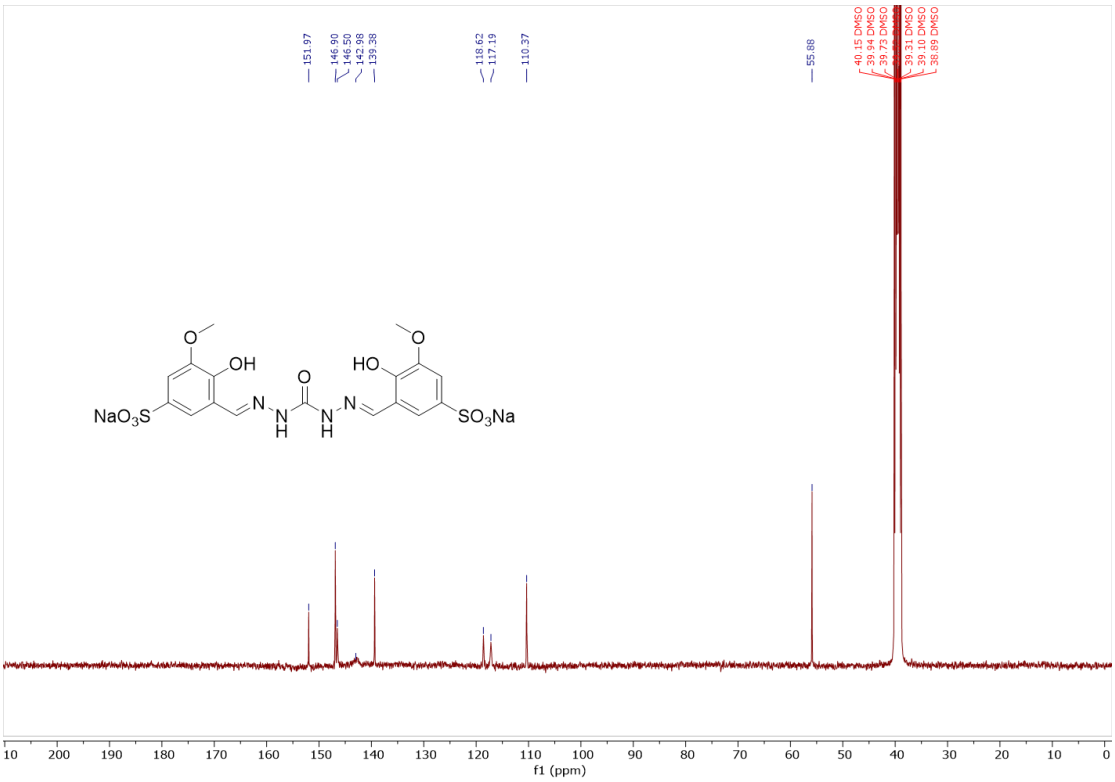

Figure A1.12: ^{13}C NMR (101 MHz, DMSO-d_6, 298 K) spectrum of **AZ26**.

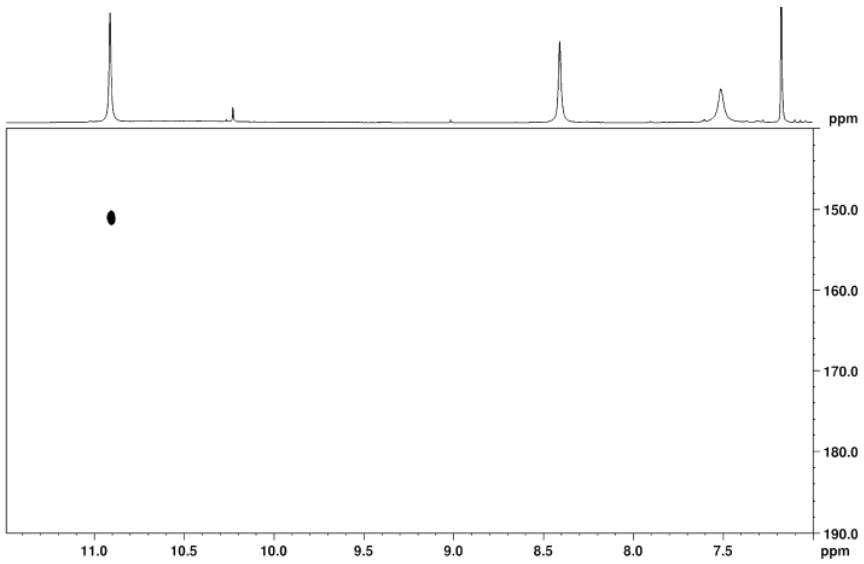

Figure A1.13: 2D ^{1}H-^{15}N HSQC spectrum of **AZ26** at 298 K in DMSO-d_6.

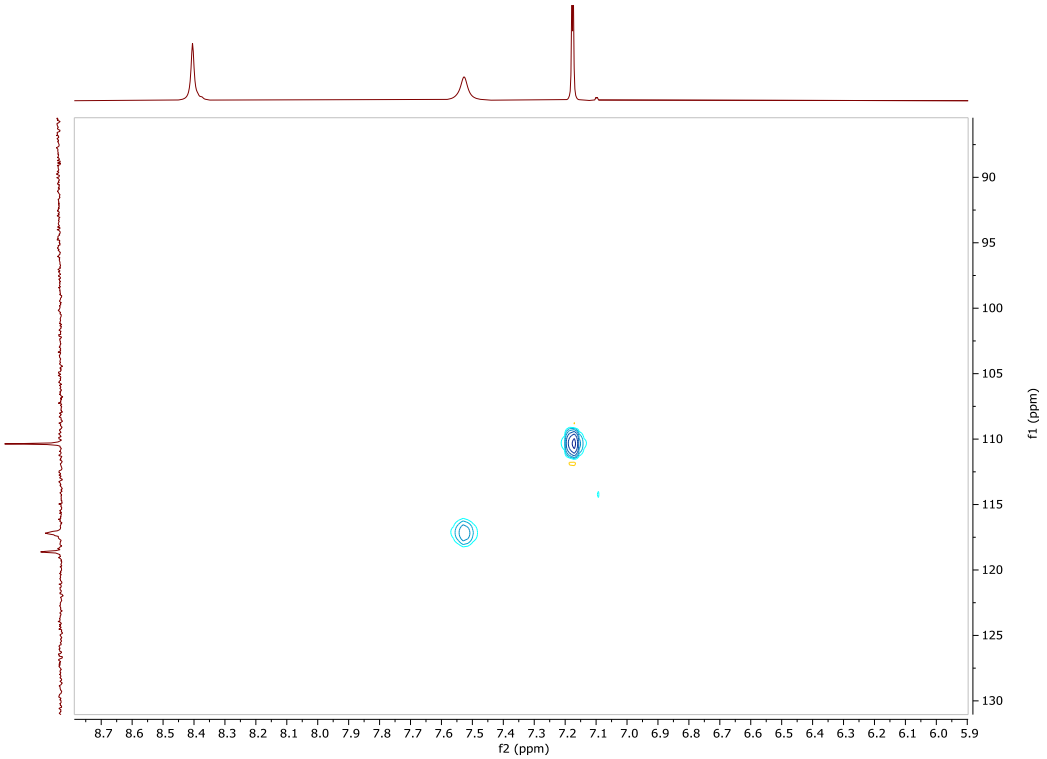

Figure A1.14: 2D ^{1}H-^{13}C HSQC spectrum of **AZ26** at 298 K in DMSO-d_6.

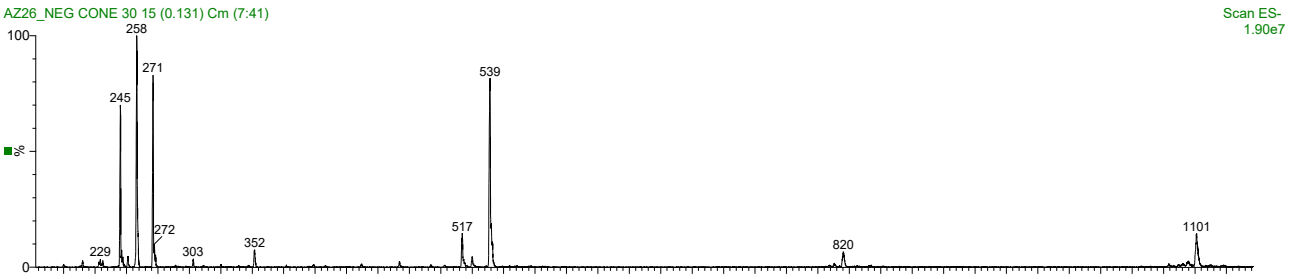

Figure A1.15: ESI-MS spectrum (negative ions) for **AZ26** in methanol.

Table A1.1: Structural parameters from the optimized geometry for the **bis-TCH** and the **bis-CH** *cis*-*cis* isomers in DMSO implicit solvent. The bond distance values are reported in angstrom, and bond and dihedral angles are reported in degrees.

bis-TCH parameter	Value	bis-CH parameter	Value
C–S (23–26)	1.680	C–O (23–50)	1.218
C–N (23–24)	1.368	C–N (23–24)	1.384
N–N (24–27)	1.352	N–N (24–26)	1.353
N–C (27–28)	1.287	N–C (26–27)	1.286
C–C (28–30)	1.454	C–C (27–29)	1.456
C–S (33–45)	1.809	C–S (32–44)	1.809
C–O (35–40)	1.374	C–O (34–39)	1.374
C–O (32–38)	1.348	C–O (31–37)	1.349
N–H (27–39)	1.790	N–H (26–38)	1.781
C–N (23–21)	1.368	C–N (23–21)	1.384
N–N (21–20)	1.352	N–N (21–20)	1.353
N–C (20–18)	1.287	N–C (20–18)	1.286
C–C (18–1)	1.454	C–C (18–1)	1.456
C–S (3–9)	1.809	C–S (3–9)	1.809
C–O (5–13)	1.374	C–O (5–13)	1.374
C–O (6–49)	1.347	C–O (6–48)	1.349
N–H (20–50)	1.791	N–H (20–49)	1.781
N–C–S (24–23–26)	123.96	N–C–O (24–23–50)	123.82
N–C–S (21–23–26)	123.97	N–C–O (21–23–50)	123.82
N–N–C (27–24–23)	120.80	N–N–C (26–24–23)	118.56
N–N–C (20–21–23)	120.81	N–N–C (20–21–23)	118.56
N–C–N (24–23–21)	112.07	N–C–N (24–23–21)	112.36
C–N–N (28–27–24)	119.52	C–N–N (27–26–24)	119.68
C–N–N (18–20–21)	119.50	C–N–N (18–20–21)	119.68
N–C–C (27–28–30)	120.20	N–C–C (26–27–29)	120.58
N–C–C (20–18–1)	120.21	N–C–C (20–18–1)	120.58
N–C–N–N (21–23–24–27)	176.50	N–C–N–N (21–23–24–26)	176.16
N–C–N–N (24–23–21–20)	176.60	N–C–N–N (24–23–21–20)	176.15
N–N–C–C (24–27–28–30)	−179.91	N–N–C–C (24–26–27–29)	−179.95
N–N–C–C (21–20–18–1)	−179.82	N–N–C–C (21–20–18–1)	−179.96

Table A1.2: Structural parameters from the optimized geometry for the **bis-TCH** and the **bis-CH** *cis*-*trans* isomers in DMSO implicit solvent. The bond distance values are reported in angstrom, and bond and dihedral angles are reported in degrees.

bis-TCH parameter	Value	bis-CH parameter	Value
C–S (23–26)	1.687	C–O (23–50)	1.224
C–N (23–24)	1.357	C–N (23–24)	1.376
N–N (24–27)	1.355	N–N (24–26)	1.355
N–C (27–28)	1.287	N–C (26–27)	1.286
C–C (28–30)	1.453	C–C (27–29)	1.456
C–S (33–45)	1.809	C–S (32–44)	1.809
C–O (35–40)	1.374	C–O (34–39)	1.374
C–O (32–38)	1.347	C–O (31–37)	1.349
N–H (27–39)	1.789	N–H (26–38)	1.781
C–N (23–21)	1.363	C–N (23–21)	1.380
N–N (21–20)	1.365	N–N (21–20)	1.362
N–C (20–18)	1.291	N–C (20–18)	1.289
C–C (18–1)	1.452	C–C (18–1)	1.455
C–S (3–9)	1.810	C–S (3–9)	1.810
C–O (5–13)	1.373	C–O (5–13)	1.373
C–O (6–49)	1.350	C–O (6–48)	1.350
N–H (20–50)	1.865	N–H (20–49)	1.854
N–C–S (24–23–26)	125.00	N–C–O (24–23–50)	124.36
N–C–S (21–23–26)	120.23	N–C–S (21–23–50)	120.95
N–N–C (27–24–23)	121.01	N–N–C (26–24–23)	118.97
N–N–C (20–21–23)	123.00	N–N–C (20–21–23)	123.51
N–C–N (24–23–21)	114.77	N–C–N (24–23–21)	114.69
C–N–N (28–27–24)	118.95	C–N–N (27–26–24)	119.16
C–N–N (18–20–21)	117.25	C–N–N (18–20–21)	117.90
N–C–C (27–28–30)	120.32	N–C–C (26–27–29)	120.70
N–C–C (20–18–1)	122.71	N–C–C (20–18–1)	122.60
N–C–N–N (21–23–24–27)	177.80	N–C–N–N (21–23–24–26)	178.11
N–C–N–N (24–23–21–20)	−5.21	N–C–N–N (24–23–21–20)	−4.84
N–N–C–C (24–27–28–30)	−179.58	N–N–C–C (24–26–27–29)	−179.93
N–N–C–C (21–20–18–1)	177.38	N–N–C–C (21–20–18–1)	177.64

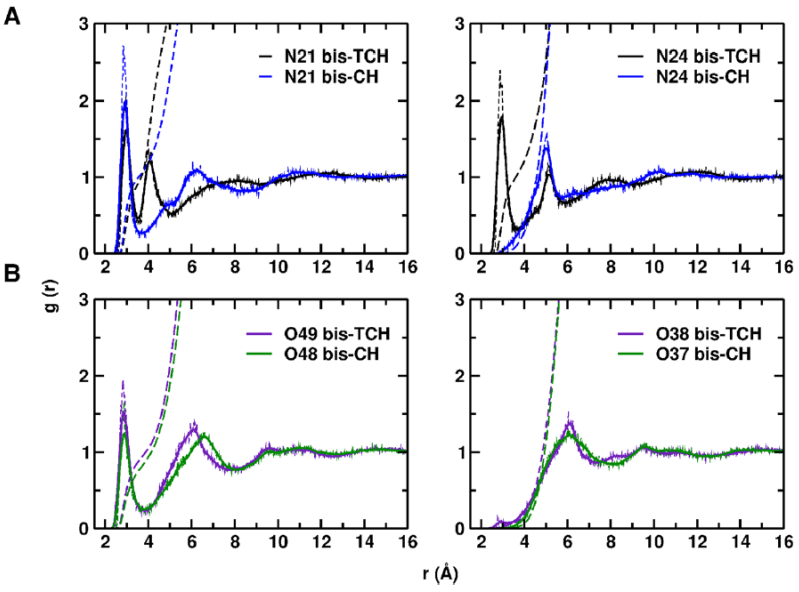

Figure A1.16: (a) RDFs (*g*(*r*)) between the N–H nitrogens from the *trans* (left) or *cis* (right) side and DMSO oxygens for **bis-TCH** and **bis-CH**. (b) RDFs between the O–H oxygens from the *trans* (left) or *cis* (right) side and DMSO oxygens for **bis-TCH** and **bis-CH**. All the RDFs are represented in dashed lines, RDFs averaged

every 20 frames in solid lines, and RDFs running coordination number in thick dashed lines. See Fig. 1.19 for the atoms' numerical labels.

Table A1.3: Structural parameters from the optimized geometry of the *cis*-*trans* **bis-TCH** and **bis-CH** in cluster representations, including two DMSO molecules. The bond distance values are reported in angstrom and the bond and dihedral angles are reported in degrees.

bis-TCH parameter	Value	bis-CH parameter	Value
C–S (23–26)	1.700	C–O (23–70)	1.230
C–N (23–24)	1.358	C–N (23–24)	1.374
N–N (24–27)	1.355	N–N (24–26)	1.357
N–C (27–28)	1.287	N–C (26–27)	1.289
C–C (28–30)	1.454	C–C (27–29)	1.457
C–S (33–45)	1.809	C–S (32–44)	1.808
C–O (35–40)	1.375	C–O (34–39)	1.375
C–O (32–38)	1.348	C–O (31–37)	1.349
N–H (27–39)	1.777	N–H (26–38)	1.755
C–N (23–21)	1.355	C–N (23–21)	1.378
N–N (21–20)	1.370	N–N (21–20)	1.366
N–C (20–18)	1.289	N–C (20–18)	1.290
C–C (18–1)	1.456	C–C (18–1)	1.455
C–S (3–9)	1.809	C–S (3–9)	1.808
C–O (5–13)	1.362	C–O (5–13)	1.374
C–O (6–49)	1.349	C–O (6–48)	1.348
N–H (20–50)	2.164	N–H (20–49)	1.931
N–C–S (24–23–26)	124.43	N–C–O (24–23–70)	124.34
N–C–S (21–23–26)	119.78	N–C–O (21–23–70)	120.54
N–N–C (27–24–23)	119.88	N–N–C (26–24–23)	117.98
N–N–C (20–21–23)	122.12	N–N–C (20–21–23)	122.4
N–C–N (24–23–21)	115.78	N–C–N (24–23–21)	115.1
C–N–N (28–27–24)	118.98	C–N–N (27–26–24)	118.83
C–N–N (18–20–21)	115.49	C–N–N (18–20–21)	116.46
N–C–C (27–28–30)	120.26	N–C–C (26–27–29)	120.22
N–C–C (20–18–1)	123.88	N–C–C (20–18–1)	122.65
N–C–N–N (21–23–24–27)	176.37	N–C–N–N (21–23–24–26)	−179
N–C–N–N (24–23–21–20)	−4.89	N–C–N–N (24–23–21–20)	−15.35
N–N–C–C (24–27–28–30)	179.65	N–N–C–C (24–26–27–29)	−179.88
N–N–C–C (21–20–18–1)	178.10	N–N–C–C (21–20–18–1)	175.16
O51(DMSO)–H22	1.815	O50(DMSO)–H22	1.827
O61(DMSO)–H25	1.824	O60(DMSO)–H25	1.782
O51(DMSO)–N21–H22	11.22	O50(DMSO)–N21–H22	11.79
O61(DMSO)–N24–H25	9.32	O60(DMSO)–N24–H25	10.45

Table A1.4: Molecular electric dipole moment (Debye) of **bis-TCH** and **bis-CH** *cis*-*trans* isomers in cluster pictures.

Dipole moment	bis-TCH	bis-CH
Total	11.2	18.6
x	−5.8	−9.2
y	7.9	14.8
z	5.4	6.6

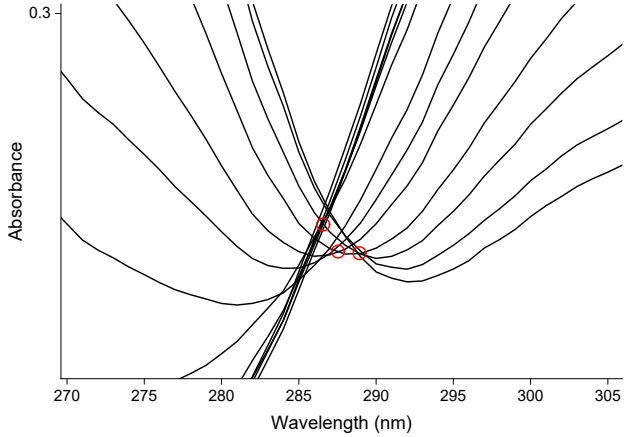

Figure A1.17: Zoom of the spectral region in which falls the isosbestic point at 288 nm for **AZ11**. The red circles indicate the various positions of the isosbestic point at different pH values.

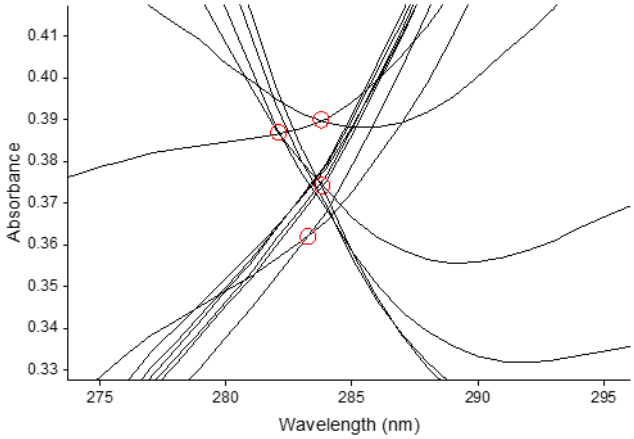

Figure A1.18: Zoom of the spectral region in which falls the isosbestic point at 284 nm for **AZ26**. The red circles indicate the various positions of the isosbestic point at different pH values.

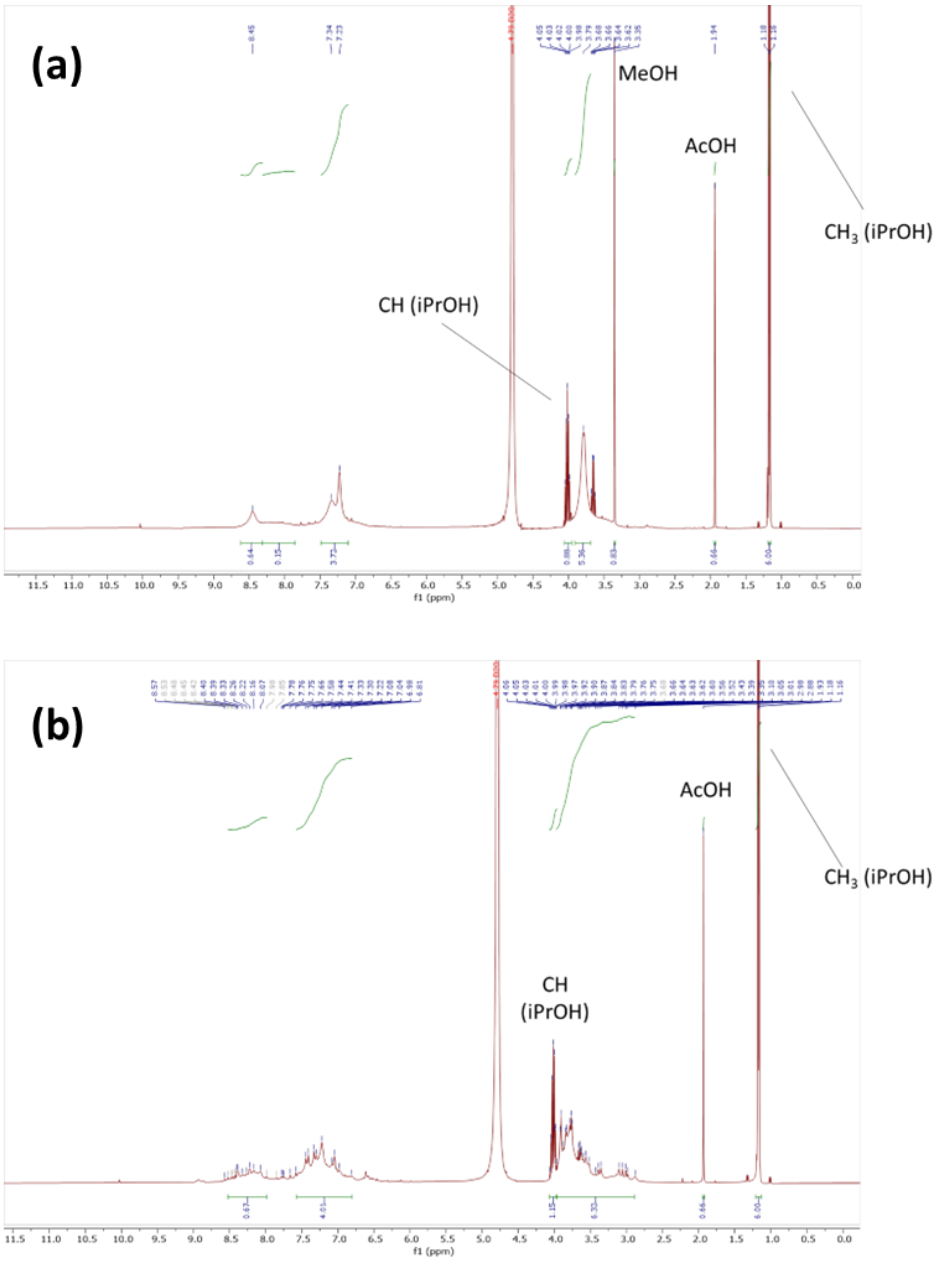

Figure A1.19: (a) ^{1}H NMR (400 MHz) spectrum of **PP9** in D_2O at 298 K. It is evident the presence of 2-propanol in the sample of the complex, together with traces of methanol and acetic acid; (b) ^{1}H NMR (400 MHz) spectrum of **PP11** in D_2O at 298 K. The unexpected high number of peaks in the spectrum suggests the formation of an equilibrium between several different complex species. It is evident the presence of 2-propanol in the sample of the complex, together with traces of acetic acid.

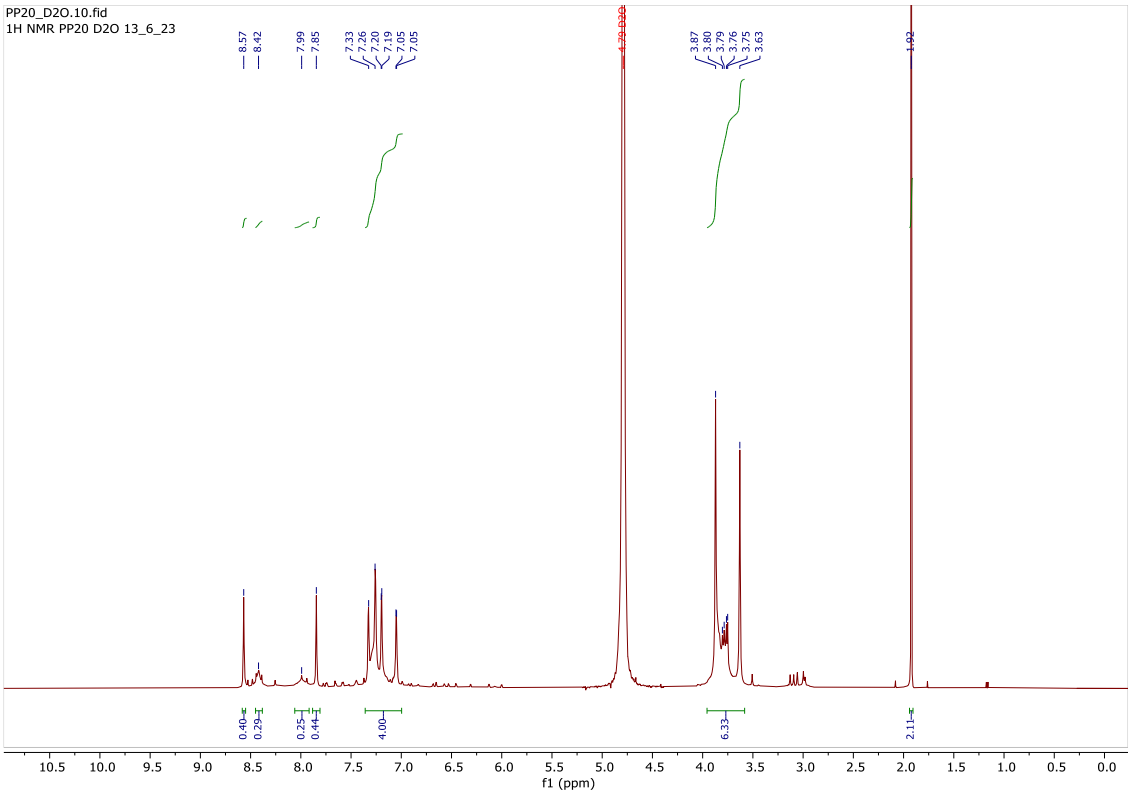

Figure A1.20: ^{1}H NMR (400 MHz) spectrum of **PP20** in D_2O at 298 K. The unexpected high number of peaks in the spectrum suggests the formation of an equilibrium between at least two different complex species. The peak at 1.92 ppm confirms the presence of the acetate ion in the structure of the complex.

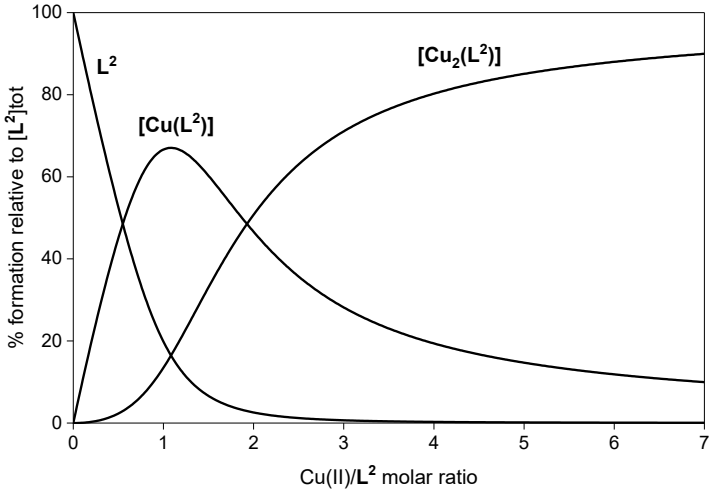

Figure A1.21: Representative distribution diagram of the **bis-CH** and Cu^{II} in aqueous solution at pH 2.5.

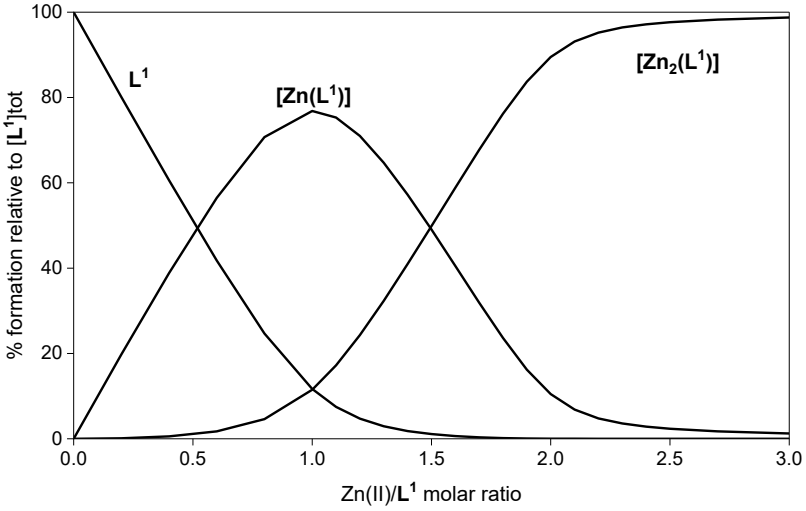

Figure A1.22: Representative distribution diagram of the **bis-TCH** and Zn^{II} in aqueous solution at pH 7.4.

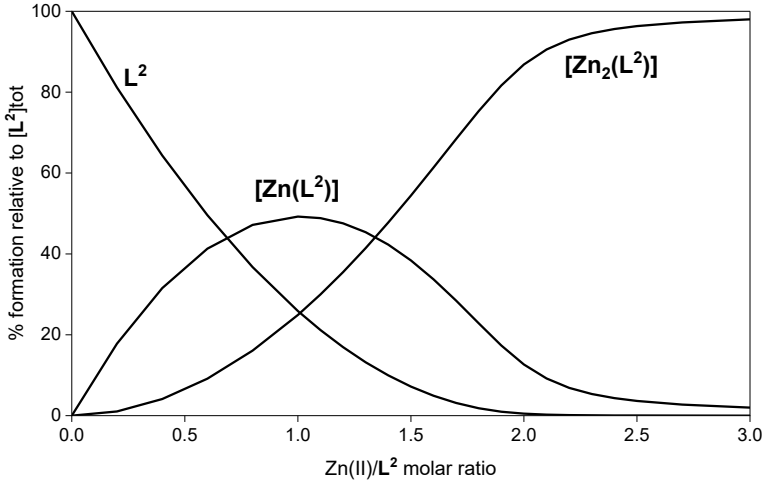

Figure A1.23: Representative distribution diagram of the **bis-CH** and Zn^{II} in aqueous solution at pH 7.4.

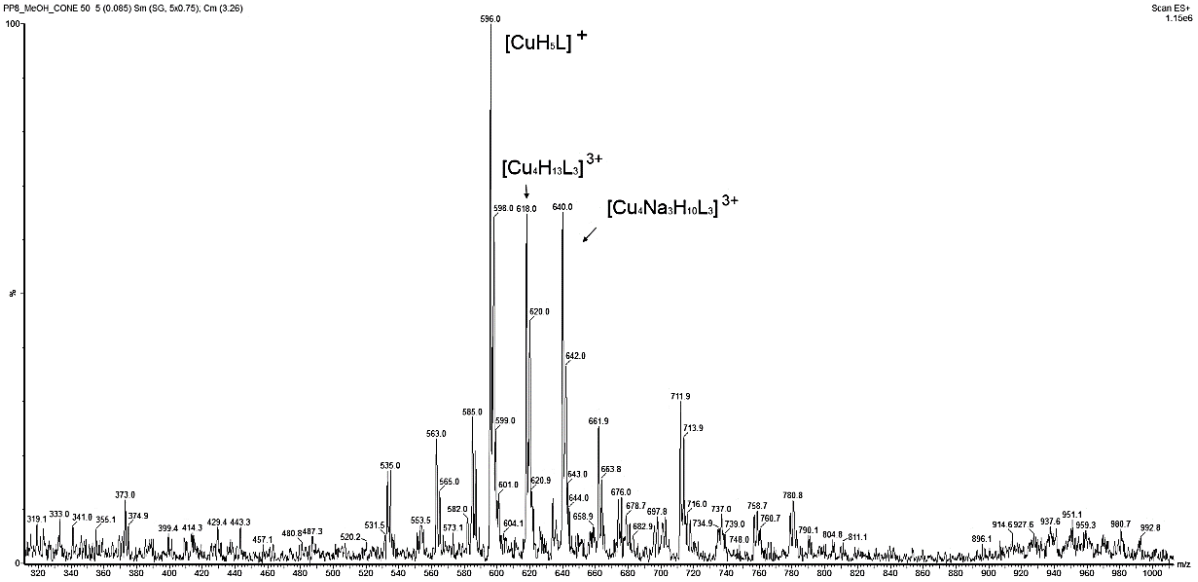

Figure A1.24: ESI-MS spectrum (positive ions) for complex **PP8** in methanol.

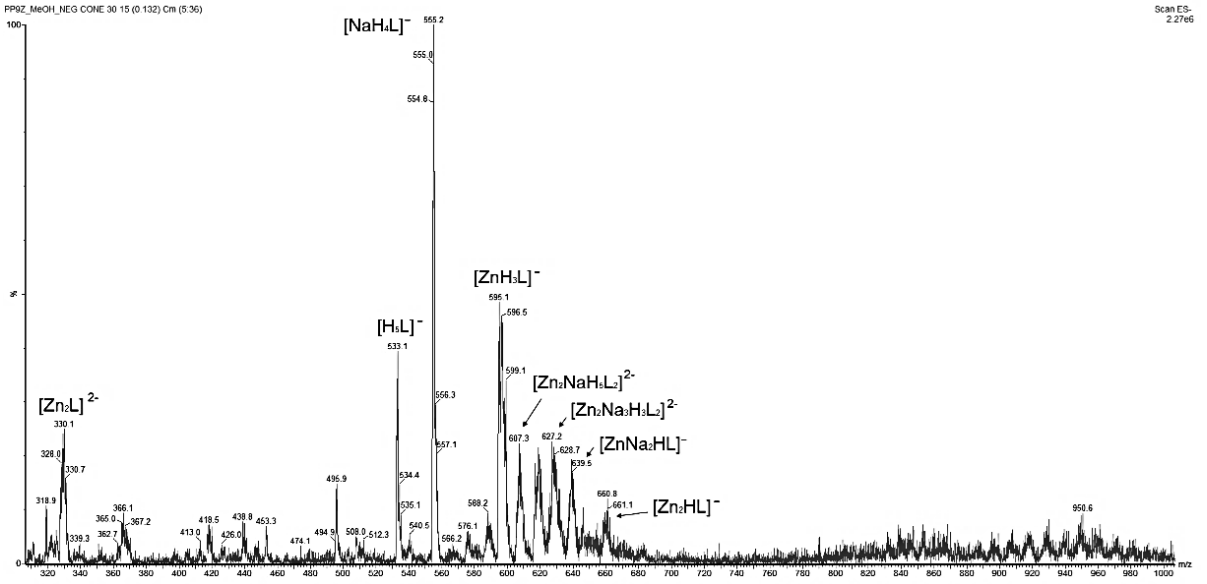

Figure A1.25: ESI-MS spectrum (negative ions) for complex **PP9** in methanol.

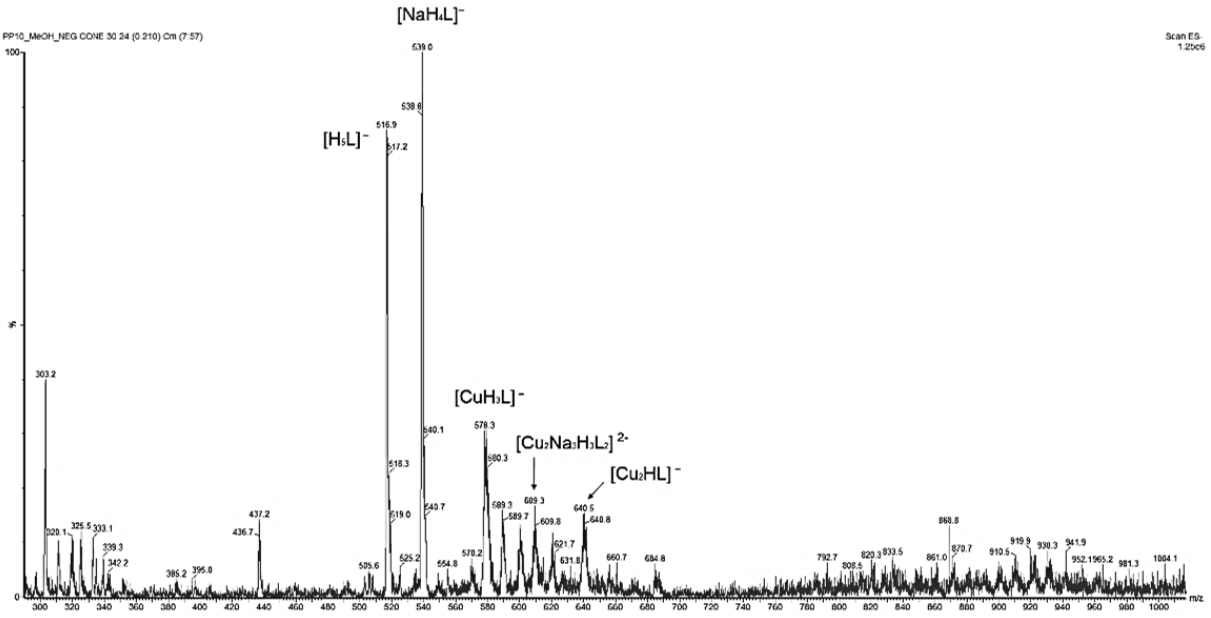

Figure A1.26: ESI-MS spectrum (negative ions) for complex **PP10** in methanol.

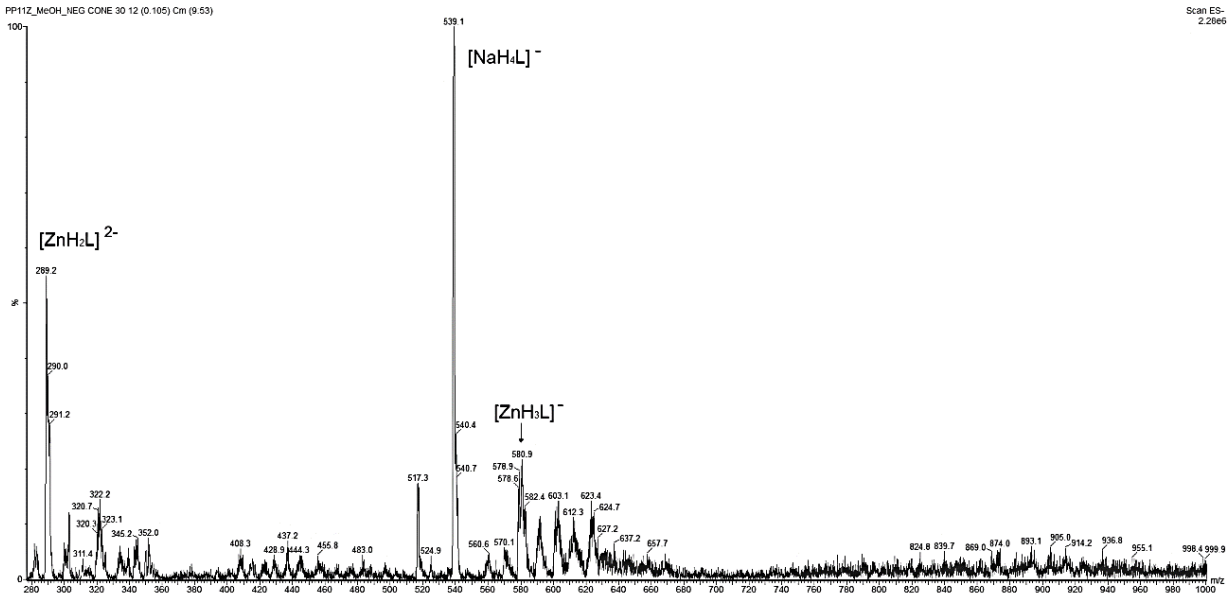

Figure A1.27: ESI-MS spectrum (negative ions) for complex **PP11** in methanol.

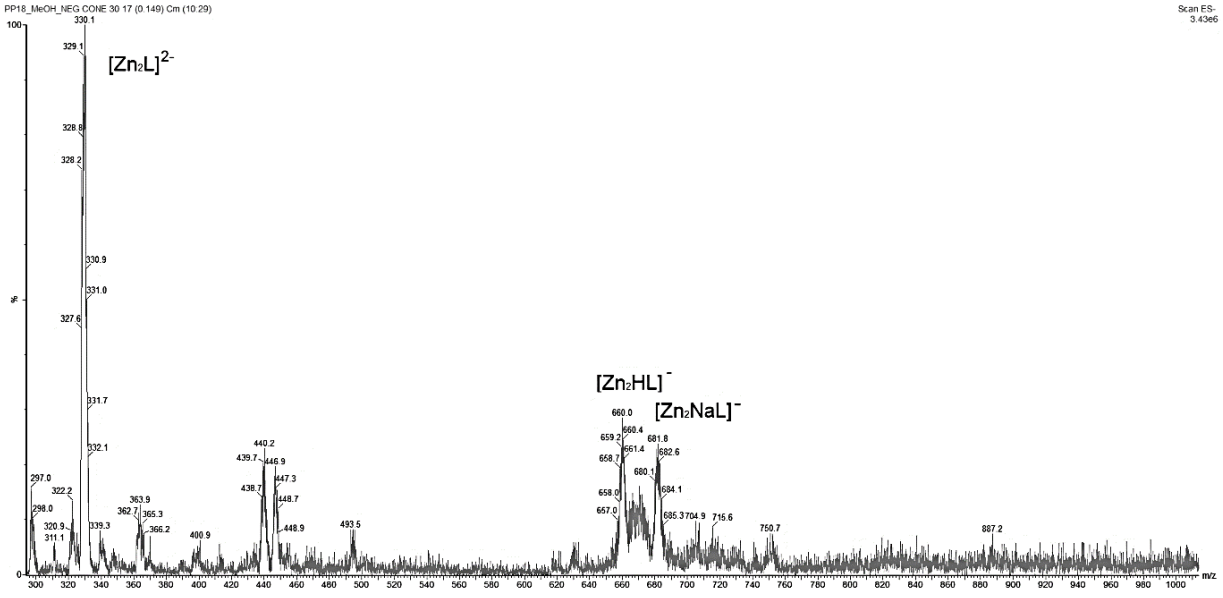

Figure A1.28: ESI-MS spectrum (negative ions) for complex **PP18** in methanol.

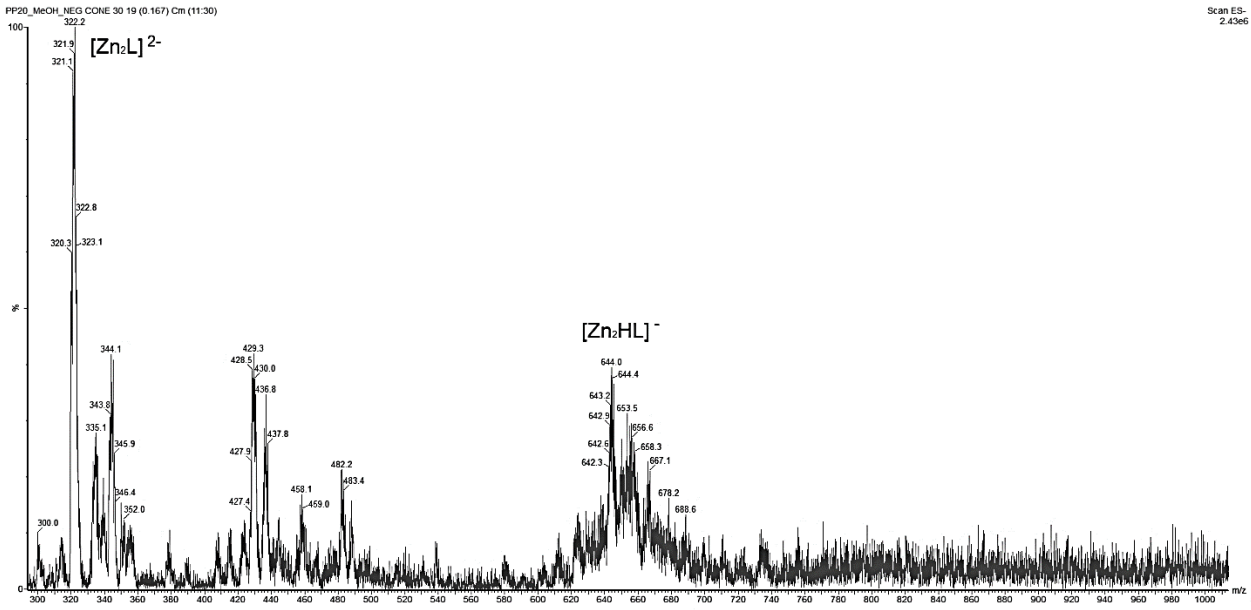

Figure A1.29: ESI-MS spectrum (negative ions) for complex **PP20** in methanol.

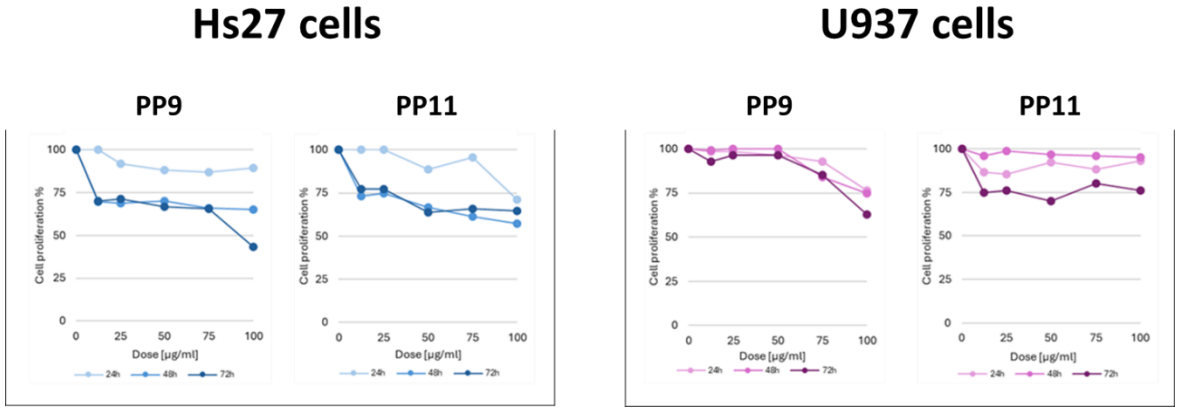

Figure A1.30: Dose–response curves obtained on Hs27 (left) and U937 cells (right) after 24, 48 and 72 h treatment with **PP9** and **PP11**. Data are expressed as cell proliferation percentage compared with control cells.

Table A1.5: GI_{50} values (µM) obtained in U937 and Hs27 cell lines after 24-, 48-, and 72 h treatment with the two ligands (**bis-TCH AZ11** and **bis-CH AZ26**) and the complexes **PP8-11**.

Compound	GI_{50} value (µM)					
	Hs27 cells (normal cells)			U937 cells (leukemia cells)		
	24 h	48 h	72 h	24 h	48 h	72 h
bis-TCH	n. a.	n. a.	n. a.	n. a.	n. a.	144.30 ± 4.66
bis-CH	n. a.	n. a.	n. a.	n. a.	n. a.	71.81 ± 6.80
PP8	n. a.	n. a.	69.50 ± 3.18	110.35 ± 4.73	120.00 ± 14.14	110.50 ± 2.82
PP10	107.75 ± 17.32	55.25 ± 7.42	53.00 ± 0.70	129.25 ± 0.35	77.00 ± 6.36	50.00 ± 14.14
PP9	n. a.	n. a.	117.75 ± 10.25	n. a.	n. a.	n. a.
PP11	n. a.	n. a.	n. a.	n. a.	n. a.	n. a.

n. a. = not active

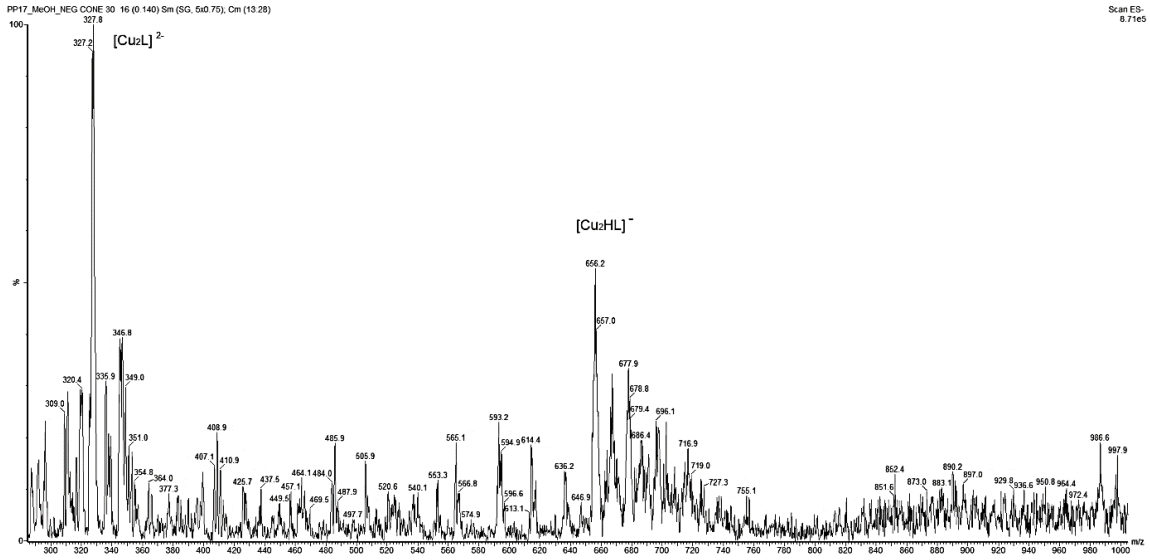

Figure A1.31: ESI-MS spectrum (negative ions) for complex **PP17** in methanol.

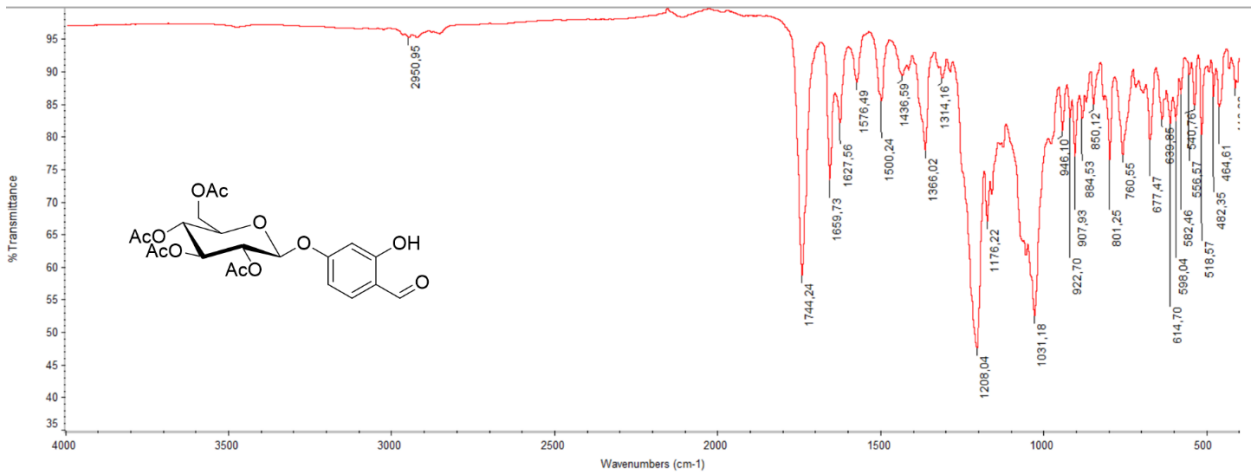

Figure A2.1: FT-IR spectrum of **FMM2**.

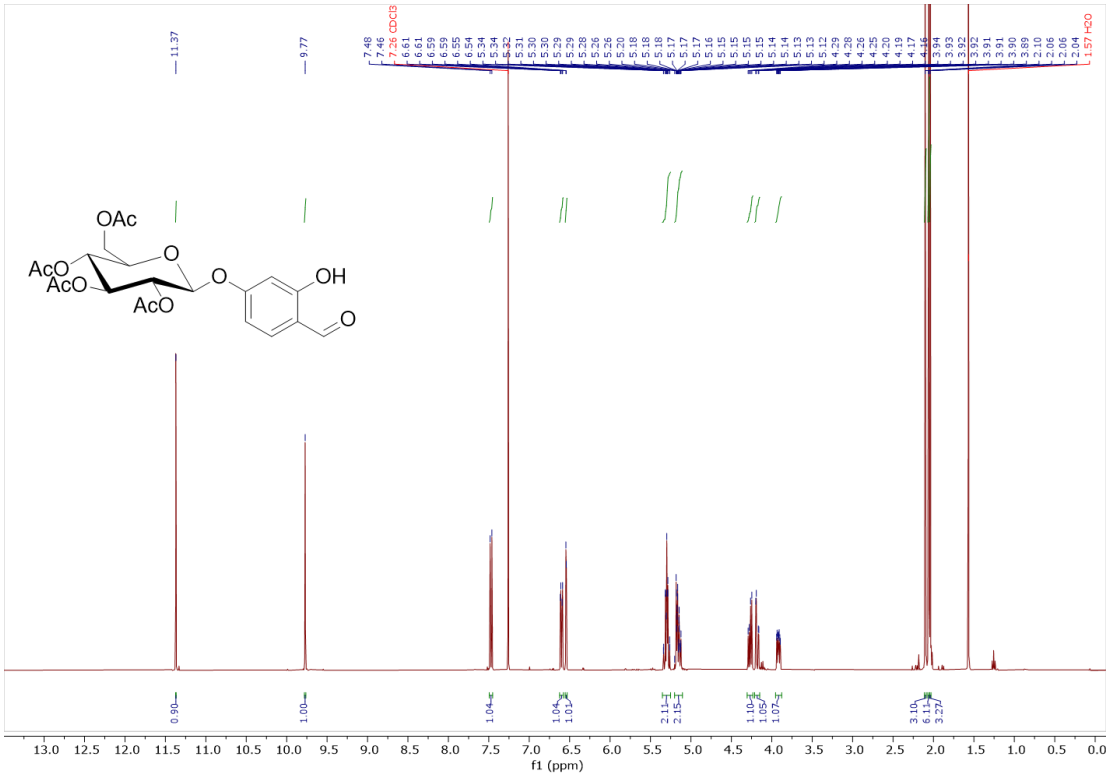

Figure A2.2: ^{1}H NMR (400 MHz, Chloroform-*d,* 298 K) spectrum of **FMM2**.

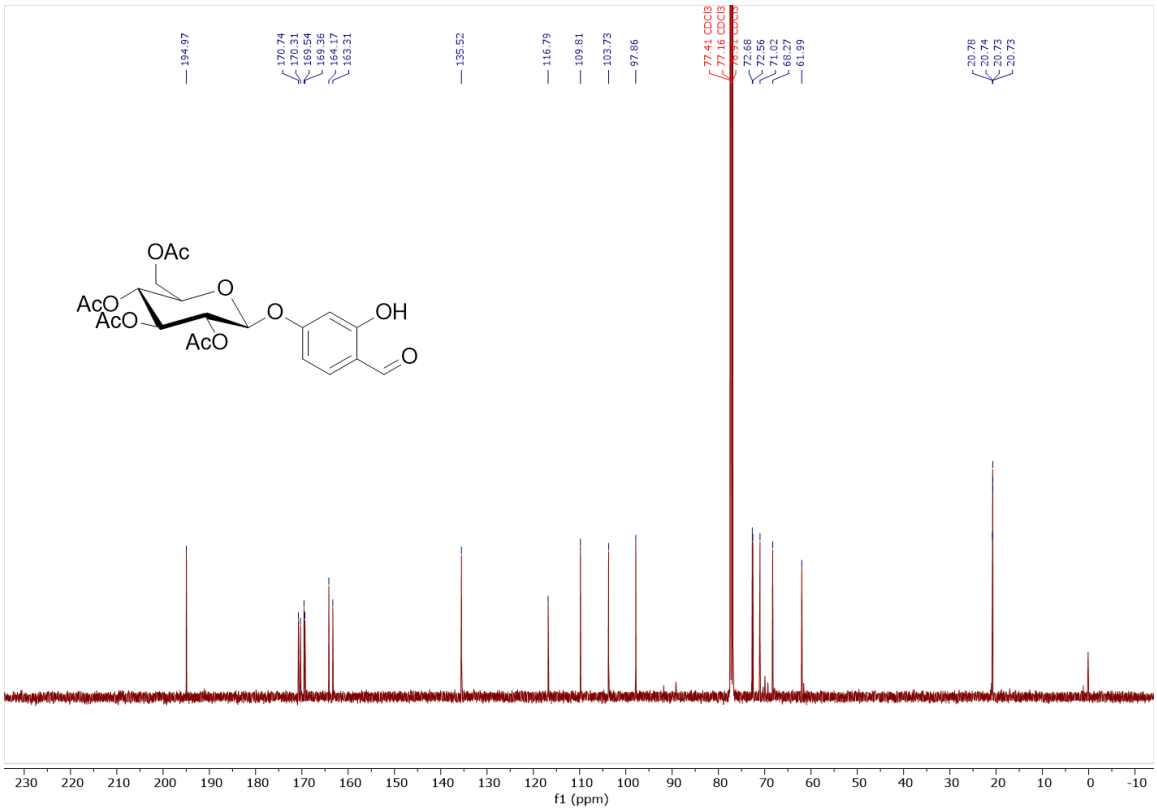

Figure A2.3: ^{13}C NMR (101 MHz, Chloroform-*d*, 298 K) spectrum of **FMM2**.

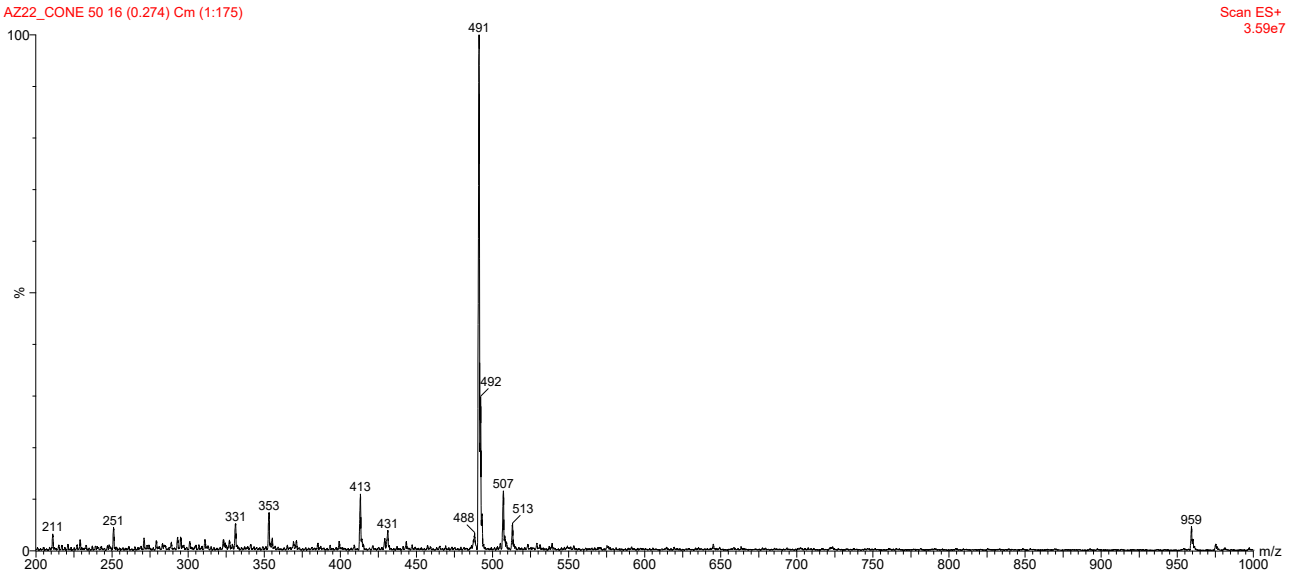

Figure A2.4: ESI-MS spectrum (positive ions) for **FMM2** (or **AZ22**) in methanol.

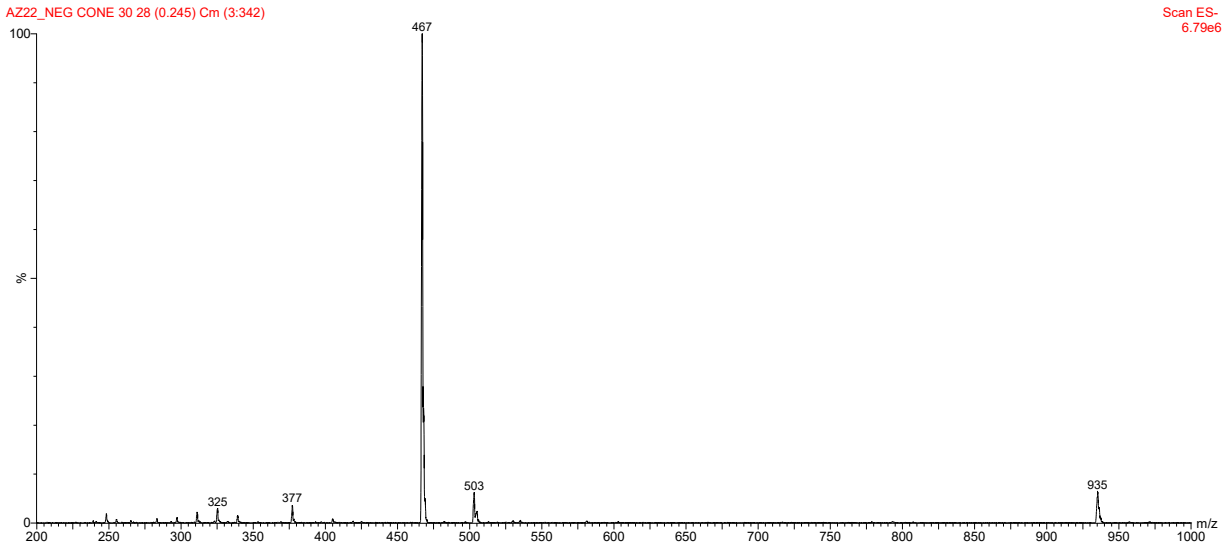

Figure A2.5: ESI-MS spectrum (negative ions) for **FMM2** (or **AZ22**) in methanol.

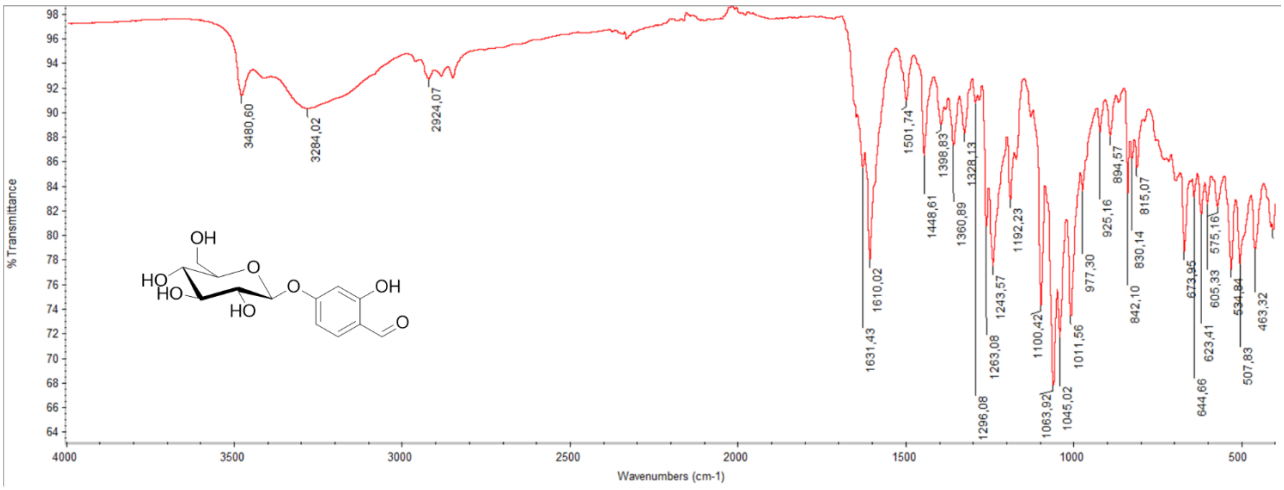

Figure A2.6: FT-IR spectrum of **AZ24**.

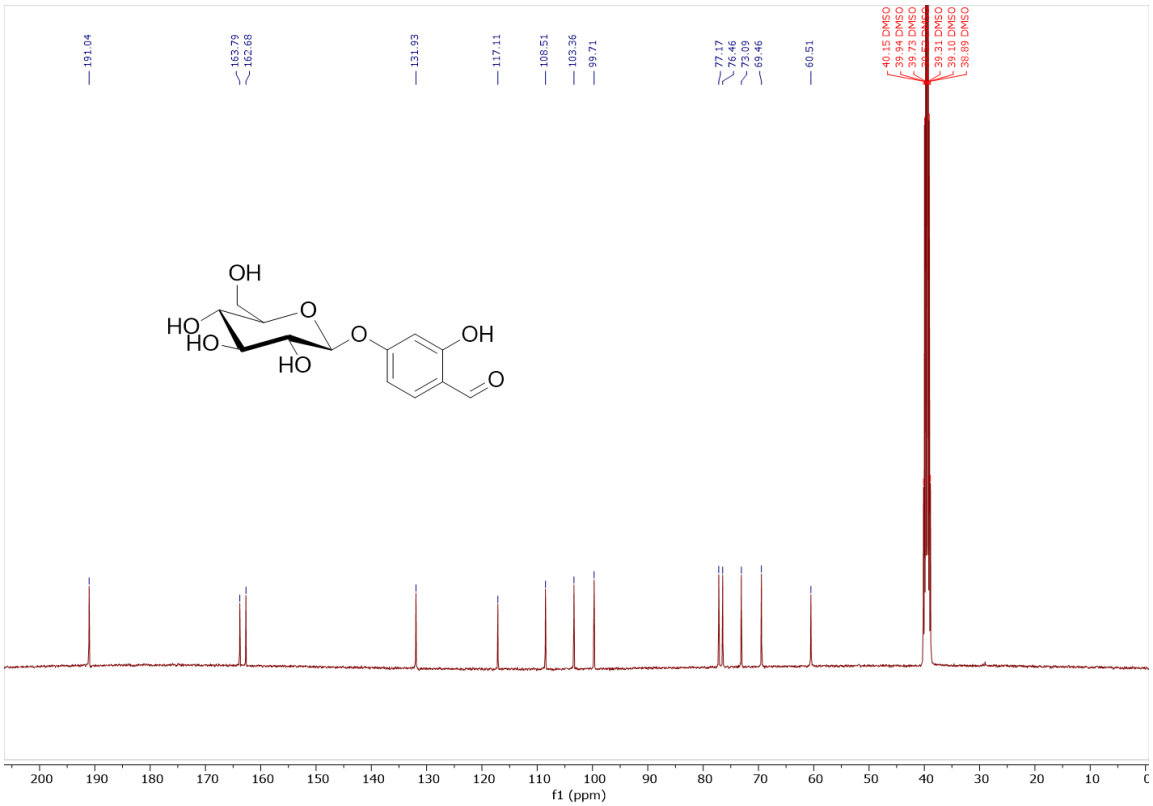

Figure A2.7: ^{13}C NMR (101 MHz, DMSO-d_6, 298 K) spectrum of **AZ24**.

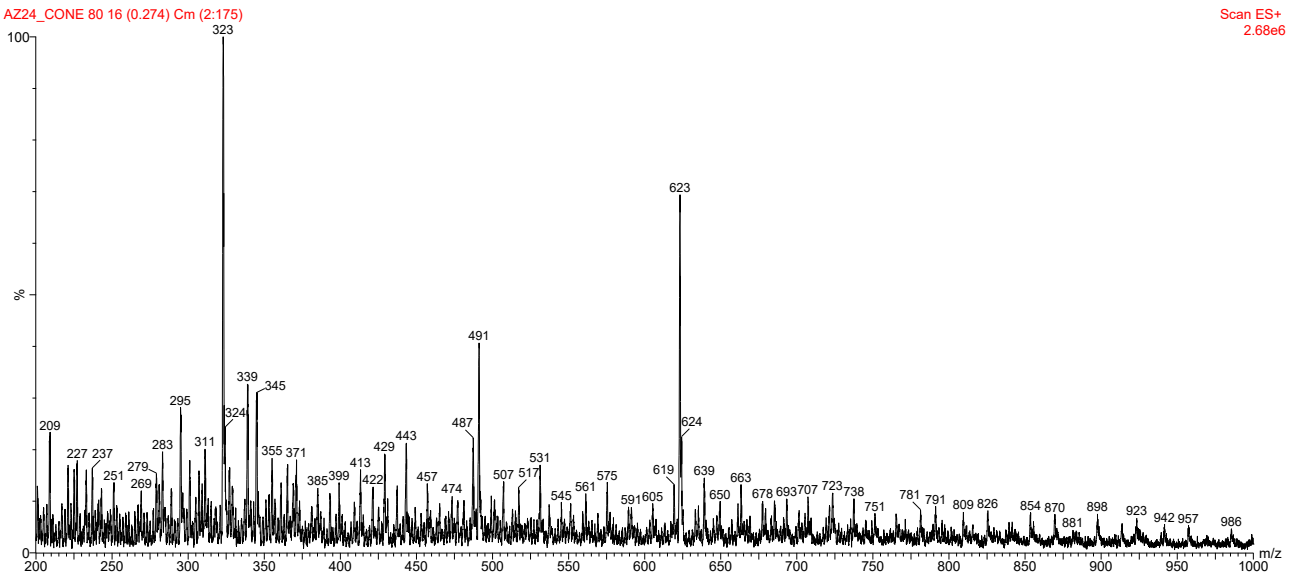

Figure A2.8: ESI-MS spectrum (positive ions) for **AZ24** in methanol.

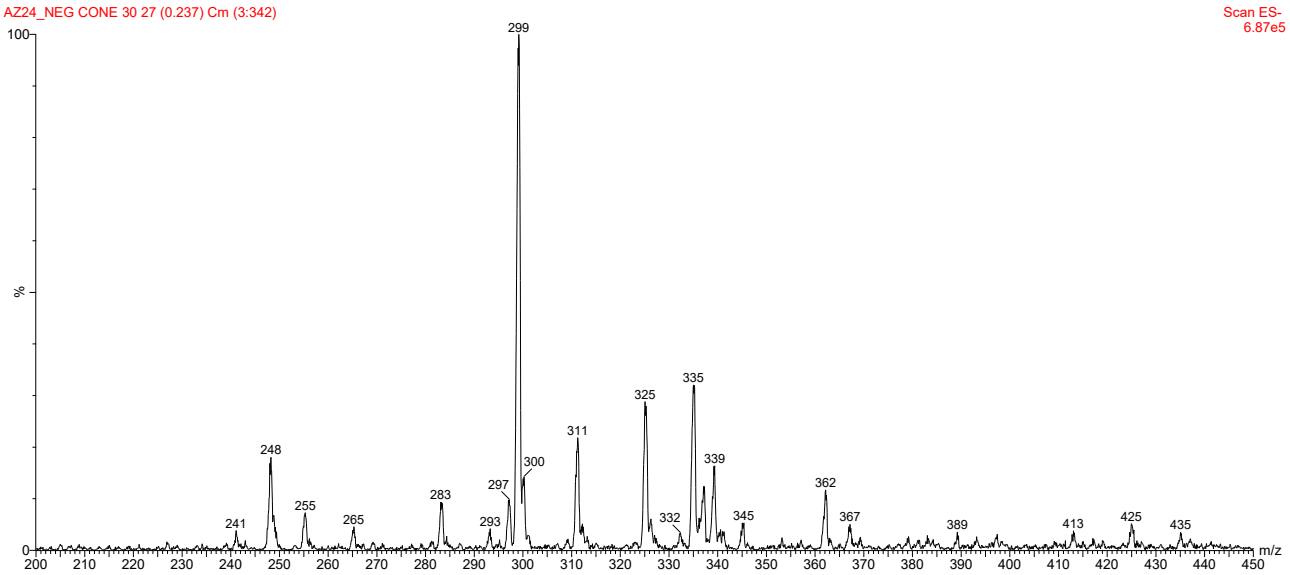

Figure A2.9: ESI-MS spectrum (negative ions) for **AZ24** in methanol.

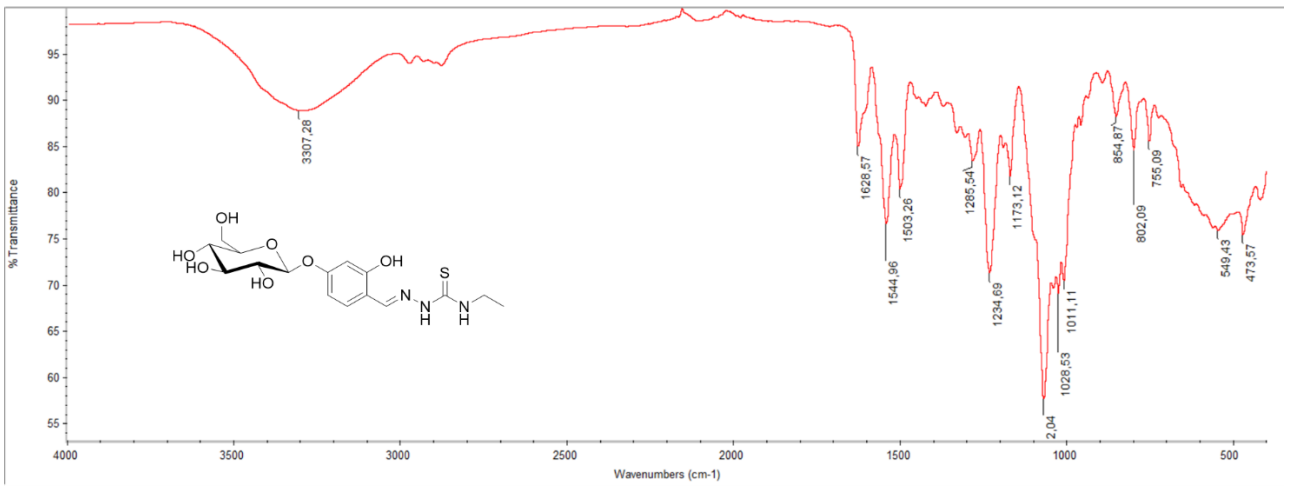

Figure A2.10: FT-IR spectrum of **FMM4Z**.

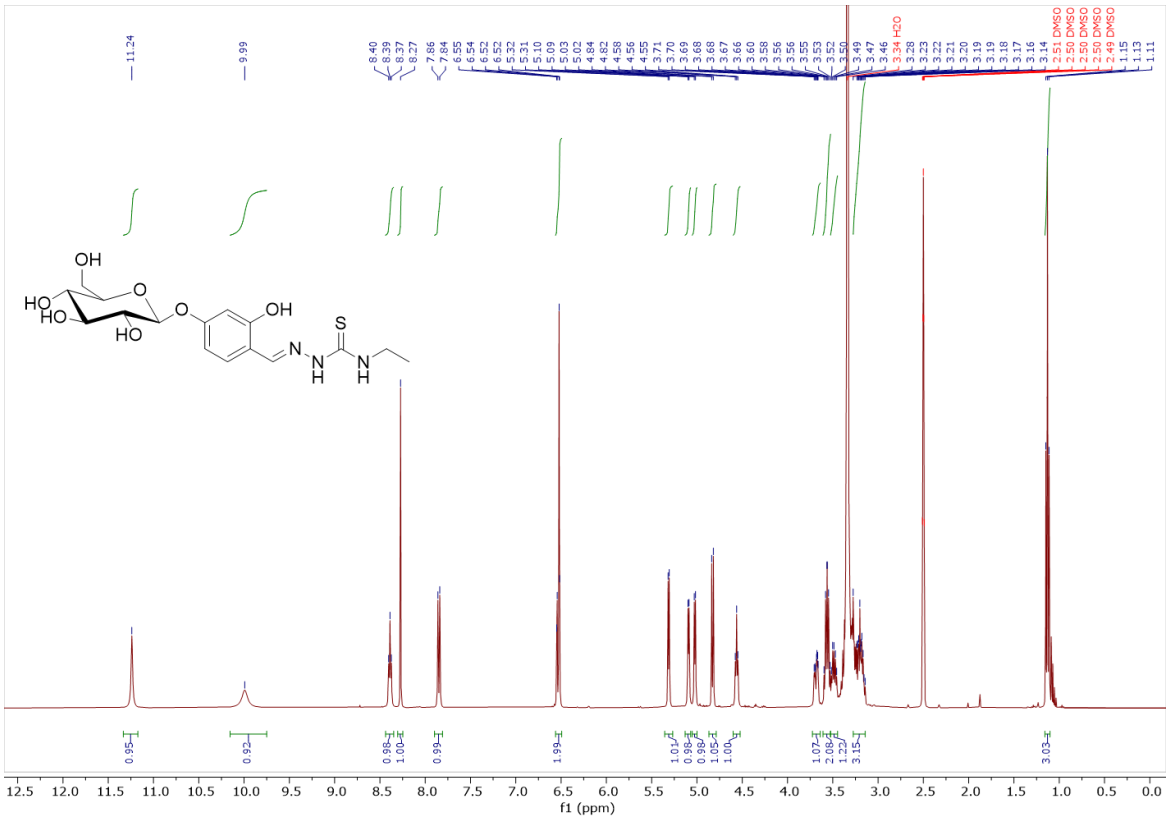

Figure A2.11: ^{1}H NMR (400 MHz, DMSO-d_6, 298 K) spectrum of **FMM4Z**.

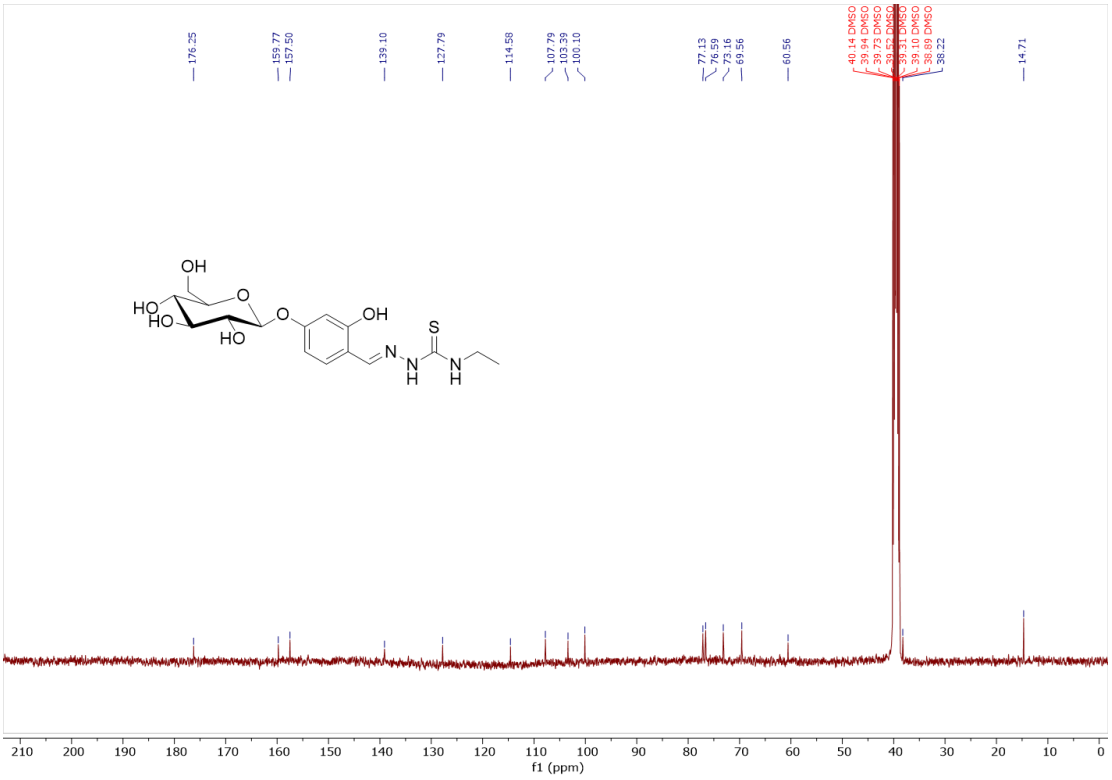

Figure A2.12: ^{13}C NMR (101 MHz, DMSO-d_6, 298 K) spectrum of **FMM4Z**.

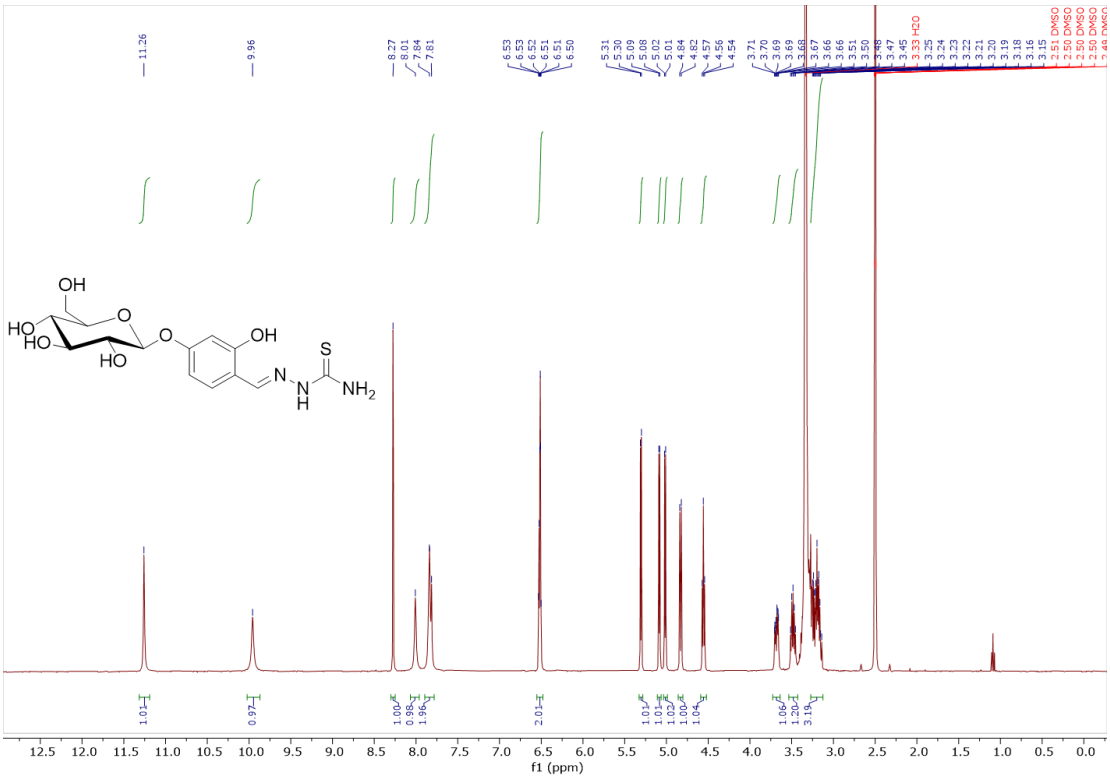

Figure A2.13: ^{1}H NMR (400 MHz, DMSO-d_6, 298 K) spectrum of **FMM8Z**.

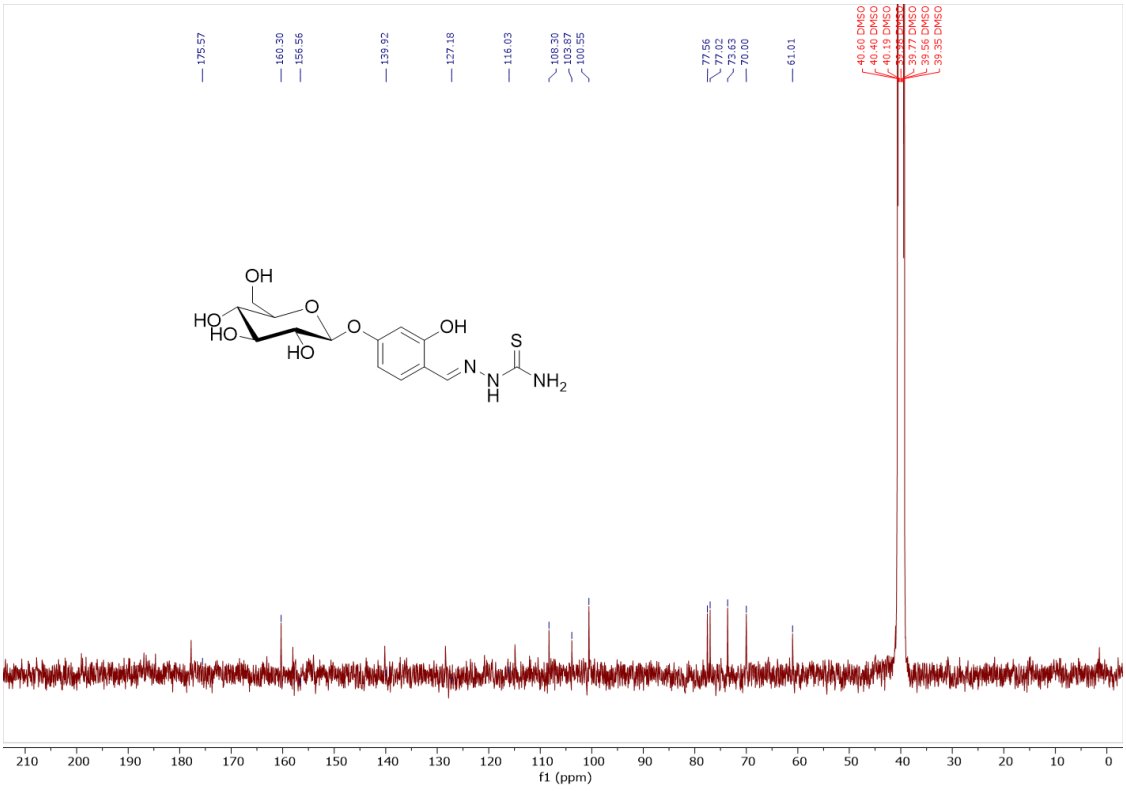

Figure A2.14: ^{13}C NMR (101 MHz, DMSO-d_6, 298 K) spectrum of **FMM8Z**.

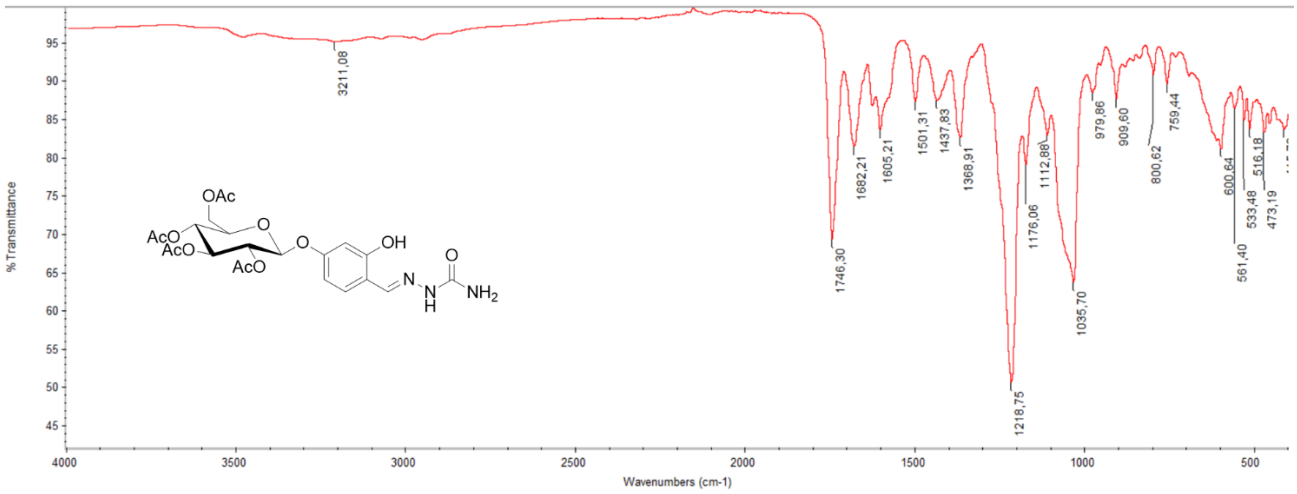

Figure A2.15: FT-IR spectrum of **CM2**.

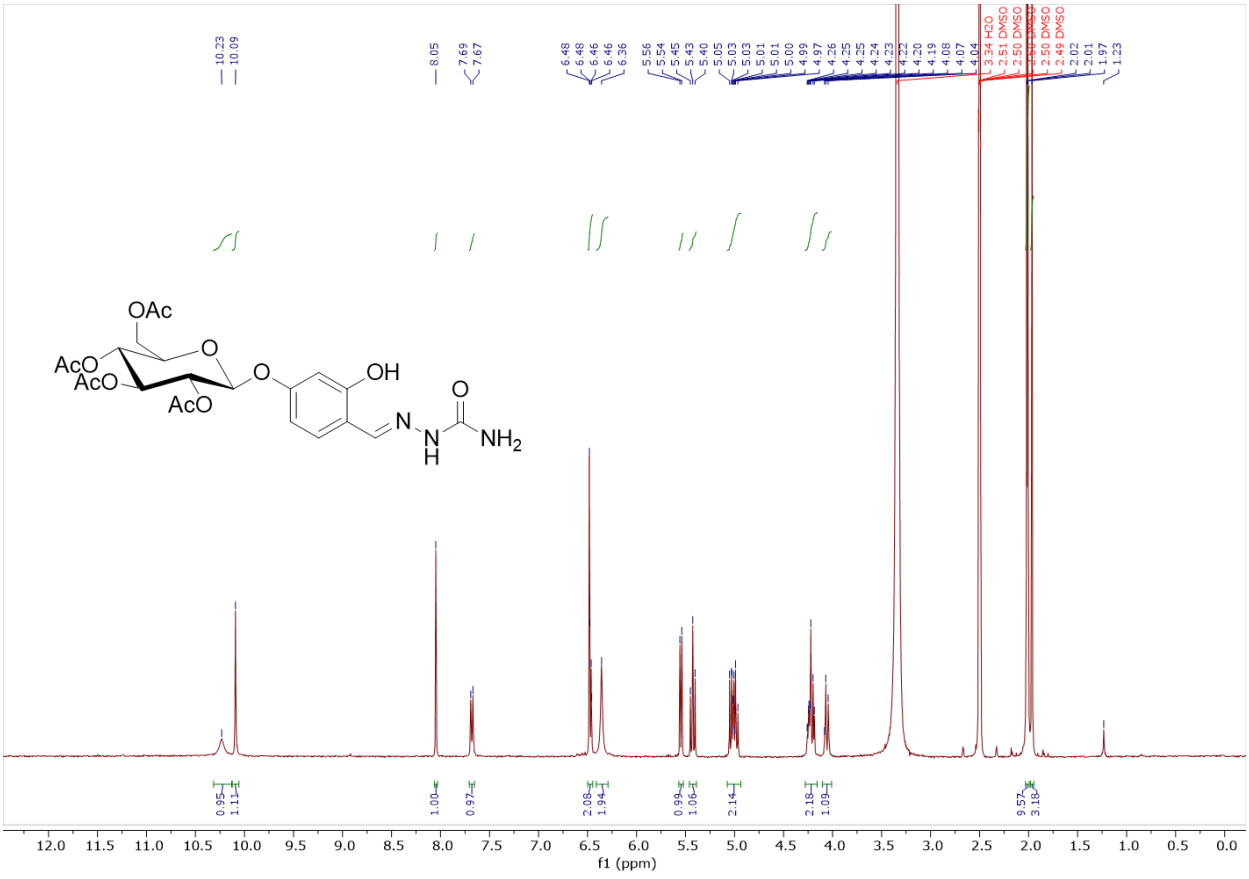

Figure A2.16: ^{1}H NMR (400 MHz, DMSO-d_6, 298 K) spectrum of **CM2**.

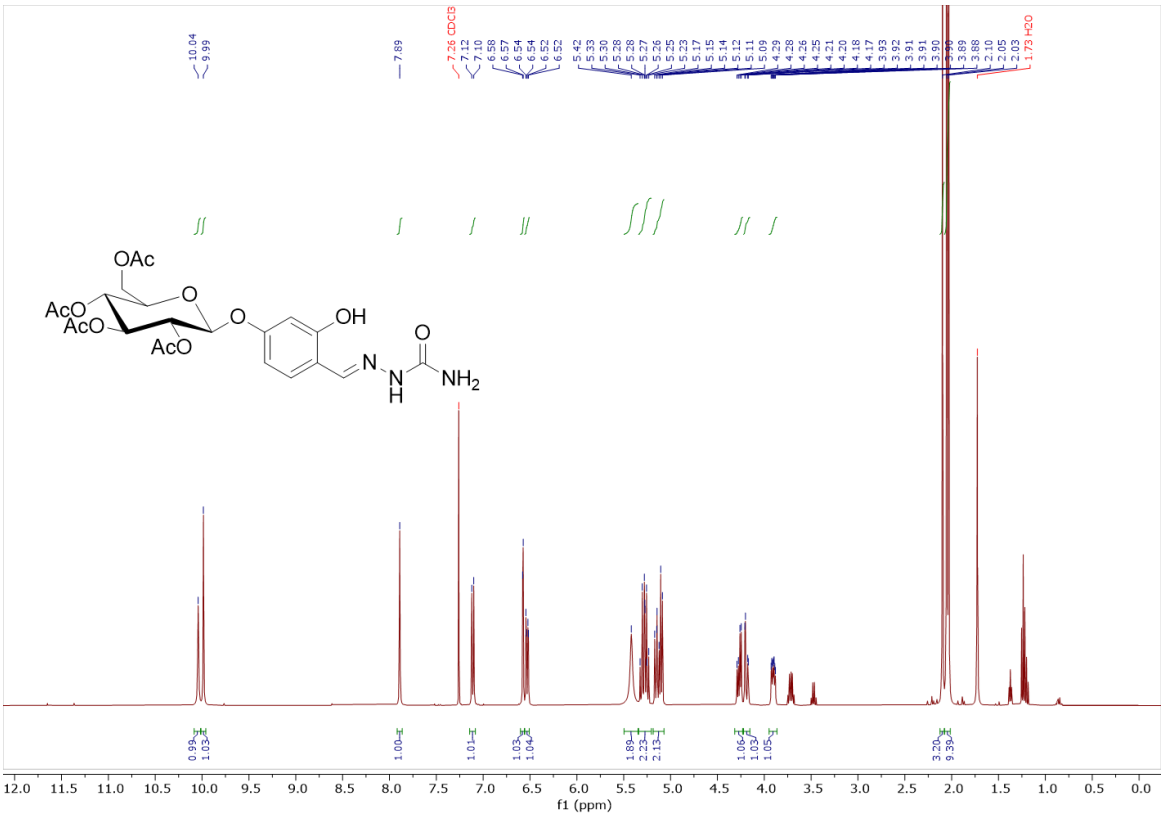

Figure A2.17: ^{1}H NMR (400 MHz, Chloroform-*d,* 298 K) spectrum of **CM2**.

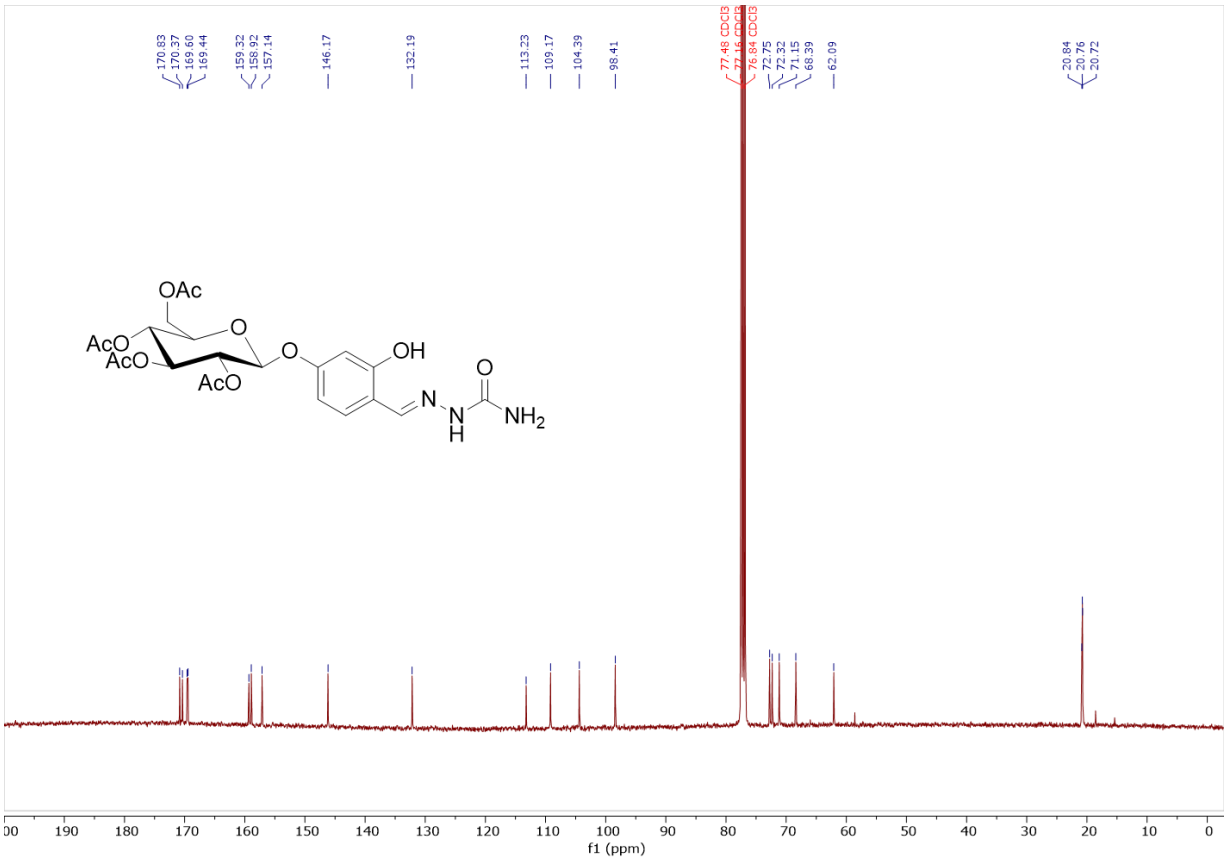

Figure A2.18: ^{13}C NMR (101 MHz, Chloroform-*d*, 298 K) spectrum of **CM2**.

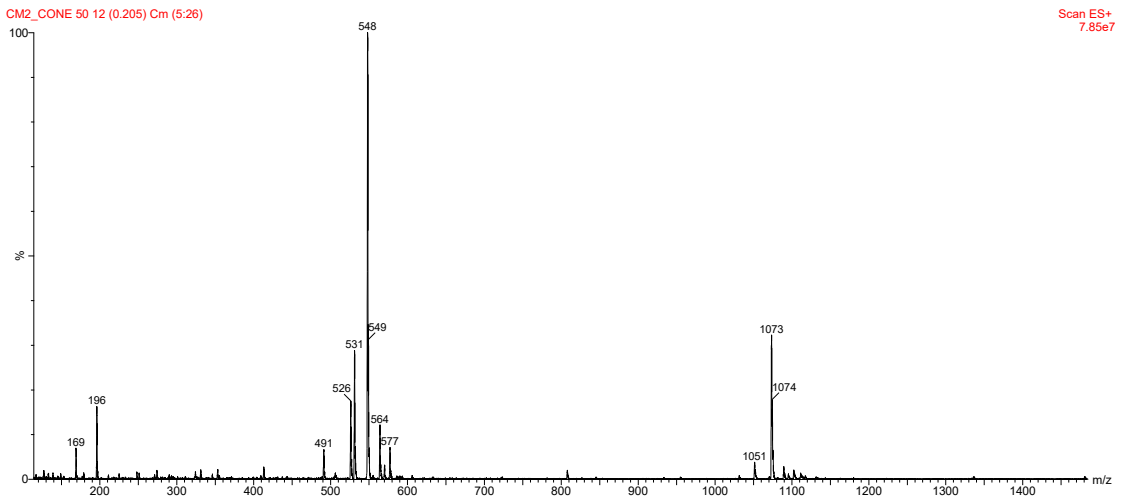

Figure A2.19: ESI-MS spectrum (positive ions) for **CM2** in methanol.

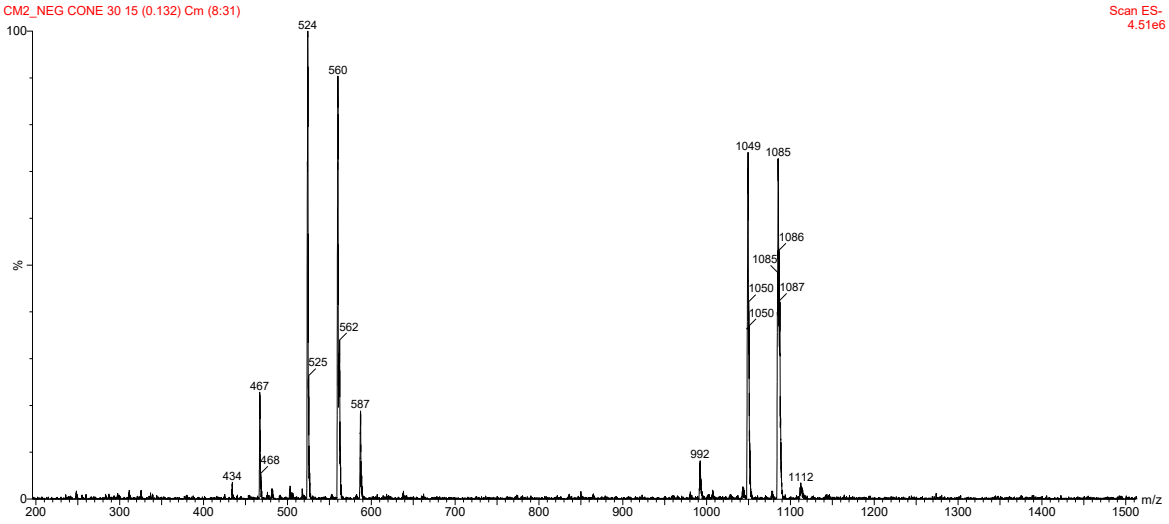

Figure A2.20: ESI-MS spectrum (negative ions) for **CM2** in methanol.

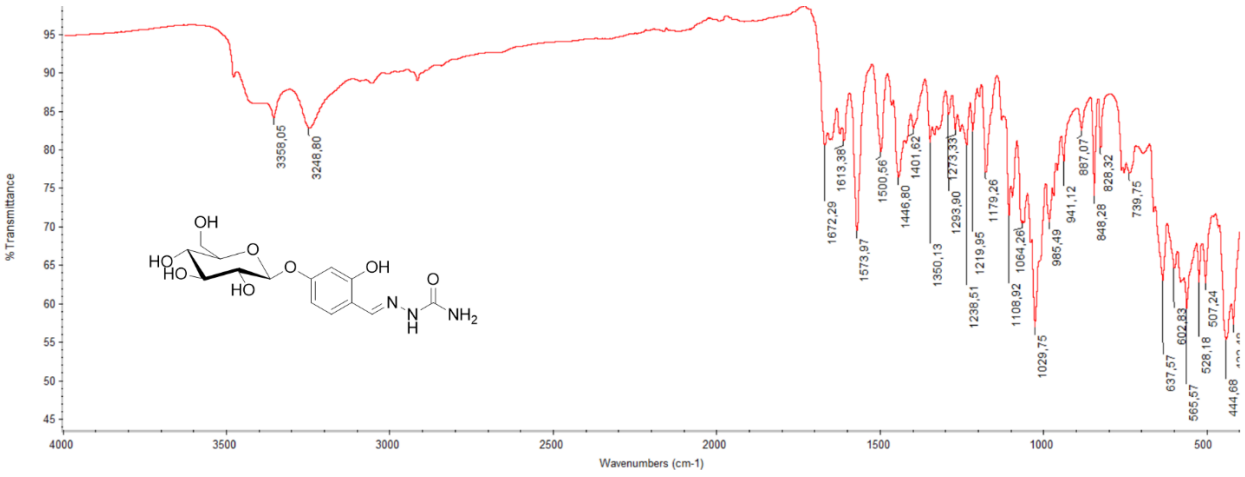

Figure A2.21: FT-IR spectrum of **CM4**.

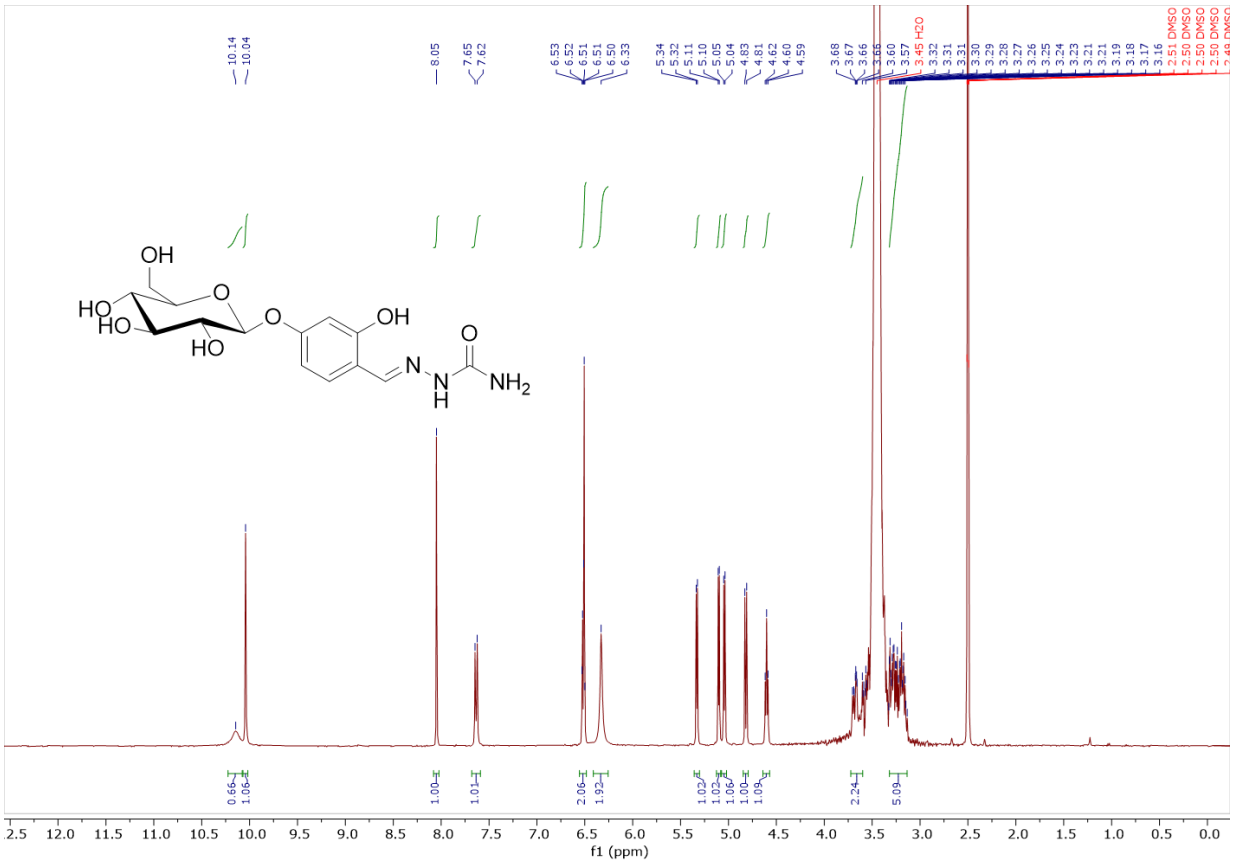

Figure A2.22: ^{1}H NMR (400 MHz, DMSO-d_6, 298 K) spectrum of **CM4**.

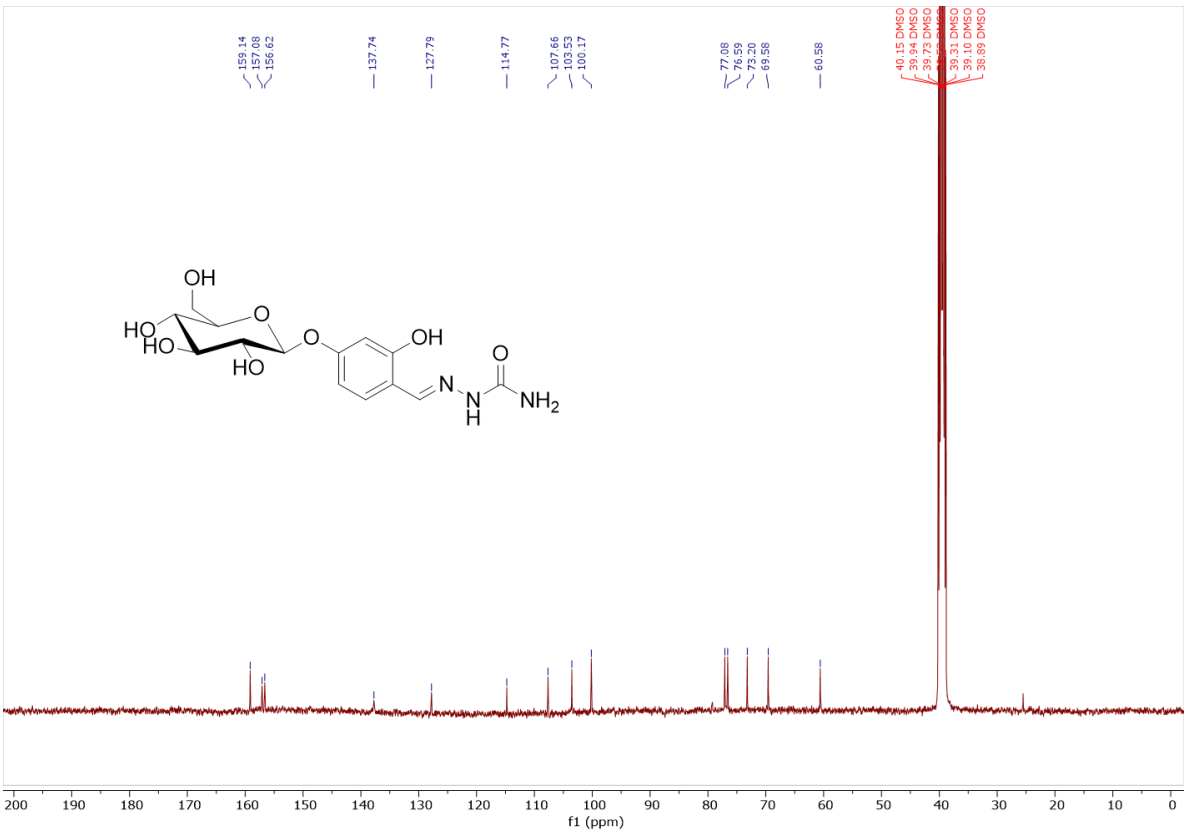

Figure A2.23: ^{13}C NMR (101 MHz, DMSO-d_6, 298 K) spectrum of **CM4**.

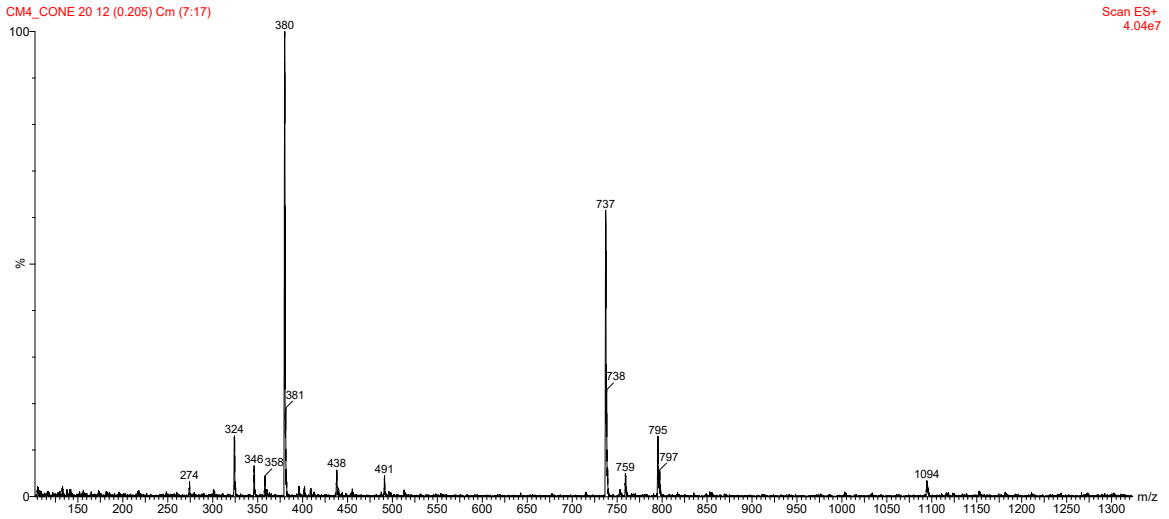

Figure A2.24: ESI-MS spectrum (positive ions) for **CM4** in methanol.

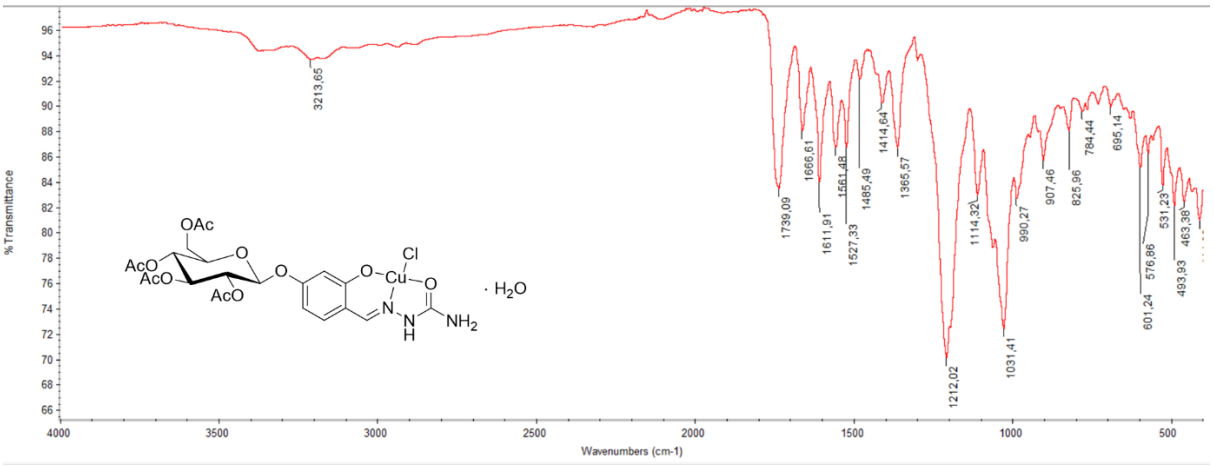

Figure A2.25: FT-IR spectrum of **CM5**.

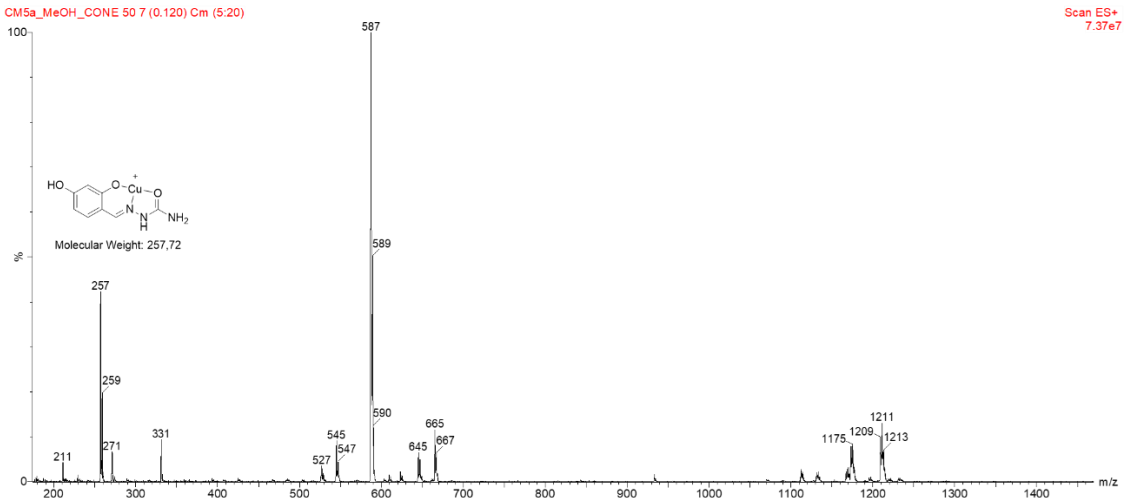

Figure A2.26: ESI-MS spectrum (positive ions) for **CM5** in methanol. The peak at m/z = 257 is associated to the fragment shown in the figure.

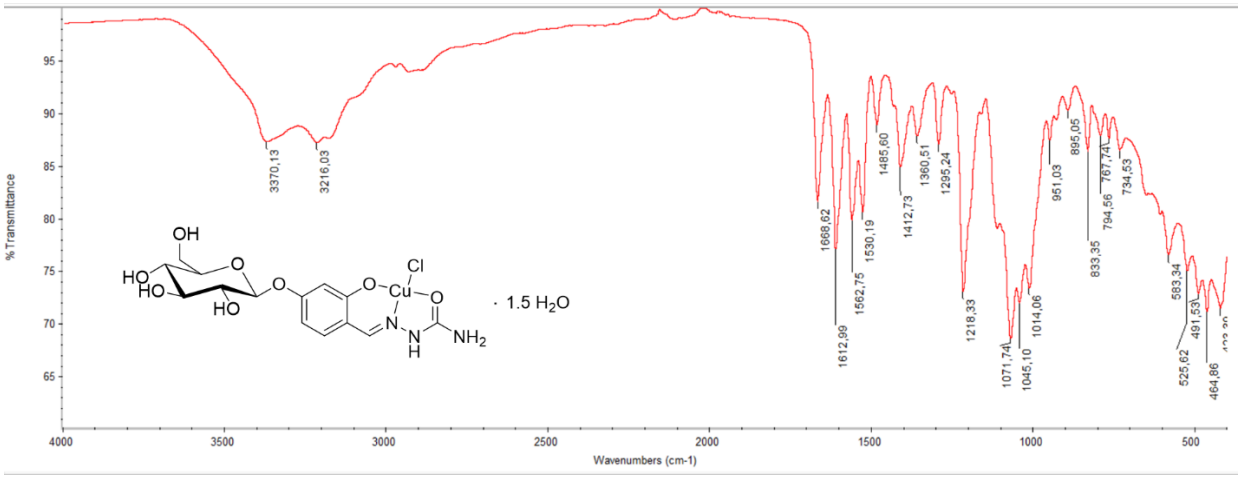

Figure A2.27: FT-IR spectrum of **CM6**.

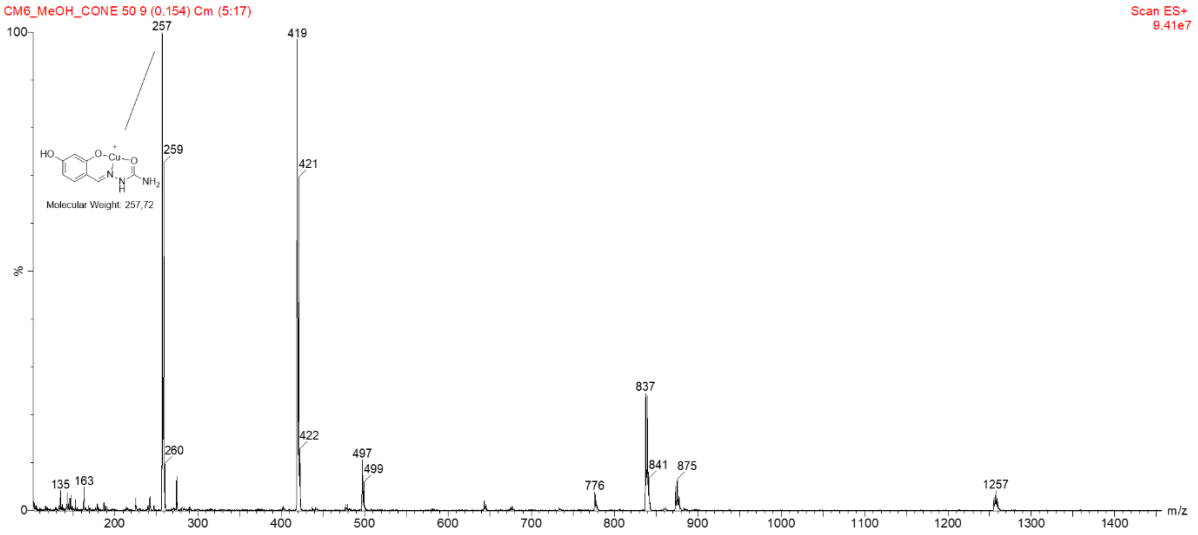

Figure A2.28: ESI-MS spectrum (positive ions) for **CM6** in methanol. The peak at m/z = 257 is associated to the fragment shown in the figure.

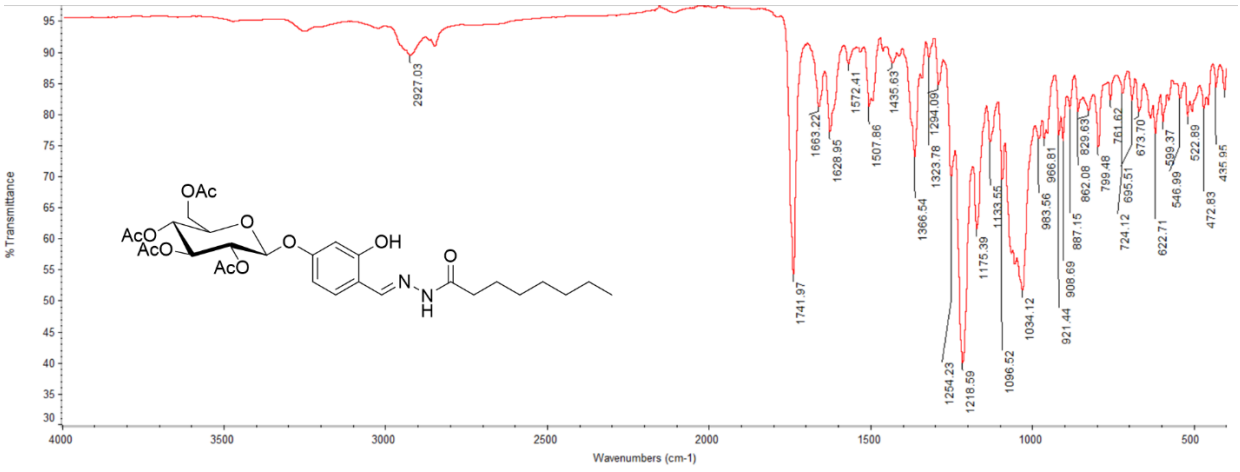

Figure A2.29: FT-IR spectrum of **CM7**.

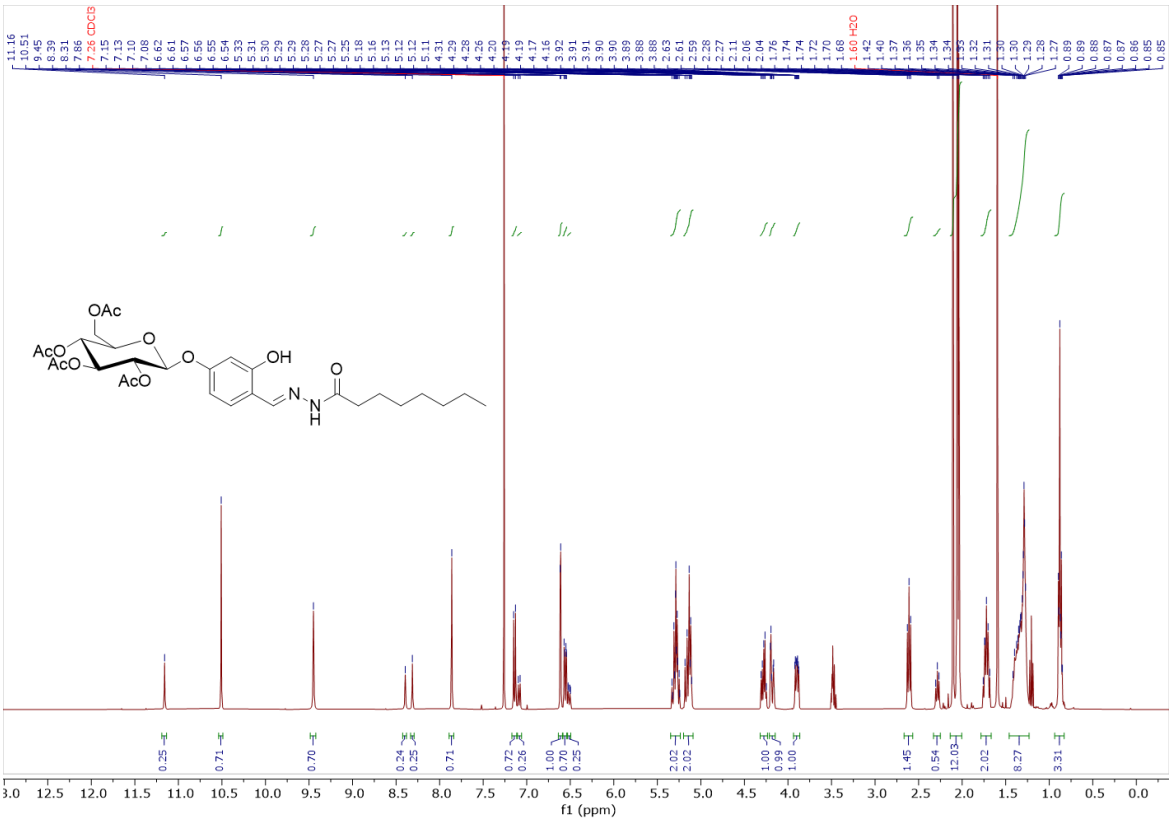

Figure A2.30: ^{1}H NMR (400 MHz, Chloroform-*d,* 298 K) spectrum of **CM7**.

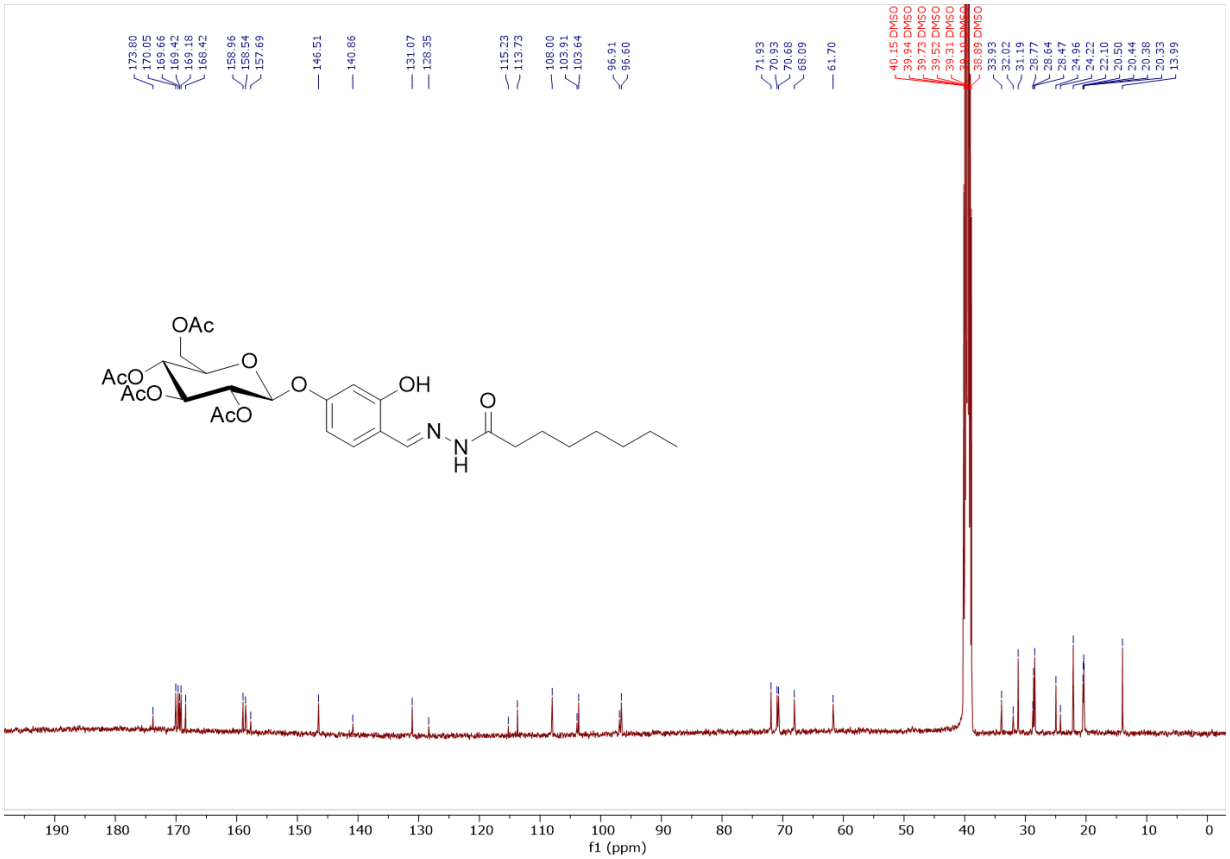

Figure A2.31: ^{13}C NMR (101 MHz, DMSO-d_6, 298 K) spectrum of **CM7**.

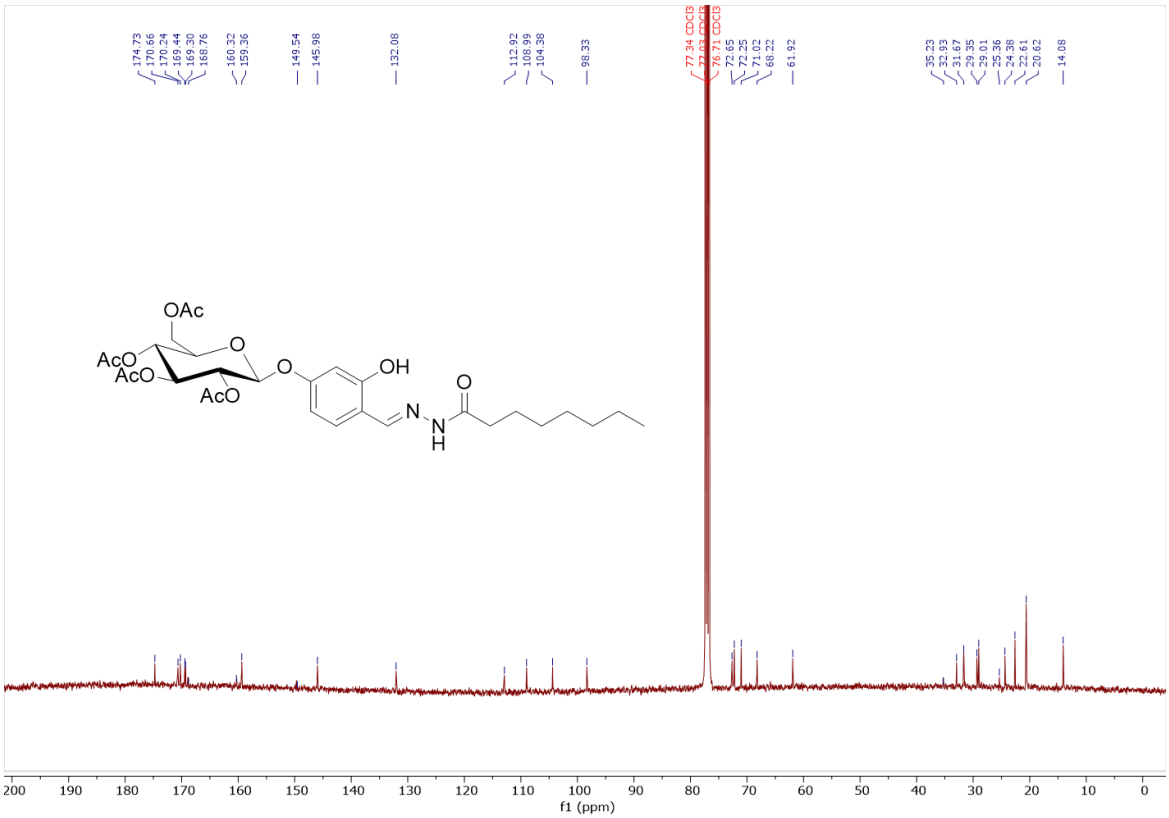

Figure A2.32: ^{1}H NMR (400 MHz, Chloroform-*d,* 298 K) spectrum of **CM7**.

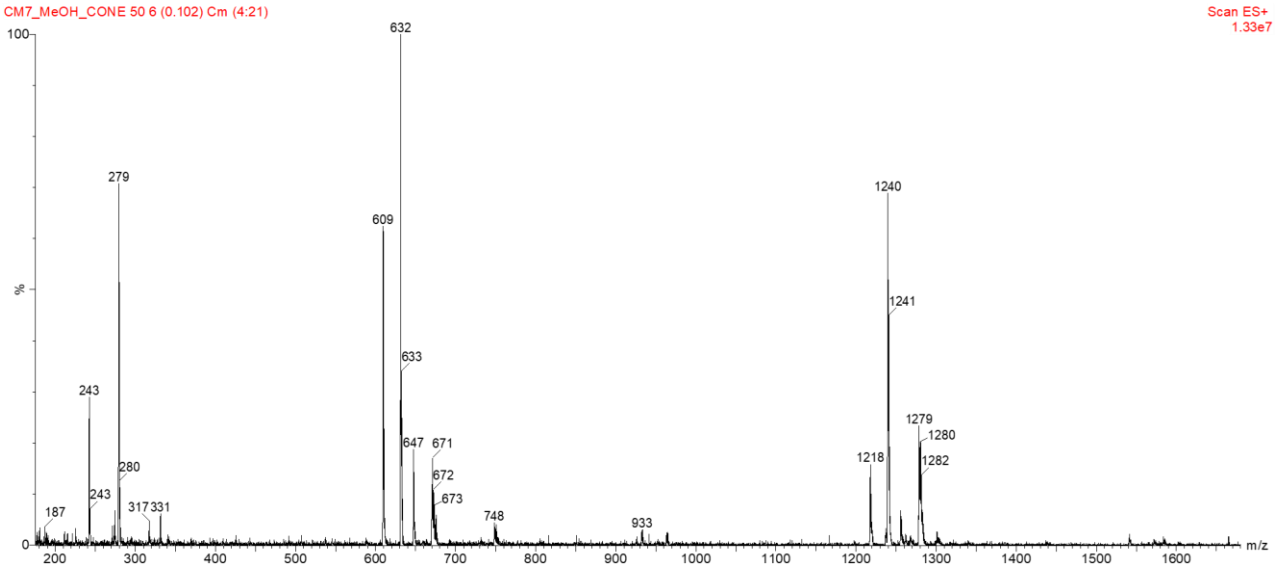

Figure A2.33: ESI-MS spectrum (positive ions) for **CM7** in methanol.

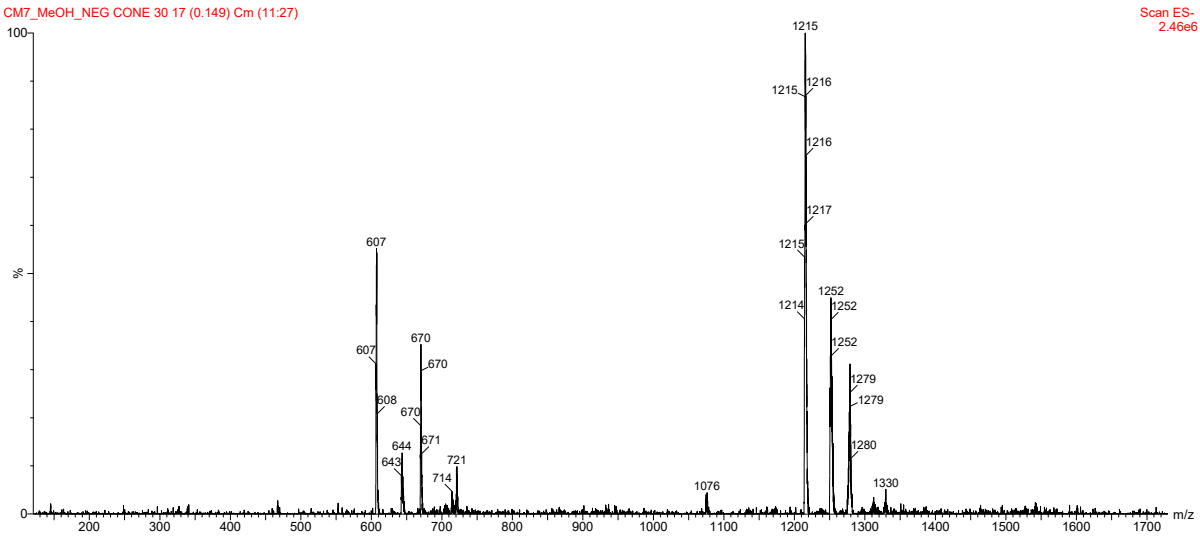

Figure A2.34: ESI-MS spectrum (negative ions) for **CM7** in methanol.

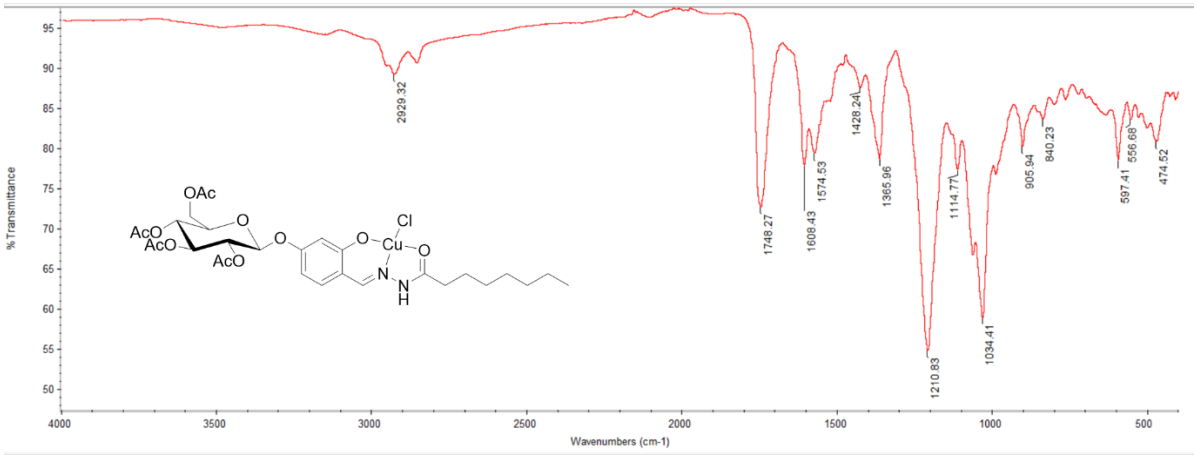

Figure A2.35: FT-IR spectrum of **CM8**.

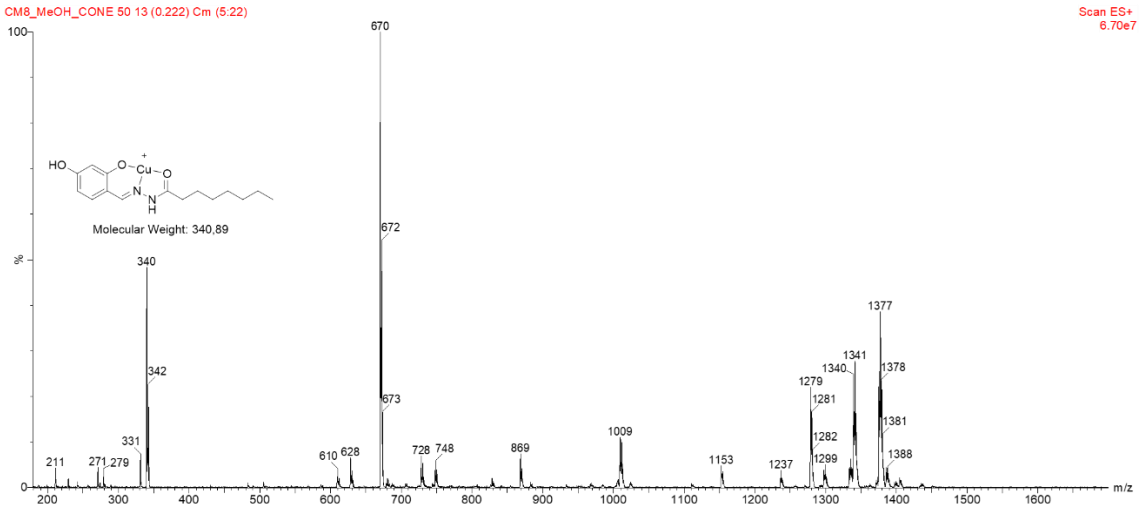

Figure A2.36: ESI-MS spectrum (positive ions) for **CM8** in methanol. The peak at m/z = 340 is associated to the fragment shown in the figure.

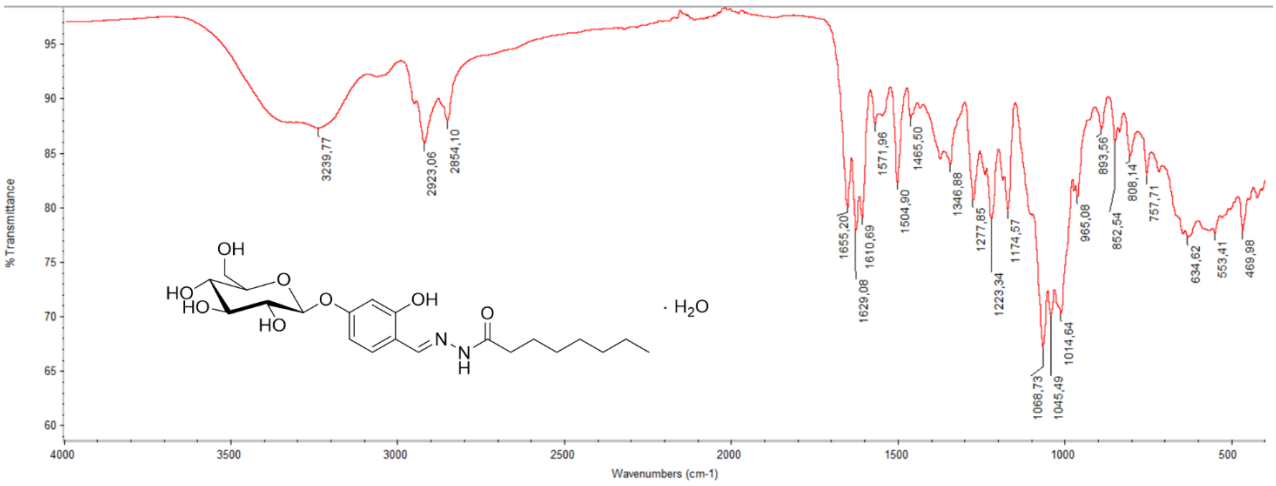

Figure A2.37: FT-IR spectrum of **CM9**.

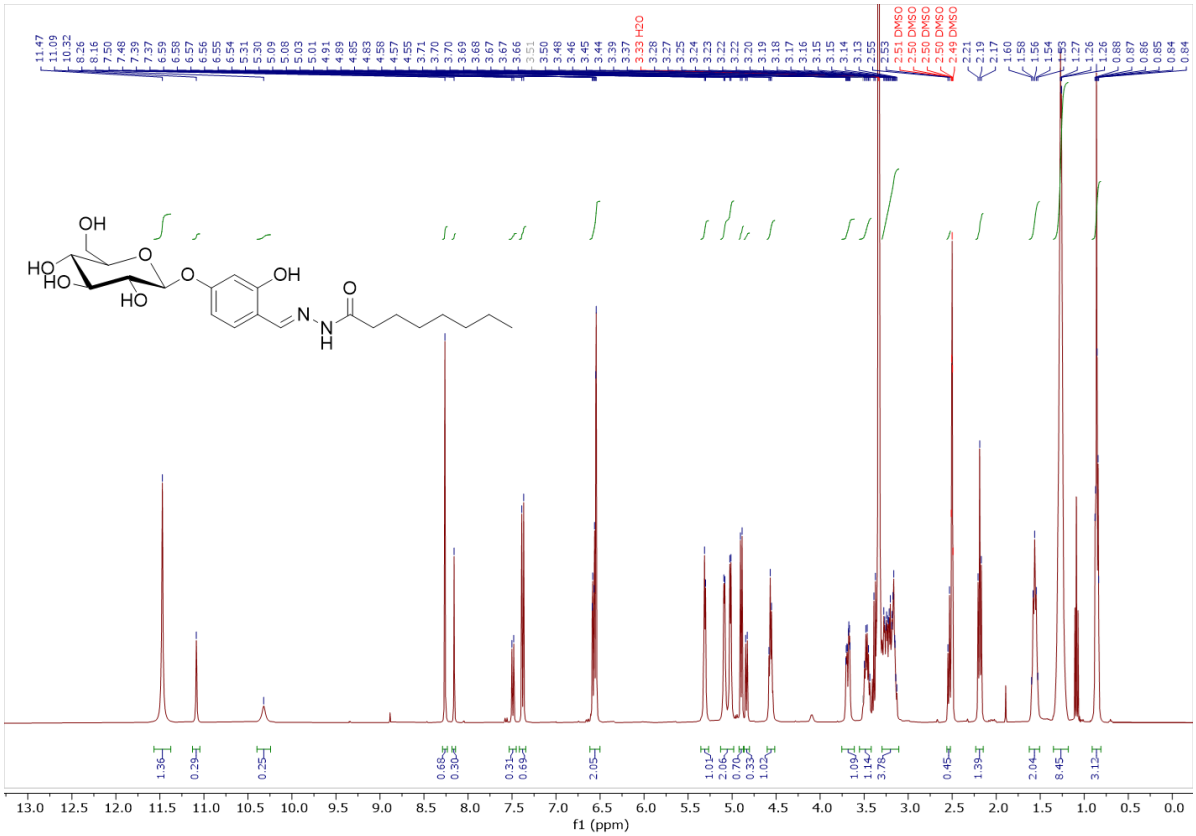

Figure A2.38: ^{1}H NMR (400 MHz, DMSO-d_6, 298 K) spectrum of **CM9**.

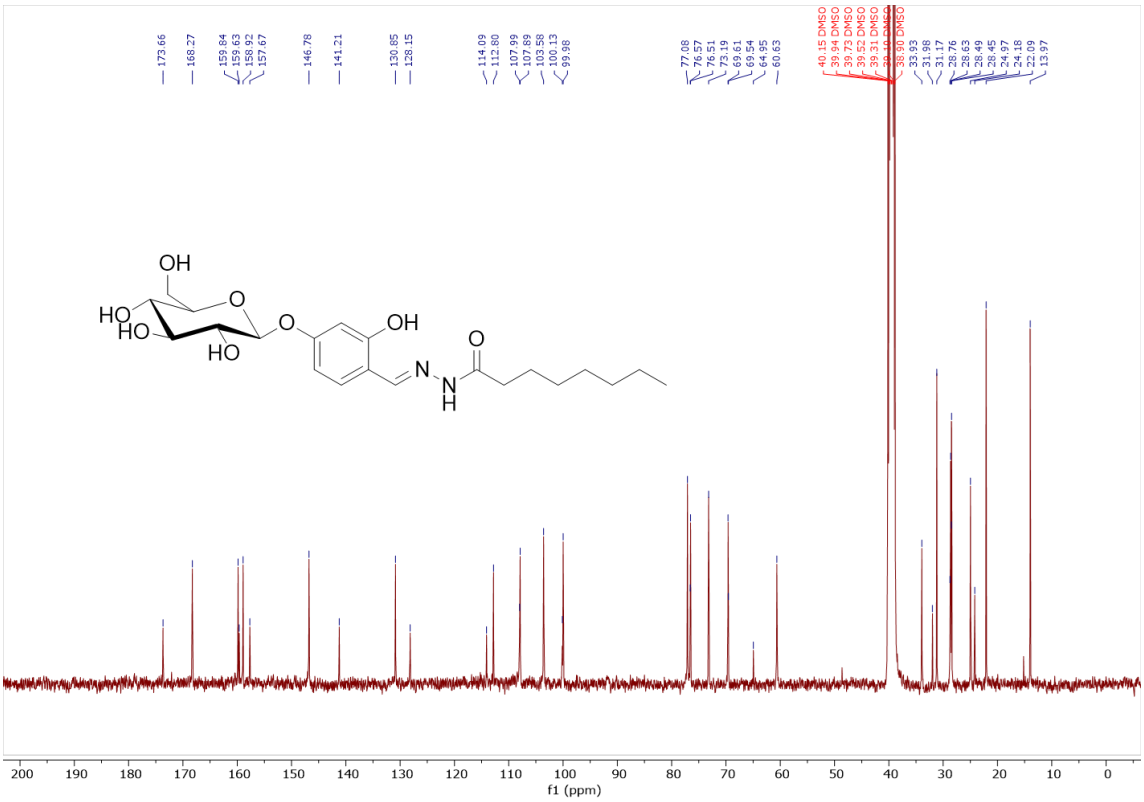

Figure A2.39: ^{13}C NMR (101 MHz, DMSO-d_6, 298 K) spectrum of **CM9**.

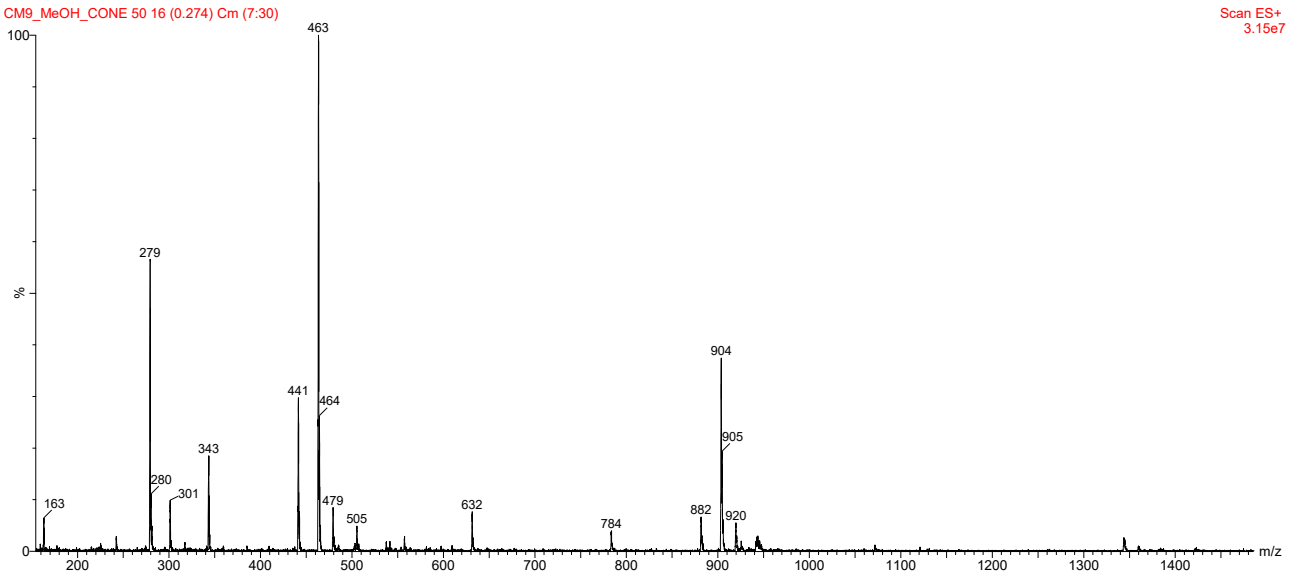

Figure A2.40: ESI-MS spectrum (positive ions) for **CM9** in methanol.

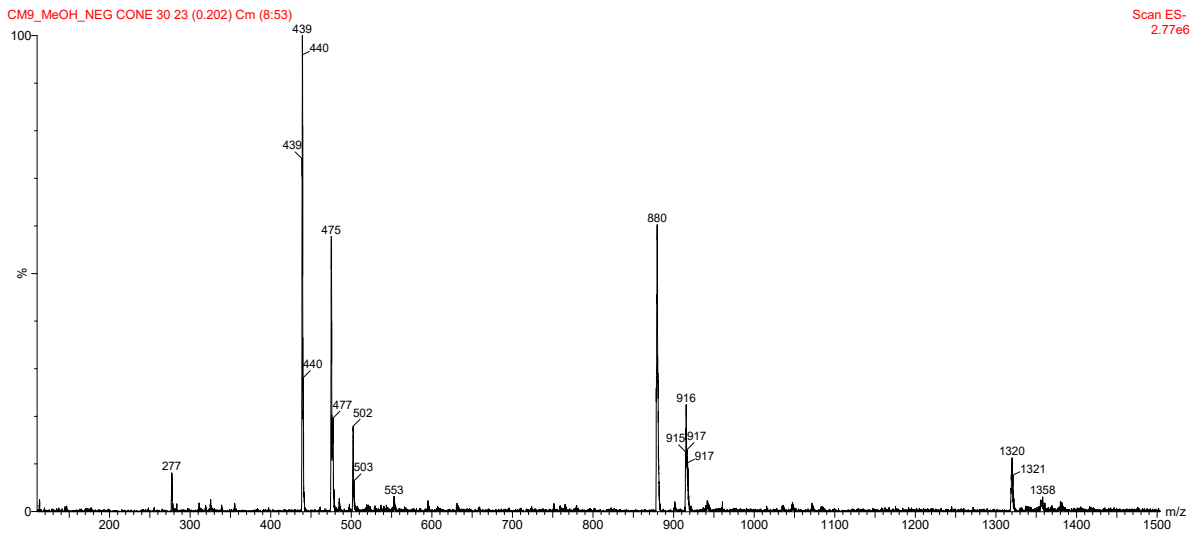

Figure A2.41: ESI-MS spectrum (negative ions) for **CM9** in methanol.

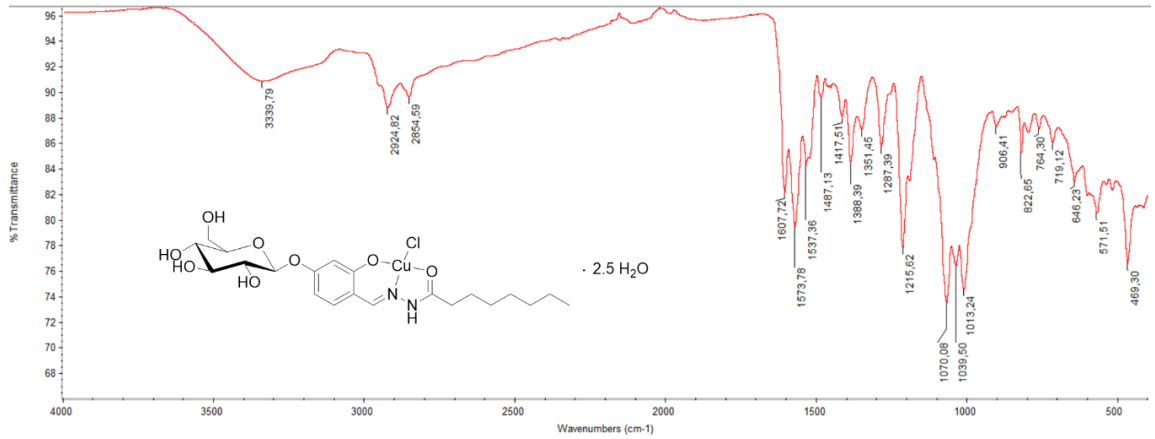

Figure A2.42: FT-IR spectrum of **CM10**.

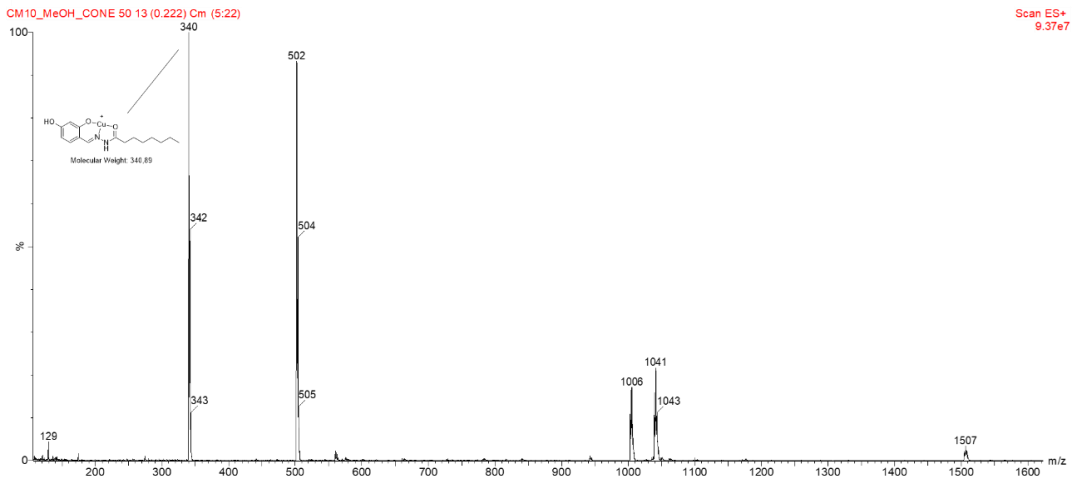

Figure A2.43: ESI-MS spectrum (positive ions) for **CM10** in methanol. The peak at m/z = 340 is associated to the fragment shown in the figure.

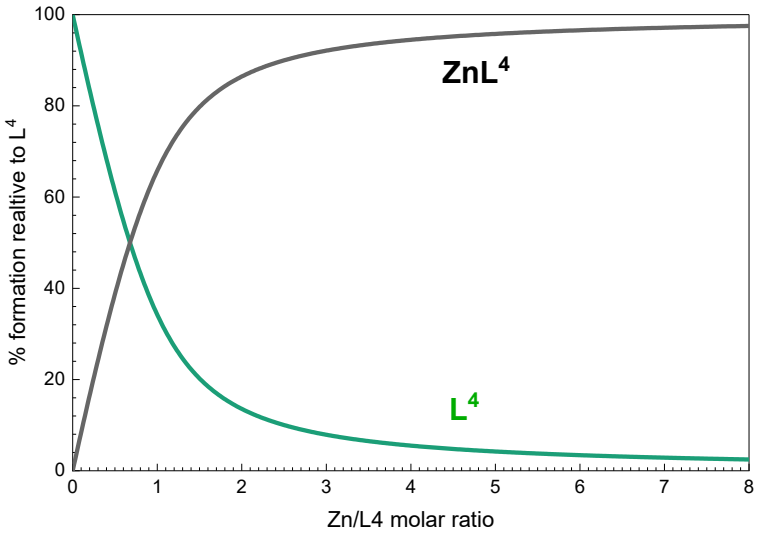

Figure A2.44: Speciation simulation for the Zn:L^4 system. The logβ(ZnL^4) value and the total concentration of ligand in solution were used as fixed parameters.

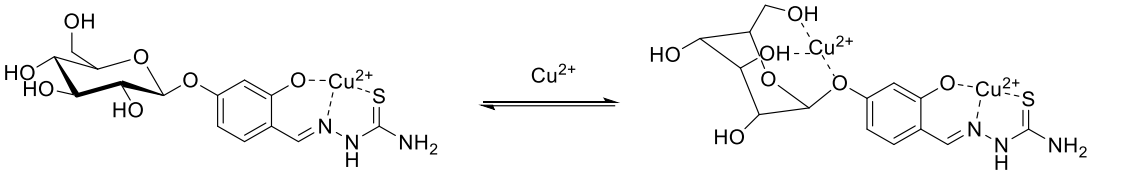

Glucosyl moiety in $^4C_1$ conformation

Hypothetical 2:1 Cu^{II}:ligand species with the glucosyl moiety in $^1C_4$ conformation

Scheme A2.1: Formation of the hypothetical 2:1 Cu^{II}:L^2 complex.

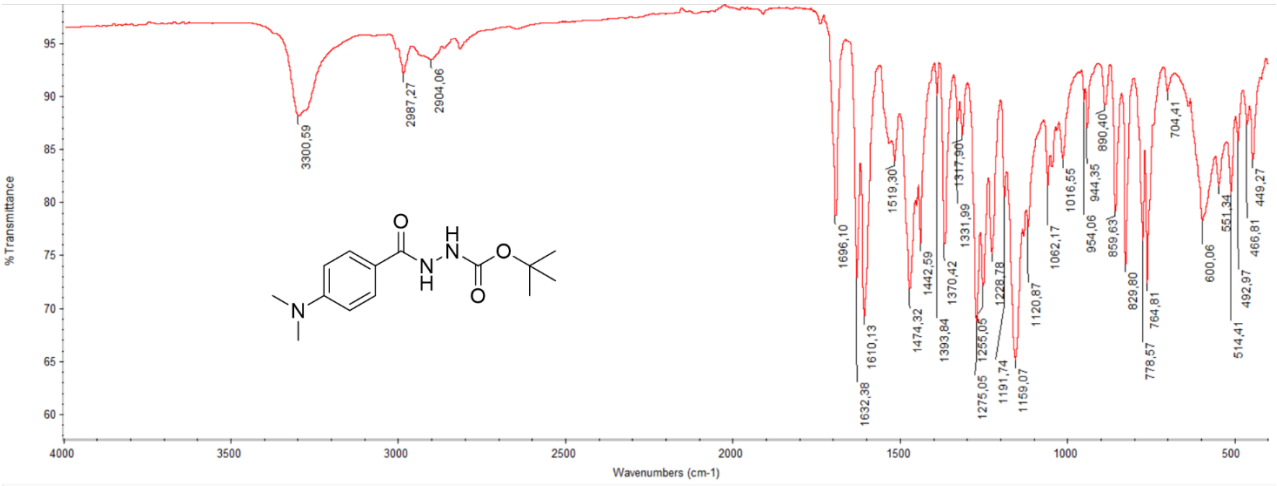

Figure A3.1: FT-IR spectrum of **AZM1b**.

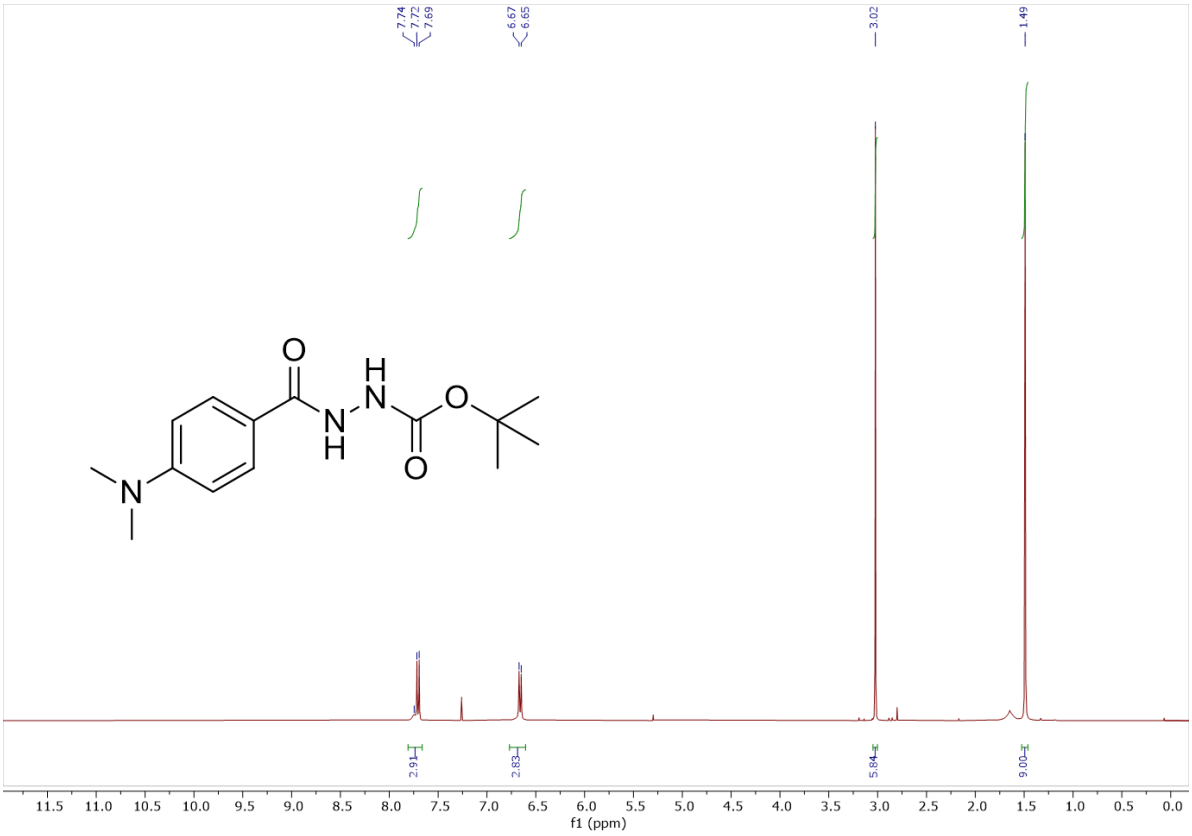

Figure A3.2: ^{1}H NMR (500 MHz, Chloroform-*d,* 298 K) spectrum of **AZM1b**.

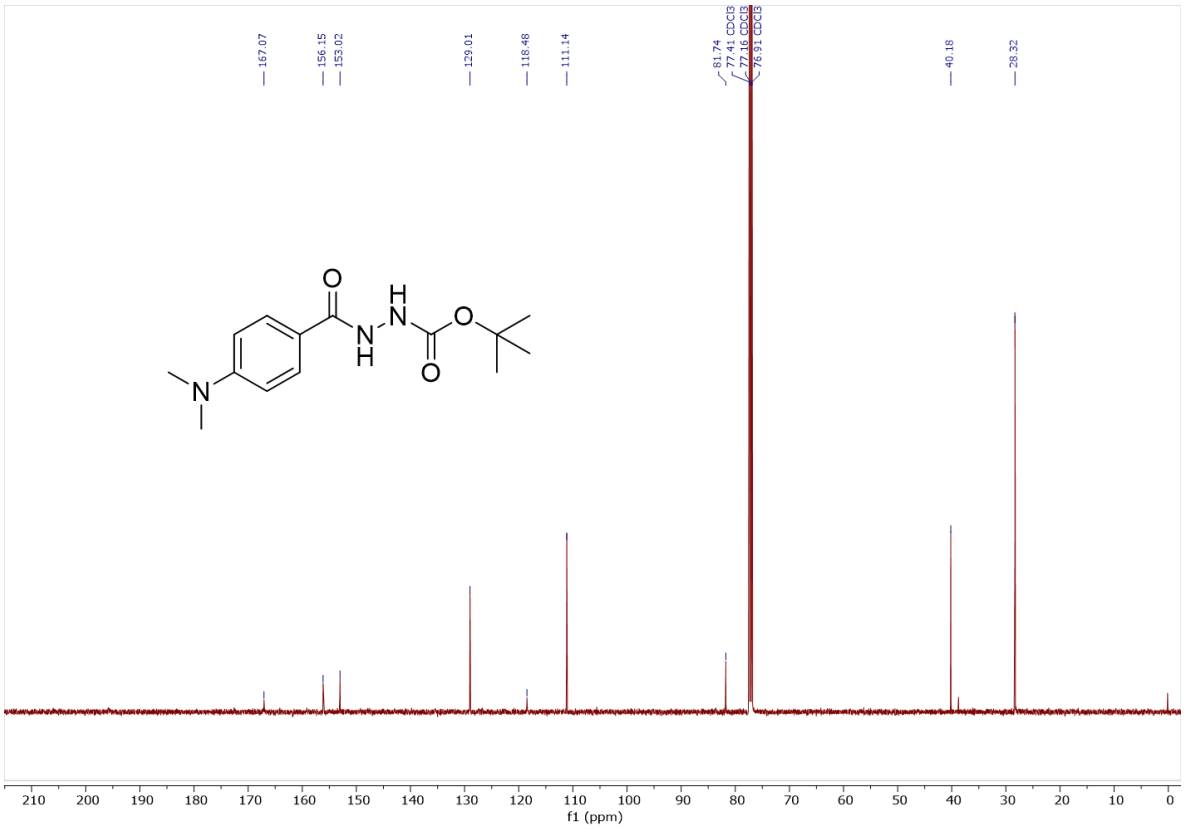

Figure A3.3: ^{13}C NMR (126 MHz, Chloroform-*d*, 298 K) spectrum of **AZM1b**.

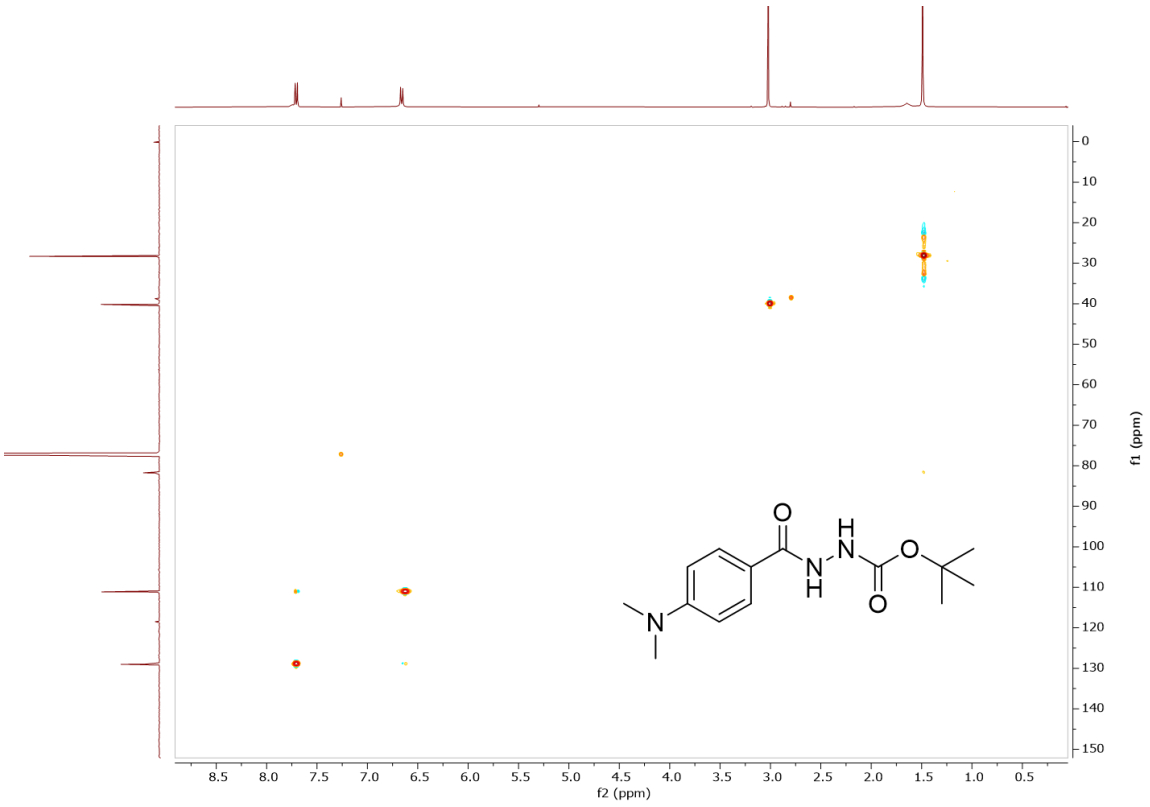

Figure A3.4: 2D ^{1}H-^{13}C HSQC spectrum of **AZM1b** at 298 K in Chloroform-*d*.

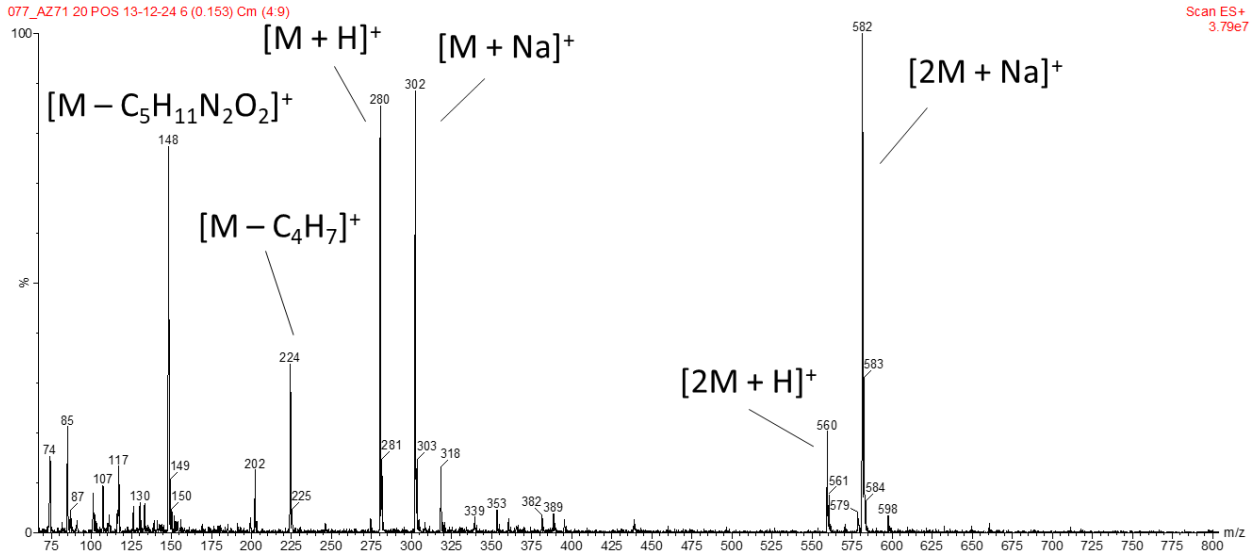

Figure A3.5: ESI-MS spectrum (positive ions) for **AZM1b** in methanol.

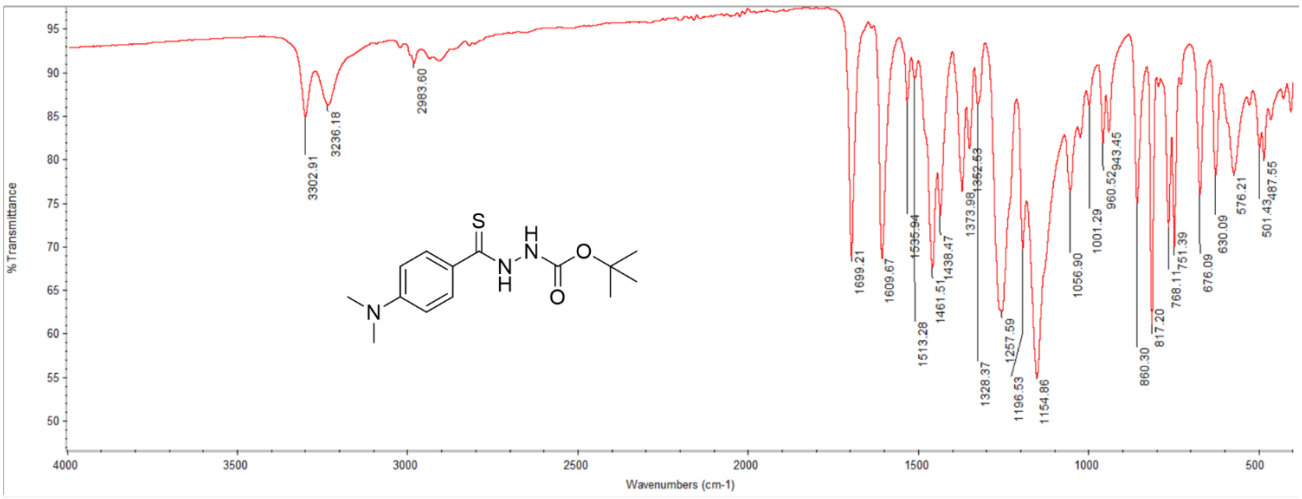

Figure A3.6: FT-IR spectrum of **AZM2c**.

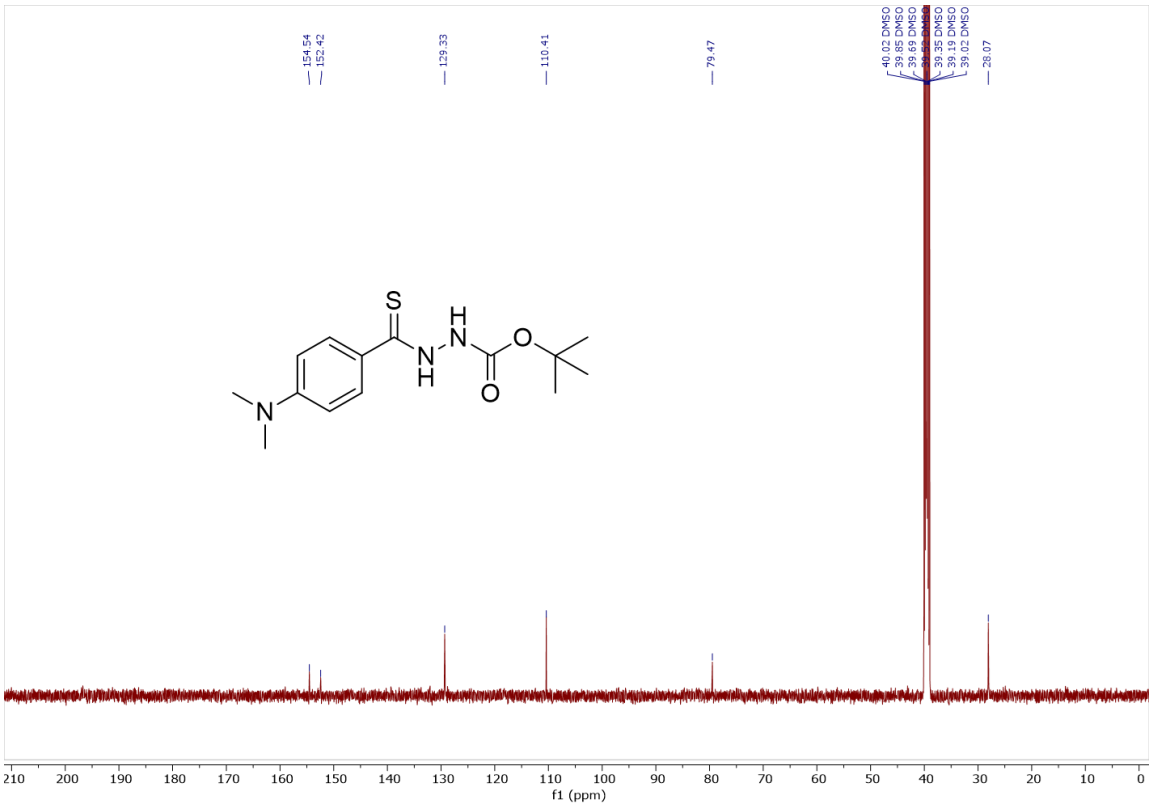

Figure A3.7: ^{13}C NMR (126 MHz, DMSO-d_6, 298 K) spectrum of **AZM2c**. The signal of methyl carbons of NMe_2 group is masked by the peaks of DMSO. There is the lack of two signals for quaternary carbons, probably due to insufficient concentration of the sample.

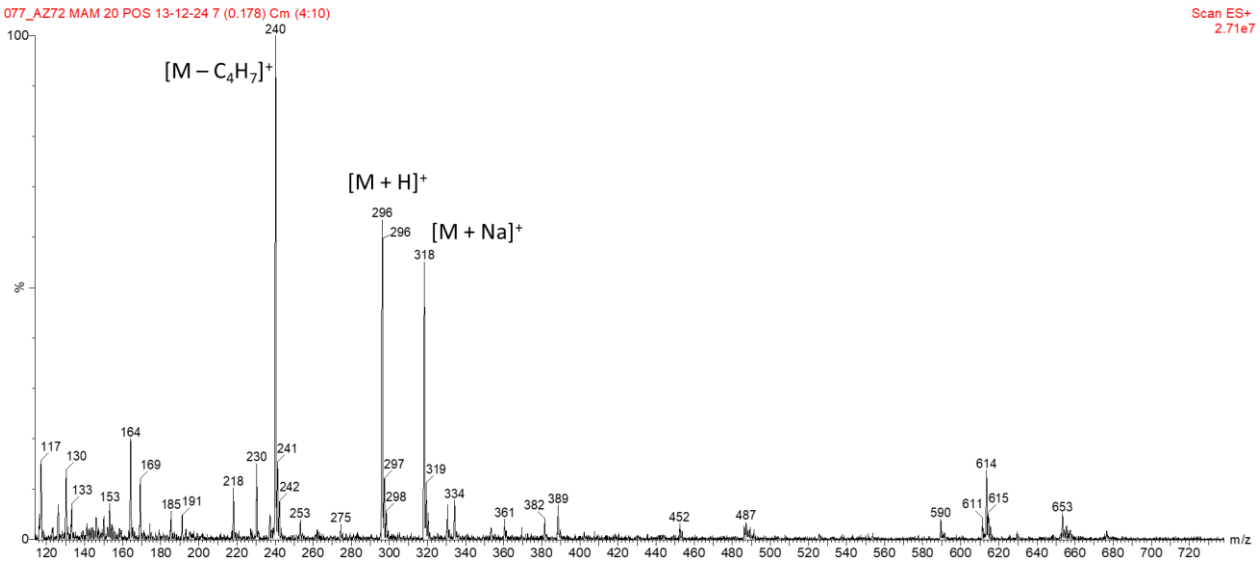

Figure A3.8: ESI-MS spectrum (positive ions) for **AZM2c** in methanol.

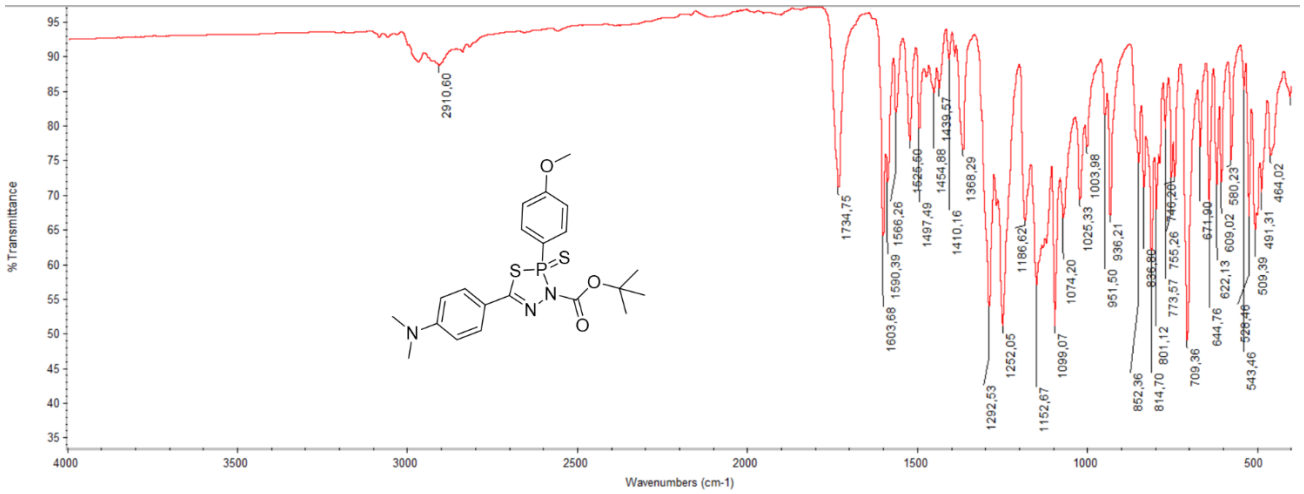

Figure A3.9: FT-IR spectrum of the side-product of the synthesis of **AZM2c**.

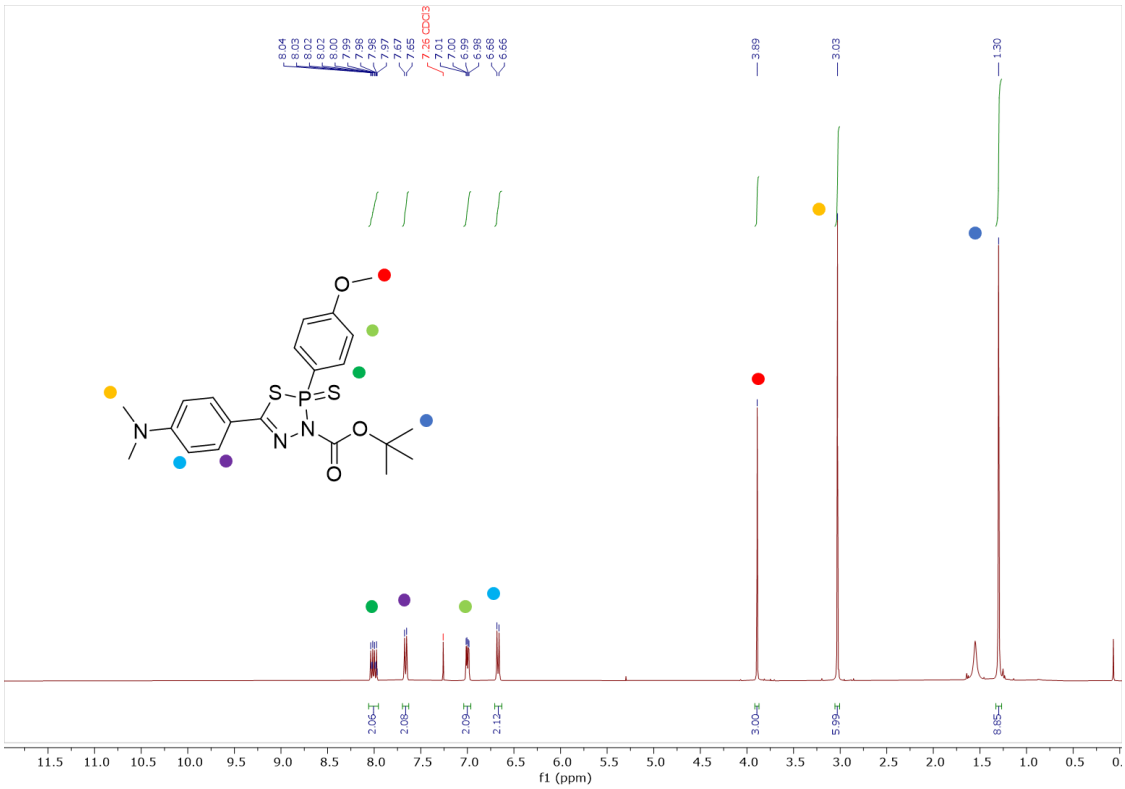

Figure A3.10: ^{1}H NMR (500 MHz, Chloroform-*d,* 298 K) spectrum of the side-product of the synthesis of **AZM2c**.

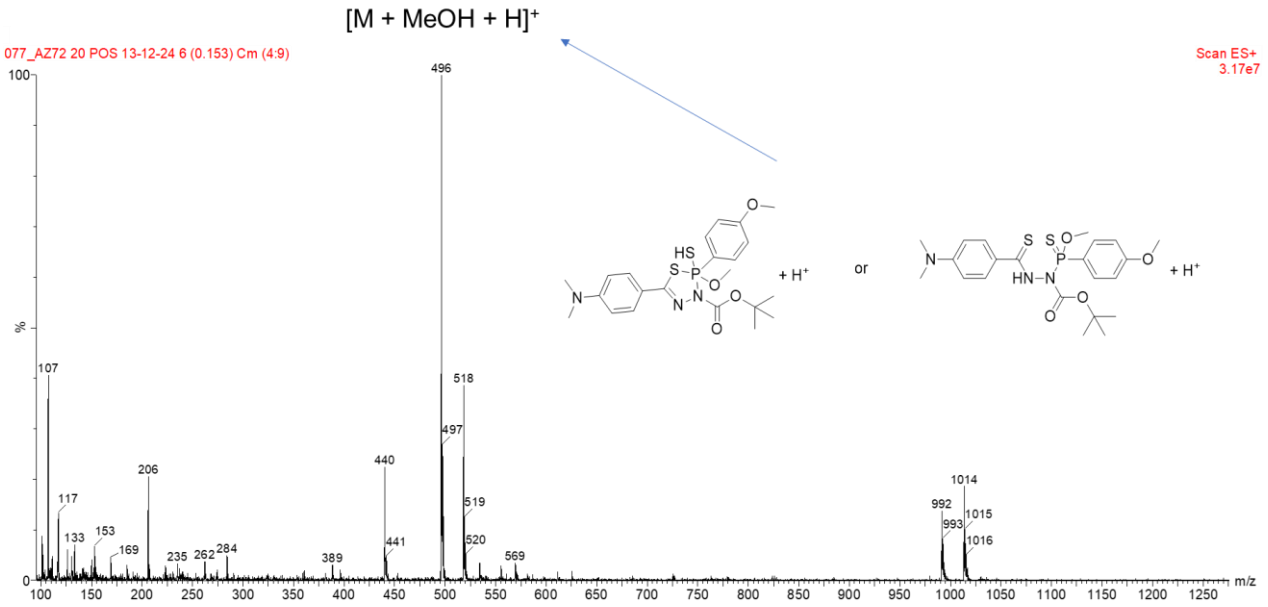

Figure A3.11: ESI-MS spectrum (positive ions) for the side-product of the synthesis of **AZM2c** in methanol.

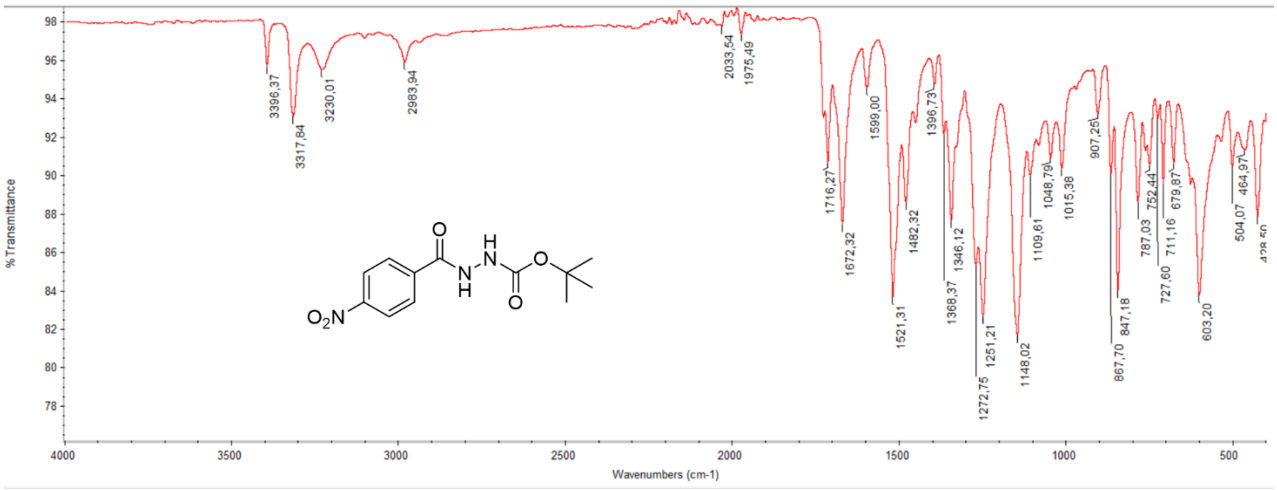

Figure A3.12: FT-IR spectrum of **AZM3**.

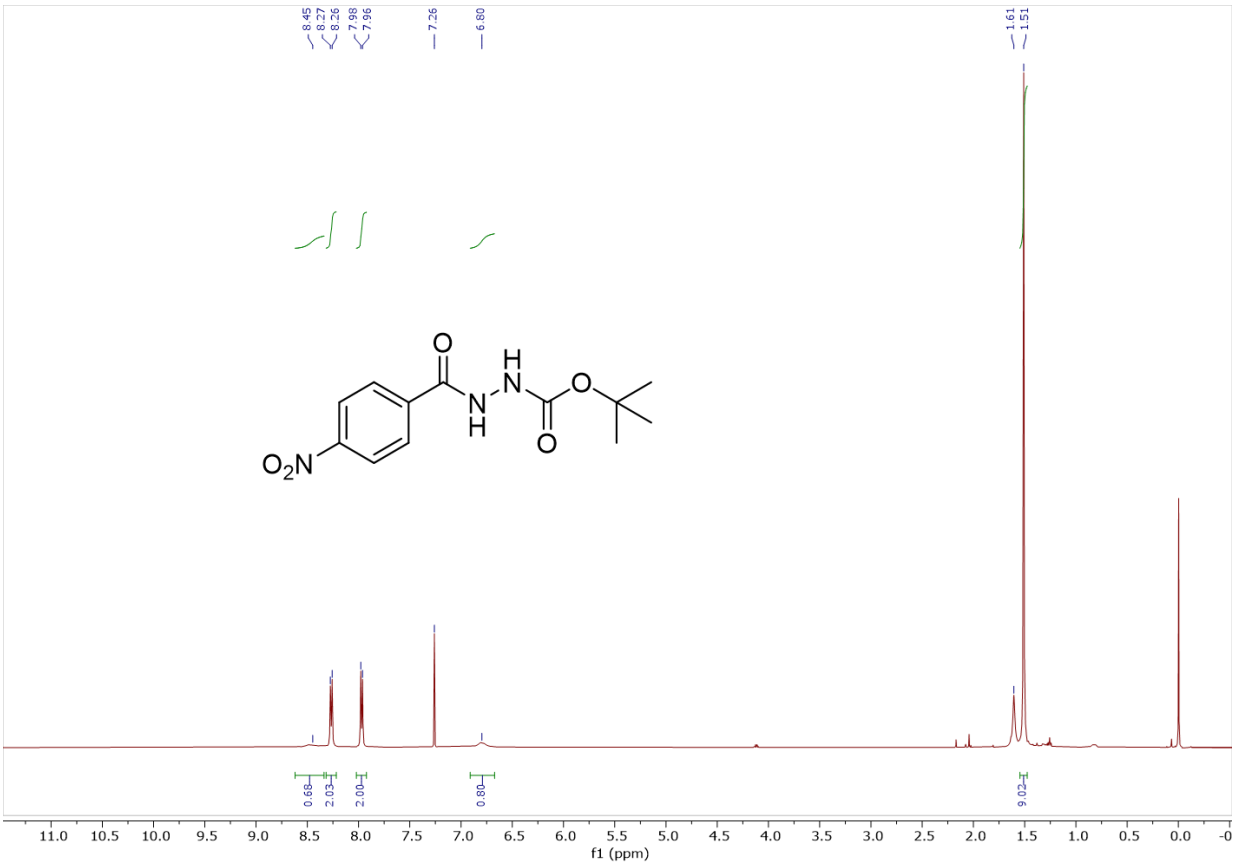

Figure A3.13: ^{1}H NMR (500 MHz, Chloroform-*d,* 298 K) spectrum of **AZM3**.

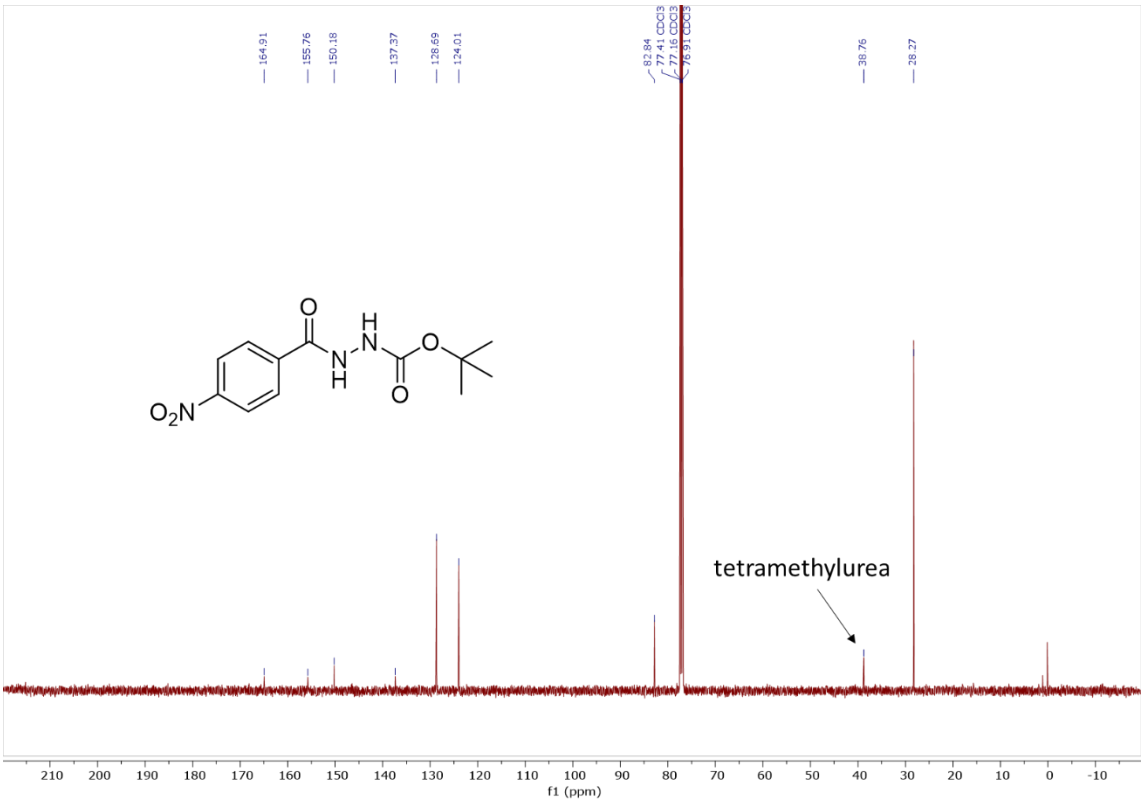

Figure A3.14: ^{13}C NMR (126 MHz, Chloroform-*d*, 298 K) spectrum of **AZM3**.

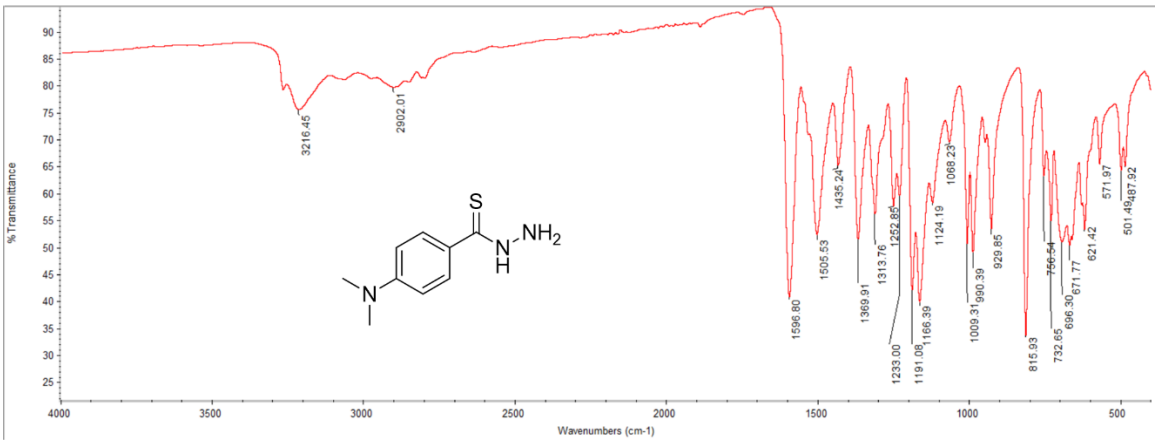

Figure A3.15: FT-IR spectrum of **AZM4c**.

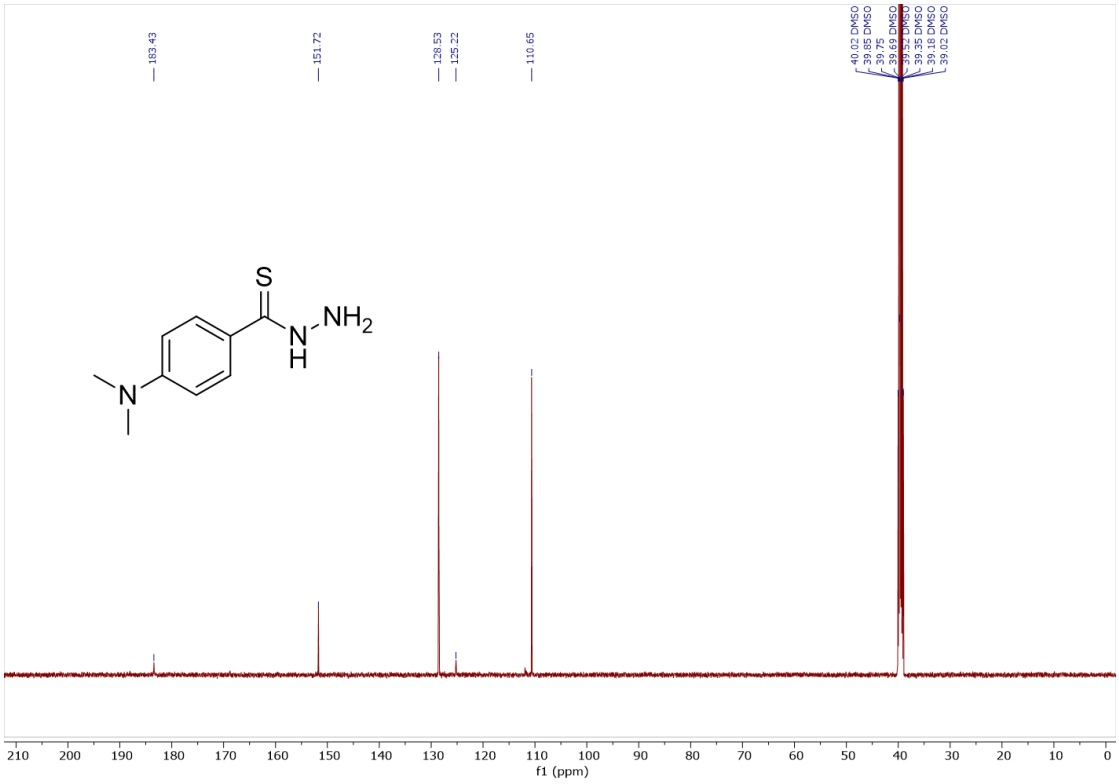

Figure A3.16: ^{13}C NMR (126 MHz, 298 K) spectrum of **AZM4c** in DMSO-d_6. The signal of methyl carbons of NMe_2 group is masked by the peaks of DMSO.

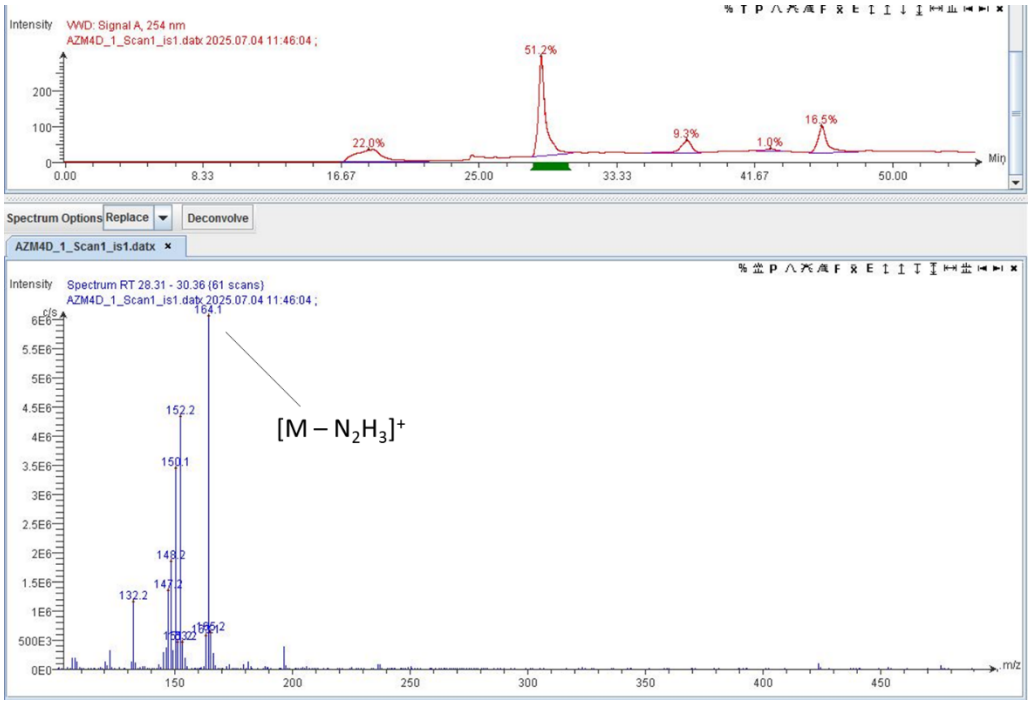

Figure A3.17: LC-MS (carrier solvent: MeCN with 0.1 % formic acid; positive ions) spectrum of **AZM4c**. Mass spectrum for the chromatographic peak of the product.

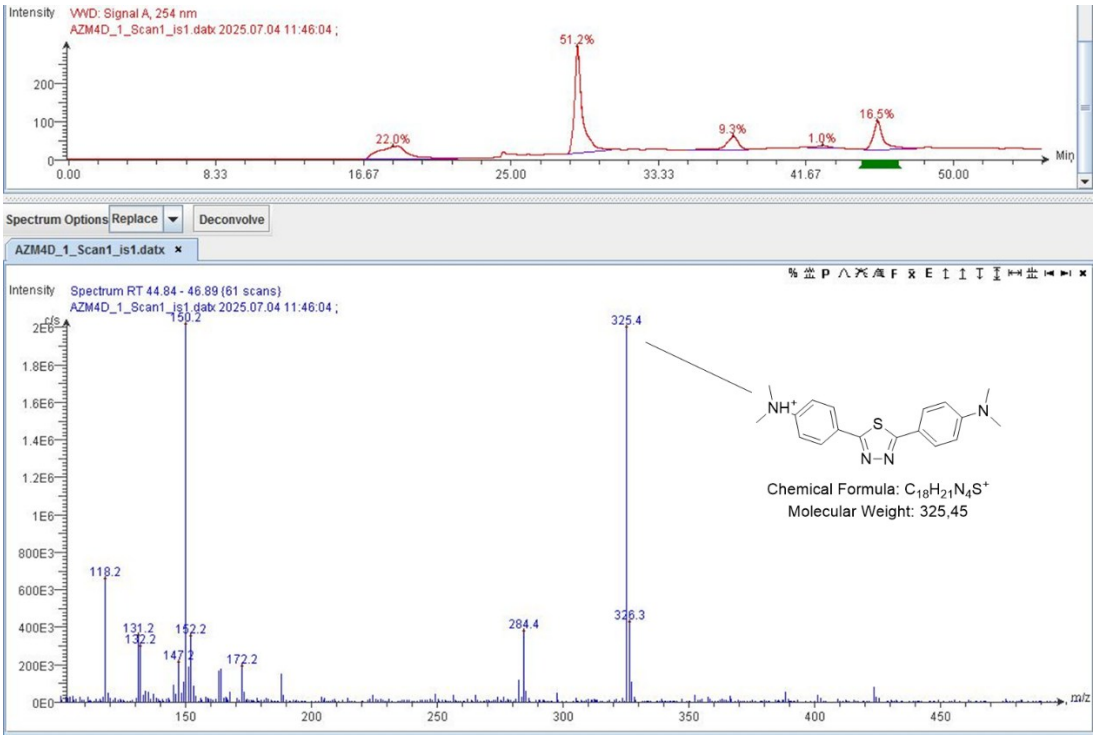

Figure A3.18: LC-MS (carrier solvent: MeCN with 0.1 % formic acid; positive ions) spectrum of **AZM4c**. Mass spectrum for the chromatographic peak of the side-product.

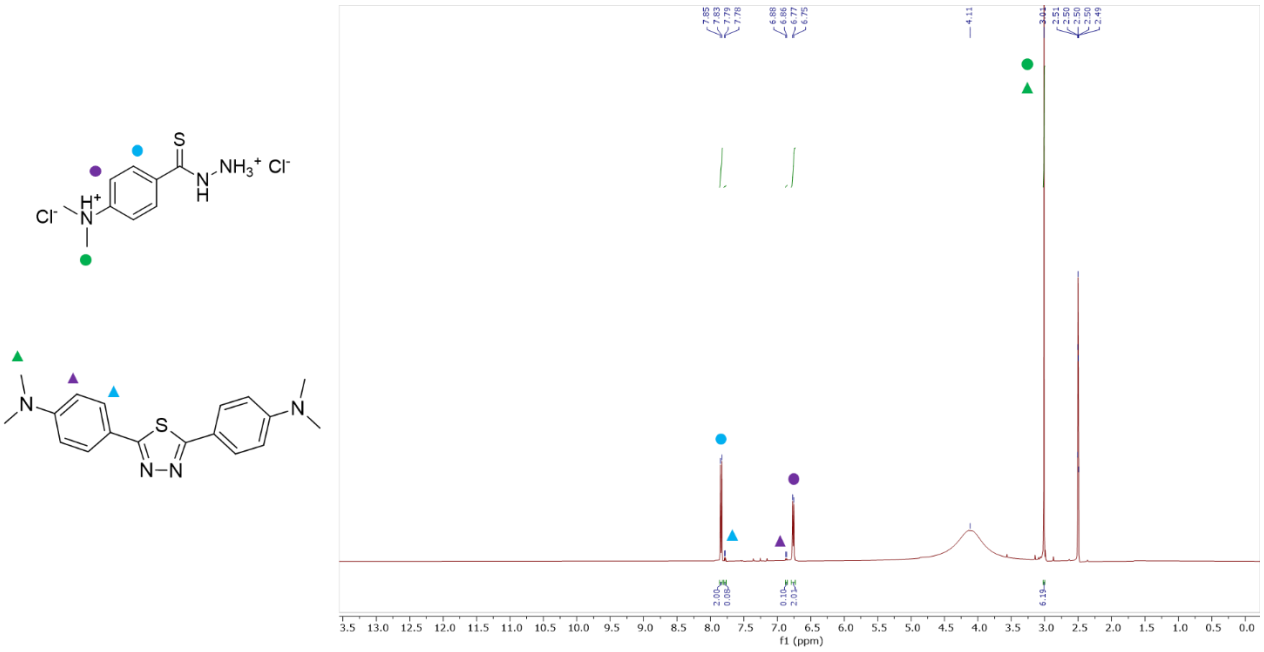

Figure A3.19: ^{1}H NMR (500 MHz, 298 K) spectrum of **AZM4_hydrochloride** in DMSO-d_6. The chemical structures of 4-(dimethylamino)benzothiohydrazide bis-hydrochloride (top) and the 1,3,4-thiadiazolic side-product (bottom) are shown on the left. It is not known the exact protonation state of the latter.

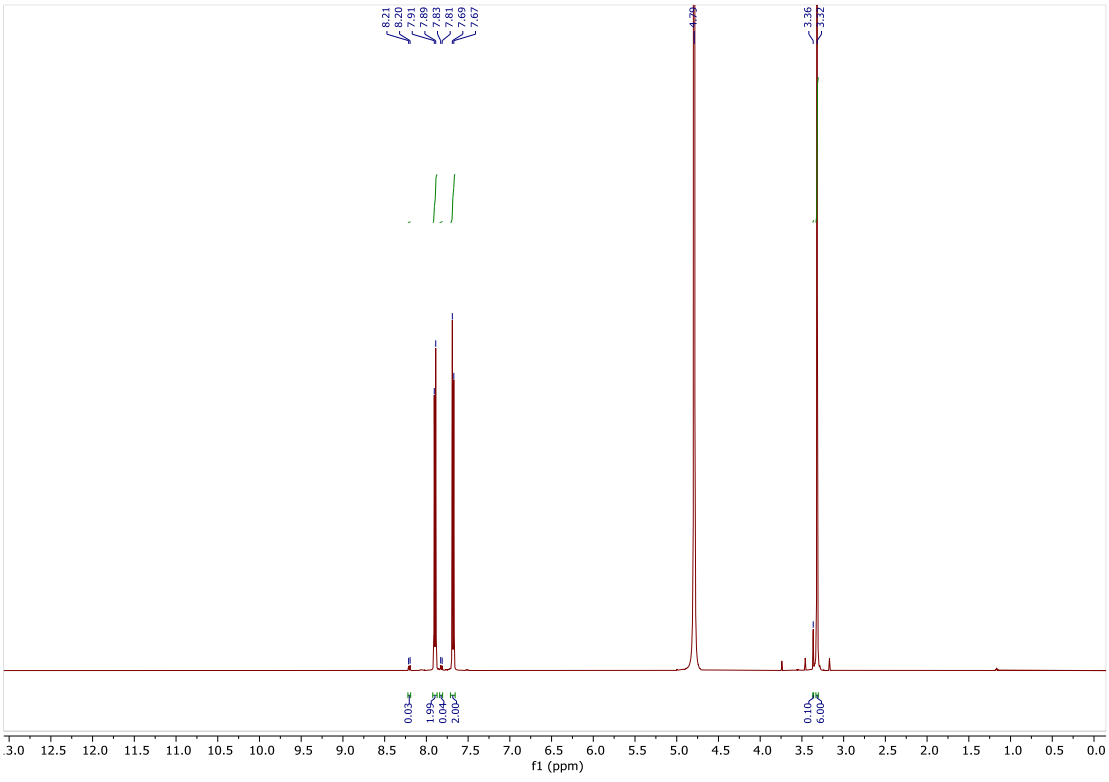

Figure A3.20: ^{1}H NMR (500 MHz, 298 K) spectrum of **AZM4_hydrochloride** in D_2O.

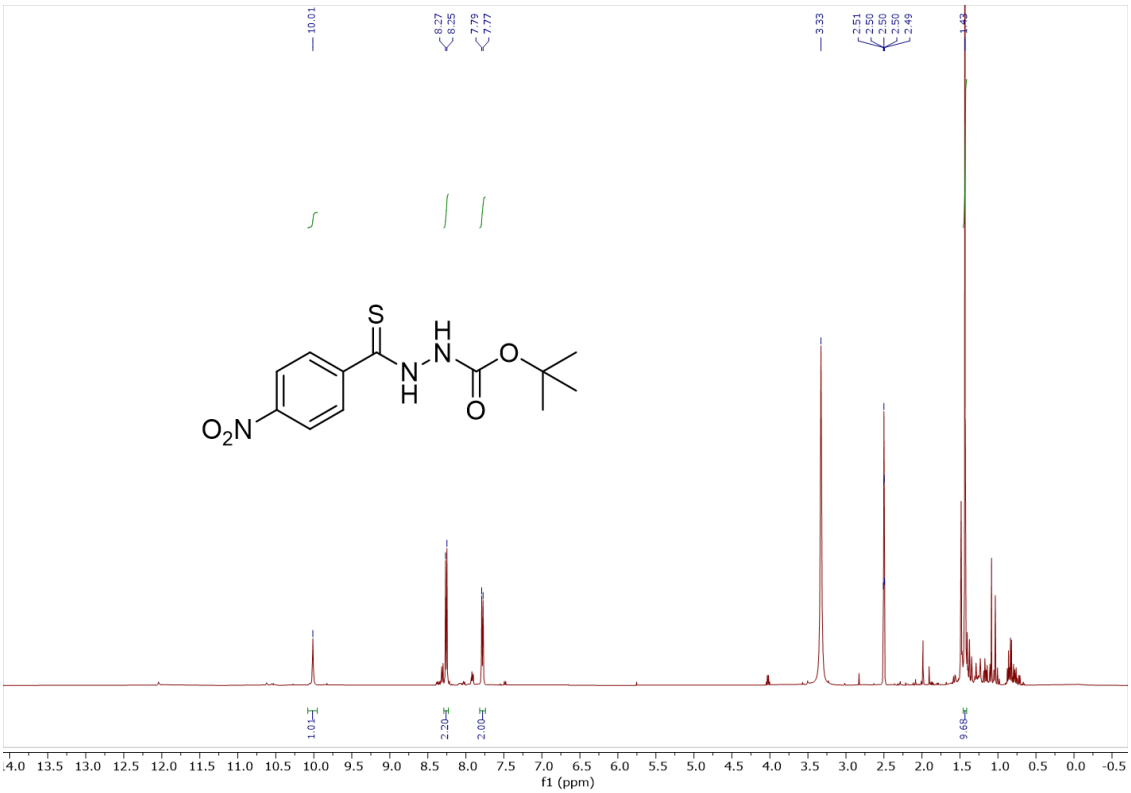

Figure A3.21: ^{1}H NMR (500 MHz, 298 K) spectrum of **AZM5a** in DMSO-d_6. The absence of the signal of one of the two NH protons is probably ascribable to the existence of the thiolene tautomer in solution: due to the highly acidic character of the resulting N=C-SH group, exchange with H_2O would be responsible for the disappearance of the peak in the spectrum.

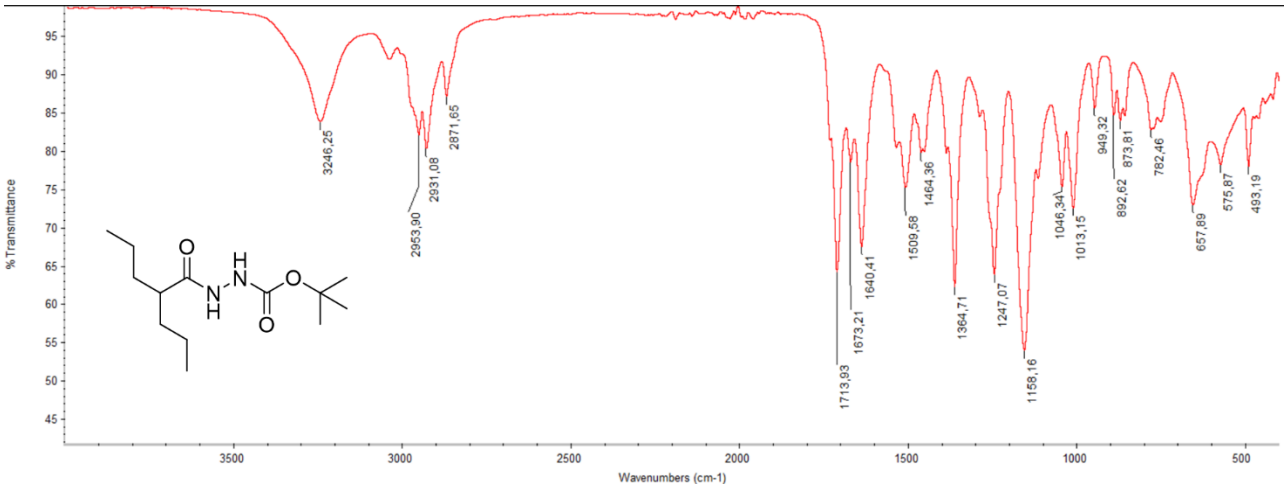

Figure A3.22: FT-IR spectrum of **AZM6**.

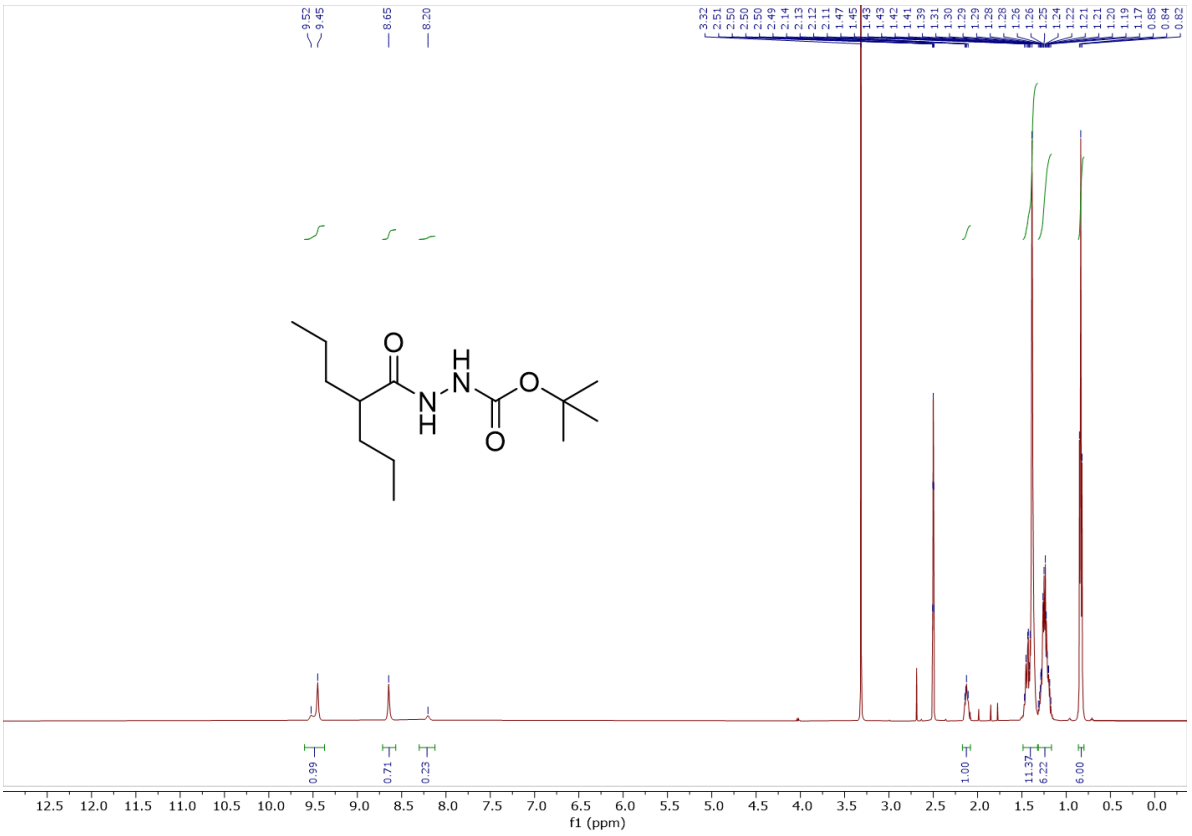

Figure A3.23: ^{1}H NMR (500 MHz, 298 K) spectrum of **AZM6** in DMSO-d_6.

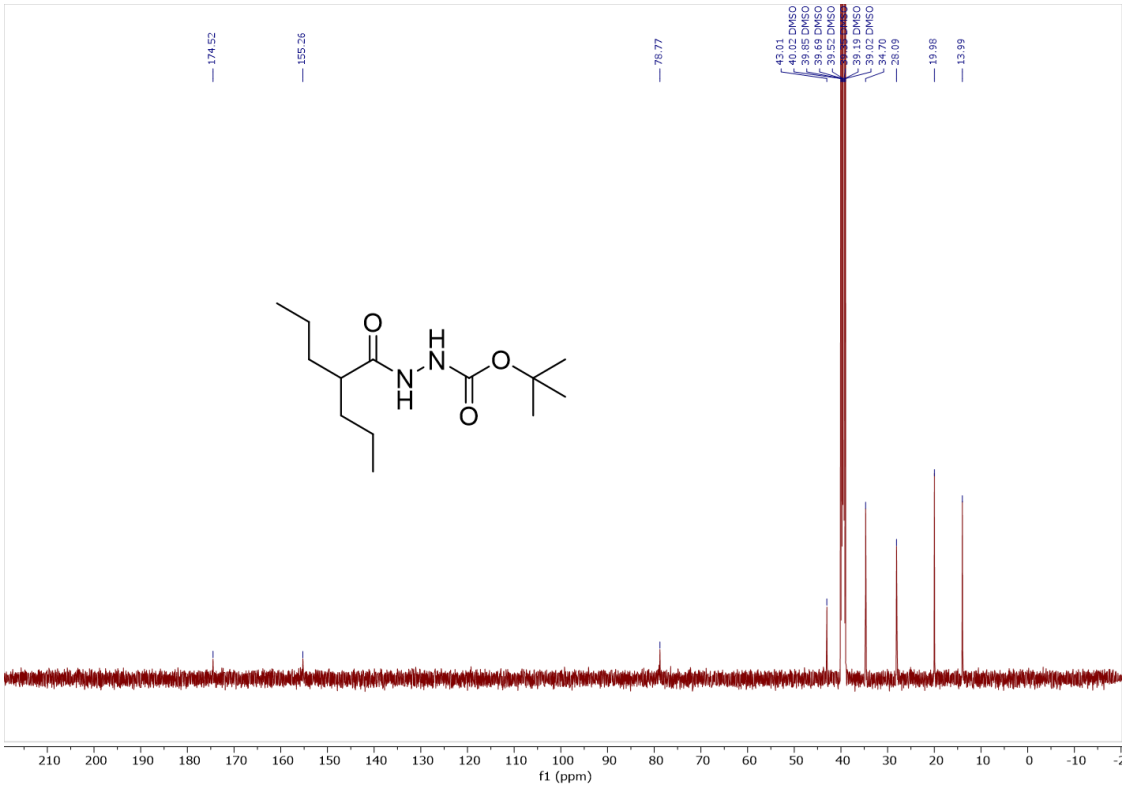

Figure A3.24: ^{13}C NMR (126 MHz, 298 K) spectrum of **AZM6** in DMSO-d_6.

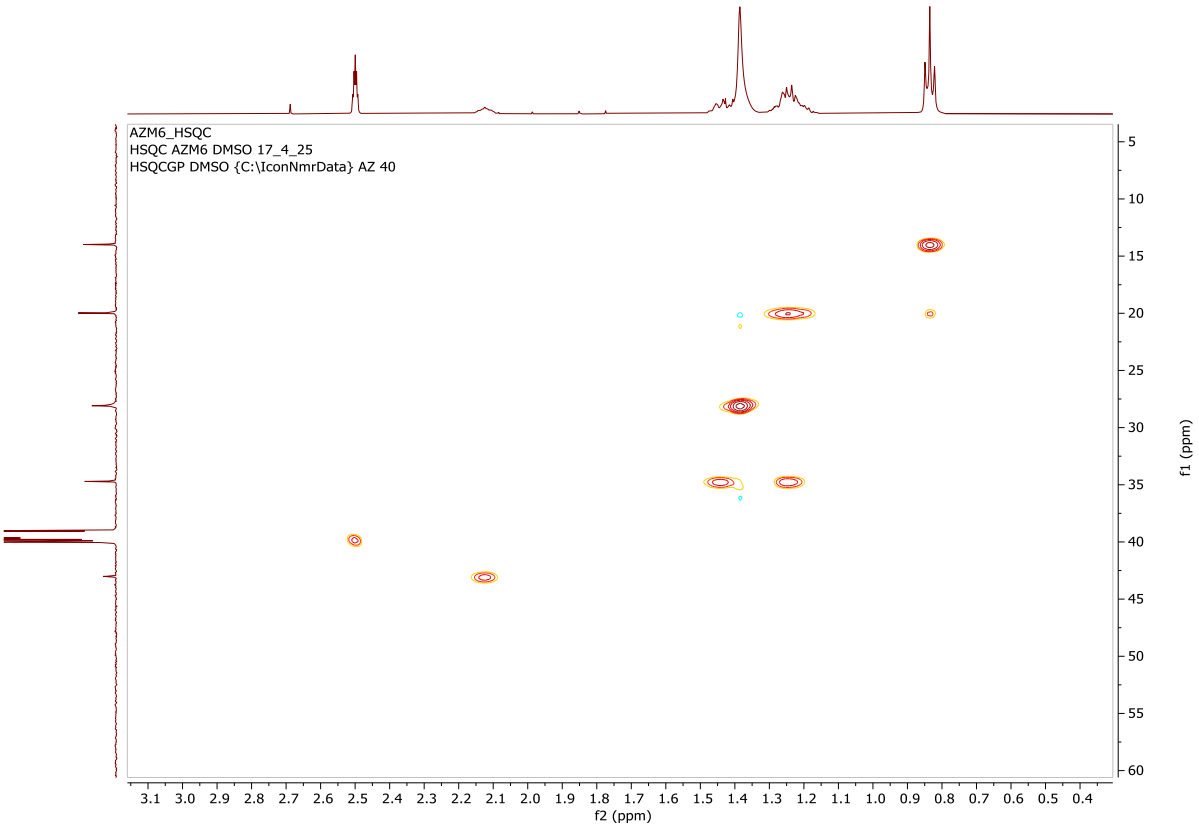

Figure A3.25: 2D ^{1}H-^{13}C HSQC spectrum of **AZM6** at 298 K in DMSO-d_6.

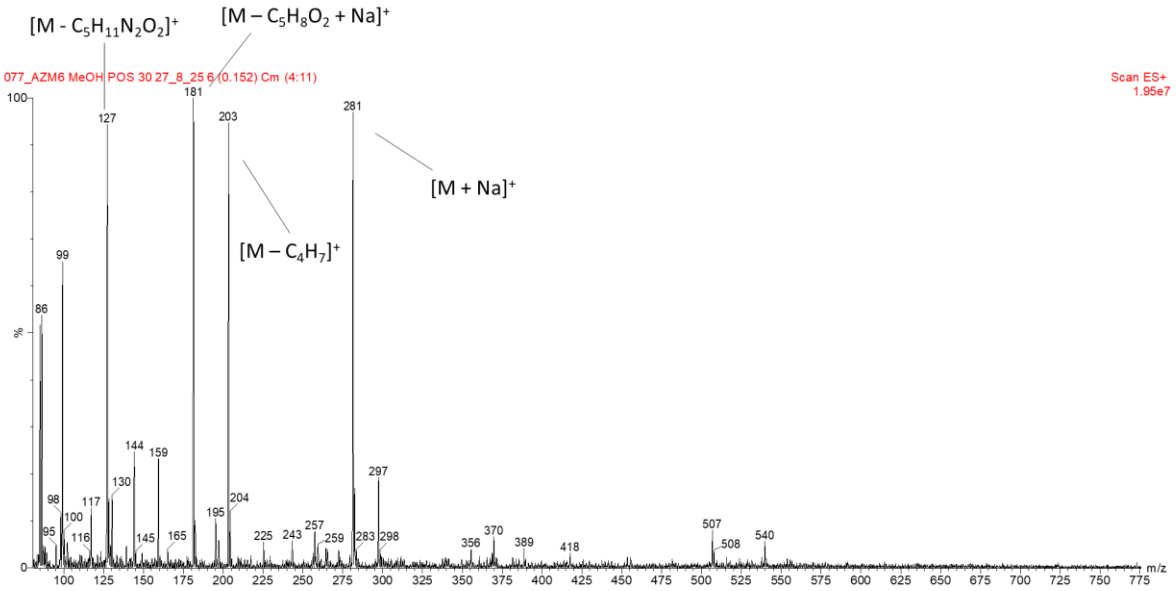

Figure A3.26: ESI-MS spectrum (positive ions) for **AZM6** in methanol.

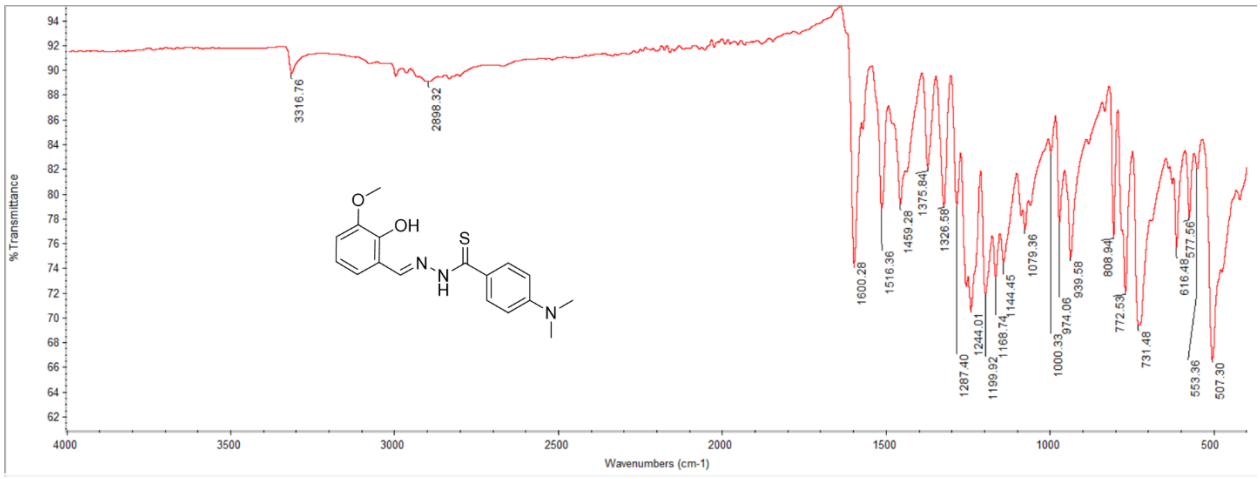

Figure A3.27: FT-IR spectrum of **AZM8a**.

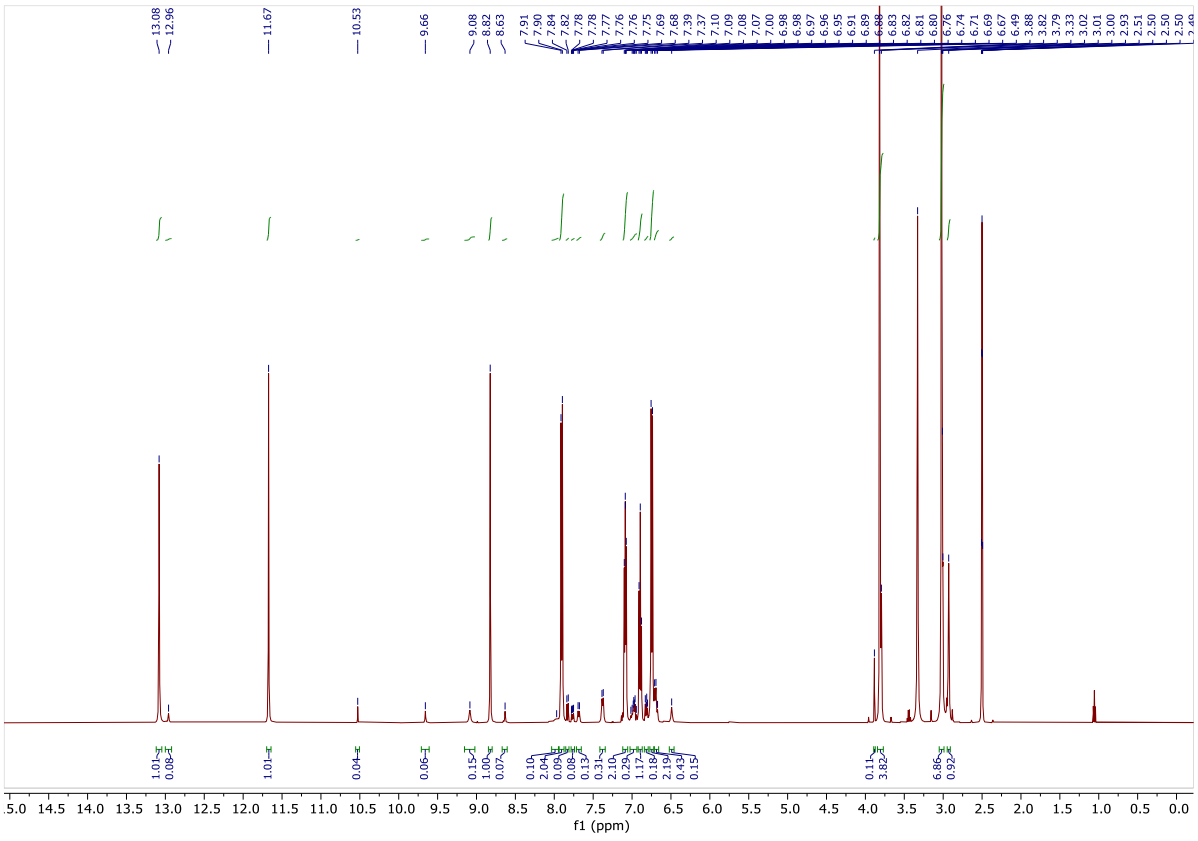

Figure A3.28: ^{1}H NMR (500 MHz, 298 K) spectrum of **AZM8a** in DMSO-d_6.

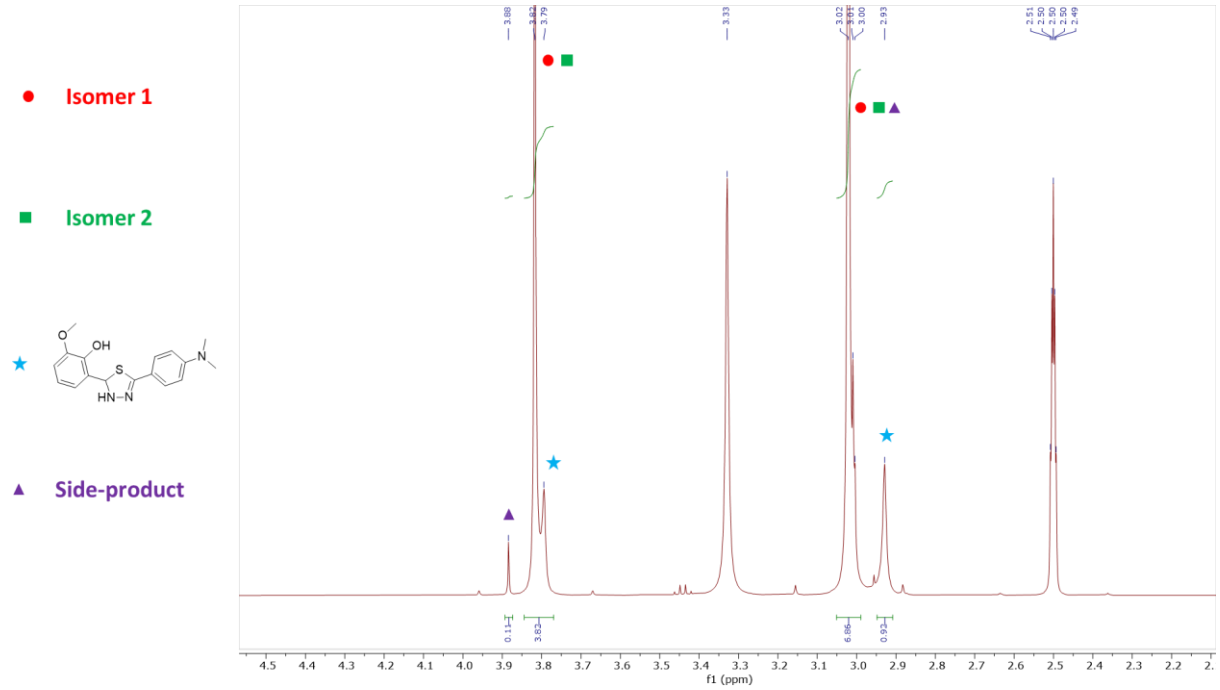

Figure A3.29: Selected range of the ^{1}H NMR (500 MHz, 298 K) spectrum of **AZM8a** in DMSO-d_6.

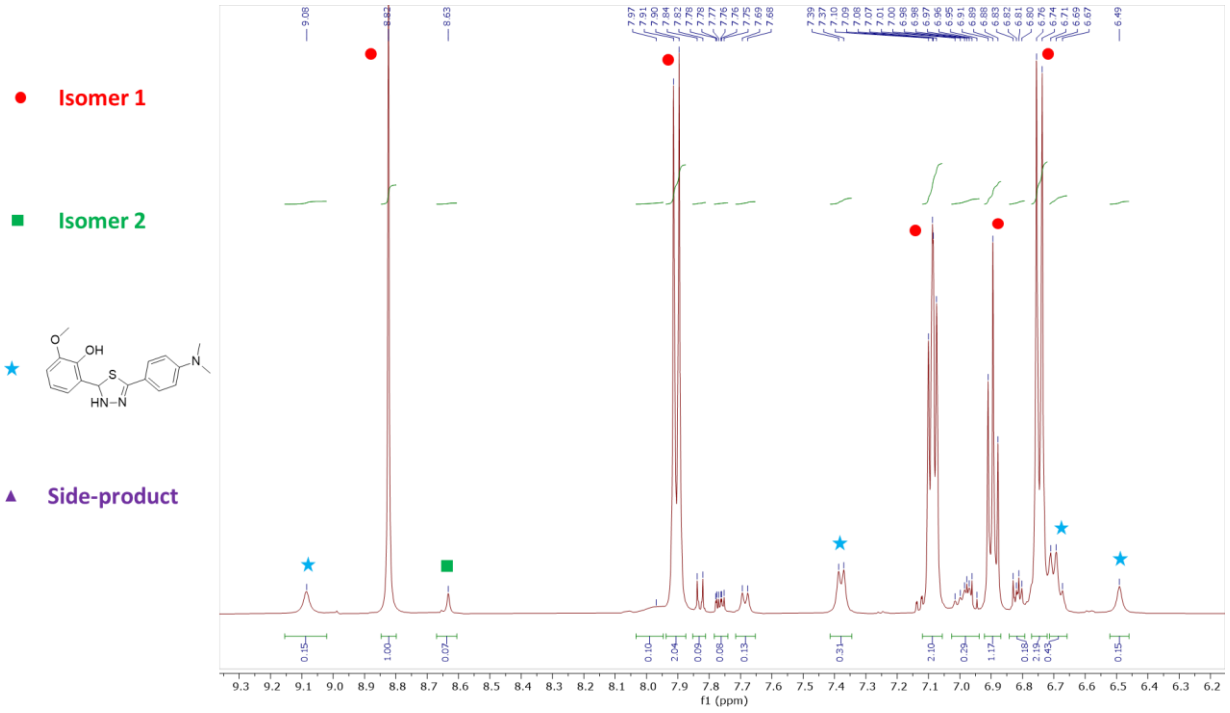

Figure A3.30: Selected range of the ^{1}H NMR (500 MHz, 298 K) spectrum of **AZM8a** in DMSO-d_6.

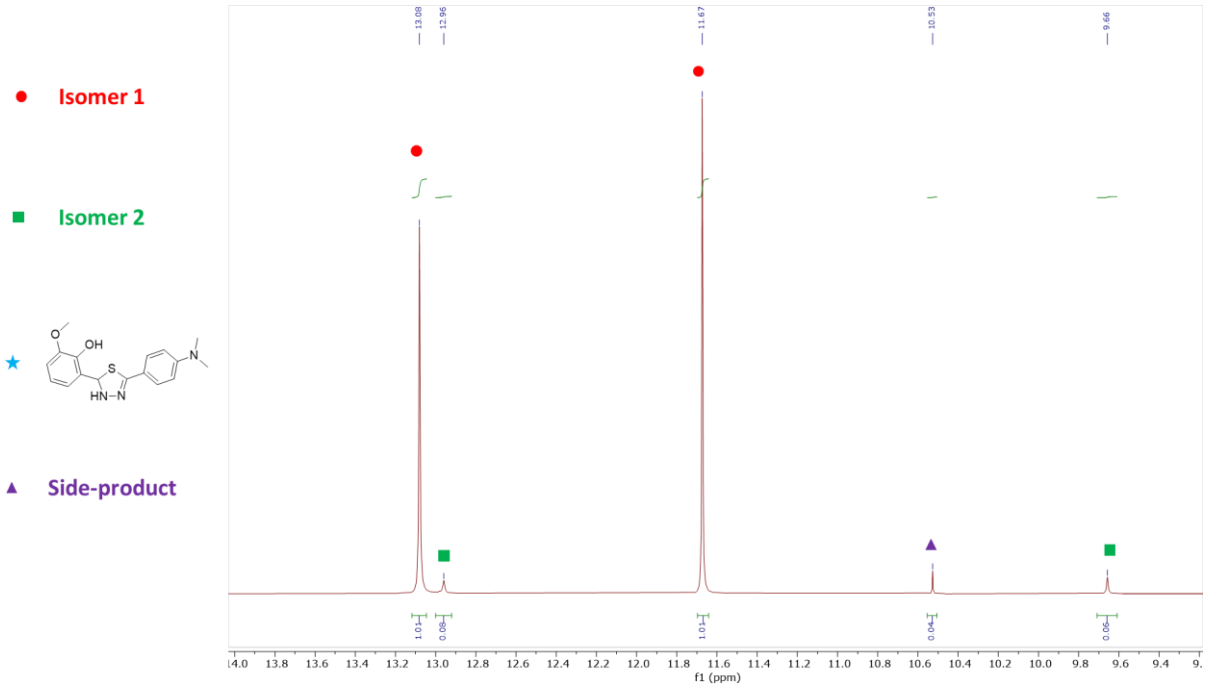

Figure A3.31: Selected range of the ^{1}H NMR (500 MHz, 298 K) spectrum of **AZM8a** in DMSO-d_6.

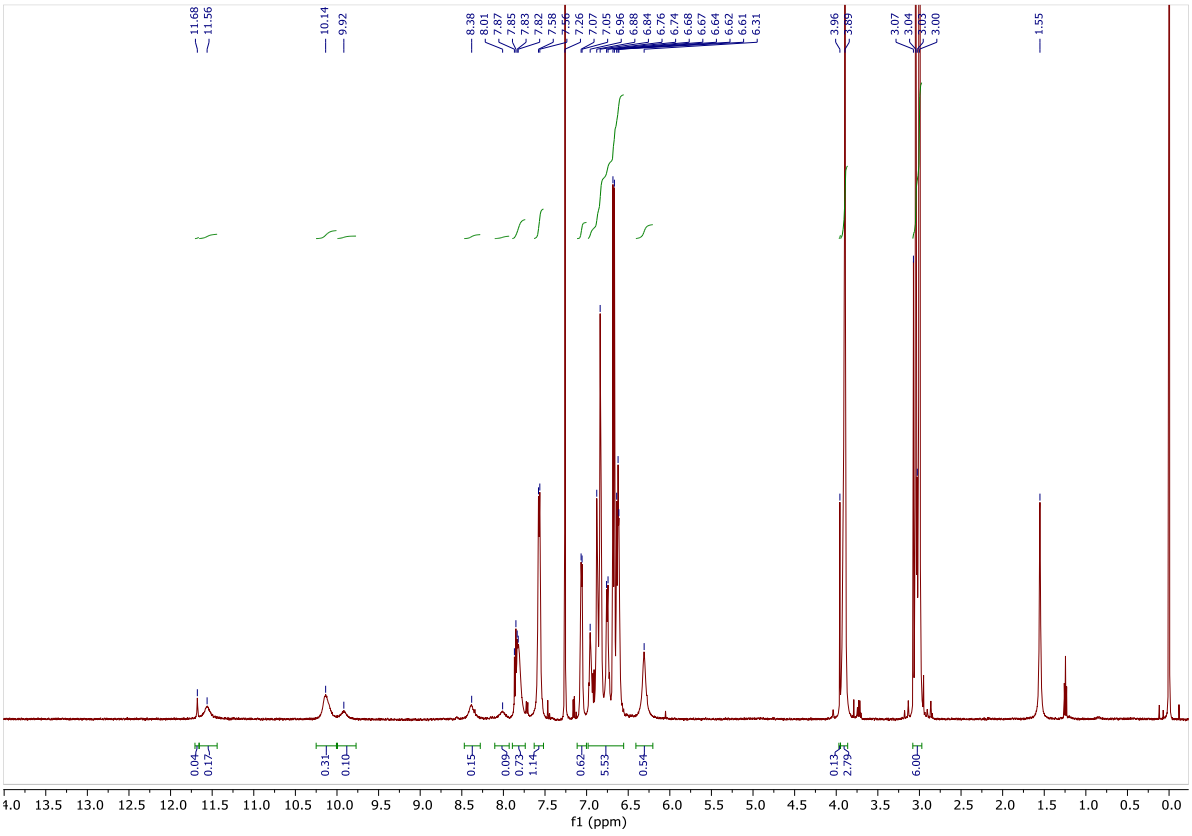

Figure A3.32: ^{1}H NMR (500 MHz, 298 K) spectrum of **AZM8a** in $CDCl_3$.

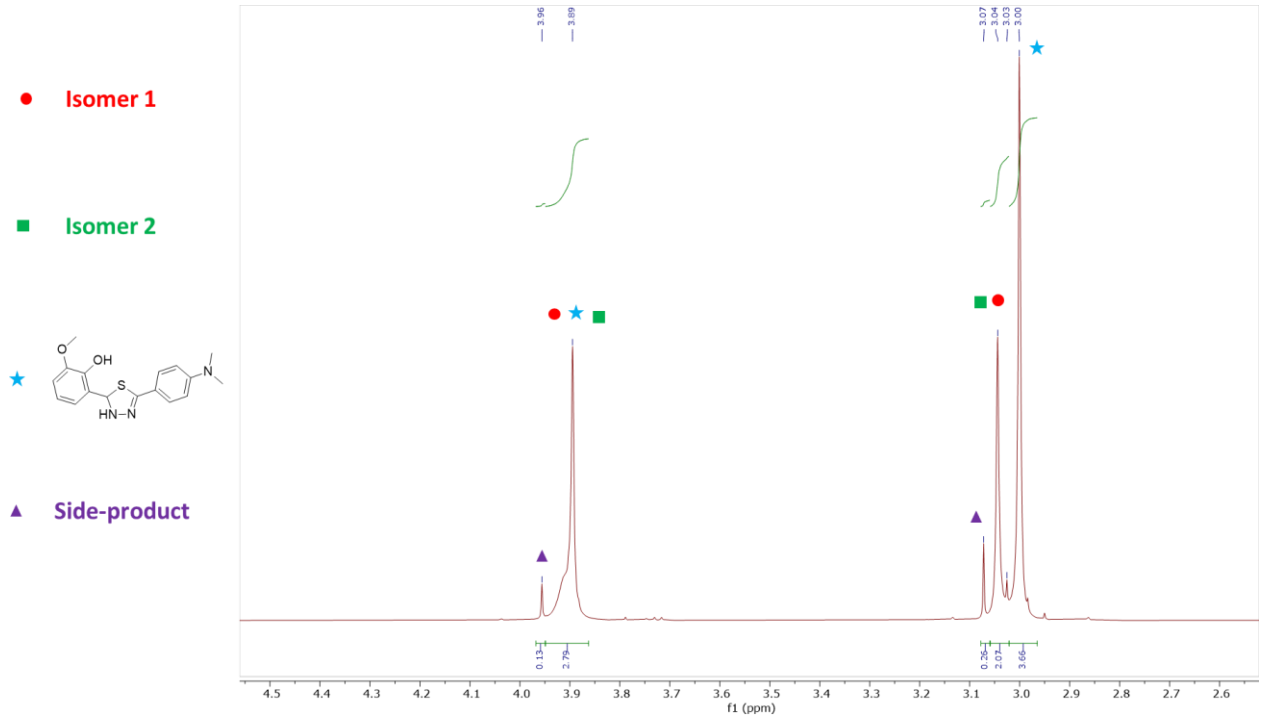

Figure A3.33: Selected range of the ^{1}H NMR (500 MHz, 298 K) spectrum of **AZM8a** in $CDCl_3$.

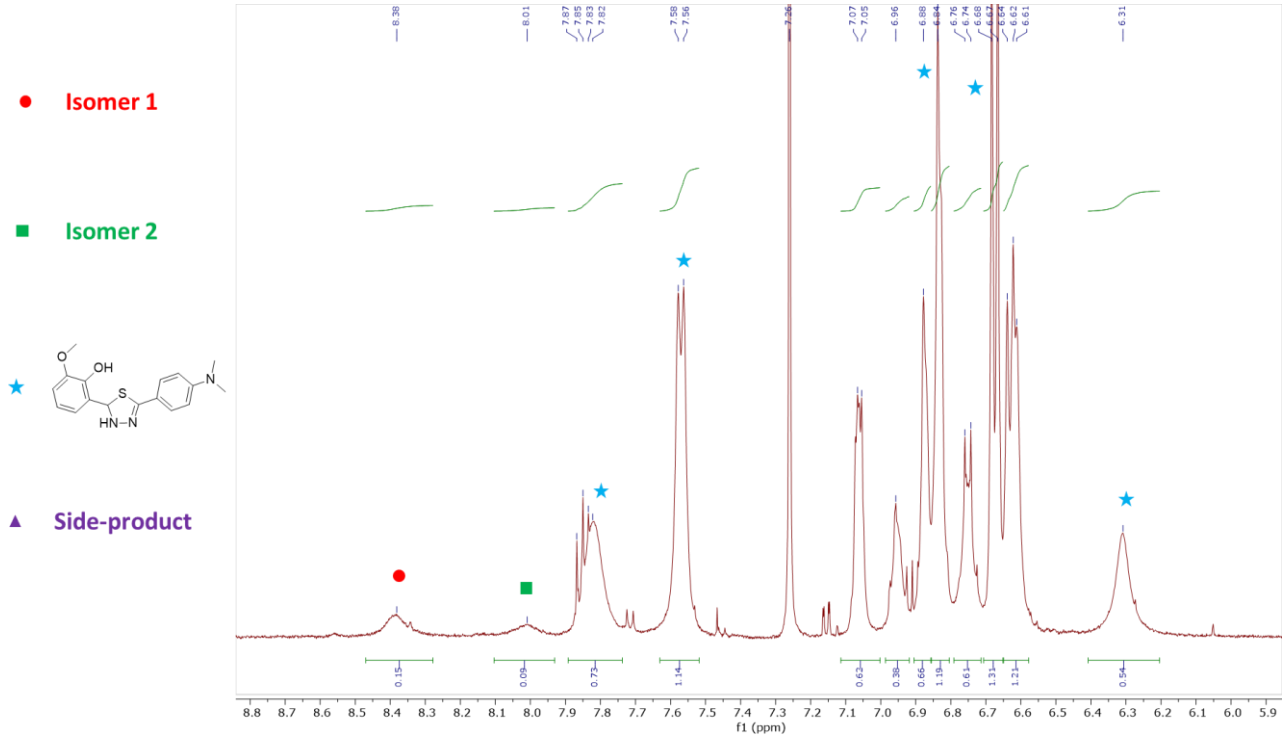

Figure A3.34: Selected range of the ^{1}H NMR (500 MHz, 298 K) spectrum of **AZM8a** in $CDCl_3$.

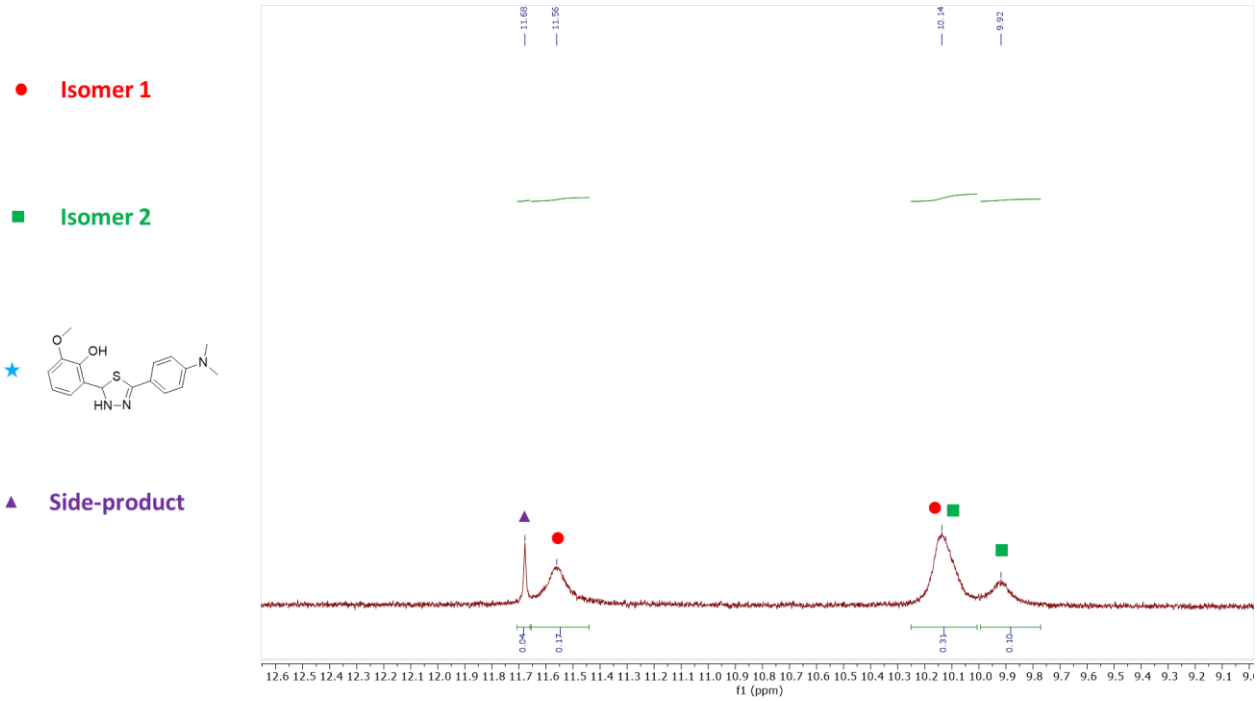

Figure A3.35: Selected range of the ^{1}H NMR (500 MHz, 298 K) spectrum of **AZM8a** in $CDCl_3$.

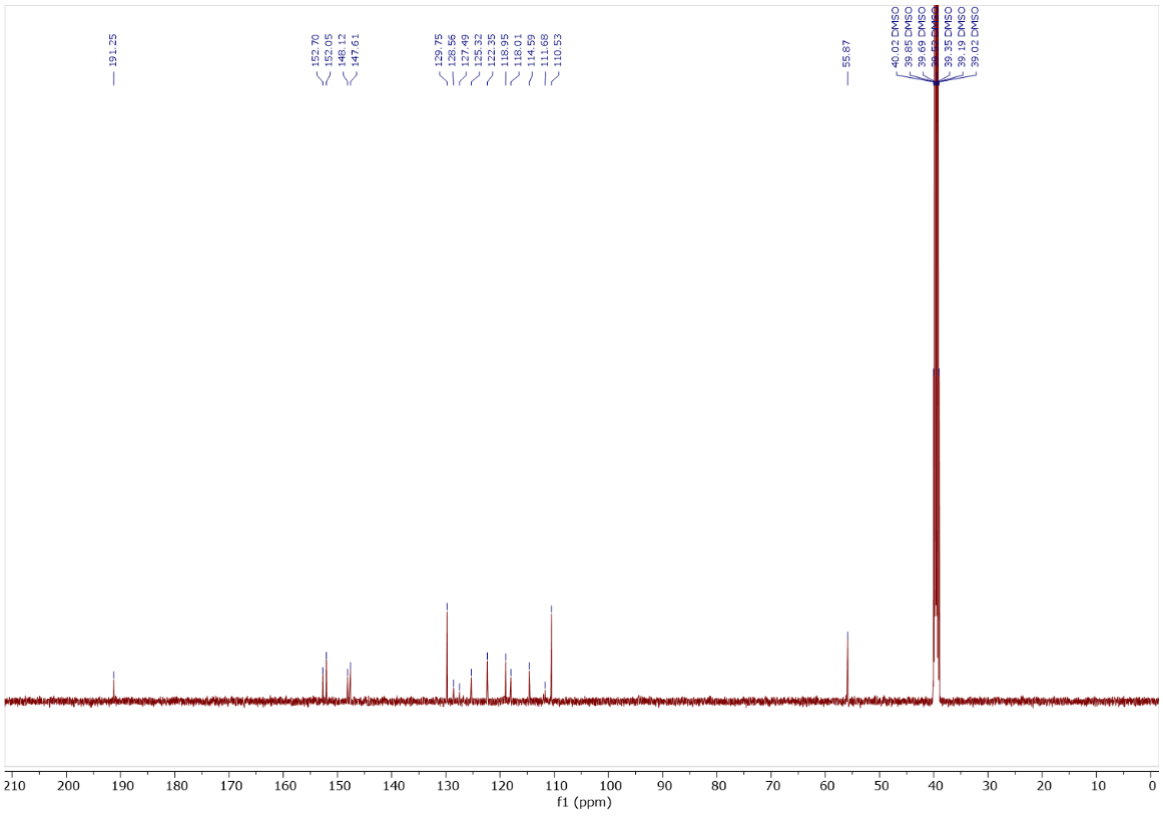

Figure A3.36: ^{13}C NMR (126 MHz, 298 K) spectrum of **AZM8a** in DMSO-d_6. The signal of methyl carbons of NMe_2 group is masked by the peaks of DMSO.

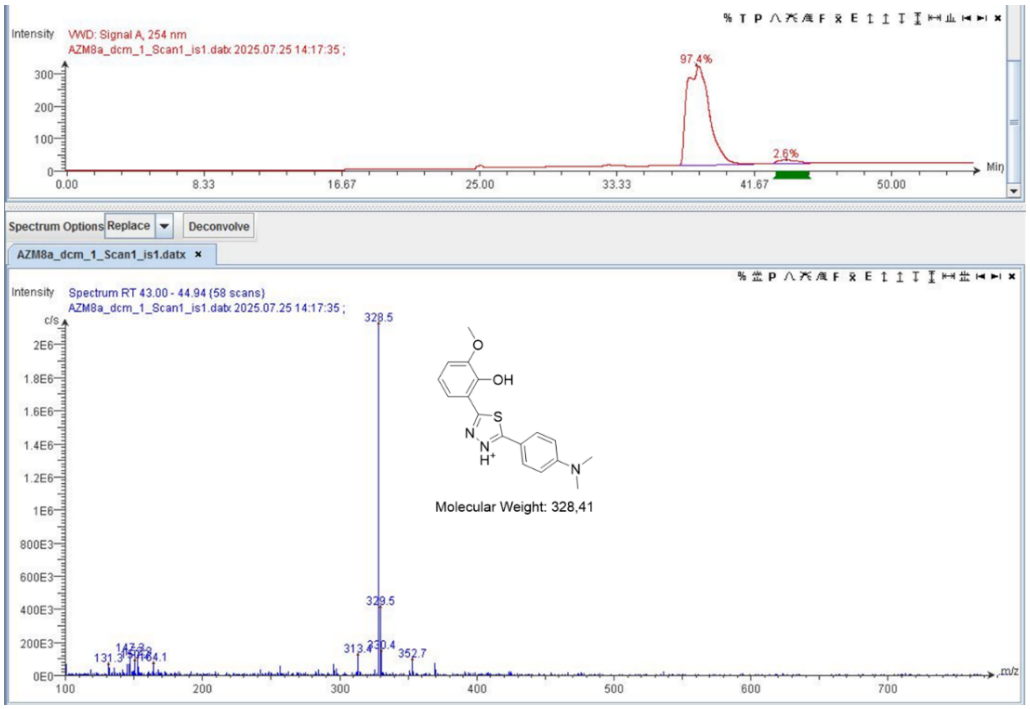

Figure A3.37: LC-MS (carrier solvent: MeCN with 0.1 % formic acid; positive ions) spectrum of **AZM8a**. Mass spectrum for the chromatographic peak of the side-product.

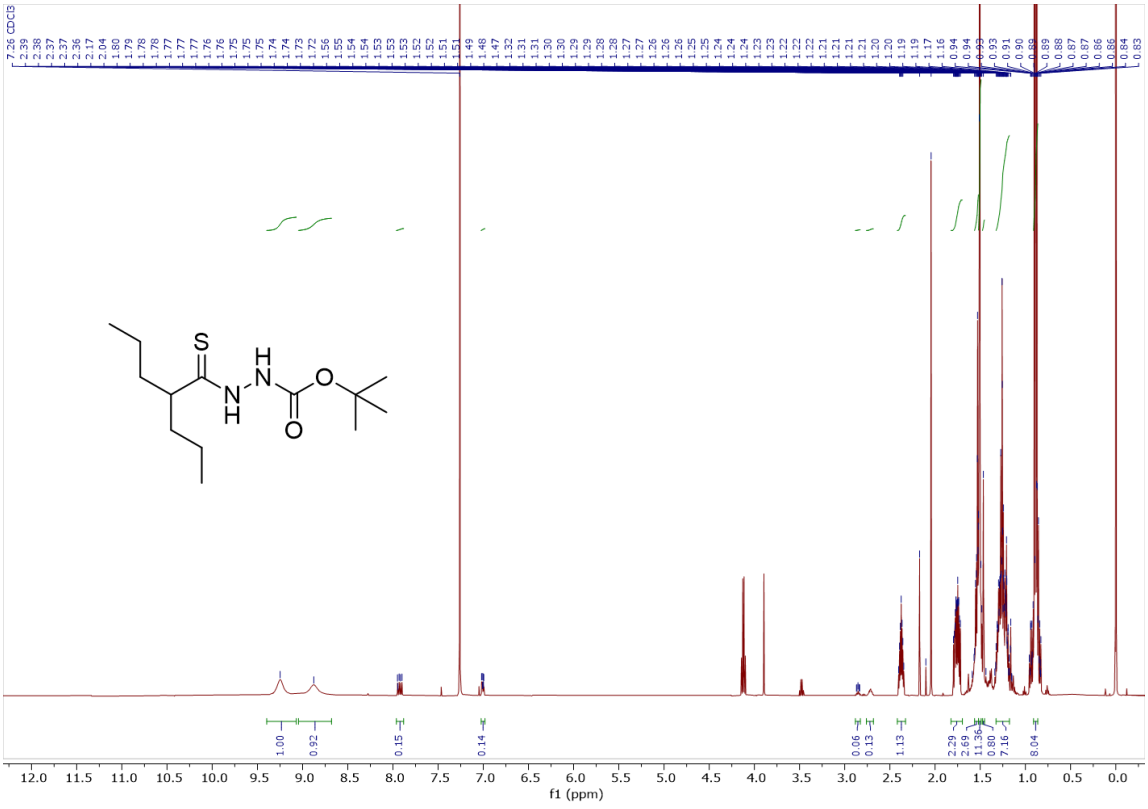

Figure A3.38: ^{1}H NMR (500 MHz, 298 K) spectrum of **AZM10** in $CDCl_3$. The spectrum indicates the presence of traces of thiadiazaphosphole side-product.

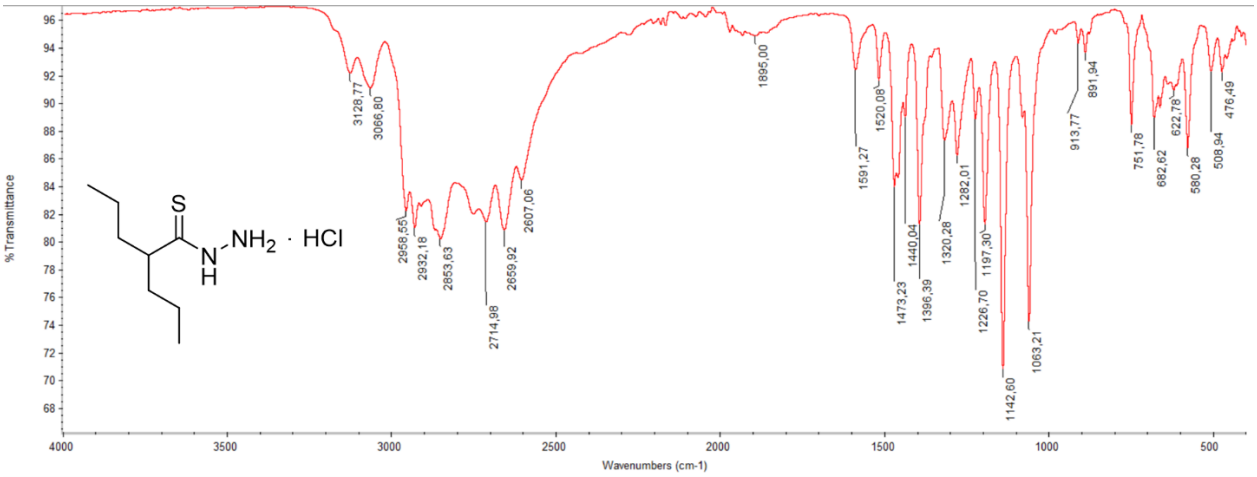

Figure A3.39: FT-IR spectrum of **AZM11**.

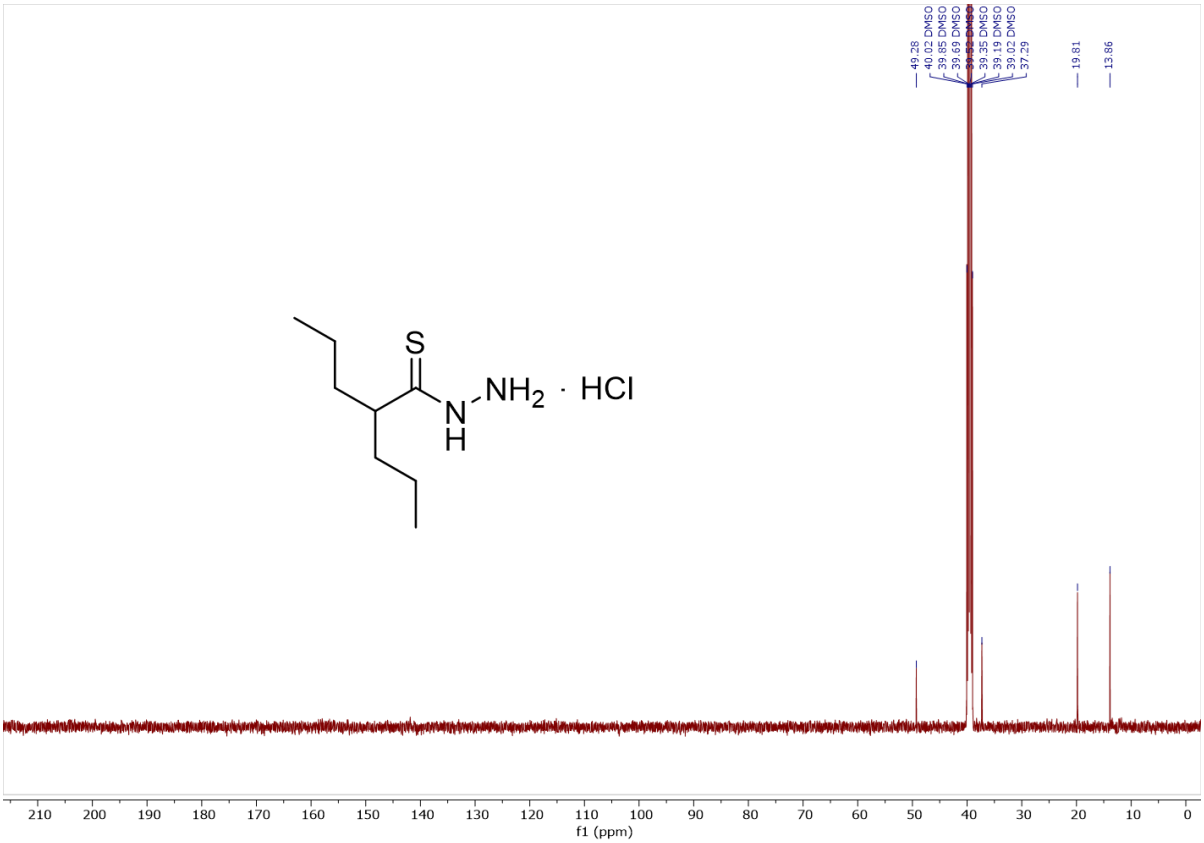

Figure A3.40: ^{13}C NMR (126 MHz, 298 K) spectrum of **AZM11** in DMSO-d_6. The lack of C=S signal is probably due to insufficient concentration of the sample.

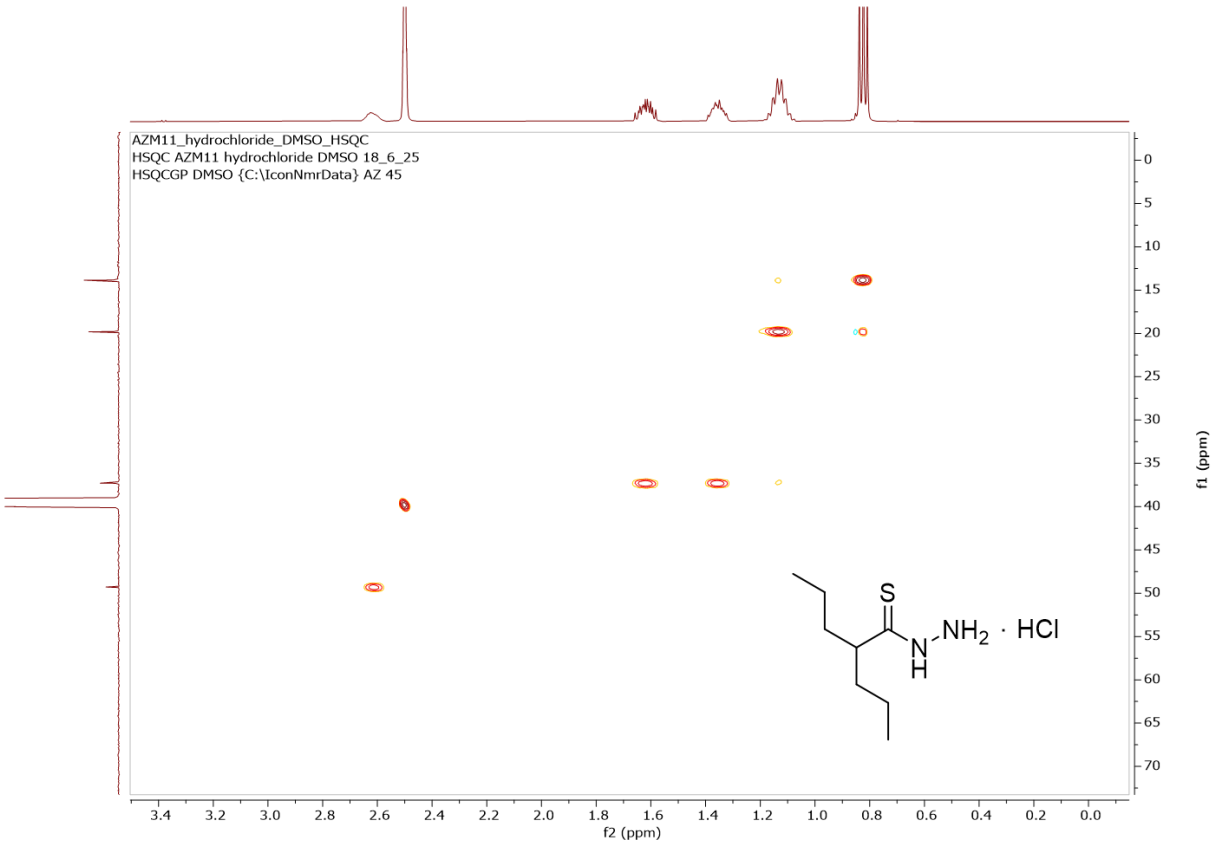

Figure A3.41: 2D ^{1}H-^{13}C HSQC spectrum of **AZM11** at 298 K in DMSO-d_6.

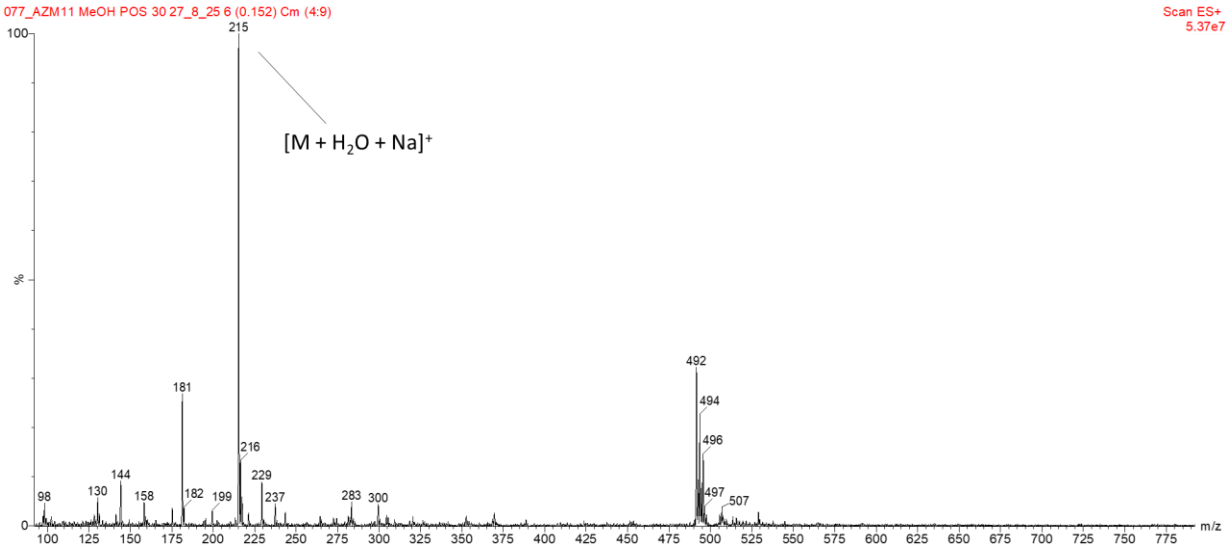

Figure A3.42: ESI-MS spectrum (positive ions) for **AZM11** in methanol.

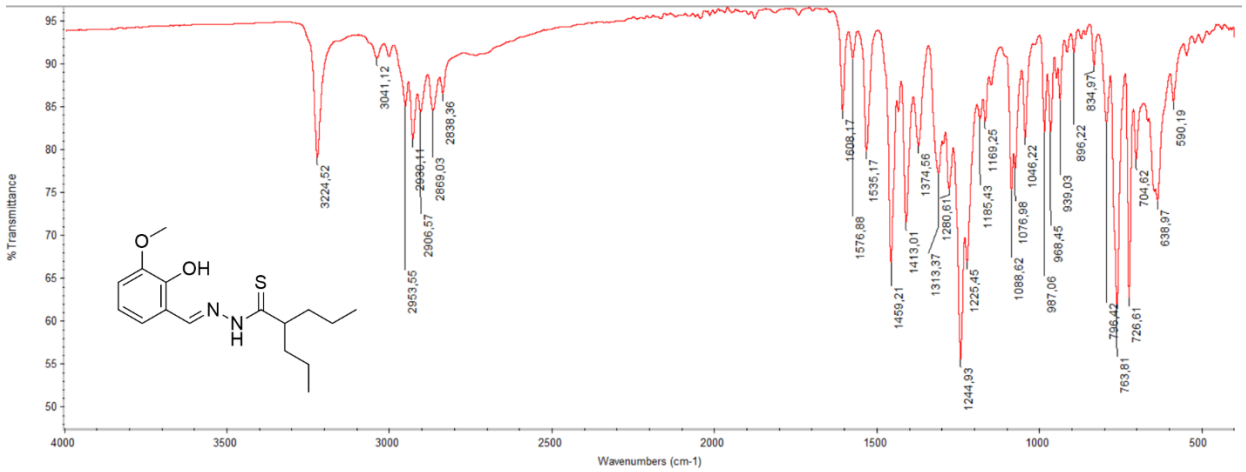

Figure A3.43: FT-IR spectrum of **AZM12**.

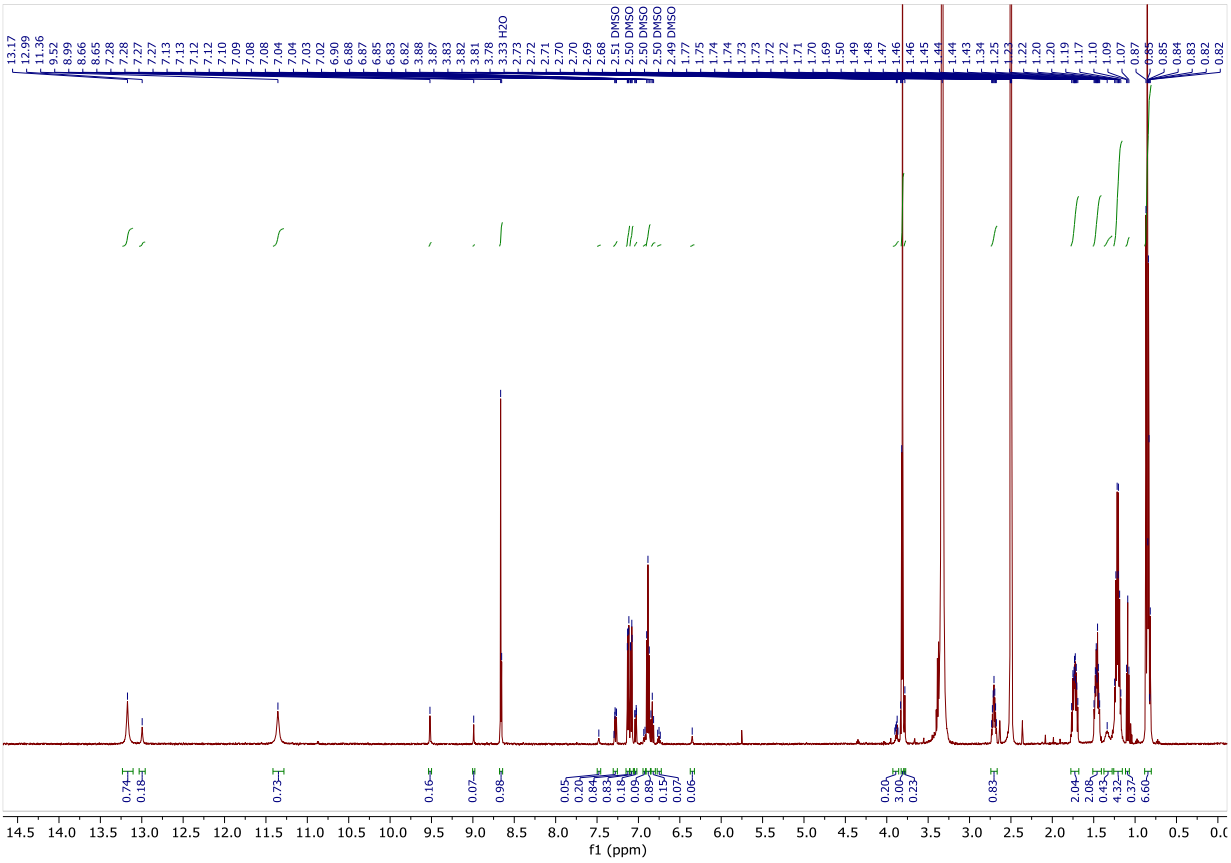

Figure A3.44: ^{1}H NMR (500 MHz, 298 K) spectrum of **AZM12** in DMSO-d_6.

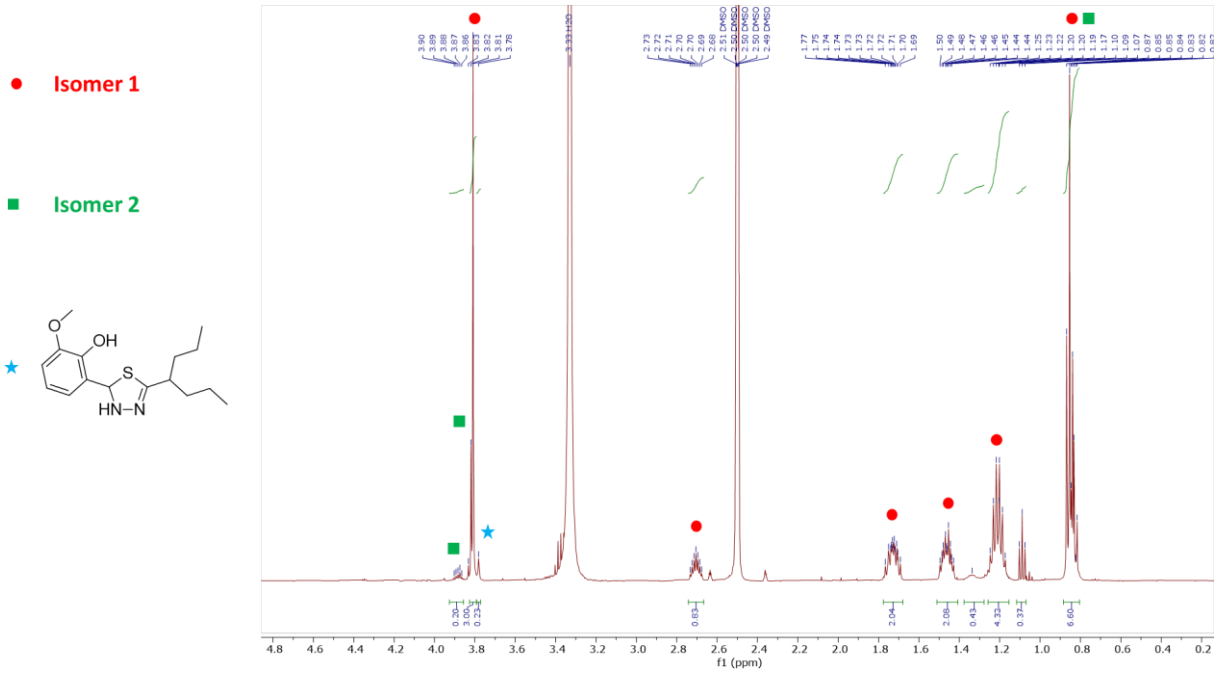

Figure A3.45: Selected range of the ^{1}H NMR (500 MHz, 298 K) spectrum of **AZM12** in DMSO-d_6.

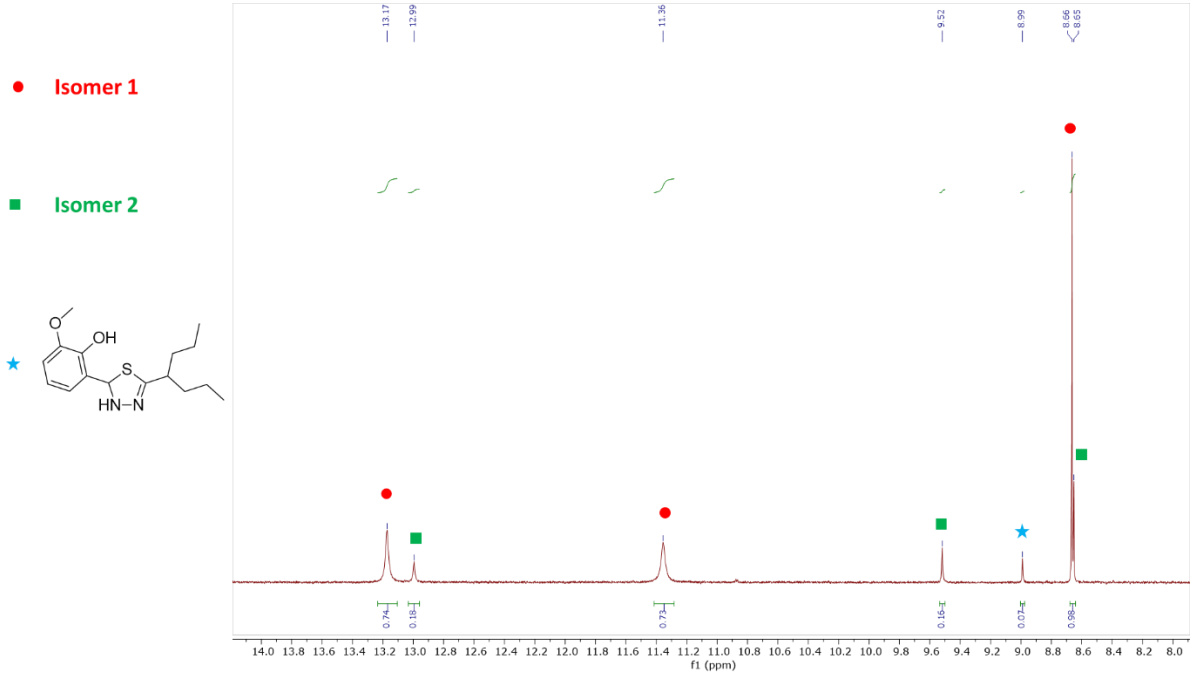

Figure A3.46: Selected range of the ^{1}H NMR (500 MHz, 298 K) spectrum of **AZM12** in DMSO-d_6.

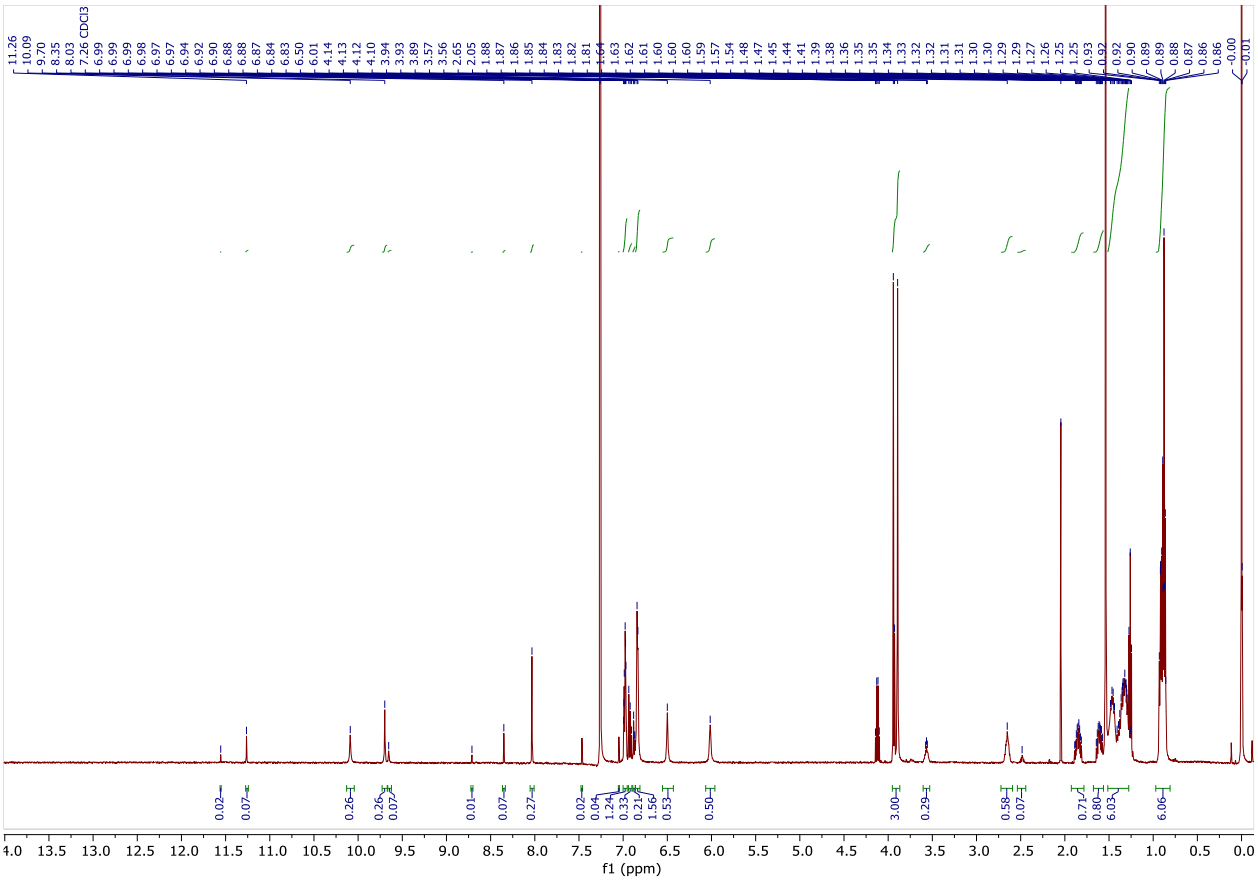

Figure A3.47: ^{1}H NMR (500 MHz, 298 K) spectrum of **AZM12** in $CDCl_3$.

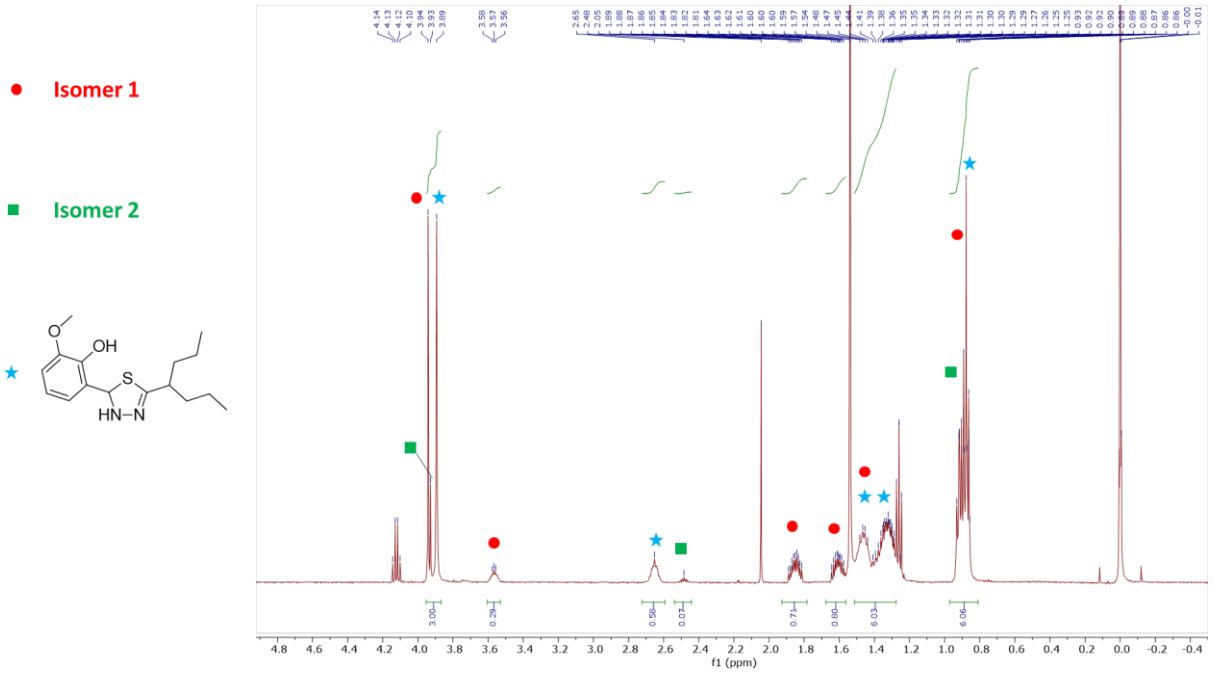

Figure A3.48: Selected range of the ^{1}H NMR (500 MHz, 298 K) spectrum of **AZM12** in $CDCl_3$.

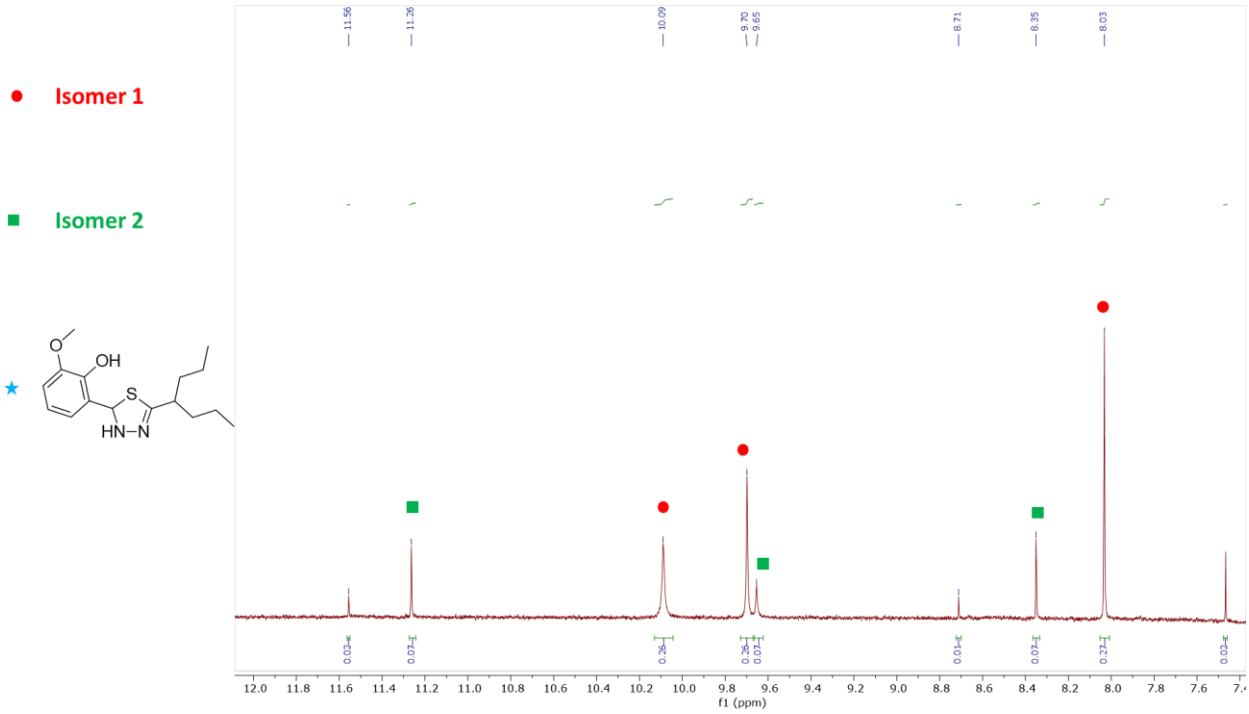

Figure A3.49: Selected range of the ^{1}H NMR (500 MHz, 298 K) spectrum of **AZM12** in $CDCl_3$.

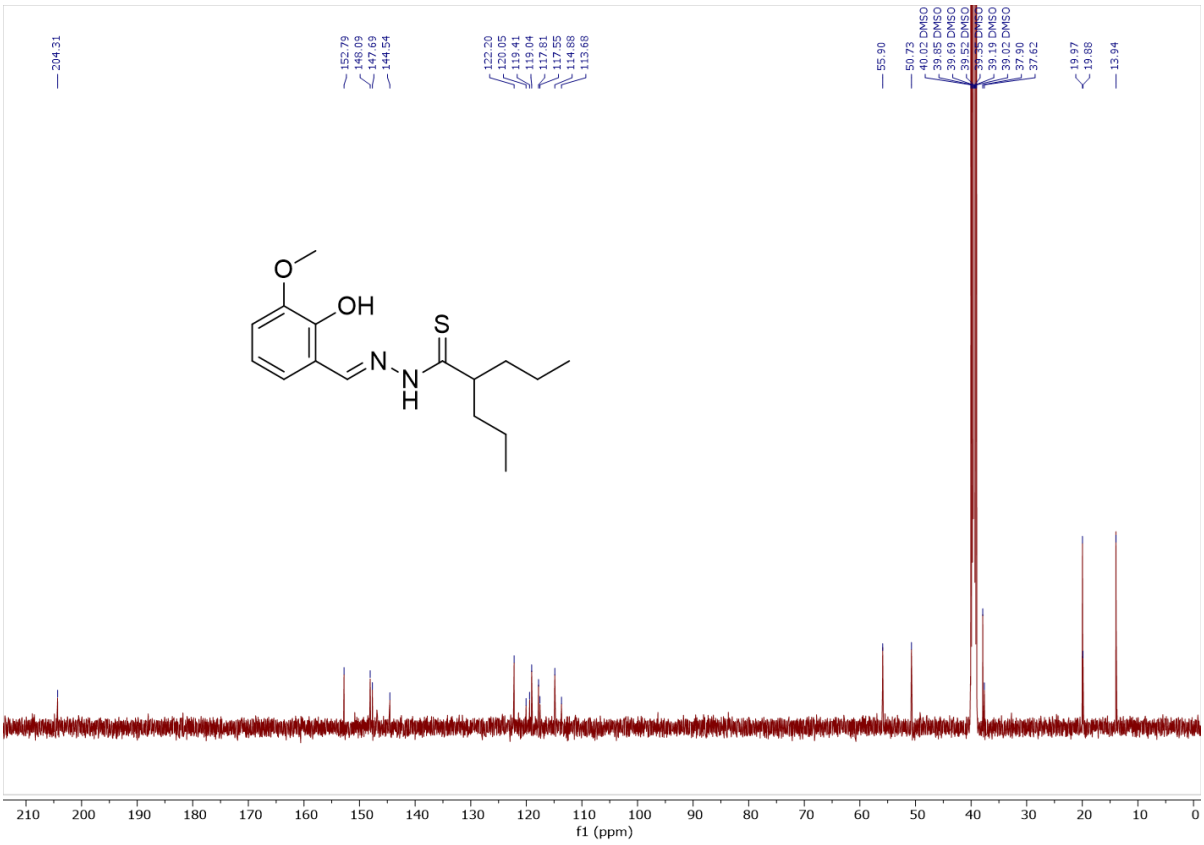

Figure A3.50: ^{13}C NMR (126 MHz, 298 K) spectrum of **AZM12** in DMSO-d_6.

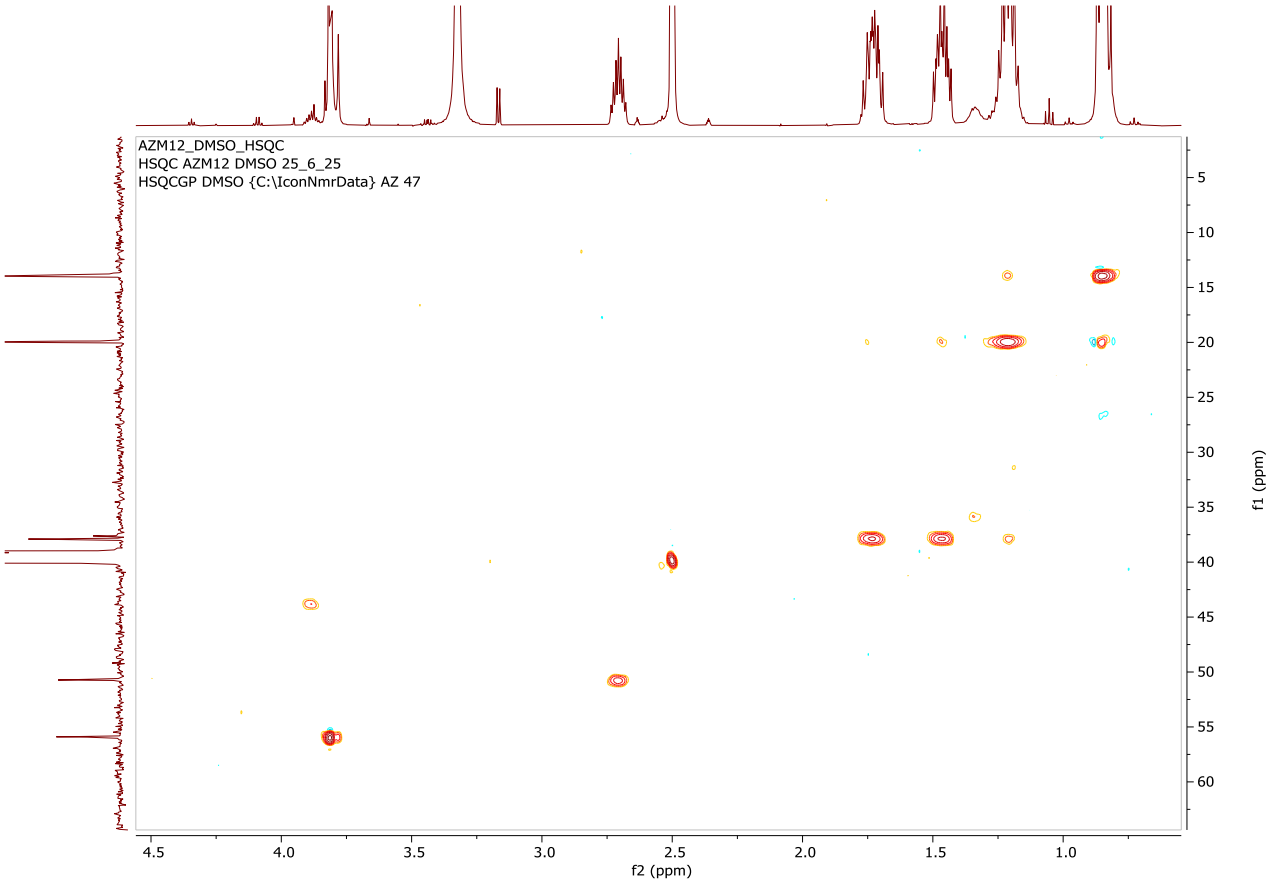

Figure A3.51: Selected range of the 2D ^{1}H-^{13}C HSQC spectrum of **AZM12** at 298 K in DMSO-d_6.

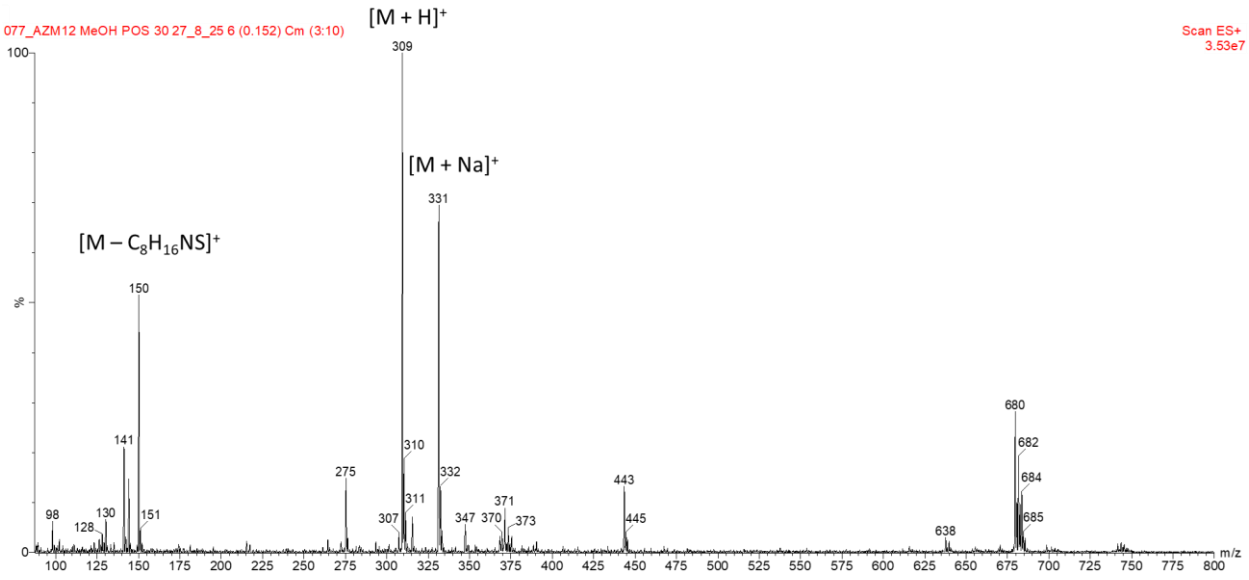

Figure A3.52: ESI-MS spectrum (positive ions) for **AZM12** in methanol.

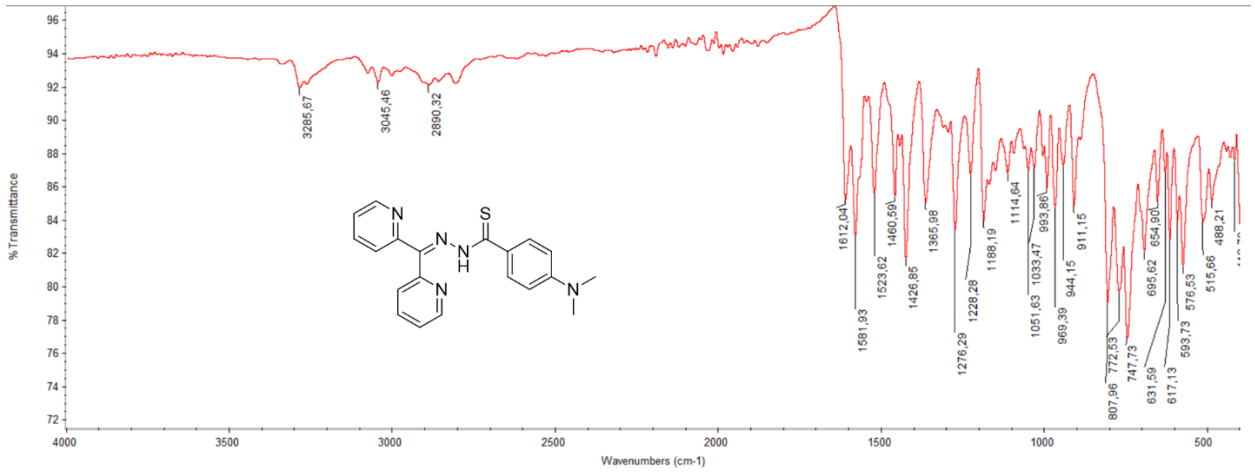

Figure A3.53: FT-IR spectrum of **AZM14b**.

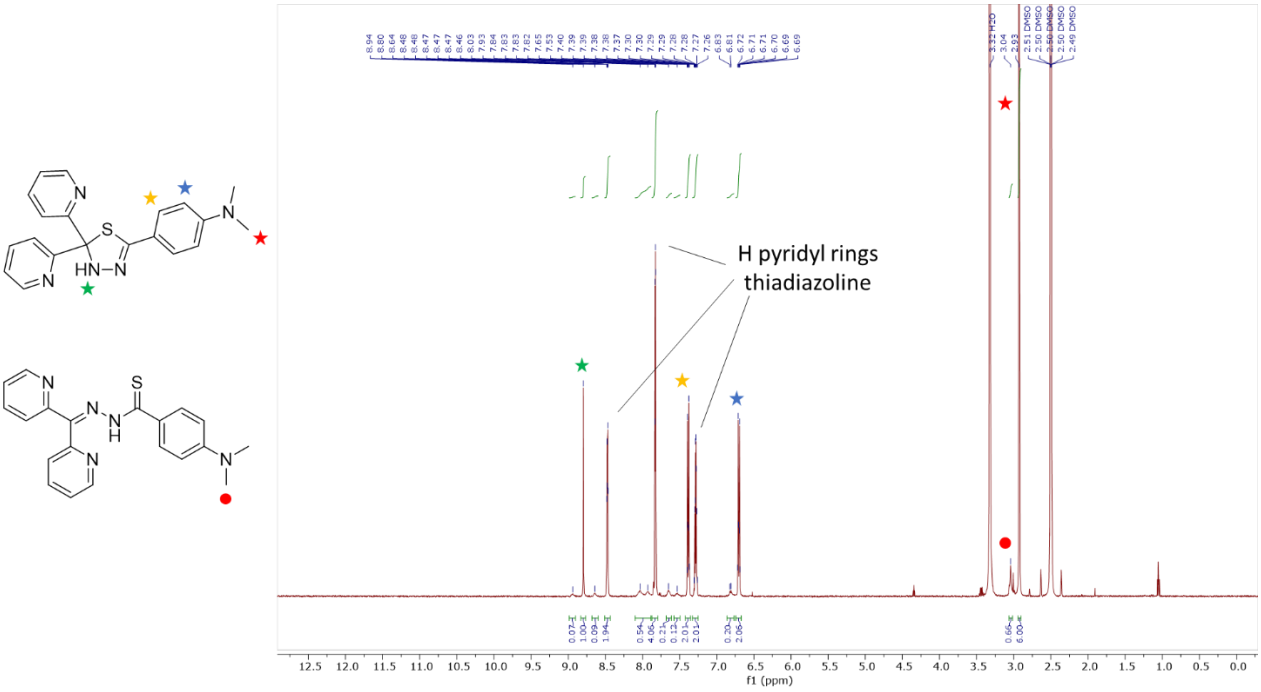

Figure A3.54: ^{1}H NMR (500 MHz, 298 K) spectrum of **AZM14b** in DMSO-d_6.

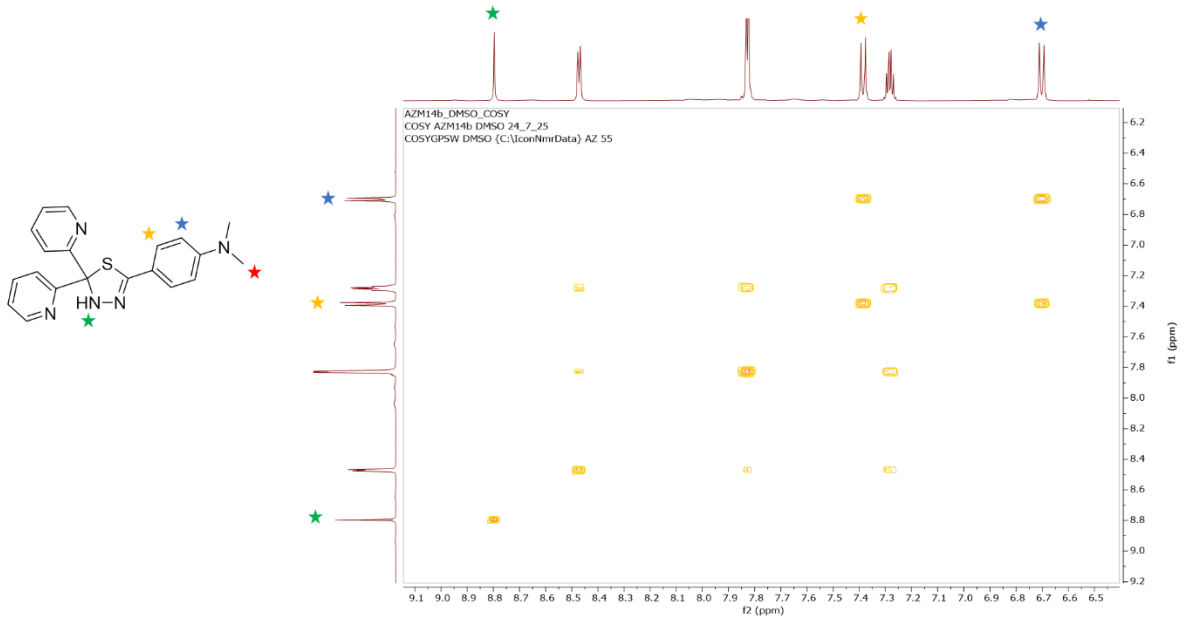

Figure A3.55: Selected range of the 2D ^{1}H-^{1}H COSY spectrum of **AZM14b** at 298 K in DMSO-d_6.

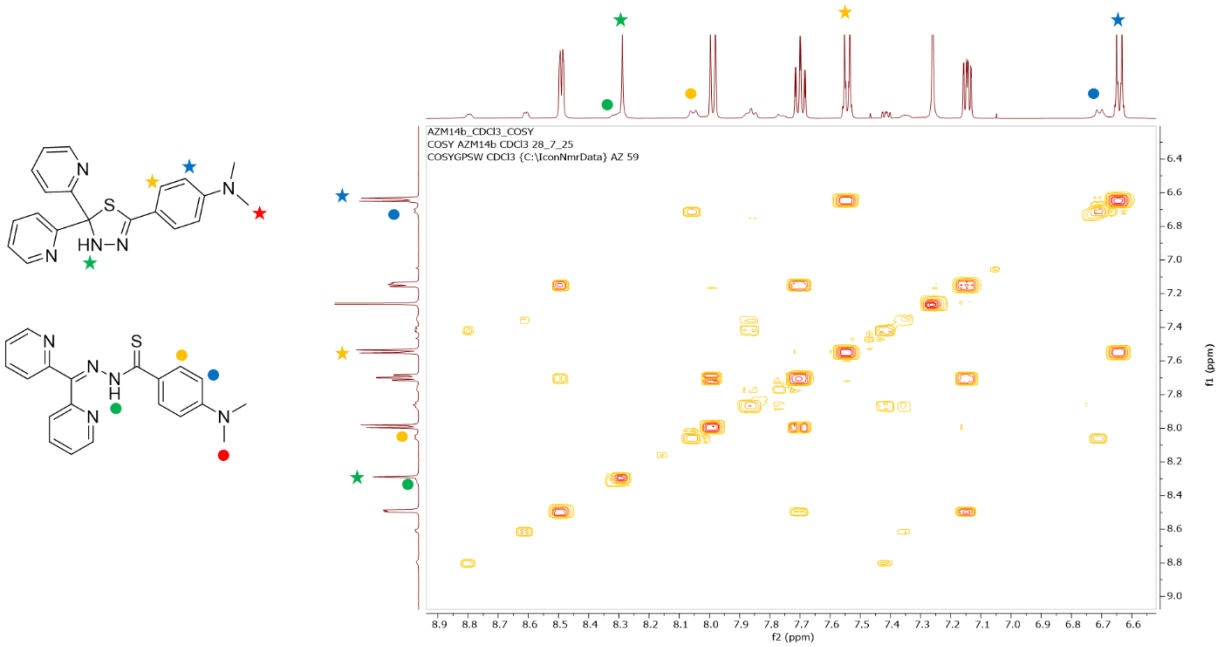

Figure A3.56: Selected range of the 2D ^{1}H-^{1}H COSY spectrum of **AZM14b** at 298 K in $CDCl_3$.

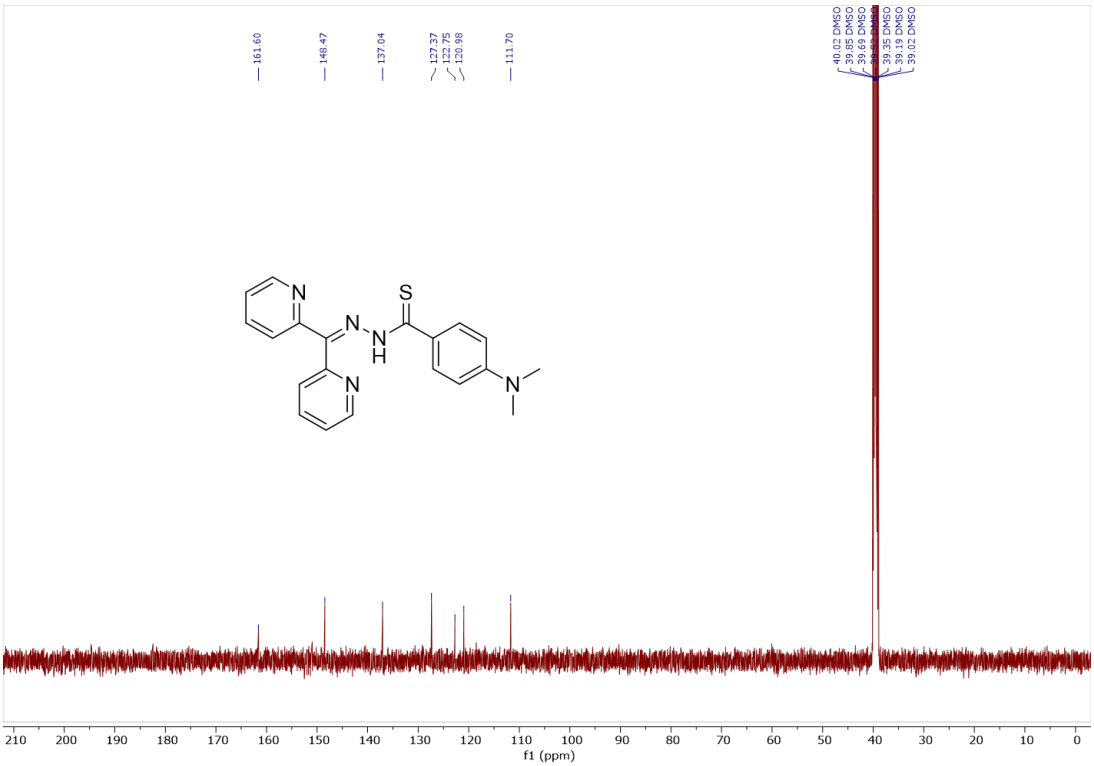

Figure A3.57: ^{13}C NMR (126 MHz, 298 K) spectrum of **AZM14b** in DMSO-d_6. The signal of methyl carbons of NMe_2 group is masked by the peaks of DMSO. The lack of some quaternary carbon signals is probably due to insufficient concentration of the sample.

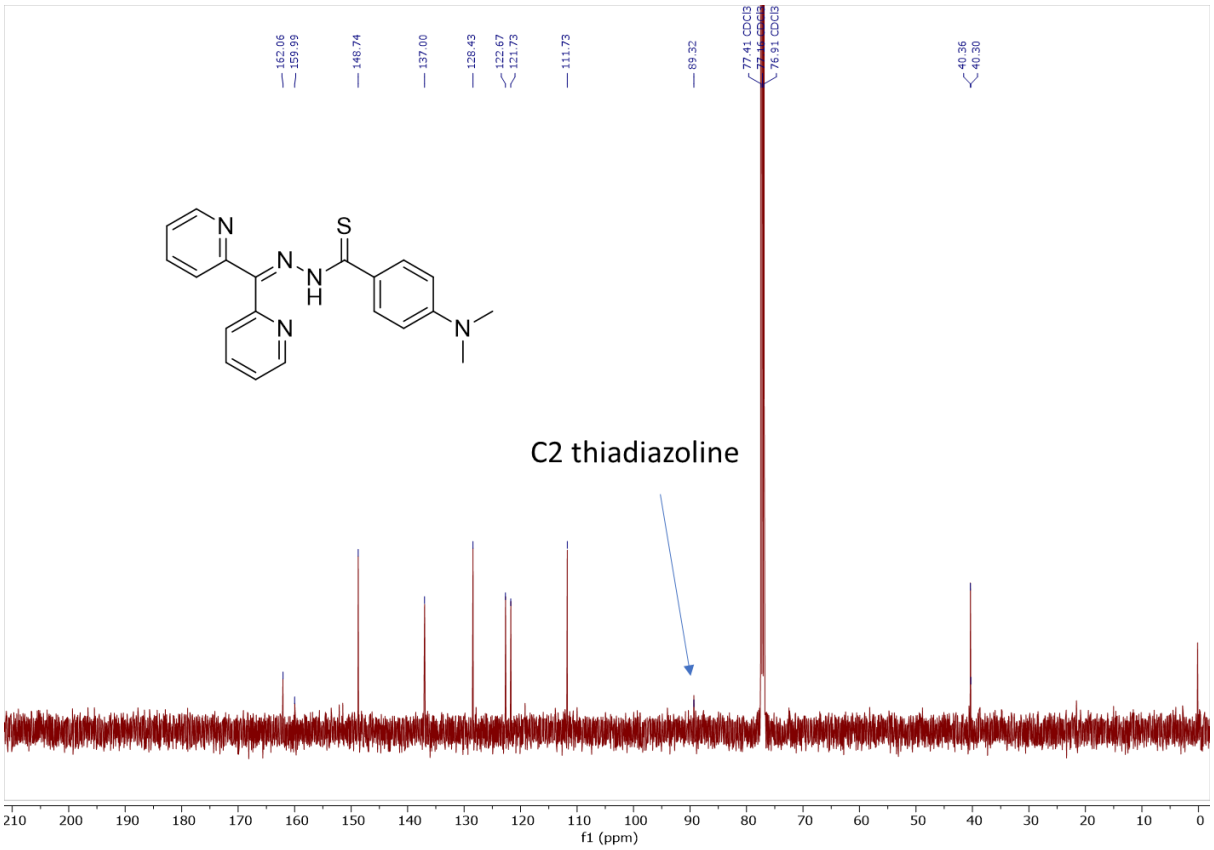

Figure A3.58: ^{13}C NMR (126 MHz, 298 K) spectrum of **AZM14b** in $CDCl_3$.

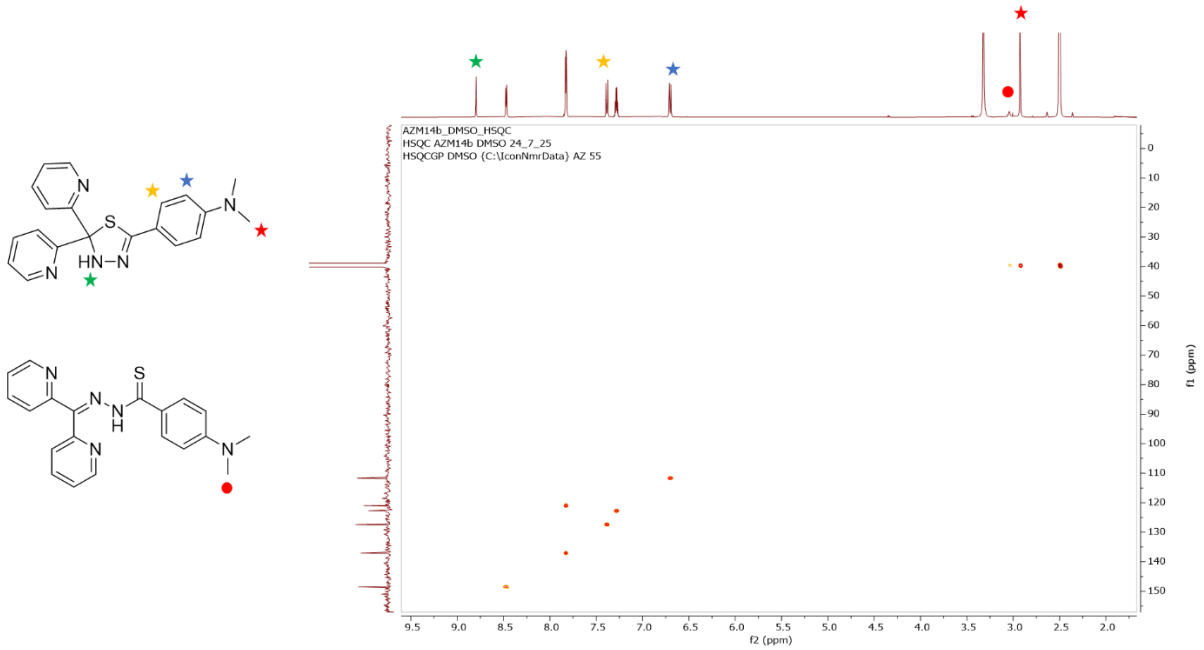

Figure A3.59: 2D ^{1}H-^{13}C HSQC spectrum of **AZM14b** at 298 K in DMSO-d_6.

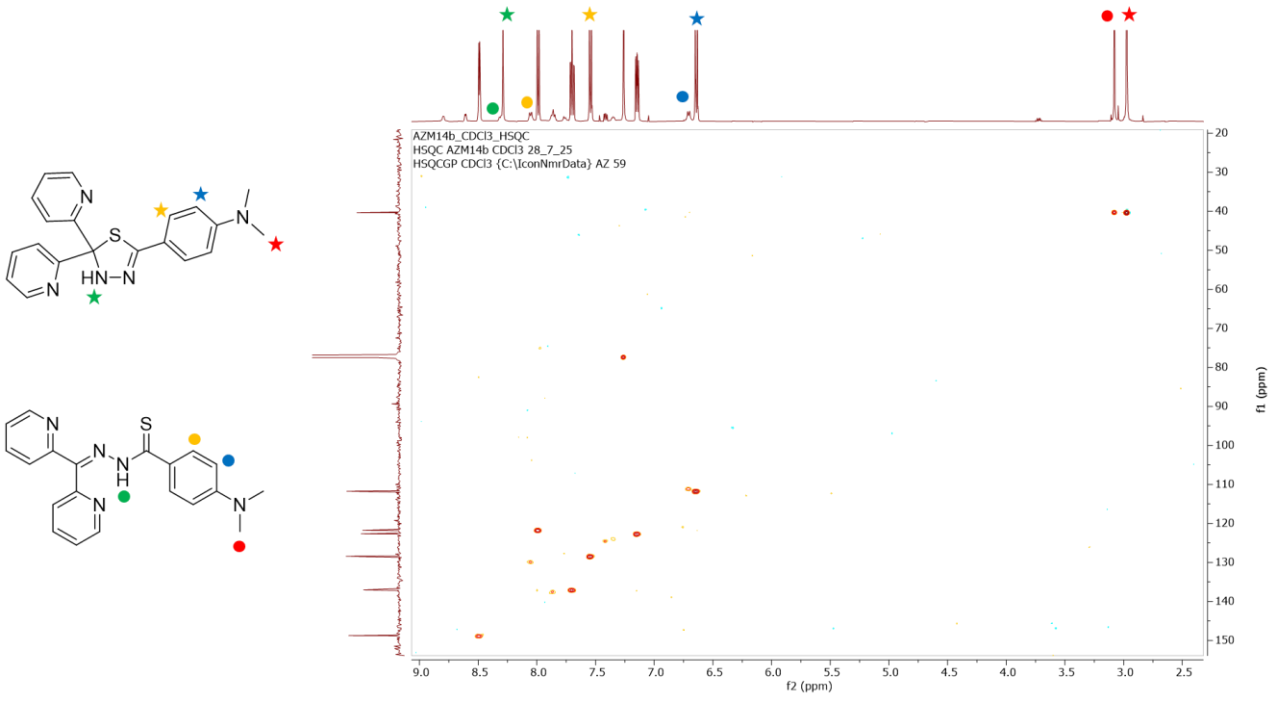

Figure A3.60: 2D ^{1}H-^{13}C HSQC spectrum of **AZM14b** at 298 K in $CDCl_3$.

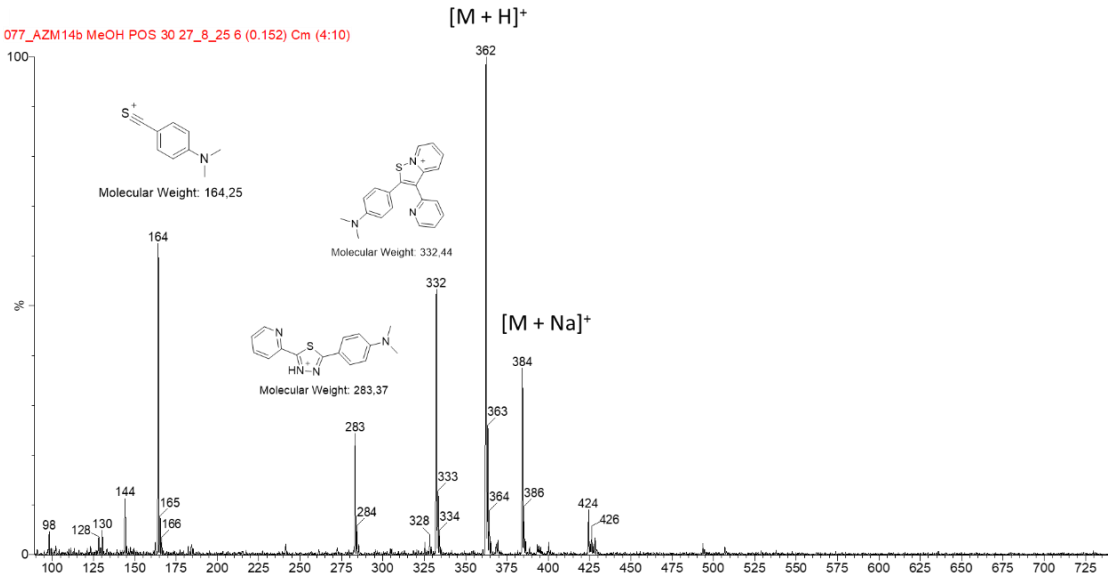

Figure A3.61: ESI-MS spectrum (positive ions, cone voltage 30) for **AZM14b** in methanol.

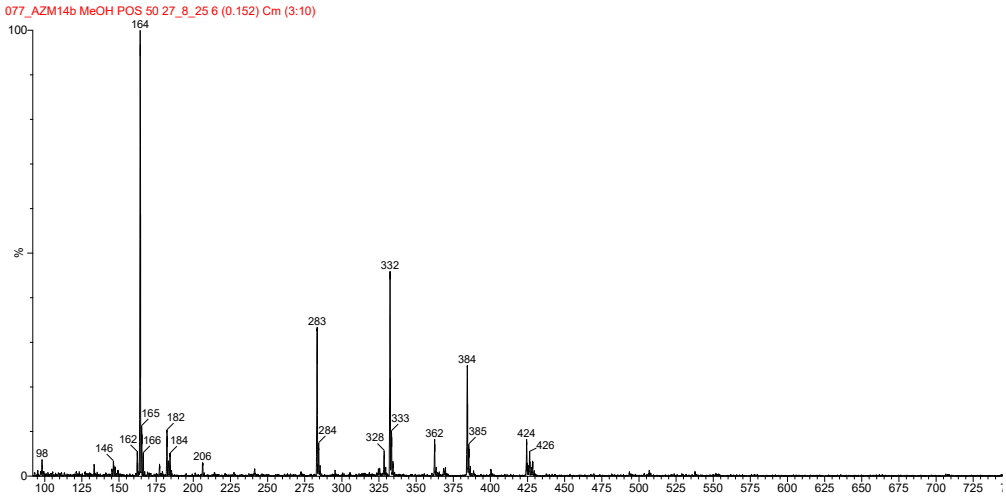

Figure A3.62: ESI-MS spectrum (positive ions, cone voltage 50) for **AZM14b** in methanol.

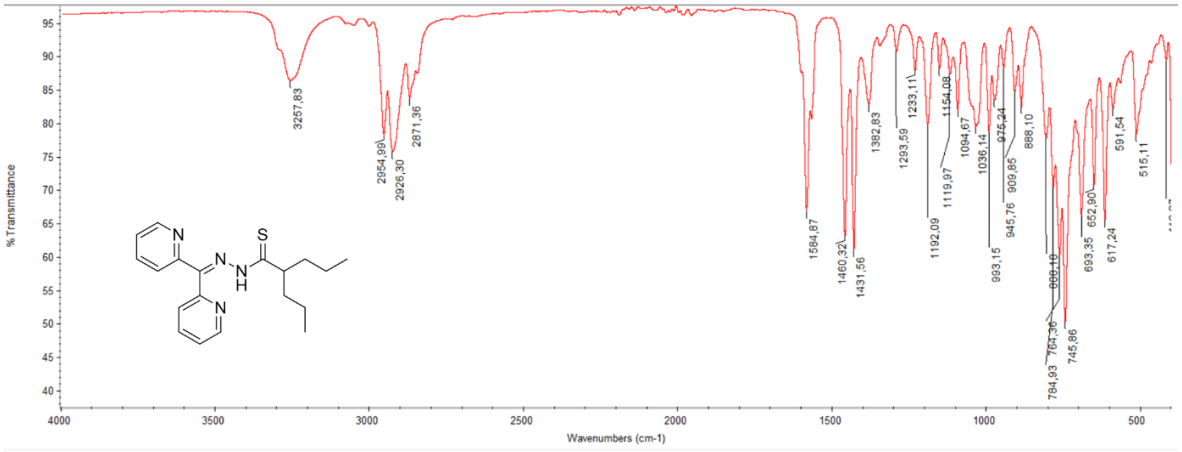

Figure A3.63: FT-IR spectrum of **AZM16**.

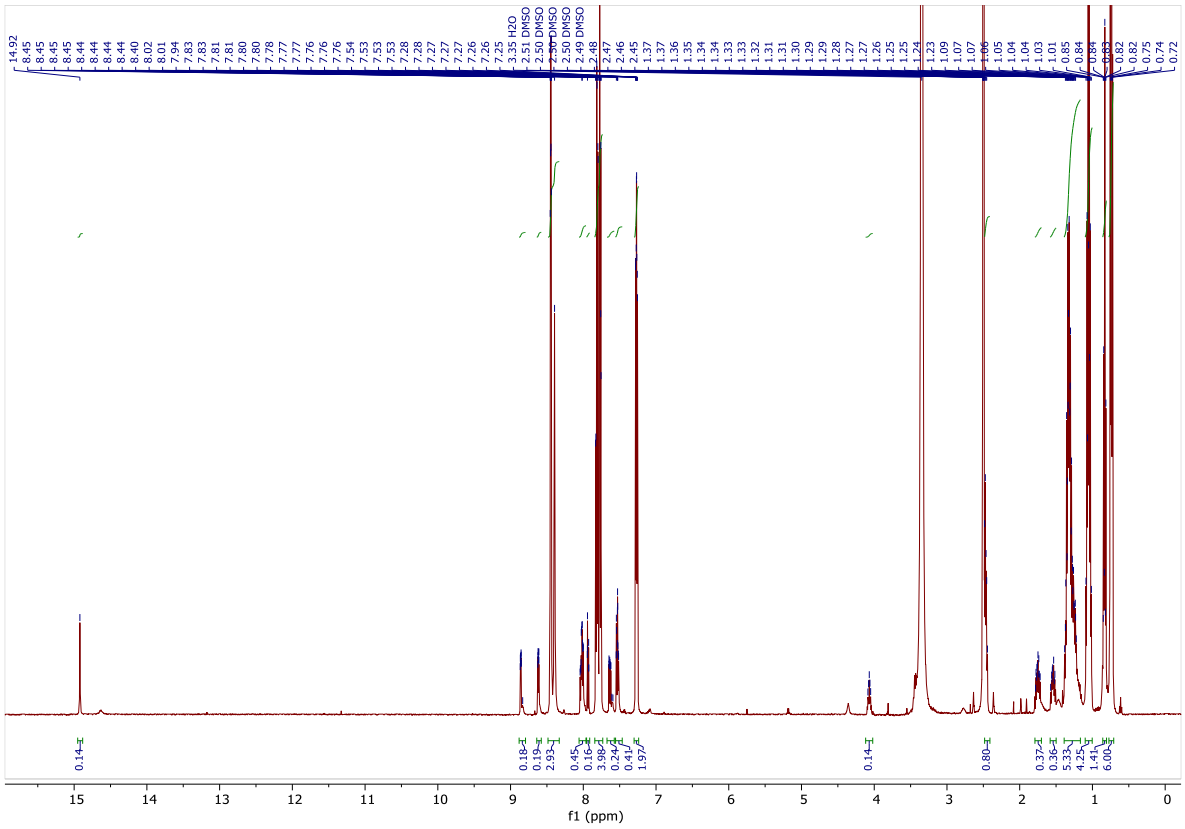

Figure A3.64: ^{1}H NMR (500 MHz, 298 K) spectrum of **AZM16** in DMSO-d_6.

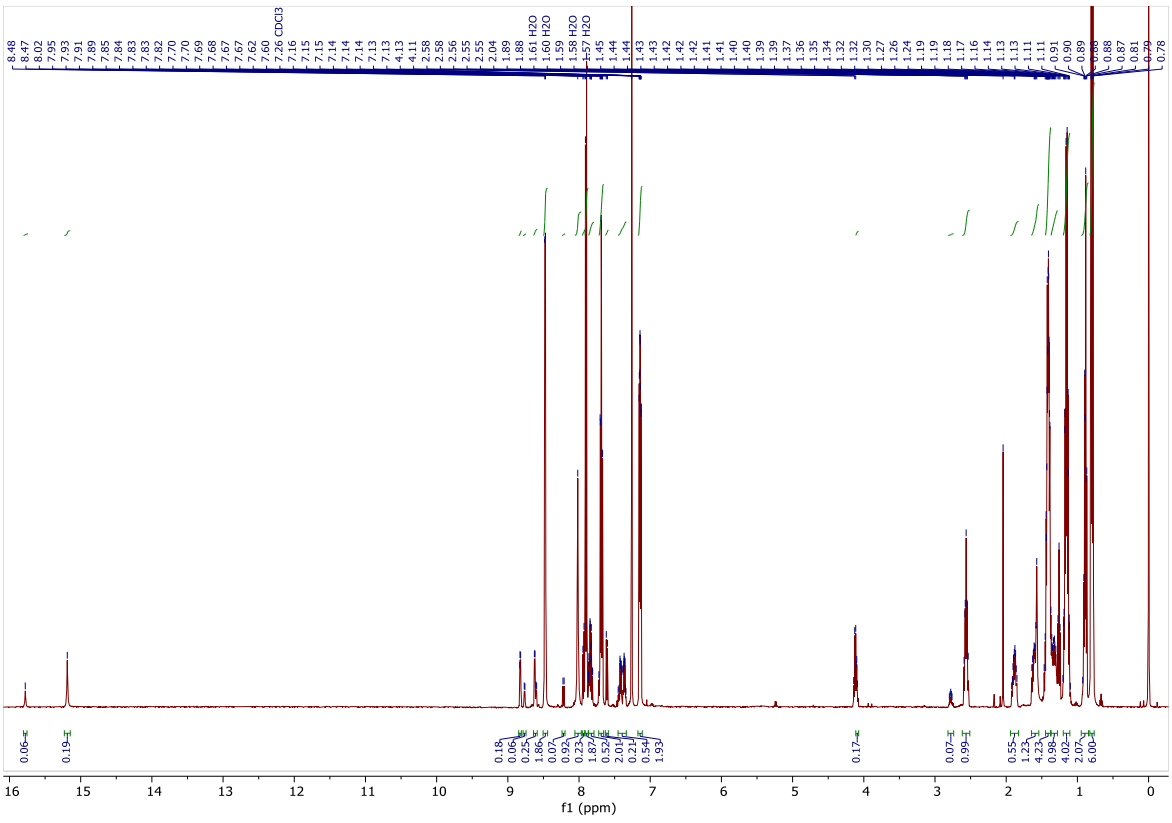

Figure A3.65: ^{1}H NMR (500 MHz, 298 K) spectrum of **AZM16** in $CDCl_3$.

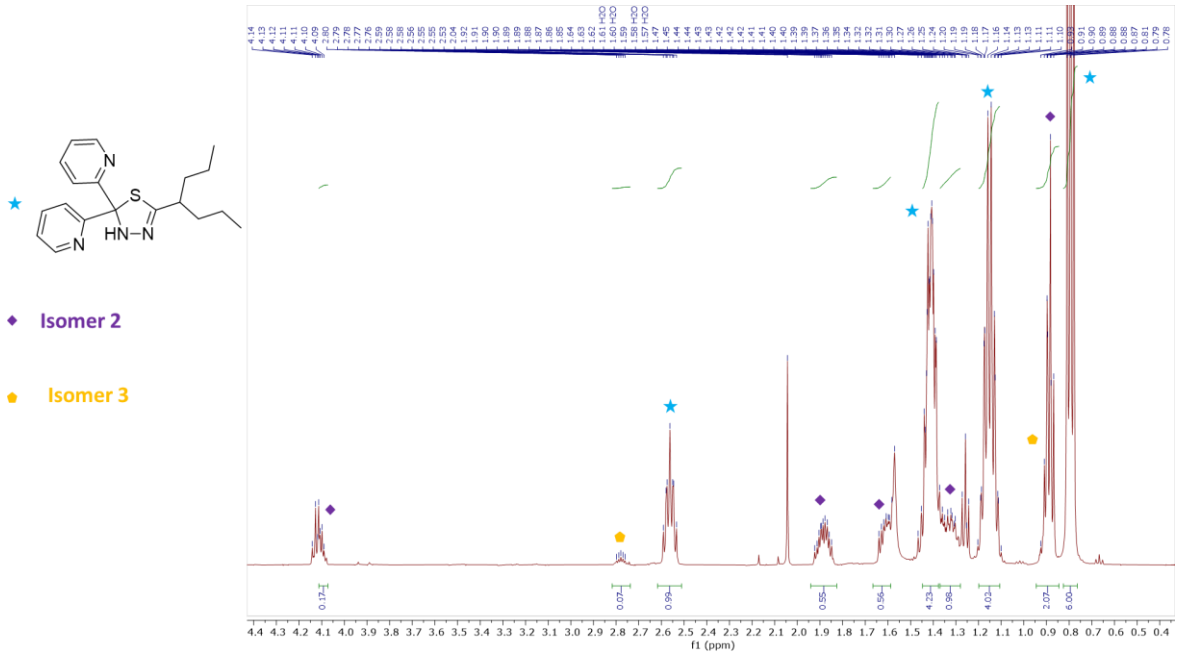

Figure A3.66: Selected range of the ^{1}H NMR (500 MHz, 298 K) spectrum of **AZM16** in $CDCl_3$.

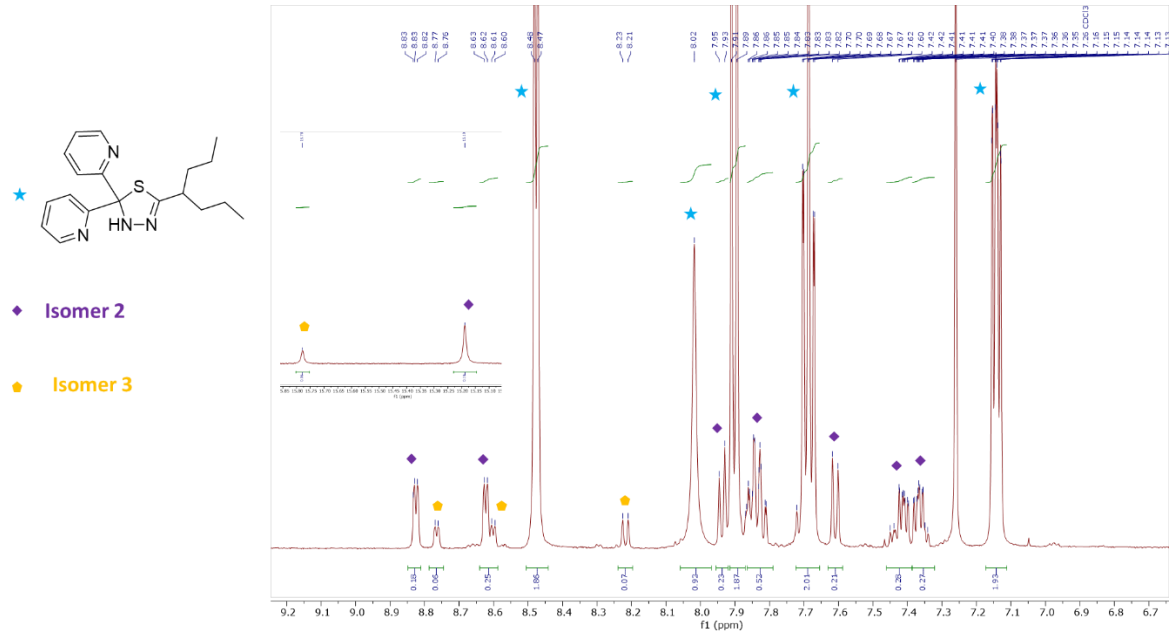

Figure A3.67: Selected range of the ^{1}H NMR (500 MHz, 298 K) spectrum of **AZM16** in $CDCl_3$. The inset shows the signals observed at 15.00 – 16.00 ppm.

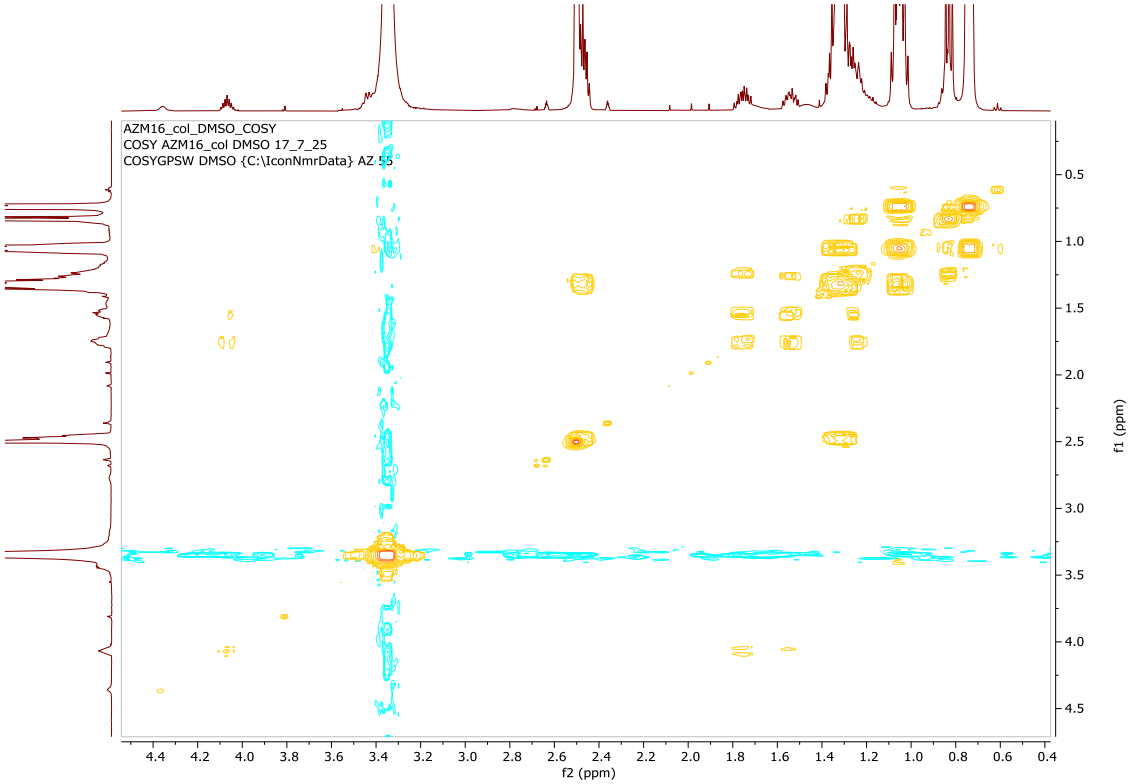

Figure A3.68: Selected range of the 2D ^{1}H-^{1}H COSY spectrum of **AZM16** at 298 K in DMSO-d_6.

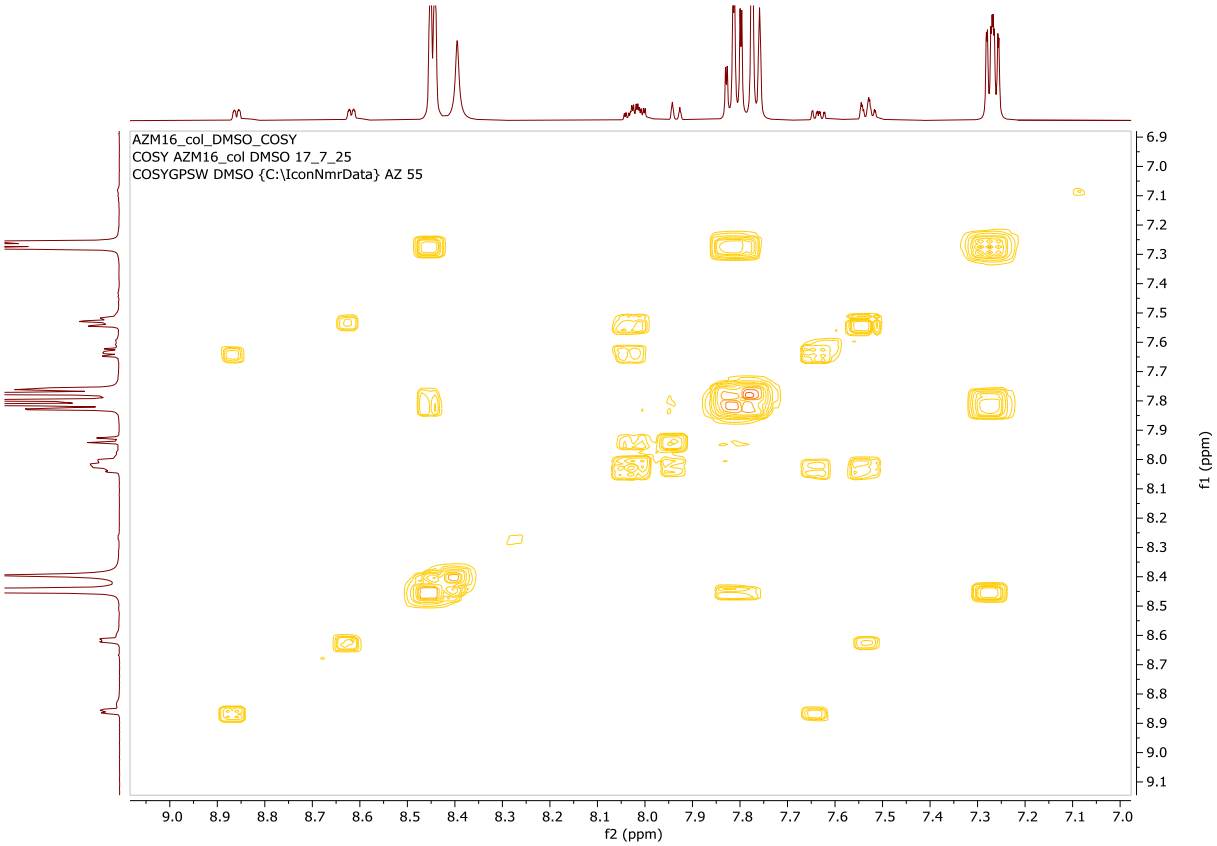

Figure A3.69: Selected range of the 2D ^{1}H-^{1}H COSY spectrum of **AZM16** at 298 K in DMSO-d_6.

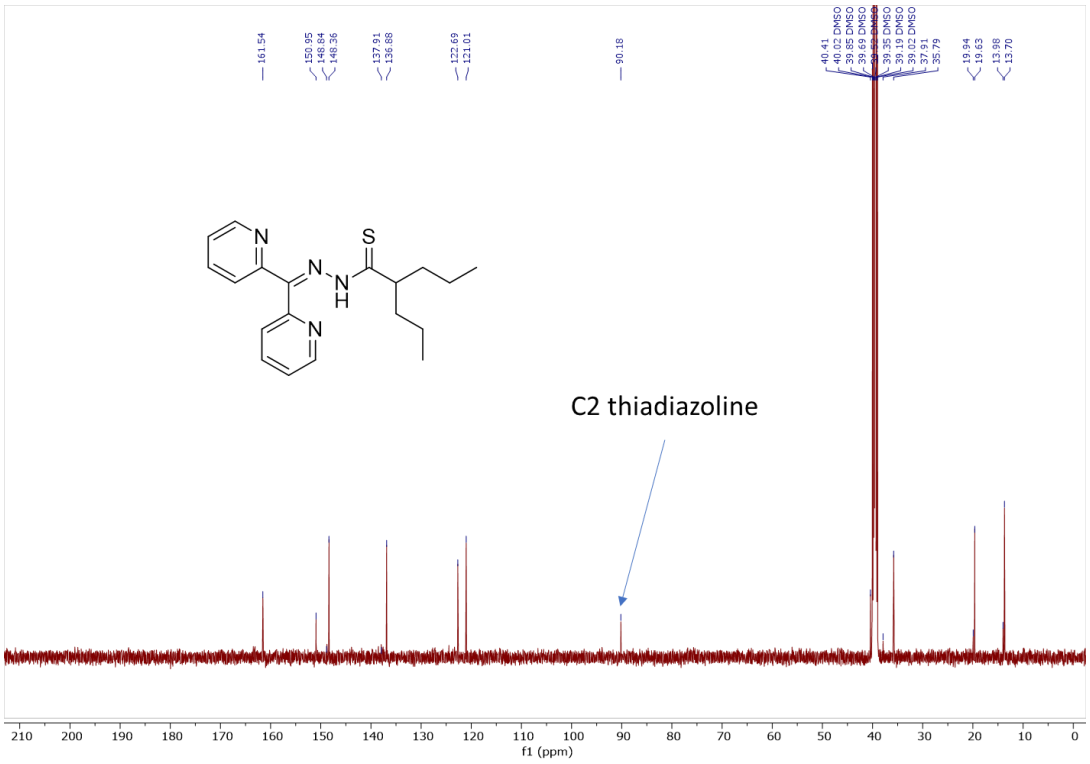

Figure A3.70: ^{13}C NMR (126 MHz, 298 K) spectrum of **AZM16** in DMSO-d_6.

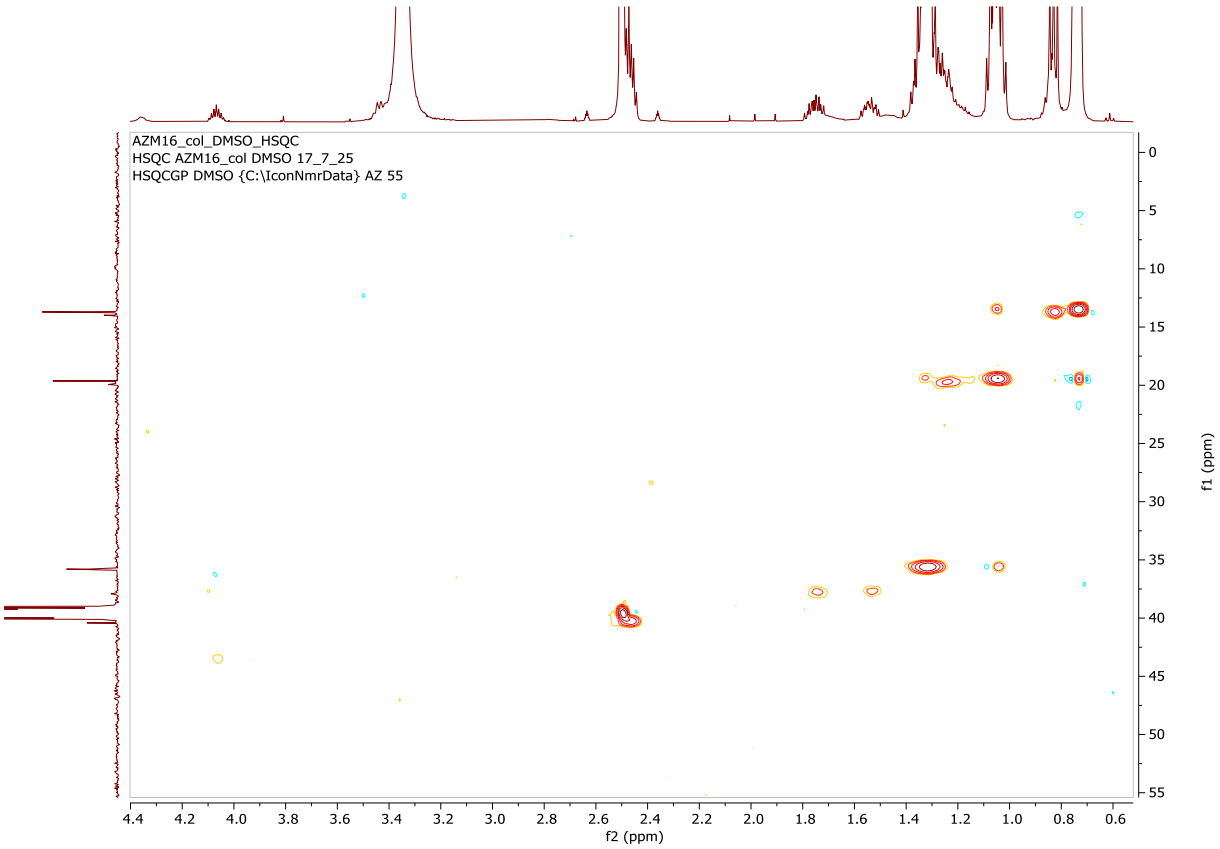

Figure A3.71: Selected range of the 2D ^{1}H-^{13}C HSQC spectrum of **AZM16** at 298 K in DMSO-d_6.

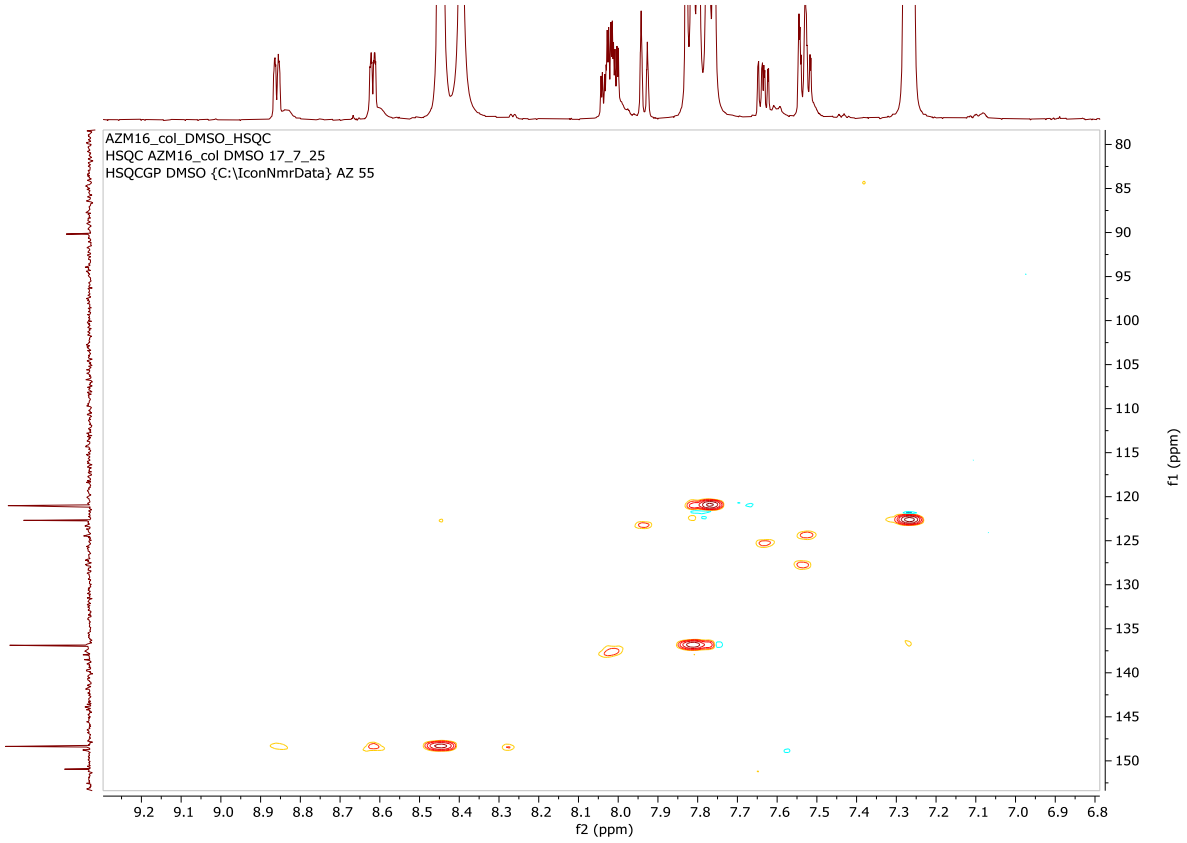

Figure A3.72: Selected range of the 2D ^{1}H-^{13}C HSQC spectrum of **AZM16** at 298 K in DMSO-d_6.

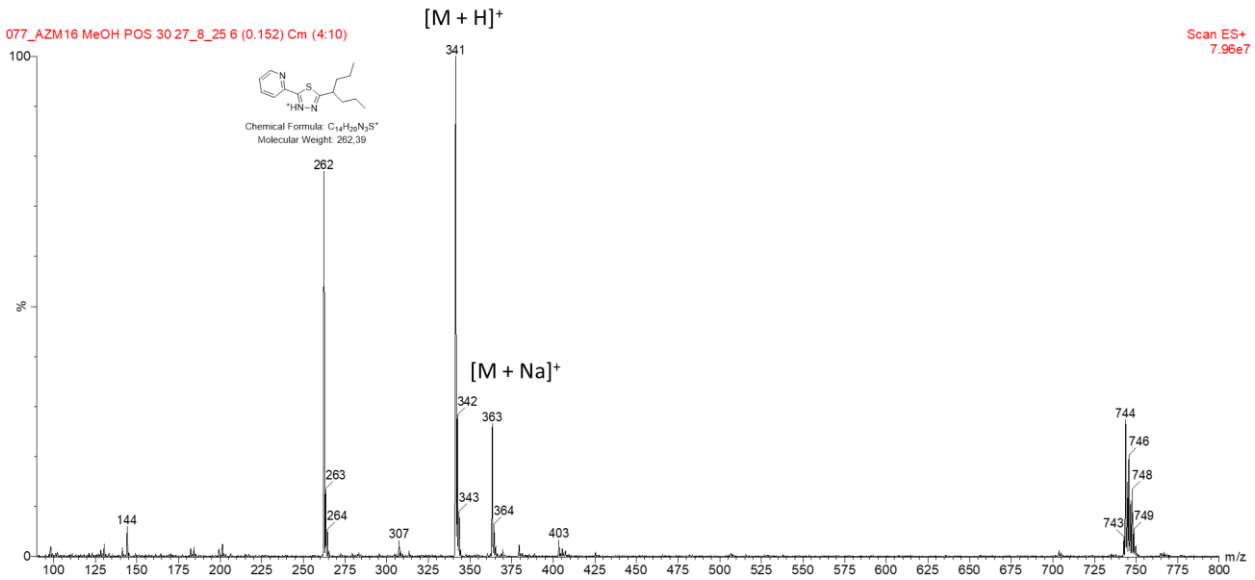

Figure A3.73: ESI-MS spectrum (positive ions, cone voltage 30) for **AZM16** in methanol.

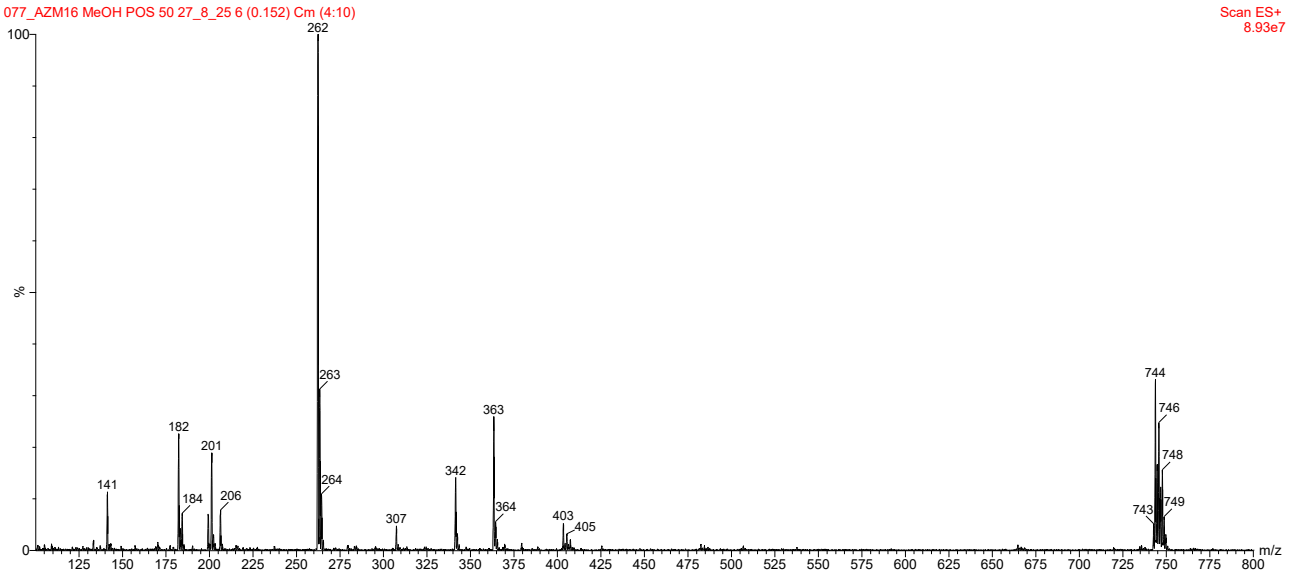

Figure A3.74: ESI-MS spectrum (positive ions, cone voltage 50) for **AZM16** in methanol.

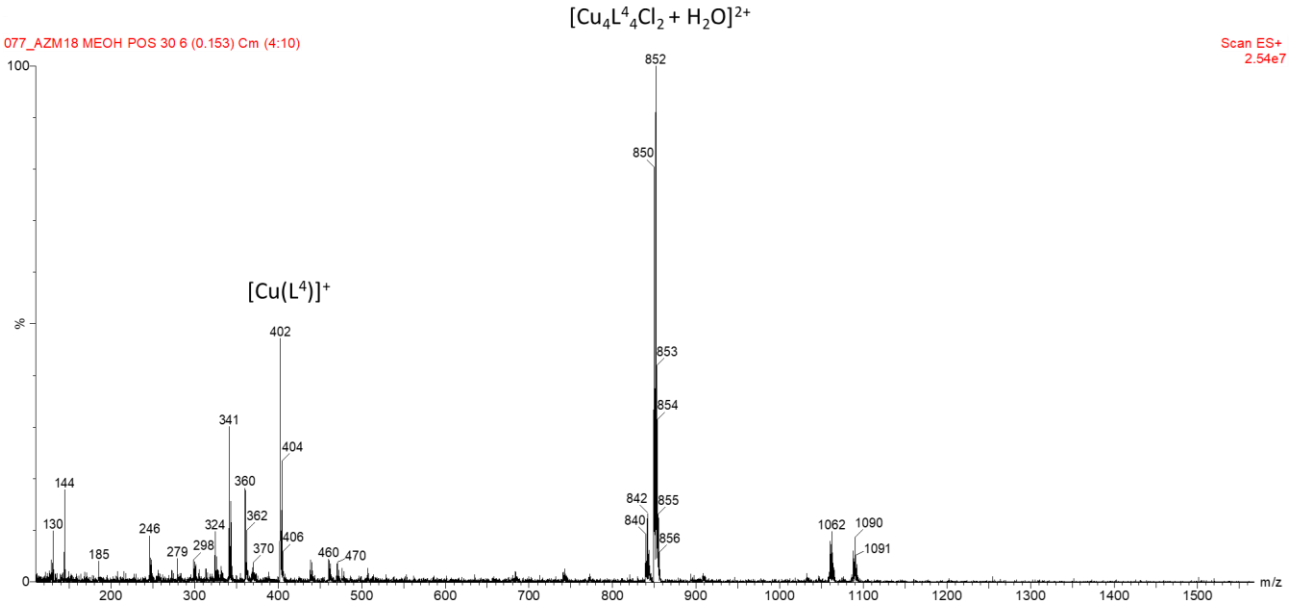

Figure A3.75: ESI-MS spectrum (positive ions) for **AZM18** in methanol.

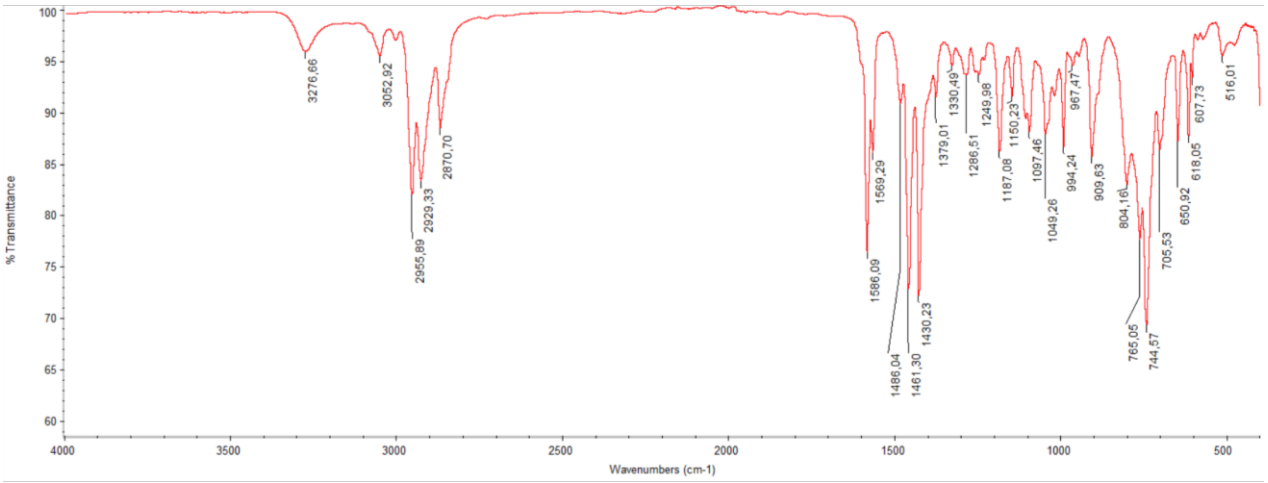

Figure A3.76: FT-IR spectrum of a solution of **AZM16** in $CDCl_3$. No bands in the range 2600 – 2500 cm^{-1} are observed.

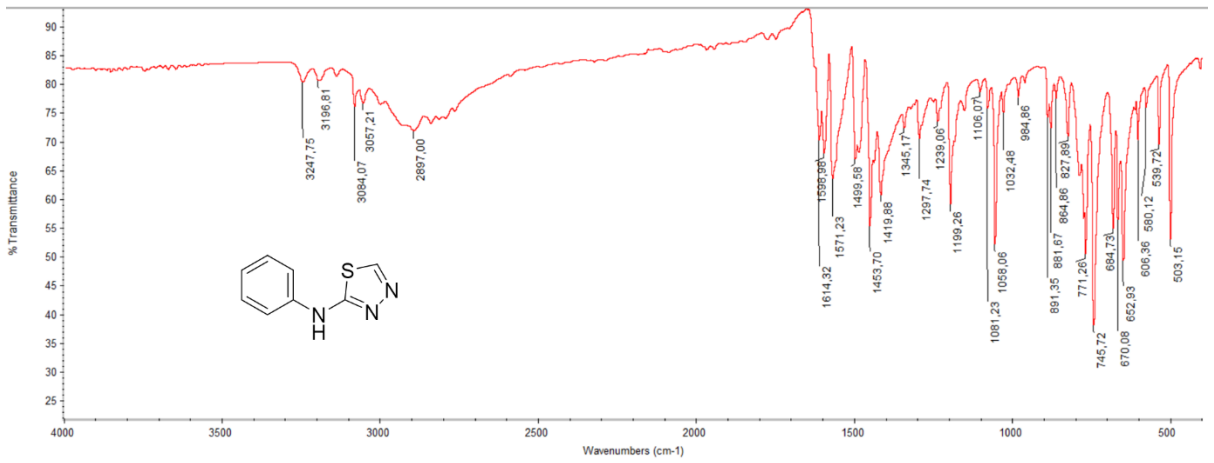

Figure A4.1: FT-IR spectrum of **AZ42**.

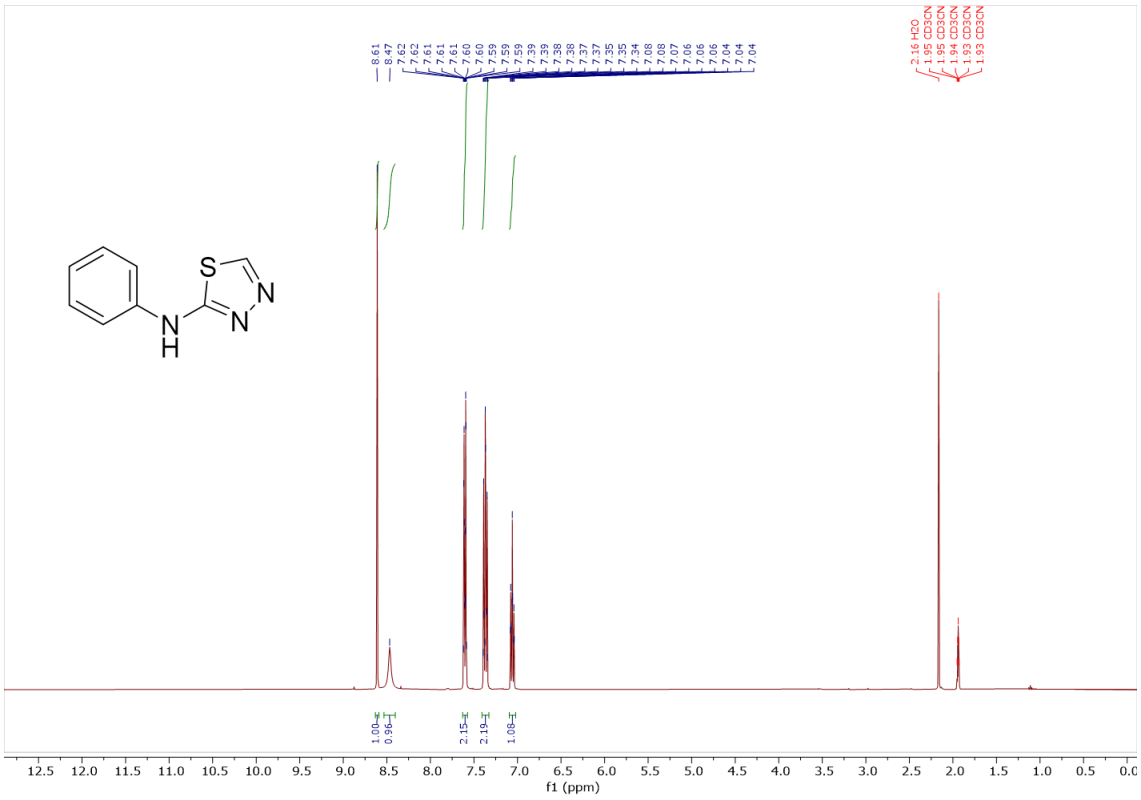

Figure A4.2: ^{1}H NMR (400 MHz, acetonitrile-d_3, 298 K) spectrum of **AZ42**.

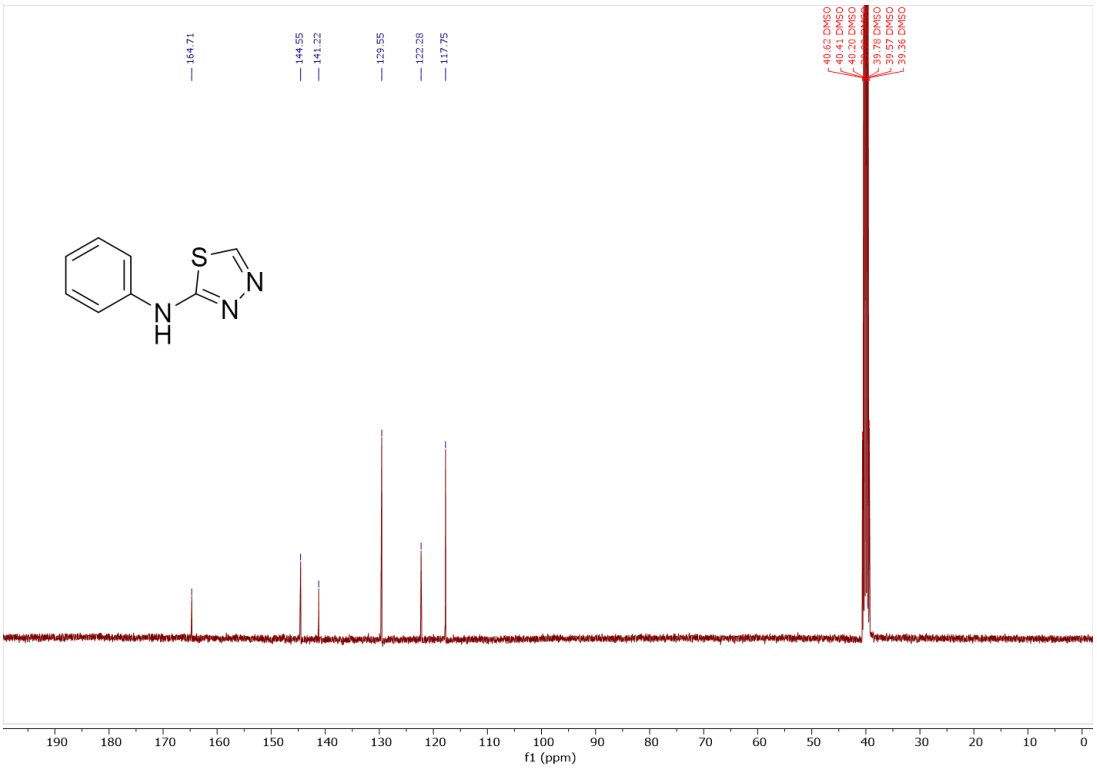

Figure A4.3: ^{13}C NMR (101 MHz, DMSO-d_6, 298 K) spectrum of **AZ42**.

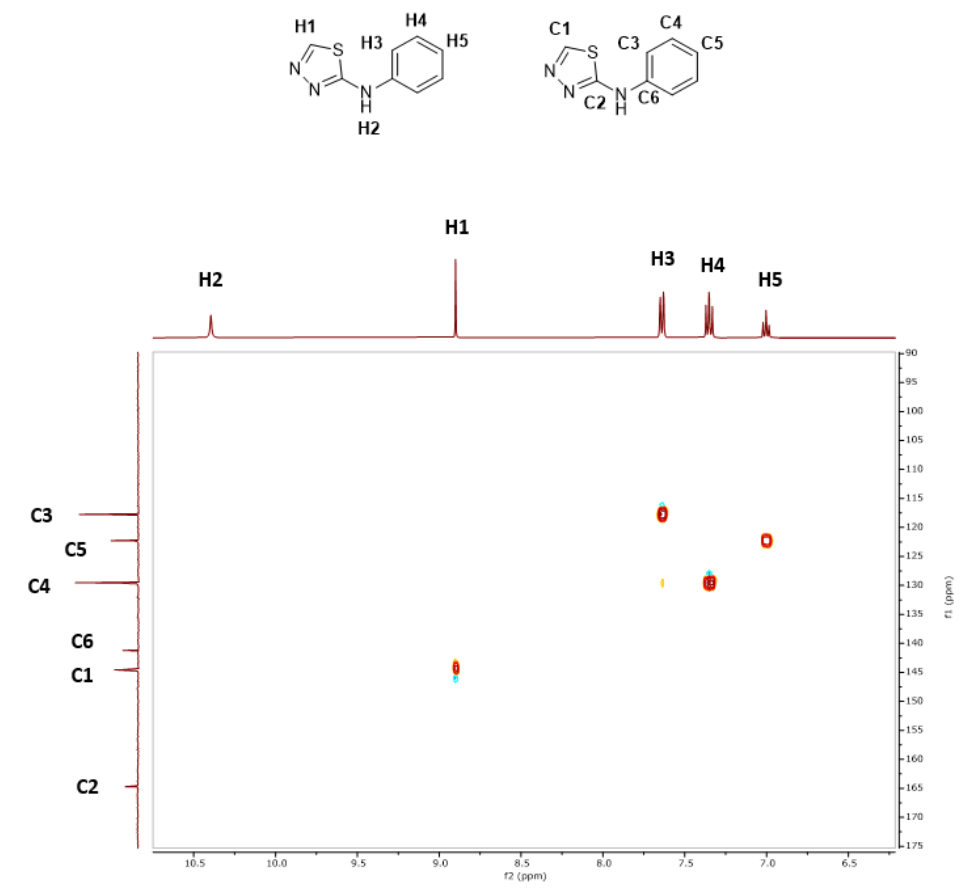

Figure A4.4: 2D ^{1}H-^{13}C HSQC spectrum of **AZ42** at 298 K in DMSO-d_6.

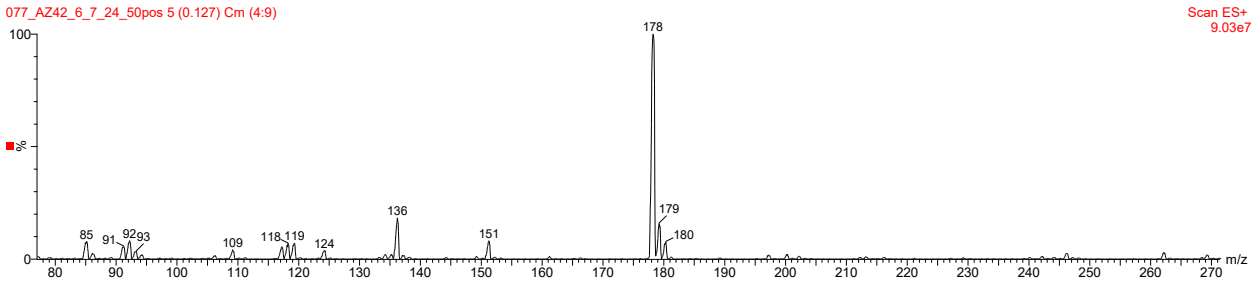

Figure A4.5: ESI-MS spectrum (positive ions) for **AZ42** in methanol.

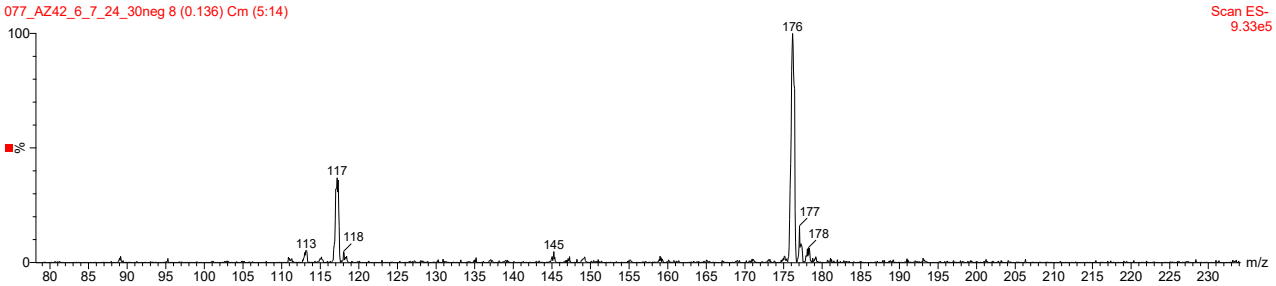

Figure A4.6: ESI-MS spectrum (negative ions) for **AZ42** in methanol.

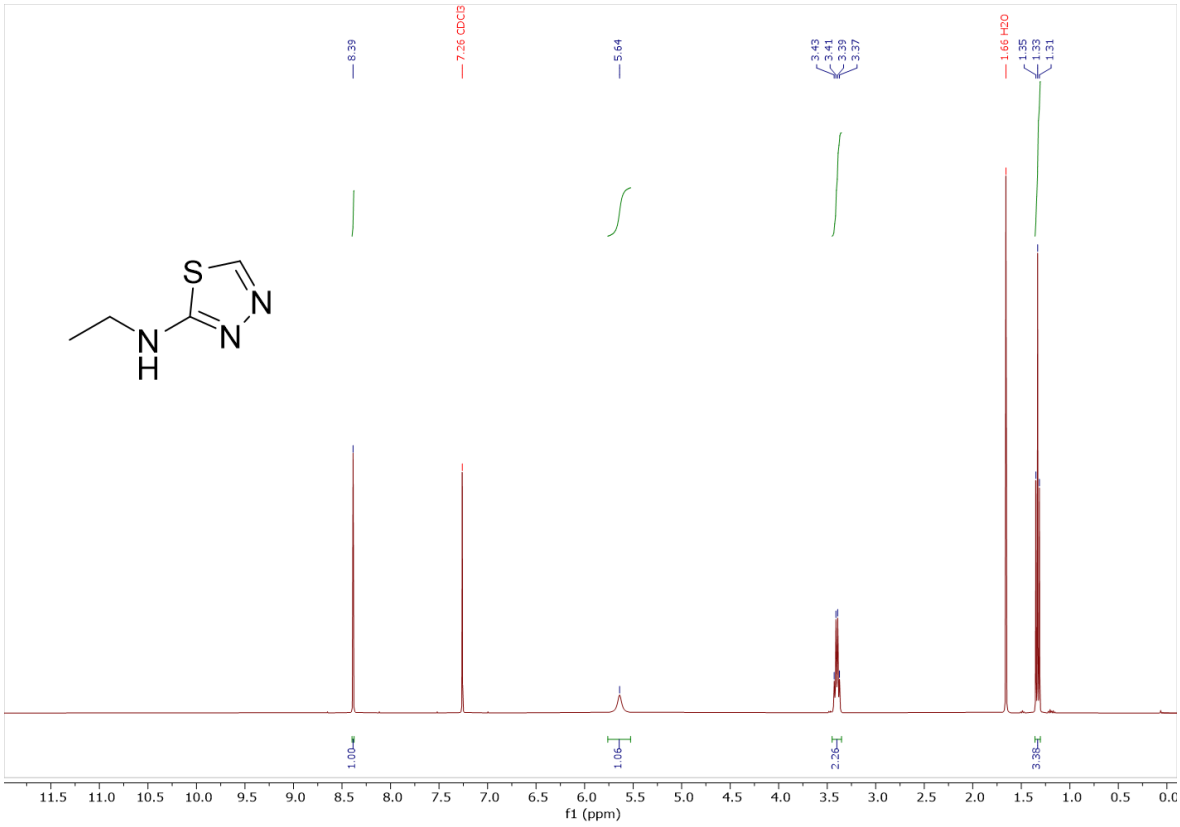

Figure A4.7: ^{1}H NMR (400 MHz, chloroform-*d*, 298 K) spectrum of **AZ50**.

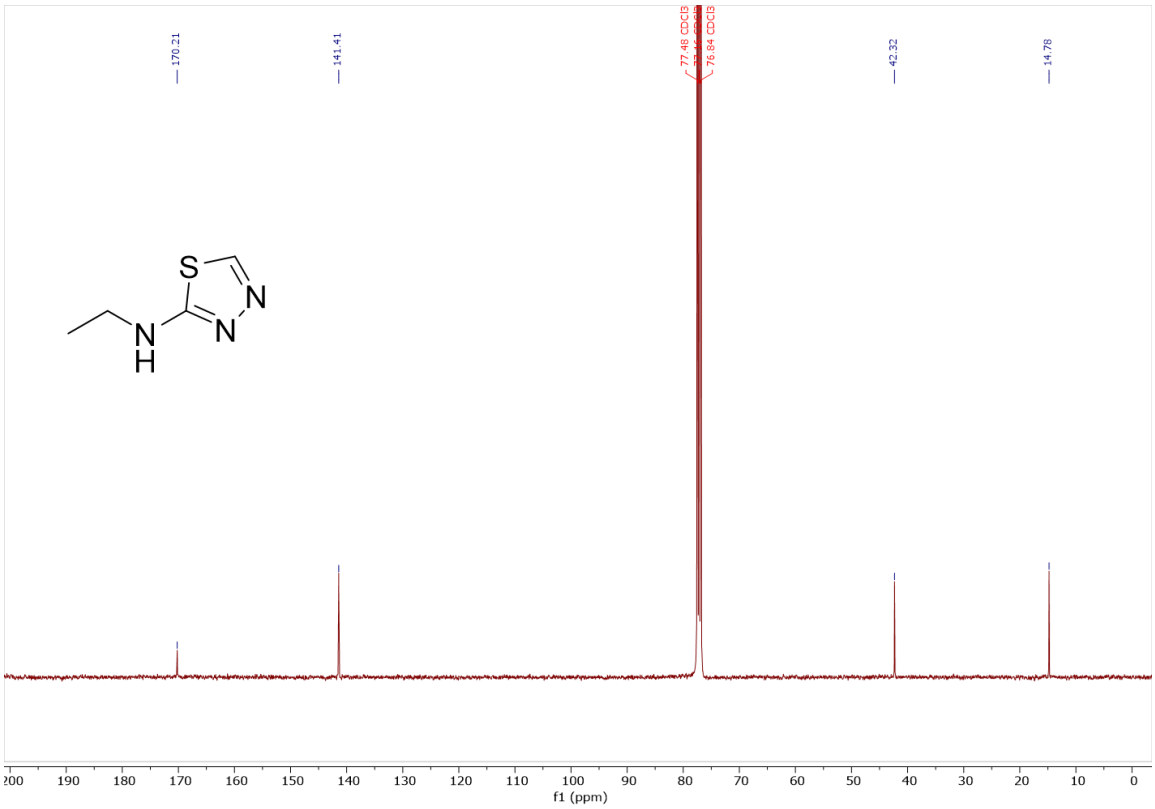

Figure A4.8: ^{13}C NMR (101 MHz, chloroform-*d,* 298 K) spectrum of **AZ50**.

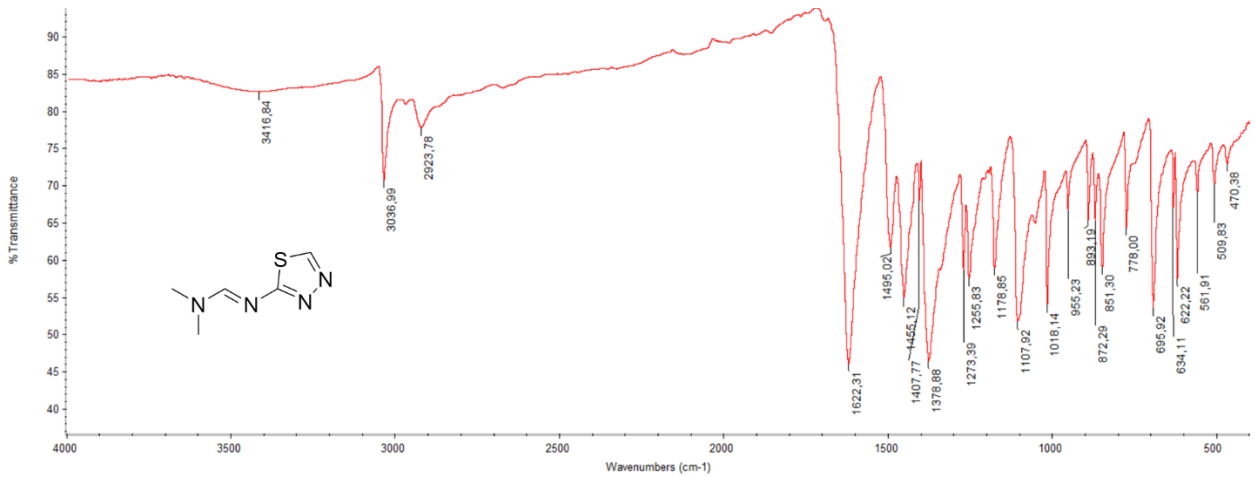

Figure A4.9: FT-IR spectrum of **AZ47**.

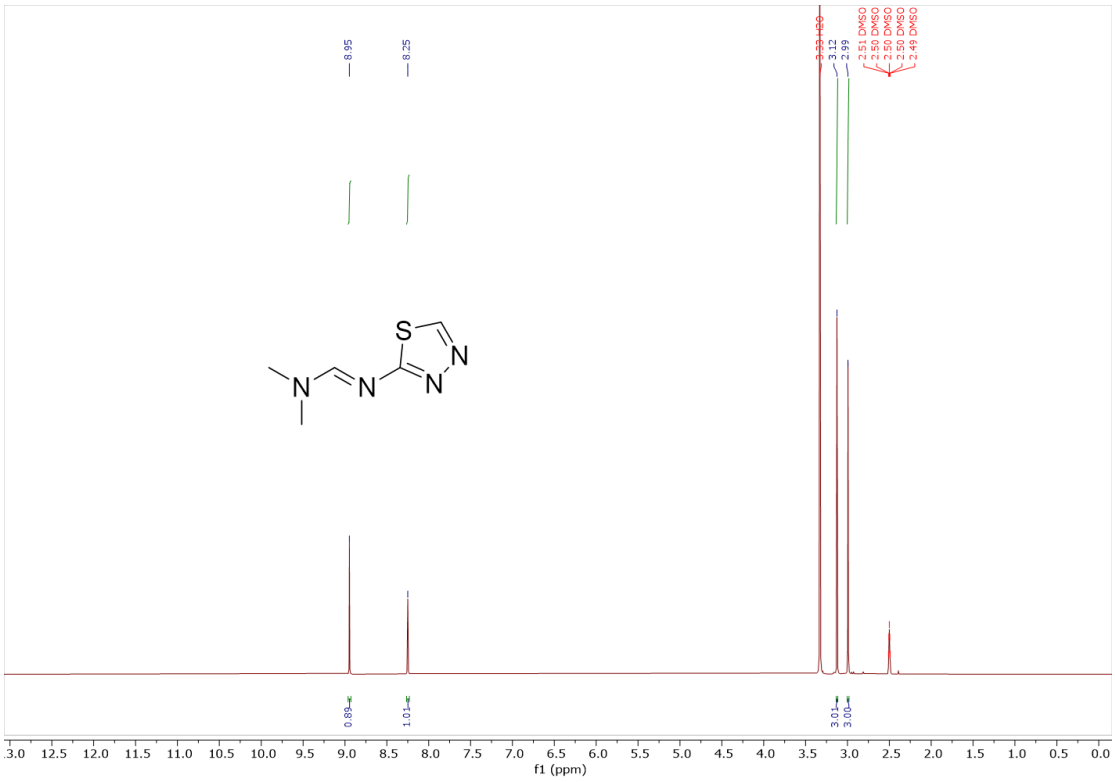

Figure A4.10: ^{1}H NMR (400 MHz, DMSO-d_6, 298 K) spectrum of **AZ47**.

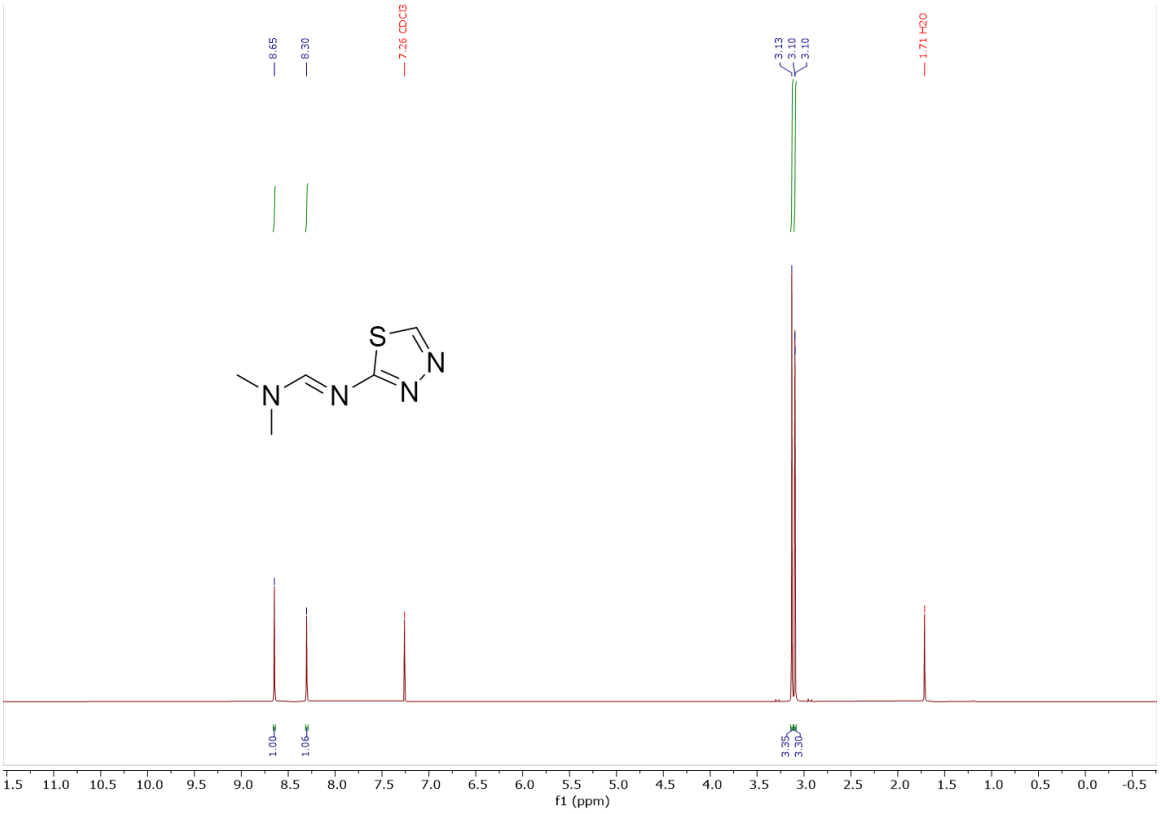

Figure A4.11: ^{1}H NMR (400 MHz, chloroform-*d*, 298 K) spectrum of **AZ47**.

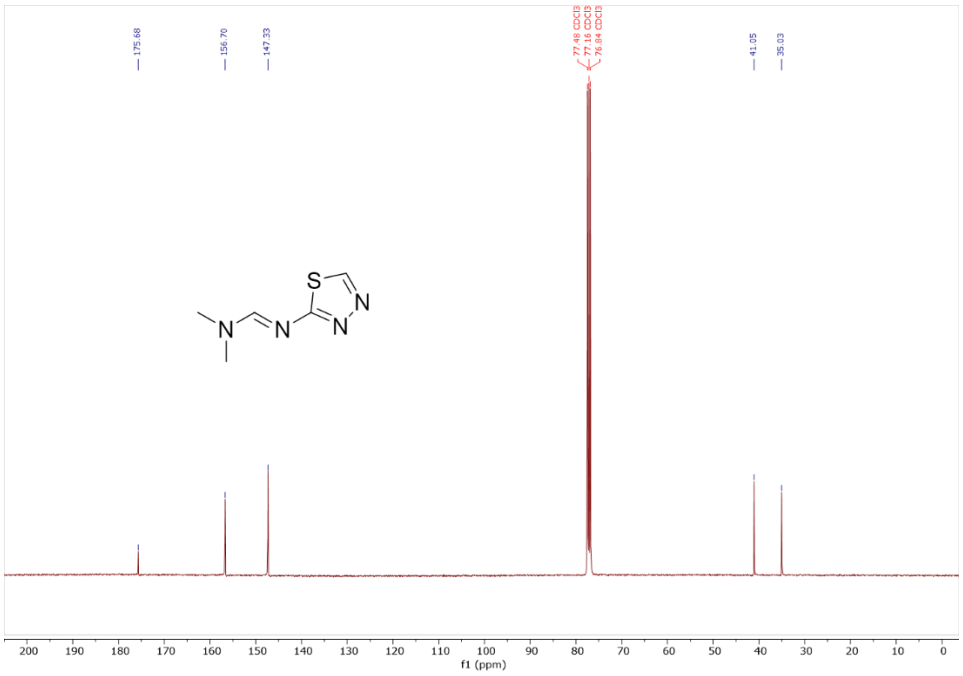

Figure A4.12: ^{13}C NMR (101 MHz, chloroform-*d,* 298 K) spectrum of **AZ47**.

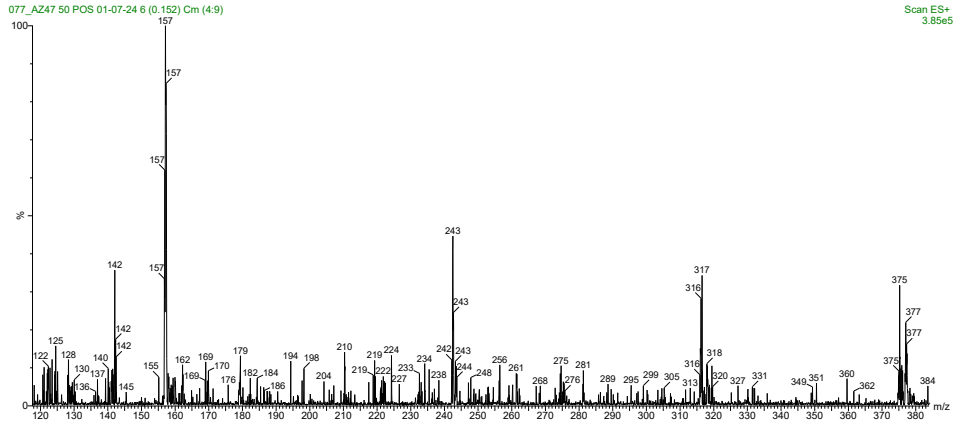

Figure A4.13: ESI-MS spectrum (positive ions) for **AZ47** in methanol.

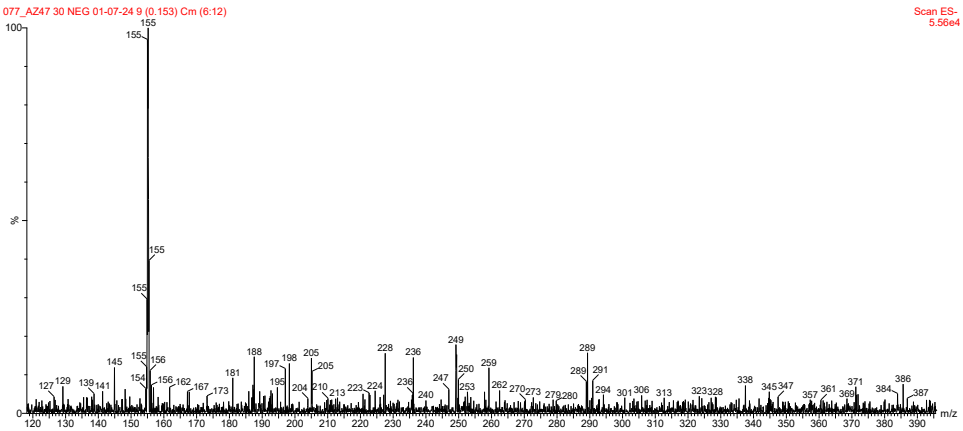

Figure A4.14: ESI-MS spectrum (negative ions) for **AZ47** in methanol.

Table A1: X-ray crystallographic data for N-(1,3,4-thiadiazol-2-yl)formamide.

Empirical formula	$4(C_3H_3N_3OS)$
Formula weight	516.5
Temperature/K	200.0
Diffractometer/detector	Bruker D8 Venture / PhotonII area
Radiation	MoKα (λ = 0.71073)
Crystal system	Monoclinic
Space group	*P* 21/n
a/Å	12.3351(5)
b/Å	10.1554(4)
c/Å	16.6886(7)
α/°	90
β/°	95.961(1)
γ/°	90
Volume/Å3	2079.24(15)
Z	4
ρcalc /g·cm^{-3}	1.650
μ/mm-1	0.51
F(000)	1056
Θ range for data	1.164 – 29.893
	-16<h<16
Index ranges	0<k<13
	0<l<22
Reflections collected	99931
Unique reflections	5130
Parameters	297
Goodness-of-fit on F^2	1.055
Final R indexes [I>=2σ	R=0.046, wR2=0.113

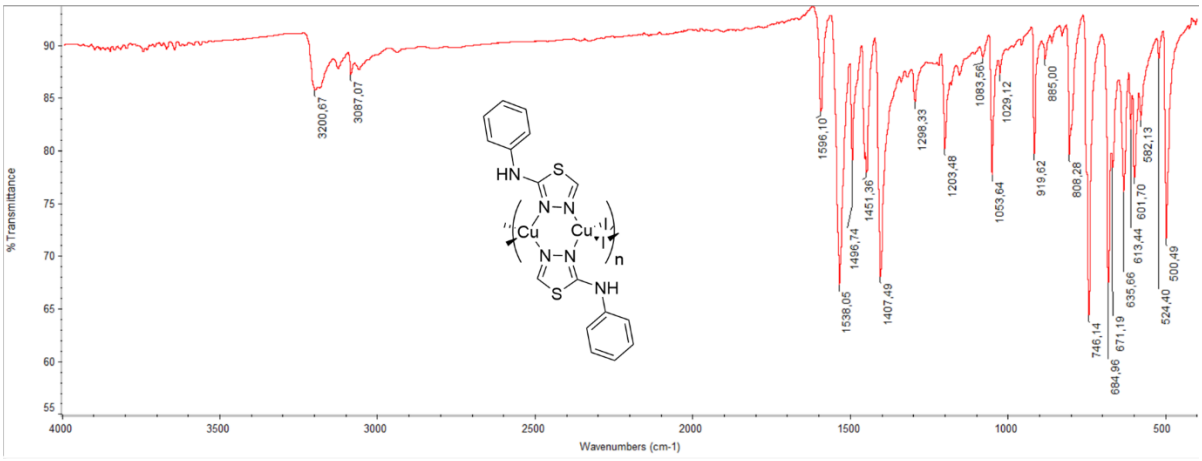

Figure A4.15: FT-IR spectrum of **AZ45**.

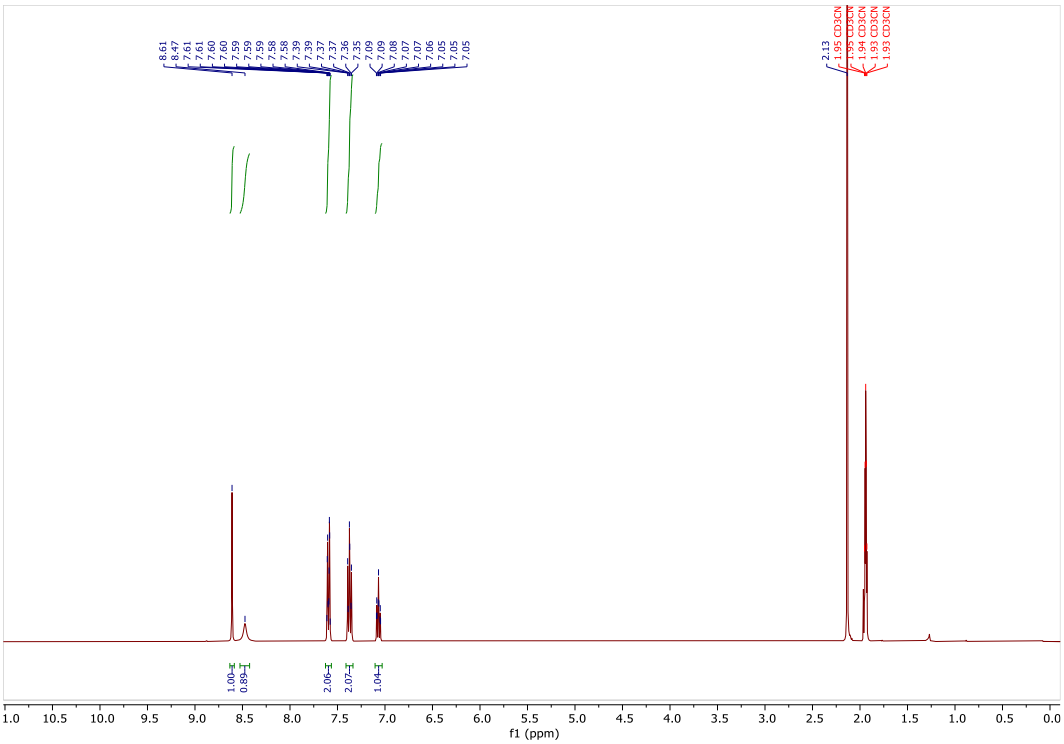

Figure A4.16: ^{1}H NMR (400 MHz, acetonitrile-d_3, 298 K) spectrum of **AZ45**.

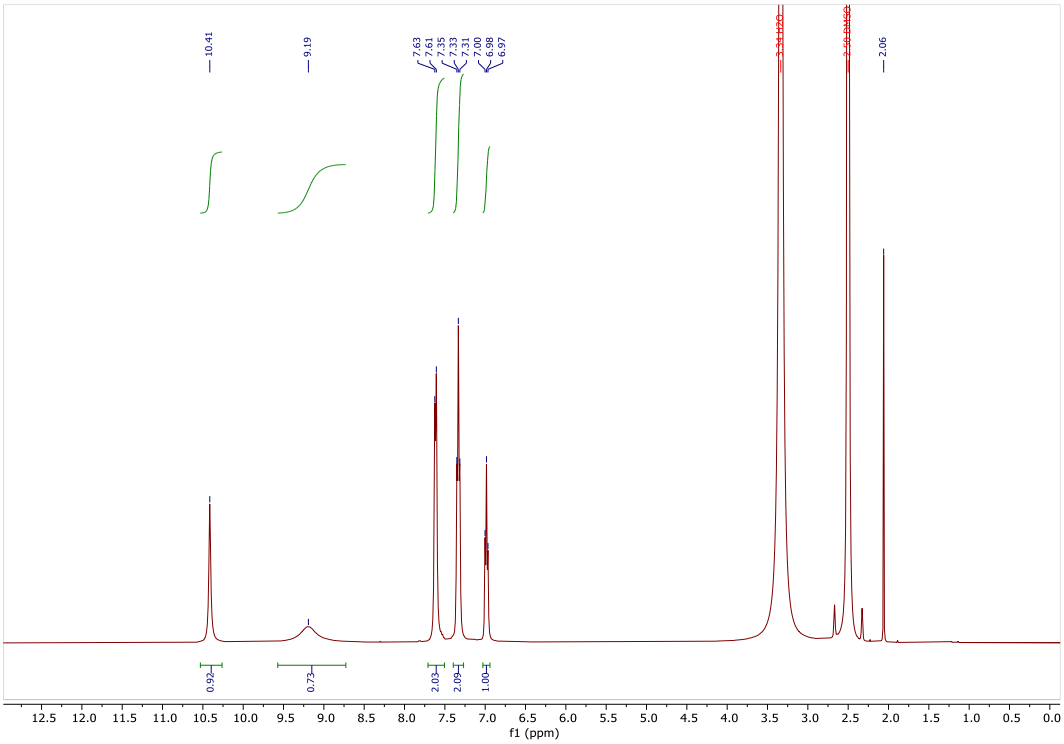

Figure A4.17: ^{1}H NMR (400 MHz, DMSO-d_6, 298 K) spectrum of **AZ45**.

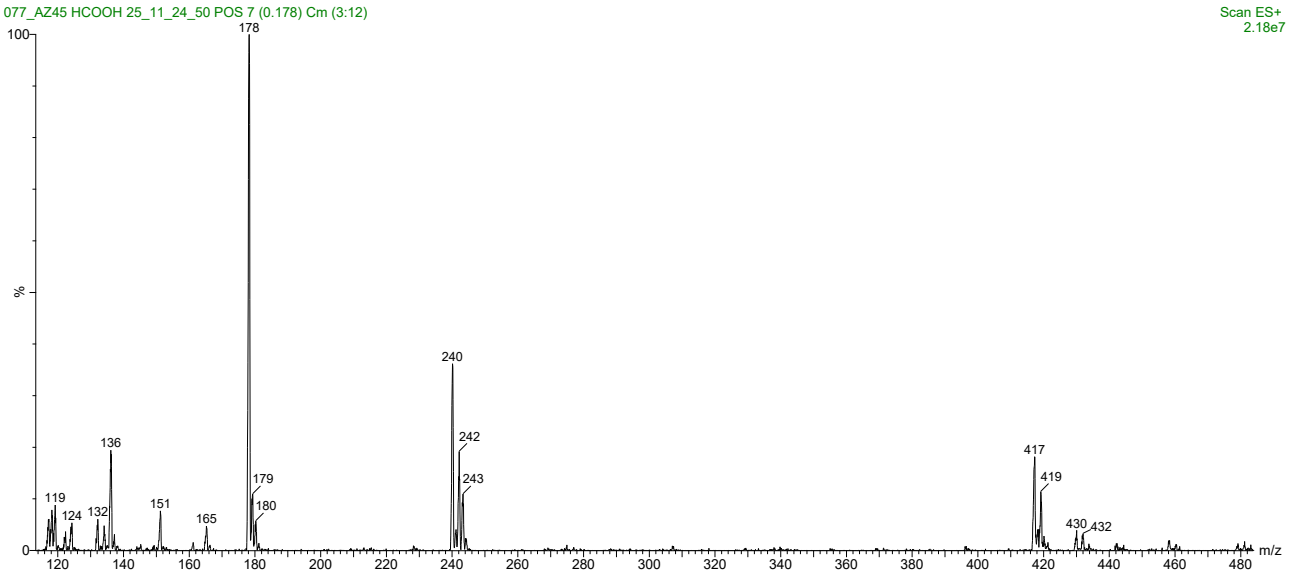

Figure A4.18: ESI-MS spectrum (positive ions) for **AZ45** in acetonitrile with one drop of formic acid.

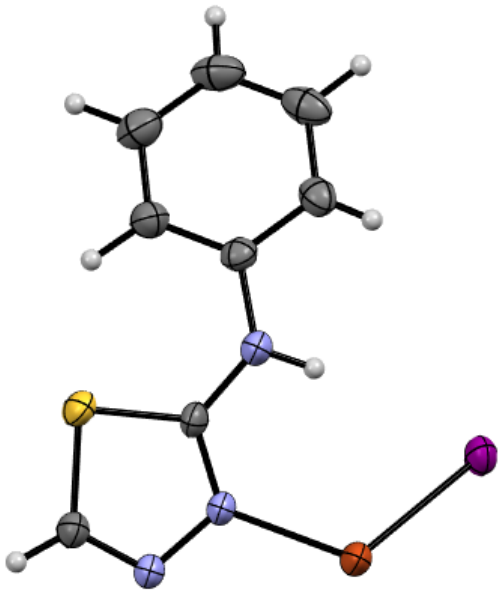

Figure A4.19: ORTEP representation of the asymmetric unit of **[CuIL]$_n$** (**AZ45**).

Table A2: X-ray crystallographic data for **AZ45**.

Compound	$[CuIL]_n$
Empirical formula	C16 H14 Cu2 I2 N6 S2
Formula weight	735.33
Temperature/K	200.0
Diffractometer/detector	Bruker D8 Venture / PhotonII area
Radiation	MoKα (λ = 0.71073)
Crystal system	Monoclinic

Space group	*P* 21/n
a/Å	7.4624(3)
b/Å	6.1009(2)
c/Å	23.0743(10)
α/°	90
β/°	98.869(1)
γ/°	90
Volume/Å3	1037.95(7)
Z	2
ρcalc /g·cm^{-3}	2.353
μ/mm-1	5.24
F(000)	696
Θ range for data	2.769 – 26.360
	-8<h<8
Index ranges	-6<k<7
	-27<l<27
Reflections collected	11145
Unique reflections	1826
Parameters	155
Goodness-of-fit on F^2	1.055
Final R indexes [I>=2σ	R=0.023, wR2=0.048

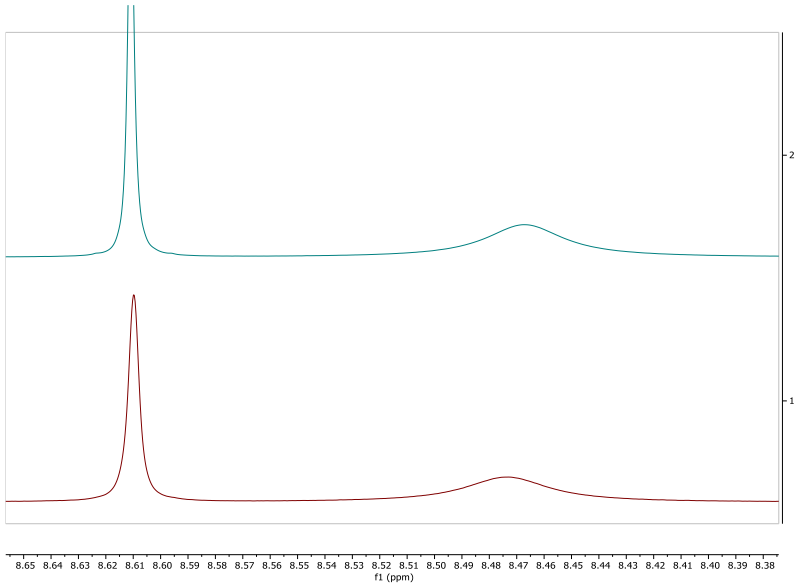

Figure A4.20: ^{1}H NMR (400 MHz, 298 K) spectra of **L** (top) and **[CuIL]$_n$** (bottom) in acetonitrile-d_3 (range: 8.38 – 8.65 ppm).

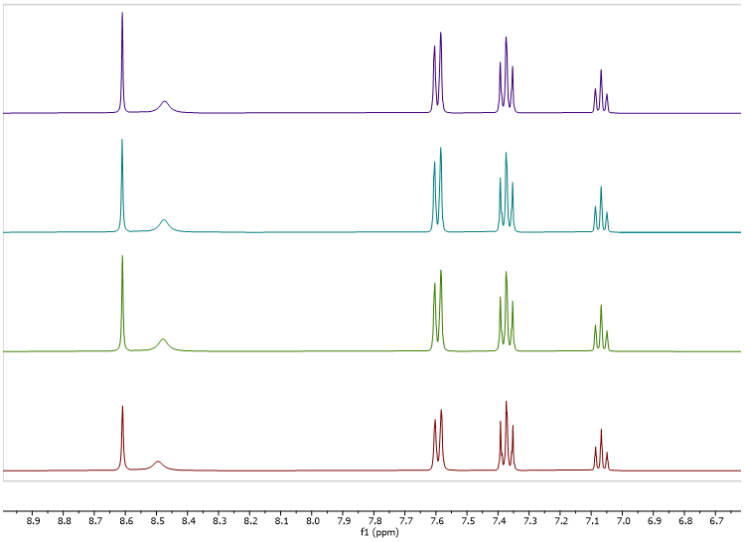

Figure A4.21: ^{1}H NMR (400 MHz, 298 K) spectrum of **[CuIL]$_n$** in acetonitrile-d_3: few minutes after sample preparation (in purple), after 24 h (in cyan), after 48 h (in green) and after 1 week (in red).

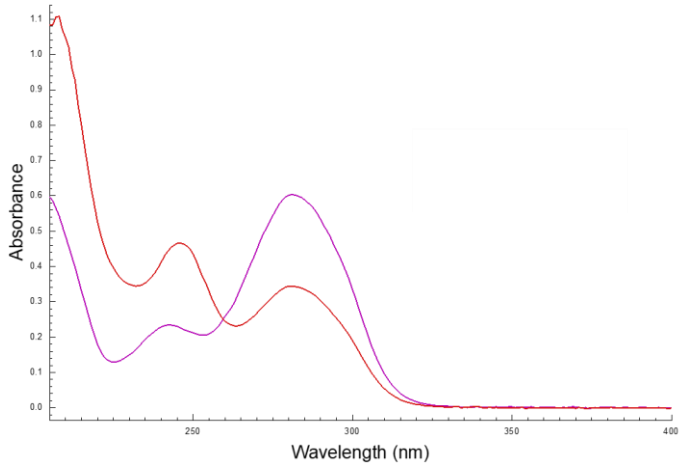

Figure A4.22: UV-visible spectra of **L** (C = 50 µM; purple line) and **[CuIL]$_n$** (C = 25 µM; red line) in acetonitrile.

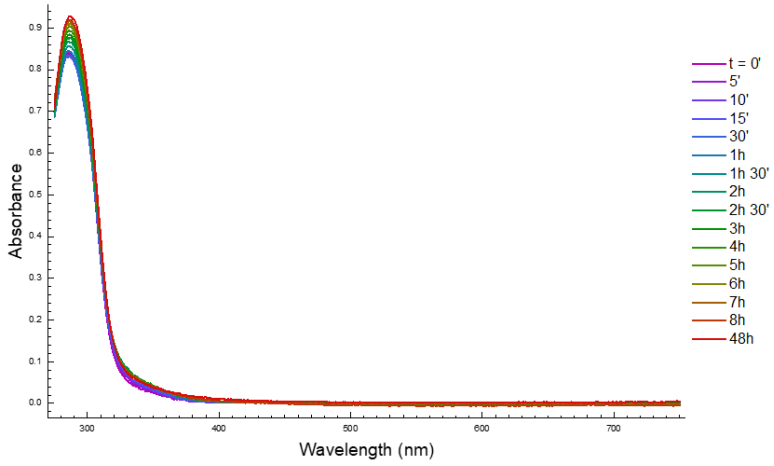

Figure A4.23: Evolution of the UV-visible spectrum of **[CuIL]$_n$** in DMSO over 48 h (C = 50 µM; r.t.).

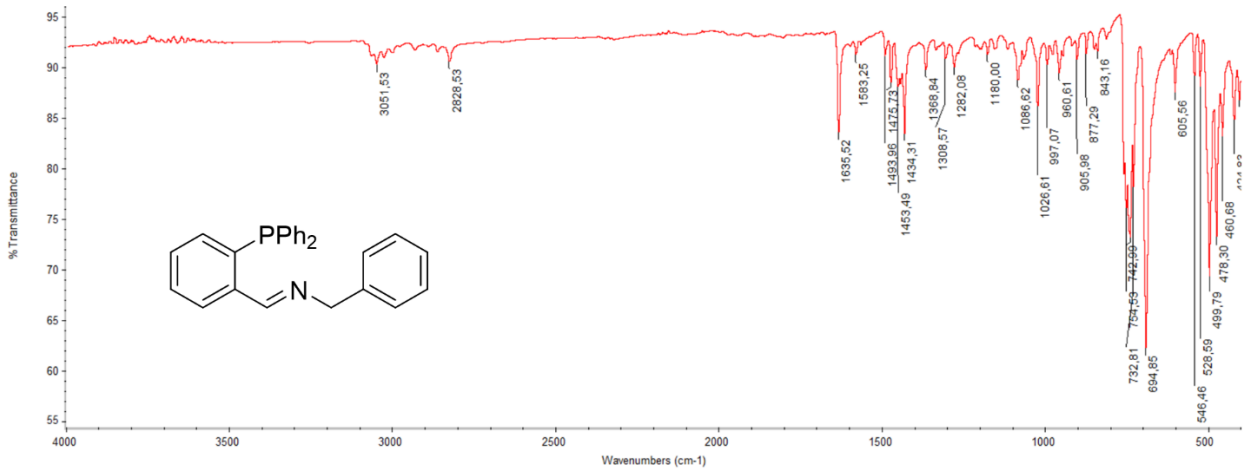

Figure A5.1: FT-IR spectrum of **AZ39**.

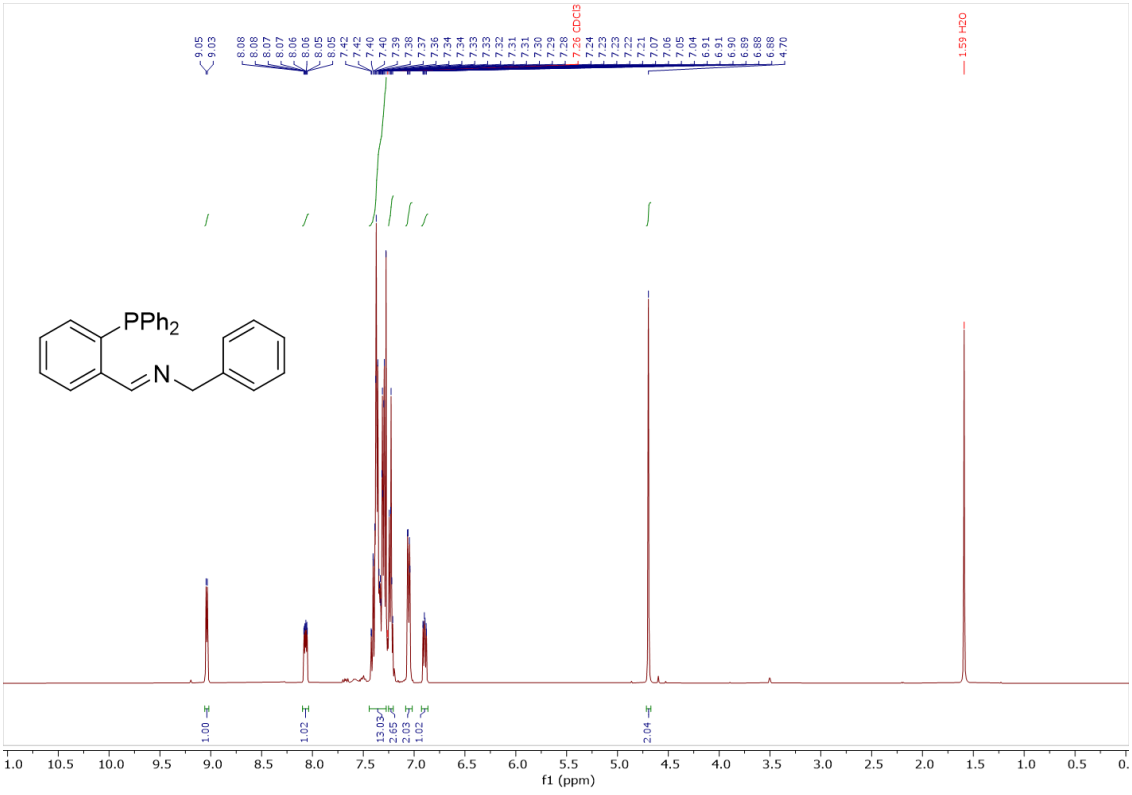

Figure A5.2: ^{1}H NMR (400 MHz, Chloroform-*d,* 298 K) spectrum of **AZ39**.

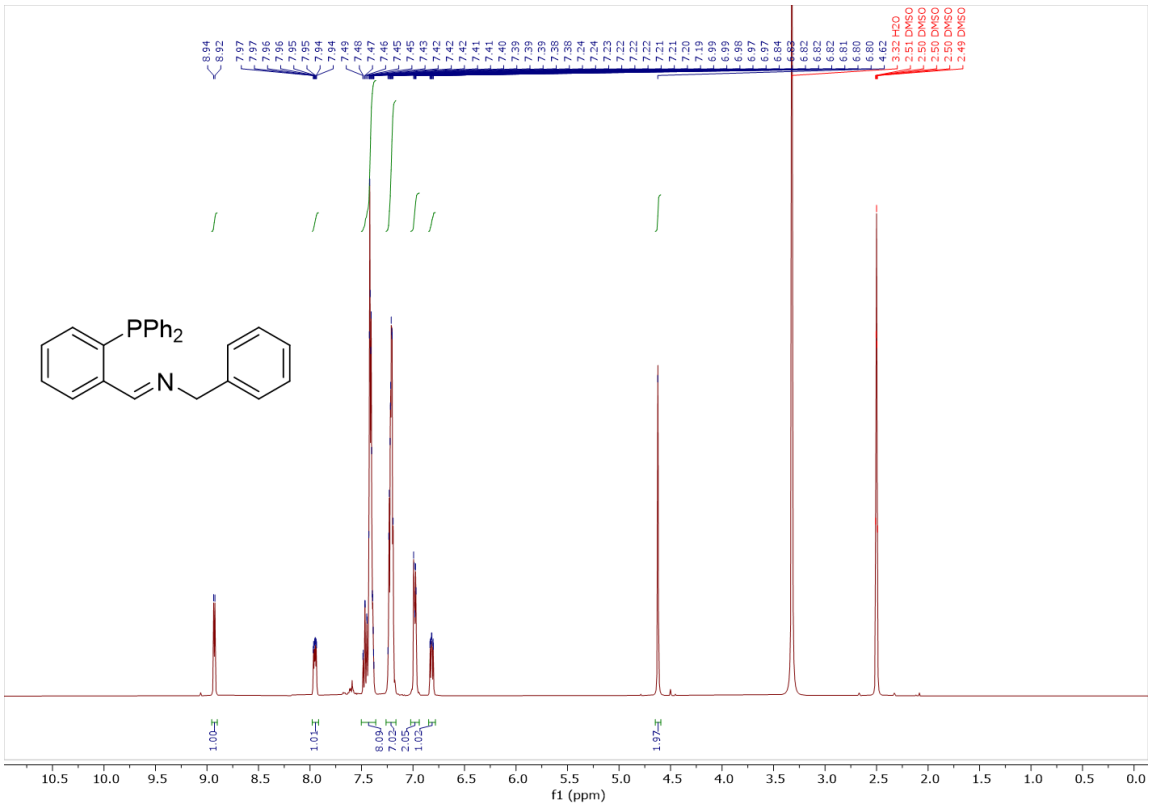

Figure A5.3: ^{1}H NMR (400 MHz, DMSO-d_6, 298 K) spectrum of **AZ39**.

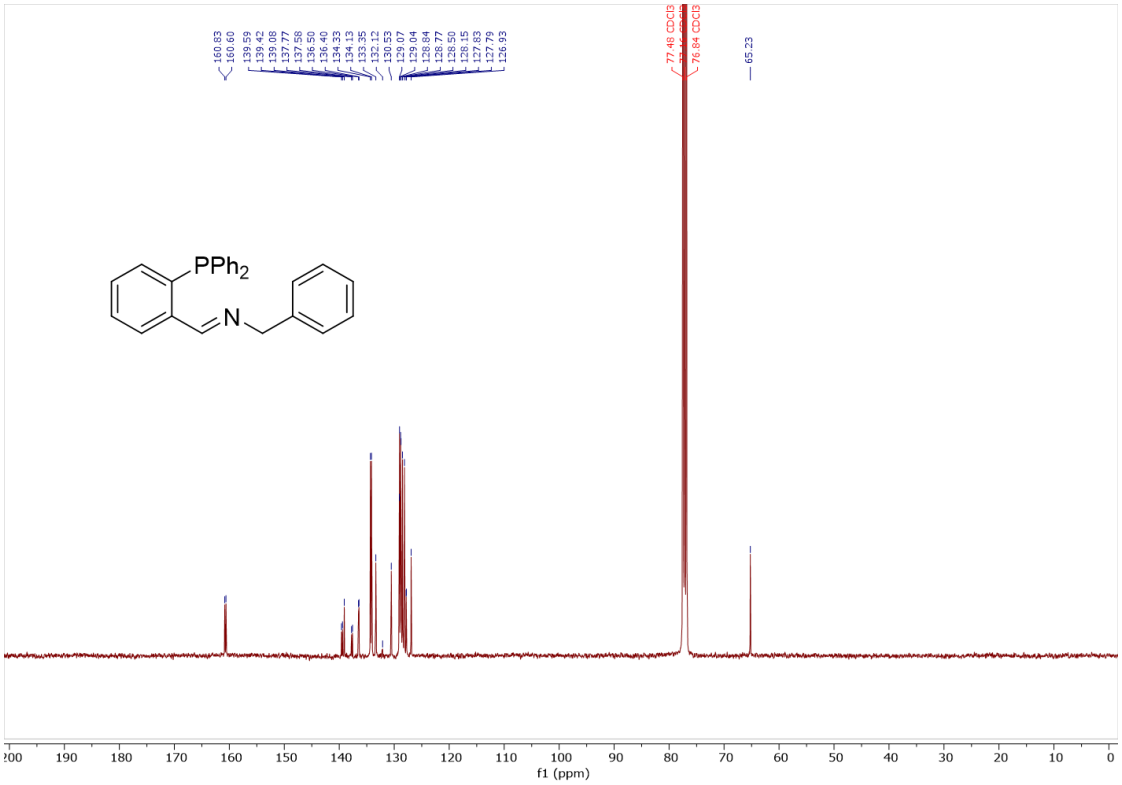

Figure A5.4: ^{13}C NMR (101 MHz, Chloroform-*d*, 298 K) spectrum of **AZ39**.

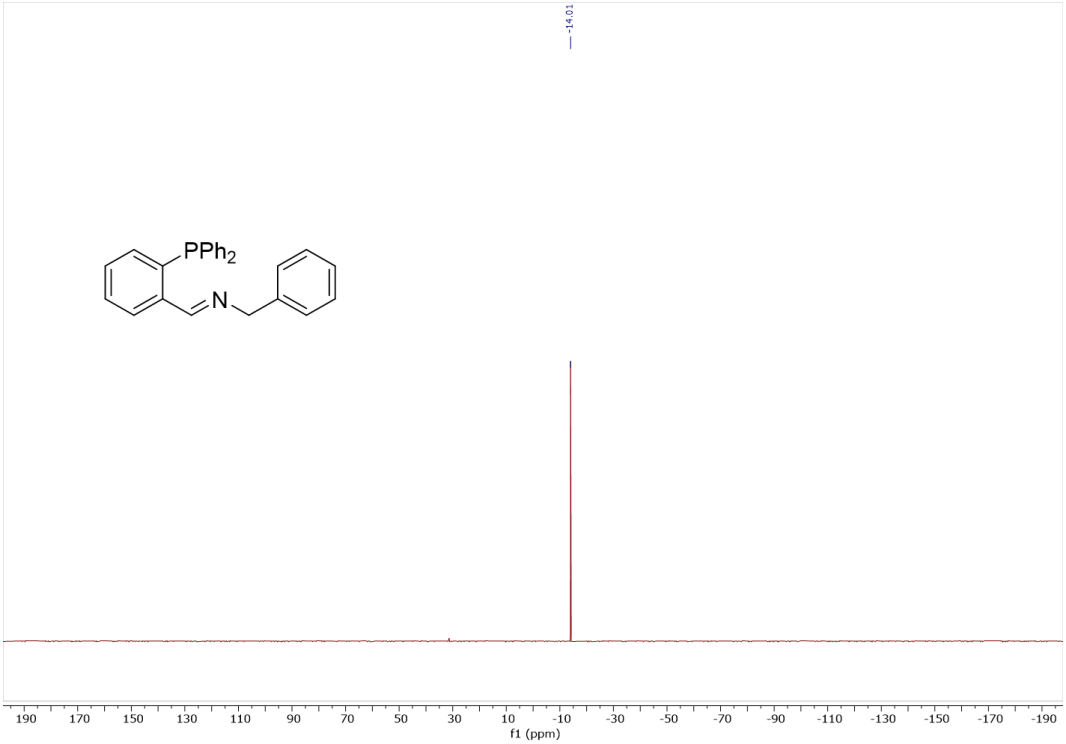

Figure A5.5: ^{31}P NMR (162 MHz, Chloroform-*d*, 298 K) spectrum of **AZ39**.

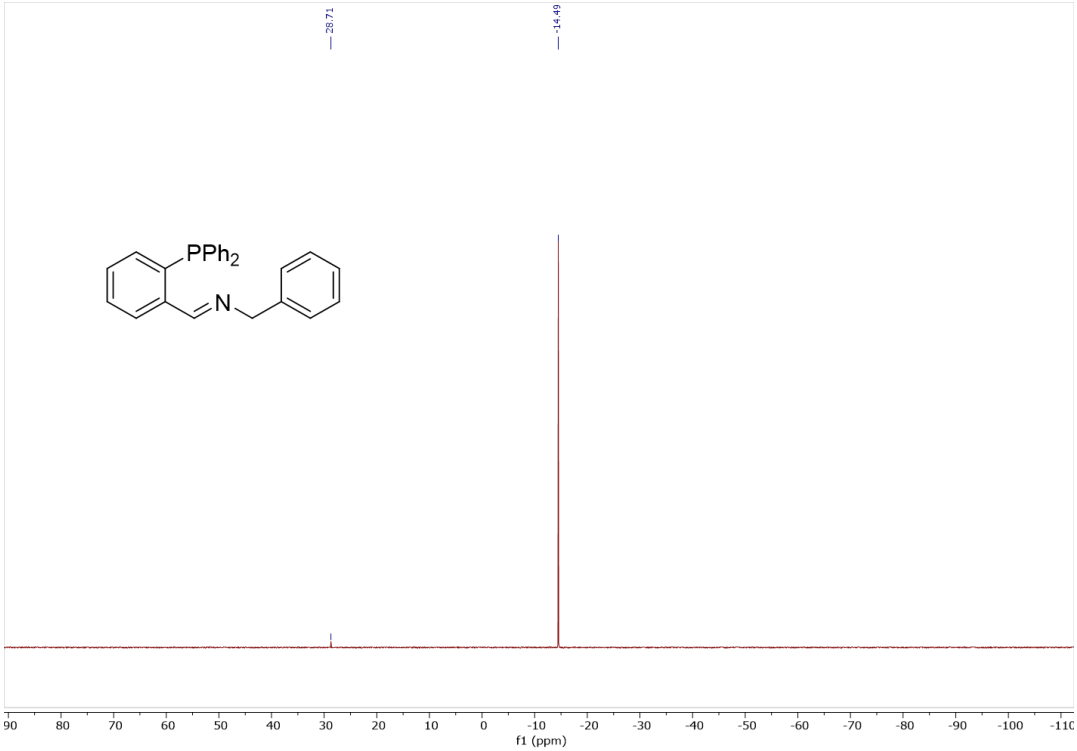

Figure A5.6: ^{31}P NMR (162 MHz, DMSO-d_6, 298 K) spectrum of **AZ39**.

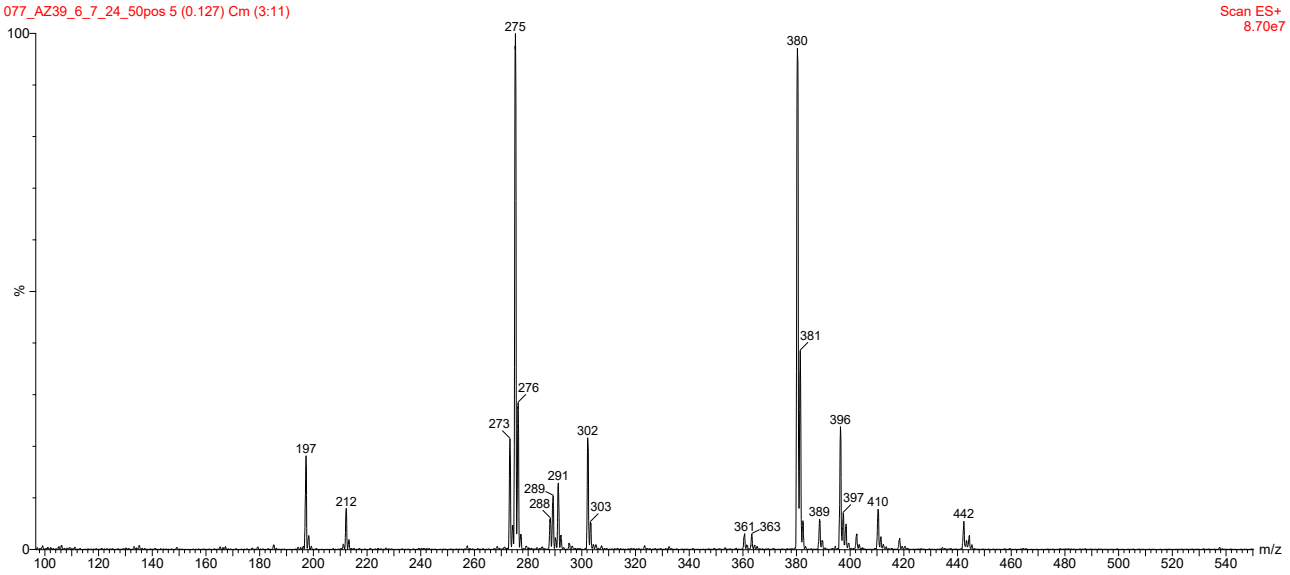

Figure A5.7: ESI-MS spectrum (positive ions) for **AZ39** in methanol.

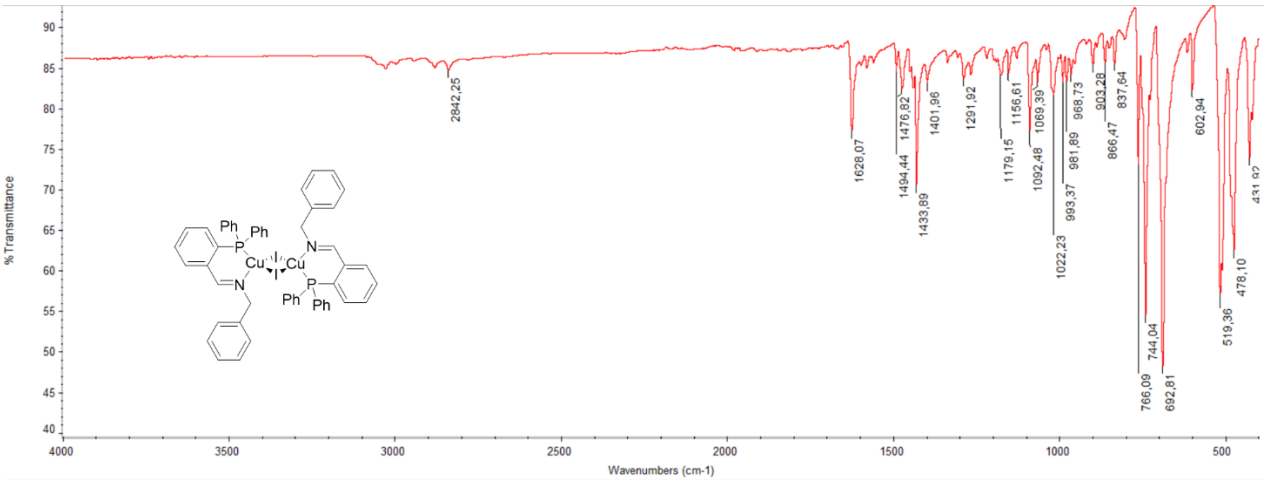

Figure A5.8: FT-IR spectrum of **AZ46**.

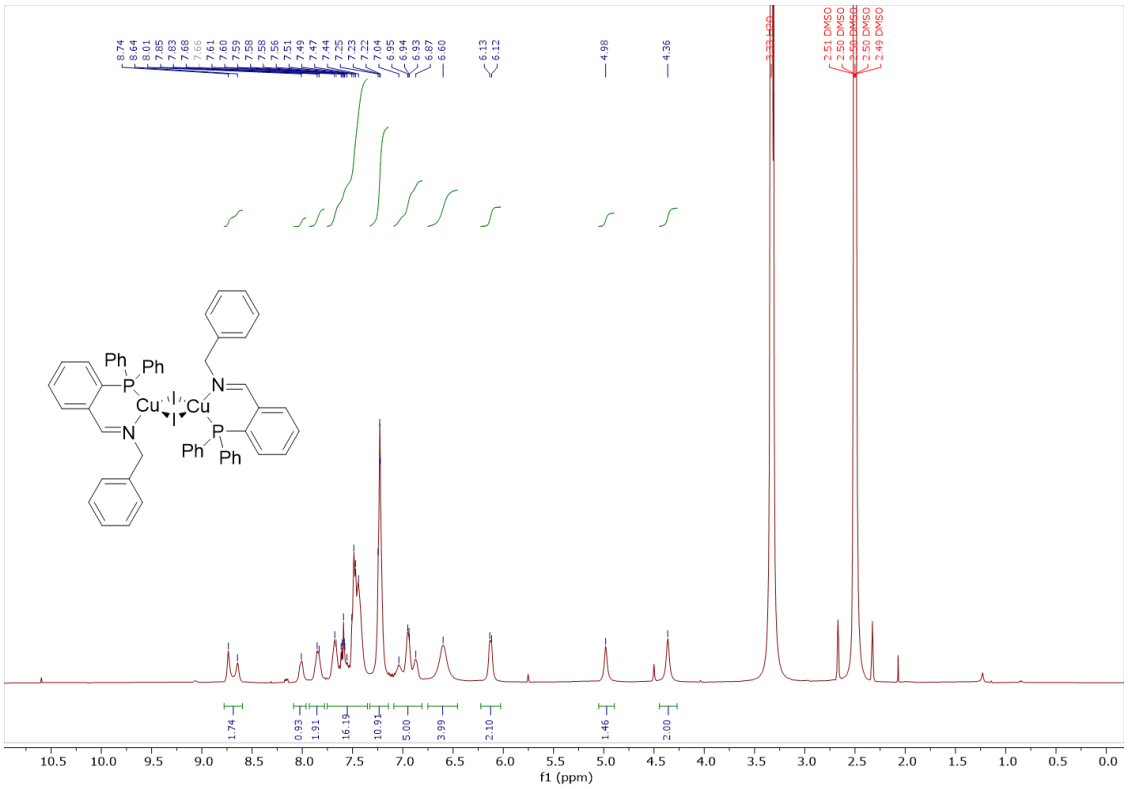

Figure A5.9: ^{1}H NMR (400 MHz, DMSO-d_6, 298 K) spectrum of **AZ46**.

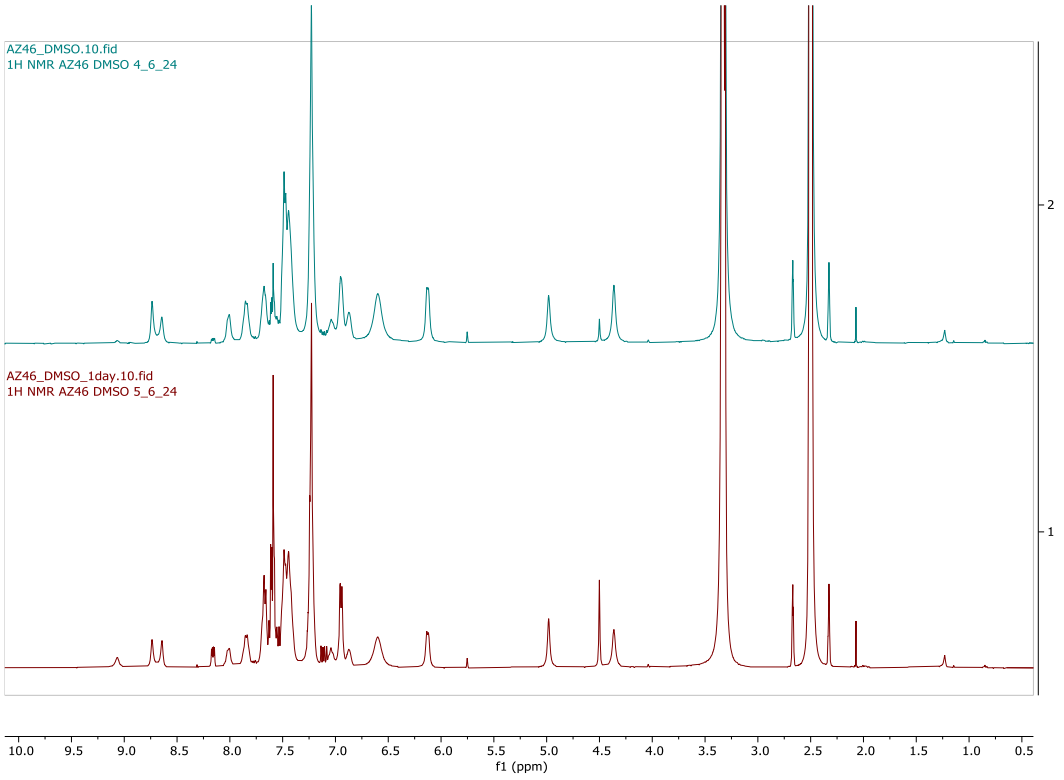

Figure A5.10: ^{1}H NMR (400 MHz, DMSO-d_6, 298 K) spectrum of **AZ46** immediately after preparation of the sample (top) and after one day (bottom).

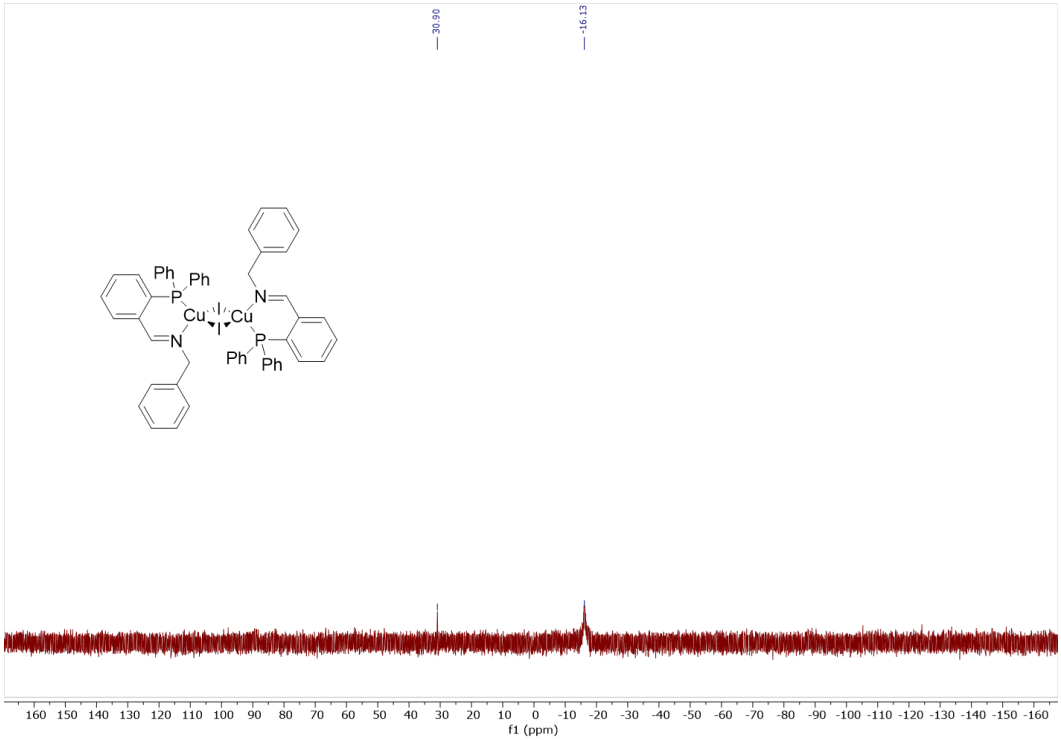

Figure A5.11: ^{31}P NMR (162 MHz, Chloroform-*d*, 298 K) spectrum of **AZ46**.

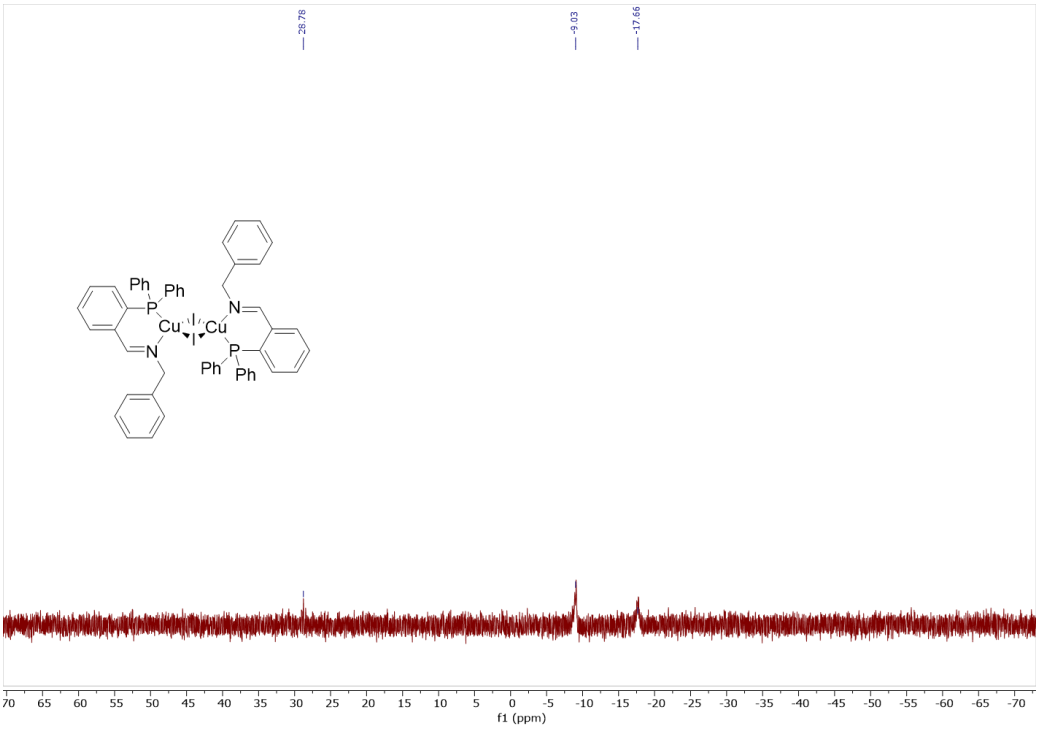

Figure A5.12: ^{31}P NMR (162 MHz, DMSO-d_6, 298 K) spectrum of **AZ46**.

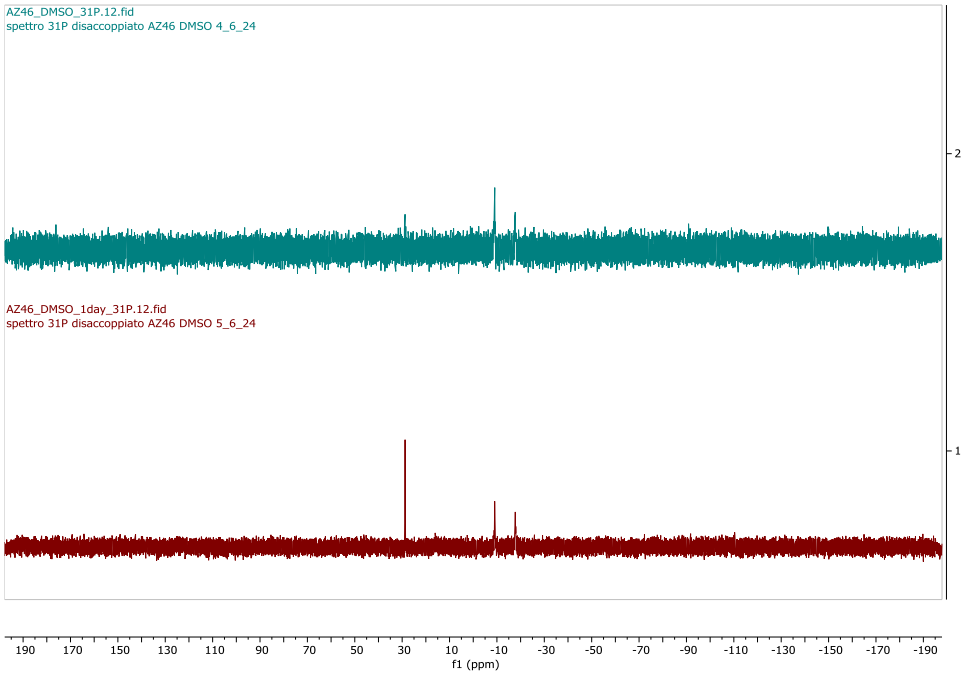

Figure A5.13: ^{31}P NMR (162 MHz, DMSO-d_6, 298 K) spectrum of **AZ46** immediately after preparation of the sample (top) and after one day (bottom).

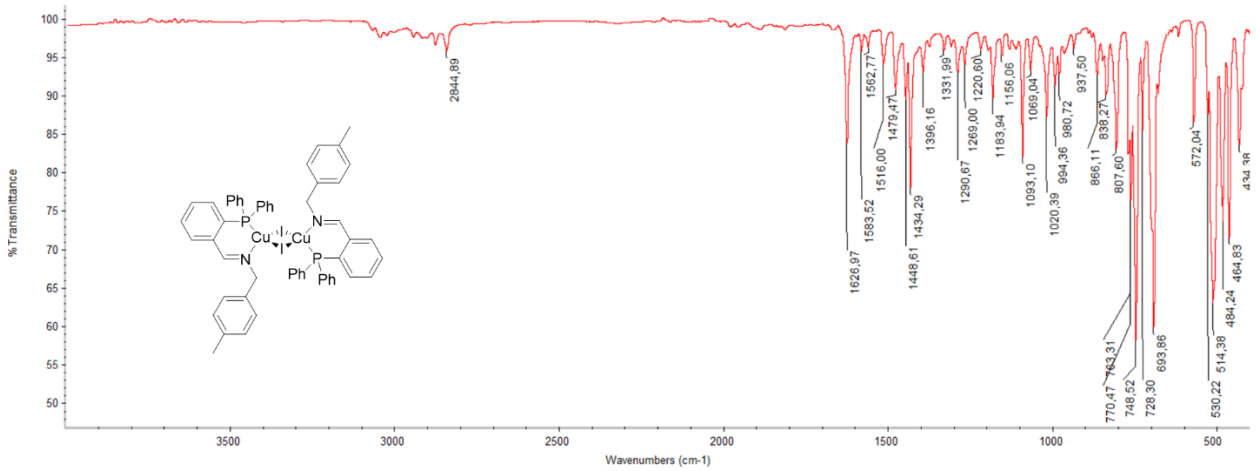

Figure A5.14: FT-IR spectrum of **AZ52**.

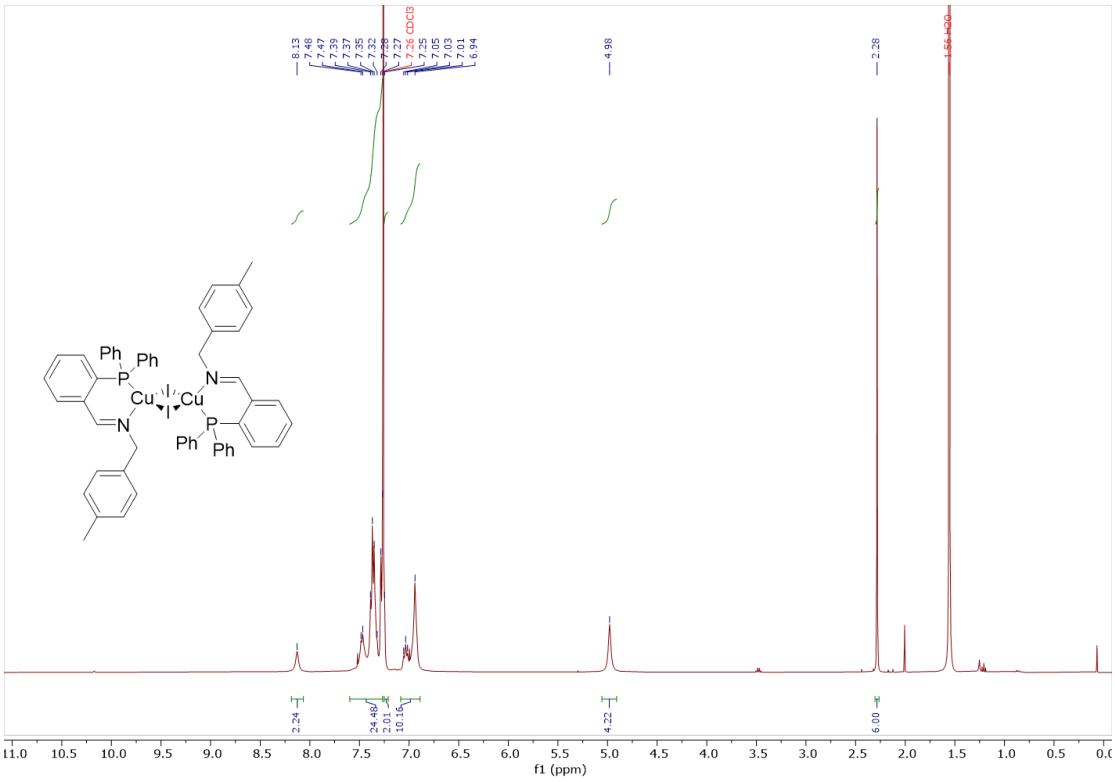

Figure A5.15: ^{1}H NMR (400 MHz, Chloroform-*d,* 298 K) spectrum of **AZ52**.

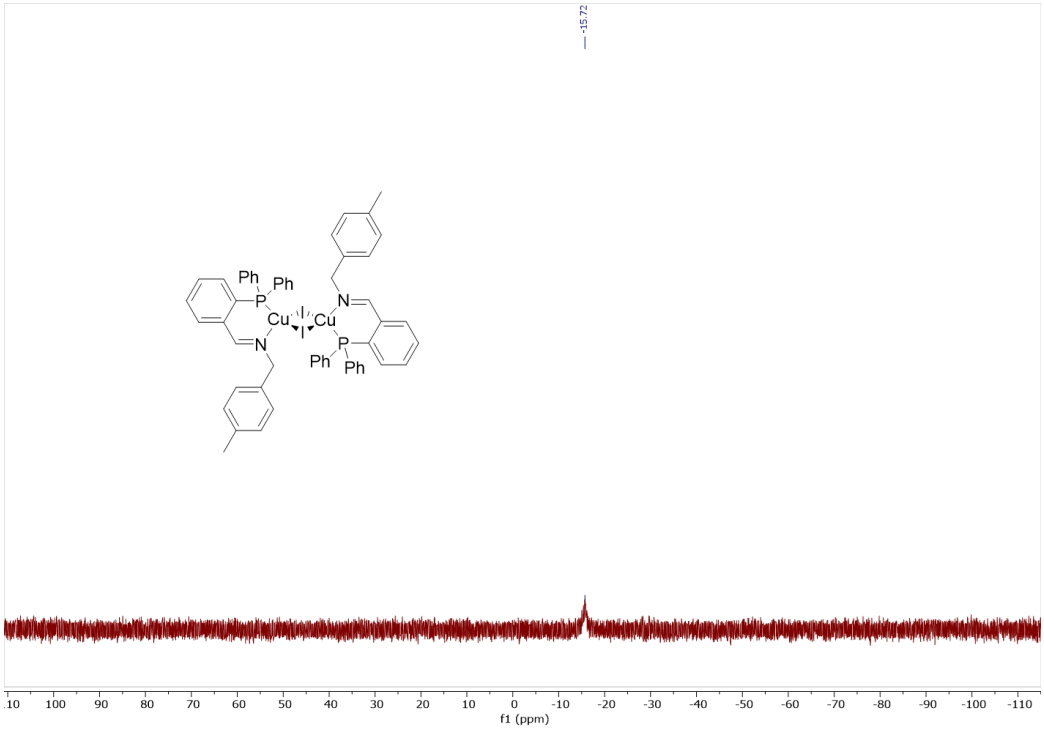

Figure A5.16: ^{31}P NMR (162 MHz, Chloroform-*d*, 298 K) spectrum of **AZ52**.

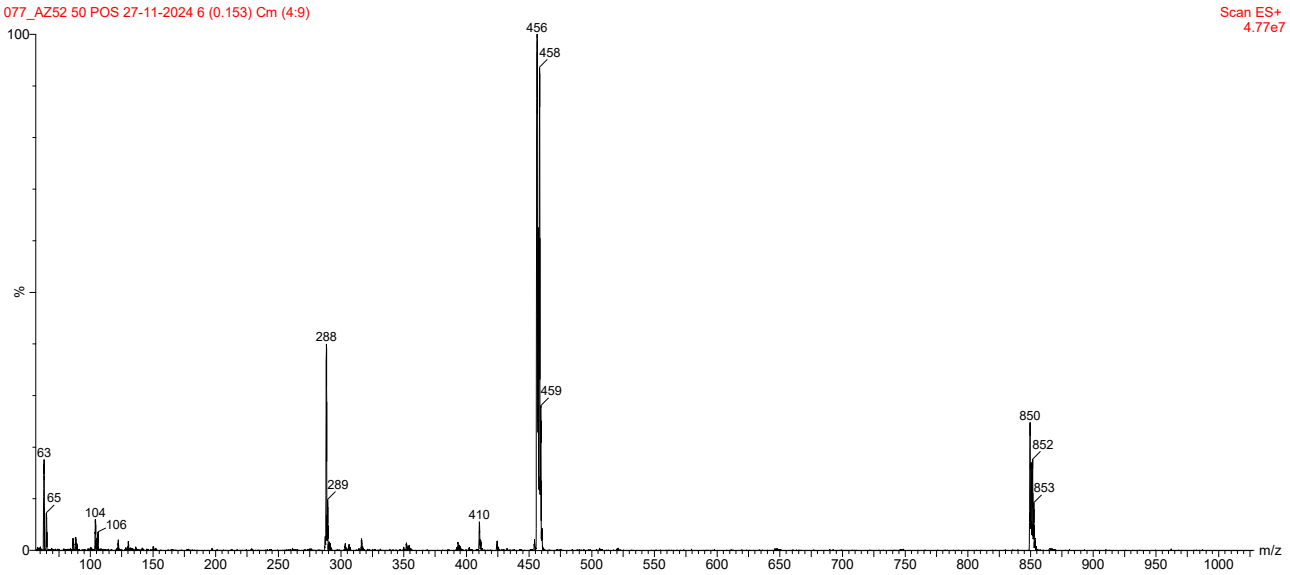

Figure A5.17: ESI-MS spectrum (positive ions) for **AZ52** in acetonitrile.

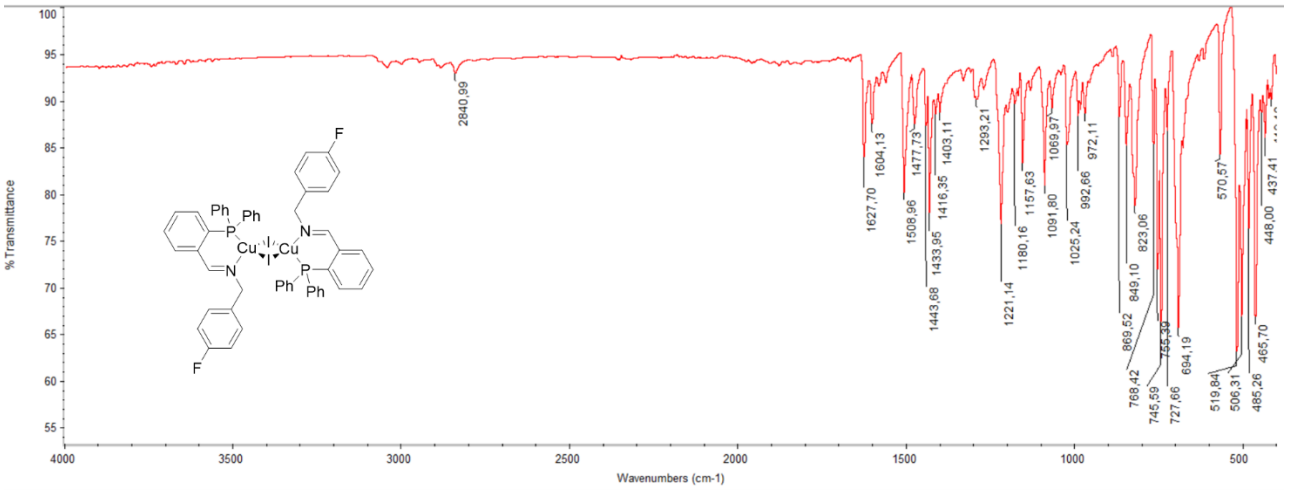

Figure A5.18: FT-IR spectrum of **AZ54**.

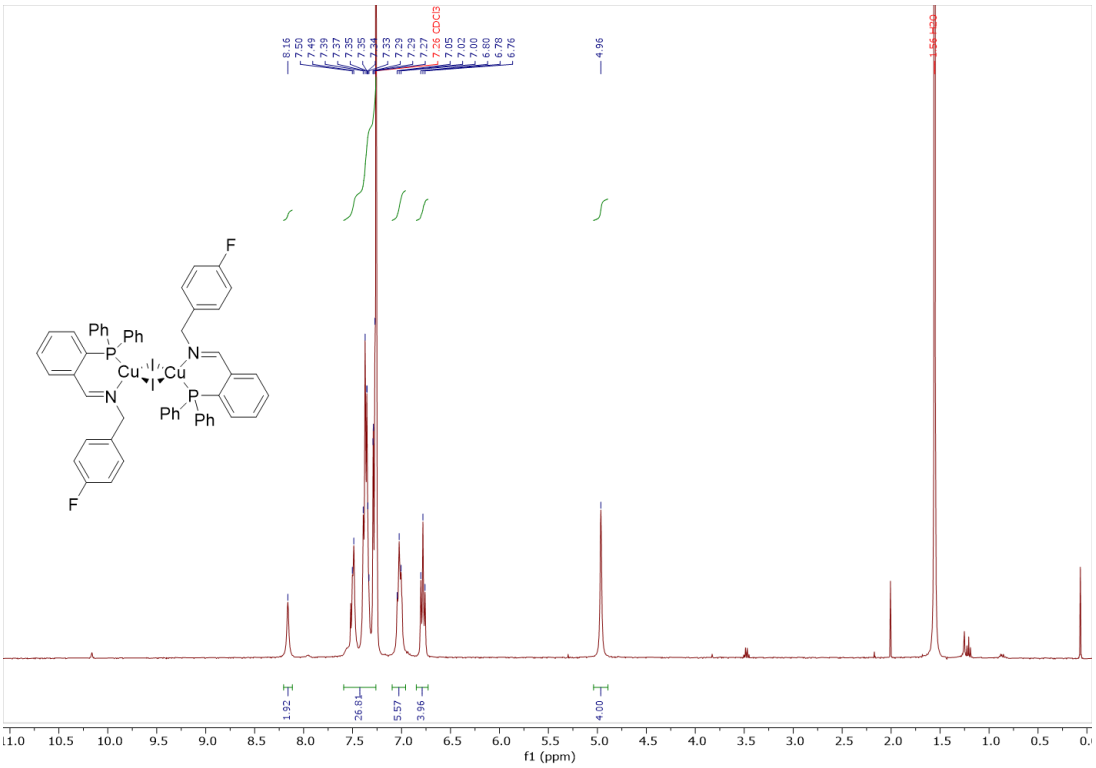

Figure A5.19: ^{1}H NMR (400 MHz, Chloroform-*d,* 298 K) spectrum of **AZ54**.

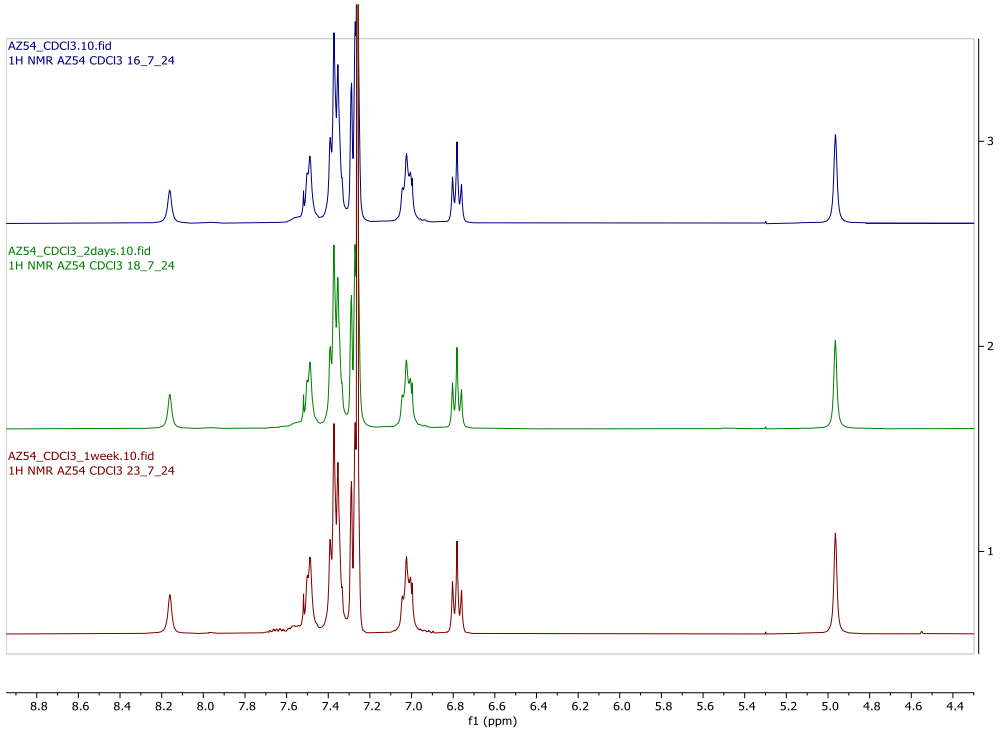

Figure A5.20: ^{1}H NMR (400 MHz, Chloroform-*d,* 298 K) spectrum of **AZ54** immediately after preparation of the sample (top), after two days (middle) and after one week (bottom).

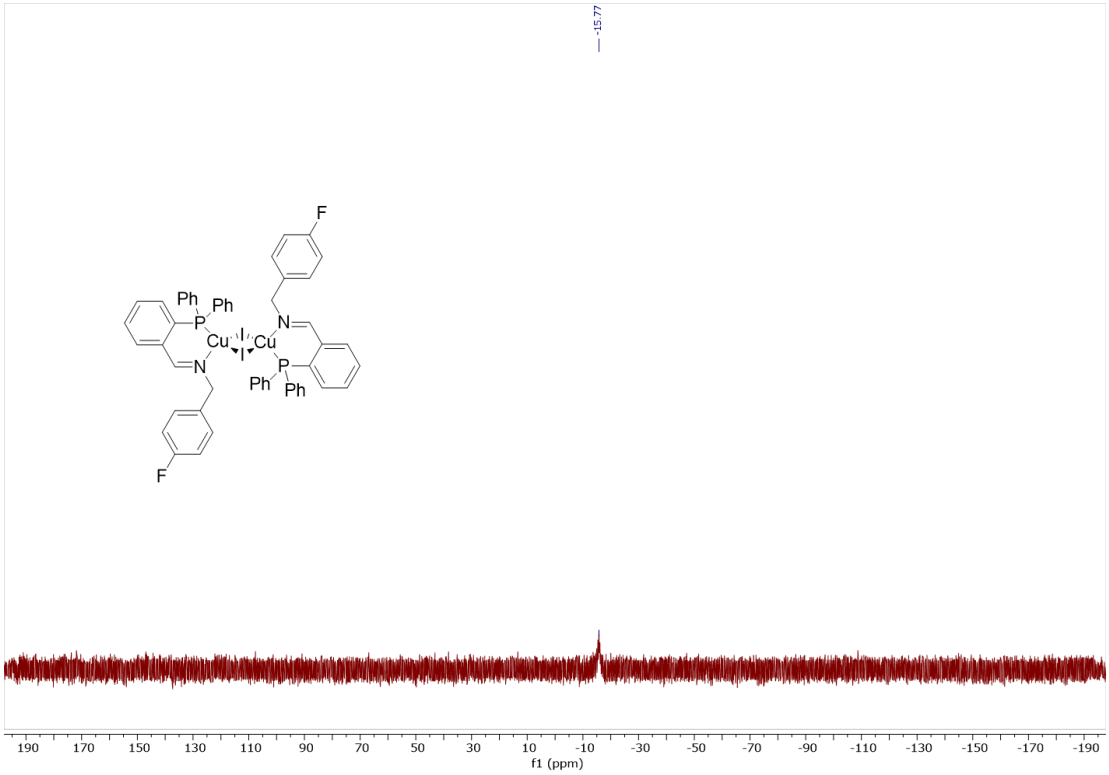

Figure A5.21: ^{31}P NMR (162 MHz, Chloroform-*d*, 298 K) spectrum of **AZ54**.

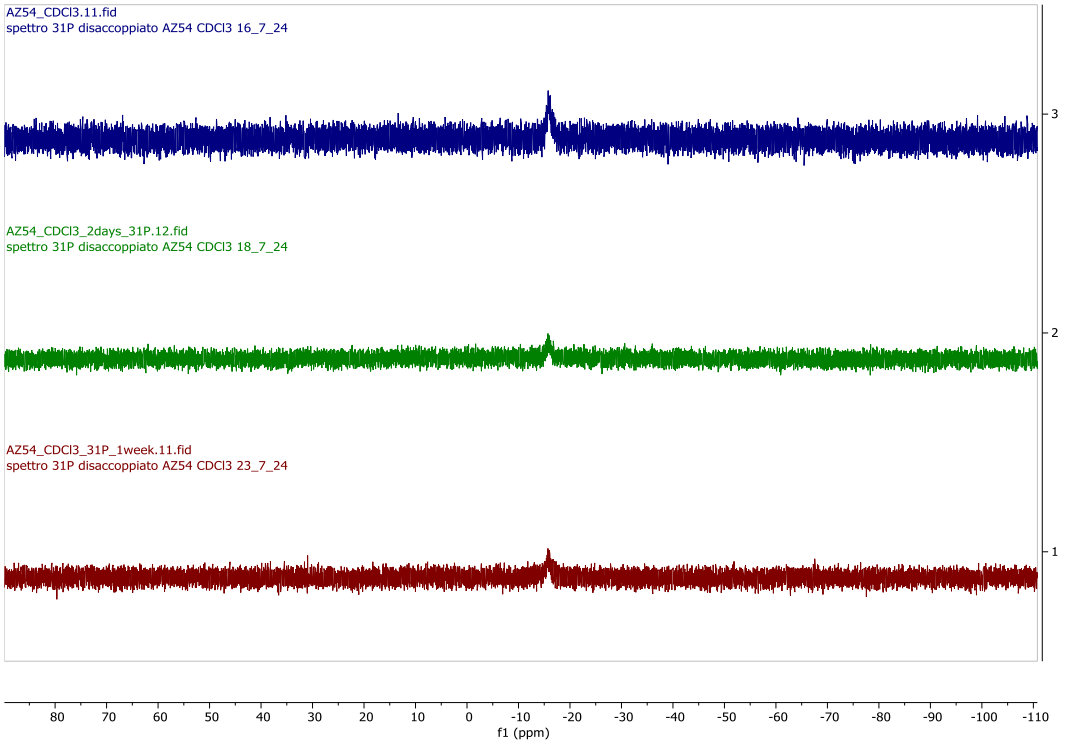

Figure A5.22: ^{31}P NMR (162 MHz, Chloroform-*d*, 298 K) spectrum of **AZ54** immediately after preparation of the sample (top), after two days (middle) and after one week (bottom).

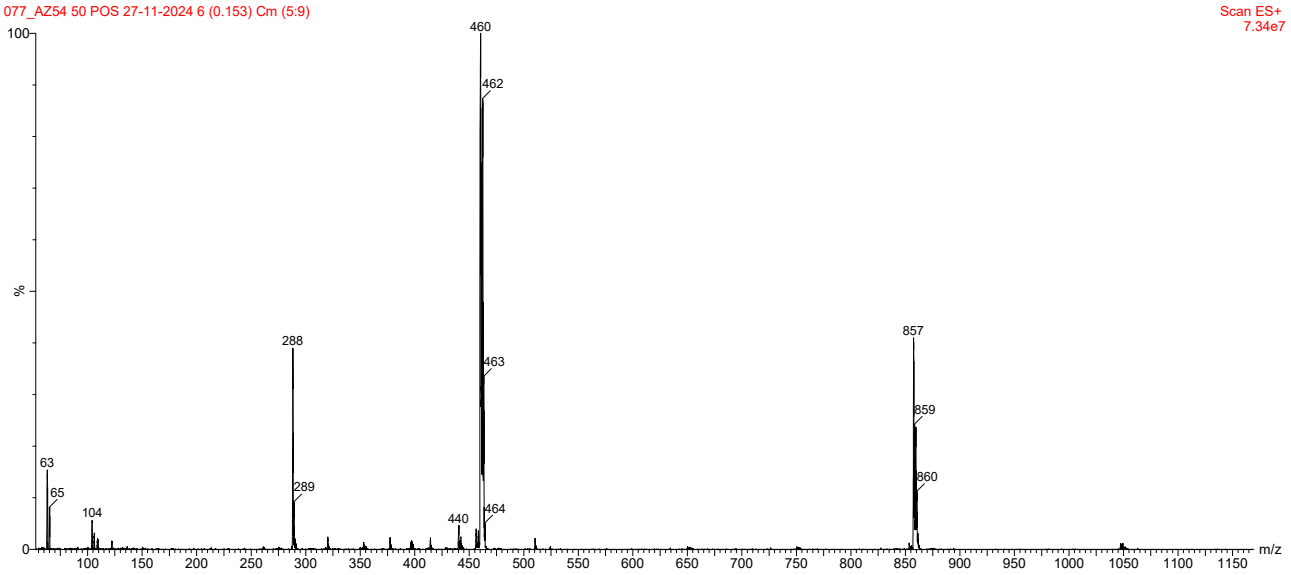

Figure A5.23: ESI-MS spectrum (positive ions) for **AZ54** in acetonitrile.

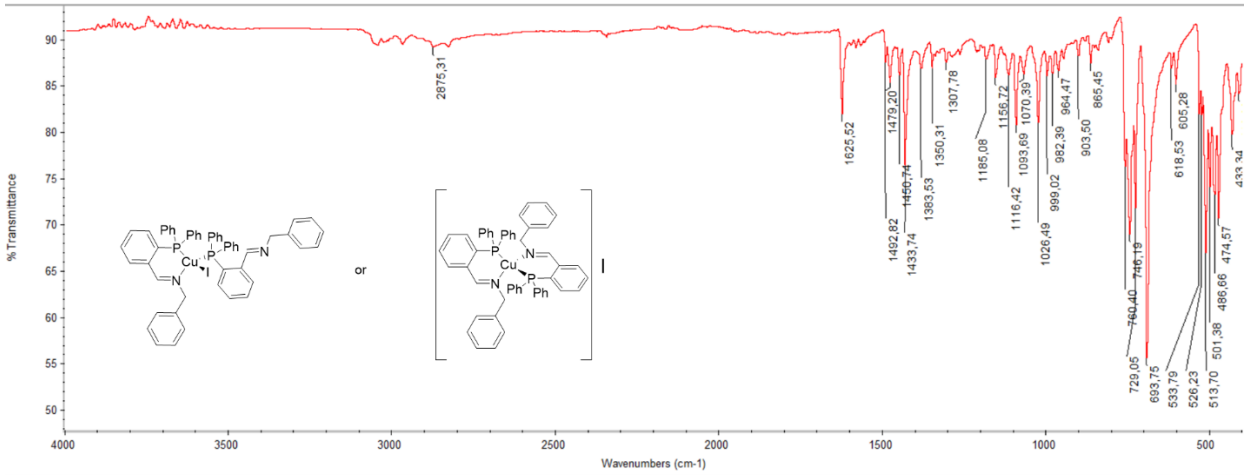

Figure A5.24: FT-IR spectrum of **AZ48**.

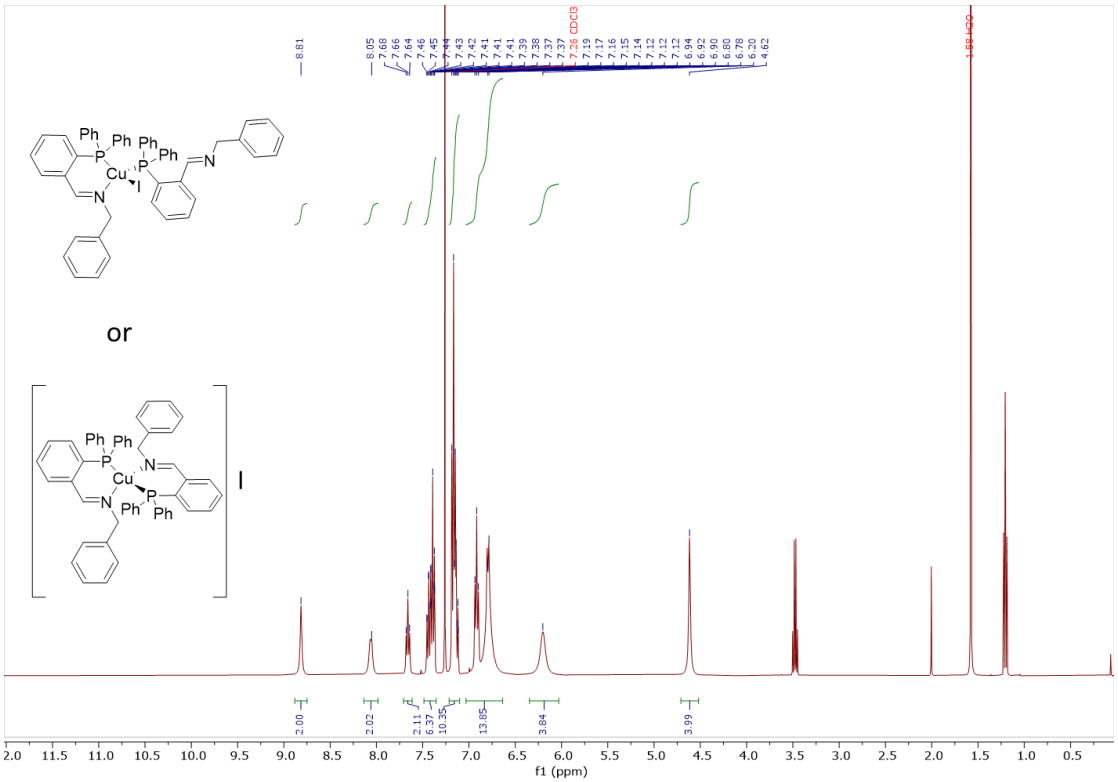

Figure A5.25: ^{1}H NMR (400 MHz, Chloroform-*d,* 298 K) spectrum of **AZ48**.

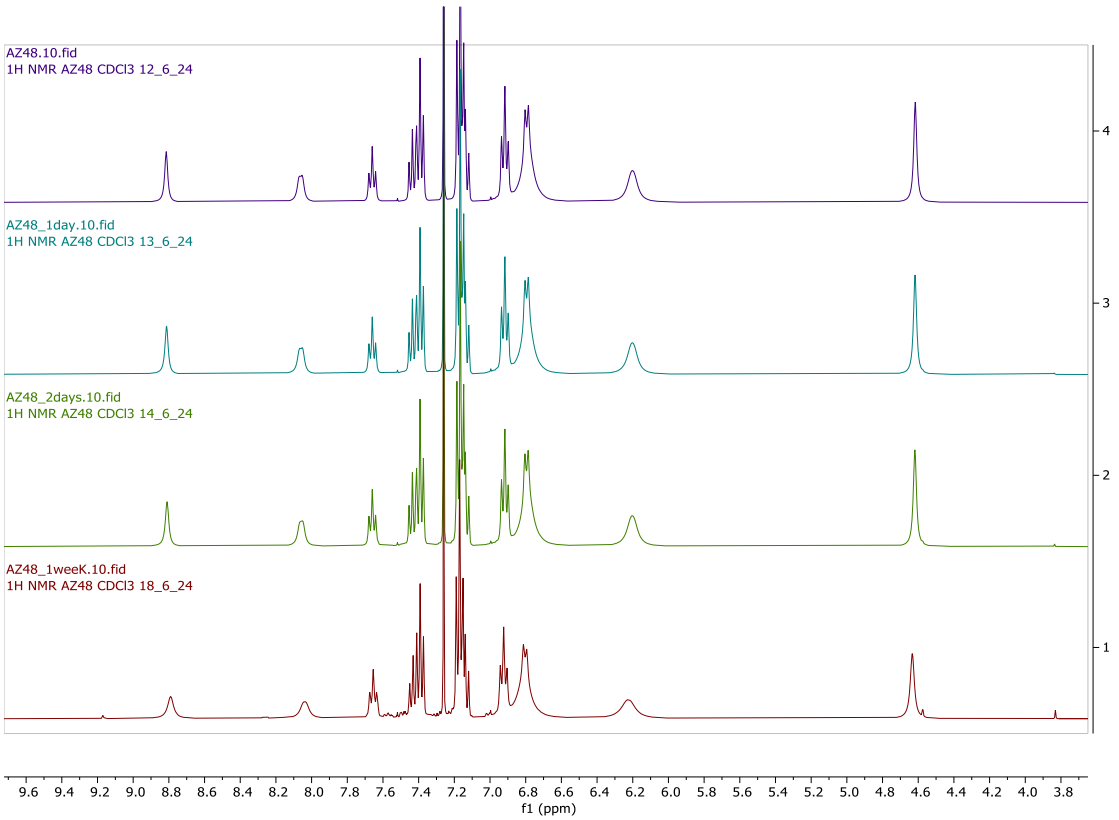

Figure A5.26: ^{1}H NMR (400 MHz, Chloroform-*d,* 298 K) spectrum of **AZ48** immediately after preparation of the sample (purple), after one day (blue-green), after two days (green) and after one week (red).

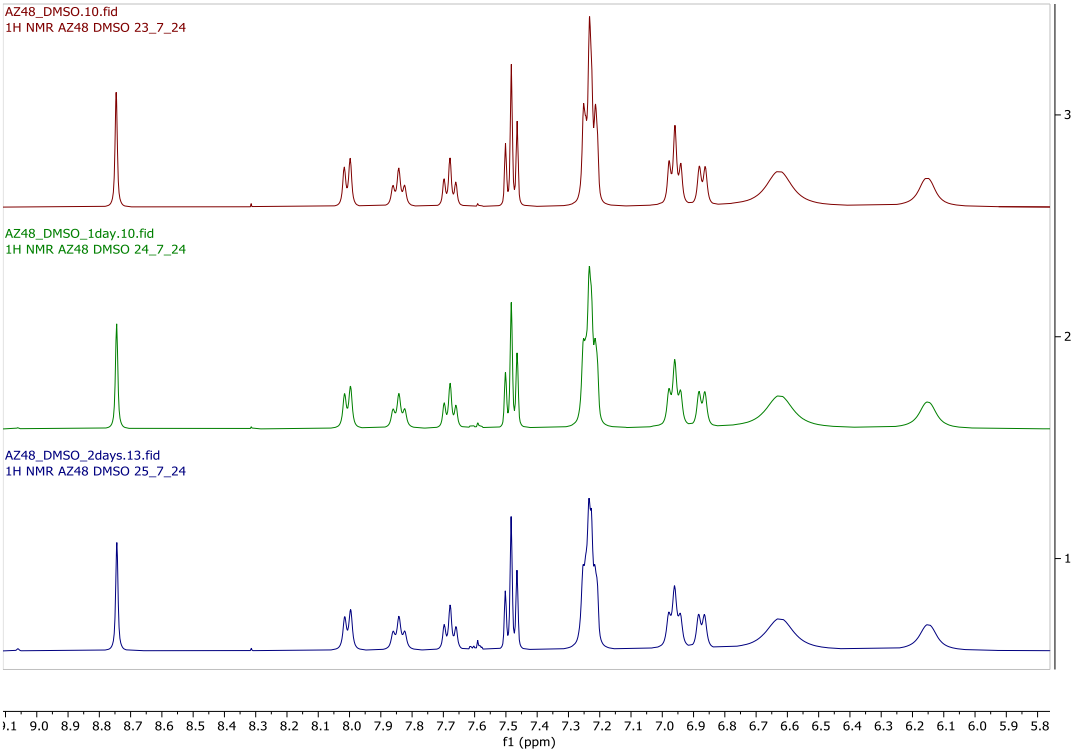

Figure A5.27: ^{1}H NMR (400 MHz, DMSO-d_6, 298 K) spectrum of **AZ48** immediately after preparation of the sample (top), after one day (middle) and after two days (green).

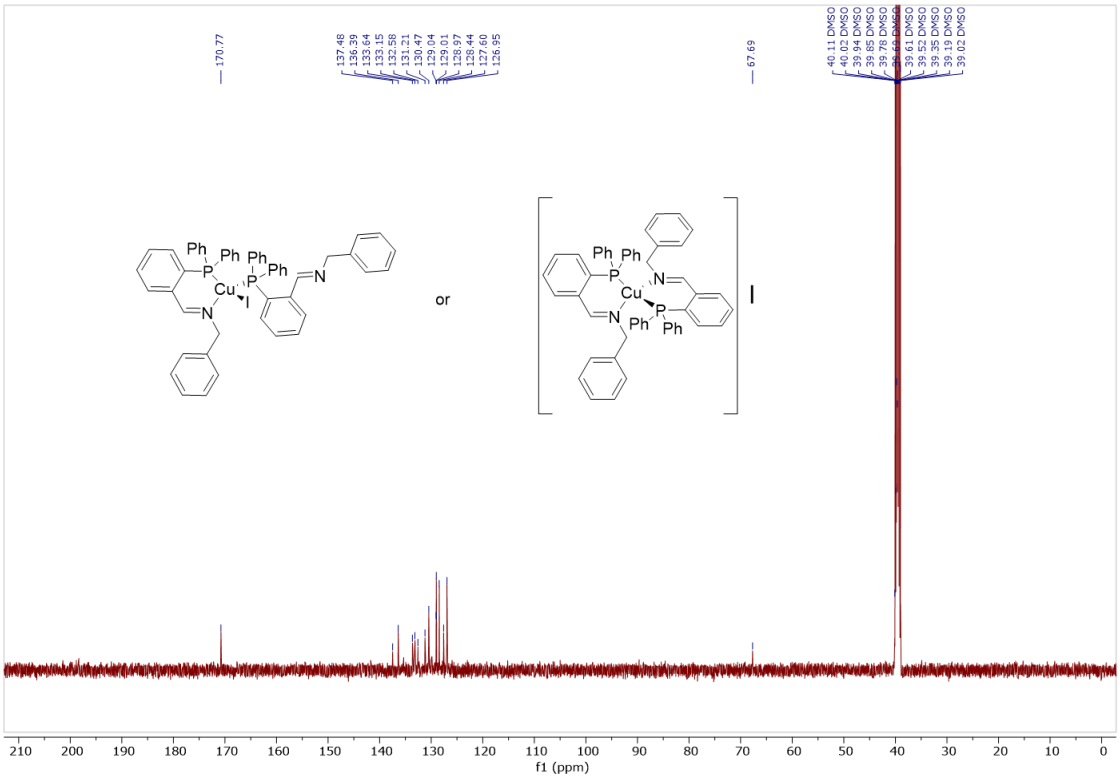

Figure A5.28: ^{13}C NMR (126 MHz, Chloroform-*d*, 298 K) spectrum of **AZ48**.

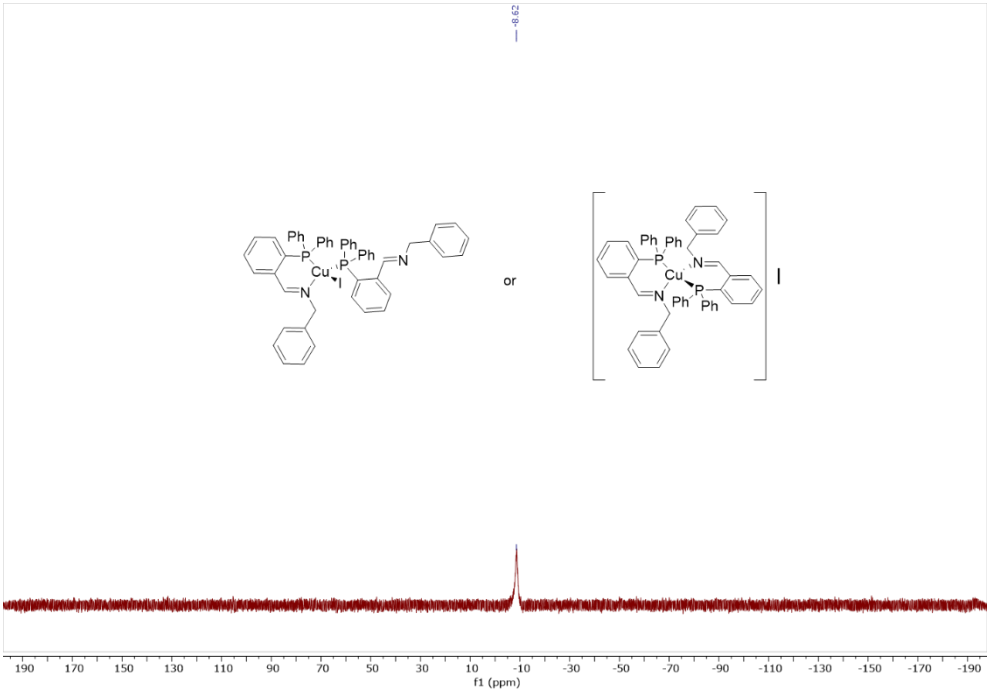

Figure A5.29: ^{31}P NMR (162 MHz, Chloroform-*d*, 298 K) spectrum of **AZ48**.

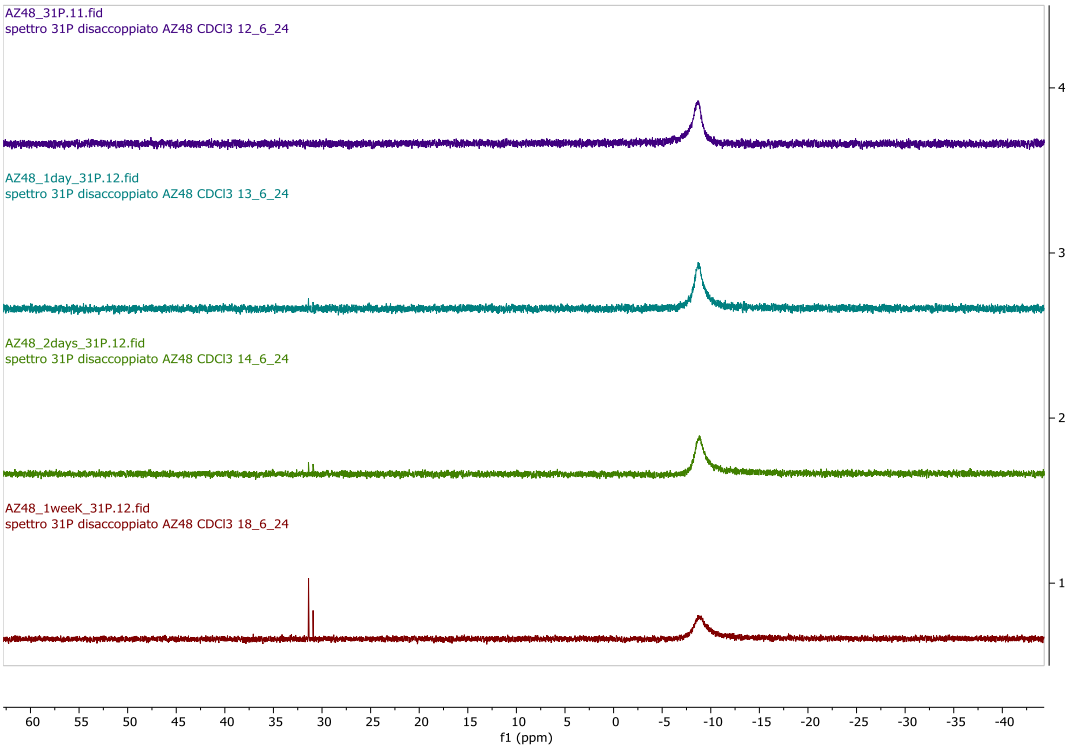

Figure A5.30: ^{31}P NMR (162 MHz, Chloroform-*d*, 298 K) spectrum of **AZ48** immediately after preparation of the sample (purple), after one day (blue-green), after two days (green) and after one week (red).

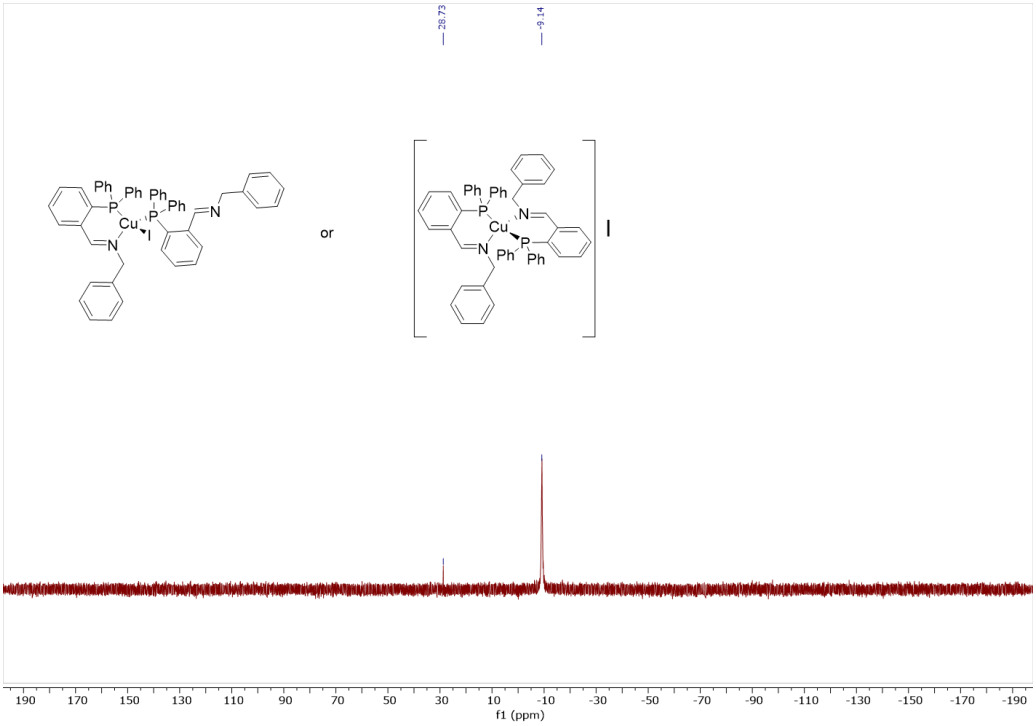

Figure A5.31: ^{31}P NMR (162 MHz, DMSO-d_6, 298 K) spectrum of **AZ48**.

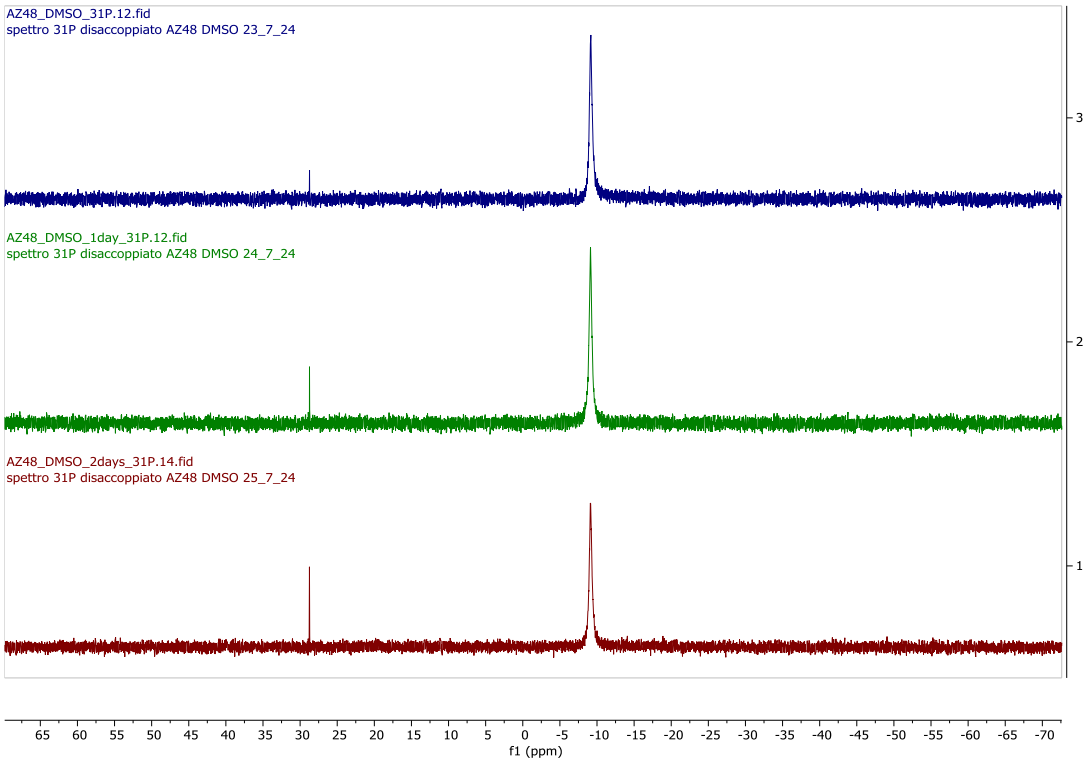

Figure A5.32: ^{31}P NMR (162 MHz, DMSO-d_6, 298 K) spectrum of **AZ48** few hours after preparation of the sample (top), after one day (middle) and after two days (bottom).

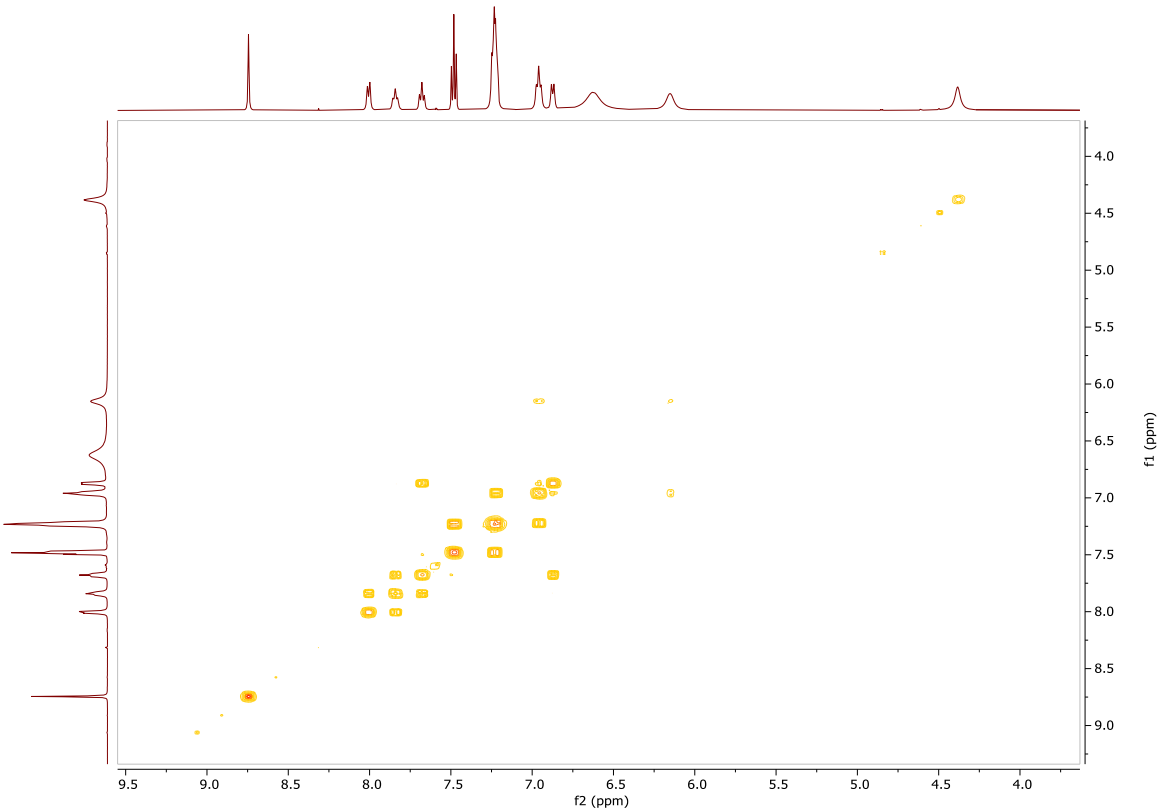

Figure A5.33: Selected range of 2D ^{1}H-^{1}H COSY spectrum of **AZ48** at 298 K in DMSO-d_6.

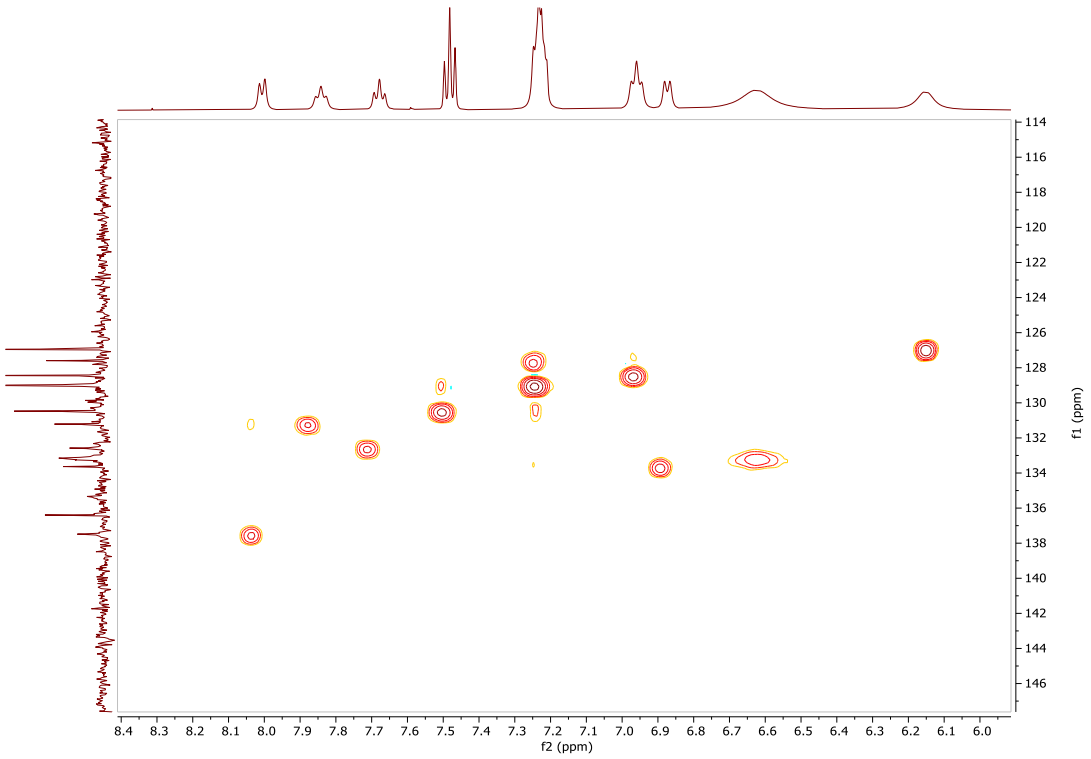

Figure A5.34: Selected range of the 2D ^{1}H-^{13}C HSQC spectrum of **AZ48** at 298 K in DMSO-d_6.

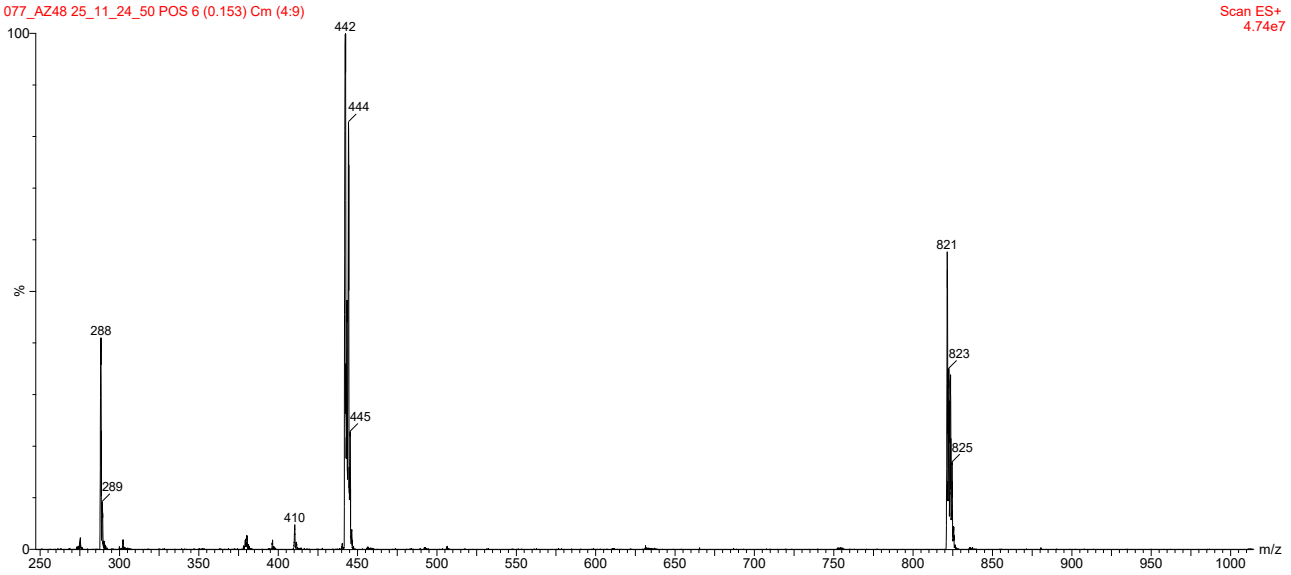

Figure A5.35: ESI-MS spectrum (positive ions) for **AZ48** in acetonitrile.

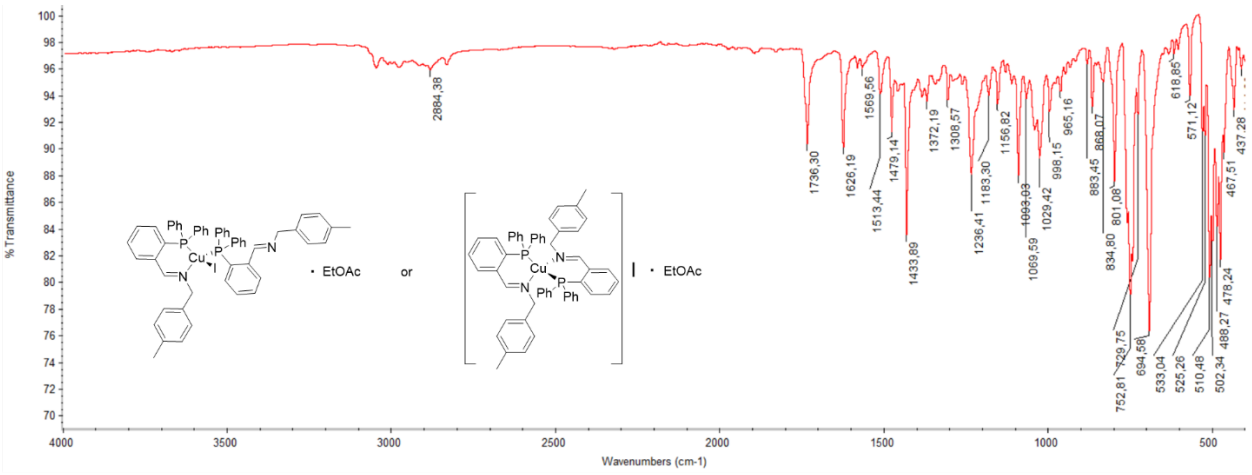

Figure A5.36: FT-IR spectrum of **AZ53**.

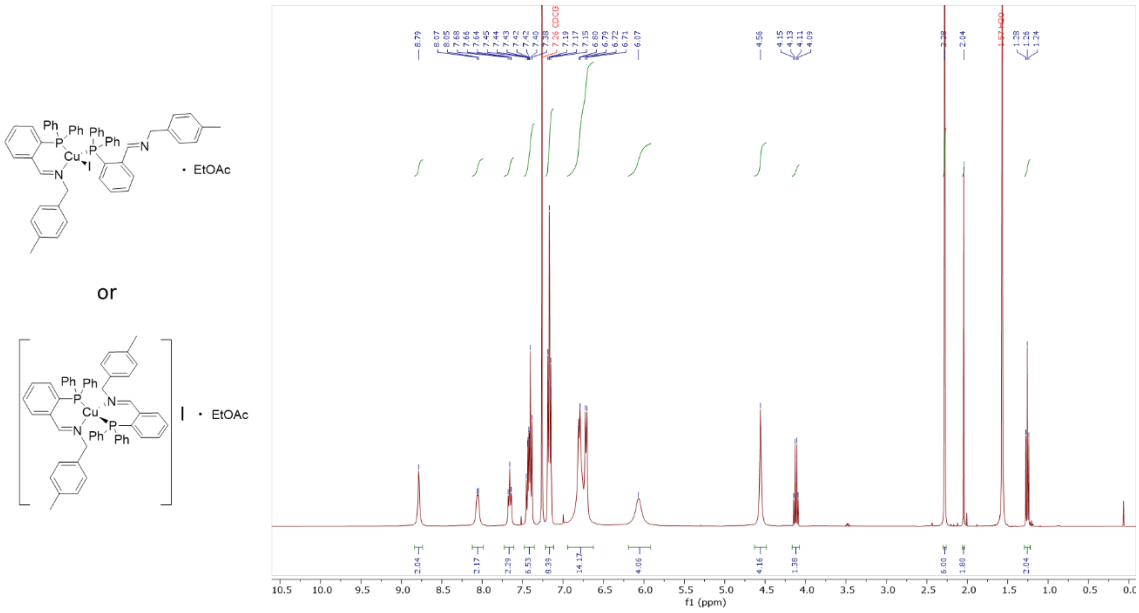

Figure A5.37: ^{1}H NMR (400 MHz, Chloroform-*d,* 298 K) spectrum of **AZ53**.

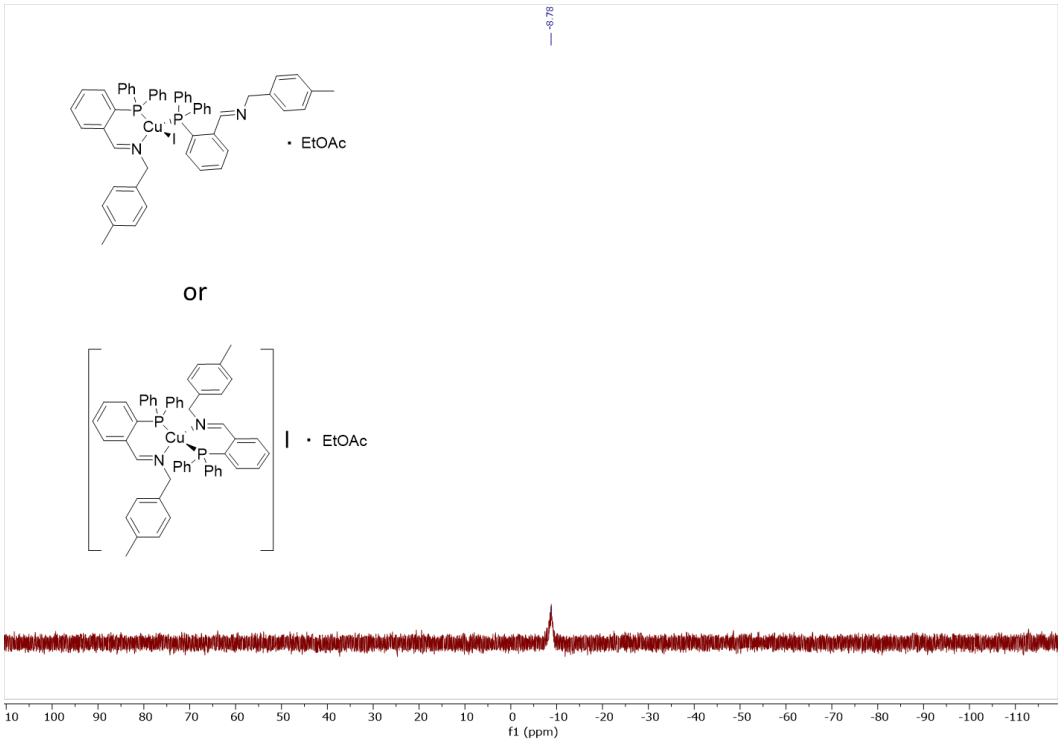

Figure A5.38: ^{31}P NMR (162 MHz, Chloroform-*d*, 298 K) spectrum of **AZ53**.

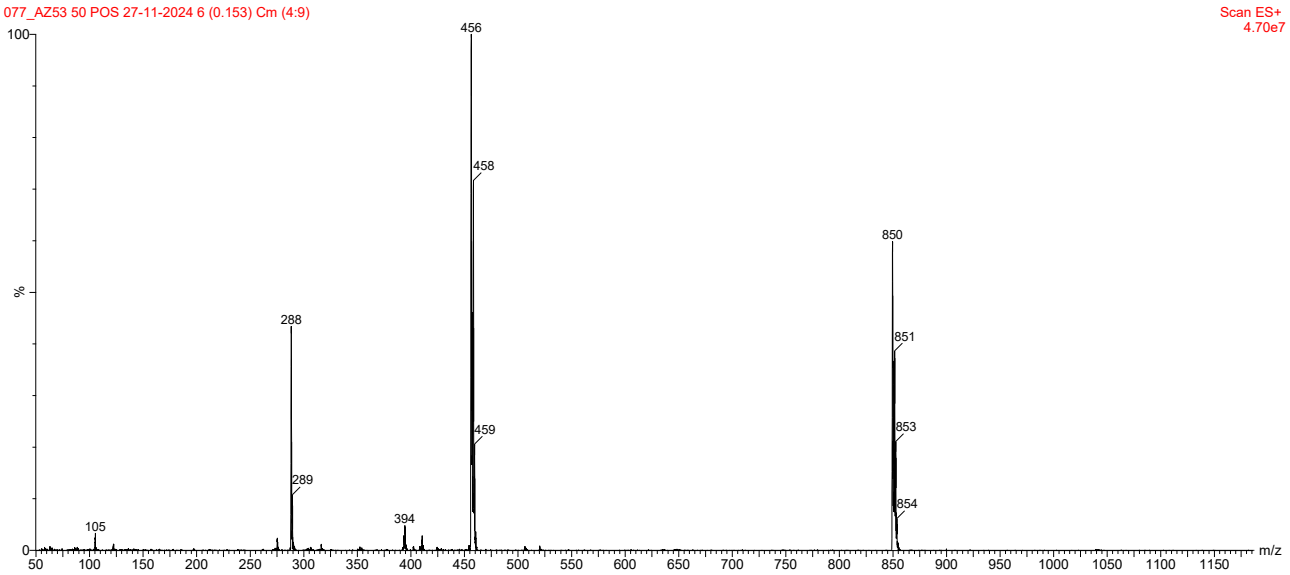

Figure A5.39: ESI-MS spectrum (positive ions) for **AZ53** in acetonitrile.

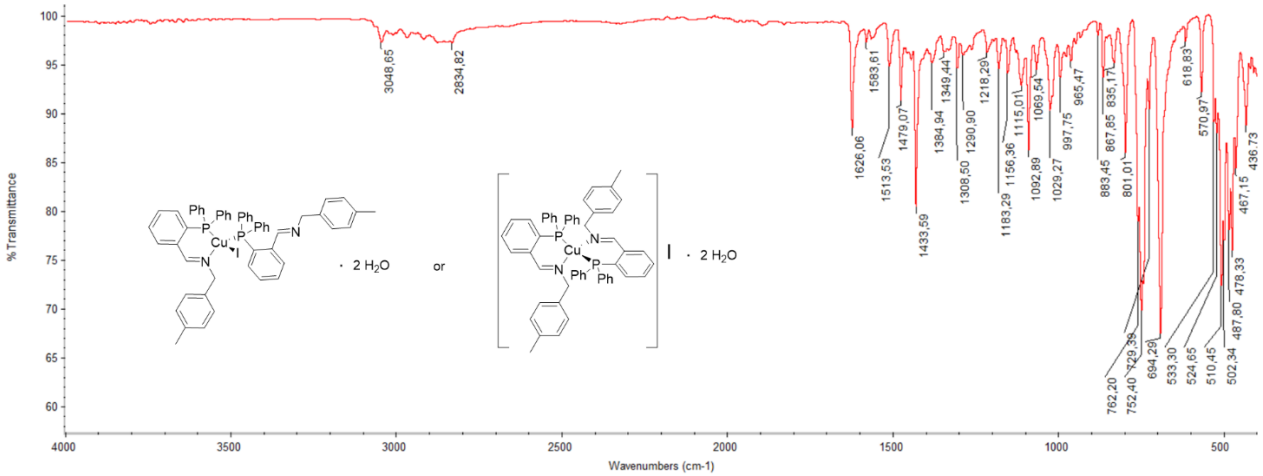

Figure A5.40: FT-IR spectrum of **AZ53a**.

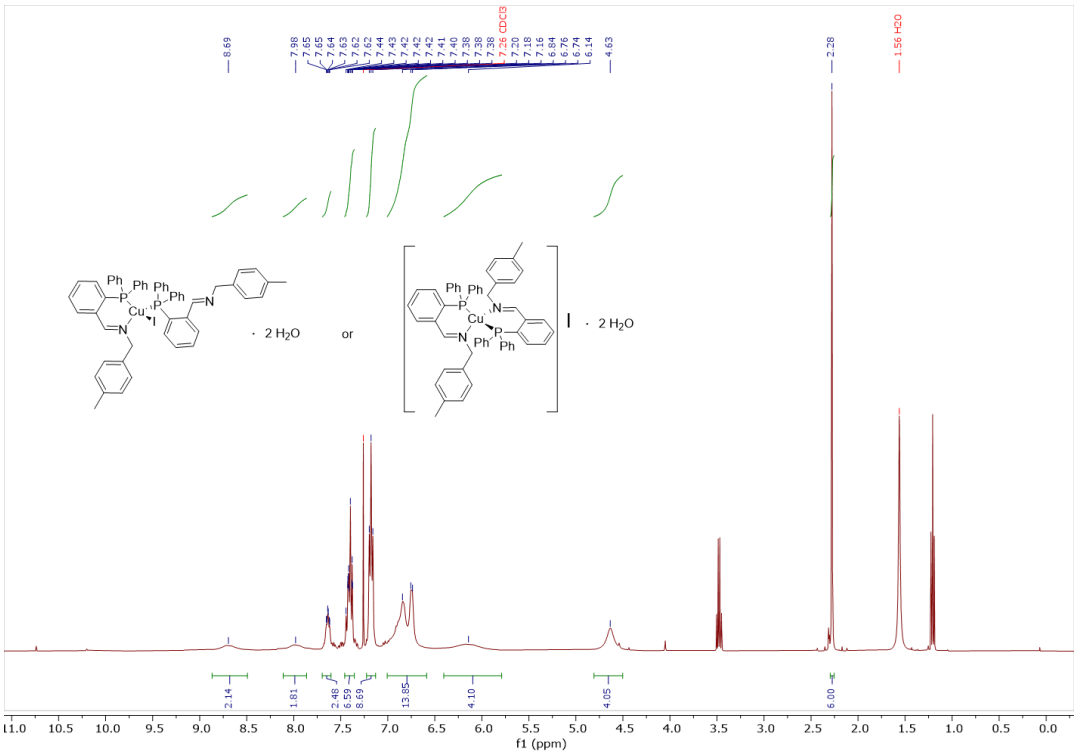

Figure A5.41: ^{1}H NMR (400 MHz, Chloroform-*d,* 298 K) spectrum of **AZ53a**.

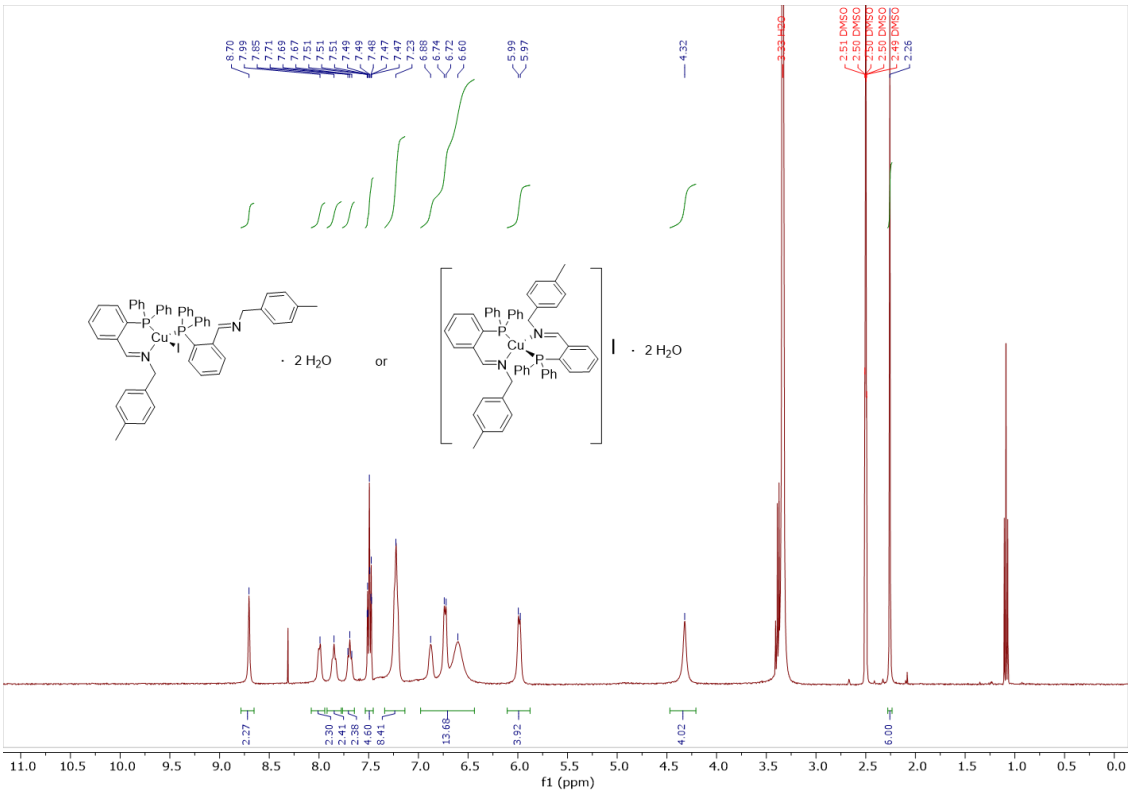

Figure A5.42: ^{1}H NMR (400 MHz, DMSO-d_6, 298 K) spectrum of **AZ53a**.

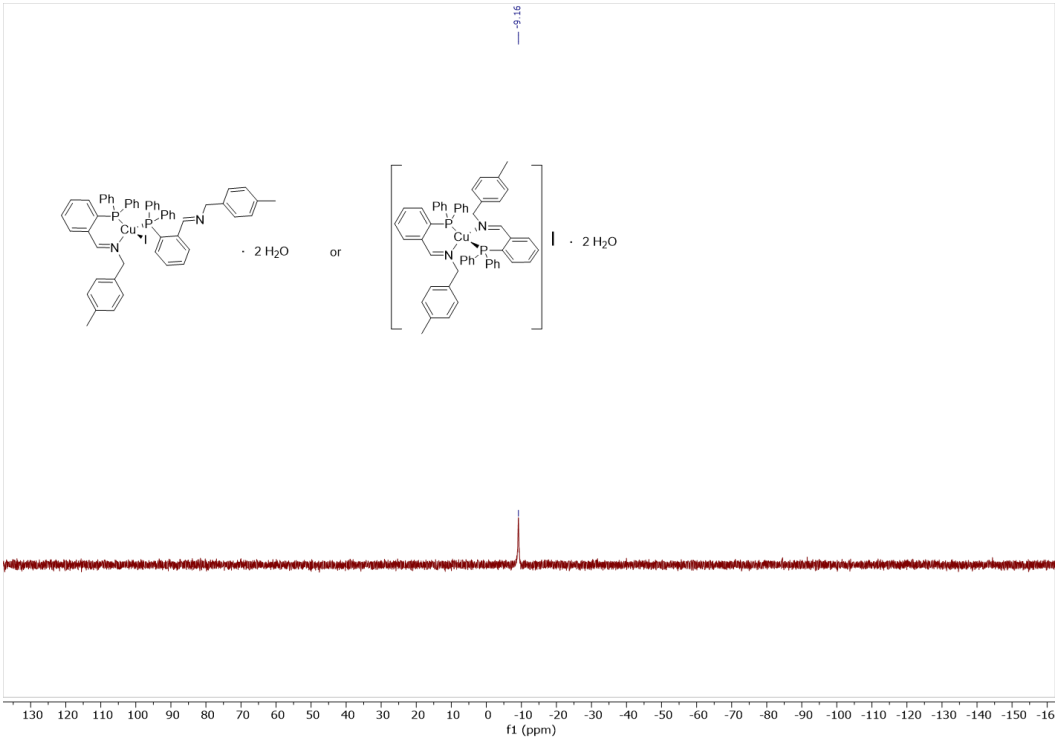

Figure A5.43: ^{31}P NMR (202 MHz, DMSO-d_6, 298 K) spectrum of **AZ53a**.

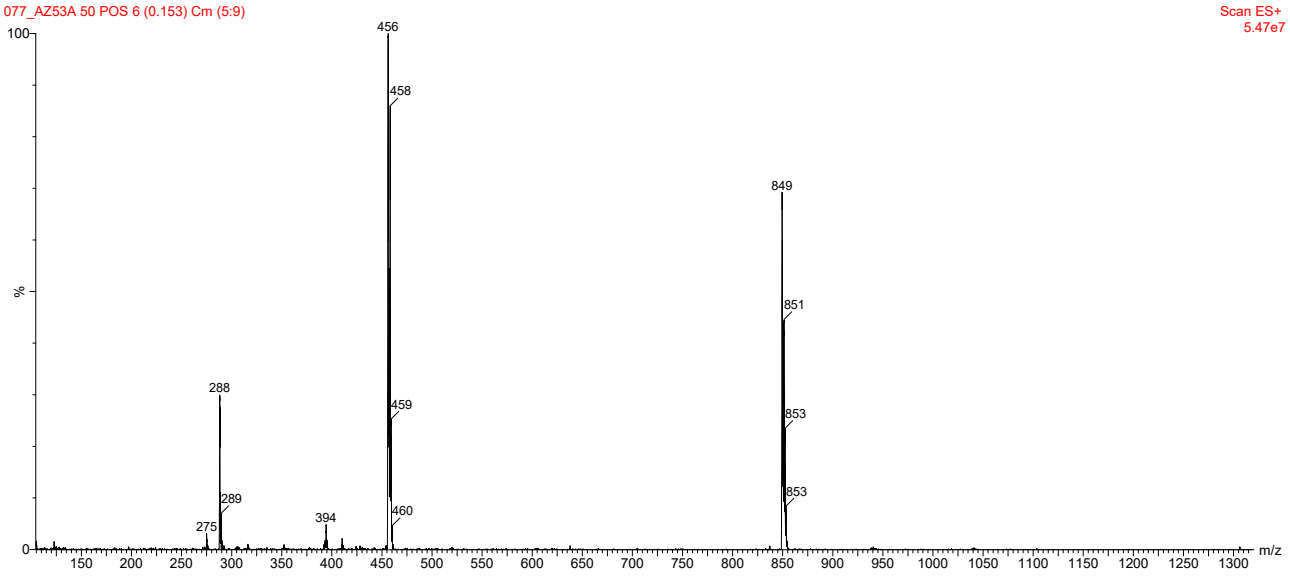

Figure A5.44: ESI-MS spectrum (positive ions) for **AZ53a** in acetonitrile.

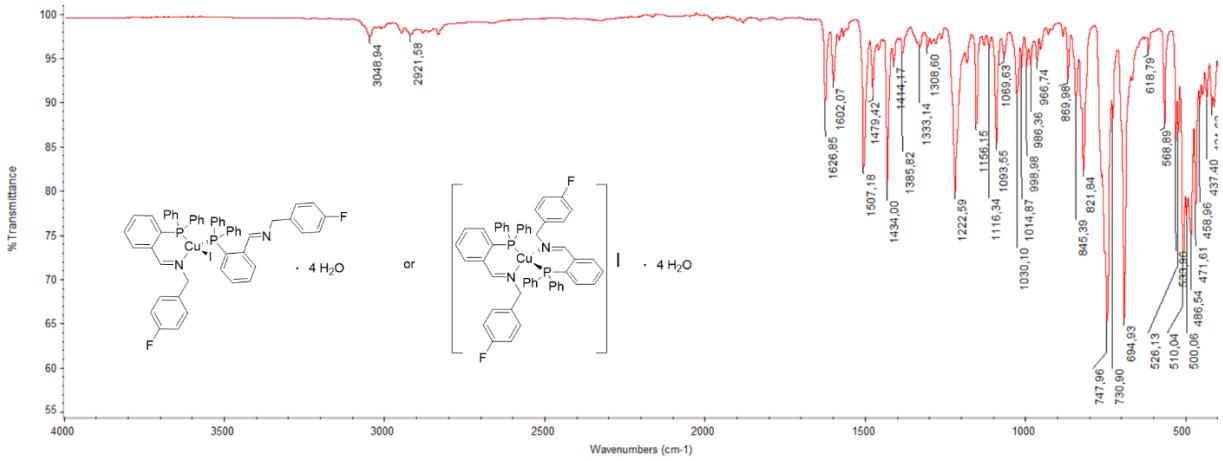

Figure A5.45: FT-IR spectrum of **AZ55a**.

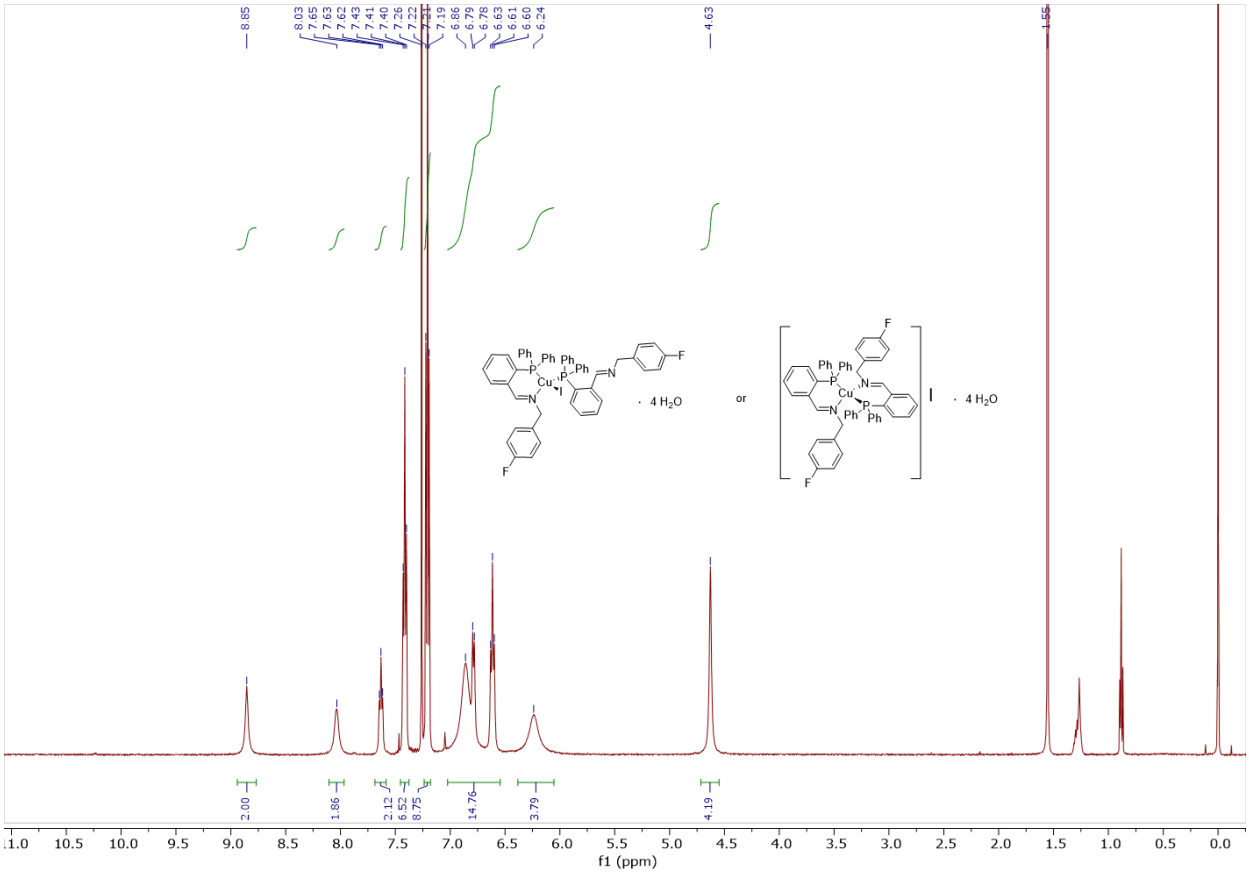

Figure A5.46: ^{1}H NMR (500 MHz, Chloroform-*d,* 298 K) spectrum of **AZ55a**.

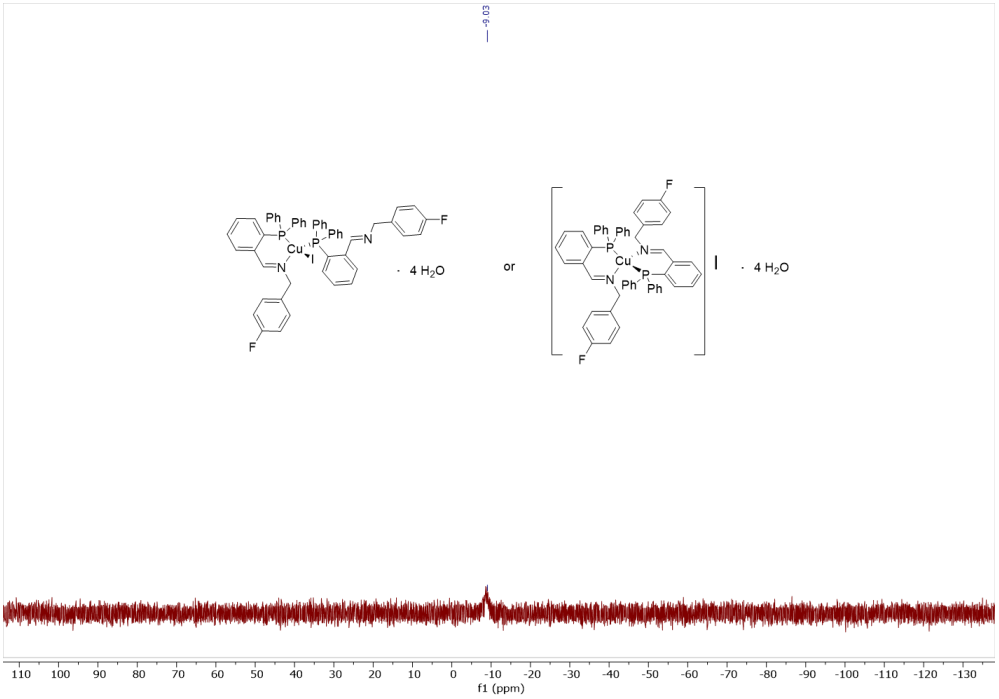

Figure A5.47: ^{31}P NMR (202 MHz, $CDCl_3$, 298 K) spectrum of **AZ55a**.

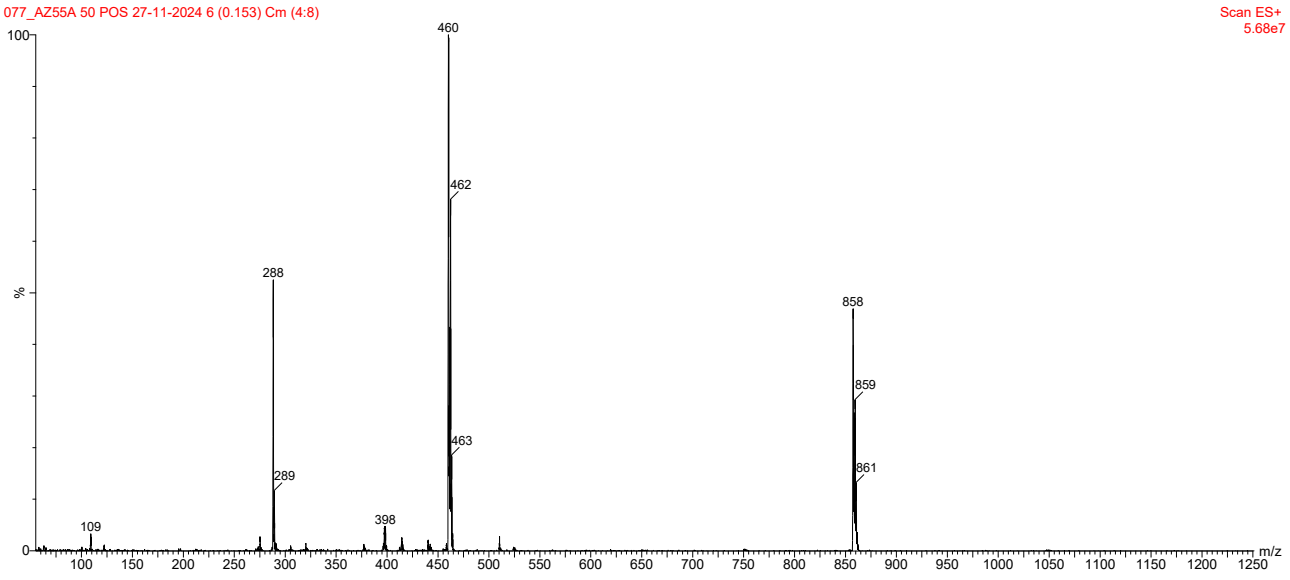

Figure A5.48: ESI-MS spectrum (positive ions) for **AZ55a** in acetonitrile.

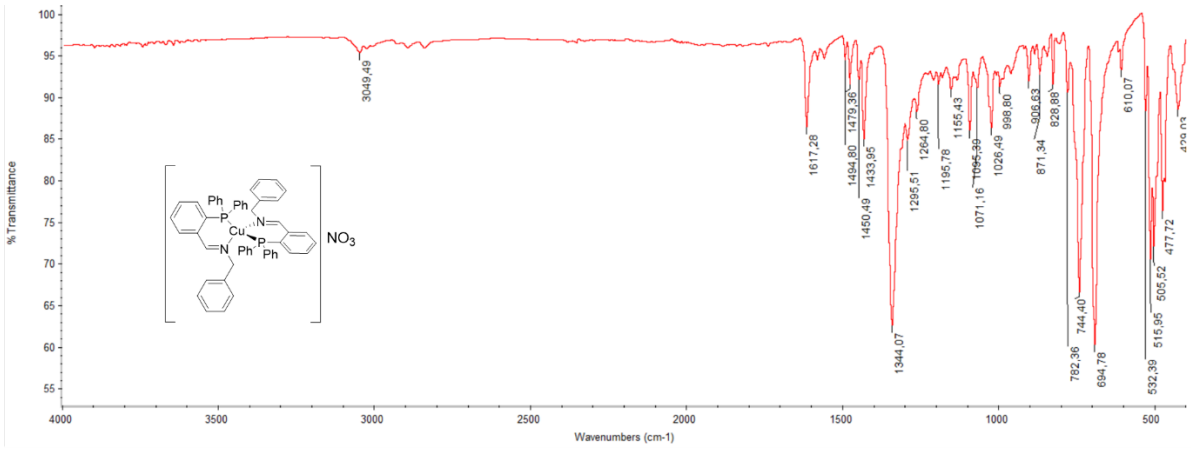

Figure A5.49: FT-IR spectrum of **AZ61**.

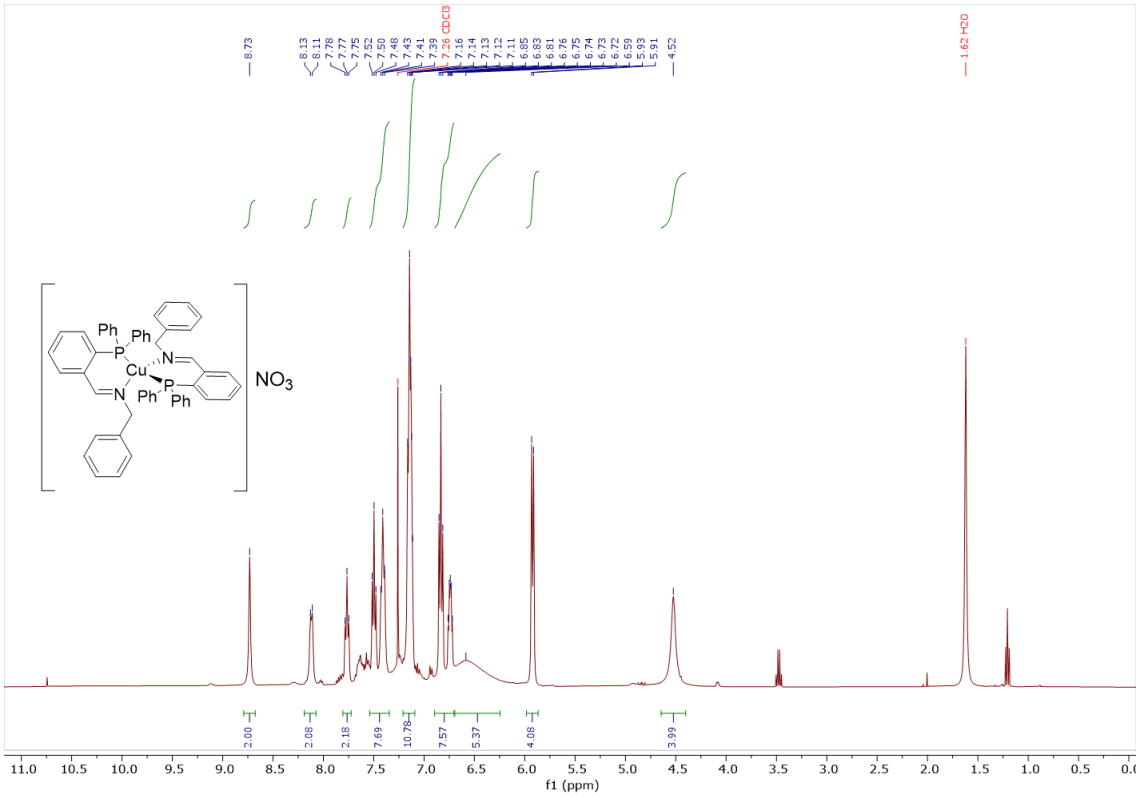

Figure A5.50: ^{1}H NMR (400 MHz, Chloroform-*d,* 298 K) spectrum of **AZ61**.

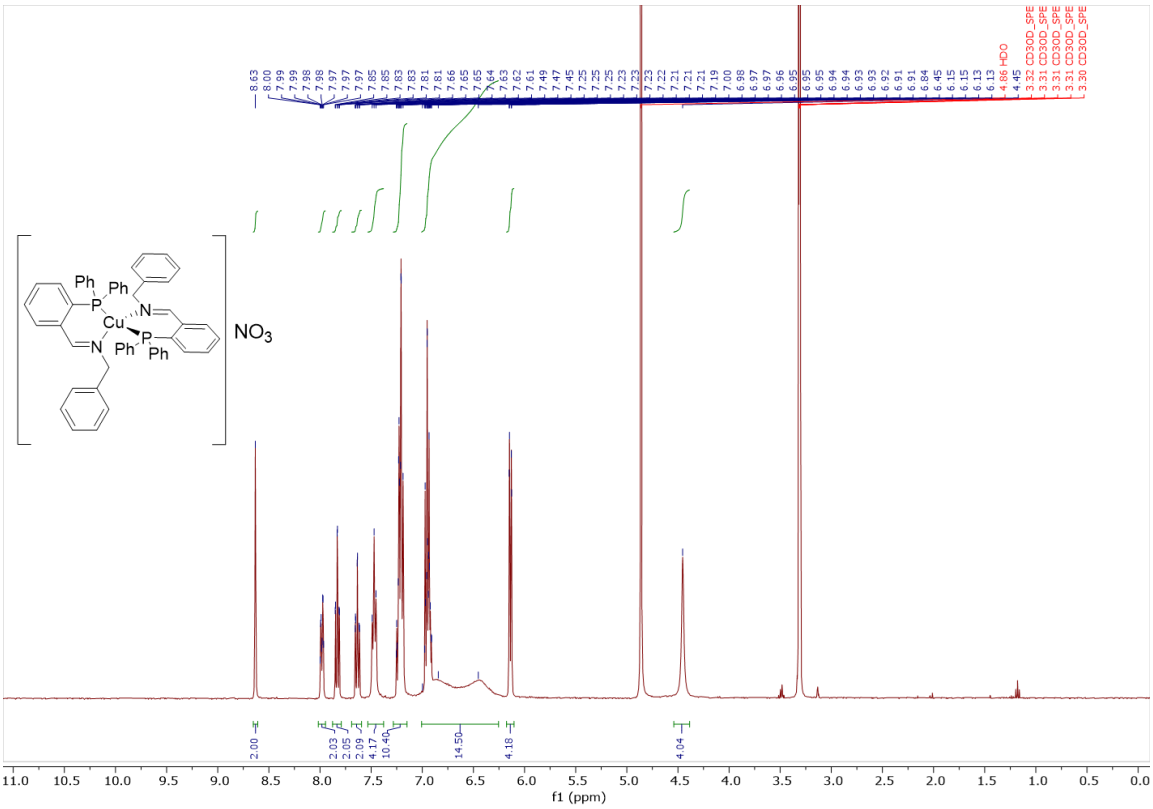

Figure A5.51: ^{1}H NMR (400 MHz, Methanol-d_4, 298 K) spectrum of **AZ61**.

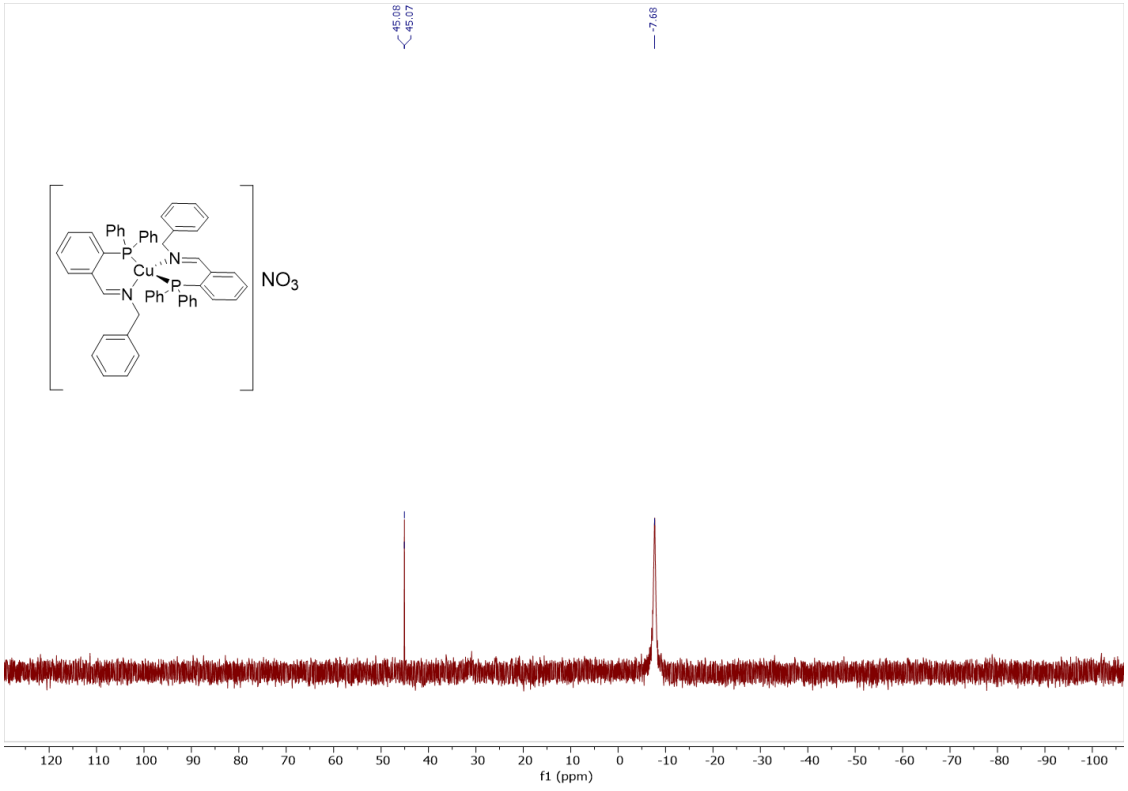

Figure A5.52: ^{31}P NMR (162 MHz, Chloroform-*d*, 298 K) spectrum of **AZ61**.

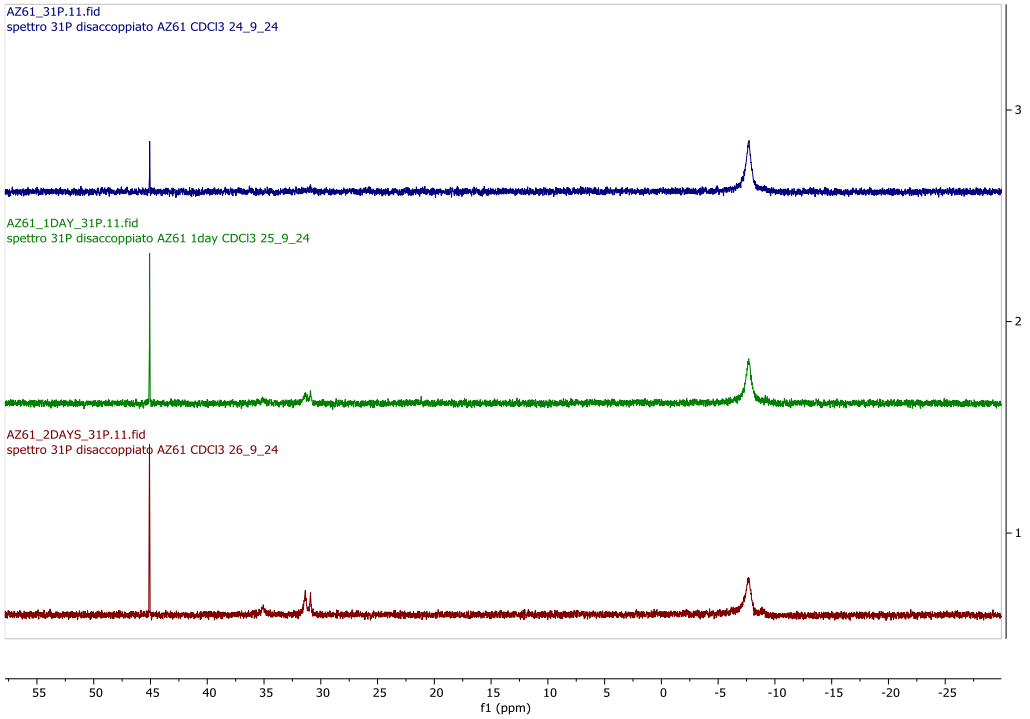

Figure A5.53: ^{31}P NMR (162 MHz, Chloroform-*d*, 298 K) spectrum of **AZ61** few hours after preparation of the sample (top), after one day (middle) and after two days (bottom).

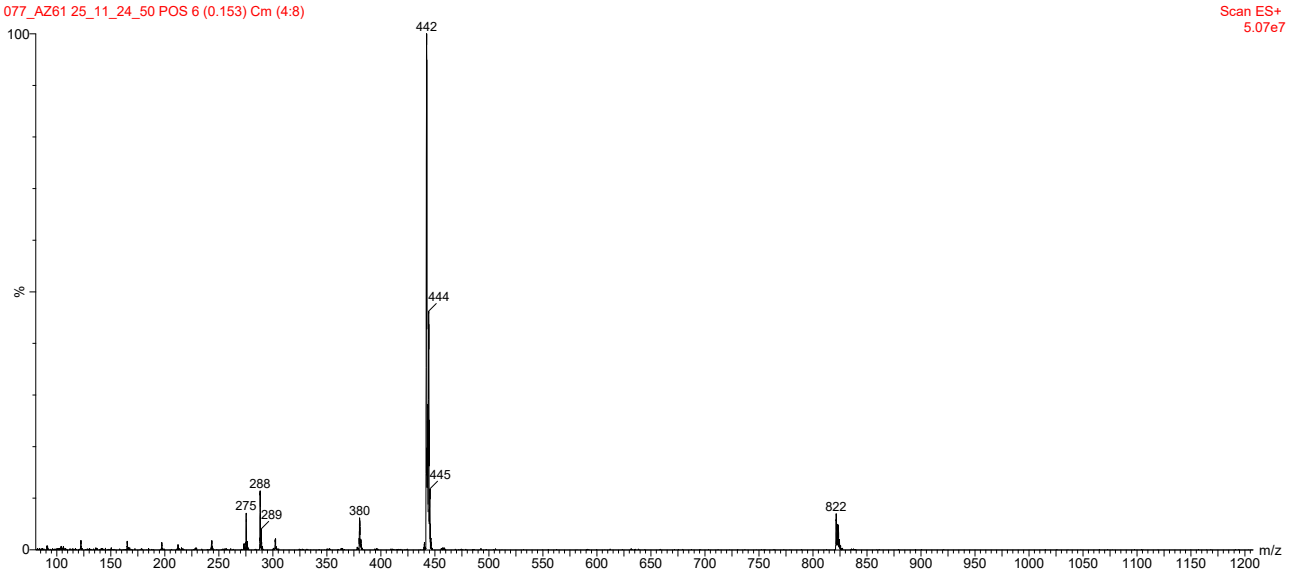

Figure A5.54: ESI-MS spectrum (positive ions) for **AZ61** in acetonitrile.

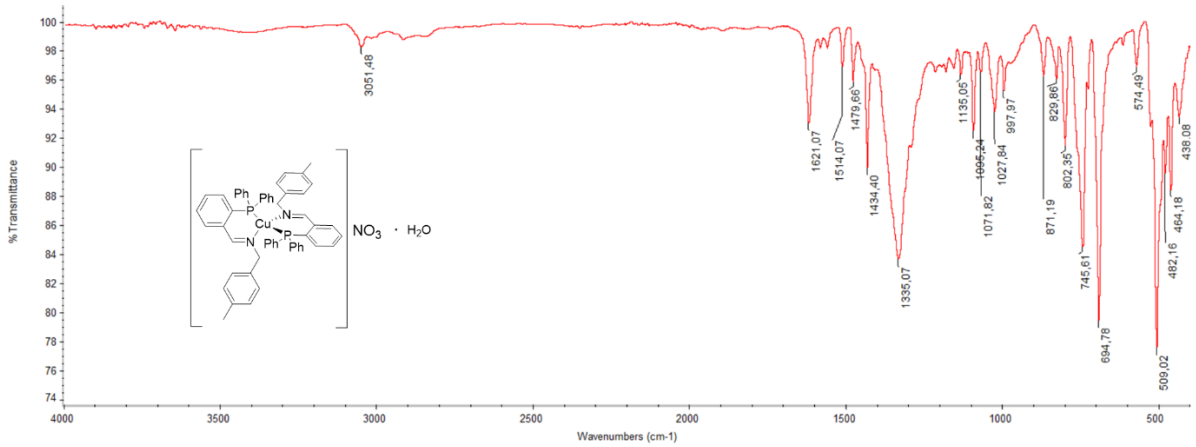

Figure A5.55: FT-IR spectrum of **AZ65**.

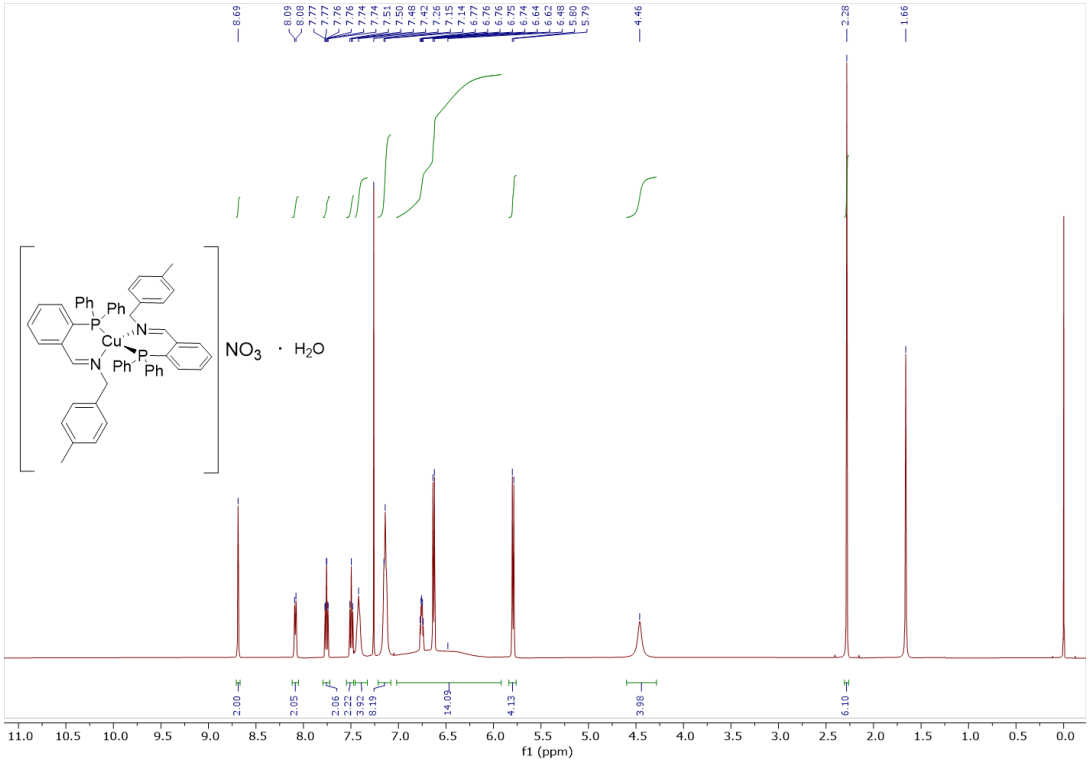

Figure A5.56: ^{1}H NMR (500 MHz, Chloroform-*d,* 298 K) spectrum of **AZ65**.

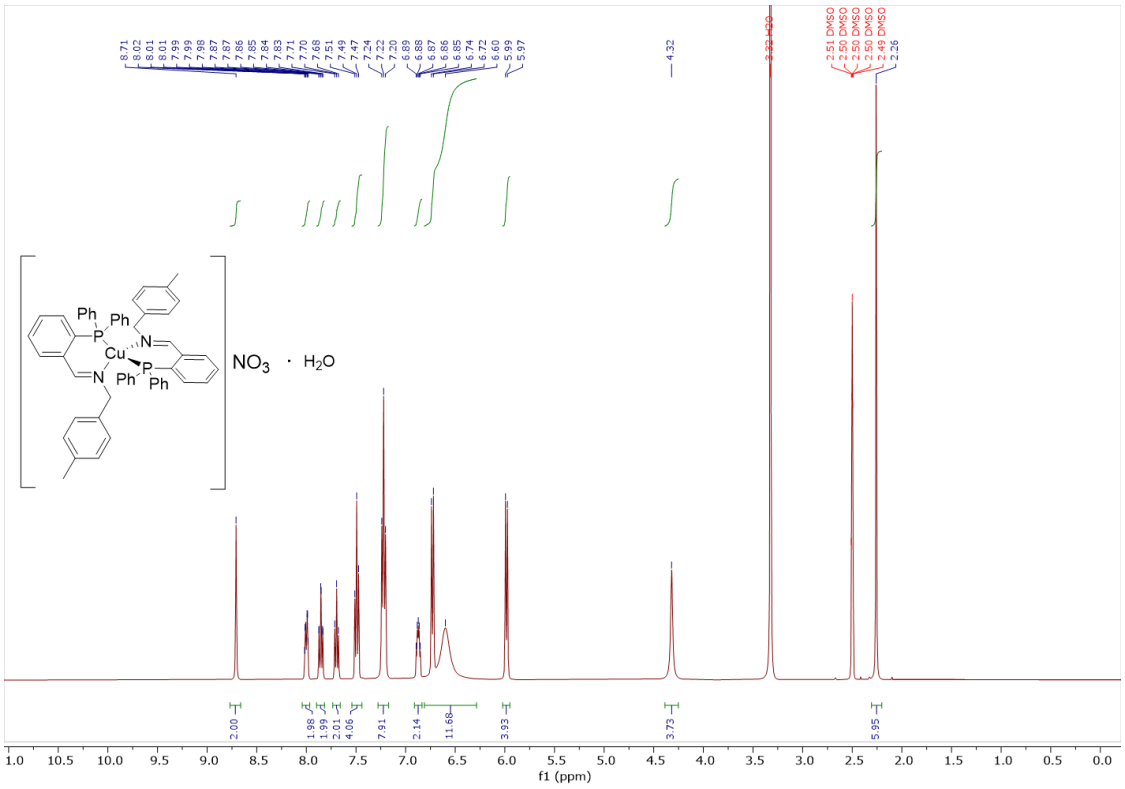

Figure A5.57: ^{1}H NMR (400 MHz, DMSO-d_6, 298 K) spectrum of **AZ65**.

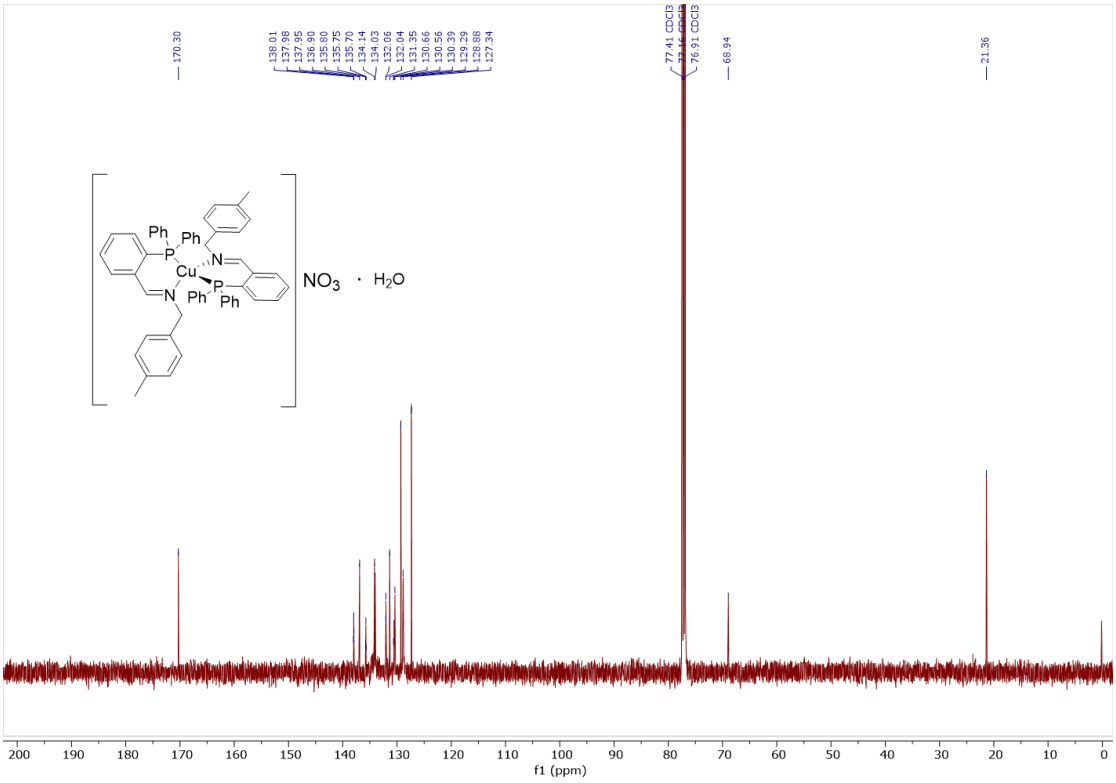

Figure A5.58: ^{13}C NMR (126 MHz, Chloroform-*d*, 298 K) spectrum of **AZ65**.

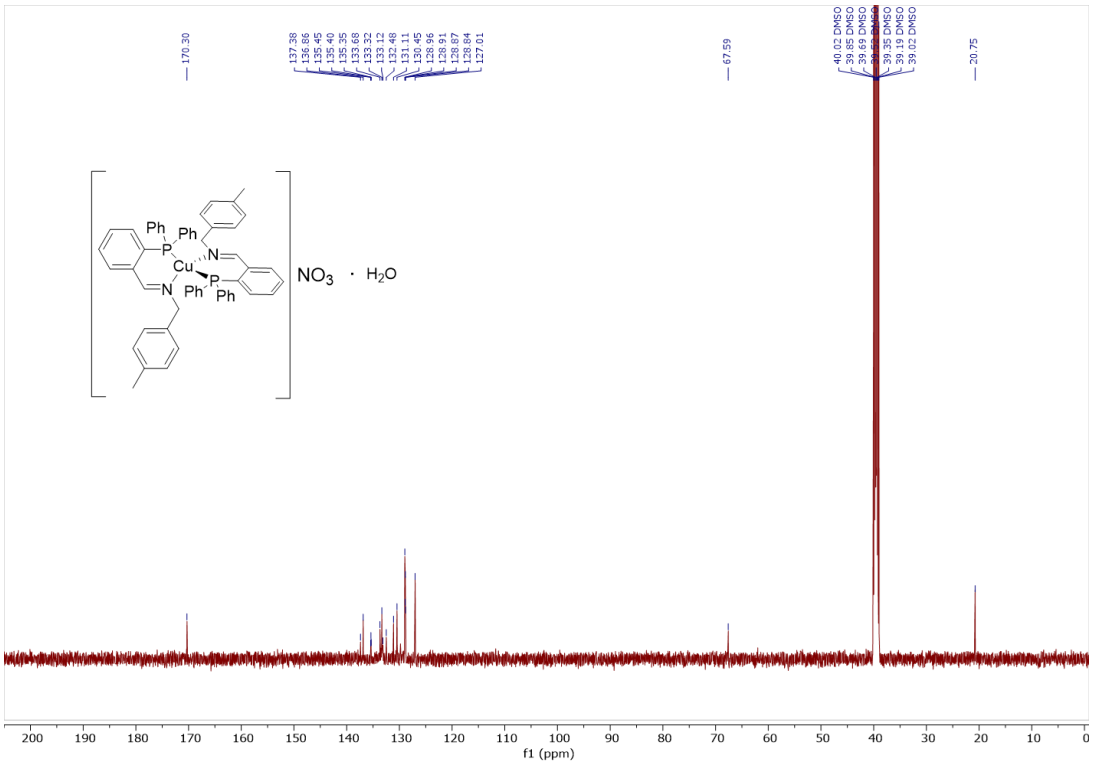

Figure A5.59: ^{13}C NMR (126 MHz, DMSO-d_6, 298 K) spectrum of **AZ65**.

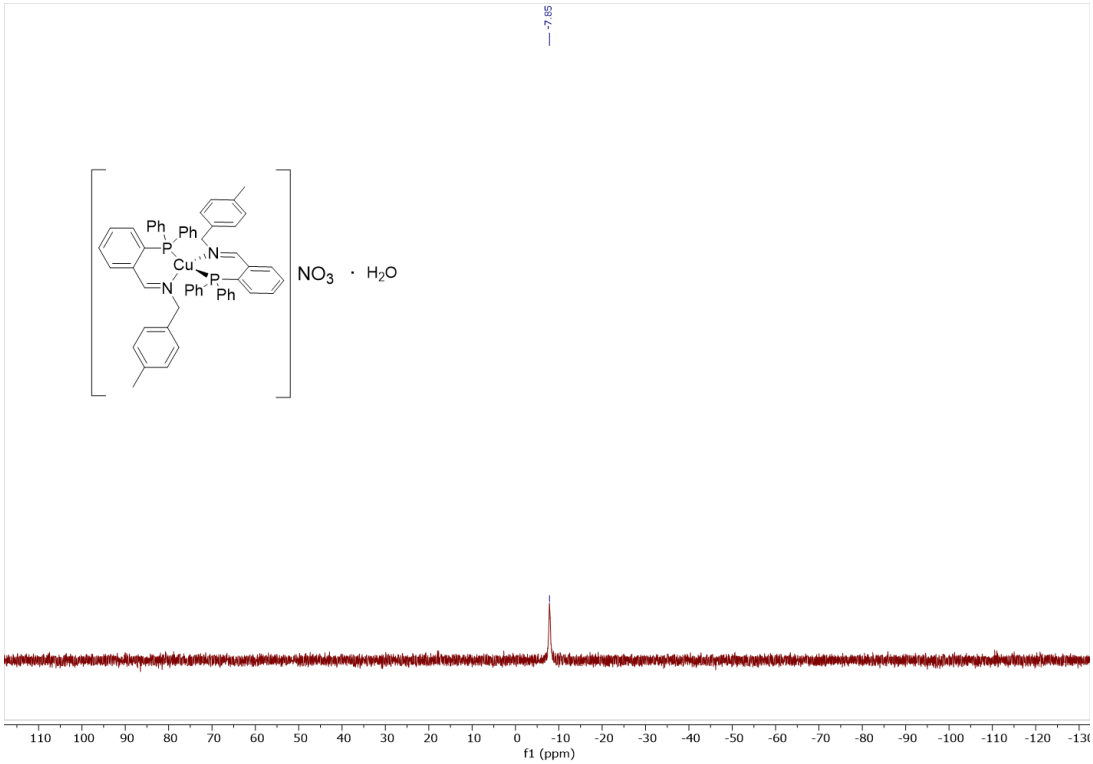

Figure A5.60: ^{31}P NMR (202 MHz, Chloroform-*d*, 298 K) spectrum of **AZ65**.

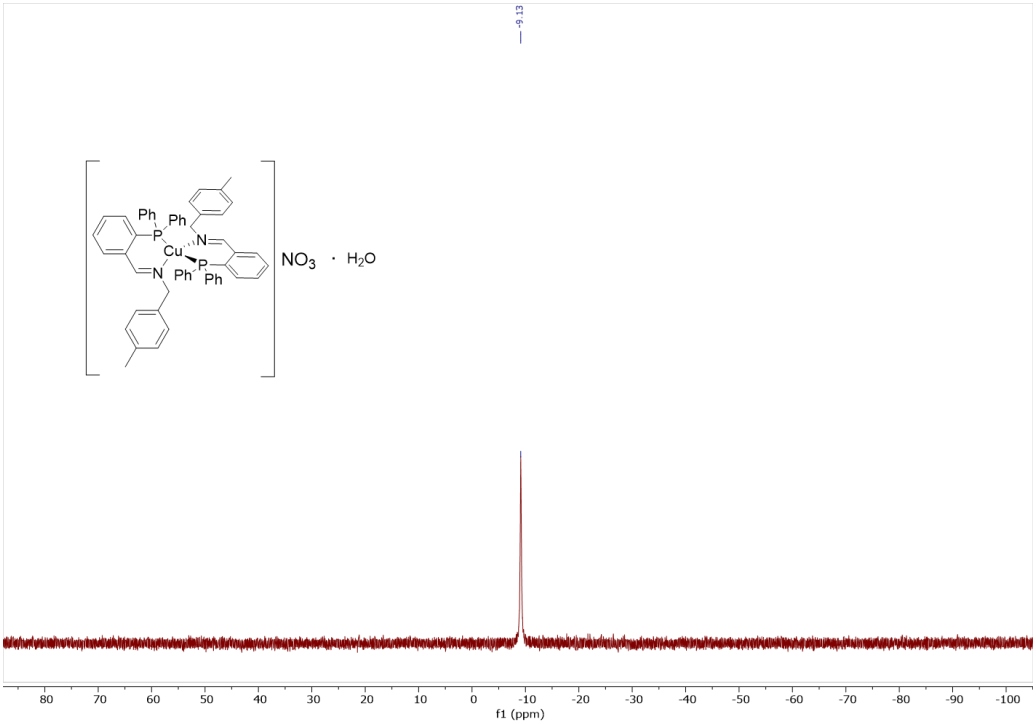

Figure A5.61: ^{31}P NMR (162 MHz, DMSO-d_6, 298 K) spectrum of **AZ65**.

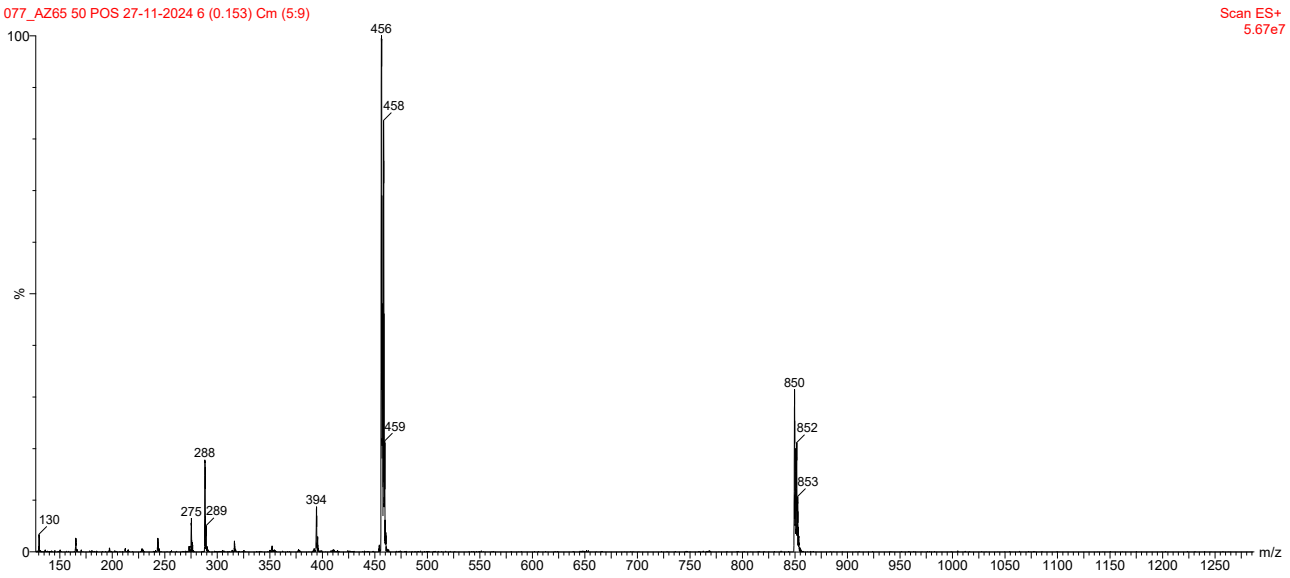

Figure A5.62: ESI-MS spectrum (positive ions) for **AZ65** in acetonitrile.

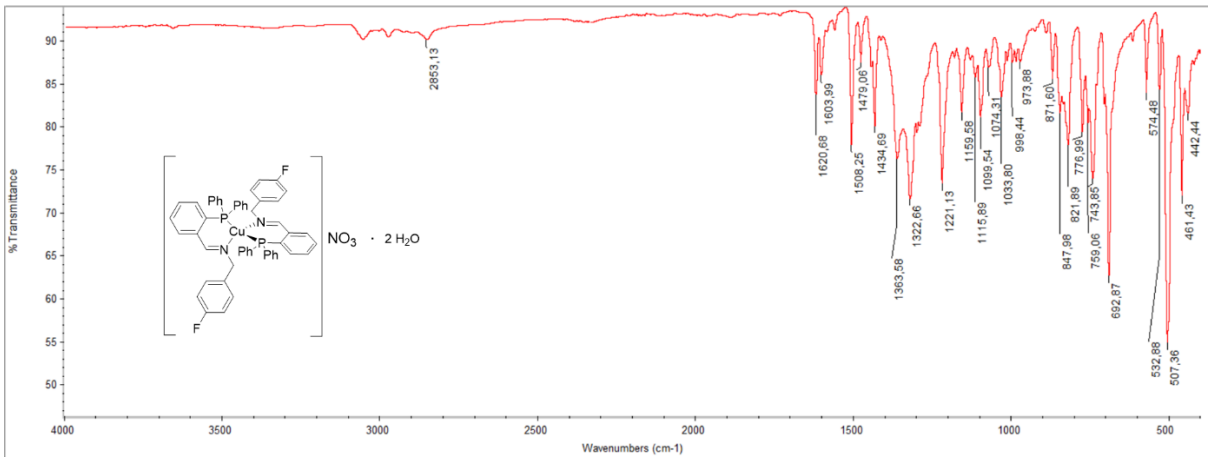

Figure A5.63: FT-IR spectrum of **AZ66**.

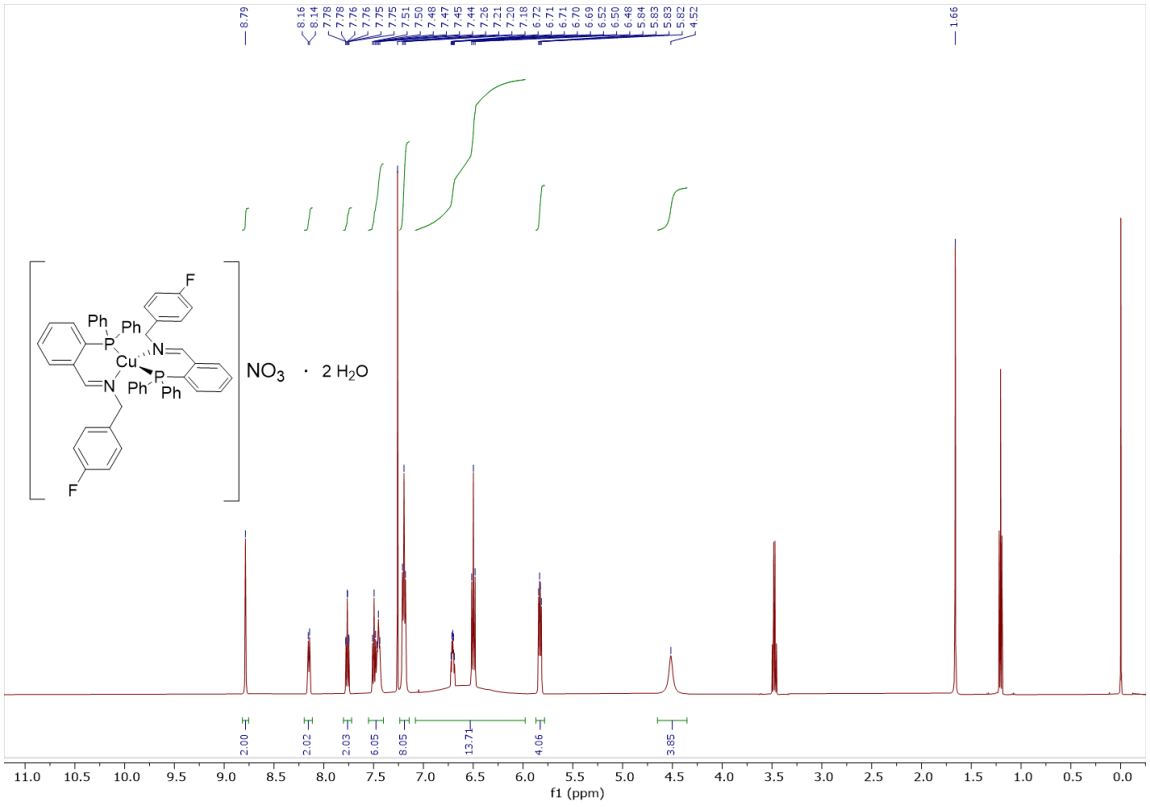

Figure A5.64: ^{1}H NMR (500 MHz, Chloroform-*d,* 298 K) spectrum of **AZ66**.

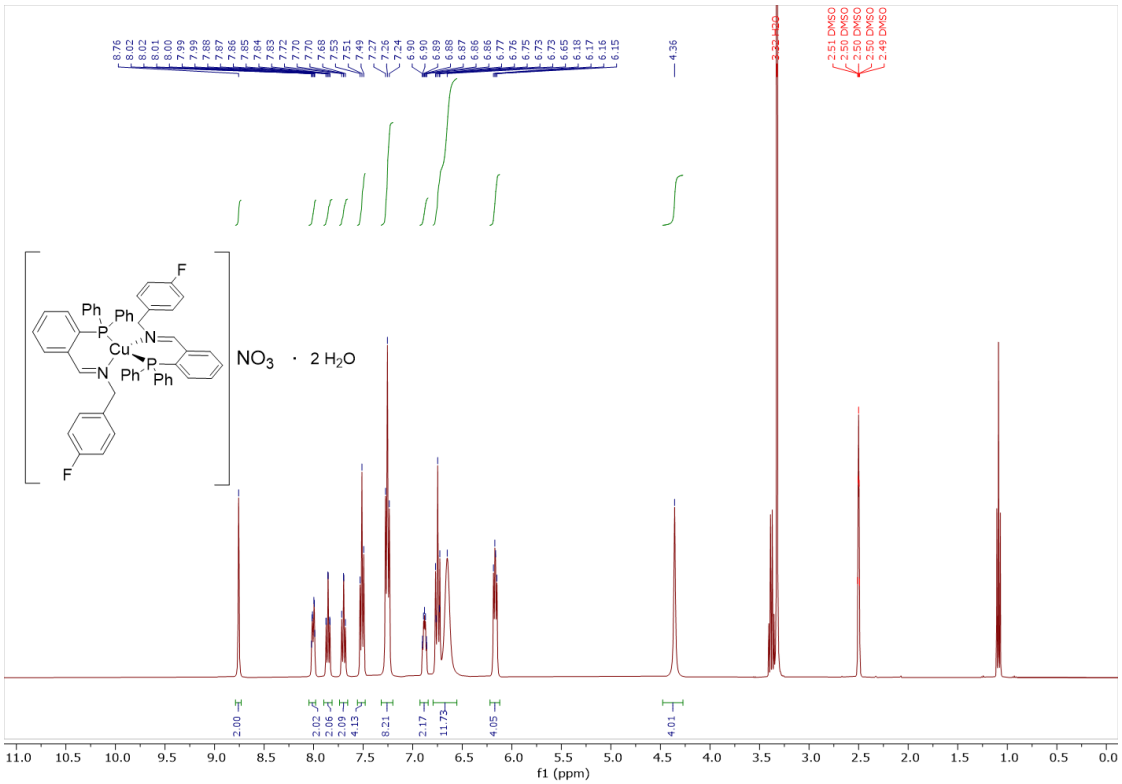

Figure A5.65: ^{1}H NMR (400 MHz, DMSO-d_6, 298 K) spectrum of **AZ66**.

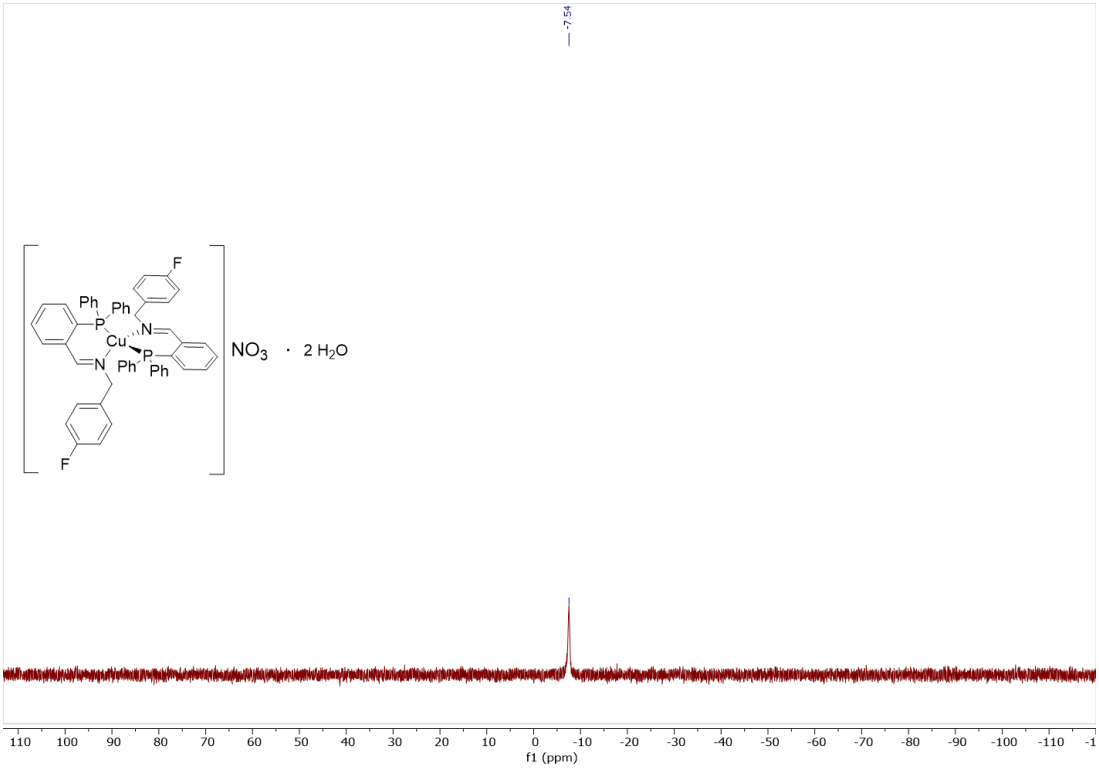

Figure A5.66: ^{31}P NMR (202 MHz, Chloroform-*d*, 298 K) spectrum of **AZ66**.

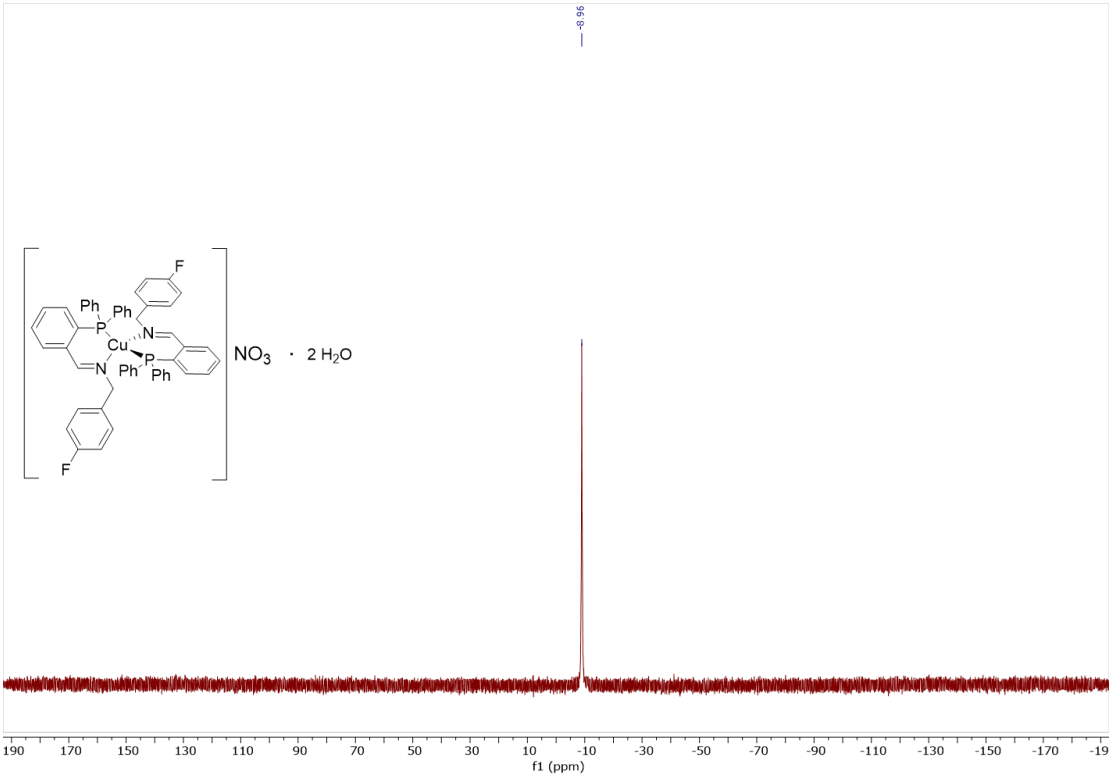

Figure A5.67: ^{31}P NMR (162 MHz, DMSO-d_6, 298 K) spectrum of **AZ66**.

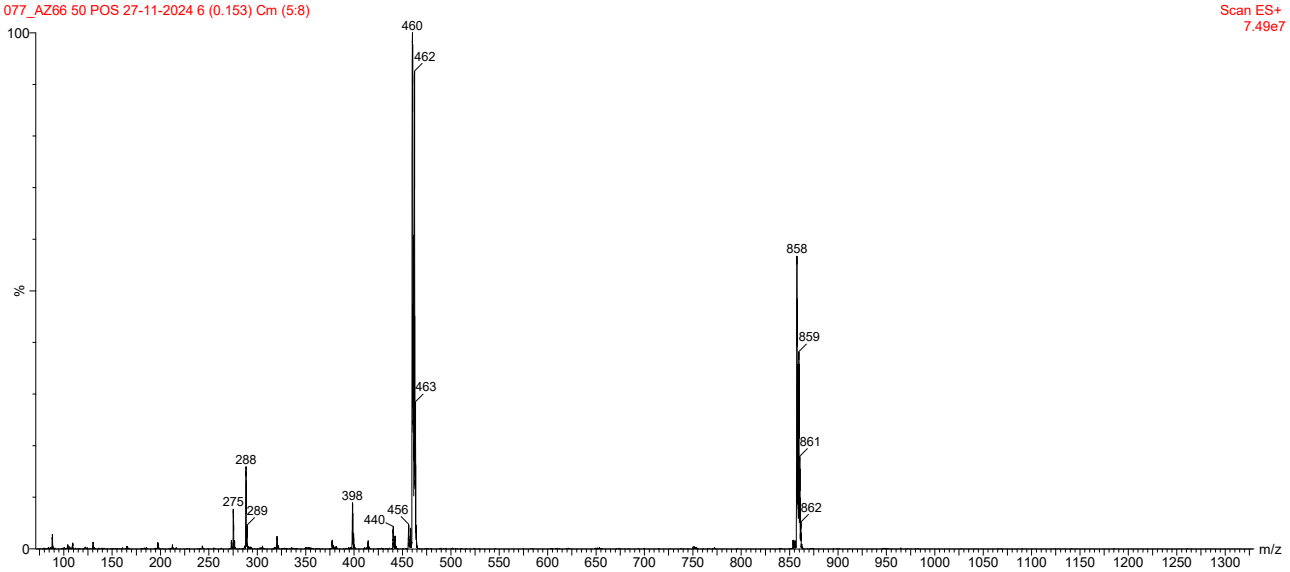

Figure A5.68: ESI-MS spectrum (positive ions) for **AZ66** in acetonitrile.

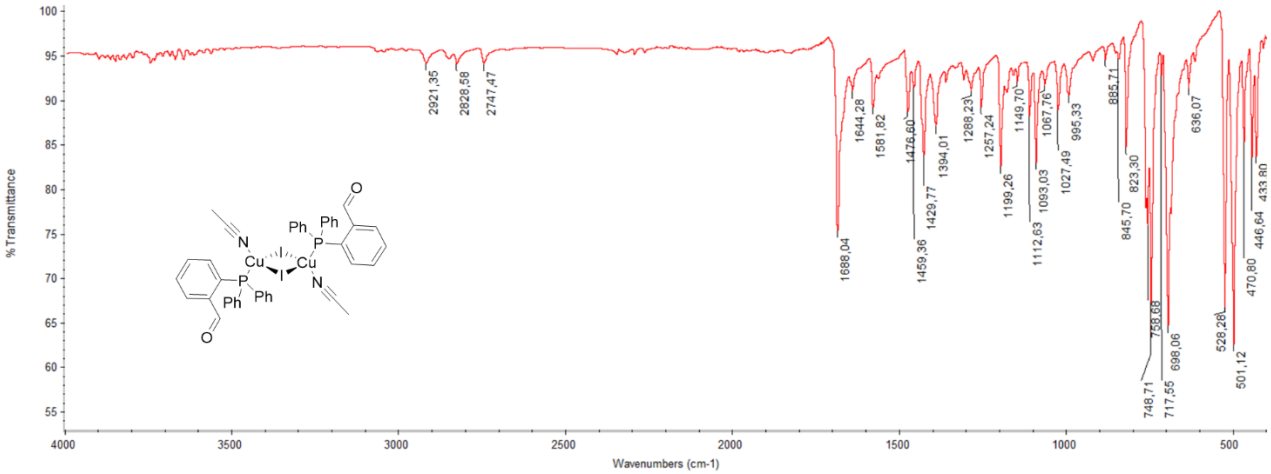

Figure A5.69: FT-IR spectrum of **AZ57**.

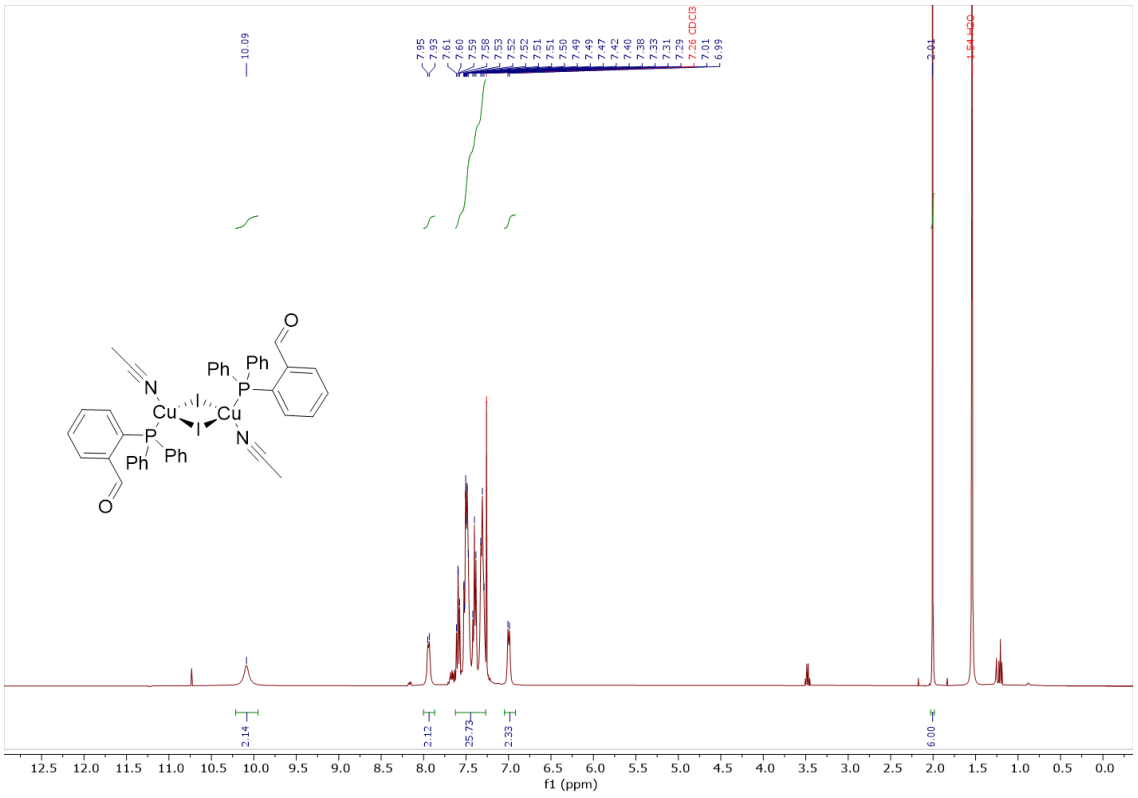

Figure A5.70: ^{1}H NMR (400 MHz, Chloroform-*d,* 298 K) spectrum of **AZ57**.

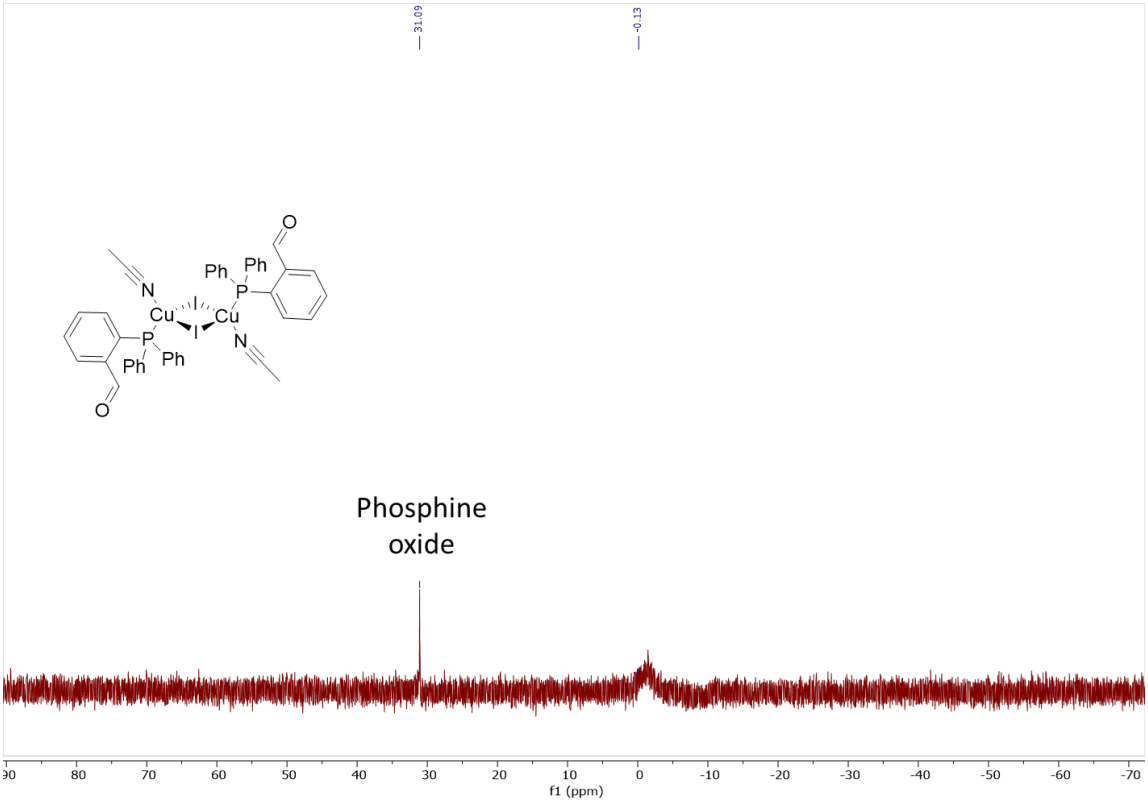

Figure A5.71: ^{31}P NMR (162 MHz, Chloroform-*d*, 298 K) spectrum of **AZ57**.

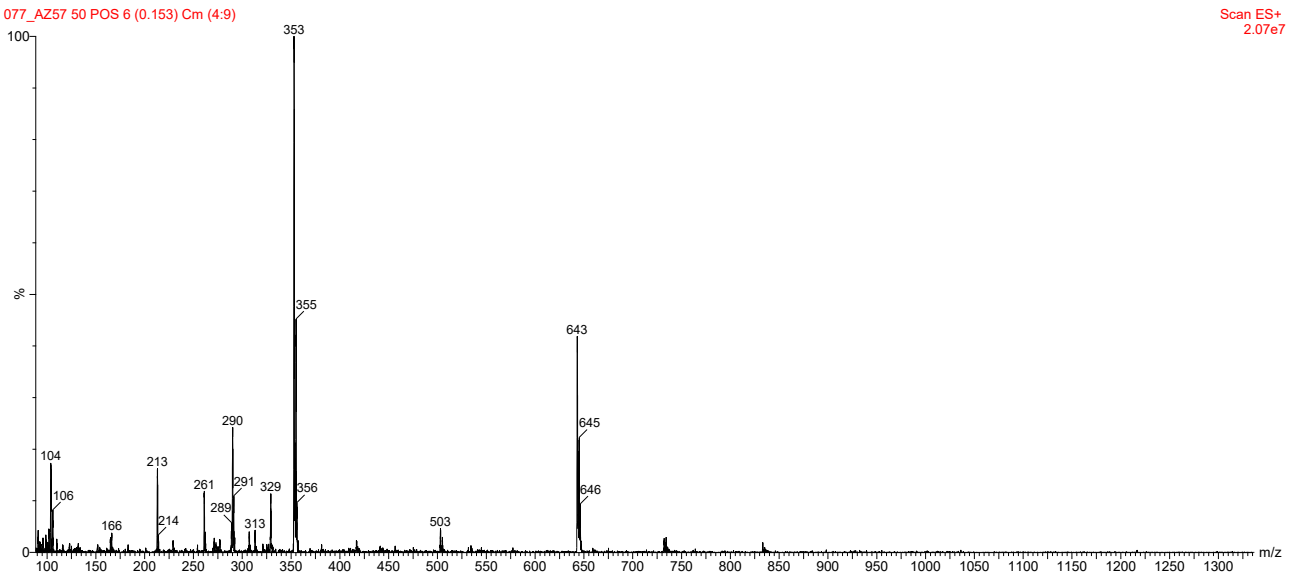

Figure A5.72: ESI-MS spectrum (positive ions) for **AZ57** in acetonitrile.

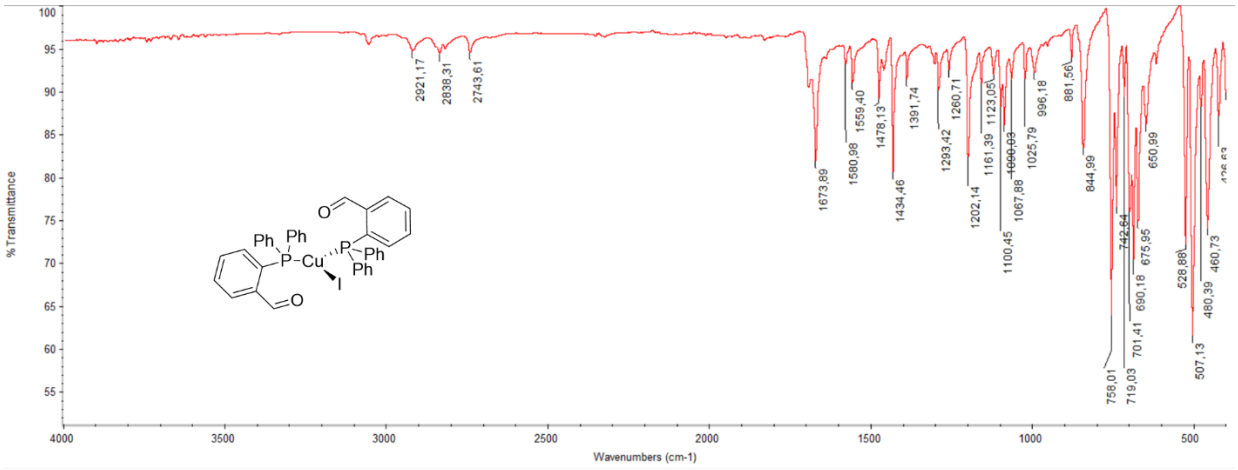

Figure A5.73: FT-IR spectrum of **AZ58**.

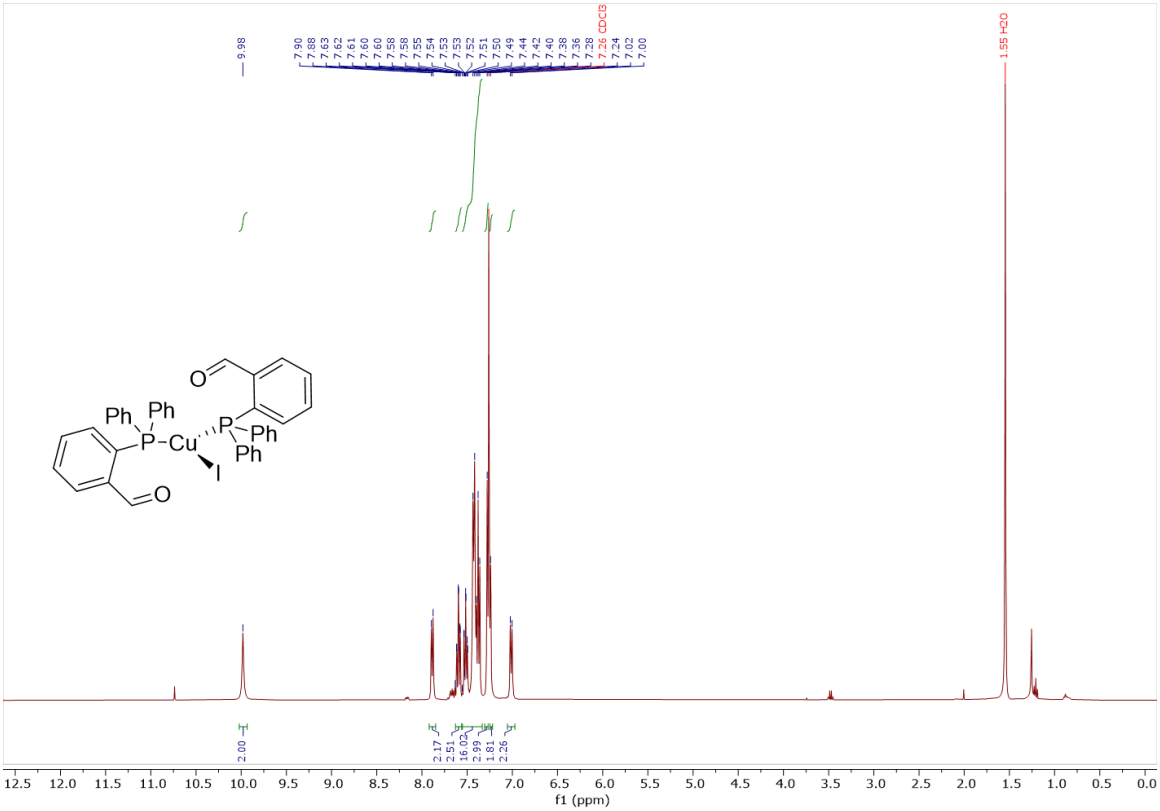

Figure A5.74: ^{1}H NMR (400 MHz, Chloroform-*d,* 298 K) spectrum of **AZ58**.

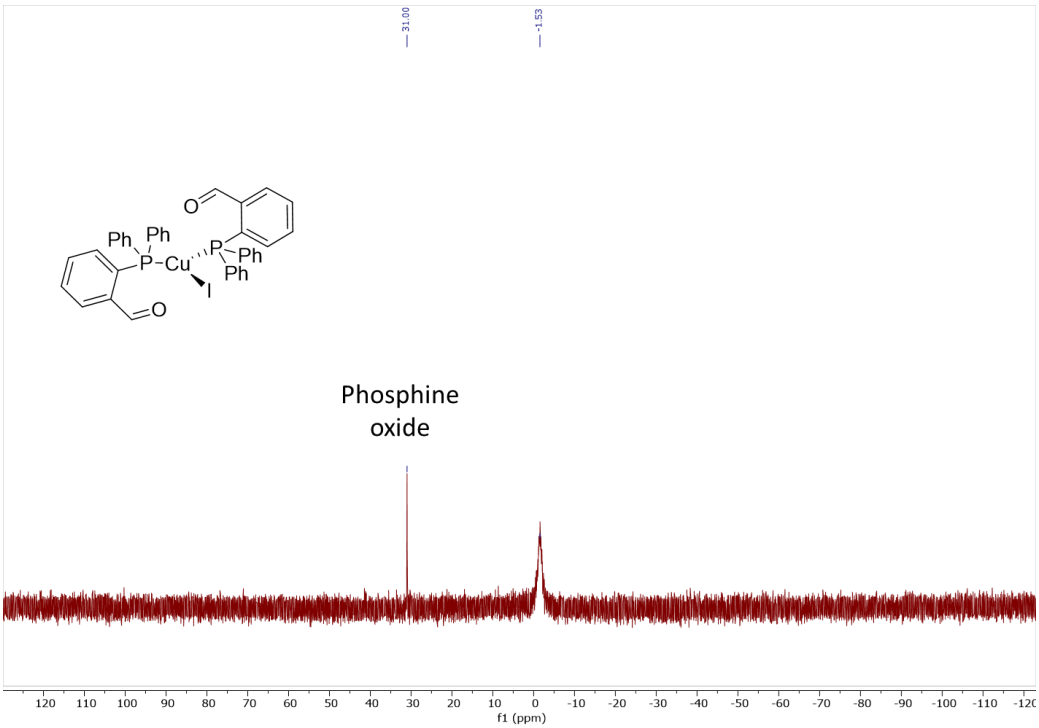

Figure A5.75: ^{31}P NMR (162 MHz, Chloroform-*d*, 298 K) spectrum of **AZ58**.

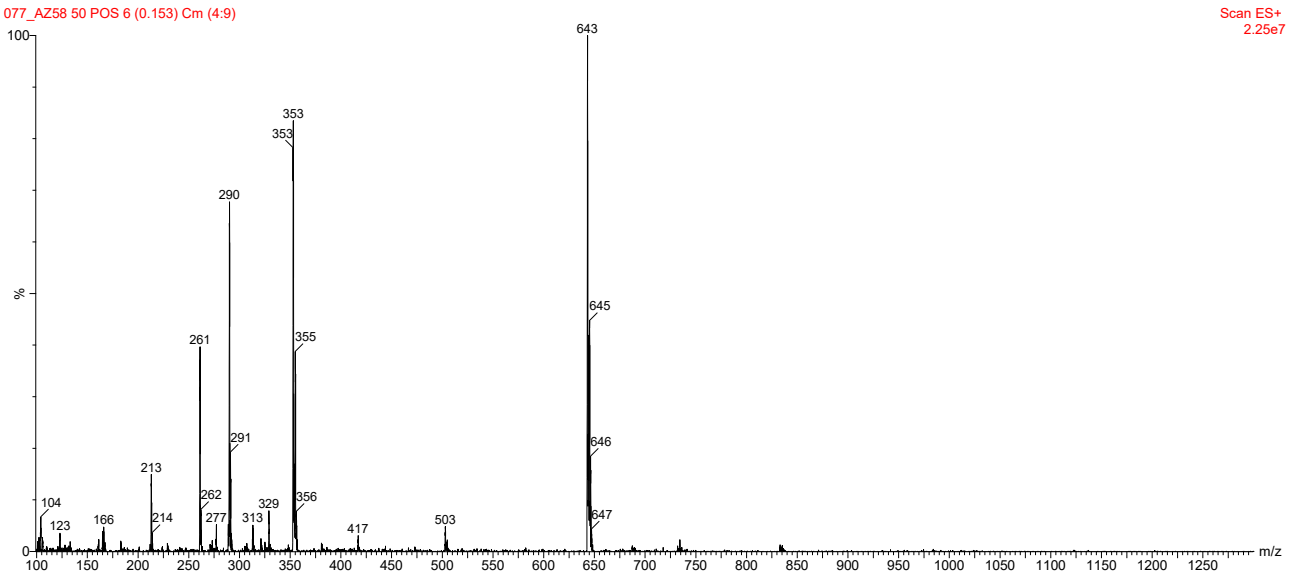

Figure A5.76: ESI-MS spectrum (positive ions) for **AZ58** in acetonitrile.

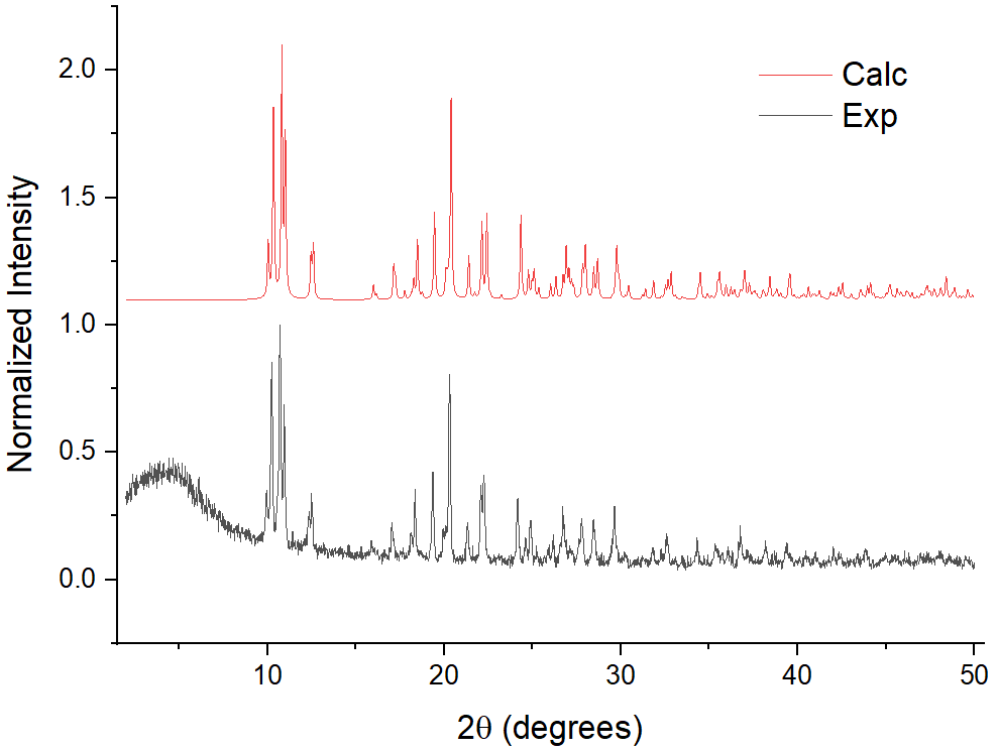

Figure A5.77: Calculated (in red) and experimental (in black) powder diffractogram of complex **AZ58**.

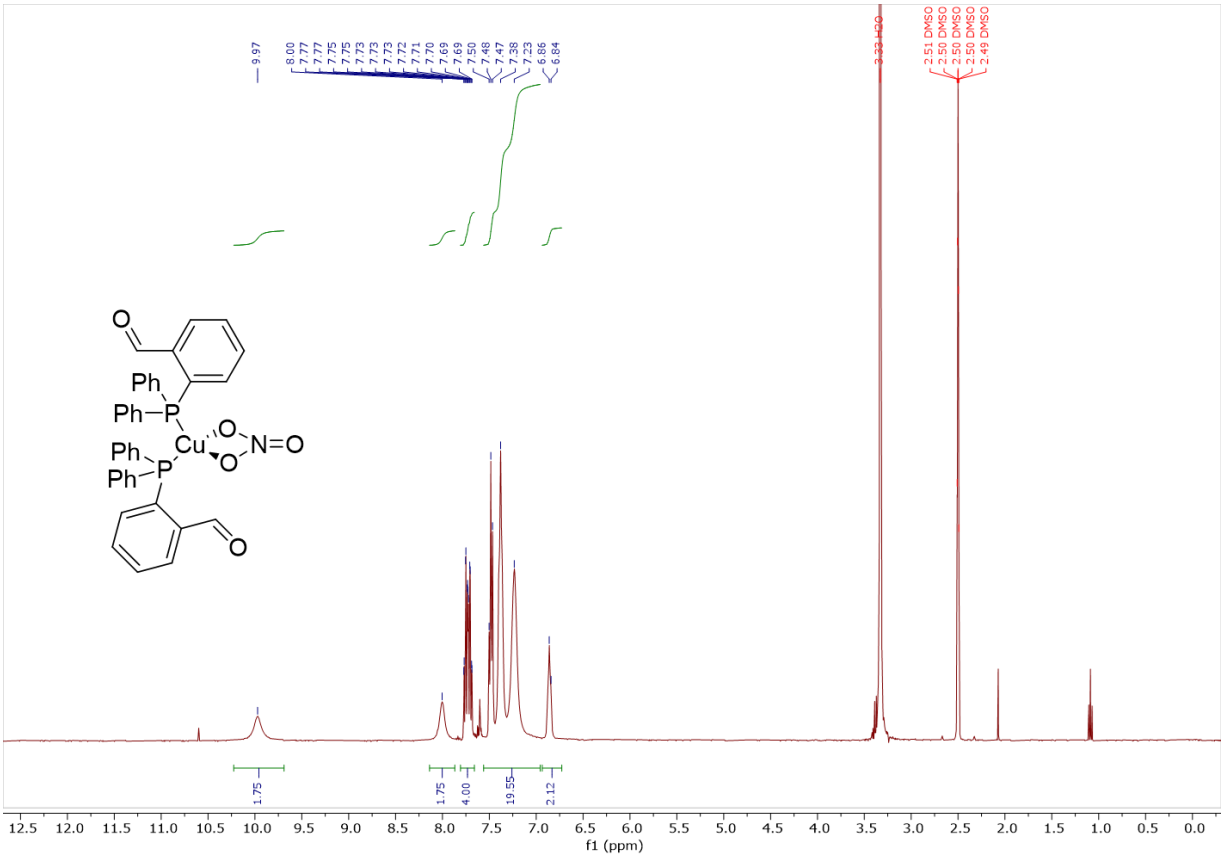

Figure A5.78: ^{1}H NMR (400 MHz, DMSO-d_6, 298 K) spectrum of **AZ67**.

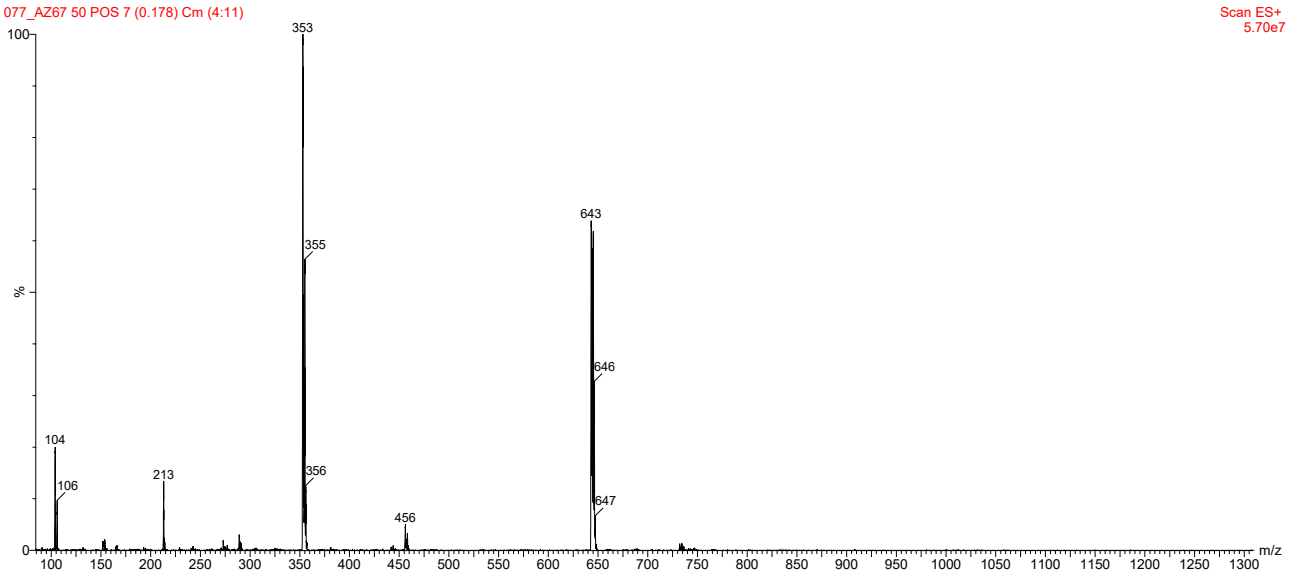

Figure A5.79: ESI-MS spectrum (positive ions) for **AZ67** in acetonitrile.